

# Simple Multiband Antenna for Mobile Phone Application Based on a Dual-arm Monopole Structure

David Delaune<sup>1</sup>, Ning Guan<sup>1</sup>, and Koichi Ito<sup>2</sup>

<sup>1</sup>Optics and Electronics Laboratory, Fujikura Ltd., Japan

<sup>2</sup>Department of Medical System Engineering, Chiba University, Japan

**Abstract**— In this paper, a printed monopole antenna for quad-band operation in the mobile phone is proposed and studied. The antenna occupies a volume of  $40 \times 20 \times 4 \text{ mm}^3$  with a very low height as compared to others, yet it can cover two wide bands centred at about 925 MHz and 1920 MHz to realize GSM/DCS/PCS/UMTS operation. Monopole-like radiation characteristics of the proposed antenna can be observed by measurements over the operating bands, where peak gains are 0.1, 0.9, 0.8, 0.5 dBi, respectively, at each of the frequency band of interest.

## 1. INTRODUCTION

Recently, multi-band operation in mobile phones tends to become popular especially for quad-band or penta-band operation [1]. For the quad-band antenna design, the targeted bands are the GSM band (880–960 MHz) and the DCS/PCS/UMTS band (1710–2170 MHz) [2]. To meet the above-mentioned requirement, a low-profile monopole antenna is a promising antenna design. In this paper, a printed monopole antenna with a very low profile and very small in size ( $0.12 \times 0.06 \times 0.01 \lambda_{925}$ , where  $\lambda_{925}$  represents the wavelength at 925 MHz) as compared to others, protruded from the top edge of the ground plane, is proposed aimed at multiband application in the mobile phone. The proposed antenna has been fabricated and results match well with the numerical simulations.

## 2. ANTENNA CONFIGURATION

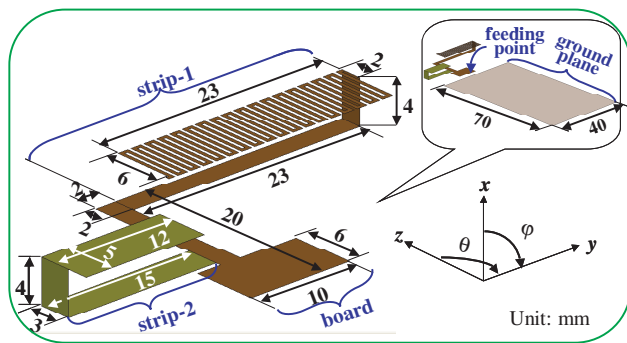


Figure 1: Composition of the antenna.

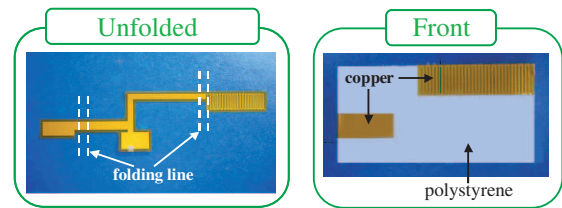


Figure 2: Pictures of the prototype antenna.

The configuration of the proposed antenna is shown in Fig. 1 and picture of the fabricated prototype is shown in Fig. 2. The antenna is located above the top edge of the system ground plane with a small distance of 3 mm between the lower part of the antenna (board) and the ground plane. The antenna is composed of two branches formed by a longer resonant strip (strip-1) and a shorter resonant strip (strip-2) located near the board, which is used to increase the bandwidth.

Strip-1 generates a fundamental mode at 925 MHz and a second mode at about 1900 MHz. This lower band is used for the GSM operation. Strip-2 generates a fundamental mode at about 2100 MHz, which overlaps with the second mode of strip-1 to form a wide band; hence, enabling the coverage of DCS/PCS/UMTS bands (Fig. 3).

Strip-1 and strip-2 are folded so that space can be saved, which is a must in requirements for mobile phone antennas, and so that frequency resonances can be arranged as described hereafter. Furthermore, the board allows a broadening of the bandwidth for strip-2 thus leading to an improved bandwidth of the whole upper band. It will be explained next as well.

Figure 4 shows the relation between modes and current distribution for both strip-1 and strip-2. From this figure, it can be seen that in both fundamental modes, the current flows on the whole

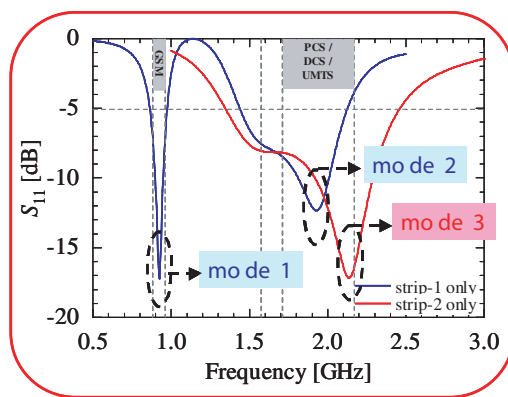


Figure 3: Input characteristics.

length of each strip and gets weaker as it propagates. Meanwhile, in the higher mode, although the current flows on the whole length of the strip, its phase changes and its direction of propagation becomes opposite at a certain point.

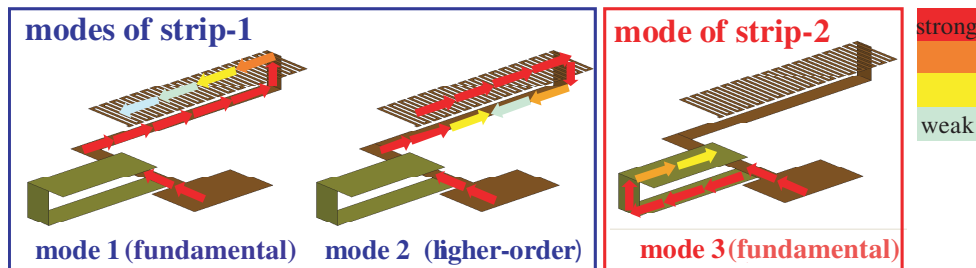


Figure 4: Relation between modes and current distribution.

In order to understand the behaviour of the proposed antenna, the influence of the folding position is analyzed first in case of strip-1 only and without any meander used. For this study, the total length of strip-1 is fixed to 60 mm, which enables a first resonance at about 925 MHz and a second one at 2610 MHz, when strip-1 is assumed to be flat and with a constant width of 2 mm. Strip-1 is then gradually folded with a height of 4 mm kept constant between the upper and lower part of the strip. The behaviour in terms of resonance and impedance variation is shown in Figs. 5 and 6, respectively.

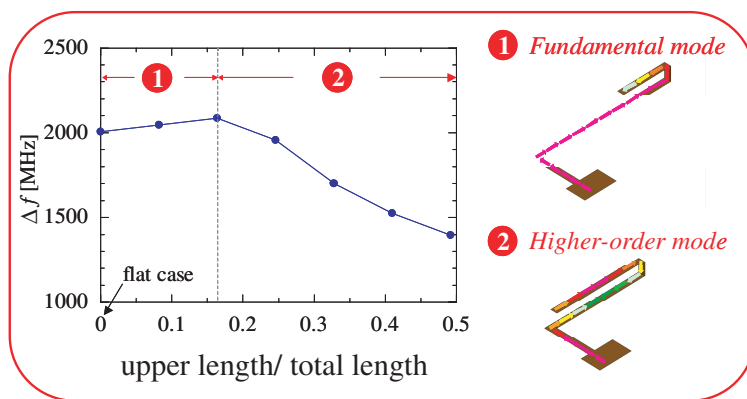


Figure 5: Variation of resonance with a change in the folding length (strip-1 only without meander).

Figure 5 shows the difference in resonance for the first and second mode with a change in the folding length. From this figure, it can be seen that the resonances of mode 1 and 2 tend to get closer to each other as the folding length is increased. As shown in Fig. 6, this phenomenon is due to the fact that, when comparing a flat strip to a fully folded one, the impedance nearby

the resonance of mode 1 gets capacitive while the one of mode 2 gets inductive. Note that the capacitive behaviour of a folded arm compared to a monopole for the first harmonic is described in details in [3]. Furthermore, referring to Fig. 4, as the current propagates along the whole length of a strip in the fundamental mode while in the higher mode it gets opposite at a certain location of the strip, the difference of behaviour in terms of impedance variation can be explained: while the antenna gets capacitive for the fundamental mode, it becomes inductive for the higher mode.

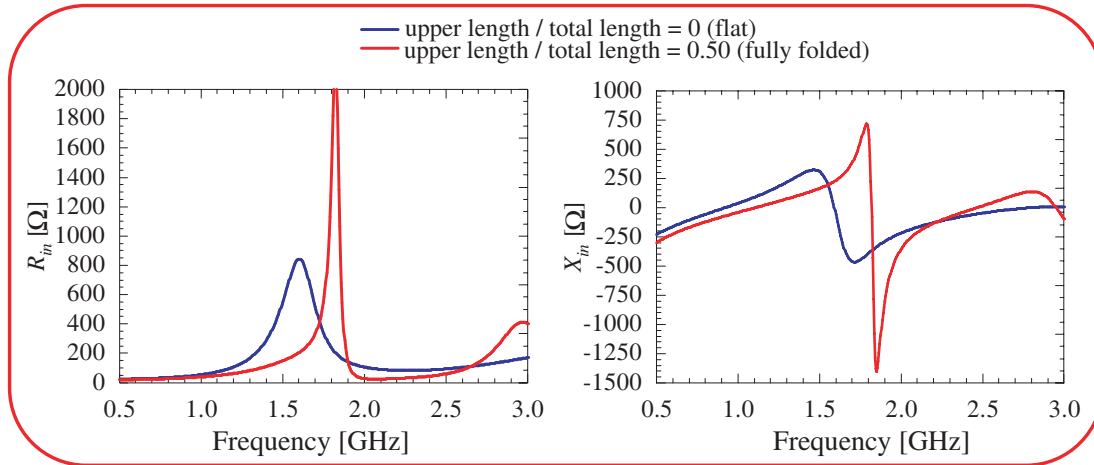


Figure 6: Variation in impedance depending on the folding length (strip-1 only without meander).

Next, in order to understand the necessity for the proposed antenna to be loaded with an extra board, the variation of behaviour when using a board or not on strip-2 is shown in Fig. 7. From this figure, it is clear the resonance is shifted towards the upper frequencies and the bandwidth broadens as compared to the case when no board is employed.

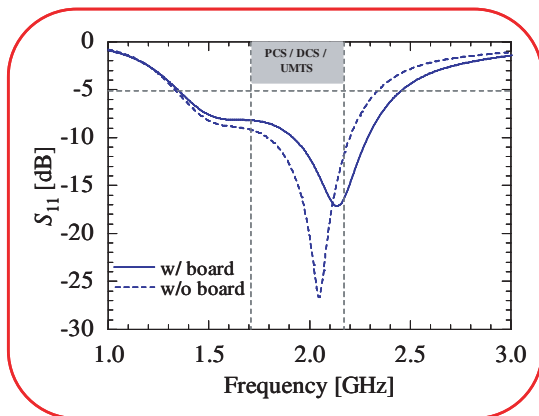


Figure 7: Variation of reflection parameters with the board (strip-2 only).

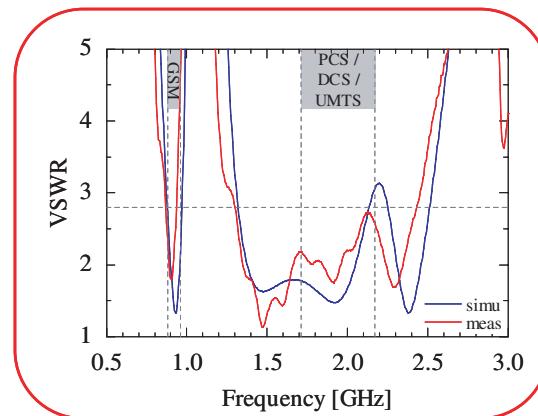


Figure 8: VSWR of the proposed antenna.

Table 1: Gain values.

Band	Peak [dBi]	Minimum [dBi]	Average [dBi]
GSM ( $f = 920$ MHz)	0.1	-1.0	-0.6
DCS ( $f = 1795$ MHz)	0.9	-3.7	-0.9
PCS ( $f = 1920$ MHz)	0.8	-3.4	-1.4
UMTS ( $f = 2045$ MHz)	0.5	-6.9	-1.6

### 3. RESULTS

Figure 8 shows the voltage standing wave ratio (VSWR) for the proposed antenna. The obtained impedance bandwidths are 100 MHz and 1130 MHz for the lower and upper band, respectively, when VSWR is chosen to be less than 3.5 and 2.8, respectively.

Radiation characteristics of the antenna are also studied (see Fig. 9). Almost omni-directional radiation patterns are observed in the xy plane and figure-of-eight shaped radiation patterns are observed in the other planes. The typical gain values are summarized in Table 1.

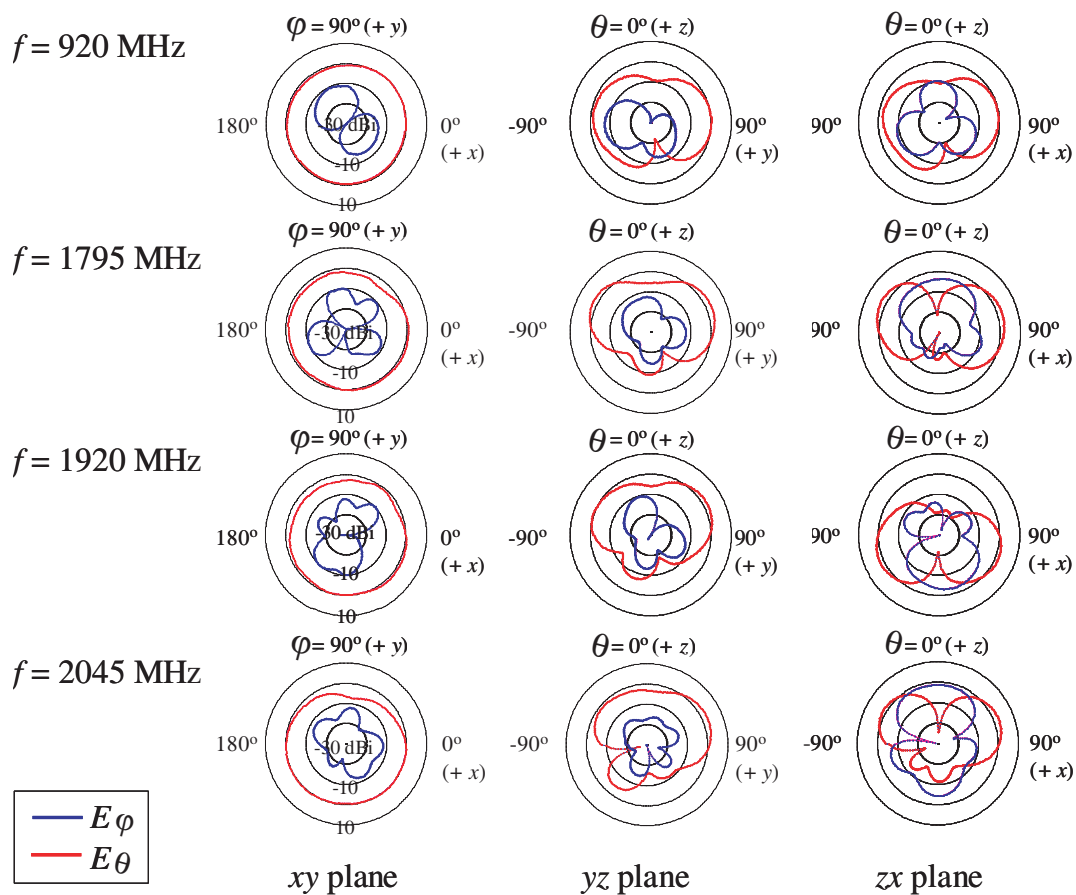


Figure 9: Radiation patterns of the proposed antenna.

### 4. CONCLUSION

A printed monopole antenna for quad-band operation in the mobile phone has been proposed and studied. The antenna occupies a volume of  $40 \times 20 \times 4 \text{ mm}^3$  with a very low height as compared to others, yet it can cover two wide bands centred at about 925 MHz and 1920 MHz to realize GSM/DCS/PCS/UMTS operation. Good radiation characteristics of the antenna over the operating bands have also been observed. The proposed antenna is very promising for application in the mobile phone as an internal antenna for quad-band operation.

### REFERENCES

1. Wong, K.-L., *Planar Antennas for Wireless Communications*, John Wiley & Sons, New York, USA, 2003.
2. Lee, H.-J., et al., "The compact quad-band planar internal antenna for mobile handsets," *Proceedings of 2007 IEEE Antennas and Propagation International Symposium*, 2045–2048, Hawaii, USA, June 2007.
3. Kraus, J. D., *Antennas*, Mc. Graw-Hill Inc., New York, USA, 1988.

# Antennas Made of Transparent Conductive Films

N. Guan<sup>1</sup>, H. Furuya<sup>1</sup>, D. Delaune<sup>1</sup>, and K. Ito<sup>2</sup>

<sup>1</sup>Optics and Electronics Laboratory, Fujikura Ltd., Japan

<sup>2</sup>Department of Medical System Engineering, Chiba University, Japan

**Abstract**— The radiation characteristics of two kinds of antennas made of transparent conductive films are investigated: a planar inverted-F antenna (PIFA) and a monopole antenna. These antennas are designed to work at 2.4 GHz and their performances are compared with each other for several films with different sheet resistivities. Wire-grid models based on the moment method are applied for the numerical analysis. It is found that the film resistance influences the performance more strongly for the PIFA than for the monopole antenna due to the cavity-like behavior of the former.

## 1. INTRODUCTION

As mobile wireless communications have progressed drastically in recent years, mobile terminals are becoming smaller and smaller, and miniaturization of the antennas installed in mobile devices is required accordingly. The designing of antennas for small mobile devices is becoming much more difficult not only because the space is getting limited but also because other electrical parts influence the performance of the antennas. Transparent conductive films, such as indium tin oxide (ITO) and fluorine-doped tin oxide (FTO) films, allow the transmission of electric currents while retaining the optical transparency [1]. Applying transparent conductive films to construct antennas is a good alternative to meet the space requirement because the transparent antennas can be installed on the surface or the display window of the mobile devices without much visible design problem [2–7]. The interference from the other electric parts can also be suppressed thanks to the location of the antenna.

In this paper, two antennas widely used for small mobile devices are investigated: a planar inverted-F antenna (PIFA) which consists of a rectangular patch and a short-pin and a monopole antenna which consists of a trapezoidal radiator [7]. Wire-grid models based on the moment method are applied for the numerical analysis. The performances of the two antennas are compared with each other for several films with different sheet resistivities. It is found that the film resistance influences the performance more strongly for the PIFA than for the monopole antenna. The difference of the performance is explained by the difference of the operating mechanism between these two antennas.

## 2. CONFIGURATIONS

Figure 1 shows the configuration of the PIFA, where the patch is made of transparent conductive film and the short-pin and ground are made of copper. Fig. 2 shows the configuration of the monopole antenna, where the trapezoidal radiator is made of transparent conductive film and the ground is made of copper.

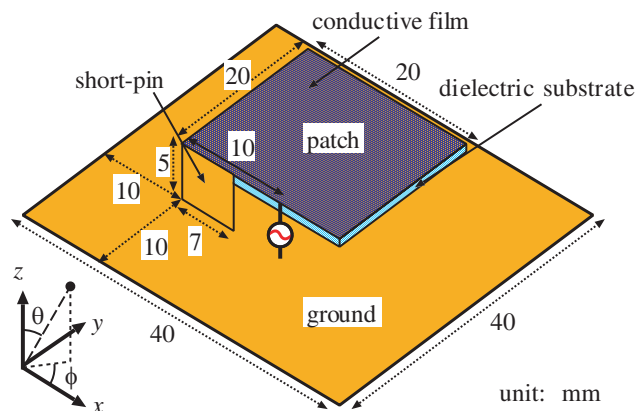


Figure 1: PIFA.

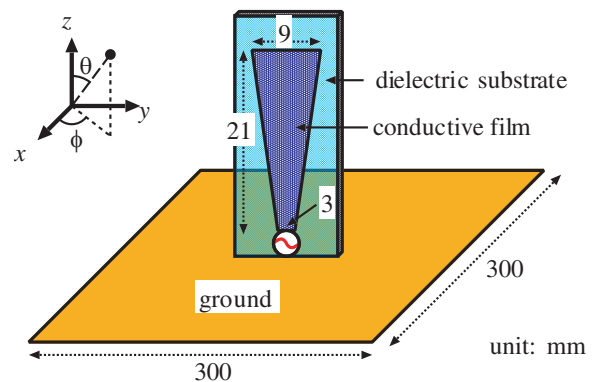


Figure 2: Monopole antenna.

The antennas are made of ITO and FTO, as well as copper as a reference. Fig. 3 shows a sample of the ITO antenna and Fig. 4 the transmittance at a wavelength of 550 nm for the ITO and FTO films. Both of the antennas are designed to work at 2.4 GHz. Fig. 5 shows the measurement of voltage standing wave ratio (VSWR) for the monopole antenna with several different films. The VSWR does not vary so much as the sheet resistivity is lower than 10 Ohm/sq. Fig. 6 shows the measurement of a radiation pattern at 2.4 GHz for the antenna. Again it is seen that the resistance does not influence the radiation pattern seriously.



Figure 3: Sample of ITO antenna.

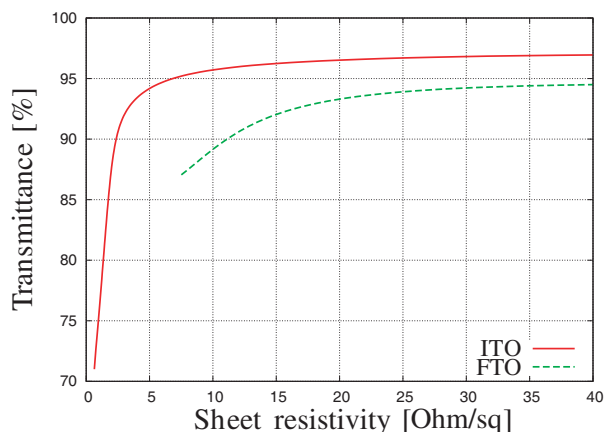


Figure 4: Transmittance of ITO and FTO films at a wavelength of 550 nm.

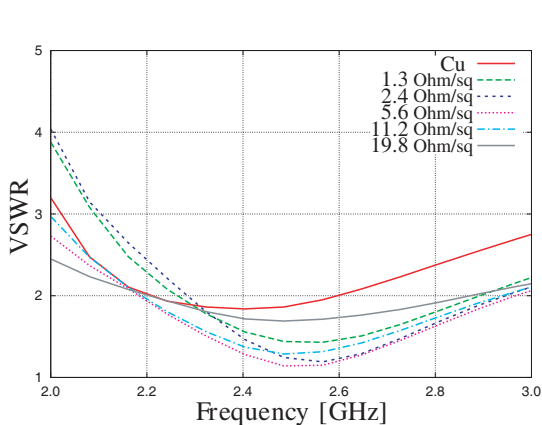


Figure 5: Measurement of VSWR for a monopole antenna.

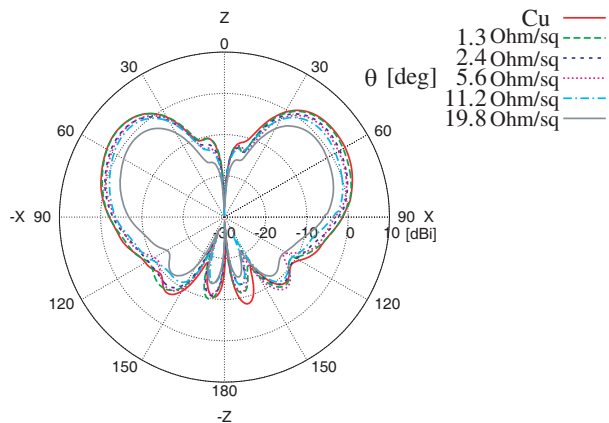


Figure 6: Measurement of  $E_\theta$  on  $xz$ -plane at 2.4 GHz for a monopole antenna.

### 3. SIMULATION

Wire-grid models by using the software Numerical Electromagnetic Code version 4 [8] are applied for the numerical analysis. The grid size is set to 0.5 mm and the wire radius to 0.15 mm. The resistance of the transparent film is taken into account by directly loading a resistance on every discretized element. Because the typical thickness of the films is several hundred nanometers, much thinner than the skin depth at the operating frequencies, the loading resistance  $R_l$  for an element is simply given by  $Rl = \rho_s \Delta l / \Delta w$ , where  $\rho_s$ ,  $\Delta l$  and  $\Delta w$  are the sheet resistivity, length and width of the element, respectively. However, due to the restriction of the software, the dielectric substrate is not included in the simulation.

Figures 7 and 8 show the calculated VSWR for the PIFA and monopole antenna, respectively. Both of the VSWRs do not vary so much as the sheet resistivity is lower than 10 Ohm/sq. Fig. 8 differs a little from Fig. 5 due to the lack of dielectric substrate in the simulation.

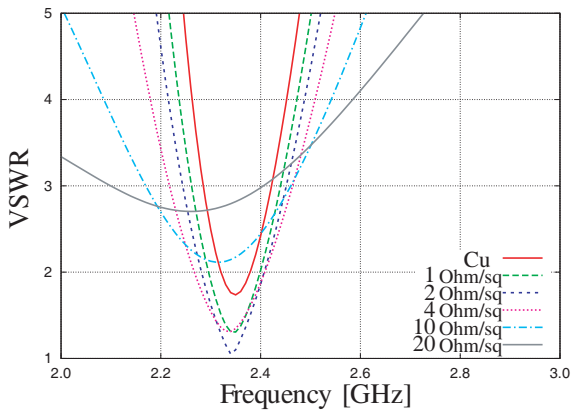


Figure 7: Calculation of VSWR for a PIFA.

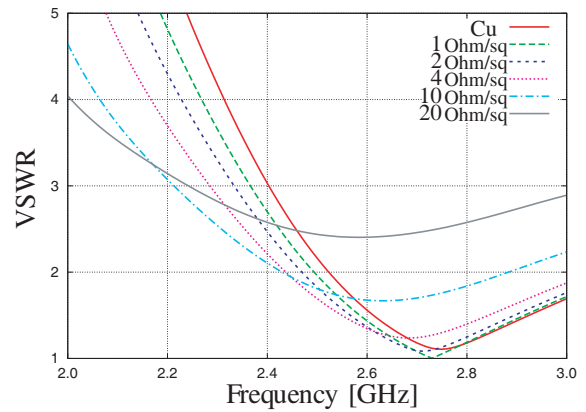
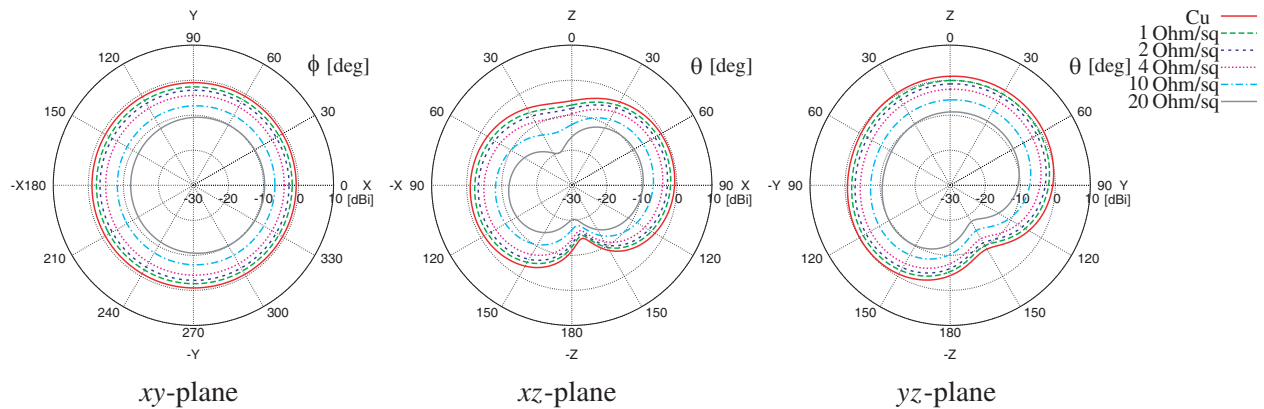
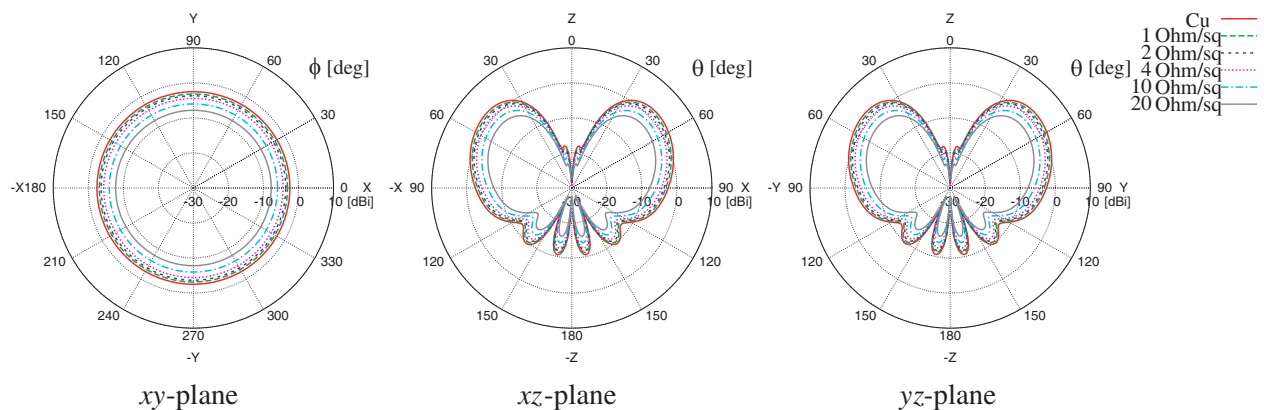


Figure 8: Calculation of VSWR for a monopole antenna.

Figures 9 and 10 show the calculated radiation patterns at 2.4 GHz for the PIFA and monopole antenna, respectively. It can be seen that the gain deterioration caused by the resistance is more serious in the PIFA than in the monopole antenna. Fig. 10 agrees with the measurement very well.

Figure 9: Calculation of  $E_\theta$  at 2.4 GHz for a PIFA.Figure 10: Calculation of  $E_\theta$  at 2.4 GHz for a monopole antenna.

Figures 11 and 12 show the calculated radiation efficiency for the PIFA and monopole antenna, respectively. The efficiency increases at the higher frequency for both of the antennas because the ratio of the radiation resistance to the ohmic resistance tends to increase as the frequency increases [9]. It is seen that the efficiency of the PIFA is lower than that of the monopole antenna for a same resistivity.

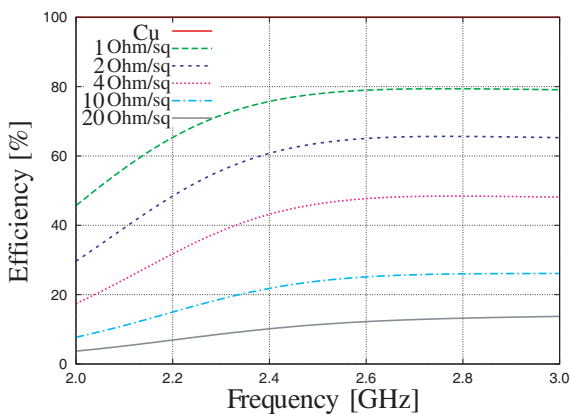


Figure 11: Calculation of efficiency for a PIFA.

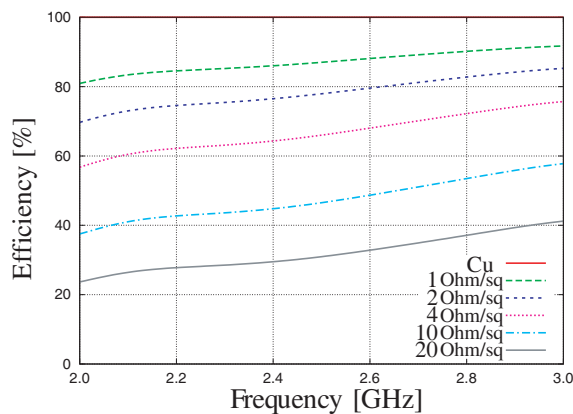


Figure 12: Calculation of efficiency for a monopole antenna.

#### 4. COMPARISON BETWEEN PIFA AND MONOPOLE ANTENNA

Figure 13 compares the maximum gain at 2.4 GHz for the PIFA and monopole antenna, where the gain is normalized to the value of the corresponding copper antenna. The gain lowering rate is 0.47 and 0.20 dB/Ohm/sq for the PIFA and monopole antenna, respectively.

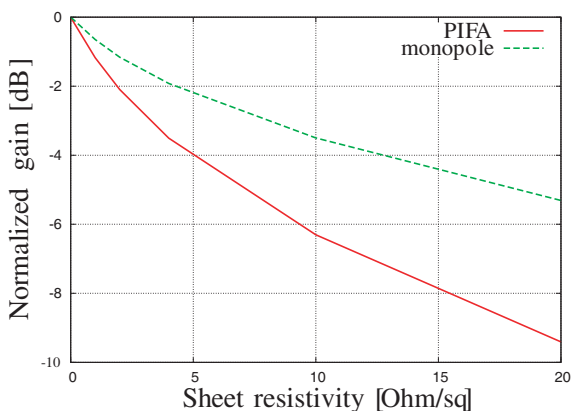


Figure 13: Gain comparison at 2.4 GHz.

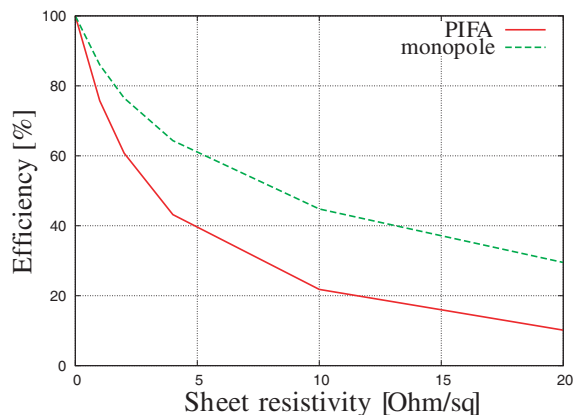


Figure 14: Efficiency comparison at 2.4 GHz.

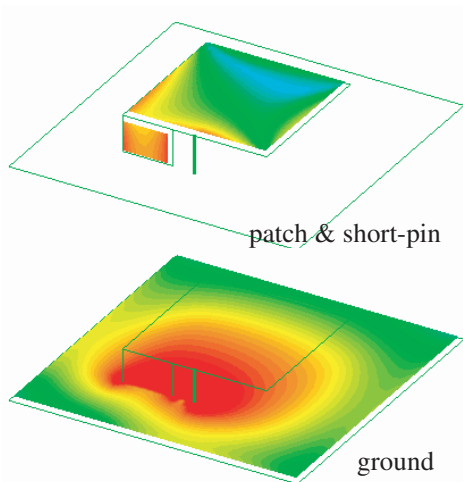


Figure 15: Current of a PIFA at 2.4 GHz.

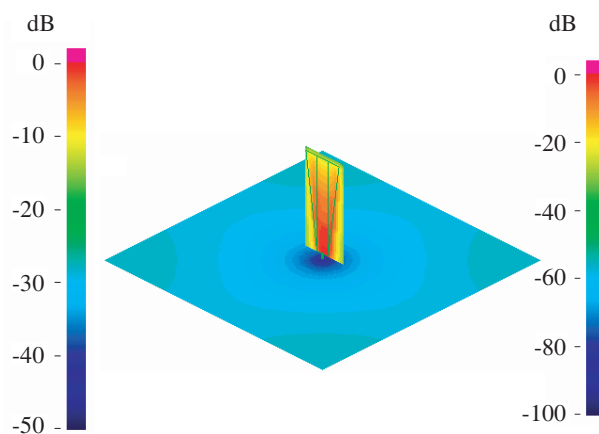


Figure 16: Current of a monopole antenna at 2.4 GHz.

Figure 14 compares the efficiency at 2.4 GHz for the two antennas. While the efficiency lowering

rate is 4.5 %/Ohm/sq for the PIFA, it is 2.7 %/Ohm/sq for the monopole antenna.

Figures 15 and 16 show the current distributions at 2.4 GHz for the PIFA and monopole antenna with perfect conductor, respectively. While the current mainly flows on the trapezoidal radiator in the monopole antenna, it flows on patch and ground in the PIFA. As a matter of fact, the PIFA behaves like a cavity and hence excites a large current on the whole patch. This is considered to be the reason why the film resistance influences the performance more strongly for the PIFA than for the monopole antenna.

Nevertheless, if an ITO film with a sufficiently small resistivity is used, radiation performance good enough for practical applications can be obtained by both antennas.

## 5. CONCLUSION

We have investigated a PIFA and a monopole antenna made of transparent conductive films. This study clarifies the fact that the influence of the film resistance on the radiation performance depends on the structure of the antennas and it provides quantitative data for the antenna design. It is expected that the transparent films can be used for both of the antennas in practical applications. It is hoped that the transparent antennas can provide a useful means for antennas integration when employed in mobile terminals in the near future.

## REFERENCES

1. Kawashima, T., H. Matsui, and T. Tanabe, "New transparent conductive films: FTO coated ITO," *Thin Solid Films*, Vol. 445, No. 2, 241–244, 2003.
2. Simons, R. N. and R. Q. Lee, "Feasibility study of optically transparent microstrip patch antenna," *IEEE AP-S Int. Symp.*, 2100–2103, Montreal, Canada, Jul. 1997.
3. Outaleb, M., J. Pinel, M. Drissi, and O. Bonnaud, "Microwave planar antenna with rf-sputtered indium tin oxide films," *Microwave and Opt. Technol. Lett.*, Vol. 24, No. 1, 3–7, 2000.
4. Mias, C., C. Tsakonas, N. Prountzos, D. C. Koutsogeorgis, S. C. Liew, C. Oswald, R. Ranson, W. M. Cranton, and C. B. Thomas, "Optically transparent microstrip antennas," *IEE Colloquium on Antennas for Automotives*, 8/1–8/6, 2000.
5. Oshima, K., N. Kidera, K. Niwano, K. Ikawa, R. Sonoda, and S. Kawasaki, "Use of a transparent conductive thin-film on a glass substrate in active integrated antenna arrays with double strong coupling," *IEEE MTT-S Int. Microwave Symp. Dig.*, 1569–1572, Seattle, USA, Jun. 2002.
6. Huang, C.-F. and L. Chen, "Realization of a printed-on-display antenna for mobile terminals," *Elect. Lett.*, Vol. 38, No. 20, 1162–1163, 2002.
7. Guan, N., H. Furuya, K. Himeno, K. Goto, and K. Ito, "Basic study on an antenna made of a transparent conductive film," *IEICE Trans. Commun.*, Vol. E90-B, No. 9, 2219–2224, 2007.
8. <http://www.llnl.gov/IPandC/technology/software/software-titles/nec.php>.
9. Guan, N., H. Furuya, D. Delaune, and K. Ito, "Radiation efficiency of monopole antenna made of a transparent conductive film," *Proc. 2007 IEEE AP-S Int. Symp.*, 221–224, Hawaii, USA, Jun. 2007.

# Application of Artificial Dielectric Material for a PIFA Antenna

Jwo-Shiun Sun<sup>1</sup>, Guan-Yu Chen<sup>1</sup>, Cheng-Hung Lin<sup>2</sup>, Kwong-Kau Tiong<sup>2</sup>, and Y. D. Chen<sup>3</sup>

<sup>1</sup>Department of Electronic Engineering, National Taipei University of Technology, Taiwan

<sup>2</sup>Department of Electrical Engineering, National Taiwan Ocean University, Taiwan

<sup>3</sup>Antenna and EMC Laboratory, High Tech Computer Corp. (HTC), Taiwan

**Abstract**— Artificial materials of periodic dielectrics which exhibit electromagnetic band-gap (EBG) performance have been proposed and applied on a planar inverted-F antenna (PIFA) design in this paper. The artificial defected dielectric material has some useful characteristics such as harmonic rejection, band suppression and surface wave suppression. A three-dimensionally periodic dielectric structure with a compact and low profile electromagnetic band gap material is presented. The artificial dielectric material (ADM) enhances radiation performance, bandwidth, radiation gain and efficiency of the designed antenna.

## 1. INTRODUCTION

A three-dimensionally periodic dielectric structure [1] with a compact and low profile electromagnetic band gap material is presented. Artificial dielectrics of FR4 permittivity are designed and fabricated by use of a patterned PCB printed circuit board. The ADM miniaturized with harmonic rejection characteristics is fabricated using periodic dielectric as resonators. In one embodiment of the implementation, the ADM substrate for a PIFA antenna comprises the frequency selective material. The general approach to reduce an antenna's size is to load the antenna with dielectric material. The AMD is better than the traditional uniform dielectric material with its good electromagnetic effects and easy integration with low profile antenna. The use of electromagnetic band-gap structures, also known as photonic band-gap structures [2, 3], for enhancing antenna performance has been widely investigated in recent years. In this paper, the ADM dielectric can do an effective function of reducing an antenna's size and improve antenna radiation efficiency.

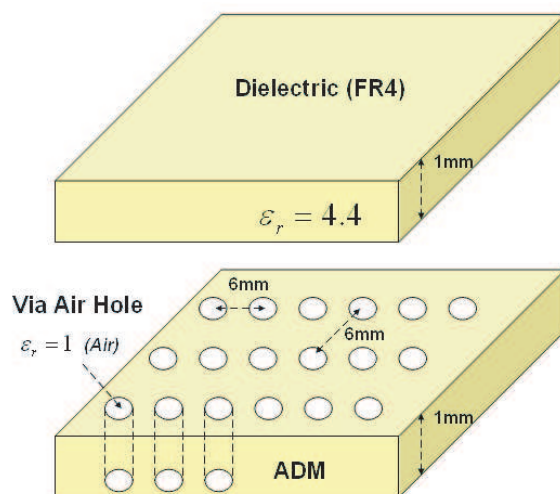


Figure 1: The proposed material for artificial dielectric material (ADM).

## 2. DESIGN AND RESULTS

ADM are periodic dielectric composite structures that forbid wave propagation of radiation for a certain frequency range. The good artificial dielectric material is better than traditional uniform dielectric material and good electromagnetic effect is easy to integrate low profile antenna design and application. Fig. 1 is the proposed AMD structure. Fig. 2 is a designed PIFA with an AMD structure. Fig. 3 shows the comparison data in between PIFA with ADM and a traditional PIFA. In this paper, the antenna design facility is suitable and effective to improve performance of total antenna radiation efficiency.

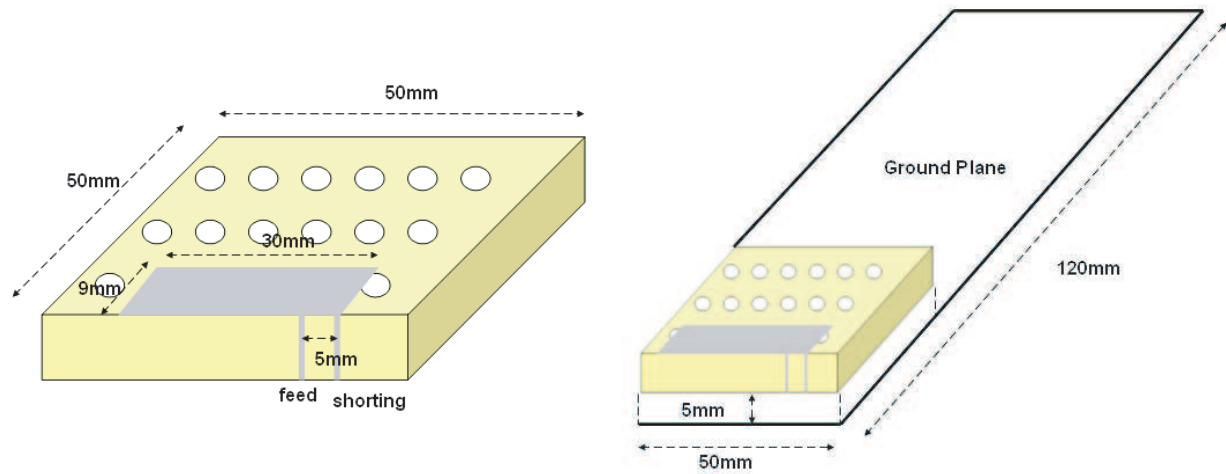


Figure 2: A designed PIFA with an AMD structure.

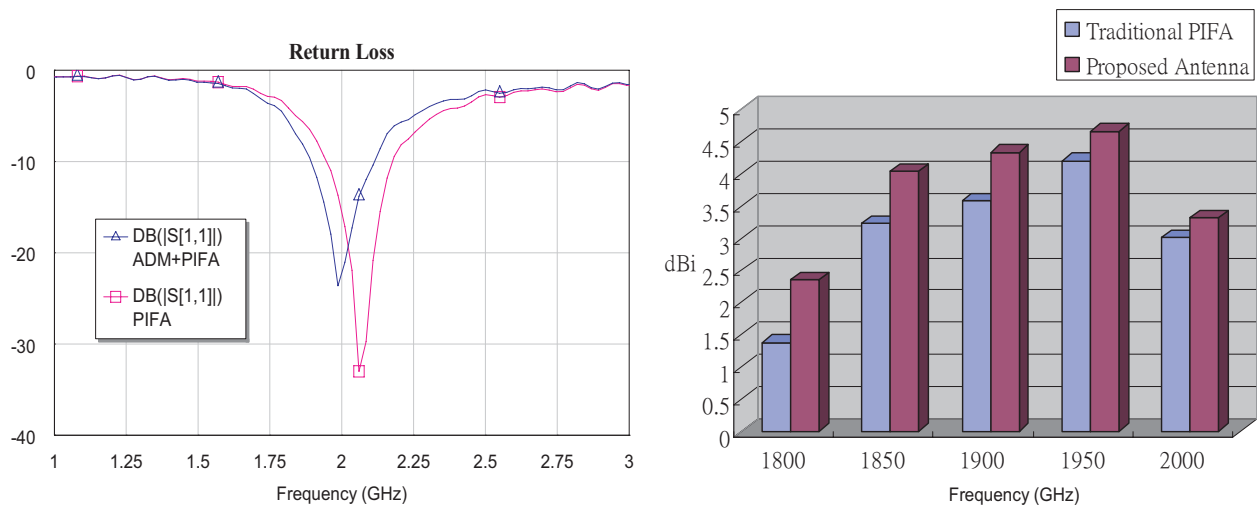


Figure 3: Comparisons of an ADM PIFA and a traditional PIFA.

### 3. CONCLUSION

The ADM applied for a PIFA antenna radiator has been developed. This designed antenna covers WCDMA and UMTS band from 1900 MHz to 2200 MHz. Evidently, it should be useful for many wireless applications.

### ACKNOWLEDGMENT

The authors would like to thank the Antenna and Wireless System Integration Department of High Tech Computer, Corp. (HTC), Taiwan for sporting the environment of measurement.

### REFERENCES

1. Munk, B. A., *Frequency Selective Surfaces: Theory and Design*, John Wiley, New York, c2000.
2. Soukoulis, C. M., *Photonic Band Gaps and Localization*, Plenum Press, New York, c1993.
3. Collin, R. E., *Field Theory of Guided Waves*, 2nd, IEEE Press, New York, c1991.

# Bandwidth Enhancement of Balanced Folded Loop Antenna Design for Mobile Handsets Using Genetic Algorithms

D. Zhou, R. A. Abd-Alhameed, and P. S. Excell

Mobile and Satellite Communications Research Centre, University of Bradford  
Richmond Road, Bradford, West Yorkshire, BD7 1DP, UK

**Abstract**— In this paper, a simple folded loop antenna (FLA) for handsets with relatively wide-band impedance, designed and optimized using genetic algorithms (GA). The FLA dimensions were optimized and evaluated using GA in collaboration with NEC-2 source code. Configuration of optimal FLA with excellent VSWR covering entirely the required GSM1800 frequency bands was found within the maximum generation. A prototype antenna was tested to verify and validate the GA-optimized antenna structure. The measured data have shown good agreement with predicted ones. Moreover, the capabilities of GA are shown as an efficient optimisation tool for selecting globally optimal parameters to be used in simulations with an electromagnetic antenna design code, seeking convergence to designated specifications.

## 1. INTRODUCTION

Recently, balanced antennas have drawn greatly interest to mobile phone antenna researchers due to their stable performance when held by mobile phone users. In the previous work [1, 2], folded dipole and loop antennas have shown the promising characteristics of balanced antennas in terms of their current distributions on ground plane, radiation performance and Specific Absorption Rate (SAR). One dramatic drawback in their proposed antennas for use in mobile handsets is the lack to provide enough impedance bandwidth to fulfill the bandwidth requirements for the current wireless mobile communications (i.e., GSM1800/1900 or UMTS). However, a wideband operation was achieved at higher central frequency 2680 MHz [3].

GA is random search methods based on the principle of natural selection and evolution [4]. An approach of using GA in cooperation with an electromagnetic simulator has been introduced for antenna designs and has become increasingly popular recently [5]. In authors' previous work [6], an example of enhancing bandwidth for mobile antennas has been demonstrated. The benefit of applying GA is that they provide fast, accurate and reliable solutions for antenna structures.

In this paper, a simple FLA for handsets with relatively wideband impedance, was designed and optimized using GA. The geometry of proposed FLA was adopted from the Morishita's work [1] (see Fig. 1) and applied here for this study due to the simple structure for the mobile antenna applications. The parameters used to define the FLA, were optimized and evaluated using GA in collaboration with NEC-2 [7, 8]. Finally, GA optimal antenna structure was verified with hardware realization. The corresponding results were compared to the predicted ones and a good agreement in VSWR was observed.

## 2. GENETIC ALGORITHMS AND ANTENNA OPTIMIZATION USING GA

A FLA was optimized with GA using real-valued chromosomes. The intended antenna was designed for GSM1800 applications (1710–1860 MHz). Performance of the randomly generated antenna samples was computed using NEC-2 and its result was compared with desired fitness using the following cost function:

$$F = \sum_{n=1}^3 W_n \cdot (1/VSWR(f_n)) \quad (1)$$

where,  $W_n$  ( $n = 1, 2, 3$ ) are the weight coefficients for the cost function and initially, they set a value of 1. Three pre-set specific frequencies 1710, 1785, and 1860 MHz were applied. GA was run to calculate and evaluate the for each erratically produced antenna structure, in order to ensure the optimal antenna operation to cover the required impedance bandwidth. The objective was to find the optimal solution that satisfies certain constraints including a specific antenna volume.

GA input parameters, their constraints and the optimal values for each specified parameter of the design geometry is presented in Table 1. Since there is no graphical abilities in NEC-2, GA generated antenna structures can be viewed using the NEC-Win Professional<sup>®</sup> simulator [9].

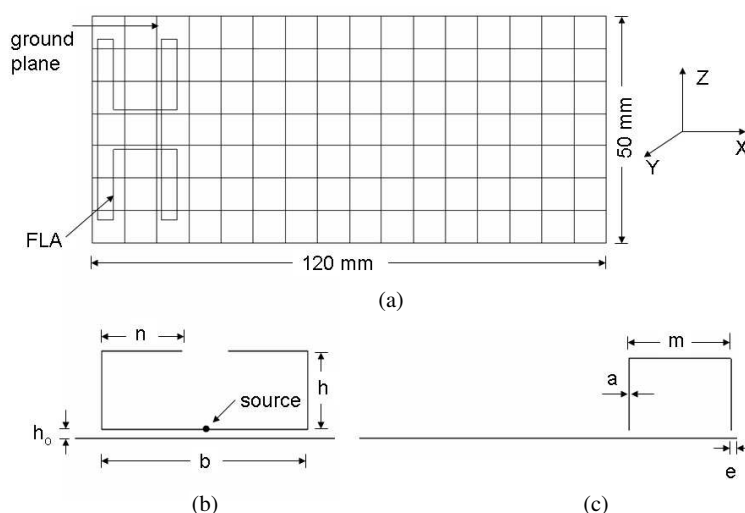


Figure 1: Antenna configuration studied, (a) balanced folded loop antenna with conducting plate, (b) front view of the antenna design, (c) side view of the antenna design.

### 3. SIMULATION AND MEASUREMENT RESULTS

Configuration of optimal FLA antennas, with excellent VSWR covering entirely the required GSM1800 frequencies bands, was found within the maximum generation; antenna parameters of the best designs are shown in Table 1. For comparison, an electromagnetic simulator based on the finite integration technique (FIT) was used to verify and validate the GA-optimized antenna structure [10]. It should be noted that thin striplines were employed in the EM modeling instead of thin wires that used in GA optimization, due to the fact for the purpose of practical implementation. Subsequently, a minor adjustment was applied to the GA-optimized antenna. The calculated antenna VSWR against frequency over the interested bands is shown in Fig. 2 and was compared to the one obtained from GA. As can be seen, an excellent agreement of antenna VSWR response was achieved. It is also notable that impedance bandwidth at  $VSWR \leq 2$  was 7.5% at central frequency  $f_0 = 1780$  MHz, compared to the bandwidth of 2.7% at  $f_0 = 1860$  MHz with a small FLA and 5.4% with using a parasitic element added to the small FLA, as reported in work [1]. The bandwidth is comparatively broadened due to the effect of capacitive coupling between the antenna and ground plane in which it dominates the frequency band.

Table 1: Summary of GA input parameters, antenna variables and best solutions.

GA parameters	FLA for GSM1800		FLA for UMTS	
	Parameters (m)	Optimal (m)	Parameters (m)	Optimal (m)
Number of population size = 6	Wire radius (a) (0.0004-0.0008)	0.00074	Wire radius (a) (0.0004-0.0008)	0.000790
Number of parameters = 7	FLA length (b) (0.03-0.04)	0.03978	FLA length (b) (0.03-0.04)	0.03690
Probability of mutation = 0.02	FLA height (h) (0.003-0.012)	0.01173	FLA height (h) (0.003-0.012)	0.01179
Maximum generation = 500	FLA arm length (n) (0.002-0.015)	0.008785	FLA arm length (n) (0.002-0.015)	0.009881
Number of possibilities = 32768	Parallel wires distance (m) (0.005-0.015)	0.01489	Parallel wires distance (m) (0.005-0.015)	0.013599
Ground plane size (120 x 50 mm)	FLA distance to GP edge (e) (0.0-0.002)	0.0008643	FLA distance to GP edge (e) (0.0-0.002)	0.001137
	Distance between FLA and GP ( $h_0$ ) (0.001-0.003)	0.001112	( $h_0$ ) (0.001-0.003)	0.001146

In addition, the same design principle and antenna geometry was applied to design and optimize antennas for 3G UMTS application. The comparative antenna VSWR (see Fig. 3) shows a good impedance matching over the intended band (11.3% at  $f_0 = 2030$  MHz).

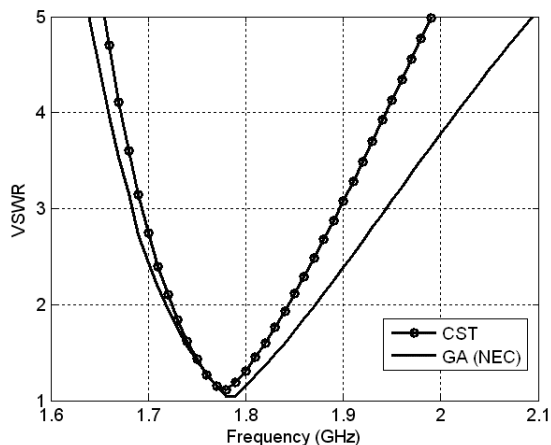


Figure 2: VSWR against frequency ( $a = 2.070$ ,  $b = 37.8802$ ,  $h = 9.9991$ ,  $h_0 = 1$ ,  $n = 13.884$ ,  $e = 0.9409$  and  $m = 12.8052$ , all dimensions in millimeters).

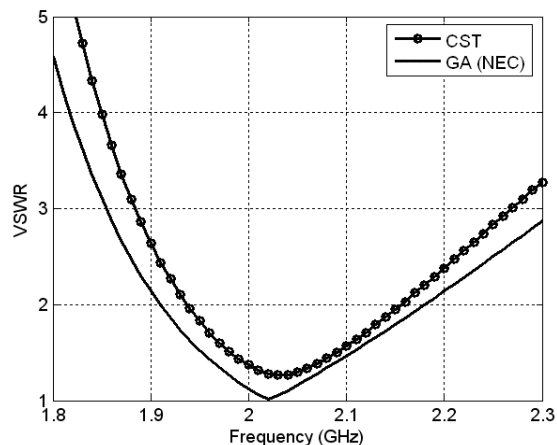


Figure 3: VSWR against frequency ( $a = 1.95144$ ,  $b = 37.0052$ ,  $h = 9.9966$ ,  $h_0 = 1$ ,  $n = 11.1638$ ,  $e = 1.8835$  and  $m = 12.9884$ , all dimensions in millimeters).

For the hardware realisation, copper sheet of thickness 0.15 mm and 0.5 mm was used for fabricating the balanced antenna and the ground plane (see Fig. 4). A balun, as a feeding network for the balanced antennas, is required to provide a balanced feed from an unbalanced source. In this study, a relatively wideband planar balun with sufficient frequency coverage and imbalance performance (covering 1.4–2.4 GHz frequencies bands with maximum 0.9 dB insertion loss in which the amplitude and phase imbalance are 0.1 dB and  $\pm 2^\circ$ , respectively) was employed to feed the prototype antenna.

Figure 5 presents the measured and simulated VSWR of the prototype antenna. As can be seen, taking into account the errors caused during antenna fabrication, a close agreement between the calculated and measured return loss was observed.

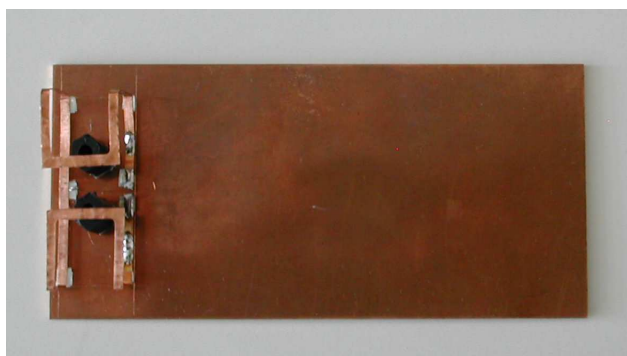


Figure 4: Photograph of fabricated prototype antenna.

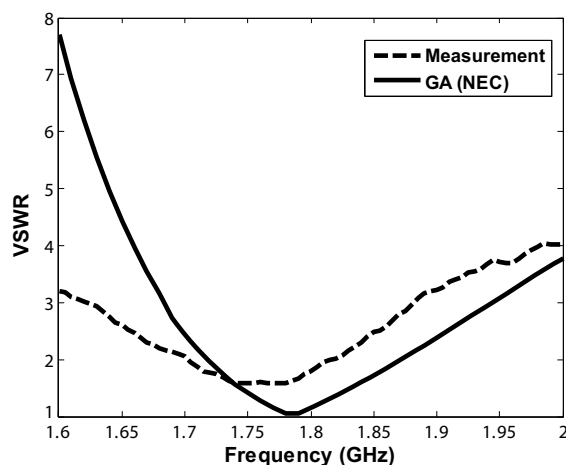


Figure 5: The simulated and Measured VSWR against operating frequency.

The radiation patterns in the z-x plane and z-y plane for the balanced folded antenna at 1780 MHz were calculated and plotted in Fig. 6, where the patterns of the proposed antenna are seen to be quite similar to each other at other frequencies inside the band. In addition, the z-x plane presents a nearly omni-directional radiation pattern in all intended frequency bands. For the GSM1800 band, the calculated peak gain was found to be 4 dBi.

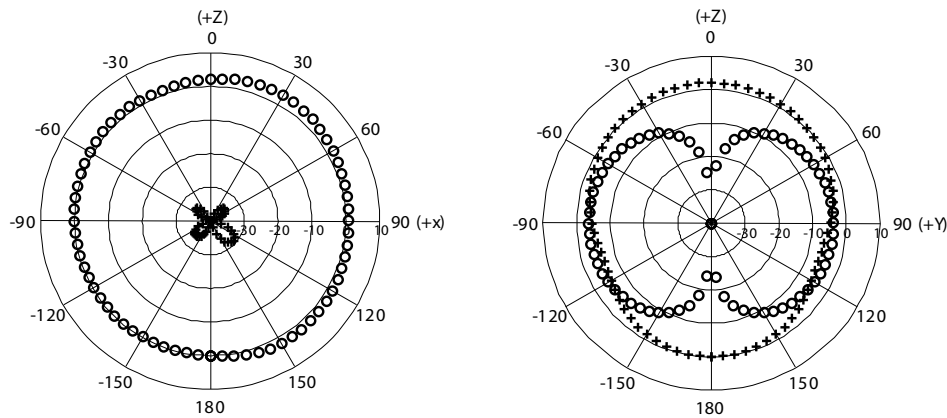


Figure 6: Radiation patterns for the proposed antenna at 1780 MHz in dBi at z-x plane (left) and z-y plane (right) ('+++ $E_{\theta}$ ' and 'ooo $E_{\varphi}$ ').

#### 4. CONCLUSIONS

A folded loop antenna with relatively wide bandwidth for mobile handsets, was designed and optimized using genetic algorithms. Performance of the GA-optimized antenna structure was validated through a hardware realization in which the simulated results show a good agreement with measured one. The GA has proven its advantage for quickly finding solutions for antenna designs as well as a robust technique to broaden the bandwidth in antenna design.

#### ACKNOWLEDGMENT

The authors would like to gratefully acknowledge the support by the Engineering and Physical Sciences Research Council (EPSRC) under grant EP/E022936.

#### REFERENCES

1. Morishita, H., Y. Kim, Y. Koyanagi, and K. Fujimoto, "A folded loop antenna system for handsets," *IEEE AP-S Proc.*, Vol. 3, 440–443, July 2001.
2. Abd-Alhameed, R. A., P. S. Excell, K. Khalil, R. Alias, and J. Mustafa, "SAR and radiation performance of balanced and unbalanced mobile antennas using a hybrid formulation," Invited paper, *IEE Proceedings-Science, Measurement and Technology Special Issue on Computational Electromagnetics*, Vol. 151, No. 6, 440–444, November 2004.
3. Hayashida, S., H. Morishita, Y. Kim, Y. Koyanagi, and K. Fujimoto, "Wideband folded loop antenna for handsets," *IEEE AP-S Proc.*, Vol. 3, 2–5, Jun. 2002.
4. Goldberg, D. E., *Genetic Algorithms in Search, Optimization and Machine Learning*, Addison-Wesley, Reading, MA, 1989.
5. Johnson, J. M. and Y. Rahmat-Samii, "Genetic algorithms in engineering electromagnetics," *IEEE Antennas and Propagation Magazine*, Vol. 39, No. 4, 7–21, 1997.
6. Zhou, D., R. A. Abd-Alhameed, C. H. See, P. S. Excell, and E. A. Amushan, "Design of quadrifilar helical and spiral antennas in the presence of mobile handsets using genetic algorithms," *Proceeding of the First European Conference on Antennas and Propagation*, Session 3PA1, Paper No. 122, Nice, France, 6–10 November, 2006.
7. Carroll, D. L., FORTRAN Genetic Algorithm Driver, Version 1.7, Download from: <http://www.staff.uiuc.edu/~carroll/ga.html>, 12/11/98.
8. Burke, G. L. and A. J. Poggio, "Numerical electromagnetics code (NEC)-method of moments," Lawrence Livermore Laboratory, Livermore, CA, 1981.
9. NEC-Win Professional V1.1, ©1997 Nittany Scientific Inc., USA.
10. Computer Simulation Technology Corporation, CST Microwave Studio, Version 5.0, Germany.

# Design Considerations of MIMO Antennas for Mobile Phones

M. Usman, R. A. Abd-Alhameed, and P. S. Excell

Mobile and Satellite Communications Research Centre  
Richmond Road, University of Bradford, Bradford, West Yorkshire, BD7 1DP, UK

**Abstract**— The paper presents a new modeling and design concept of antennas using polarization diversity of  $2 \times 2$  and  $3 \times 3$  Multiple Input Multiple Outputs (MIMO) system that is proposed for future mobile handsets. The channel capacity is investigated and discussed over Raleigh fading channel and compared to a linear/planner antenna array MIMO channel. The capacity is also discussed over three types of power azimuth spectrums. The results are compared to the constraints capacity limits in which the maximum capacity observed.

## 1. INTRODUCTION

MIMO for short, which stands for Multiple Input, Multiple Output systems are theoretically able to provide increased throughput, and better error performance than traditional systems [1–5]. The particular aspect that is used by MIMO systems is called *Multi-Path* propagation [2, 5]. This effect occurs when the radio signals sent from the transmitter bounce off intermediate objects before reaching the receiver. Some of these reflected signals may travel along entirely separate paths, and even reach the receiver at different times. Currently, there are a number of MIMO applications, development platforms, and tools that are showing great promise in the quest for wireless systems with higher bandwidth and greater capabilities. The major advantage of MIMO technology is the digital beam forming, which is now making its way out of research laboratories and into real-world applications with great speed. Spatial correlation using polarization issues for MIMO applications has great interest since the size of the actual radiating elements can be reduced [6–12]. This study has great advantages if a MIMO system needs to be implemented on a mobile handset. This paper will consider the spatial polarization technique and how this technique can improve the capacity of the system. A MIMO system of  $2 \times 2$  and  $3 \times 3$  elements will be considered for implementations on mobile handsets. This will be discussed under Raleigh fading channel and the results will be compared to linear or planer array antenna MIMO system. More over different types of power azimuth spectrums will be considered for system evaluation.

## 2. SUMMERY OF THE METHOD

For a system having  $N$  transmitters and  $N$  receivers the channel capacity can be given by [1];

$$C = E \log_2 \left| \left( I + \frac{P_t}{n_t \sigma} H H^* \right) \right| \quad (1)$$

where  $I$  is the identity matrix of  $n_r \times n_r$  dimensions.  $P_t$  is the total average transmitted power.  $\sigma$  is the variance of the noise power,  $H$  is the channel transfer matrix of size  $n_r \times n_t$ .  $E()$  is the expectation average and ‘\*’ is the conjugate transpose operation.

If the receiver and transmitter spatial matrixes are none then the matrix  $H H^*$  can be rewritten as follows:

$$H H^* = W_r G_w W_t^* \quad (2)$$

where  $W_r$  and  $W_t$  are the spatial matrices of the receiver and transmitter respectively.  $G_w$  is the matrix that defines the channel properties. For example the elements of the  $G_w$  matrix in Raleigh fading channel are complex guassian distributed elements. Since the space availability on the transmitter side then the spatial matrix of the transmitter for maximum channel capacity can be given as an identity matrix. Therefore Eq. (2) can be reduced to the following:

$$H H^* = W_r G_w \quad (3)$$

The elements of the spatial matrix  $W_r$  can be stated as follows:

$$W_{r_{i,j}} = \frac{\oint (E_{ai} \cdot E_i)(E_{aj} \cdot E_i)^* d\Omega}{\sigma_1 \sigma_2} \quad (4)$$

where

$$\sigma_1 = \oint_s (E_{ai} \cdot E_i)^2 d\Omega \quad (5)$$

$$\sigma_2 = \oint_s |E_{aj} \cdot E_i|^2 d\Omega \quad (6)$$

$$\oint_s = \int_{\phi_1}^{\phi_2} \int_{\theta_1}^{\theta_2} \quad (7)$$

$$d\Omega = \sin \theta d\theta d\phi \quad (8)$$

and  $E_a$  is the electric field of the radiating element.  $E_i$  is the incident field on the receiver side.

Using polarization concept we assume that there were three dipoles collocated over the  $z$  axis and centered at origin point as shown in Figure 1. We restrict our study to three radiating elements and in which the mutual coupling are ignored and they will located with respect to the elevation angle (it is the polarization angle in our case). We reduced the complicity of the method implementation by using short dipoles in which the field can be easily stated (as example for a short dipole oriented in the  $z$  axis the total field is  $E_\theta = \sin \theta$ ).

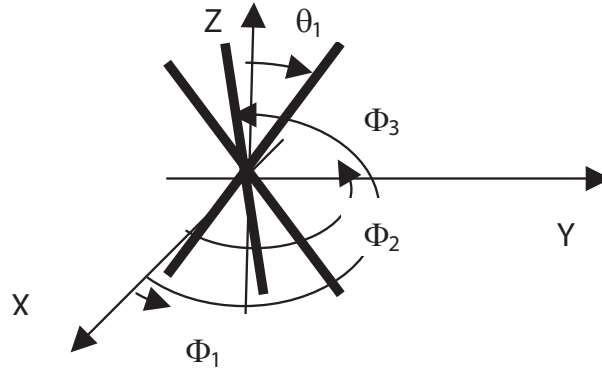


Figure 1: Basic antenna geometry.

The direction of a dipole oriented in  $\theta_d$  and  $\phi_d$  can be expressed as follows:

$$\hat{\mathbf{d}} = \sin \theta_d \cos \phi_d \hat{\mathbf{a}}_x + \sin \theta_d \sin \phi_d \hat{\mathbf{a}}_y + \cos \theta_d \hat{\mathbf{a}}_z \quad (9)$$

Then the radiated field of this dipole can be given as follows:

$$E_a = E_{\theta a} \hat{\mathbf{a}}_\theta + E_\phi \hat{\mathbf{a}}_\phi \quad (10)$$

where

$$E_\theta(\theta, \phi) = \hat{\mathbf{d}} \cdot \hat{\mathbf{u}}_\theta \quad (11)$$

$$E_\phi(\theta, \phi) = \hat{\mathbf{d}} \cdot \hat{\mathbf{u}}_\phi \quad (12)$$

$$\hat{\mathbf{u}}_\theta = \cos \theta \cos \phi \hat{\mathbf{a}}_x + \cos \theta \sin \phi \hat{\mathbf{a}}_y + \sin \theta \hat{\mathbf{a}}_z \quad (13)$$

and

$$\hat{\mathbf{u}}_\phi = -\sin \phi \hat{\mathbf{a}}_x + \cos \phi \hat{\mathbf{a}}_y \quad (14)$$

### 3. SIMULATION AND MEASUREMENT RESULTS

If the signal to noise ratio is high then the channel capacity can be given by [5]:

$$C = \sum_{i=1}^n \left( I + \frac{P}{n_T \sigma} \lambda_i \right) \quad (15)$$

where  $\lambda_i$  for  $i = 1, 2, 3$  are the eigen values of the matrix given in Eq. (3). However, the channel capacity is also computed for comparison using Eq. (1). The incident fields are assumed to have uniform distribution over the range 0 to  $2\pi$  for azimuth angle  $\phi$  and  $30^\circ$  over the elevation angle at the horizontal plane for urban channel. For suburban channel the variation over elevation angle is similar to urban channel where as the azimuth will have laplacian spectrum distribution of various  $\sigma_\phi = 5^\circ, 10^\circ, 15^\circ$  and  $20^\circ$ .

The  $E_\phi$  and  $E_\theta$  of the incident fields were assumed independent over all angles of  $\theta$  and  $\phi$ , and their variations are uniform over the channel properties under considerations. It was also assumed that the phase variations are uniform over 0 to  $2\pi$ .

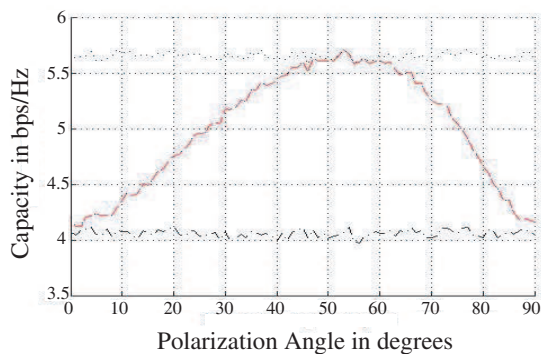


Figure 2: The channel capacity of  $2 \times 2$  MIMO system as oriented in Figure 1 as a function of the polarization angle. ('...': upper limit of  $2 \times 2$  MIMO fading channel, '-.-.-': upper limit of  $2 \times 1$  MIMO fading channel, Capacity using Eq. 1: red line, Capacity using Eq. 15: blue dots).

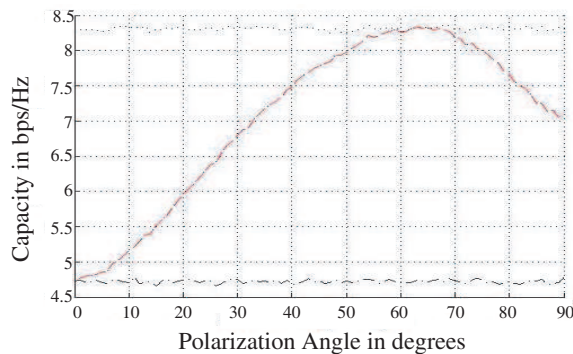


Figure 3: The channel capacity of  $3 \times 3$  MIMO system as oriented in Figure 1 as a function of the polarization angle. ('...': upper limit of  $3 \times 3$  MIMO fading channel, '-.-.-': upper limit of  $3 \times 1$  MIMO fading channel, Capacity using Eq. 1: red line, Capacity using Eq. 2: blue dots).

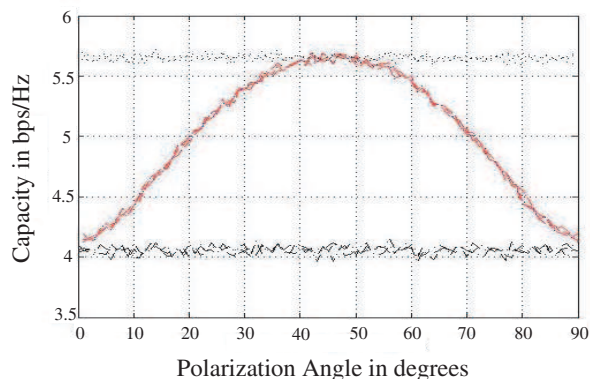


Figure 4: The channel capacity of  $2 \times 2$  MIMO system as oriented in Figure 1 (the antennas are rotated by 90 degrees over azimuth angle) as a function of the polarization angle. ('...': upper limit of  $3 \times 3$  MIMO fading channel, '-.-.-': upper limit of  $3 \times 1$  MIMO fading channel, Capacity using Eq. 1: red line, Capacity using Eq. 2: blue dots). The elevation angle is varied uniformly over 30 degrees at the horizontal plane, whereas azimuth angle varied as Laplacian spectrum of different values of  $\sigma_\phi$  (5, 10, 15, 20 degrees for the geometry presented in Figure 1) in which the azimuth direction randomly selected between 0 and  $2\pi$ .

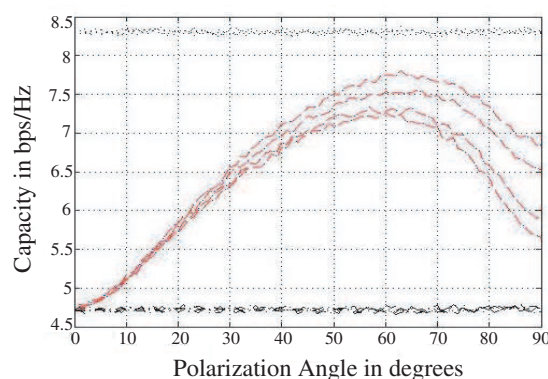


Figure 5: The channel capacity of  $3 \times 3$  MIMO system as oriented in Figure 1 (the antennas are located at 90, 210 and  $-30^\circ$  azimuth angles) as a function of the polarization angle. ('...': upper limit of  $3 \times 3$  MIMO fading channel, '-.-.-': upper limit of  $3 \times 1$  MIMO fading channel, Capacity using Eq. 1: red line, Capacity using Eq. 2: blue dots). The elevation angle is varied uniformly over 30 at the horizontal plane, whereas azimuth angle varied as Laplacian spectrum of different values of  $\sigma_\phi$  (5, 10, 20, 30 degrees for the geometry presented in Figure 1) in which the azimuth direction randomly selected between 0 and  $2\pi$ .

Channel capacity of  $2 \times 2$  MIMO and  $3 \times 3$  MIMO systems for urban channel are shown in Figures 2 and 3. The antennas for  $2 \times 2$  MIMO are located at  $\phi = 0^\circ$  and  $\phi = 180^\circ$  where as

for  $3 \times 3$  MIMO at  $\phi = 0^\circ, 120^\circ$  and  $240^\circ$ . In these figures a closed form solutions of the  $W_r$  are found and then the capacity was evaluated under Raleigh channel in which the average was taken over 1000 complex samples and in each point the transfer function was normalized to have a good prediction of the maximum variation of the spatial matrices using these types of antennas. It is simply can be noticed that the maximum capacities for  $2 \times 2$  MIMO and  $3 \times 3$  MIMO occur at around  $55^\circ$  and  $63^\circ$ . These angles are recommended to represent the othogonalities of the spatial fields required by the antennas given in Figure 1.

Similarly, for Suburban channel the capacity of  $2 \times 2$  and  $3 \times 3$  MIMO system are shown in Figures 4 and 5 respectively for various values of  $\sigma_\phi$ . It should be noted that the maximum capacity limits for  $2 \times 2$  MIMO channel were achieved for all values presented for  $\sigma_\phi$  where as for the  $3 \times 3$  MIMO were slightly reduced as  $\sigma_\phi$  is increasing.

Basically, the MIMO channel capacity for different transmitted power is shown in Figure 6. In this example the variations of the elevation angle is considered between  $\theta = 0$  to  $\pi$  where as in azimuth are similar to that presented in Figures 2 and 3. It is clearly the maximum capacities are proportional linearly with the transmitted power in which the maximum location for each transmitted power is fixed at around  $63^\circ$ .

Figure 7 demonstrates the capacity variations for urban channel using ring array of three elements. The channel capacity was reached when the ring radius was about  $\lambda/4$  (i.e., the separated distance between the radiating elements was around  $\lambda/2$ ). Comparing the antenna sizes in Figures 1 and 7, it is evidence that the spatial polarization diversity has the ability to achieve the maximum capacity with certain constraints on the field orthogonalites.

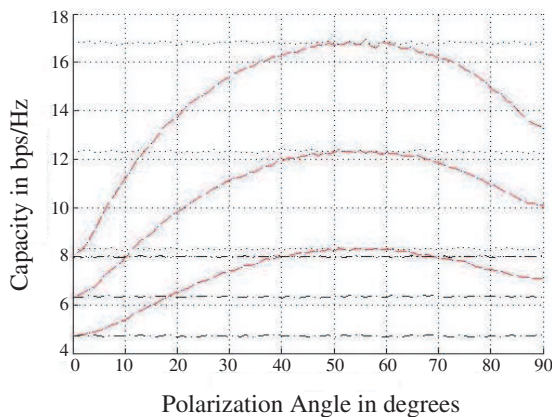


Figure 6: The channel capacity of  $3 \times 3$  MIMO system as oriented in Figure 1 as a function of the polarization angle for different SNR starting from 10 dB, 15 dB and 20 dBs. ('...': upper limit of  $3 \times 3$  MIMO fading channel, '-.-.-': upper limit of  $3 \times 1$  MIMO fading channel, Capacity using Eq. 1: red line, Capacity using Eq. 2: blue dots). The elevation angle is varied uniformly over 180 degrees at the horizontal plane.

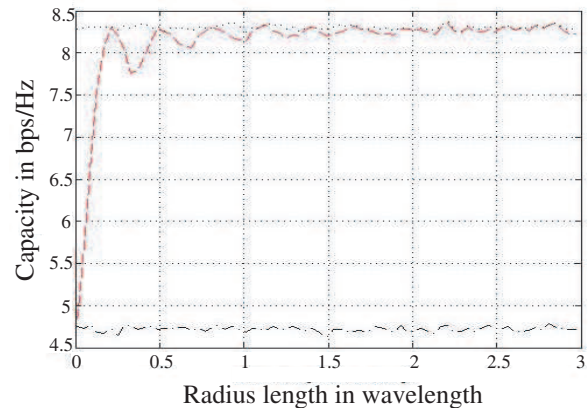


Figure 7: The channel capacity of  $3 \times 3$  MIMO system as oriented on a ring (the antennas are located at  $0, 120$  and  $-120$  azimuth angles) as a function of the radius distance in wavelength (c). ('...': upper limit of  $3 \times 3$  MIMO fading channel, '-.-.-': upper limit of  $3 \times 1$  MIMO fading channel, red line, Capacity using Eq. 2: blue dots).

#### 4. CONCLUSIONS

The channel capacity of a simple  $2 \times 2$  and  $3 \times 3$  MIMO systems using spatial polarization diversity was presented for different channel assumptions. The presented results show that the maximum channel capacity within small volume space can be reached with careful selection of the spatial field's orthoanlities. The results also compared to planner array MIMO system operation in which the antenna size considered was much larger to the MIMO system presented here. However, the work is still in progress to include the mutual coupling between the antennas and implementation on the mobile handset.

## REFERENCES

1. Foschini, G. J. and M. J. Gans, "On limits of wireless communication in a fading environment when using multiple antennas," *Wireless Personal Commun.*, Vol. 6, No. 3, 311–335, Mar. 1998.
2. Foschini, G. J. and R. A. Valenzuela, "Initial estimation of communication efficiency of indoor wireless channel," *Wireless Networks*, Vol. 3, 141–154, 1997.
3. Wallace, J. W. and M. A. Jensen, "Modeling the indoor MIMO wireless channel," *IEEE Trans. Antennas Propag.*, Vol. 50, No. 5, 591–599, May 2002.
4. Wallace, J. W., M. A. Jensen, A. L. Swindlehurst, and B. D. Jeffs, "Experimental characterization of the MIMO wireless channel: Data acquisition and analysis," *IEEE Trans. Wireless Commun.*, Vol. 2, No. 2, 335–343, Mar. 2003.
5. Gesbert, D., H. Bölcskei, D. A. Gore, and A. Paulraj, "Outdoor MIMO wireless channels: Model and performance prediction," *IEEE Trans. Commun.*, Vol. 50, No. 12, 1926–1934, Dec. 2002.
6. Dong, L., H. Choo, R. W. Heath, and H. Ling, "Simulation of MIMO channel capacity with antenna polarization diversity," *IEEE Trans. Wireless Commun.*, Vol. 4, No. 4, 1869–1873, Jul. 2005.
7. Winters, J. H., J. Salz, and R. D. Gitlin, "The impact of antenna diversity on the capacity of wireless communication systems," *IEEE Trans. Commun.*, Vol. 42, 1740–1751, Feb. 1994.
8. Andrews, M. R., P. P. Mitra, and R. deCarvalho, "Tripling the capacity of wireless communications using electromagnetic polarization," *Nature*, Vol. 409, No. 6818, 316–318, Jan. 2001.
9. Svantesson, T., "On capacity and correlation of multi-antenna systems employing multiple polarizations," *IEEE Int. Antennas Propagation Symp. Digest*, 202–205, San Antonio, TX, Jun. 2002.
10. Stancil, D. D., A. Berson, J. P. Van't Hof, R. Negi, S. Sheth, and P. Patel, "Doubling wireless channel capacity using co-polarised, co-located electric and magnetic dipoles," *Electron. Lett.*, Vol. 38, No. 14, 746–747, Jul. 2002.
11. Andersen, J. B. and B. N. Getu, "The MIMO cube—A compact MIMO antenna," *5th Int. Symp. Wireless Personal Multimedia Communications*, 112–114, Honolulu, HI, Oct. 2002.
12. Xu, H., M. J. Gans, N. Amitay, and R. A. Valenzuela, "Experimental verification of MTMR system capacity in controlled propagation environment," *Electron. Lett.*, Vol. 37, No. 15, 936–937, Jul. 2001.

# A Simple Antenna Design of Implantable RFID based on EFAB Technology

Donghui Guo<sup>1,2</sup>, Huajun Chen<sup>1</sup>, and L. L. Cheng<sup>3</sup>

<sup>1</sup>EDA Lab, Physics Department, Xiamen University, Fujian 361005, China

<sup>2</sup>Department of Electronic Engineering, Xiamen University, Fujian 361005, China

<sup>3</sup>Electronic Engineering Department, City University of Hong Kong, China

**Abstract**— This paper is to present a new technology for implantable RFID antenna design. As implantable RFID are popularly used as active devices for animal identification, bio-medical sensor etc. Size miniature and high working efficiency are the basic requirements for these implantable devices which cause no discomforts for a body. A new MEMS process called EFAB is introduced. The implantable RFID antenna design is based on the use of micro-coil. With EFAB design rules and parameters, the simulation results have shown that we can satisfy the requirements of implantable RFID antenna.

## 1. INTRODUCTION

As the development of the micro-electronics and wireless communication technologies, the Radio Frequency Identification (RFID) [1–6] is getting mature and is widely used in different areas, especially indoor monitoring system, logistic management system and one-card-for-all payment system. Besides, for those bio-medical electronic devices that have to be implanted inside the human or animal bodies such as nervous muscular stimulators, implanted hearing aid devices etc. [7–13], they need to use passive RFID technology to achieve wireless transferring electronic signals and power. With integrating of the RFID and sensing devices, we can develop an implantable bio-medical device that can be used as an identification and physiology monitoring. On the other hand, for those RFID implanted sensing device which can obtain non-stopping energy supply without using battery or power source. Recently, the implantable RFID technology is a hot topic for researchers to work hard.

Differing than those current mature consumer RFID technologies, in order to make the RFID device to satisfy the requirements to implant devices into human or animal bodies, especially it has to satisfy the safety standards for the RFID EMC and the miniature size constraint for an implanted device. Not only to consider the absorption effects of the transmission and reception of electro-magnetic waves for animals also side-effects which hurt an animal when a device is implanted into its body. For this reason, the size of the device has to be as small as possible in order to reduce the influencing effects caused by the implanted device [14]. In addition, the device has to be communicated with the outside world within a workable distance. It is obvious that the antenna design of the RFID device is very important

This paper is trying to introduce an antenna design with a multi-layer MEMS based on EFAB technology [15]. Based on the requirements of implanted antenna, computer simulations have been done in order to design the RFID device antenna structure.

## 2. THE DESIGN REQUIREMENTS OF IMPLANTED RFID

RFID uses wireless communication technologies to achieve the data exchange between IC card and system [1]. For those international standards, such as ISO10536, ISO14443, ISO15693, ISO18000, they are working on ISM band at 135 kHz, 13.56 MHz, 433 MHz, 915 MHz and 2.45 GHz respectively. For the devices to be implanted into an animal body, we have to consider effects due to the absorption of electromagnetic wave by the organs and how it influencing to the health conditions and activities of these organs. For this reason, we intend to avoid loss or absorption of EM wave inside the body of an animal. In normal condition, the EM wave inside the animal body, the rate of attenuation or absorption of EM wave is proportional to the square root of the transmit frequency [16]. Hence, the frequencies of implanted RFID is preferable to be chosen at lower frequency bands, however, this will need a larger inductive coupling antenna. Of course, it is illogical or impracticable for an implanted device with a too big size. In this case, the working frequency for an implanted RFID is chosen at 13.56 MHz.

Lots of international companies have developed of 13.56 MHz RFID chip-products, such like, Siemens, Sony, Philips, Atmel etc. recently, the built-in capacitance of these RFID chips is in

the range of  $100 \sim 200$  pF and the external inductance needed is greater than 689 nH. (if built-in capacitance of 200 pF is assumed). For normal RFID cards, if the printed circuit technology is used and it is easy to achieve the inductance value by using a large antenna coil. However, for an implanted application, we need the size of the antenna has to be small, so we decide to use MEMS technology [17] to minimize the antenna size. There are a lot of design methods for the antenna coil [18–22], although there are differences in formulating methods for calculating the inductance value, on the whole, the inductance value of the antenna coil design is closely related to several parameters of the antenna structure, for instance, the number of turns, radius, line width and the separation between turns of an antenna coil. Therefore, this paper will base on these parameters mentioned above to design the implanted RFID antenna.

It is mainly through the coupling EM field of body antenna to the system antenna in order to perform the wireless data exchange for the implanted RFID of an animal. The performance of the data communication mainly depends on the energy coupling transmission efficiency ( $\eta_{12}$ ) between the inside-body antenna and the outside-system antenna. The  $\eta_{12}$  can be represented as shown in Equation (1) [23]:

$$\eta_{12} = \frac{1}{1 + \frac{1}{k^2 Q_1 Q_2}} \quad (1)$$

where  $Q_1$  and  $Q_2$  are the quality factor of transmitting and receiving antenna respectively,  $k$  is magnetic induction coupling coefficient.

$$k = \frac{M_{ab}}{\sqrt{L_a L_b}} \quad (2)$$

where  $M_{ab}$  is the mutual inductance coefficient,  $L_a$  and  $L_b$  are the inductance values of two antennas respectively.

It is obvious, the larger the  $Q$  factor and coupling coefficient  $k$  of the antenna, the efficiency of the antenna power will be better and the communication quality will be higher.

In this case, when the system frequency and the built-in capacitance of the RFID chip are well defined, then the inductance value  $L$  of the antenna coil will be fixed as well. For the mutual inductance coefficient  $M$ , it is mainly related to the positions of the transmitting and receiving antennas and the coefficient is depending on the antenna directions. Usually the transmitting and the receiving antenna coils are in the same axis will have a larger mutual inductance coefficient and the closer of the two antenna positions, the coupling coefficient will be larger. Therefore, our implantable RFID antenna design is mainly paying attention only to the antenna inductance value  $L$  to be chosen and also how to increase the  $Q$  factor of the antenna.

Of course, the power coupling coefficient between antennas is related to the implanted device position, depth and organization of the animal. It will change according to the EM wave power absorption of the body of a creature (SAR, Specific Absorption Rate) [16, 24, 25]. In this paper, we shall not discuss the problem due to the coupling coefficient of RFID inside body. It is our future work and detail analysis will be done in the future.

### 3. ANTENNA DESIGN BASED ON EFAB TECHNOLOGY

The miniature RF antenna is made by using the MEMS planar technology on the silicon substrate [26–28]. The antenna made by the planar technology has a disadvantage of using large silicon area and contacts to the silicon substrate will be occurred, hence the loss is high and will have a smaller  $Q$  value. The miniature of RFID antenna could not achieved with these conditions. If we adopt multilayer technology for antenna coils, less area are needed and also we can avoid contacts to the substrate, this will cause less loss hence the antenna  $Q$  factor will be increased. In this case, a new kind of MEMS technology-EFAB [15] is introduced for implanted RFID antenna design.

#### 3.1. EFAB Technology

EFAB technology is an additive micro-fabrication process based on multi-layer selective electro-deposition of metals (MEMS technology). The process is designed to help rapidly form multiple independently-patterned metal layers on top of one another. This enables designers to create intricate 3D geometries with micron-level precision. EFAB is a batch process like semiconductor manufacturing in which many devices are built simultaneously on wafers, allowing volume production at low cost. The essence of this approach is a basic three-step process that is used to generate

each layer. This repeats as many times as there are layers to build the desired complex devices. The complete flow of the EFAB technology [29] is shown in Figure 1. These steps are: (a) Patterned layer deposition; (b) Blanket layer deposition and (c) Planarization. (d) After planarization of the layer, this layer may serve as the new substrate, allowing the process cycle ('a' through 'c') repeats until the full desired height of the device is achieved; (e) Finally, after all layers are completed, a release etchant removes the sacrificial metal, leaving behind the free standing device.

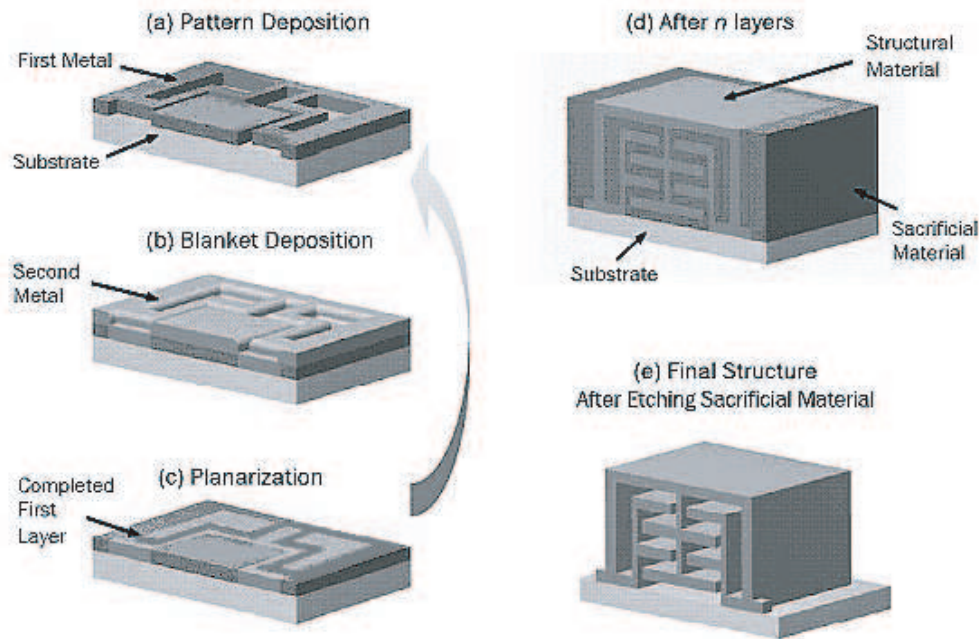


Figure 1: EFAB technology process [21].

EFAB technology at the moment can provide thickness of each layer from 2–10  $\mu\text{m}$  and it can make devices up to 20 layers or more. Multilayer structure can make device harder and bigger than the MEMS technology. EFAB technology can choose any metal which can be metal plated or alloys (for example, nickel, copper, silver, gold or nickel cobalt metal alloy etc.) to build the structure of the device, but there is a constraint condition, that is, the metal structure must not be affected after etching sacrificial material.

### 3.2. The Miniature Coil Antenna Design Method

SolidWorks is a kind of 3D graphical EDA tool and SolidWorks uses 3D mechanical design software to design and manufacture MEMS and microdevices as part of a single solution. SolidWorks software is the recommended design software for EFAB Access and enables viewing of 3D micro geometry as it will appear when fabricated in layers and the structure data file [29]. ANSOFT HFSS is an EM field analysis software tool which can output compatible SolidWorks data file format. These two software tools are used for the antenna coil miniature design in this paper.

For a dedicated area of chip size of the antenna, it can acquire the inductance value of the antenna coil by increasing the coil layers. Firstly, the single layer coil structure has to be well defined. This layer diagram is shown in Figure 2 and the top view and the cross-section layer of this layer have been shown in Figure 2(a) and (b) respectively. Among them, the line width of coil ( $w$ ), the separation between strip lines ( $s$ ) and the thickness of line ( $h$ ). The antenna adopts nickel-cobalt (the electrical resistivity  $10.5 \mu\Omega\text{-cm}$ ) material, the substrate is using alumina (the electrical resistivity is  $10^{14} \Omega\text{s-cm}$ , relative permeability is 9.9), among them, the choice of material of the antenna is providing by EFAB technology related factory [29]. The port 1 and port 2 in Figure 2(a) are the input and output ports of the antenna respectively, The calculation method of the parameters  $S$  and the admittance  $Y_{11}$  based on the two-port network [30], we can obtain the antenna value  $L$  and  $Q$ .

$$L = \text{Im}(1/Y_{11})/2\pi f \quad (3)$$

$$Q = \text{Im}(1/Y_{11})/\text{Re}(1/Y_{11}) \quad (4)$$

From the equations above, admittance parameter  $Y_{11}$  is converted from the two-port network parameter  $S$ ,  $f$  is the working frequency of the antenna coil.

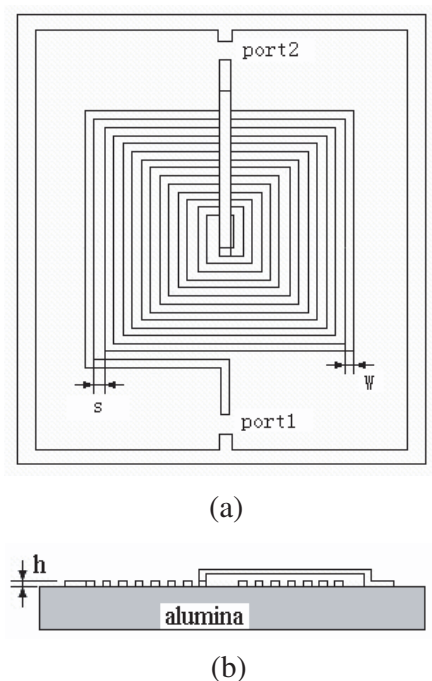


Figure 2: Configuration of the inductive coil antenna. (a) Top view diagram, (b) Cross-section diagram.

According to Equations (3) and (4), for a fixed antenna structure and a single layer antenna coil, the simulation analysis is carrying out. Firstly, the changing of the inductance values and  $Q$  values are being observed, hence the structure parameters (coil number, strip line width and strip line separations) are being fixed. After that, for two layer antenna coils, the changing of the inductance and  $Q$  values will be investigated when the separations (distances) of the layers are changing. For this we can find out the optimized separation for the two layer coils. Finally, we will obtain the decided inductance values by increasing the numbers of the coil layer.

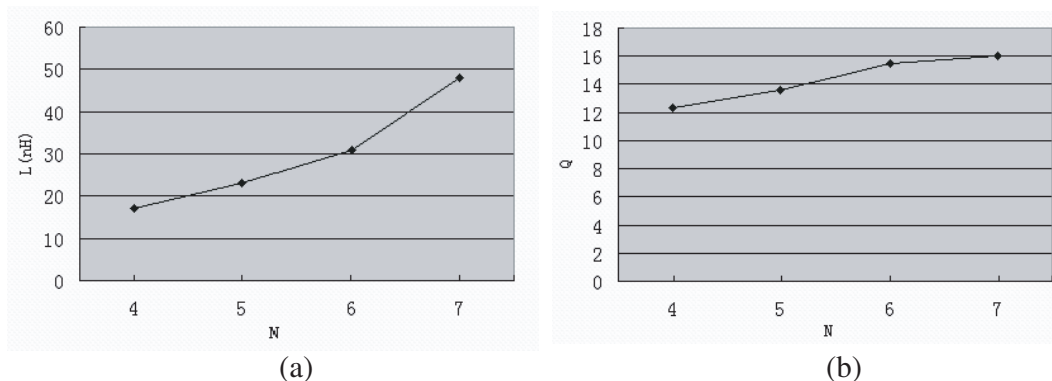


Figure 3: Inductance ( $L$ ) and quality factor ( $Q$ ) vs coil turn ( $N$ ). (a)  $N$  vs  $L$ , (b)  $N$  vs  $Q$ .

#### 4. DESIGN BY COMPUTER SIMULATION

We have to do analysis on the number ( $N$ ) of turns of the first layer inductive coil. As shown in Figure 3, the numbers ( $N$ ) of turns of the inductive coil are: 4, 5, 6 and 7 respectively. It shows the corresponding inductance values ( $L$ ) at the dedicated frequency of the coil for  $Q$  is the maximum. The design for other parameters ( $w = 50 \mu\text{m}$ ,  $s = 50 \mu\text{m}$ ,  $h = 10 \mu\text{m}$ ) of the coil are based on the data provided by EFAB for minimal size for the first layer. In Figure 3, it shows that as the number of turns of the coil increased, the values of the inductance  $L$  and  $Q$  factor are also increased. For

this reason, the decided inductance value can be obtained through the increment of the number of turns of the coil. However this will increase the area size of the coil. As shown in Figure 3(b), when the number turns of coil has increased from 6 to 7, but it has found that  $Q$  value has insignificantly increased. Hence, for a chosen area size of silicon, since we can choose the maximum number of turns of coil but we have to consider the change of  $Q$  value. As we can see  $Q$  value is close to constant after the number of turns reaches certain value.

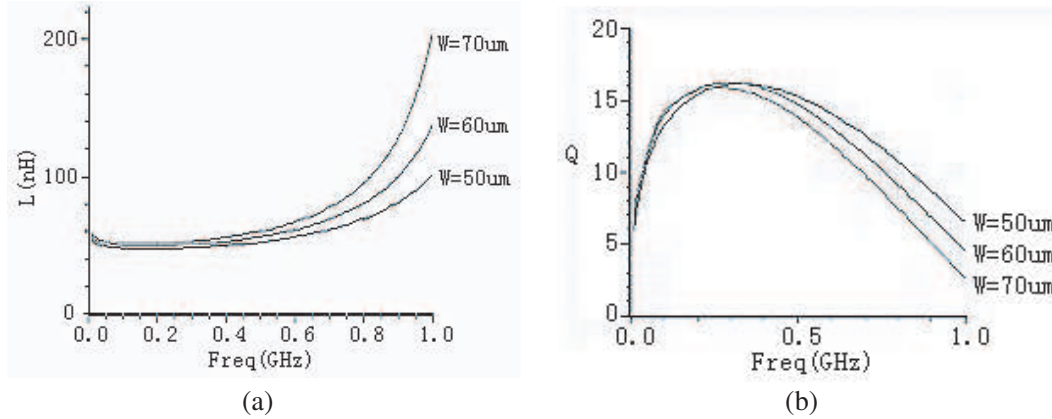


Figure 4:  $L$  and  $Q$  vs frequency with different strip width ( $w$ ). (a) Freq. vs  $L$ , (b) Freq. vs  $Q$ .

Following the number of turns of coil has fixed as  $N = 7$ , and other parameter are set to be  $s = 50 \mu\text{m}$ ,  $h = 10 \mu\text{m}$ . The strip width is changing respectively with  $50 \mu\text{m}$ ,  $60 \mu\text{m}$  and  $70 \mu\text{m}$ . Computer simulations for the structure of the antenna coil are being done. The results as shown in Figure 4, although the maximum value of  $Q$  is basically unchanged, as the frequency has been increased, the wider of the strip width will cause the  $Q$  value drops faster.  $L$  increases as the strip width  $w$  increases, but not much change when the  $Q$  is the maximum. The inductance values for maximum  $Q$  are  $48 \text{ nH}$ ,  $50 \text{ nH}$  and  $53 \text{ nH}$  respectively for  $w$  equals  $50 \mu\text{m}$ ,  $60 \mu\text{m}$  and  $70 \mu\text{m}$  respectively. As shown in Figure 3 and 4, the influence of the number of turns of the coil to the value of inductance of the antenna coil is greater than the changing of width of the strip. Therefore, in the design, usually we mainly reduce the width of the strip and increase the number of turns of the coil.



Figure 5: Cross-section view of two-layered configuration.

According to the above analysis and the required area of the antenna is  $1500 \times 1500 \mu\text{m}^2$ . Then you can obtain parameters of the first layer inductive coil as:  $N = 7$ ,  $w = 50 \mu\text{m}$ ,  $s = 50 \mu\text{m}$ ,  $h = 10 \mu\text{m}$ . One more layer will be added on top of the first layer and the coil of the new layer will use the same parameters of the first layer. The cross-section of the two-layer structure is shown in Figure 5. The separation of the two coil layers is  $t$ . When  $t$  has the value of  $10 \mu\text{m}$ ,  $20 \mu\text{m}$  and  $30 \mu\text{m}$  respectively, the coil inductance value  $L$  and  $Q$  value are shown in Figure 6. When the  $t$  become larger, the  $Q$  value is increasing as well but the  $L$  value is reducing in the corresponding frequency point. Compare with Figures 4 and 6, that is to compare a single layer coil and a double layer coil, as the number of layer increased, it increases the inductance value  $L$  and also the  $Q$  value. The effect of increase the number of layers is much better than simply increase the value of  $t$ . Therefore we set  $t = 10 \mu\text{m}$  and then increase the number of layers to get a high value of  $L$ .

Summarize the analytical results above, the final setting for the parameters of the turns of the coil as:  $N = 7$ ,  $w = 50 \mu\text{m}$ ,  $s = 50 \mu\text{m}$ ,  $h = 10 \mu\text{m}$ ,  $t = 10 \mu\text{m}$ . Totally it is the 4-layer coil structure, as shown in Figure 7. Its physical volume on the whole is:  $1500 \times 1500 \times 70 \mu\text{m}^3$ . The computer simulation has shown the inductance value of the coil as  $L = 702 \text{ nH}$  and  $Q = 18$ . These values can meet the specification requirement of the RFID system for real applications.

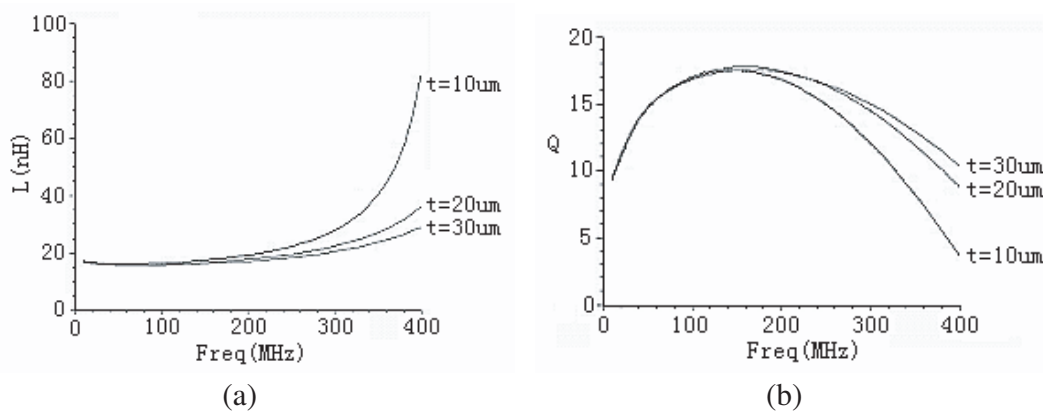


Figure 6:  $L$  and  $Q$  vs frequency with various separations between the two-layer coil. (a) Freq. vs  $L$ , (b) Freq. vs  $Q$ .



Figure 7: Cross-section view of a four-layered configuration.

## 5. CONCLUSION

In the future, it is a trend for implanted RFID technology for widely used as for animal identification. It will be used as wireless monitoring, physiology function assistance etc. However, antenna design is the major issue of the implanted RFID applications. For those biological electronic medical treatment devices implanted into the human body, it has to be physically relatively small and the power efficiency has to be high in order to transmit and receive data wirelessly. We use EFAB to design the four layer antenna coil which is mentioned above and has a size of  $1.5 \times 1.5 \times 0.07 \text{ mm}^3$ . Its inductance is 702 nH and the  $Q$  is 18. This fulfill the specification requirement for 13.56 MHz band RFID and can be used by most of the chip set produced by RFID micro-electronics in the 13.56 MHz band. For this reason, the design can be used for the need of the implanted device satisfactory.

## REFERENCES

1. Curty, J.-P., et al., *Design and Optimization of Passive UHF RFID Systems*, Springer, New York, 2007.
2. Friedman, D., H. Heinrich, and D. W. Duan, "A low-power CMOS integrated circuit for field-powered radio frequency identification tags," *Solid-State Circuits Conference, IEEE International*, 294–295, 474, 6–8 Feb. 1997.
3. Galbraith, D. C., M. Soma, and R. L. White, "A wide-band efficient inductive transdermal power and data link with coupling insensitive gain," *IEEE Trans. Biomed. Eng.*, Vol. BE-34, 265–275, 1987.
4. Troyk, P. R. and M. Edington, "Inductive links and drivers for remotely-powered telemetry systems," *Proc. Antennas and Propagation Symposium*, Vol. 1, 60–62, 2000.
5. Abrial, A., J. Bouvier, M. Renaudin, etc., "A new contactless smart card IC using an on-chip antenna and an asynchronous microcontroller," *IEEE J. Solid-State Circuits*, Vol. 36, 1101–1107, July 2001.
6. Raker, P., L. Connell, T. Collins, and D. Russell, "Secure contactless smartcard ASIC with DPA protection," *IEEE J. Solid-State Circuits*, Vol. 36, 559–565, Mar. 2001.
7. Heetderks, W. J., "RF powering of millimeter- and submillimeter-sized neural prosthetic implants," *IEEE Trans. Biomed. Eng.*, Vol. 35, 323–327, May 1988.
8. Zierhofer, C. M. and E. S. Hochmair, "High-efficiency coupling-insensitive transcutaneous power and data transmission via an inductive link," *IEEE Trans. Biomed. Eng.*, Vol. 37, 716–722, July 1990.

9. Galbraith, D. G., M. Soma, and R. L. White, "A wide-band efficient inductive transdermal power and data link with coupling insensitive gain," *IEEE Trans. Biomed. Eng.*, Vol. 34, 265–275, Apr. 1987.
10. Zierhofer, C. M., I. J. Hochmair-Desoyer, and E. S. Hochmair, "Electronic design of a cochlear implant for multichannel high-rate pulsatile stimulation strategies," *IEEE Trans. Rehab. Eng.*, Vol. 3, 112–116, Mar. 1995.
11. Liu, W., et al., "A neuro-stimulus chip with telemetry unit for retinal prosthetic device," *IEEE J. Solid-State Circuits*, Vol. 35, 1487–1497, Oct. 2001.
12. Suaning, G. J. and N. H. Lovell, "CMOS neuro-stimulation ASIC with 100 channels, scalable output, and bidirectional radio-freq. telemetry," *IEEE Trans. Biomed. Eng.*, Vol. 48, 248–260, Feb. 2001.
13. Troyk, P. R., I. E. Brown, W. H. Moore, etc., "Development of BION technology for functional electrical stimulation: Bidirectional telemetry," *Proc. 23rd IEEE-EMBS Conference*, Vol. 2, 1317–1320, 2001.
14. Troyk, P. R. and M. Edgington, "Inductive links and drivers for remotely-powered telemetry systems," *Antennas and Propagation Society Symposium, IEEE International*, Vol. 1, 60–62, 2000.
15. <http://www.microfabrica.com>, 20 Sept. 2005.
16. Durney, C. H., M. F. Iskander, H. Massoudi, etc., "An empirical formula for broad band SAR calculations of prolate spheroidal models of humans and animals," *IEEE Trans. Microwave Theory Tech.*, Vol. 27, 758–763, 1979.
17. Keith, B., *ASIC Design in the Silicon Sandbox: A Complete Guide to Building Mixed-signal Integrated Circuits*, McGraw-Hill Professional, New York; McGraw-Hill [distributor], London, 2007.
18. Ytterdal, T., Y. Cheng, and T. A. Fjeldly, *Device Modeling for Analog and RF CMOS Circuit Design*, Chichester, England; Wiley, Hoboken, NJ, 2003.
19. Burghartz, J. N., "Spiral inductors on silicon-status and trends," *International Journal of RF and Microwave Computer-Aided Engineering*, Vol. 8, Issue 6, 422–432, 1998.
20. Ruehli, A. E., "Equivalent circuit models for three-dimensional multiconductor systems," *IEEE Trans. Microwave Theory and Techniques*, Vol. 22, Issue 3, 216–221, 1974.
21. Niknejad, A. M., R. Gharpurey, and R. G. Meyer, "Numerically stable Green function for modeling and analysis of substrate coupling in integrated circuits," *IEEE Trans. CAD*, Vol. 17, Issue 4, 305–315, 1998.
22. Greenhouse, H. M., "Design of planar rectangular microelectronic inductors," *IEEE Trans. Parts, Hybrids, and Packaging*, Vol. 10, No. 2, 101–9, June 1974.
23. Hochmair, E. S., "System optimization for improved accuracy in transcutaneous signal and power transmission," *IEEE Trans. Biomed. Eng.*, Vol. 31, 177–186, Feb. 1984.
24. Hand, J. W., J. L. Cheetham, and A. J. Hind, "Absorbed power distributions from coherent microwave arrays for localized hyperthermia," *IEEE Trans. Microwave Theory and Techniques*, Vol. 34, Issue 5, 484–489, May 1986.
25. Chang, H. C. and K. K. Mei, "Penetration of a focused electromagnetic pulse into a biological material and its application to hyperthermia," *Antennas and Propagation Society International Symposium*, Vol. 1, 544–547, 26–30 June 1989.
26. Kim, Y. J. and M. G. Allen, "Surface micromachined solenoid inductors for high frequency applications," *IEEE Trans. Comp., Packag., Manufact. Technol.*, Vol. 21, 26–33, Jan. 1998.
27. Yoon, J. B., B. K. Kim, C. H. Han, etc., "Surface micromachined solenoid on-Si and on-glass inductors for RF applications," *IEEE Lett. Electron Device*, Vol. 20, 487–489, Sept. 1999.
28. Chen, Y. E., Y. K. Yoon, J. Laskar, etc., "A 2.4 GHz integrated CMOS power amplifier with micromachined inductors," *Microwave Symposium, IEEE International*, 523–526, June 2001.
29. EFAB Access Design Guide [EB/OL]. <http://www.microfabrica.com/efabaccess/designtools/EFAB%20Access%20Design%20Guide%20v1.21.pdf>, 20 Sept. 2005.
30. Koutsoyannopoulos, Y. K. and Y. Papananos, "Systematic analysis and modeling of integrated inductors and transformers in RF IC design," *IEEE Trans. Circuits and Systems II: Analog and Digital Signal Processing*, Vol. 47, Issue 8, 699–713, Aug. 2000.

## Advances in RF Bioeffect Mechanisms

Asher R. Sheppard<sup>1</sup>, Mays L. Swicord<sup>2</sup>, and Quirino Balzano<sup>3</sup>

<sup>1</sup>Asher Sheppard Consulting, Redlands, CA 92373, USA

<sup>2</sup>Motorola Inc, Ft. Lauderdale, FL 33304, USA

<sup>3</sup>Department of Electrical and Computer Engineering, University of Maryland  
College Park, MD 20742, USA

**Abstract**— This paper analyzes the many established and speculative biophysical mechanisms of interaction between RF energy and living tissue to assess the possible biological effects of exposures at or below the level of endogenous electric fields (generally, 1 to  $10^2$  V·m<sup>-1</sup>), with emphasis on conditions where temperature increases are insignificant ( $\ll$  1 K). Two RF mechanisms plausibly may affect biological matter under the exposure conditions stated above. For frequencies below approximately 150 MHz, shifts in the rate of chemical reactions can be mediated by radical pairs and at all frequencies, dielectric and resistive loss mechanisms dissipate the incident energy and increase the entropy of the affected biological system.

### 1. INTRODUCTION

The complexity of interactions of electromagnetic fields up to  $10^{12}$  Hz with the ions, atoms and molecules of biological systems has given rise to a large number of established and speculative biophysical mechanisms applicable over a wide range of time and distance scales, field amplitudes, frequencies, and waveforms. This paper focuses on the physical principles that guide quantitative assessment of mechanisms applicable for exposures at or below the level of endogenous electric fields associated with development, wound healing, and excitation of muscles and the nervous system (generally, 1 to  $10^2$  V·m<sup>-1</sup>), with emphasis on conditions where temperature increases are insignificant ( $\ll$  1 K).

### 2. BRIEF OVERVIEW OF RF MECHANISMS

Experiment and theory demonstrate possible demodulation at membrane barriers for frequencies  $\lesssim$  10 MHz, but not at higher frequencies [2]. Although signal levels somewhat below system noise can be detected, signal-to-noise ratios substantially less than 0.1 cannot be overcome by cooperativity, signal averaging, coherent detection, or by nonlinear dynamical systems. Sensory systems and possible effects on biological magnetite suggest paradigms for extreme sensitivity at lower frequencies, but there are no known radiofrequency analogues. At the molecular level, vibrational modes are so overdamped by water molecules that excitation of molecular modes below the far infrared cannot occur [6].

The hypothesis of nonlinear effects triggered by demodulation of RF carriers amplitude modulated at extremely low frequencies suffers from strong attenuation that can be theoretically evaluated and has been demonstrated experimentally. The magnitude of a demodulated electric field generated by a nonlinear mechanism can be estimated from fundamental relationships of physical electronics that show that the down conversion of the envelope of an RF carrier by its nature must attenuate the amplitude of the modulating signal. For an ideal hypothetical lossless detection process where the reverse biased nonlinear device acts as a lossless capacitor  $C$ , the attenuation of  $I$ , the current across the energy gap at a material discontinuity, is inversely proportional to the angular frequency  $\omega$  ( $= 2\pi f$ ) of the signal, that is, the gap voltage  $V(\omega) = I/j\omega C$ . Consequently, in the example of a 900 MHz carrier amplitude-modulated at 16 Hz, a perfect square law detector would attenuate the signal power at base band in the proportion 16/900,000,000, or by about 77 dB. An attenuation of 90–100 dB is more likely because of leakage losses across the hypothesized potential barrier in living tissue. For attenuation of this order, a  $10^{-3}$  W (1 mW) RF carrier 100% amplitude modulated at 16 Hz can be expected to yield a demodulated signal power of no more than  $10^{-12}$  W at the 16-Hz baseband frequency.

A recent experiment obtained measurements showing that the ELF E-field detected by a nonlinear material from an incident ELF amplitude-modulated RF electric field of  $100$  V·m<sup>-1</sup> would be no more than approximately  $3 \times 10^{-3}$  V·m<sup>-1</sup> in the ELF band [1]. Consequently, the voltage across a  $10^{-8}$  m thick membrane could be no more than  $3 \times 10^{-11}$  V. This astonishingly small signal is approximately  $10^7$  times (140 dB) smaller than the low-frequency membrane voltage noise that

limits physiologically significant events in excitable cells [3–5] and would be equally far below the cell membrane voltage noise of  $10^{-6} \text{ V}\cdot\text{Hz}^{-1/2}$  observed by Roa and Pickard [7] in the band from 1 Hz to  $10^4$  Hz. These fundamental considerations show that for any practical exposure the demodulated ELF signal that may exist across the membrane would be irretrievably lost in membrane noise.

RF magnetic fields through spin-correlated interactions between radical pairs allow for the possibility of RF effects on a variety of biological reactions involving pairs of radicals. RF magnetic field effects on a photochemical reaction yield in solution have been observed at discrete frequencies in the range 1 to 80 MHz using a  $300 \mu\text{T}$  RF magnetic field [8, 9]. The molecular hyperfine coupling constant sets the limit for energy level splitting of a radical pair causing RF resonance effects to be limited to frequencies below approximately 150 MHz.

The radical pair mechanism is due to the quantum mechanical relation between electron spins, so it escapes the limitations of S/N ratio that affect the detection of demodulated RF signals or the energy requirements that limit the effects of damped molecular vibrations.

### 3. CONCLUSION

Two mechanisms plausibly may affect biological matter under common RF exposure conditions, which are characterized by a negligible ( $\ll 1$  K) temperature increase. For frequencies below approximately 150 MHz, shifts in the rate of certain chemical reactions can be mediated by spin-coupled radical pairs independent of a temperature increase and at all frequencies dielectric and resistive loss mechanisms dissipate the incident energy and increase the entropy of the affected biological system.

### REFERENCES

1. Balzano, Q., V. Hodzic, R. W. Gammon, and C. C. Davis, "A doubly resonant cavity for detection of RF demodulation by living cells," *Bioelectromagnetics*, published on line 27 September 2007 in advance of print, 2007.
2. Barsoum, Y. H. and W. F. Pickard, "Radio-frequency rectification in electrogenic and nonelectrogenic cells of *Chara* and *Nitella*," *Journal of Membrane Biology*, Vol. 65, 81–87, 1982.
3. Billimoria, C. P., R. A. DiCaprio, J. T. Birmingham, L. F. Abbott, and E. Marder, "Neuro-modulation of spike-timing precision in sensory neurons," *Journal of Neuroscience*, Vol. 26, 5910–5919, 2006.
4. Jacobson, G. A., K. Diba, A. Yaron-Jakoubovitch, Y. Oz, C. Koch, I. Segev, and Y. Yarom, "Subthreshold voltage noise of rat neocortical pyramidal neurones," *The Journal of Physiology Online*, Vol. 564, 145–160, 2005.
5. Kole, M. H. P., S. Hallermann, and G. J. Stuart, "Single Ih channels in pyramidal neuron dendrites: properties, distribution, and impact on action potential output," *Journal of Neuroscience*, Vol. 26, 1677–1687, 2006.
6. Prohofsky, E. W., "RF absorption involving biological macromolecules," *Bioelectromagnetics*, Vol. 25, 441–451, 2004.
7. Roa R. L. and W. F. Pickard, "The use of membrane electrical noise in the study of *Characean* electrophysiology," *J. Exp. Bot.*, Vol. 27, 460–472, 1976.
8. Timmel, C. R. and K. B. Henbest, "A study of spin chemistry in weak magnetic fields," *Philosophical Transactions of the Royal Society of London A*, Vol. 362, 2573–2589, 2004.
9. Woodward, J. R., C. R. Timmel, K. A. McLauchlan, and P. J. Hore, "Radio frequency magnetic field effects on electron-hole recombination," *Physical Review Letters*, Vol. 87, 1–4, 2001.

# SAR of Wireless Communication Terminals Operated near the Human Body Using the Example of PCMCIA Data Cards

Y. Zhou, J. Streckert, H. Ndoumbè Mbonjo Mbonjo, and V. Hansen  
University of Wuppertal, Germany

**Abstract**— The objective of this study is to examine how the specific absorption rates evoked by wireless communication terminals operated near the body are influenced by e.g., the antenna topology or by the topology of the entire device or by the choice of the transmitter frequency. The influence on the communication characteristics of the devices is likewise to be regarded in this process. By means of computer simulations, four rf devices (cordless phone base station, wireless LAN router, notebook data card and Bluetooth stick) embedded in typical scenarios involving high-resolution 3D computer models of adult and adolescent persons were considered. In this respect, the present paper shows examples for notebooks with PCMCIA data cards.

## 1. INTRODUCTION

Many wireless communication terminals are operated neither in direct contact to the human body nor far away, but often at distances of some centimetres to some decimetres. Typical examples are base stations of cordless phones, wireless LAN routers and data cards for notebooks. While the human exposure to rf sources in physical contact to the body, e.g., mobile phones, on the one hand and to quasi-uniform plane waves radiated from far sources on the other hand has extensively been discussed in the community, only little is known about the effect of near-body sources. In order to fill this gap, the Federal Office for Radiation Protection has initiated a project within the framework of the German Mobile Telecommunication Research Programme entitled “Study on the influence of antenna topologies and topologies of entire devices of wireless communication terminals operated near the body on the resulting SAR values”. About 50 different scenarios are examined in the study. This paper presents examples for PCMCIA data cards.

## 2. METHODS

The exposure of a user to the radiated electromagnetic fields of wireless communication terminals is expressed by means of the specific absorption rate (SAR) within the human body

$$SAR = \frac{\Delta P_d}{\Delta m}, \quad (1)$$

where  $\Delta P_d$  is the dissipated power due to rf absorption in a biological tissue element of mass  $\Delta m$ .

Since the measurement techniques proposed so far for compliance tests are not applicable to anatomical bodies, the SAR distribution for the present context can only be determined from numerical calculations with the help of electromagnetic field solvers using computer models for the human body as well as for the communication terminals.

$$SAR = \frac{1}{2} \frac{\sigma}{\rho} |\vec{E}|^2 \quad (2)$$

$E$  denotes the peak value of the electrical field strength and  $\sigma$  and  $\rho$  the electrical conductivity (in S/m) and the density (in kg/m<sup>3</sup>) of the tissue, respectively.

From such calculations, the two important characteristic parameters, whole-body SAR and maximum localized SAR (related to 10 g tissue mass), are derived and related to the internationally recommended basic restrictions [1] for general public exposure (Table 1).

Four voxel-based anatomical body models developed from the data set of the ‘visible human project’ are used (adult and adolescent, both standing and sitting) with an inhomogeneous spatial resolution varying from 1 mm to 4 mm. Since the computer models for the terminals have to be configured with special care of the antenna design the antenna and neighboring parts are resolved with 1 mm. The models for the human body and for the terminal under test are embedded in user-typical environments comprising desk and chair (consisting of metallic frames and wooden plates) and a grounded floor, but due to the local character of the sources with respect to the SAR in the body the scenario is not surrounded by a specific room geometry. The related field problem of the total scenario is solved using a parallelized FDTD in-house code running on a multiprocessor system.

Table 1: Basic restrictions for general public exposure in the frequency range 100 kHz–10 GHz [1].

Whole-body SAR $SAR_{wb}$	Localized SAR in head and trunk (related to 10 g tissue mass) $SAR^{10g}_{trunk}$	Localized SAR in limbs (related to 10 g tissue mass) $SAR^{10g}_{trunk}$
0.08 W/kg	2 W/kg	4 W/kg

For the investigations the following widely used types of wireless communication terminals were selected based on a market analysis: PCMCIA data card for operation of GPRS, UMTS and W-LAN, Bluetooth USB adapter, W-LAN router and DECT base station. The commercially acquired terminals are taken apart in order to develop the respective computer models of the terminals. A second device of each type is used to calculate and to measure the free-space radiation diagram in order to perform a mutual quality check between theory and practice.

The field and SAR distributions as well as the radiation patterns are computed for the various scenarios and for the relevant frequencies. Hereby, the total scenario containing the radiating terminal, the human body and the nearer environment (table, chair etc.) represents an equivalent source. The resulting SAR values and the radiation characteristics serve as a reference for the following step: The topology of the terminal and/or the antenna design is modified and the effect on the SAR and on the radiation pattern is investigated.

The alteration of the gain function  $G_{scenario}(\theta, \varphi)$  and of the total radiated power  $P_{scenario}$  is taken here as a first criterion for the direction-dependent channel capacity deviation  $\Delta C(\theta, \varphi)$  between the modified and the reference scenario and thereby for the conservation of communication quality:

$$\Delta C(\theta, \varphi) = C_{mod}(\theta, \varphi) - C_{ref}(\theta, \varphi) = \log_2 \left( \frac{P_{scenario, mod} G_{scenario, mod}(\theta, \varphi)}{P_{scenario, ref} G_{scenario, ref}(\theta, \varphi)} \right) \text{ [bps/Hz]}. \quad (3)$$

Equation. (3) can be deduced from the usual channel capacity formulas (e.g., [2]) introducing far-field conditions in free space and a matched detector with a constant system noise power fairly below the received power and with an antenna optimally directed to the source at any position.

The main objective of the procedure is to find design rules for minimizing the SAR while maintaining or improving the channel capacity.

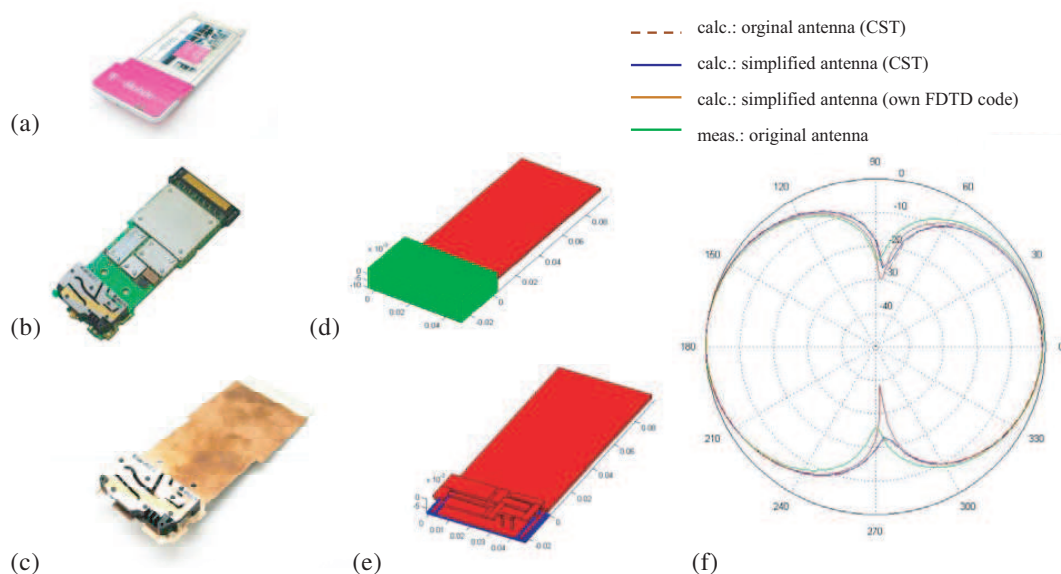


Figure 1: PCMCIA multiband data card: (a) outer view; (b) inner structure; (c) phantom card with original antenna; (d) computer model (closed); (e) computer model (open); (f) horizontal radiation pattern ( $\vartheta = 90^\circ$ ) for horizontal polarisation, comparison measurement/calculation (FIT [3]/FDTD).

### 3. RESULTS

In the following the results of three exemplary scenarios are presented involving a notebook with a PCMCIA data card as transmitter. The outer and inner view of the original card as well as a phantom card for measurement purposes (with the original antenna, but omitted electronic circuits) and the computer model are shown in Figs. 1(a)–(e). Fig. 1(f) gives a comparison of the measured and calculated radiation pattern for the card fed with a 900 MHz cw signal under free space conditions.

As a first scenario an adolescent sitting on a chair with a notebook on the lap is regarded. Fig. 2 shows the computer model of the scenario in a 3D representation (a) and a sagittal cut through the ‘visible human’ model (b). A PCMCIA data card plugged into the left side of the laptop (c) emits signals at a frequency of 900 MHz in the GPRS mode.

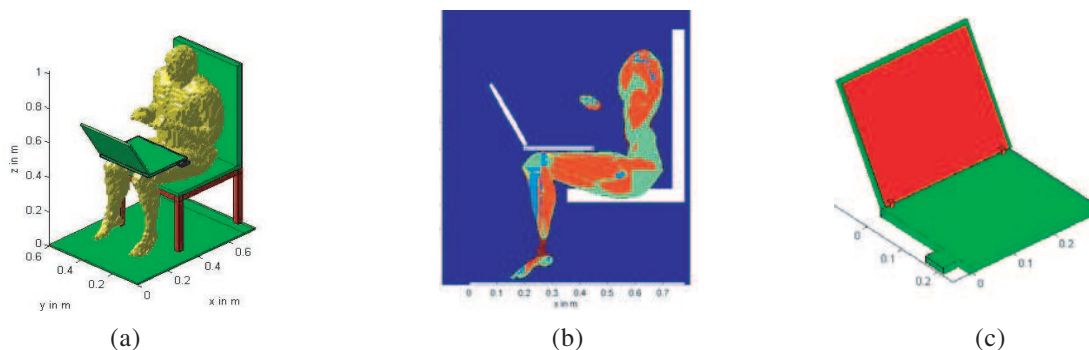


Figure 2: Sitting adolescent with laptop and PCMCIA data card in GPRS mode as rf source. (a) 3D representation; (b) longitudinal cut at  $y = 0.24$  m; (c) computer model of the laptop (red: metal kernel; green: plastic shell).

Figure 3 shows the electrical field and the SAR distribution for the same section plane as in Fig. 2(b) assuming a transmitted power of 240 mW (maximum for GPRS power class 4). It is obvious that the field penetrates the leg only in the direct neighbourhood of the transmitting antenna. Accordingly, the SAR is there at its largest. SAR values of  $SAR_{wb} = 1.93$  mW/kg and  $SAR^{10g}_{max} = 75$  mW/kg occur, whereby the maximum is related to 10 g tissue mass of cubic volume and is located at (0.43 m, 0.246 m, 0.465 m), i.e., in the upper left region of the left thigh.

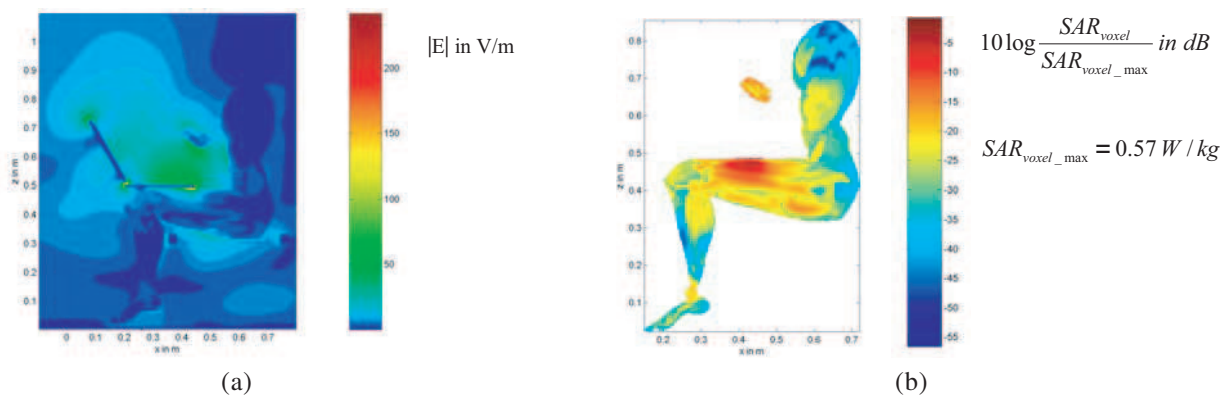


Figure 3: Electrical field distribution (a) and SAR distribution (b) in a longitudinal cut at  $y = 0.24$  m caused by the PCMCIA data card emitting at 900 MHz.  $SAR_{voxel\_max}$  refers only to the cut shown here..

The next two scenarios concern the exposure of an adult by the PCMCIA data card (GPRS mode) for two different positions of the card in the notebook. In the first case, the card is positioned at the left side of the keyboard (Fig. 4(a)), in the second case at the rear side of the display (Fig. 4(b)). The person is sitting at a desk in front of the notebook.

The comparison of the field and SAR distributions for the cut  $x = 0.73$  m is shown in Fig. 5. For the rear side position of the card (case b) in Fig. 4) the field and SAR distribution (Figs. 5(b) and (d)) is rather symmetrical while for the left side position larger values occur in the left part of the

body. The absolute SAR values are substantially lower for the rear position. The whole body SAR reduces by a factor of 5.3 (from  $625 \mu\text{W}/\text{kg}$  to  $118 \mu\text{W}/\text{kg}$ ) and the maximum of the localized SAR ( $\text{SAR}_{\text{max}}^{10\text{g}}$ ) from  $65 \text{ mW}/\text{kg}$  to  $10 \text{ mW}/\text{kg}$ . This decay can be attributed to different accounts: The larger source-body distance of 20 cm introduces a decay factor of approx. 1.8. Due to the altered feedback of the notebook in the rear position the antenna mismatch is changed causing a drop of the power radiated from the PCMCIA data card by a factor of 1.26. The largest effect (factor 2.3), however, is contributed by the shielding of the mainly metallic display of the notebook.



Figure 4: Side (a) and rear (b) position of the PCMCIA data card plugged into the notebook.

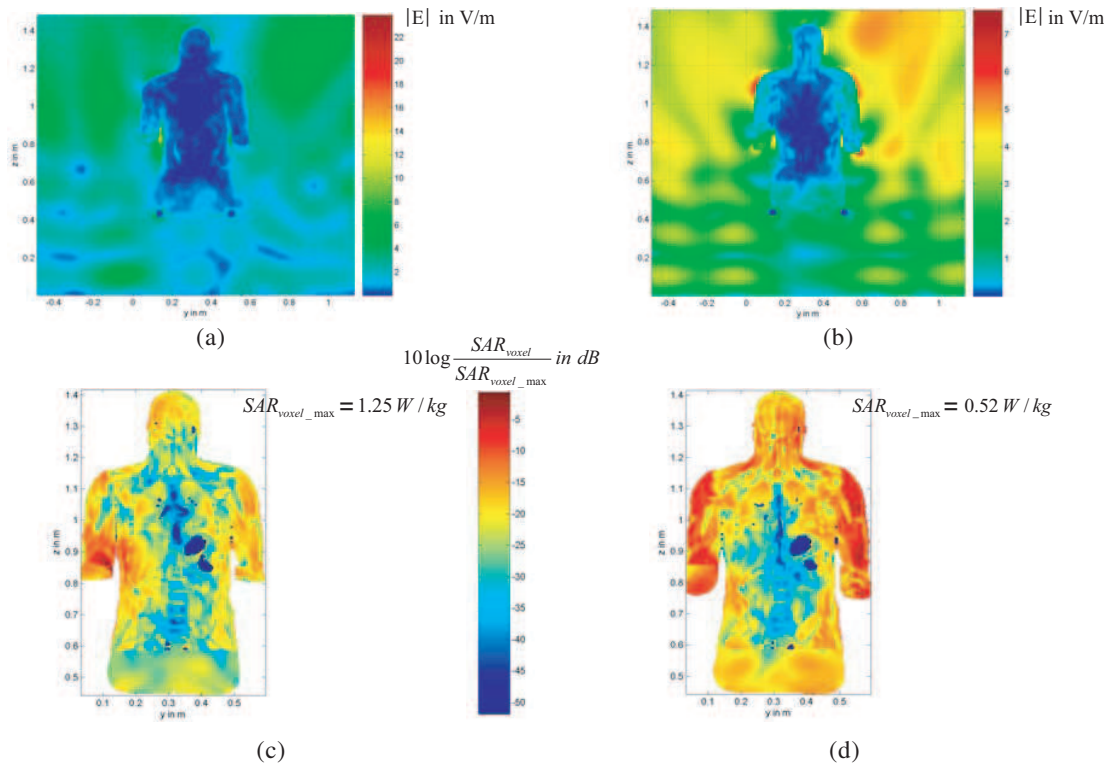


Figure 5: Electrical field (a), (b) and SAR (c), (d) distribution in the cut  $x = 0.73 \text{ m}$  (looked at from behind) for the adult exposed to a 900 MHz field from a PCMCIA data card radiating 240 mW placed in a notebook (a), (c) on the left side of the keyboard, (b), (d) on the rear side of the display.

Though the power dissipated in the shell of the notebook and in the lossy parts of the card increases by 131%, the power radiated from the modified total scenario (including body, notebook, desk, chair and earthed floor) is only 5% lower than the power for the reference scenario (side position) yielding a slight drop of the averaged channel capacity deviation  $\Delta C_{\text{avg}}$  of 0.08 bps/Hz. In Fig. 6 a colour map with the spatial dependency of the channel capacity deviation  $\Delta C(\theta, \varphi)$

defined in Eq. (3) is plotted assuming for both scenarios the same detector in the far field in free space. This plot can be used to estimate the decrease/increase of the channel capacity of a specific communication system embedded in a well-defined outer environment. Obviously, there are many directions where the channel capacity of the modified scenario  $C_{\text{mod}}(\theta, \varphi)$  exceeds  $C_{\text{ref}}(\theta, \varphi)$ . However, a final decision of the consequences for the absolute channel capacity in a user-specific transmission system can only be taken if the properties of the actual detector and the near and far environmental structures contributing to multi-path propagation are given.

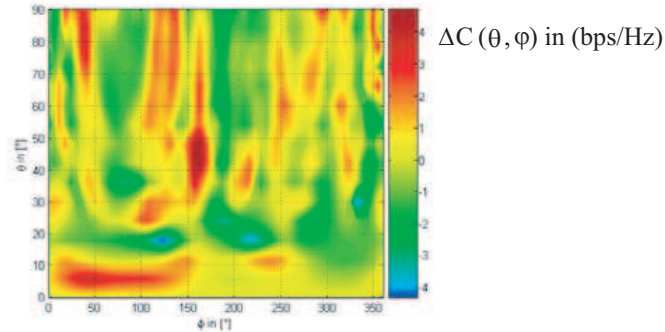


Figure 6: Channel capacity deviation  $\Delta C(\theta, \varphi)$  (cf. Eq. (3)) between the above described scenarios using the sources according to Fig. 4 ((a): reference; (b): modified).

#### 4. CONCLUSIONS

Reducing the SAR in the human body by changing the topology of wireless terminals seems to be possible without degrading the quality of communication. While the absolute SAR values for a single transmitter are usually very low compared to the basic restrictions, the increasing use of multiple sources in home and office environments justifies the request for a SAR minimisation of any contributing source.

#### REFERENCES

1. ICNIRP: "Guidelines for limiting exposure to time-varying electric, magnetic, and electromagnetic fields (up to 300 GHz)," *Health Physics*, Vol. 74, 494–522, 1998.
2. Paulraj, A., R. Nabar, and D. Gore, *Introduction to Space-time Wireless Communications*, Cambridge University Press, Cambridge, 2003.
3. CST GmbH: Microwave Studio<sup>TM</sup> Version 5.12, Darmstadt, Germany, 2005.

# An Improved Doppler Parameter Estimator for Synthetic Aperture Radar

Y. Li, H. Fu, and P. Y. Kam

Department of Electrical and Computer Engineering, National University of Singapore  
S117576, Singapore

**Abstract**— To achieve a high quality synthetic aperture radar (SAR) image, the motion caused by the radar and/or the moving target needs be compensated for coherent processing, and this requires the accurate estimation of the Doppler parameters of the received signals. A new, approximate, maximum likelihood (ML) estimator in the time domain is obtained recently to jointly estimate the Doppler parameters, and it is shown to have much better performance than that of an existing approximate ML estimator in the literature, for the values of the Doppler parameters of interest. The effects of the parameter estimation errors on the SAR system performance are analyzed. By revealing the relationship between the range/azimuth resolution of SAR imaging and the estimation accuracy of the Doppler parameters, we show that our new estimator can be applied in SAR imaging to improve the image quality.

## 1. INTRODUCTION

With the reputation of high resolution and impressive quality of image, synthetic aperture radar (SAR) has played an important role in cartography, oceanography, and numerous military applications [1]. Since the signal energy from a point target is spread in range and azimuth, the purpose of SAR focussing is to collect this dispersed energy into a single pixel in the output image. The optimum focusing of the SAR data is a space-variant and two-dimensional operation, which makes SAR processing a challenge. The most popular SAR processing algorithm is the Range-Doppler technique [2] and its variations; see [3] and [4]. The method is efficient, and in principle, solves the problems of azimuth focussing and range cell migration correction. These imaging algorithms require the accurate estimation of the Doppler parameters, namely, the centroid Doppler frequency and the frequency rate, to perform coherent processing. Our main goal here is to estimate accurately the Doppler parameters to compensate for the motion caused by the radar or the moving targets. This compensation is challenging and important for moving targets, where the motion is non-cooperative as in inverse SAR (ISAR) [5]. Without correct motion compensation, the image quality may be degraded in several ways, such as shifting, distortion, defocusing and so on. The traditional estimation for the centroid Doppler frequency and the frequency rate is usually performed separately for simplicity by using clutter-locking and autofocus technologies, respectively [6]. However, this leads to error propagation, and thus, the optimal estimator is to jointly implement clutter-locking and autofocus. The conventional joint estimation in the frequency domain [7] is a two-dimensional, nonlinear search. Unfortunately, there is still no exact, closed-form solution for solving the general nonlinear programming problem, and the search complexity is high. In this paper, we present a new, approximate, maximum likelihood (ML) estimator in the time domain. It shows that for the range of values of interest of the Doppler parameters [6], our estimator leads to a better performance than that of the only other existing approximate, ML estimator in the time domain, i.e., the Djuric-Kay (DK) estimator [8].

This paper is organized as follows. In Section 2, we first model the SAR echo response. Then, the new, approximate, ML Doppler parameter estimator for SAR Doppler signals is presented in Section 3. The effects and criteria of the estimation errors are discussed in Section 4. Numerical results in Section 5 show the better performance of our improved estimator. Finally, conclusions are given in Section 6.

## 2. MODELING OF SAR ECHO RESPONSE

Assume the SAR transmits narrowband pulses, typically the linear FM, or “chirp”, signals [6]

$$p(t) = \sum_n a(t - nT_p) \quad (1)$$

where  $a(t) = \exp[j2\pi(f_c t + K_t^2/2)]$ ,  $|t| \leq \tau_p/2$ ,  $T_p$  is the pulse repetition interval, and the summation is over the aperture time. Here,  $f_c$  is the starting frequency at  $t = 0$ ,  $K$  is the chirp rate, and  $\tau_p$

is the pulse length. The bandwidth of the transmitted signal is  $B = K\tau_p$ . An advantage of the chirp signal is that the time resolution in the matched filter output does not depend on input pulse length  $\tau_p$ , but only on the pulse bandwidth  $B$ . The geometry of the SAR is given in Fig. 1. A

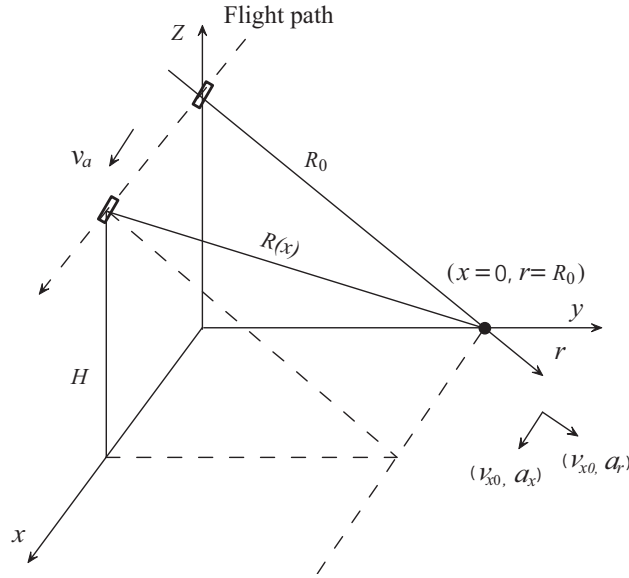


Figure 1: Geometry of SAR.

reference point on the target is assumed to be at the position  $(x = 0, r = R_0)$  at time 0, and moves with velocity components  $v_{x0}$ ,  $v_{r0}$  and acceleration components  $a_x$  and  $a_r$ . Without considering the path loss and noise, and assuming the range does not change within one pulse, the received signal in the azimuth-range domain  $(x, r)$  is

$$v(x, r) = \sum \exp \left\{ j \frac{4\pi}{\lambda} R(x) - \frac{j4\pi}{c} [f_c r + K(r - R(x))^2/2] \right\} \quad (2)$$

where  $\lambda$  is the wavelength of the transmitted SAR signals,  $R(x)$  is the range between the target and the radar at azimuth position of  $x$ , and  $c$  is the speed of light. Then, the impulse response  $h(x, r)$  is given by [4]

$$h(x, r) = h_1(x, r) \otimes h_2(x, r) \quad (3)$$

where  $\otimes$  denotes a two-dimensional convolution,  $h_1(x, r)$  and  $h_2(x, r)$  are given, respectively, by

$$h_1(x, r) = \exp \left[ j \frac{4\pi}{\lambda} r \right] \delta(r - R(x)) \quad (4)$$

$$h_2(x, r) = \frac{2}{cv_a} \delta(x) \exp[-j2\pi(f_c r + Kr^2/2)] \quad (5)$$

where  $\delta(r)$  is Dirac's delta function, and  $v_a$  is the velocity of radar. Therefore, the target can be reconstructed by sequentially correlating the return signal  $v(x, r)$  with the responses  $h_2(x, r)$  and  $h_1(x, r)$ . The correlation with  $h_2(x, r)$  is standard, referred to as the range compression. After range compression, the correlation with the two-dimensional, range-dependent, azimuth response function  $h_1(x, r)$  is more challenging, where interpolation of the discrete azimuth response over the adjacent range bins is necessary to combat the range cell migration. In most SAR scenarios, the Doppler signal of a discrete backscattering point, obtained after the range compression and range cell migration compensation, is appropriately modeled by a chirp signal [6]

$$r(k) = \alpha \exp [j(\phi + \omega_d k + \omega_r k^2/2)] + n(k) \quad k = 0, \dots, N-1 \quad (6)$$

where  $k$  is the discrete time index in the slow time domain, corresponding to the  $k$ th pulse transmission time [6]. Here,  $r(k)$  is the received Doppler signal sample,  $\alpha$  is the signal amplitude, and

$\{n(k)\}$  is a sequence of independent, identically  $\mathcal{CN}(0, \sigma^2)$  distributed, Gaussian noise samples<sup>1</sup>. The basis of the signal model in (6) is that the range  $R(x)$  can be approximated accurately by its second-order Taylor series around  $x = 0$  during the coherent processing interval, where the coefficients are the phase  $\phi$ , the centroid Doppler frequency  $\omega_d$ , and the frequency rate  $\omega_r$ , respectively. The signal model (6) is suitable for both stationary and moving targets. The feature of the targets is reflected by the variant range  $R(x)$ . When the target is stationary,  $R(x)$  is only dependent on the radar motion. When the target is moving,  $R(x)$  depends on both the velocity and acceleration rate of the moving targets and the motion of the radar. We consider  $\phi$ ,  $\omega_d$  and  $\omega_r$  as unknown but deterministic parameters. Denote  $\mathbf{p} = [\phi \ \omega_d \ \omega_r]^T$  as the parameter vector to be estimated.

### 3. ML DOPPLER PARAMETER ESTIMATION

At each time  $k = N - 1$ , we estimate the parameter vector  $\mathbf{p}$  based on all the received signal samples  $\mathbf{r} = [r(0) \ \cdots \ r(N - 1)]^T$ . Given the  $N$  sample measurements, the ML estimates are the values of  $\phi$ ,  $\omega_d$  and  $\omega_r$  that maximize the likelihood function  $p(\mathbf{r}|\phi, \omega_d, \omega_r)$ . Following our technique in [9], an approximate ML estimate of  $\mathbf{p}$  can be shown to be concisely expressed as [10]

$$\hat{\mathbf{p}}^{(N-1)} = \sum_{k=0}^{N-1} \mathbf{w}(k) \angle r(k) \quad (7)$$

where the weight vector  $\mathbf{w}(k) = [w_\phi(k) \ w_{\omega_d}(k) \ w_{\omega_r}(k)]^T$  is given by

$$\mathbf{w}(k) = \frac{1}{\Omega} \begin{bmatrix} |r(k)| \sum_{j=0}^{N-2} |r(j)| j \sum_{\tau=1}^{N-1-j} |r(j+\tau)|(j+\tau)\rho \\ - |r(k)| \sum_{j=0}^{N-2} |r(j)| \sum_{\tau=1}^{N-1-j} |r(j+\tau)|(2j+\tau)\rho \\ 2 |r(k)| \sum_{j=0}^{N-2} |r(j)| \sum_{\tau=1}^{N-1-j} |r(j+\tau)|\rho \end{bmatrix} \quad (8)$$

where  $\Omega = \sum_{k=0}^{N-1} |r(k)| \sum_{j=0}^{N-2} |r(j)| j \sum_{\tau=1}^{N-1-j} |r(j+\tau)|(j+\tau)\rho$ , and  $\rho = \tau^2[j(j+\tau) - k(2j+\tau) + k^2]$ .

From (7), we note that the estimator is a weighted linear combination of the phases of the received signal samples. It makes use of both the magnitudes and the phases of the received signals. The derivation is made under no assumption on the phase model of the received signals. Only an assumption of high signal-to-noise ratio (SNR) is made. Thus, its performance is expected to be better than that of the DK estimator, which is also an approximate, ML estimator, valid for high SNR, in which only the phase information was exploited based on an approximate phase noise model proposed in [11].

The measured phases of the received signals  $\{r(k)\}$  are their principal values, which are generated as  $\arctan \frac{r_I(k)}{r_R(k)}$ , and are all wrapped into the interval  $[-\pi, \pi)$ . Thus, phase unwrapping is necessary to obtain the absolute value of  $\angle r(k)$ . Here, the phase information  $\angle r(k)$  is obtained via the aid of the Fu-Kam phase unwrapping algorithm proposed in [9], which makes use of the continuous updating nature of the estimator (7). The algorithm makes the “best” prediction of the  $2\pi$ -phase interval for the phase at the next time point by using the parameter estimates obtained at the current time. Specifically, suppose at time point  $k$ , the estimates  $\hat{\phi}^{(k)}$ ,  $\hat{\omega}_d^{(k)}$  and  $\hat{\omega}_r^{(k)}$  have been computed from (7), respectively. We take

$$\hat{\psi}^{(k)}(k+1) = \hat{\phi}^{(k)} + \hat{\omega}_d^{(k)}(k+1) + \hat{\omega}_r^{(k)}(k+1)^2/2 \quad (9)$$

as the prediction of the phase  $\angle r(k+1)$  at time  $(k+1)$ , given the measurements up to time  $k$ . The phase of  $r(k+1)$  is then unwrapped to the value lying in the interval  $[\hat{\psi}^{(k)}(k+1) - \pi, \hat{\psi}^{(k)}(k+1) + \pi)$ . This is done by adding multiples of  $\pm 2\pi$  to the principal value of  $\angle r(k+1)$  when the absolute difference between  $\hat{\psi}^{(k)}(k+1)$  and the principal value of  $\angle r(k+1)$  is greater than  $\pi$ .

<sup>1</sup>Throughout this paper,  $\mathcal{CN}(u, \Sigma)$  denotes a complex, Gaussian random variable with mean  $u$  and variance  $\Sigma$ .  $|\cdot|$  denotes an absolute value. The subscripts  $R$  and  $I$  denote the real and image part, respectively.

#### 4. EFFECTS AND CRITERIA OF ESTIMATION ERRORS

The estimation errors in  $\omega_d$  and  $\omega_r$  can cause linear phase errors and quadratic phase errors. Assume the knowledge of  $\phi$  is available. The actual values for  $\omega_d$  and  $\omega_r$  are denoted as  $\omega_{d_0}$  and  $\omega_{r_0}$ , respectively, and the corresponding estimation errors are denoted as  $\bar{\omega}_d$  and  $\bar{\omega}_r$ , respectively. Then, the continuous estimated Doppler signal of (6) in the slow time domain is given by

$$\hat{r}(s) = \exp [j (\phi + \omega_{d_0}s + \omega_{r_0}s^2/2)] \exp [j\bar{\omega}_d s] \exp [j\bar{\omega}_r s^2/2]. \quad (10)$$

Multiplication by  $\exp[j\bar{\omega}_d s]$  means the Fourier transform of  $\hat{r}(s)$  will be shifted in the frequency domain. This leads to a displacement in the image domain. Similarly, multiplication by a phase term of quadratic phase error (QPE)  $\exp[j\bar{\omega}_r s^2/2]$  before Fourier transforming introduces a spreading out or defocusing in the frequency (imaging) domain. Uncompensated QPE is a major concern in phase error budgets for a coherent imaging system. It is common practice to use  $\pi/4$ ,  $\pi/2$  or  $\pi$  rad as an acceptable level of uncompensated QPE [12, pp. 209], depending on the applications. The effect of a  $\pi/2$  QPE broadens the resolution by 10 percent and reduces the peak intensity by 0.5 dB. Without loss of generality, we take  $\text{QPE} \leq \pi/4$  as the criterion. At the Doppler band edges, i.e.,  $s = S/2$  where  $S$  is the aperture time of SAR, for negligible mismatch we require the phase error in (10) due to a mismatch of  $\omega_r$  to be limited by

$$|\bar{\omega}_r S^2/8| \leq \pi/4. \quad (11)$$

Since the spatial resolution  $\rho_a$  in azimuth of SAR equals the product of the sensor speed  $v_a$  and the time resolution  $1 = B_D$  where  $B_D = \omega_r S/2\pi$  we have

$$|\bar{\omega}_r| \leq \frac{\rho_a^2 \omega_{r_0}^2}{2\pi v_a}. \quad (12)$$

On the other hand, the range migration caused by the uncompensated linear phase error should be limited by the range resolution  $\rho_r$ . Given the Doppler parameters  $\omega_{d_0}$  and  $\omega_{r_0}$ , the range  $R(s)$  at time  $s$  can be rewritten as

$$R(s) = R_0 - (\lambda\omega_{d_0}/4\pi)s - (\lambda\omega_{r_0}/8\pi)s^2. \quad (13)$$

If we require that  $|\lambda\bar{\omega}_d S/8\pi| \leq \rho_r$ , then we have

$$|\bar{\omega}_d| \leq \frac{4\rho_r \rho_a \omega_{r_0}}{\lambda v_a}. \quad (14)$$

From the error criteria of  $\omega_r$  and  $\omega_d$  given in (12) and (14), we can see that the estimation error in the frequency rate  $\omega_r$  affects the azimuth resolution  $\rho_a$  in a square-root mode, and the estimation error in  $\omega_d$  affects both  $\rho_a$  and  $\rho_r$  in a linear mode. Thus, the improvement in the estimation accuracy of  $\omega_d$  and  $\omega_r$  can refine both the range resolution and the azimuth resolution.

#### 5. NUMERICAL RESULTS

In this section, the numerical and simulation results of the error variances of our estimator (7) are presented, and compared with those of the DK estimator in [8]. Without loss of generality, we focus on the performances of the estimator for the frequency rate  $\omega_r$ , whose performance is evaluated by the inverse variances given by  $-10 \log_{10} E[|\hat{\omega}_r - \omega_{r_0}|^2]$  dB. The inverse Cramer-Rao lower bound (ICRLB) is given as the benchmark for comparison, and is also computed in dB. The number of simulation runs is set to  $10^6$ .

Figure 2 shows the better performance of our estimator than that of DK for the values of interest of the Doppler parameters. It can be seen that for the small value of  $\omega_{r_0} = 0.002$ , the performance of our estimator is very near the ICRLB. The threshold SNR of our estimator is only 2 dB, while it is nearly 10 dB for the DK estimator. Thus, a great performance improvement can be achieved by our new approximate ML estimator. The improved estimation of the Doppler parameters, in turn, results in a better system performance, such as a finer range and/or azimuth resolution. Alternatively, our estimator can be seen to be more power efficient as it can achieve the same the performance as that of the DK estimator, but with much lower SNR. Due to the nature of the Fu-Kam phase unwrapping algorithm, the performance of our estimator is expected to be sensitive

to the actual values taken on by the Doppler parameters to be estimated [9]. With the increase in the values taken on by the parameters, the performance of our estimator degrades. However, in practice, the values of the Doppler parameters are usually small for the satellite, airborne, or spaceborne radar, since in comparison with the radar, the radial velocity of the moving targets on the ground is small. For the case of parameters with large values, some center-frequency techniques can be used to reduce the parameter values [13], where our improved estimator has the advantage.

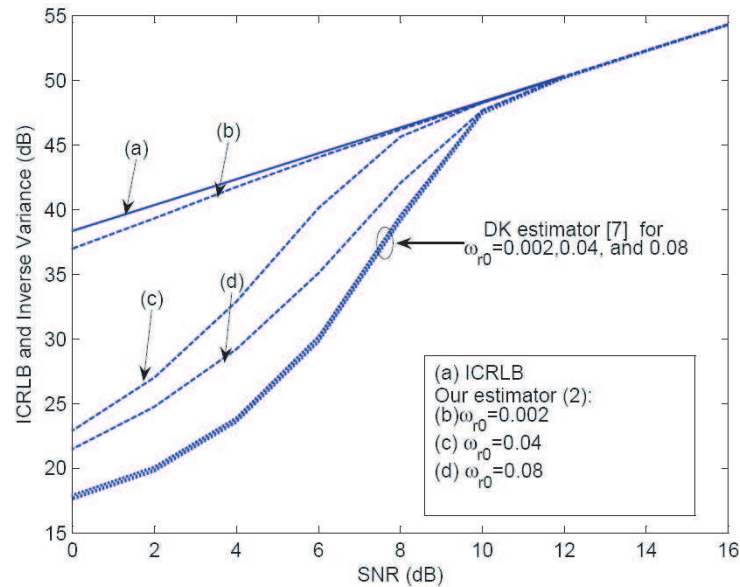


Figure 2: Performance comparison of ML-based estimators for  $\omega_r$ , with  $\omega_{d_0} = 0.05$ ,  $\phi_0 = 0.25\pi$  and  $N = 11$ .

## 6. CONCLUSION

In this paper, an improved approximate ML estimator for the chirp parameters was derived in the time domain. The estimator is promising in practice for estimating the Doppler parameters of SAR and improving its imaging quality, especially for moving targets. The effects of the estimation errors of the Doppler parameters were analyzed, and the criteria for the error limits were given. Our improved estimator can also be applied to space-time adaptive processing (STAP) to improve the target detection probability, and other applications.

## REFERENCES

1. Richards, M. A., *Fundamentals of Radar Signal Processing*, McGraw-Hill, New York, 2005.
2. Wu, C., "A digital system to produce imagery from sar data," *Proc. of the AIAA Systems Design Driven by Sensors Conference*, Oct. 1976.
3. Cumming, I. G. and J. R. Bennett, "Digital processing of seasat sar data," *Proc. of ICASSP*, 710–718, Apr. 1976.
4. Wu, C., K. Y. Liu, and M. Jin, "Modeling and a correlation algorithm for spaceborne sar signals," *IEEE Trans. Aerosp. and Electron. Syst.*, Vol. 18, 563–574, 1982.
5. Li, J., R. Wu, and V. C. Chen, "Robust autofocus algorithm for isar imaging of moving targets," *IEEE Trans. Acoustics, Speech and Signal Process.*, Vol. 37, 1056–1069, July 2001.
6. Curlander, J. C. and R. N. McDonough, *Synthetic Aperture Radar Systems and Signal Processing*, John Wiley and Sons, Inc., 1992.
7. Abatzoglou, T. J., "Fast maximum likelihood joint estimation of frequency and frequency rate," *IEEE Trans. Aerospace and Electron. Sys.*, Vol. 22, 708–715, Nov. 1986.
8. Djuric, P. M. and S. M. Kay, "Parameter estimation of chirp signals," *IEEE Trans. Acoustics, Speech and Signal Process.*, Vol. 38, 2118–2126, Dec. 1990.
9. Fu, H. and P. Y. Kam, "Map/ml estimation of the frequency of a single sinusoid in noise," *IEEE Trans. Signal Process.*, Vol. 55, 834–845, Mar. 2007.

10. Li, Y., H. Fu, and P. Y. Kam, "An improved, approximate, time-domain ml estimator of chirp signal parameters and its performance," *IEEE Trans. Singal Process.*, 2007.
11. Tretter, S., "Estimating the frequency of a noisy sinusoid by linear regression," *IEEE Trans. Info. Theory*, Vol. 31, 832–835, Nov. 1985.
12. Carrara, W. G., R. S. Goodman, and R. M. Majewski, *Spotlight Synthetic Aperture Radar: Signal Processing Algorithms*, Artech House, Boston, 1995.
13. Fowler, M. L., "Phase-based frequency estimation: a review," *Digital Signal Process.*, 590–615, Apr. 2002.

# Performance Investigation of the Flat Antenna Based on Metamaterials

Dexin Ye<sup>1,2</sup>, Lixin Ran<sup>1,2</sup>, and Jin Au Kong<sup>1,3</sup>

<sup>1</sup>The Electromagnetics Academy at Zhejiang University, Zhejiang University, Hangzhou 310058, China

<sup>2</sup>Department of Information and Electronic Engineering, Zhejiang University, Hangzhou 310027, China

<sup>3</sup>Research Laboratory of Electronics, Massachusetts Institute of Technology, Cambridge, MA 02139, USA

**Abstract**— The flat antennas made of different metamaterials including isotropic and uniaxial metamaterials are investigated. The radiation property and gain are obtained. Based on the relationship between the aperture of parabola antenna, we give a detailed instruction on the design of the flat antenna using metamaterials with proper permittivity and permeability.

## 1. INTRODUCTION

Metamaterials are a sort of artificial composite materials possessing extraordinary EM properties [1], which have excited imaginations of physicists and engineers in the past few years. As the theoretical study of metamaterials developed, more and more artificial structures are designed in which the permittivity and permeability [2] are negative, or some of them are negative. Also epsilon-near-zero and mu-near-zero materials may be properly synthesized as metamaterials at the desired frequency, by embedding suitable inclusions in a host medium [3–5]. Typical applications of these materials are perfect lenses [6] that are not limited to the usual wavelength limits by employing double negative indexes materials, and most recently, cloaks of invisibility constructed by artificially structured gradient metamaterials [7]. Antennas are also a field in which metamaterials find their amazing applications. In this paper, we discuss two kind of materials which can increase the gain of antenna. The energy radiated by a source embedded in the isotropic metamaterial slab is concentrated in a narrow cone in the surrounding media.

## 2. HORIZONTAL ELECTRIC DIPOLE (HED) IN THE ANISOTROPIC MATERIAL

The anisotropic medium is characterized by the constitutive parameters

$$\bar{\bar{\epsilon}} = \begin{bmatrix} \epsilon_{rx} & 0 & 0 \\ 0 & \epsilon_{ry} & 0 \\ 0 & 0 & \epsilon_{rz} \end{bmatrix} \quad \bar{\bar{\mu}} = \begin{bmatrix} \mu_{rx} & 0 & 0 \\ 0 & \mu_{ry} & 0 \\ 0 & 0 & \mu_{rz} \end{bmatrix} \quad (1)$$

The dispersion relation for the TE wave (the electric field is polarized in the  $y$ -direction) is

$$\frac{k_z^2}{\mu_{rx}\epsilon_{ry}} + \frac{k_x^2}{\epsilon_{ry}\mu_{rz}} = k_0^2 \quad (2)$$

While TM wave is

$$\frac{k_z^2}{\epsilon_{rx}\mu_{ry}} + \frac{k_x^2}{\mu_{ry}\epsilon_{rz}} = k_0^2 \quad (3)$$

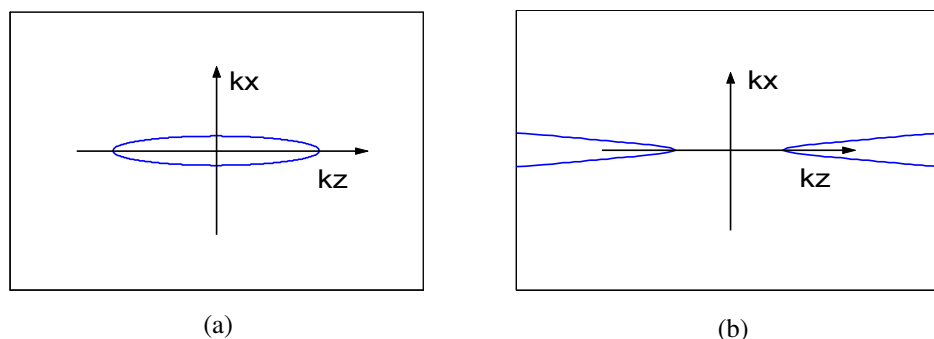


Figure 1.

If  $\varepsilon_{rx} = \varepsilon_{ry} = 1$ ,  $\mu_{rx} = \mu_{ry} = 1$  the dispersion relation become

$$k_z^2 + \frac{k_x^2}{\mu_{rz}} = k_0^2 \quad (\text{for TE}), \quad \text{and} \quad k_z^2 + \frac{k_x^2}{\varepsilon_{rz}} = k_0^2 \quad (\text{for TM}) \quad (4)$$

We can find the electromagnetic wave will propagation in a narrow channel when  $\mu_{rz}$  and  $\varepsilon_{rz}$  are near to zero. The shape of the dispersion relation only depends on the sign of  $\varepsilon_{rz}$ : it is an ellipse for positive  $\varepsilon_{rz}$  and a hyperbola for negative  $\varepsilon_{rz}$  [8, 9] as shown in Fig. 1. Therefore this material will have an important effect in focusing of the beam, which can increase the directivity of the antenna.

### 3. THE PERFORMANCE OF CYLINDRICAL WAVE IN ANISOTROPIC MATERIAL

In order to confirm this phenomenon, we use simulations to model a line source ( $z$  direction) put in the middle of the slab (2D) made of the material with above-mentioned parameter. The geometry of the slab is:  $L = 9$  (cm) ( $x$  direction  $-4.5$ – $4.5$ ),  $H = 5$  (cm) ( $y$  direction  $3.5$ – $8.5$ ) and the slab is surrounded by the isotropic material with  $\varepsilon$  and  $\mu$  are unity. The parameters of this slab are  $\varepsilon_{ry} = 1$  and  $\varepsilon_{rz} = 0.001$ , Calculated radiation patterns in  $E$ -plane are illustrated in Fig. 2. We can see that the wavelength in the slab is nearly equal to that in the air, so the wave is normal incidence with absolute matching.

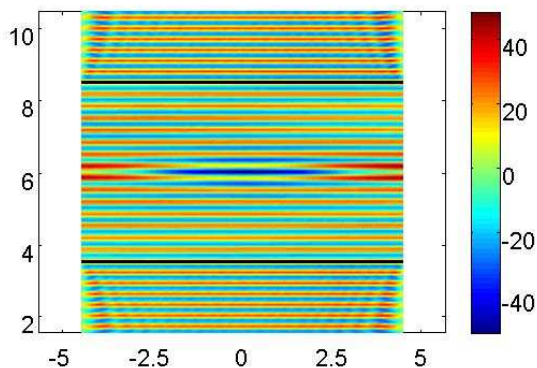


Figure 2: The performance of cylindrical wave in anisotropic material. Cylindrical wave is excited in the middle and electric field  $E$  is in the  $z$  direction.

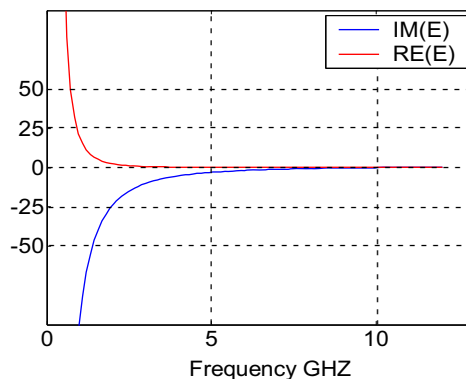


Figure 3: Drude model.

### 4. THE RADIANT PATTERN AND DIRECTIVITY OF HORIZONTAL ELECTRIC DIPOLE (HED) IN THE ANISOTROPIC MATERIAL

In the following discussion, we put a horizontal electric dipole (HED  $y$  direction) in the anisotropic material. An electric dipole is located in the middle of the slab made of the material with above-mentioned parameter. The geometry of the slab is that:  $L = 105$  (mm) ( $z$  direction),  $W = 300$  (mm) ( $x$  direction) and  $H = 300$  (mm) ( $y$  direction) and the slab is backed with a PEC. The constitutive parameters of medium are  $\varepsilon_{rz} = \mu_{rz} = 0.02i$  at the frequency of 10 GHz, we use Drude model to describe the dielectric behavior of plasma material, determined by the plasma frequency and the collision frequency representing damping effects. The Drude model is illustrated in Fig. 3, where the loss tangential is at experimental level, and the other components of  $\varepsilon$  and  $\mu$  are unity.

Calculated radiation patterns in  $H$ -plane and  $E$ -plane are illustrated in Fig. 4 and Fig. 5 and the HPBW is 3.0 degree for the  $H$ -plane and 3.0 degree for the  $E$ -plane, respectively.

### 5. FLAT ANTENNA MADE OF ARTIFICIAL STRUCTURES BASED ON AN EXTENDED S-GEOMETRY OF SPLIT-RING RESONATORS

The anisotropic metamaterial sample based on an extended  $S$ -geometry of split-ring resonators [10] is shown in Fig. 6. The elementary cell is composed of an FR4 substrate of height  $L = 10$  mm in the  $z$  direction, of thickness  $d = 1$  mm in the  $y$  direction, and of relative permittivity equal to 4.6 (measured at 10 GHz). The other dimensions of the sample are:  $w1 = 2.4$  mm,  $w2 = 1.6$  mm,

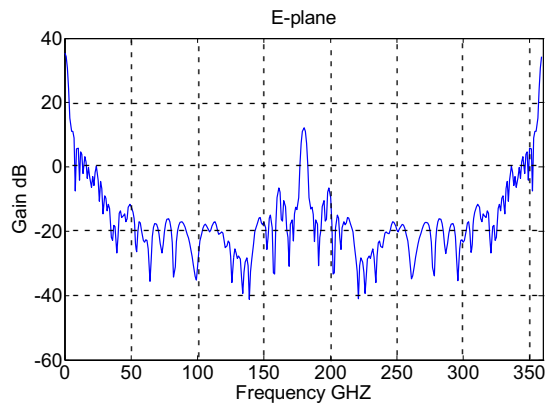


Figure 4: The simulated gain (in dB) as function of angle  $\varphi$  in  $E$ -plane.

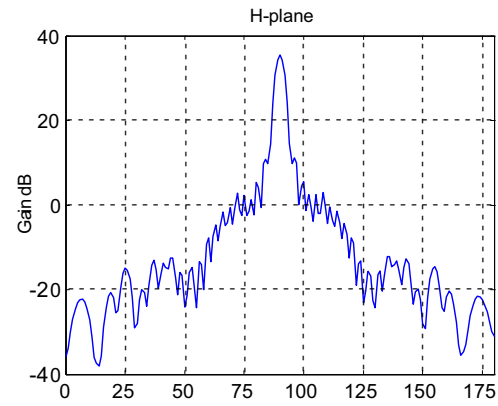


Figure 5: The simulated gain (in dB) as function of angle  $\theta$  in  $H$ -plane.

$w_3 = 3.6$  mm,  $w_4 = 0.4$  mm,  $h = 2.8$  mm, and  $c = 0.4$  mm. We can get the  $S$ -parameter as follows Fig. 7.

The structure exhibits two left-handed pass bands above 9.5 GHz, as shown in Fig. 7, where the effective permittivity and permeability have been obtained by computing the reflection coefficients and transmission coefficients of a wave normally incident on a slab of the metamaterial [11, 12] followed by a retrieval process [13], Fig. 8. We can find the  $\mu$  will be near to zero when the frequency is about 13.764 GHz.

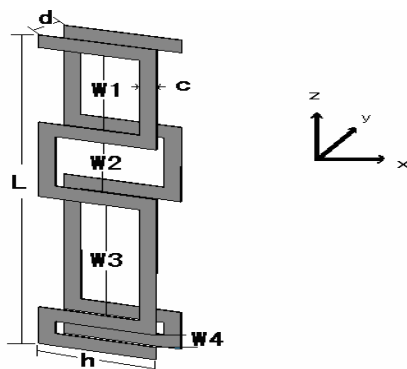


Figure 6: Definition of the parameters characterizing the unit cell of the metamaterial ( $c$  is constant for all metallizations).

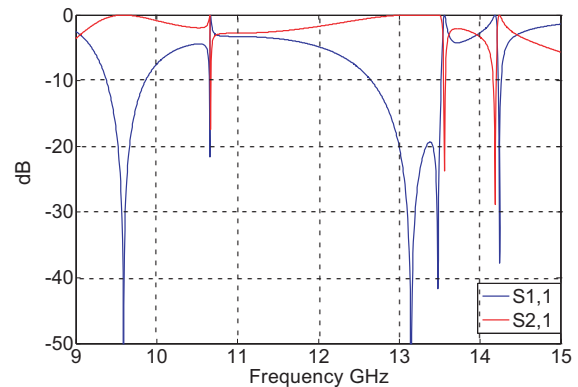


Figure 7: The  $S$ -parameters characterizing the unit cell of the metamaterial.

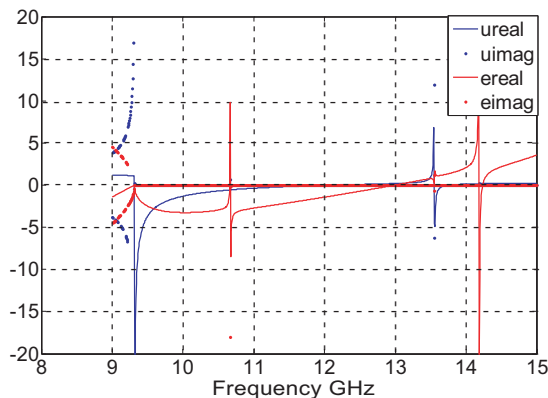


Figure 8: The retrieval parameters (refraction index).

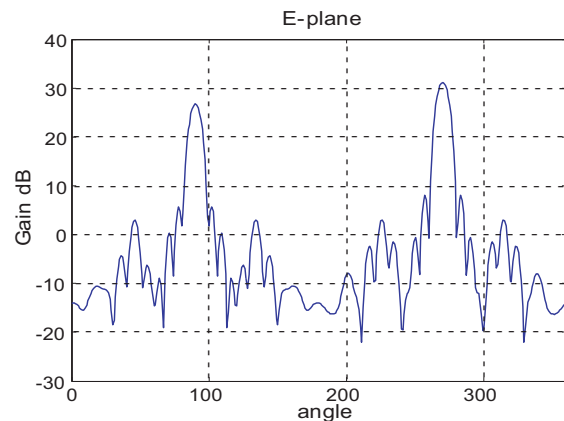


Figure 9: The simulated gain (in dB) as function of angle  $\varphi$  in  $E$ -plane in above-mentioned structure.

So we simulate this structure made of multilayer at 13.764 GHz and get the radiate pattern and the gain (in dB) as function of angle  $\varphi$  in  $E$ -plane as shown in Fig. 9. We can see that the mu-near-zero can enhance the directivity of the flat antenna largely.

## 6. CONCLUSION

In conclusion, we use an anisotropic metamaterial to realize a kind of flat antenna. Our simulation results successfully demonstrated the enhanced gain of the antenna.

## ACKNOWLEDGMENT

This work is supported by the NSFC (Nos. 60531020, 60671003), ZJNSF (No. R105253), the NCET-07-0750, and the Ph.D. Programs Foundation of MEC (No. 20070335120).

## REFERENCES

1. Veselago, V. G., *Sov. Phys. Usp.*, Vol. 10, 509, 1968.
2. Alù, A. and N. Engheta, *J. Opt. Soc. Am. B*, Vol. 23, 571, 2006.
3. Pendry, J., *IEEE Trans. Microwave Theory Tech.*, Vol. 47, 2075, 1999.
4. Smith, D., *Phys. Rev. Lett.*, Vol. 85, 2933, 2000.
5. Chen, H., L. Ran, D. Wang, J. Huangfu, Q. Jiang, and J. A. Kong, *Appl. Phys. Lett.*, Vol. 88, 031908, 2006.
6. Pendry, J. B., *Phys. Rev. Lett.*, Vol. 85, 3966, 2000.
7. Schurig, D., J. J. Mock, B. J. Justice, S. A. Cummer, J. B. Pendry, A. F. Starr, and D. R. Smith, [www.scienceexpress.org/19 October2006/10.1126/science.1133628](http://www.scienceexpress.org/19%20October2006/10.1126/science.1133628).
8. Kong, J. A., *Electromagnetic Wave Theory*, EMW, Cambridge, MA, 2000.
9. Grzegorzcyk, T. M., M. Nikku, X. D. Chen, B. I. Wu, and J. A. Kong, *IEEE Trans. Microwave Theory Tech.*, Vol. 53, 1443, 2005.
10. Chen, H., L. Ran, J. Huangfu, X. Zhang, K. Chen, T. M. Grzegorzcyk, and J. A. Kong, *Prog. Electromagn. Res.*, to be published.
11. Smith, D. R., S. Schultz, P. Markoš, and C. M. Soukoulis, *Phys. Rev. B*, Vol. 65, 195104, 2002.
12. Kong, J. A., *Prog. Electromagn. Res.*, Vol. 35, 1, 2002.
13. Chen, X., T. M. Grzegorzcyk, B.-I. Wu, J. P. Jr., and J. A. Kong, *Phys. Rev. E*, Vol. 70, 016608, 2004.

# The Prevention of Multipactor Discharge in Rectangular Waveguide Loaded with Uniaxial Metamaterial

Wanzhao Cui<sup>1</sup>, Zhiyu Wang<sup>2</sup>, Tao Jiang<sup>2</sup>  
Dongxing Wang<sup>2</sup>, Wei Ma<sup>1</sup>, and Lixin Ran<sup>2</sup>

<sup>1</sup>National Key Laboratory of Space Microwave Technology  
Xi'an Institute of Space Radio Technology, Xi'an 710000, China

<sup>2</sup>The Electromagnetics Academy at Zhejiang University  
Zhejiang University, Hangzhou 310027, China

**Abstract**— Uniaxial metamaterial is used to reduce the possibility of multipactor discharge in rectangular waveguide. Single-negative permeability metamaterial can produce both double positive and double negative passband below the cutoff frequency of the hollow waveguide, depending on the orientation of its optic axis. The metamaterial is inserted in the middle of the waveguide, repeated along the direction of the axis. The TE wave is guided in the region of the uniaxial media. In the other region around, the wave becomes evanescent and attenuates exponentially. As a result, the normal component of electric field reduces sharply near the metal boundary, which in agreement with the simulation results. So the probability of electron emission at the metal surface would decrease.

## 1. INTRODUCTION

Multipactor discharge is a resonant vacuum discharge frequently observed in microwave systems. The phenomenon of resonant secondary emission multiplication was first recognized and described by Farnsworth [1] in 1934. Intensive researches of the mechanism and the prevention of such phenomenon have been done [2–5]. The main mechanism behind the multipactor discharge is the avalanche caused by secondary electron emission. Electrons accelerated by electric fields impact a surface and release a larger number of secondary electrons. Then all the electrons may in turn be accelerated by the electric fields and made to impact again.

Waveguides containing anisotropic negative materials have unique propagation characteristics [6–8] and can provide valuable applications in prevention of multipactor discharge. In this paper, the general rules of TE and TM wave decomposition in anisotropic metamaterials will be obtained and waves in waveguides partially filled with anisotropic metamaterials will be studied in detail. The result shows normal component of electric field attenuates sharply near the metal boundary, which would help to reduce the probability of the multipactor discharge.

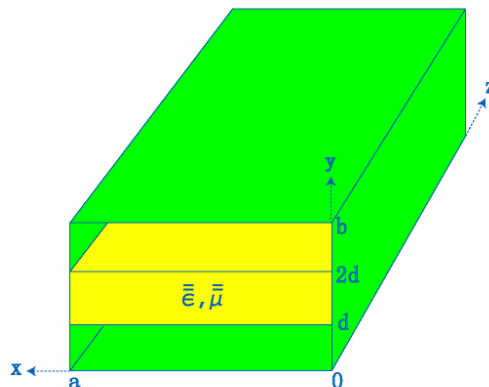


Figure 1: The structure of the model.

## 2. EXISTENCE OF MODE IN RECTANGULAR WAVEGUIDE PARTIALLY FILLED WITH UNIAXIAL METAMATERIAL

In this paper, we consider a rectangular waveguide partially filled with uniaxial metamaterial, shown in Figure 1, where the permittivity and permeability are as follows.

$$\bar{\bar{\epsilon}} = \begin{bmatrix} \epsilon_x & & \\ & \epsilon_y & \\ & & \epsilon_z \end{bmatrix} \quad (1)$$

$$\bar{\bar{\mu}} = \begin{bmatrix} \mu_x & & \\ & \mu_y & \\ & & \mu_z \end{bmatrix} \quad (2)$$

Using Maxwell Equations, we can get the Helmholtz equation. We need to do the TE and TM wave decomposition in one direction, in order to get the dispersion relation. In the following sections, we will discuss about the TE mode in  $z$  direction and TE mode in  $x$  direction.

### 2.1. TE<sub>z</sub> Mode Analysis

In TE<sub>z</sub> mode, we have  $E_z = 0$ . Then we can get the dispersion relations Eq. (3), and the restriction Eq. (4). Let  $\bar{k} = \hat{z}k_z + \hat{s}k_s$ , we write Eq. (5). Then Maxwell's two curl equations become Eq. (6). From Helmholtz equation, and considering the boundary conditions of vanishing tangential electric fields on the metallic wall surfaces, we obtain Eq. (7), where  $k_x = \frac{\pi}{a}$ . We assume  $A_2 = 1$  for simplification.

$$\begin{cases} k_z^2 = \omega^2 \epsilon_x \mu_y - k_x^2 \frac{\mu_x}{\mu_z} - k_y^2 \frac{\mu_y}{\mu_z} \\ k_z^2 = \omega^2 \epsilon_y \mu_x - k_x^2 \frac{\mu_x}{\mu_z} - k_y^2 \frac{\mu_y}{\mu_z} \end{cases} \quad (3)$$

$$\frac{\epsilon_x}{\epsilon_y} = \frac{\mu_x}{\mu_y} \quad (4)$$

$$k_z^2 = \omega^2 \epsilon_s \mu_s - \frac{\mu_s}{\mu_z} (k_x^2 + k_y^2) \quad (5)$$

$$\begin{cases} (\omega^2 \bar{\mu} \bar{\epsilon} - k_z^2) \bar{E}_s = i\omega \bar{\mu} \nabla_s \times \bar{H}_z \\ (\omega^2 \bar{\mu} \bar{\epsilon} - k_z^2) \bar{H}_s = \nabla_s \frac{\partial H_z}{\partial z} \end{cases} \quad (6)$$

$$\begin{cases} H_{z1} = A_1 \cos k_x x \cos[k_{y1}(3d - y)] e^{ik_z z} \\ H_{z2} = \cos k_x x [A_2 e^{ik_{y2} y} + B_2 e^{-ik_{y2} y}] e^{ik_z z} \\ H_{z3} = A_3 \cos k_x x \cos k_{y3} y e^{ik_z z} \end{cases} \quad (7)$$

After fulfilling the boundary conditions at  $y = d, 2d$ , the characteristic equation takes the following form, Eq. (8):

$$\frac{k_{y1}}{\epsilon_{y1}} \tan k_{y1} d + \frac{k_{y2}}{\epsilon_{y2}} \tan \frac{1}{2} k_{y2} d = 0 \quad (8)$$

where

$$\mu_{x2} = \mu_{y2} = \mu_0 \quad (9)$$

$$\epsilon_{x2} = \epsilon_{y2} = \epsilon_0$$

$$k_{y3} = k_{y1} \quad (10)$$

### 2.2. TE<sub>x</sub> Mode Analysis

In TE<sub>x</sub> mode, we have  $E_x = 0$ . Same as the TE<sub>z</sub> mode we get Eqs. (11–14).

$$k_z^2 = \omega^2 \epsilon_s \mu_x - k_x^2 \frac{\mu_x}{\mu_s} - k_y^2 \quad (11)$$

$$\frac{k_{y1}}{\epsilon_{y1}} \tan k_{y1} d + \frac{k_{y2}}{\epsilon_{y2}} \tan \frac{1}{2} k_{y2} d = 0 \quad (12)$$

where

$$\mu_{y2} = \mu_{z2} = \mu_0 \quad (13)$$

$$\epsilon_{y2} = \epsilon_{z2} = \epsilon_0$$

$$k_{y3} = k_{y1} \quad (14)$$

### 3. DETERMINATION OF $k_y$ USING ITERATIVE METHOD

In Eqs. (8) and (12),  $k_{y1}$ ,  $k_{y2}$  and  $k_z$  have not yet been found. One procedure that can be used to accomplish this will be to solve Eq. (5) or (11) for  $k_{y1}$  and  $k_{y2}$  in two different media respectively, and then substitute these expressions in Eqs. (8) and (12) [9]. The new form will be a function of  $k_z$ . Thus for a given frequency, a particular value of  $k_z$  will satisfy the new form of Eqs. (8) and (12). That value of  $k_z$  can be found iteratively. We do this using the MATLAB. The results are shown in the next section.

### 4. ANALYTICAL RESULT

In TE<sub>z</sub> mode, considering the frequency band we care (below the cutoff frequency of the hollow waveguide), and let  $a = 0.015$  m,  $b = 0.0075$  m,  $d = 0.0025$  m,

$$\mu_z = 1 + \frac{(2\pi \cdot 5 \cdot 10^9)^2}{(2\pi \cdot 5 \cdot 10^9)^2 - (1 \cdot 10^9)^2 - \omega^2} \quad (15)$$

we can get the iterative solution of  $k_z$ ,  $k_{y1}$ ,  $k_{y2}$ ,  $E_y$ , shown in the following figures. When  $\mu_z$  is

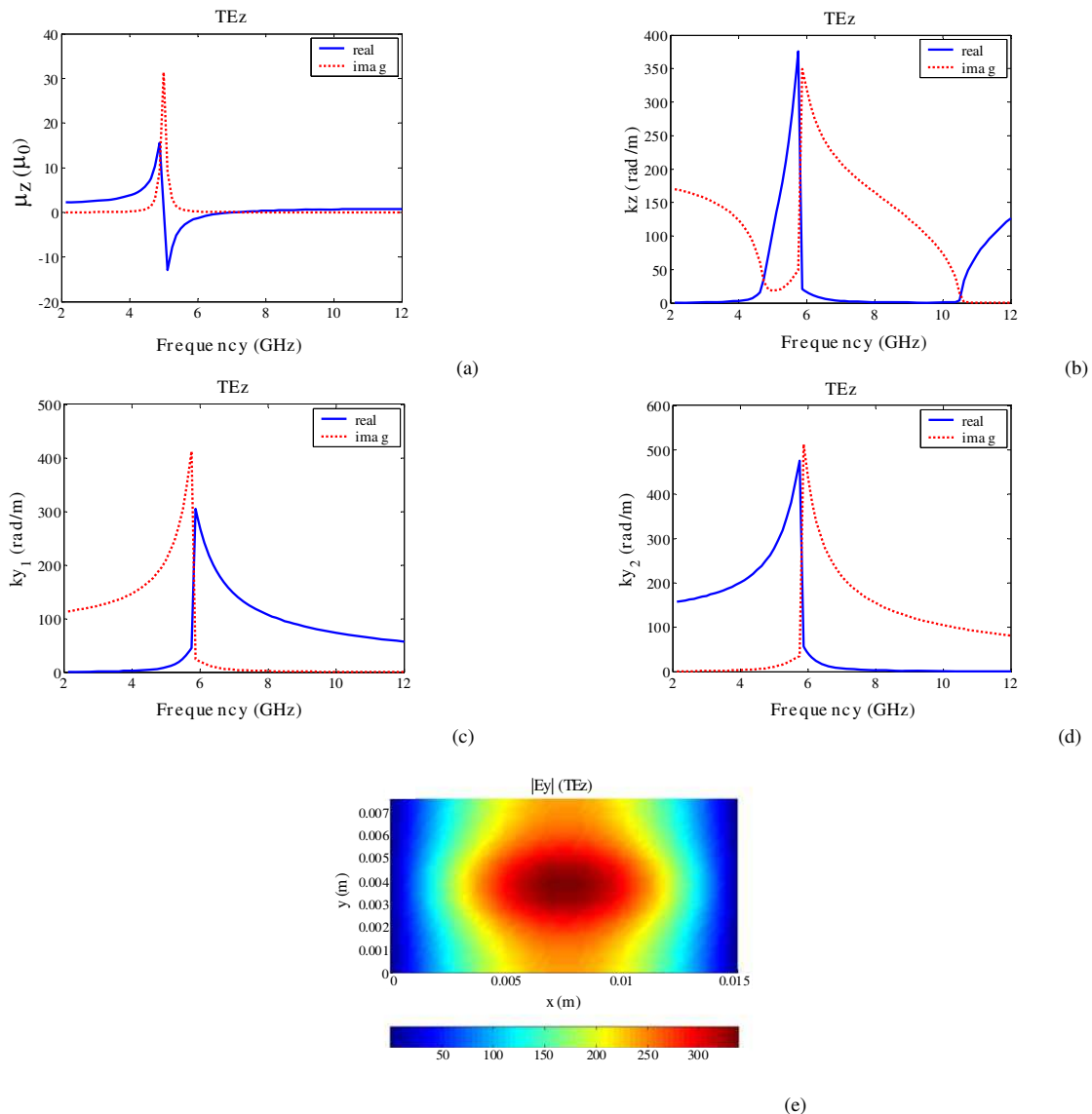


Figure 2: (a) Lorentz model of  $\mu_z$ ; (b)  $k_z$  of the TE<sub>z</sub> wave; (c)  $k_y$  in the air region; (d)  $k_y$  in the uniaxial media; (e) The distribution of the magnitude of  $E_y$  in the cross section of the partially filled waveguide.

below zero, the partially filled rectangular waveguide has a double positive passband, demonstrated

by the positive value of  $k_z$  at 5–7 GHz. Figure 2(c), (d) show that: in this frequency band, the  $y$  component of  $k$  is large in Region 2 with lower imaginary part, while close to zero in Region 1 with large consumption. Thus the TE wave is guided in the region of the uniaxial media. In the other region around, the wave becomes evanescent and attenuates exponentially.

In TEx mode, let  $\mu_x$  be the same lorentz model as above, we can also get the solution. The partially filled rectangular waveguide has a double negative passband. The large positive value of  $k_z$  appears below the resonating frequency (5 GHz) with large imaginary part, because of the imaginary part of  $\mu_x$ . The result figures are as follows. (Figure 3)

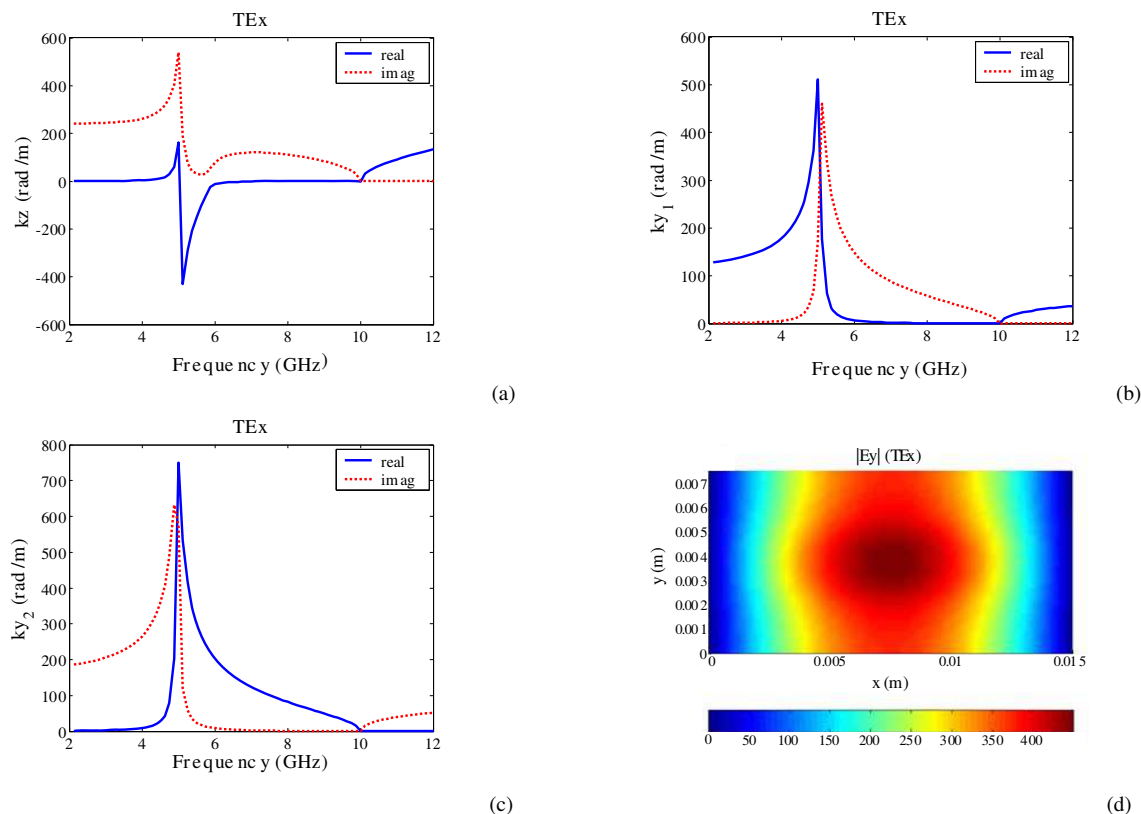


Figure 3: (a)  $k_z$  of the TEx wave; (b)  $k_y$  in the air region; (c)  $k_y$  in the uniaxial media; (d) The distribution of the magnitude of  $E_y$  in the cross section of the partially filled waveguide.

### 5. SIMULATION RESULT

To verify our results, we do the simulation of the same model in the commercial software CST. The above result matches well with the simulation one. The distribution of  $E_y$  are shown below.

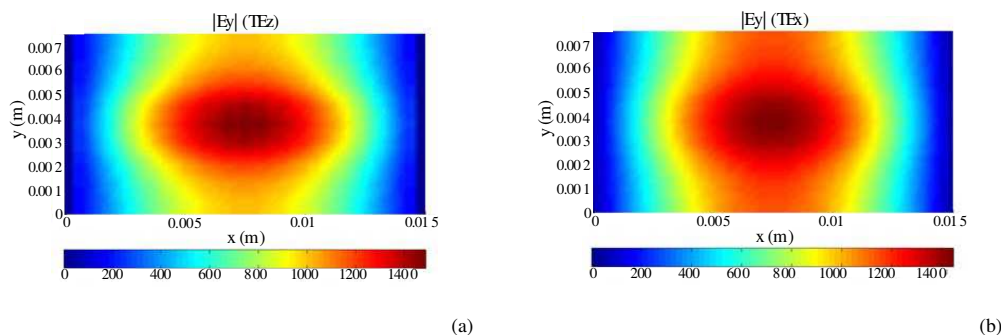


Figure 4: The distribution of the magnitude of  $E_y$  in  $z$ -cutting plane. (a) TEz mode, (b) TEx mode.

(Figure 4) We find that both the propagation directions are the same with calculation by watching the phase changing while the wave moving in  $z$  direction.

## 6. CONCLUSION

From the discussion above, we can see the normal component of electric field reduces sharply near the metal boundaries at  $y = 0$  and  $y = 3d$ . So the probability of electron emission at the metal surface would decrease. This would help to reduce the probability of the multipactor discharge.

## ACKNOWLEDGMENT

This work is supported by the National Key Laboratory Foundation (No. 9140C5304020704), the NSFC (Nos. 60531020, 60671003), ZJNSF (No. R105253), the NCET-07-0750, and the Ph.D. Programs Foundation of MEC (No. 20070335120).

## REFERENCES

1. Farnsworth, P. T., "Television by electron image scanning," *J. Franklin Inst.*, Vol. 218, 411–444, 1934.
2. Vaughan, J. R. M., "Multipactor," *IEEE Transactions on Electron Devices*, Vol. 35, No. 7, July 1988.
3. Hatch, A. J. and H. B. Williams, "Multipacting modes of high-frequency gaseous breakdown," *The Physical Review*, Second Series, Vol. 112, No. 3, November 1, 1958.
4. Torregrosa, G., A. Coves, C. P. Vicente, A. M. Perez, B. Gimeno, and V. E. Boria, "Time evolution of an electron discharge in a parallel-plate dielectric-loaded waveguide," *IEEE Electron Device Letters*, Vol. 27, No. 7, July 2006.
5. Kishek, R. A., Y. Y. Lau, L. K. Ang, A. Valfells, and R. M. Gilgenbach, "Multipactor discharge on metals and dielectrics: Historical review and recent theories," *Physics of Plasmas*, Vol. 5, No. 5, May 1998.
6. Wu, B.-I., T. M. Grzegorzcyk, Y. Zhang, and J. A. Kong, "Guided waves with imaginary transverse wave number in a slab waveguide with negative permittivity and permeability," *J. Appl. Phys.* 93, 9386–9388, 2003.
7. Xu, Y., "A study of waveguide filled with anisotropic metamaterials," *Microwave and Optical Technology Letters*, Vol. 41, No. 5, June 5, 2004.
8. Xu, H., Z. Wang, T. Jiang, D. Wang, J. Hao, J. Dai, L. Ran, J. A. Kong, and L. Zhou, "Resonance-induced transparencies of opaque waveguides: Effective-medium models for waveguides," not published yet.
9. Balanis, C. A., *Advanced Engineering Electromagnetics*, John Wiley & Sons, Inc. 395–407, 1989.

# Cloak Changing with Background

Jingjing Zhang<sup>1,2</sup>, Jiangtao Huangfu<sup>1,2</sup>, Yu Luo<sup>1</sup>  
Hongsheng Chen<sup>1,2</sup>, Jin Au Kong<sup>1,2</sup>, and Bae-Ian Wu<sup>2</sup>

<sup>1</sup>The Electromagnetics Academy at Zhejiang University  
Zhejiang University, Hangzhou 310058, China

<sup>2</sup>Research Laboratory of Electronics, Massachusetts Institute of Technology  
Cambridge, Massachusetts 02139, USA

**Abstract**— Coordinate transformation approach has previously been used for designing cloak which can shield an interior region in a homogeneous medium. In this letter, we consider the case where the background is no longer a homogeneous medium and determine the relative constitutive parameters of the cloak according to the multilayered background. We propose the parameters of cylindrical cloak structures working in multilayered media and the scheme of specifying these parameters could also be applied to the design of cloak in arbitrary isotropic background. The theoretical analysis based on coordinate transformation is given and numerical simulations are performed to illustrate these properties. The simulation results show that the cloaking with the proposed parameters performs well in these inhomogeneous background medium. Potential applications are also discussed.

## 1. INTRODUCTION

Recently the idea of using the coordinate transformation approach to design a cloak of invisibility has attracted many people [1–20]. Pendry et al., [1] first suggested that by surrounding the object to be cloaked by a metamaterial shell of spatially varying parameters, the light paths could be smoothly bent around the center of the shell so that the electromagnetic field can be excluded from the concealed volume without perturbing the exterior fields. D. Schurig et al., have shown how to calculate the material properties associated with a coordinate transformation and used these properties to perform ray tracing with detailed examples of spherical and cylindrical cloaks [2]. Full wave numerical simulations on cylindrical cloaking were presented by Cummer [3]. The interactions between EM waves and a general class of cloaks have also been analytically studied, yielding a better physical interpretation [4, 5]. The first experimental demonstration of such a cloak at microwave frequencies showing a reduced reflection and shadow [6] arouses people's interests in putting cloaking into reality and studying its applications [7–14].

To our best knowledge, all researches on cloaking reported so far have been focused on the case in which the background is one single homogeneous medium [13–20]. However, the performances of cloaking in layered media, which should be very common in real life, have not been considered. For example, sometimes we want to conceal a ship sailing in the sea. In this letter, we will study the cases when the cloak is placed at the interfaces of layered media. We focus our analysis on the two-dimensional cylindrical cloaking, but it can also be extended to the three-dimensional spherical case. By using the coordinate transformation approach presented in [2], the effective permittivity and permeability of these cloaks as a function of space are calculated. The performances of the cloaking are evaluated with simulations using finite element method (FEM), and the potential applications of these cases are discussed.

## 2. CLOAKING FOR MULTI-LAYERED MEDIA

Suppose that the Jacobian transformation matrix [2] between the transformed coordinate and the original coordinate is:

$$\Lambda_{\alpha}^{\alpha'} = \frac{\partial x^{\alpha'}}{\partial x^{\alpha}}. \quad (1)$$

The associated permittivity and permeability tensors become:

$$\varepsilon^{i'j'} = |\det(\Lambda_i^{i'})|^{-1} \Lambda_i^{i'} \Lambda_j^{j'} \varepsilon^{ij}, \quad (2a)$$

$$\mu^{i'j'} = |\det(\Lambda_i^{i'})|^{-1} \Lambda_i^{i'} \Lambda_j^{j'} \mu^{ij}. \quad (2b)$$

For an inhomogeneous media, the permittivity tensor  $\varepsilon^{ij}$  and the permeability tensor  $\mu^{ij}$  can thus be expressed in the form:

$$\varepsilon^{ij} = \varepsilon^{ij}(x^\alpha), \quad (3a)$$

$$\mu^{ij} = \mu^{ij}(x^\alpha). \quad (3b)$$

We shall express  $x^\alpha$  in terms of  $x^{\alpha'}$ , since  $x^\alpha = f(x^{\alpha'})$ , and the associated permittivity and permeability become:

$$\varepsilon^{i'j'} = |\det(\Lambda_i^{i'})|^{-1} \Lambda_i^{i'} \Lambda_j^{j'} \varepsilon^{ij}(f(x^{\alpha'})), \quad (4a)$$

$$\mu^{i'j'} = |\det(\Lambda_i^{i'})|^{-1} \Lambda_i^{i'} \Lambda_j^{j'} \mu^{ij}(f(x^{\alpha'})). \quad (4b)$$

For the following cylindrical cloak transformation which radially maps points from a radius  $\rho$  to a radius  $\rho'$  and has the identity mapping for the axial transformation, we have:

$$\rho' = \rho, \quad \theta' = \theta, \quad \text{and} \quad z' = z \quad (\text{for } \rho > R_2), \quad (5a)$$

$$\rho' = R_1 + \frac{R_2 - R_1}{R_2} \rho, \quad \theta' = \theta, \quad \text{and} \quad z' = z \quad (\text{for } \rho < R_2). \quad (5b)$$

Thus the Jacobian transformation matrix is:

$$(\Lambda_j^{i'}) = \begin{pmatrix} \frac{\rho'}{\rho} - \frac{R_1 x^2}{\rho^3} & -\frac{R_1 xy}{\rho^3} & 0 \\ -\frac{R_1 xy}{\rho^3} & \frac{\rho'}{\rho} - \frac{R_1 y^2}{\rho^3} & 0 \\ 0 & 0 & 1 \end{pmatrix}. \quad (6)$$

Now we consider the case where the axis of the cylinder is located at  $y = 0$  and the background is a two-layered medium with the interface located at  $y = d$  and parallel to  $x$  axis, as shown in Fig. 1. The permittivity and permeability of the original space can be written as:

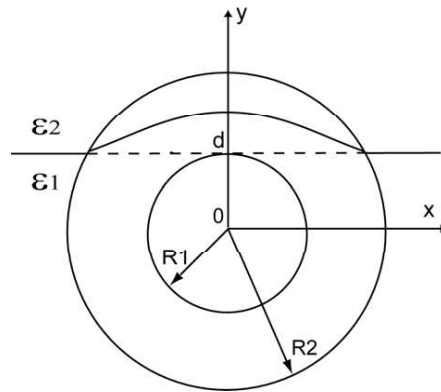


Figure 1: Simplified model to analyze the cloaking in layered background. The curve which identifies the interface of two layers inside the cloak is described by Equation 11.

$$\varepsilon^{ij} = \begin{cases} \varepsilon_1 & \text{for } y < d \\ \varepsilon_2 & \text{for } y > d \end{cases}, \quad (7a)$$

$$\mu^{ij} = \mu_0, \quad (7b)$$

or

$$\varepsilon^{ij} = \varepsilon_1 \text{sgn}(d - y) + \varepsilon_2 \text{sgn}(y - d), \quad (8a)$$

$$\mu^{ij} = \mu_0, \quad (8b)$$

where  $\text{sgn}(x)$  is defined as

$$\text{sgn}(x) = \begin{cases} 0 & x \leq 0 \\ 1 & x > 0 \end{cases}.$$

So the associated permittivity and permeability of cloaking become:

$$\varepsilon^{i'j'} = \left( \begin{array}{c} \varepsilon_1 \text{sgn} \left( d - \frac{(\rho' - R_1)R_2}{(R_2 - R_1)} \sin \theta \right) + \\ \varepsilon_2 \text{sgn} \left( \frac{(\rho' - R_1)R_2}{(R_2 - R_1)} \sin \theta - d \right) \end{array} \right) \begin{bmatrix} \frac{\rho - R_1}{\rho} & 0 & 0 \\ 0 & \frac{\rho}{\rho - R_1} & 0 \\ 0 & 0 & \left( \frac{R_2}{R_2 - R_1} \right)^2 \frac{\rho - R_1}{\rho} \end{bmatrix}, \quad (9a)$$

$$\mu^{i'j'} = \mu_0 \begin{bmatrix} \frac{\rho - R_1}{\rho} & 0 & 0 \\ 0 & \frac{\rho}{\rho - R_1} & 0 \\ 0 & 0 & \left( \frac{R_2}{R_2 - R_1} \right)^2 \frac{\rho - R_1}{\rho} \end{bmatrix}. \quad (9b)$$

It can be easily seen that because the background is layered, the cloak is divided into two parts by the interface and the parameters of the cloak in the two parts are also different. In particular, if  $d \neq 0$ , which means the cylindrical cloak is asymmetrically located at the interface, the interface inside the cloak is no longer a straight line, but a curve described as the function below, which is shown by the curve in Fig. 1:

$$d - \frac{(\rho' - R_1)R_2}{(R_2 - R_1)} \sin \theta = 0, \quad (10)$$

or

$$\rho' = R_1 + \frac{d(R_2 - R_1)}{R_2 \sin \theta}. \quad (11)$$

From Equation 10, if  $d = 0$ , we have two solutions:  $\rho' = R_1$  or  $\theta = k\pi$ , and the solution  $\theta = k\pi$  corresponds to a straight line along the original interface. It means that in the case where the cloak is placed symmetrically at the interface of a two-layered medium, we could simply choose the parameters with respect to the backgrounds in the two equal halves in the configuration of the cloaking setup.

For a multi-layered case, the function of the curved interface inside the cloak can be obtained in the same way and is expressed as follows:

$$\rho'_i = R_1 + \frac{(R_2 - R_1)d_i}{R_2 \sin \theta}, \quad (12)$$

where  $d_i$  corresponds to the location of the  $i$ th layer.

We now use finite element based numerical simulation to study the cloaking performance. The simulation quantities are normalized to unity and all domain boundaries are perfectly matched layers to prevent reflections. The operating frequency is 2 GHz. The inner radius of the cloak is 0.1 m while the outer radius is 0.2 m in all the simulations and we only consider TE polarization. The axis of the cylinder is located at  $x = 0$  m,  $y = 0$  m and is in the  $z$  direction. Fig. 2 illustrates the effects of cloaking for 4 different cases where the interface between the two media is at  $y = 0$  m, which separates the cylinder into two equal halves. The arrows indicate the directions of incidence. Sub figures (a), (b), (c), and (d) show the electric field distributions of the original space when a Gaussian beam is incident on the interface in four different situations. (a) corresponds to a normal incidence from air to Teflon ( $\varepsilon_r = 2$ ); (b) corresponds to an oblique incidence from air to Teflon with an incident angle of 45 degree; (c) shows the case where a Gaussian beam is obliquely incident from a denser medium (with a permittivity of 4) to air with an incident angle of 45 degree. In this case, the electromagnetic wave is reflected completely due to total internal reflection. In (d), we add a PEC (perfect electric conductor) sheet at the interface of air and Teflon and observe the electric field distribution. Next we place a cloaked cylinder at the interface in the aforementioned way and simulate the field distributions in the four cases corresponding to (a), (b), (c), and (d). The parameters of the cloak are defined in Equation 9. Compared with the original electric field distribution shown in (a), (b), (c), and (d), the directions of the transmitted and reflected beams appear undisturbed after passing the cylindrical shells, which are shown in (e), (f), (g), and (h). The scattering introduced by the cloaking is very small, which could be attributed to numerical artifacts. However, sometimes we are only able to cover the object with half of the shell. For instance, if we want to hide a building on the ground, we might only be able to cover the part above the ground. From the example shown in Fig. 2(k) (l), we find that if the ground can be considered as PEC or total reflection occurs at the interface, then the scattering of the obstacle is

still greatly reduced with only half of the cloak shell. But if the ground cannot be considered as a PEC at certain frequency range, i.e., significant reflection and transmission occurs at the interface, then covering the object with only half of the cloak is not enough to conceal it, which is shown in Fig. 2(i) (j).

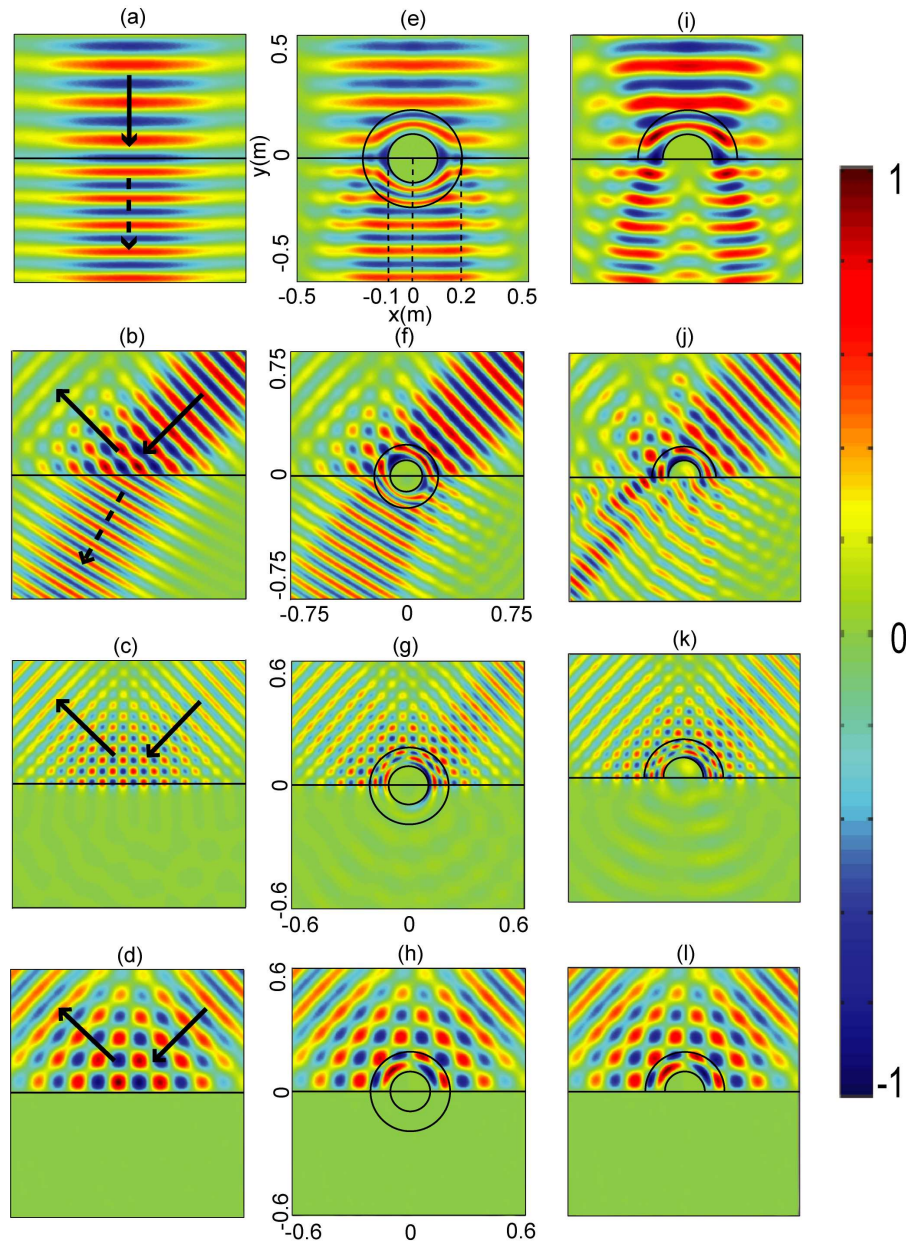


Figure 2: (a) A Gaussian beam normally incident from air to Teflon. (b) A Gaussian beam obliquely incident from air to Teflon with an incident angle of 45 degree. (c) A Gaussian beam incident from a material (with permittivity 4) to air. Total reflection occurs for an incident angle of 45 degree. (d) A Gaussian beam incident from air onto a PEC boundary. (e) The electric field distribution when a cloak is placed symmetrically at the interface of case (a). (f) The electric field distribution when a cloak is placed symmetrically at the interface of case (b). (g) The electric field distribution when a cloak is placed symmetrically at the interface of case (c). (h) The electric field distribution when a cloak is placed symmetrically at the interface of case (d). (i) The electric field distribution when the obstacle in case (e) is covered by only half of the cloak. (j) The electric field distribution when the obstacle in case (f) is covered by only half of the cloak. (k) The electric field distribution when the obstacle in case (g) is covered by only half of the cloak. (l) The electric field distribution when the obstacle in case (h) is covered by only half of the cloak.

### 3. DISCUSSIONS AND APPLICATIONS

The study of cloaking when the background media is no longer homogeneous is very useful in practical situations. For example, we may want to conceal an object which is placed in layered media or at the interface of two different materials, like a ship in the sea. From the simulation, we can see that by wrapping the obstacle with a cloak shell, it can be invisible to electromagnetic observations. But if we are only able to cover half of the obstacle, invisibility will not be obtained except under certain condition.

### 4. CONCLUSION

The parameters for cloaking in layered media and gradually changing media are studied theoretically in this paper and numerical simulations are done to demonstrate the performances of cloaking in different related cases. The scheme of obtaining the parameters can be applied in the design of cloaking in arbitrary isotropic background. And the applications of different cases in practical situations are discussed.

### ACKNOWLEDGMENT

This work is sponsored by the Chinese National Science Foundation under Grant Nos. 60531020, 60671003 and 60701007, the NCET-07-0750, the ZJNSF (R105253), the Ph.D. Programs Foundation of MEC (No. 20070335120), the ONR under Contract No. N00014-01-1-0713, and the Department of the Air Force under Air Force Contract No. F19628-00-C-0002.

### REFERENCES

1. Pendry, J. B., D. Schurig, and D. R. Smith, *Science*, Vol. 312, 1780, 2006.
2. Schurig, D., J. B. Pendry, and D. R. Smith, *Opt. Express*, Vol. 14, 9794, 2006.
3. Cummer, S. A., B.-I. Popa, D. Schurig, D. R. Smith, and J. B. Pendry, *Phys. Rev. E*, Vol. 74, 036621, 2006.
4. Chen, H., B.-I. Wu, B. Zhang, and J. A. Kong, *Phys. Rev. Letts.*, Vol. 99, 063903, 2007.
5. Zhang, B., H. Chen, B.-I. Wu, Y. Luo, L. Ran, and J. A. Kong, *Phys. Rev. B*, Vol. 76, 121101(R), 2007.
6. Schurig, D., J. J. Mock, B. J. Justice, S. A. Cummer, J. B. Pendry, A. F. Starr, and D. R. Smith, *Science*, Vol. 314, 5801, 2006.
7. Cai, W., U. K. Chettiar, A. V. Kildishev, and V. M. Shalaev, *Nature Photonics*, Vol. 1, 224–227, 2007.
8. Cummer, S. A. and D. Schurig, *New J. Phys.*, Vol. 9, No. 3, 2007.
9. Rahm, M., D. Schurig, D. A. Roberts, S. A. Cummer, and D. R. Smith, eprint arXiv: 0706.2452, 2007.
10. Chen, H. and C. T. Chan, *Appl. Phys. Letts.*, Vol. 90, 241105, 2007.
11. Sihvola, A., *Progress In Electromagnetics Research*, RIER 66, 191–198, 2006.
12. Rahm, M., S. A. Cummer, D. Schurig, J. B. Pendry, and D. R. Smith, eprint ArXiv: 0711.1846, 2007.
13. Smolyaninov, I. I., Y. J. Hung, and C. C. Davis, eprint ArXiv 0709.2862, 2007.
14. Yaghjian, A. D. and S. Maci, eprint ArXiv 0710.2933, 2007.
15. Cai, W., U. K. Chettiar, A. V. Kildishev, and V. M. Shalaev, *Appl. Phys. Letts.*, Vol. 91, 111105, 2007.
16. Ruan, Z., M. Yan, C. W. Neff, and M. Qiu, *Phys. Rev. Letts.*, Vol. 99, 113093, 2007.
17. Yan, M., Z. Ruan, and M. Qiu, eprint ArXiv 0706.0655, 2007.
18. Zolla, F., S. Guenneau, A. Nicolet, and J. B. Pendry, *Opt. Letts.*, Vol. 32, 9, 2007.
19. Wood, B. and J. B. Pendry, *J. Phys.*, Vol. 19, 076208, (9pp), 2007.
20. Hendi, A., J. Henn, and U. Leonhardt, *Phys. Rev. Letts.*, Vol. 97, 073902, 2006.

# Electromagnetic Absorption by Metamaterial Grating System

Xiaobing Cai and Gengkai Hu

School of Science, Beijing Institute of Technology, Beijing 100081, China

**Abstract**— Total absorption of electromagnetic waves is demonstrated in a system composed of zero-order metamaterial grating and rearward metamaterial wall. The grating and the wall are separated by an air gap. Two mechanisms are shown to account for this absorption. The first one is due to the existence of standing waves in both the grooves of the grating and the air gap. These standing waves trap the electromagnetic waves and induce an oscillating surface charge density on the grating surface. The second one is due to surface plasmons at the interface between the air gap and metamaterial wall, the width of the air gap is a key parameter for the total absorption.

## 1. INTRODUCTION

Recently, metamaterial is under an intense study due to its potential applications, such as imaging [1], cloaking [2, 3]. In this paper, we will discuss the possibility of using metamaterial grating as microwave absorbing structures. It is well known, surface waves can be excited and propagate along the interface between two media with opposite permittivity (or permeability) [4]. The surface wave decays exponentially on either side of the interface, so by carefully choosing the damping factor of the metamaterial, the incident energy can be confined and dissipated. However, surface wave cannot be directly excited by a propagating wave. Usually two methods are used to remedy this, one way is to utilize the attenuated total reflection (ATR) setup [5], the other makes use of diffraction grating [6]. The principle of the two methods is firstly to transform the propagating wave into evanescent one, and then the evanescent wave excites in turn surface waves at interface under proper condition. If another metamaterial is placed behind the grating separated by an air gap, the transformed evanescent wave can then excite surface waves at the interface between the air and the rearward metamaterial, leading to energy dissipation. This principle may provide a new absorption mechanism, so the objective of this paper is to illustrate in detail the interaction mechanism between a metamaterial grating and a metamaterial wall separated by an air gap.

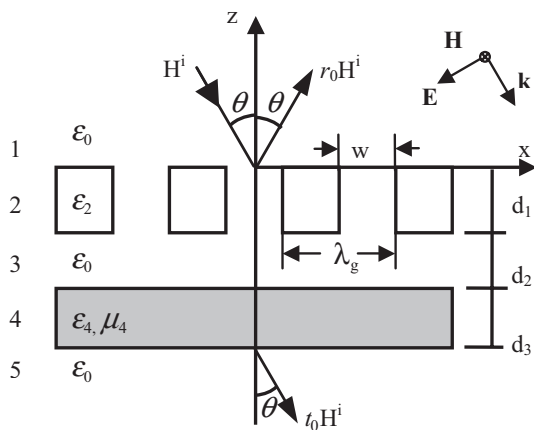


Figure 1: Configuration of the proposed microwave absorbing structure. (1) vacuum, (2) metamaterial diffraction grating, (3) air gap, (4) metamaterial, (5) vacuum.

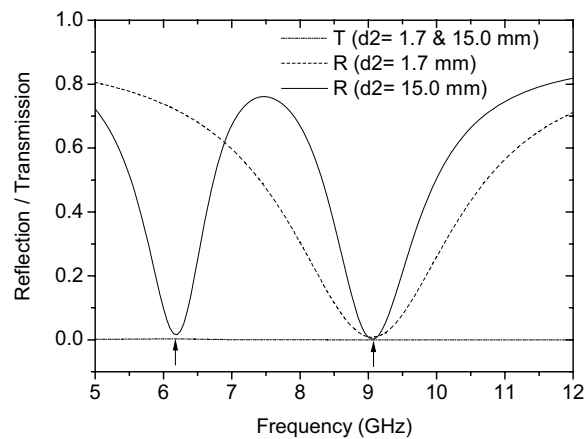


Figure 2: The reflectance and transmittance of the diffraction grating back with a negative permittivity metamaterial for different values of  $d_2$  (i.e., width of the air gap). Total absorptions take place at 6.1 GHz and 9.05 GHz, respectively.

## 2. REFLECTION OF THE FIVE-LAYER GRATING SYSTEM

The sketch of the proposed model is shown in Figure 1, we have a five-layer system. A diffraction grating (layer 2) made of a metamaterial is placed in front of another homogenous metamaterial (layer 4). An air gap separates the grating from the metamaterial. The grating is constructed by

periodically arranging metamaterial strips in vacuum with a period  $\lambda_g$ . The propagating wave is incident to the grating from the upper half space at a random angle  $\theta$ . For simplicity, the grating vector lies in the  $x$  direction, and the normal to the grating plane coincides with  $z$  direction, as shown in Figure 1. Basically the metamaterial can be chosen freely, either dielectric or magnetic. As for the  $p$ -polarized wave shown in Figure 1, the ridge of the grating is taken to be a metamaterial with a negative dielectric constant, while the metamaterial of the layer 4 can have negative permittivity, negative permeability or both simultaneously (LHM) [7]. To obtain the electromagnetic diffraction properties for the grating structure, the widely recognized rigorous coupled-wave analysis (RCWA) can be used [8], which is highly efficient for the investigation of the binary grating.

Due to the surface plasmon polariton excitation, gratings can exhibit absorption anomalies [9, 10], these gratings are mainly etched on a metal sheet, corresponding to the situation  $\varepsilon_2 = \varepsilon_3 = \varepsilon_4 = \varepsilon_5$  in Figure 1. Since the surface plasmon can only be excited when the incident wavelength equals to the grating period, the bandwidth of the absorption in the frequency spectrum due to surface plasmon are therefore limited. However, the grating can also support the waveguide modes [11–13], in this case, the bandwidth of the absorption can be expected to extend much wider than that due to the surface plasmon mechanism. This may make the grating as an efficient mechanism for microwave absorption.

Figure 2 shows the reflection and transmission curves for two grating structures with different air gaps  $d_2 = 1.7$  mm and  $d_2 = 15.0$  mm, respectively. We assume  $\theta = 0$  in the following analysis, except mentioned else. The material parameters of the grating and the rearward metamaterial are chosen to be nondispersive:  $\varepsilon_1 = \varepsilon_3 = \varepsilon_5 = 1$ ,  $\varepsilon_2 = -25.0 + 6.0i$ , and  $\varepsilon_4 = -1.0 + 0.1i$ . The structural parameters are taken as:  $\lambda_g = 10.0$  mm,  $w = 1.5$  mm,  $d_1 = 10.0$  mm, and  $d_3 = 30.0$  mm.

It is found that when the air gap is relatively small ( $d_2 = 1.7$  mm), the greatest absorption with the minimum reflection appears at 9.05 GHz. At this frequency, no energy is found to travel forward in the region 5, since the transmittance is kept as low as  $10^{-5}$  as compared to the norm of the incident wave. The result also show that the increase of  $d_3$  can even reduce the transmission in the region 5, with little interference to the reflection waves in the region 1. For the air gap  $d_2 = 15.0$  mm, two absorption peaks with low transmissions appear at 6.2 GHz and 9.05 GHz, respectively. The reason for these phenomena is due to the formation of wave guide mode in the air gap, this will be explained in detail in the following.

### 3. ABSORPTION DUE TO WAVEGUIDE MODES

It is shown previously that the width of the air gap is an important parameter to control the reflectance and transmittance properties of the system. Figure 3 gives the variation of reflection as function of the width of the air gap for the incident wave of 6.2 GHz and 9.05 GHz, respectively, the other parameters are kept unchanged. It's interesting to note that the reflectance varies periodically with increasing the width of the air gap. Except the first minimum reflection point, the intervals between the two adjacent minimum reflections equal exactly to the half of the incident wavelength, i.e., 16.6 mm and 24.2 mm for the two considered frequencies, respectively.

Figure 4 shows the variations of  $|\mathbf{H}(x, z)|$  as function of  $x$  and  $z$  over 5 periods of the grating

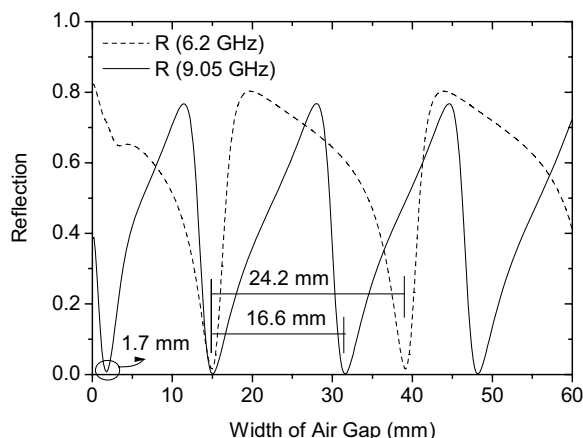


Figure 3: The reflective curves are periodic by increasing the width of the air gap between the diffraction grating and metamaterial.

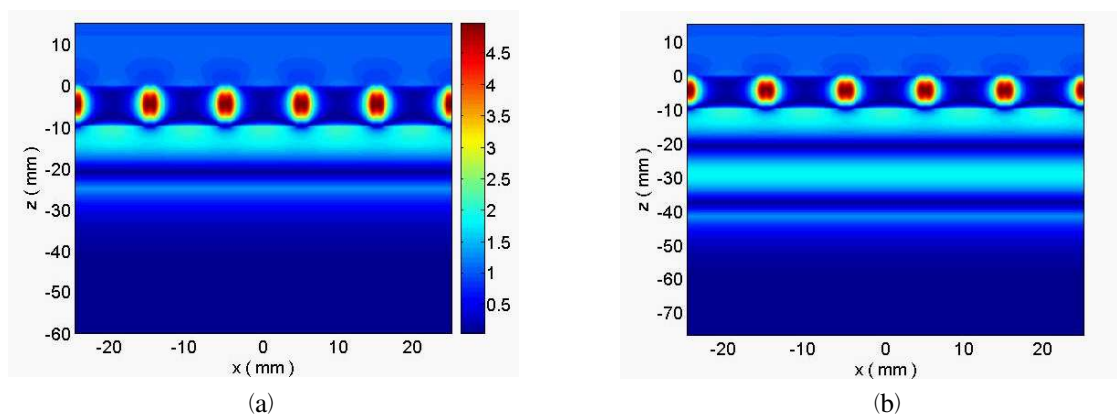


Figure 4: (a) Distribution of magnetic field  $|\mathbf{H}(x, z)|$  as function of  $x$  and  $z$  over five pitches of the grating with  $\lambda_g = 10.0$  mm,  $d_2 = 15.0$  mm, half wavelength standing wave lies in the air gap,  $-25 < z < -10$  mm, (b)  $d_2 = 31.6$  mm, a whole period of the standing wave lies in the air gap,  $-41.6 < z < -10$  mm.

for the air gap of  $d_2 = 15.0$  mm and  $d_2 + \lambda_0/2 = 31.6$  mm, corresponding to the second and third minimum reflection points in Figure 3. Where  $\lambda_0$  is the wavelength for the incident wave, and the incident wave frequency is 9.05 GHz. We found that for these two widths of the air gap, the magnetic field concentrations in the grooves of the different gratings are similar, about 5.5 times higher than the amplitude of the incident field. The concentrated magnetic field will induce a high instantaneous charge density on the surfaces of the grooves, thus greatly enhances the absorbing efficiency [9]. There are also standing waves developed in the air gap for larger air gaps, as shown in Figure 4(a) and (b). The phase delay in Figure 4(b) has  $\pi$  difference compared to the phase delay in Figure 4(a), these explain the intervals between the two adjacent minimum reflections in Figure 3 is exactly the half of the wavelength. As long as the air gap allows the standing waves to form, this means the width of the air gap is probably  $n\lambda_0/2$ , the air gap works like a vessel with dissipative walls (grating and metamaterial). The dissipation together with absorption in the grooves leads to the minimum reflection shown in Figure 3. Moreover, the formation of standing waves in the air gap (the region 3) is due to the multireflection of the two boundaries of the grating and the rearward metamaterial ( $\varepsilon_4 < 0$ ). If a metamaterial with  $\mu_4 < 0$  is used as the rearward wall, it also forbids waves to propagate through, standing waves can also be formed. Figure 5 shows the variation of reflectance as function of the air gap for the frequency 9.05 GHz. The rearward metamaterial is chosen as  $\mu_4 = -1.0 + 0.1i$ ,  $\varepsilon_4 = 1$ . A notable difference from the result in Figure 3 is that the first two absorption peaks in Figure 5 are well separated by a half wavelength, verifying the condition for the waveguide mode. The first absorption peak in Figure 3 is due largely to the surface resonance at the interface between the air and the metamaterial in case of the  $p$ -polarized

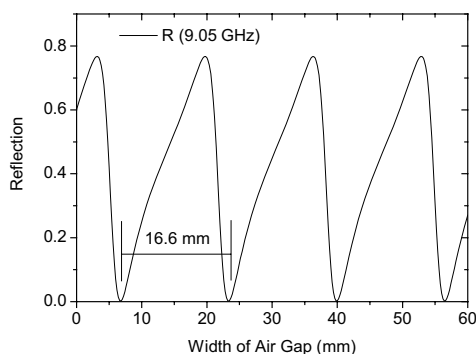


Figure 5: The variation of the reflective curves by increasing of the width of the air gap between the diffraction grating and the metamaterial with a negative permeability, all absorption peaks are due to the formation of standing wave.

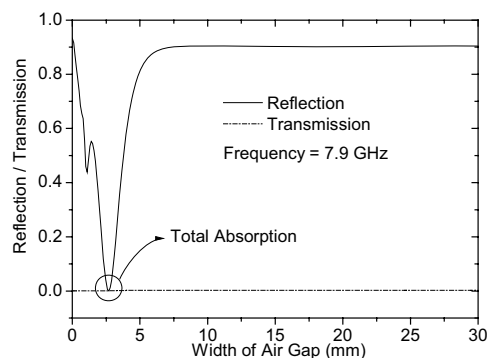


Figure 6: The reflection and transmission at 7.9 GHz for different values of the width of the air gap  $d_2$ . While the grating is lossless, total absorption only takes place at  $d_2 = 2.7$  mm.

wave. However, the surface wave can not be formed for a rearward metamaterial with  $\mu_4 < 0$ , so the first absorption peak appeared in Figure 5 is due to the waveguide mode.

#### 4. ABSORPTION DUE TO SURFACE WAVES

Through the waveguide resonance of the grating, the incident propagating wave can be transformed into evanescent one, and then the latter excites surface wave at the interface between the air and the metamaterial under the following relation [5]:

$$\frac{k_{3,zm}}{\varepsilon_3} + \frac{k_{4,zm}}{\varepsilon_4} = 0. \quad (1)$$

The width of the air gap between the grating and the metamaterial is a critical parameter in this process, this width should ensure the formation of the surface wave at the interface. A slight increase of the width would allow the localized modes to reemit in the forward direction and form propagating waves again [11]. In order to further illustrate this point, a model with a lossless grating and a lossy metamaterial is proposed. We change the material parameters as:  $\varepsilon_2 = -25.0$ ,  $\varepsilon_4 = -1.2 + 0.12i$ , again the other parameters are kept unchanged. Since in this case only the metamaterial (the region 4) has a damping coefficient, it is the unique part that the incident energy could be absorbed. The reflection as function of the width of the air gap at 7.9 GHz is presented in Figure 6, the frequency 7.9 GHz is chosen here, since without considering the loss of the grating, the minimum reflection shifts from 9.05 to 7.9 GHz. As shown in Figure 6, the air gap plays a completely different role, it excites surface waves at the interface between air and the metamaterial instead of setting up standing waves, there is no periodicity at all in the air gap. The reflection peak at  $d_2 = 2.7$  mm in Figure 6 corresponds to that at  $d_2 = 1.7$  mm in Figure 3 when loss of the grating is not considered. As shown in Figure 7, a clear surface resonance is observed at the interface between the air gap and the metamaterial at  $z = -12.7$  mm. Since the grating is lossless, the only role of the grating is to transform the plane waves into evanescent ones without attenuation, so all the incident energy are damped at the interface between the air gap and the metamaterial due to the surface wave.

For the  $p$ -polarized illumination, the surface resonance not only can be excited for the case that the metamaterial has a negative permittivity [4], but also can be set up at the interface of air and LHM [5]. By this way, the evanescent wave will penetrate into the LHM and be absorbed if the LHM is lossy. Figure 8 illustrates the reflectance of the diffraction grating with a LHM as the rearward metamaterial for different widths of the air gap. As a reference, the circles represent the reflectance of the diffraction grating ( $\varepsilon_2 = -25.0$ ) without the LHM behind, the transmittance is nearly to 1. When a LHM with  $\varepsilon_4 = -10.0 - 2.0i$ ,  $\mu_4 = -1.0 - 0.1i$  is placed behind the grating with a distance  $d_2 = 2.5$  mm, the surface waves will be excited at the 8.7 GHz, leading to an absorption peak. Now turning the LHM to be matched with vacuum, i.e., the impedance  $Z = \sqrt{\mu_4/\varepsilon_4} = Z_0$  ( $Z_0$  is the impedance of the vacuum), the surface waves will be also induced at 7.5 GHz for the

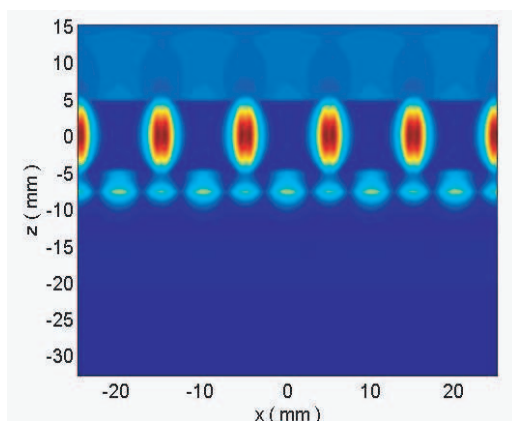


Figure 7: Distribution of magnetic field  $|\mathbf{H}(x, z)|$  as function of  $x$  and  $z$  over five pitches of the grating with  $\lambda_g = 10.0$  mm,  $d_2 = 2.7$  mm. Strong surface waves are observed at the interface of  $z = -12.7$  mm.

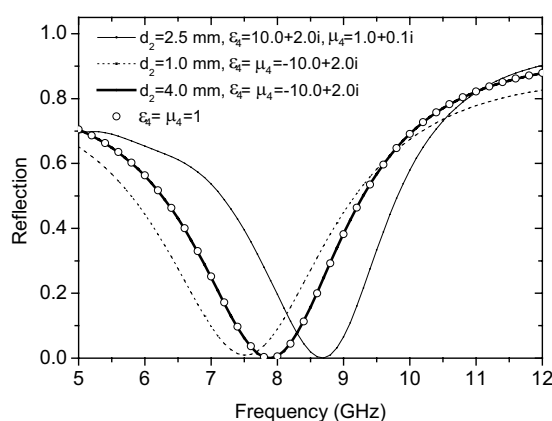


Figure 8: Reflections of diffraction grating back with a LHM at different distances.

distance between the grating  $d_2 = 1.0$  mm. If this distance is enlarged to a certain value, e.g.,  $d_2 = 4.0$  mm, no surface waves will appear at the interface between the LHM and the air. So the evanescent wave generated by the grating will reemit and penetrate into the LHM. Since a matched LHM can not reflect plane waves, the rearward LHM has no effect on the reflectance or transmittance of the gratings. It is demonstrated clearly in Figure 8 that the thick black line agrees exactly with the reference cycles, implying that the matched LHM has the same role as the air.

## 5. CONCLUSION

Microwave absorptions are examined for a system of a metamaterial grating and a rearward metamaterial separated by an air gap. It is found that the air gap plays an important role on the absorbing efficiency. While the width of the air gap is relatively small, surface waves can be excited at the interface between the air and the metamaterial, these surface waves are damped along the interface. When the width of air gap becomes large, standing waves can be formed in the air gap. These standing waves together with the high field concentration in the grooves of the grating, can lead to the total dissipation of the incident energy. For the  $p$ -polarized illumination, only the materials with negative permittivity or LHM can be used for exciting surface wave. However, the rearward metamaterials with negative permittivity, or negative permeability or both can be used to set up standing waves. This absorption mechanism is expected to have potential application in the microwave absorbing structures.

## ACKNOWLEDGMENT

This work is supported by the National Natural Science Foundation of China under Grants No. 10325210 and 90605001, National Basic Research Program of China through grant 2006CB601204.

## REFERENCES

1. Pendry, J. B., "Negative refraction makes a perfect lens," *Phys. Rev. Lett.*, Vol. 85, 3966–3969, 2000.
2. Pendry, J. B., "Controlling electromagnetic fields," *Science*, Vol. 312, 1780–1782, 2006.
3. Schurig, D., J. J. Mock, B. J. Justice, S. A. Cummer, J. B. Pendry, A. F. Starr, and D. R. Smith, "Metamaterial electromagnetic cloak at microwave frequencies," *Science*, Vol. 314, 977–980, 2006.
4. Raether, H., *Surface Plasmons on Smooth and Rough Surfaces and on Gratings*, Springer-Verlag, Berlin, 1988.
5. Ruppin, R., "Surface polaritons of a left-handed medium," *Phys. Lett. A*, Vol. 277, 61–64, 2000.
6. Bliokh, Y. P., J. Felsteiner, and Y. Z. Slutsker, "Total absorption of an electromagnetic wave by an overdense plasma," *Phys. Rev. Lett.*, Vol. 95, 165003 (1–4), 2005.
7. Veselago, V. G., "The electrodynamics of substances with simultaneously negative values of  $\epsilon$  and  $\mu$ ," *Sov. Phys. Usp.*, Vol. 10, 509–514, 1968.
8. Moharam, M. G., E. B. Grann, D. A. Pommet, and T. K. Gaylord, "Formulation for stable and efficient implementation of the rigorous coupled-wave analysis of binary gratings," *J. Opt. Soc. Am. A*, Vol. 12, 1068–1076, 1995.
9. Sobnack, M. B., W. C. Tan, N. P. Wanstall, T. W. Presit, and J. R. Sambles, "Stationary surface plasmons on a zero-order metal grating," *Phys. Rev. Lett.*, Vol. 80, 5667–5670, 1998.
10. López-Rios, T., D. Mendoza, F. J. Garía-Vidal, J. Sánchez-Dehesa, and B. Pannetier, "Surface shape resonances in lamellar metallic gratings," *Phys. Rev. Lett.*, Vol. 81, 665–668, 1998.
11. Porto, J. A., F. J. Garía-Vidal, and J. B. Pendry, "Transmission resonances on metallic grating with very narrow slits," *Phys. Rev. Lett.*, Vol. 83, 2845–2848, 1999.
12. Popov, E., M. Nevière, S. Enoch, and R. Reinisch, "Theory of light transmission through subwavelength periodic hole arrays," *Phys. Rev. B*, Vol. 62, 16100–16108, 2000.
13. Barbara, A., P. Quémerais, E. Bustarret, and T. Lopez-Rios, "Optical transmission through subwavelength metallic gratings," *Phys. Rev. B*, Vol. 66, 161403 (1–4), 2002.

# Designed Fano Resonance in Semiconductor Devices

H. C. Liu, C. Y. Song, Z. R. Wasilewski, J. A. Gupta, and M. Buchanan  
Institute for Microstructural Sciences, National Research Council, Ottawa K1A 0R6, Canada

**Abstract**— We investigate Fano resonance mediated by intersubband and phonon coupling in specially designed GaAs/AlGaAs quantum well infrared photodetectors. This work presents a new approach for realizing designed quantum interference.

## 1. INTRODUCTION

Fano resonance [1] is seen in many areas of physics including atomic and molecular spectroscopy, quantum optics [2], quantum transport [3], and more. In order to make use of this quantum interference effect, e.g., for lasing without inversion [2], it is highly desirable if one can design a Fano resonance quantum structure with controlled coupling strength. Semiconductor quantum well is a model system [4, 5] and offers this possibility. The nano-scale quantum structures designed and studied in this work are based on the well celebrated GaAs/AlGaAs semiconductor materials system. Here the intersubband transition involved in our specially designed GaAs/AlGaAs quantum-well structure is of bound-to-quasibound nature. The coupling is with a particular longitudinal optical (LO) phonon mode, and the Fano resonance is revealed in photocurrent spectra. The important feature with the present system is that the characteristics of the Fano resonance, such as coupling strength, can be designed and tuned by device parameters and bias voltage. This offers good potentials for making use of the effect in achieving practical devices. Our initial work has been reported in Ref. [6].

## 2. IDEA AND APPROACH

A Fano resonance mediated by the coupling between intersubband transition and optical phonon may be expected [7]. However, for a simple GaAs/AlGaAs square quantum well, it is difficult to experimentally observe the effect. In such a structure, the strongest phonon mode is the bulk GaAs one. In an actual experiment measuring either transmission or photocurrent spectra, the GaAs substrate completely absorbs the incident light in the optical phonon region. The other possibility involves the AlAs-like phonon in the barrier region. However, the AlAs-like phonon is mostly in the barrier and the coupling region is mostly from the barrier region immediately next to the well. The phonon absorption in the bulk of the barrier region obscures the Fano feature.

With the design flexibility of quantum well system, we use the pure AlAs LO phonon which has an energy of about  $400\text{ cm}^{-1}$  (50 meV) and which does not overlap with other strong absorption features. If the LO phonon mode of an incorporated AlAs layer overlaps strongly with the intersubband transition final states, a Fano resonance should be observable. Following the above considerations, a structure was designed as shown schematically in Fig. 1, in which a thin layer of AlAs is inserted next to the well region. To investigate the Fano resonance, photocurrent spectroscopy technique was employed due to its high sensitivity. For an efficient extraction of photo-excited electrons, the AlAs layer must be kept thin. The coupling mechanism is also shown schematically in Fig. 1. Another possibility of achieving a designed Fano resonance is by tunnel-coupling, involving only electronic transitions [5, 8, 9].

## 3. EXPERIMENTAL AND ANALYSIS

The quantum-well sample was grown on a semi-insulating GaAs substrate by molecular beam epitaxy. It has 40 GaAs/AlAs/AlGaAs quantum wells, consisting of 13.6-nm GaAs wells with their center 10 nm doped with Si to a density of  $2 \times 10^{17}\text{ cm}^{-3}$ , 0.67-nm thin AlAs “phonon” layers, and 53.8-nm  $\text{Al}_{0.09}\text{Ga}_{0.91}\text{As}$  barriers. Mesa devices were made using standard GaAs micro-fabrication methods. A 45-degree facet was polished for light coupling (see inset to Fig. 2), and the device chip was mounted in a helium optical cryostat and cooled to 9 K. Photocurrent spectra were collected using a Fourier transform infrared spectrometer with our device as the detector. Only *p*-polarized response was observed, confirming the intersubband nature of the transition process. The entire optical path was under vacuum to eliminate water absorption. Note that this device can serve as a practical infrared detector with good performance, for example, the temperature for background limited infrared performance is about 30 K.

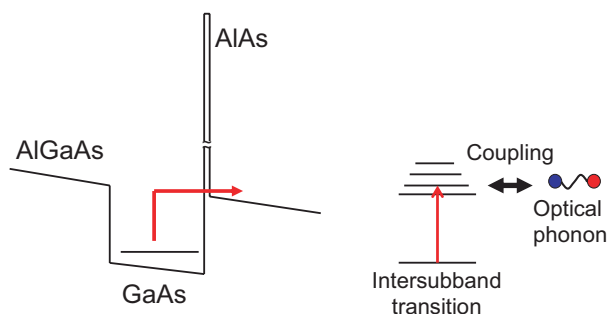


Figure 1: Schematic bandedge diagram (left) and Fano coupling between bound-to-quasibound intersubband transition and optical phonon (right).

Figure 2 presents the measured photocurrent spectra. The upper panel shows a typical quantum-well infrared photodetector response except for the feature at  $395\text{ cm}^{-1}$ , which is expanded in the lower panel. Immediately recognizable is the standard asymmetrical Fano resonance lineshape. We have observed the Fano features on other samples with a range of quantum-well parameters.

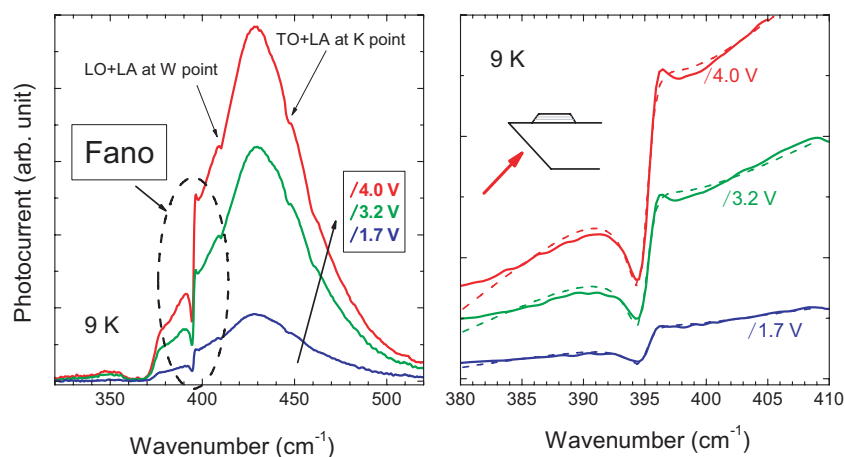


Figure 2: Photocurrent spectra for three bias voltages. The negative bias polarity corresponds to the band profile shown in Fig. 1. The right panel expands the Fano resonance region. The dashed lines are the fits to the Fano formula. The inset schematically shows the light coupling and mesa device geometry.

In contrast, a standard quantum-well infrared photodetector covering the similar spectral region shows only pure phonon absorption features all previously identified (see, for example, Ref. [10]). A typical spectrum from one of our detectors [11] is shown in Fig. 3 in which all phonon features are marked. This device is a simple multiple quantum-well structure with doped GaAs wells and  $\text{Al}_{0.05}\text{Ga}_{0.95}\text{As}$  barriers (for more details see Ref. [11]). Since the incident light passes through the substrate before reaching the quantum wells, the GaAs optical phonon absorption results in a zero response region from about  $270$  to  $290\text{ cm}^{-1}$ . Two-phonon absorption features at high symmetry points (X, K, and W) are indicated. Moreover the  $\text{Al}_{0.05}\text{Ga}_{0.95}\text{As}$  barrier AlAs-like phonon also gives rise to an absorption feature at  $366\text{ cm}^{-1}$ , however this dip should be partially due to the W-point TO + TA two-phonon absorption at  $363\text{ cm}^{-1}$ . Although the expected K-point LO + LA absorption is at  $403\text{ cm}^{-1}$  (LA = longitudinal acoustical), the arrow at  $403\text{ cm}^{-1}$  is unlabelled since we do not see this dip in other samples. All these absorption processes simply produce dips in the spectrum, in sharp contrast to the Fano resonance feature seen in Fig. 2.

A standard Fano resonance absorption spectral shape is described by the following expression:

$$\frac{\left(q + \frac{E - E_{res}}{\Delta E}\right)^2}{1 + \left(\frac{E - E_{res}}{\Delta E}\right)^2}, \quad (1)$$

where  $q$  is the Fano parameter,  $E$  is the photon energy,  $E_{res}$  is the resonance position, and  $\Delta E$

is the linewidth parameter. For our case shown in Fig. 2, the photocurrent Fano resonance is superimposed on the usual intersubband detector response. After subtracting a sloped background and fitting the experimental spectrum to expression (1), we get  $E_{res} = 395.1 \pm 0.1 \text{ cm}^{-1}$  independent of voltage, and  $q = 0.77 \pm 0.06$ ,  $0.61 \pm 0.02$ , and  $0.56 \pm 0.02$  for voltages  $-1.7$ ,  $-3.2$ , and  $-4.0 \text{ V}$ , respectively. The decrease of the  $q$  value with voltage indicates a weakening of the coupling. For the background subtraction, since the Fano feature is much narrower than the bound-to-quasibound intersubband transition spectrum, a second-order polynomial function is used in the small spectral region as in the lower part of Fig. 2. In fact, the quadratic part is very small and the subtracted background is practically a linear slope. The fitting results are shown in Fig. 2 by dashed lines.

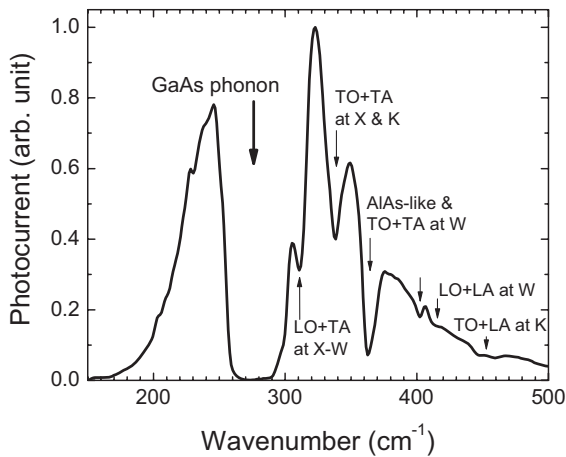


Figure 3: Photocurrent spectrum of a standard GaAs/Al<sub>0.05</sub>Ga<sub>0.95</sub>As quantum-well infrared photodetector. Phonon absorption features are marked. Device parameters are given in Ref. [10].

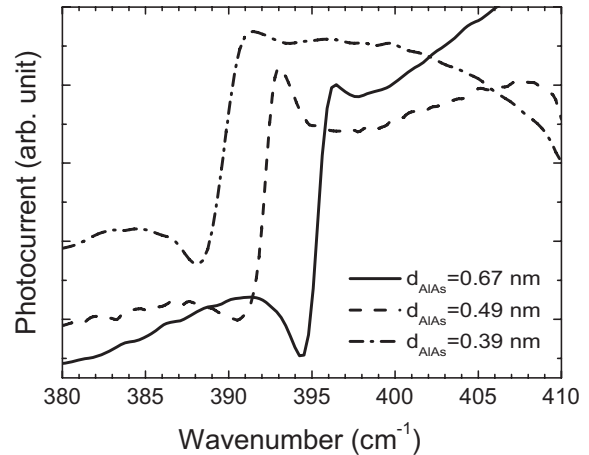


Figure 4: Photocurrent Fano resonance features for three samples with different AlAs thin barrier thickness ( $d_{\text{AlAs}}$ ). The solid curve is from the same sample as Fig. 2. All spectra were taken under negative bias voltages and at 9 K.

The fitted resonance energy ( $395 \text{ cm}^{-1}$ ) is slightly lower than the bulk AlAs phonon value. Such shift is expected from the confinement and zone folding effect in the thin (0.67 nm) AlAs layer [12, 13]. Quantitatively, the bulk AlAs LO phonon energy is  $402 \text{ cm}^{-1}$  at room temperature [14], and at 10 K, it blue-shifts to  $405 \text{ cm}^{-1}$  [15]. The confinement effect causes a red-shift of about  $10 \text{ cm}^{-1}$  for a 0.67-nm-thick AlAs layer [12], leading to an expected value of  $395 \text{ cm}^{-1}$  — in perfect agreement with experiment.

Moreover the confinement induced shift can be used to confirm that the Fano feature observed here is indeed related to the thin AlAs layer. We have measured other samples with varying AlAs layer thickness ( $d_{\text{AlAs}}$ ) and three are shown in Fig. 4. The resonance positions are seen at  $E_{res} = 389$ ,  $391$ , and  $395 \text{ cm}^{-1}$  for the three samples with  $d_{\text{AlAs}} = 0.39$ ,  $0.49$ , and  $0.67 \text{ nm}$ , respectively. The expected total shift [12] is about  $6 \text{ cm}^{-1}$  which is precisely what we observe, i.e.,  $395 - 389 \text{ cm}^{-1}$ . Note that a controversy exists over the precise mechanism for the cause of the shift. For these very thin AlAs layers, segregation may play an important role. However, also note that we are comparing our experimentally observed shifts with reported experimental results in Ref. [12].

#### 4. DISCUSSION AND CONCLUSIONS

It is interesting to note that experimental evidence of Fano resonance involving intraband transitions had been seen in more confined systems of quantum wires [16] and dots [17]. There [16, 17], however, the observations seemed to be more “accidental” than designed, in contrast to the present work. In the quantum-well intersubband system, Imamoğlu et al. and Faist et al. studied quantum interference [5, 8, 9] and Fano resonance [8, 9, 18] for potentially reaching gain without inversion [2, 19]. However, only electronic intersubband processes were involved in that study. Intersubband and phonon coupling was also shown in optically pumped intersubband Raman lasers [20]. There, the intersubband transitions were all bound-to-bound, resulting in intersubband plasmons or polarons. It can be argued that in the Raman laser case [20], phonons are playing a useful and active role. An intriguing possibility [21] is to realize a laser working at a phonon mode frequency — “phonon

laser". The present work demonstrates a possible route by using the Fano interference. Of course here we are studying a near equilibrium system (non-inverted). The next step is to explore the interference in a near-inverted or inverted system. An interesting gain spectrum should be observed and perhaps even gain without inversion.

#### ACKNOWLEDGMENT

We thank R. Wang and R. Dudek for technical assistance, H. Luo for providing the standard detector, and E. Dupont and D. Lockwood for comments. This work was supported in part by the NRC GHI program.

#### REFERENCES

1. Fano, U., *Phys. Rev.*, Vol. 124, 1866, 1961.
2. Nikonov, D. E., A. Imamoglu, and M. O. Scully, *Phys. Rev. B*, Vol. 59, 12212, 1999.
3. Martins, G. B., C. A. Busser, K. A. Al-Hassanieh, E. V. Anda, A. Moreo, and E. Dagotto, *Phys. Rev. Lett.*, Vol. 96, 066802, 2006.
4. Capasso, F., *Science*, Vol. 235, 172, 1987.
5. Faist, J., F. Capasso, C. Sirtori, L. N. Pfeiffer, and K. W. West, *Nature*, Vol. 390, 589, 1997.
6. Liu, H. C., C. Y. Song, J. A. Gupta, Z. R. Wasilewski, and M. Buchanan, *Appl. Phys. Lett.*, Vol. 91, 131121, 2007.
7. Jin, K. J., S. H. Pan, and G. Z. Yang, *Phys. Rev. B*, Vol. 51, 9764, 1995.
8. Imamoglu, A. and R. J. Ram, *Opt. Lett.*, Vol. 19, 1744, 1994.
9. Schmidt, H., K. L. Campman, A. C. Gossard, and A. Imamoglu, *Appl. Phys. Lett.*, Vol. 70, 3455, 1997.
10. Blakemore, J. S., *J. Appl. Phys.*, Vol. 53, R123, 1982.
11. Luo, H., H. C. Liu, C. Y. Song, and Z. R. Wasilewski, *Appl. Phys. Lett.*, Vol. 86, 231103, 2005.
12. Tanino, H. and S. Amano, *Surface Science*, Vol. 267, 422, 1992.
13. Yu, G., N. L. Rowell, D. J. Lockwood, and Z. R. Wasilewski, *Appl. Phys. Lett.*, Vol. 83, 3683, 2003.
14. Wasilewski, Z. R., M. M. Dion, D. J. Lockwood, P. Poole, R. W. Streater, and A. J. SpringThorpe, *J. Appl. Phys.*, Vol. 81, 1683, 1997.
15. Jusserand, B. and J. Sapriel, *Phys. Rev. B*, Vol. 24, 7194, 1981.
16. Sa'ar, A., A. Givant, S. Calderon, O. Ben-Shalom, E. Kapon, A. Gustafsson, D. Oberli, and C. Caneau, *Superlattices and Microstructures*, Vol. 19, 217, 1996.
17. Lelong, P., S.-W. Lee, K. Hirakawa, and H. Sakaki, *Physica E*, Vol. 7, 174, 2000.
18. Faist, J., F. Capasso, A. L. Hutchinson, L. Pfeiffer, and K. W. West, *Phys. Rev. Lett.*, Vol. 71, 3573, 1993.
19. Harris, S. E., *Phys. Rev. Lett.*, Vol. 62, 1033, 1989.
20. Liu, H. C., C. Y. Song, Z. R. Wasilewski, A. J. SpringThorpe, J. C. Cao, C. Dharma-Wardana, G. C. Aers, D. J. Lockwood, and J. A. Gupta, *Phys. Rev. Lett.*, Vol. 90, 077402, 2003.
21. Wolff, P. A., *Phys. Rev. Lett.*, Vol. 24, 266, 1970.

# Formulation of Scintillations for Optical Incidence of Arbitrary Field Profile

Y. Baykal<sup>1</sup>, H. T. Eyyuboğlu<sup>1</sup>, and Y. Cai<sup>2</sup>

<sup>1</sup>Department of Electronic and Communication Engineering, Çankaya University  
Öğretmenler Cad. 14, Yüzüncüyıl 06530 Balgat Ankara, Turkey

<sup>2</sup>Max-Planck-Research-Group, Institute of Optics, Information and Photonics, University of Erlangen  
Staudtstr. 7/B2D-91058 Erlangen, Germany

**Abstract**— Scintillation index on the receiver axis is formulated in random medium when an optical source with an arbitrary field profile is employed. To represent the arbitrary source field profile, source is decomposed into pixels and the incident field to form the scintillations is expressed as the superposition of the fields from each pixel area. Thus obtained arbitrary field distribution is then introduced into the weak atmospheric turbulence formulation by using Rytov method. Our result, which is in summation and integral forms, reduces correctly to the known scintillation index of a Gaussian beam wave in atmospheric turbulence.

## 1. INTRODUCTION

Detailed theoretical and experimental work studying various aspects of the scintillations in atmospheric turbulence appear in the literature [1–4]. These studies mainly cover the beams of Gaussian shape and the special cases of plane and spherical beams. It is well known that the scintillation index in weak turbulence is not only a function of the wavelength, path length, and the structure constant but also depends on the beam size. Optimal beams are investigated [5] in random media. Recently, we have formulated the correlations for general-type beams in turbulence [6] in which the general beam is described as the superposition of many sets of multimode contents, each mode being off-axis Hermite-Gaussian. As special cases of our formulation in Ref. 6, the scintillations of various types of beams such as higher-order single-mode, multimode, off-axis Hermite-Gaussian, Hermite-sinusoidal-Gaussian, higher-order annular, flat-topped-Gaussian beams can be evaluated in turbulence. We have also reported [7] the scintillation calculations of flat-topped-Gaussian beams in random medium. Lately, Liu et al., [8] reviewed in detail the effects of the scintillations on atmospheric optical access communication links. In this paper, we present the formula for the on-axis scintillation index in weak turbulence when a source with an arbitrary field distribution is used. We want to understand whether certain special type of beams will help to reduce the degrading effects of atmospheric turbulence.

## 2. FORMULATION

At the source plane ( $z = 0$ ) we take incremental areas with corner points  $\left[ (s_{n,m})_x - \frac{\Delta s_x}{2}, (s_{n,m})_y - \frac{\Delta s_y}{2} \right]$ ,  $\left[ (s_{n,m})_x + \frac{\Delta s_x}{2}, (s_{n,m})_y - \frac{\Delta s_y}{2} \right]$ ,  $\left[ (s_{n,m})_x + \frac{\Delta s_x}{2}, (s_{n,m})_y + \frac{\Delta s_y}{2} \right]$ ,  $\left[ (s_{n,m})_x - \frac{\Delta s_x}{2}, (s_{n,m})_y + \frac{\Delta s_y}{2} \right]$ , whose center points are  $\mathbf{s}_{n,m} = \left[ (s_{n,m})_x, (s_{n,m})_y \right]$  where  $(s_{n,m})_x, (s_{n,m})_y$  represent the  $x$  and  $y$  components of the center point  $\mathbf{s}_{n,m}$ , the ranges of  $n$  and  $m$  being from  $-N$  to  $N$ , and  $-M$  to  $M$ , respectively. Center point  $\mathbf{s}_{0,0} = (0, 0)$  is the point at the origin. The index  $n$  is positive in  $+s_x$  direction,  $n$  increases as  $s_x$  increases, and  $n$  is negative in  $-s_x$  direction,  $n$  decreases as  $s_x$  decreases. The same relationship exists between  $m$  and  $s_y$ .

The incident field (free space field) at the receiver point  $[\mathbf{r} = (\mathbf{p}, z)]$  originating from the source incremental area having the center point  $\mathbf{s}_{n,m} = \left[ (s_{n,m})_x, (s_{n,m})_y \right]$  can be found by using the Huygens-Fresnel principle as

$$u_{n,m}^{FS}(\mathbf{p}, z) = \frac{k \exp(ikz)}{2\pi iz} \int_{(s_{n,m})_x - \frac{\Delta s_x}{2}}^{(s_{n,m})_x + \frac{\Delta s_x}{2}} \int_{(s_{n,m})_y - \frac{\Delta s_y}{2}}^{(s_{n,m})_y + \frac{\Delta s_y}{2}} \mathbf{d}^2 \mathbf{s} u_{n,m}(\mathbf{s}, z = 0) \exp \left[ \frac{ik}{2z} (\mathbf{s} - \mathbf{p})^2 \right], \quad (1)$$

where  $u_{n,m}(\mathbf{s}, z = 0)$  is the field at the source plane,  $k$  is the wave number,  $\mathbf{s} = (s_x, s_y)$  and  $\mathbf{p} = (p_x, p_y)$  are the transverse source and receiver coordinates, respectively.

For sufficiently small incremental area, i.e., when  $\Delta s_x \rightarrow 0$  and  $\Delta s_y \rightarrow 0$ , one can reasonably approximate that the integrand in Eq. (1) does not vary with the transverse source coordinate,  $\mathbf{s}$ . Thus, for each receiver point  $\mathbf{p} = (p_x, p_y)$ , the value of the integrand stays constant, and this constant is calculated by evaluating the integrand at  $\mathbf{s}_{n,m} = [(s_{n,m})_x, (s_{n,m})_y]$ , i.e.,

$$u_{n,m}(\mathbf{s}, z=0) \exp \left[ \frac{ik}{2z} (\mathbf{s} - \mathbf{p})^2 \right] \cong u_{n,m}(\mathbf{s}_{n,m}, z=0) \exp \left[ \frac{ik}{2z} (\mathbf{s}_{n,m} - \mathbf{p})^2 \right] = \text{constant}, \quad (2)$$

Using Eq. (2) in Eq. (1), inserting  $\mathbf{s}_{n,m} = [(s_{n,m})_x, (s_{n,m})_y]$ ,  $\mathbf{p} = (p_x, p_y)$ , and performing the integration, Eq. (1) becomes

$$u_{u,m}^{FS}(\mathbf{p}, z) = \frac{k \exp(ikz)}{2\pi iz} \Delta s_x \Delta s_y u_{n,m} \left[ (s_{n,m})_x, (s_{n,m})_y, z=0 \right] \exp \left( \frac{ik}{2z} \left\{ [(s_{n,m})_x - p_x]^2 + [(s_{n,m})_y - p_y]^2 \right\} \right), \quad (3)$$

Total incident field (free space field) at the receiver point  $[\mathbf{r} = (\mathbf{p}, z)]$ , originating from the total source aperture, i.e., originating from the contributions of all source incremental areas having the center points  $[(s_{n,m})_x, (s_{n,m})_y]$ , is found as

$$u^{FS}(\mathbf{p}, z) = \sum_{n=-N}^N \sum_{m=-M}^M u_{n,m}^{FS}(\mathbf{p}, z), \quad (4)$$

Inserting Eq. (3) into Eq. (4), we have

$$u^{FS}(\mathbf{p}, z) = \sum_{n=-N}^N \sum_{m=-M}^M \frac{k \exp(ikz)}{2\pi iz} \Delta s_x \Delta s_y u_{n,m} \left[ (s_{n,m})_x, (s_{n,m})_y, z=0 \right] \times \exp \left( \frac{ik}{2z} \left\{ [(s_{n,m})_x - p_x]^2 + [(s_{n,m})_y - p_y]^2 \right\} \right), \quad (5)$$

On-axis scintillation index in weak turbulence is well known to be [9]

$$m^2 = 4 \langle \chi^2 \rangle = 4 \left\langle \frac{1}{2} [\psi + \psi^*]^2 \right\rangle, \quad (6)$$

where  $\chi$  and  $\psi$  represent the log-amplitude and wave fluctuations at the origin of the receiver plane, and  $\langle \rangle$  denotes the ensemble average. Rytov method solution for  $\psi$  is

$$\psi = \frac{k^2}{2\pi u^{FS}(\mathbf{p} = \mathbf{0}, L)} \int_{V'} d^3 r' n_1(\mathbf{p}', z') u^{FS}(\mathbf{p}', z') \frac{\exp(ik|\mathbf{r} - \mathbf{r}'|)}{|\mathbf{r} - \mathbf{r}'|}, \quad (7)$$

where  $\mathbf{r}' = (\mathbf{p}', z') = (p'_x, p'_y, z')$ ,  $\mathbf{r} = (\mathbf{p} = \mathbf{0}, L) = (p_x = 0, p_y = 0, z = L)$ ,  $L$  being the link distance. Integration in Eq. (7) is over the volume  $V'$  with  $d^3 r' = dp'_x dp'_y dz'$ , and  $n_1$  is the random part of the refractive index given by

$$n_1(p'_x, p'_y, z') = \int_{-\infty}^{\infty} \int_{-\infty}^{\infty} \exp(i\kappa_x p'_x + i\kappa_y p'_y) dZ_n(\kappa_x, \kappa_y, z') \quad (8)$$

where  $\kappa_x$  and  $\kappa_y$  are the spatial frequencies in  $x$  and  $y$  directions, respectively,  $dZ_n(\kappa_x, \kappa_y, z')$  is the random amplitude of the spectrum of the refractive index fluctuations representing the integrations with respect to  $\kappa_x$  and  $\kappa_y$ .

For  $u^{FS}(\mathbf{p}', z')$  in Eq. (7), by inserting from Eq. (5) the arbitrary source field profile at the receiver point  $[\mathbf{r} = (\mathbf{p}, z)]$  and substituting for thus evaluated  $\psi$  in Eq. (6), the on-axis scintillation

index for the arbitrary source field profile is found. In our formulation, paraxial approximation is used, and the integration over  $dp'_x dp'_y$  is performed by the use of Eq. (7.374.8) of Ref. 10. We note that, in the derivation, similar procedure as in Ishimarus formulation [11] for the Gaussian beam wave source field is used. Instead of including the lengthy algebra involved in the derivations, we present below our result directly. Hence, in the end, the on-axis scintillation index for the arbitrary source field profile is found to be

$$m^2 = 4\pi \text{Re} \left\{ \int_0^L d\eta \int_0^\infty \kappa d\kappa \int_0^{2\pi} d\theta [Y_1(\eta, \kappa, \theta) + Y_2(\eta, \kappa, \theta)] \Phi_n(\kappa) \right\}, \quad (9)$$

where  $\Phi_n(\kappa)$  is the spectral density of the index of refraction fluctuations,  $\kappa = \sqrt{\kappa_x^2 + \kappa_y^2}$ ,  $\kappa = \kappa_x / \cos \theta = \kappa_y / \sin \theta$ , and

$$Y_1(\eta, \kappa, \theta) = \frac{V(\eta, \kappa, \theta)V(\eta, -\kappa, \theta)}{W^2}, \quad (10)$$

$$Y_2(\eta, \kappa, \theta) = \frac{|V(\eta, \kappa, \theta)|^2}{W^2}, \quad (11)$$

$$V(\eta, \kappa, \theta) = \frac{ik}{L} \exp \left[ -\frac{i(L-\eta)\eta}{2kL} \kappa^2 \right] \sum_{n=-N}^N \sum_{m=-M}^M u_{n,m} [(s_{n,m})_x, (s_{n,m})_y, z=0] \exp \left[ \frac{ik(s_{n,m})_x^2}{2L} \right] \\ \times \exp \left[ \frac{ik(s_{n,m})_y^2}{2L} \right] \exp \left\{ \left[ \frac{i(s_{n,m})_x(L-\eta)}{L} \right] \kappa \cos \theta \right\} \exp \left\{ \left[ \frac{i(s_{n,m})_y(L-\eta)}{L} \right] \kappa \sin \theta \right\}, \quad (12)$$

and

$$W = \frac{1}{L} \sum_{n=-N}^N \sum_{m=-M}^M u_{n,m} [(s_{n,m})_x, (s_{n,m})_y, z=0] \exp \left[ \frac{ik}{2L} (s_{n,m})_x^2 + \frac{ik}{2L} (s_{n,m})_y^2 \right], \quad (13)$$

Introducing the arbitrary source field distribution,  $u_{n,m} [(s_{n,m})_x, (s_{n,m})_y, z=0]$  in Eqs. (12) and (13), and performing the integrations in Eq. (9), on-axis scintillation index for the chosen source field profile is calculated.

### 3. CHECK CASE

As a check point, Eq. (9) is evaluated for the known Gaussian beam wave scintillation index. For this purpose, arbitrary source field distribution is taken as

$$u_{n,m} [(s_{n,m})_x, (s_{n,m})_y, z=0] = A \exp \left\{ -\frac{1}{2} k\alpha \left[ (s_{n,m})_x^2 + (s_{n,m})_y^2 \right] \right\}, \quad (14)$$

together with  $N = M = \infty$ . Here  $\alpha = 1/(k\alpha_s^2) + i/F$ ;  $\alpha_s$  and  $F$  being the Gaussian source size and the focal length, respectively. Also taking  $(s_{n,m})_x = n\Delta s_x$  and  $(s_{n,m})_y = m\Delta s_y$ , multiplying Eqs. (12) and (13) by  $\Delta s_x \Delta s_y$  [note that multiplying both Eq. (12) and Eq. (13) by  $\Delta s_x \Delta s_y$  will not change Eqs. (10) and (11)], letting  $\Delta s_x \rightarrow 0$  and  $\Delta s_y \rightarrow 0$ , and using the definition of integral; the summations in Eqs. (12) and (13) will be converted into integrations over the continuous transverse source coordinates. Performing these integrations, substituting the thus obtained  $V$  and  $W$  into Eqs. (10) and (11);  $Y_1$  and  $Y_2$  valid for the special case of the Gaussian beam are found. Then these  $Y_1$  and  $Y_2$  are employed in Eq. (9). When the integrations over  $\theta$  and  $\kappa$  are taken in Eq. (9) under Kolmogorov spectrum, the scintillation index on the receiver axis for the Gaussian beam wave is found as the limiting case.

### 4. CONCLUSION

The scintillation index formula is presented from which the intensity fluctuations due to a source with an arbitrary field distribution can be numerically evaluated on the receiver axis and in weak turbulence. In our future work, we will evaluate this formula in atmospheric optical links to figure out the optimum source field profile that will minimize the scintillation noise in such links.

**ACKNOWLEDGMENT**

Y. Cai gratefully acknowledges support from the Alexander von Humboldt Foundation.

**REFERENCES**

1. Andrews, L. C., R. L. Phillips, and C. Y. Hopen, *Laser Beam Scintillation with Applications*, SPIE, Bellingham, Washington, 2001.
2. Banakh, V. A. and V. L. Mironov, "Influence of the diffraction size of a transmitting aperture and the turbulence spectrum on the intensity fluctuations of laser radiation," *Sov. J. Quantum Electr.*, Vol. 8, No. 7, 875–878, 1978.
3. Andrews, L. C., R. L. Phillips, C. Y. Hopen, and M. A. Al-Habash, "Theory of optical scintillation," *J. Opt. Soc. Am. A*, Vol. 16, No. 6, 1417–1429, 1999.
4. Toyoda, M., "Intensity fluctuations in laser links between the ground and a satellite," *Appl. Opt.*, Vol. 44, No. 34, 7364–7370, 2005.
5. Schulz, T. J., "Optimal beams for propagation through random media," *Opt. Lett.*, Vol. 30, No. 10, 1093–1095, 2005.
6. Baykal, Y., "Formulation of correlations for general type beams in atmospheric turbulence," *J. Opt. Soc. Am. A*, Vol. 23, No. 4, 889–893, 2006.
7. Baykal, Y. and H. T. Eyyuboglu, "Scintillation index of flat-topped-Gaussian beams," *Appl. Opt.*, Vol. 45, No. 16, 3793–3797, 2006.
8. Liu, Q., C. Qiao, G. Mitchell, and S. Stanton, "Optical wireless communication networks for first- and last-mile broadband access [Invited]," *J. Opt. Net.*, Vol. 4, No. 12, 807–828, 2005.
9. Andrews, L. C. and R. L. Phillips, *Laser Beam Propagation through Random Media*, SPIE, Bellingham, Washington, 2005.
10. Gradshteyn, I. S. and I. M. Ryzhik, *Tables of Integrals, Series and Products*, Academic Press, New York, 2000.
11. Ishimaru, A., "Fluctuations in the parameters of spherical waves propagating in a turbulent atmosphere," *Radio Sci.*, Vol. 4, No. 4, 295–305, 1969.
12. Ishimaru, A., *Wave Propagation and Scattering in Random Media*, Academic, New York, 1978.

# Propagation of Partially Coherent Beams after a Source Plane Ring Aperture

H. T. Eyyuboğlu<sup>1</sup>, Y. K. Baykal<sup>1</sup>, and Y. Cai<sup>2</sup>

<sup>1</sup>Department of Electronic and Communication Engineering, Çankaya University  
Öğretmenler Cad. 14, Yüziüncüyıl, 06530 Balgat, Ankara, Turkey

<sup>2</sup>Max-Planck-Research-Group, Institute of Optics, Information and Photonics, University of Erlangen  
Staudtstr. 7/B2D-91058 Erlangen, Germany

**Abstract**— The propagation properties of partially coherent beams passing through a source placed ring aperture are examined. The derivation is based on the lowest order general beam formulation, such that our results are applicable to a wide range of beams. In this study, our focus is on fundamental Gaussian, cosh-Gaussian, cos-Gaussian, sinh-Gaussian, sine-Gaussian and annular beams. The aperture consists of inner and outer parts, thus the middle hollow part appears in the form of a ring. The propagation environment is turbulent.

From the graphical outputs of the beams investigated, it is seen that despite the existence of the circular ring, during propagation, the beams tend to retain the basic profiles similar to the case of no aperture, but depending on the inner and outer radius dimensions, the propagated beams are reduced in intensity levels and become more spread. It is further observed that, when the inner part of the aperture has nonzero radius, ring formations are developed at the outer edges of the receiver plane intensities.

## 1. INTRODUCTION

In practical optical communication equipment, an aperture confinement of some type, usually a circular shape, is readily built into the transmission apparatus. Here we also introduce an inner part so that the eventual configuration is in the form of a ring consisting of an inner and outer radius.

In literature, many sources have investigated the propagation of laser beams with a source aperture confinement, usually coupled with the representation of the propagation environment as  $ABCD$  matrix. In these works, the propagation medium is mostly taken to be free space, rather than turbulent atmosphere. A collection of such studies is found in [1–8].

Recently there has also appeared a study concerning the propagation of beams in turbulent atmosphere incorporating a source aperture confinement [9].

Our goal in this paper has been to extend the aperture treatment to the case of selected general beams. Hence, this study is aimed at the in-turbulence propagation analysis of beams passing through a source aperture configuration. In particular, within the context of general beam, our graphical results cover cosh-Gaussian, sine-Gaussian and annular beams.

## 2. FORMULATION

As shown in [10], the source field of most popular beams contains a summation of two terms. In radial coordinates, the mutual coherence function of partial coherent version of such beams is given as

$$\Gamma_s(s_1, s_2, \phi_{1s}, \phi_{2s}) = \exp \left\{ \frac{-0.25}{\sigma_s^2} [s_1^2 + s_2^2 - 2s_1s_2 \cos(\phi_{1s} - \phi_{2s})] \right\} \\ \sum_{t_1=1}^2 \sum_{t_2=1}^2 C_{t_1} C_{t_2}^* \exp \{ -[k\alpha_{t_1} s_1^2 + jV_{t_1} s_1 (\cos \phi_{1s} + \sin \phi_{1s})] \\ - [k\alpha_{t_2}^* s_2^2 - jV_{t_2}^* s_2 (\cos \phi_{2s} + \sin \phi_{2s})] \} \quad (1)$$

$s_1, s_2, \phi_{1s}$  and  $\phi_{2s}$  refer to the two distinct source coordinates,  $\sigma_s$  is the partial coherence parameter.  $k = 2\pi/\lambda$  is the wave number with  $\lambda$  being the wavelength,  $\alpha = 1/(k\alpha_0^2) + j/(2F_0)$  where  $\alpha_0$  and  $F_0$  respectively indicate radial Gaussian source size and focusing parameter. Via the amplitude parameters  $C$ , displacement parameters  $V$  and  $\alpha$  together with their  $t_1$  and  $t_2$  subscripts, it is possible to configure the general beam so that it will deliver fundamental Gaussian, cosh-Gaussian,

cos-Gaussian, sinh-Gaussian, sine-Gaussian and annular beams [11]. We assume that prior to propagation, the source given by Eq. (1) passes through a ring aperture with internal radius of  $a$  and outer radius of  $b$  as shown in Figure 1.

The average intensity falling on a receiver plane which is  $L$  distance apart from the source plane, can be calculated in terms of the Huygens-Fresnel integral as shown below [10]

$$\begin{aligned} \langle I_r(r, \phi_r) \rangle &= \frac{k^2}{(2\pi L)^2} \int_a^{b/2} \int_0^{2\pi} \int_a^{b/2} \int_0^{2\pi} ds_1 d\phi_{1s} ds_2 d\phi_{2s} \Gamma_s(s_1, s_2, \phi_{1s}, \phi_{2s}) s_1 s_2 \\ &\times \exp \left\{ \frac{jk}{2L} [-2rs_1 \cos(\phi_r - \phi_{1s}) + s_1^2 + 2rs_2 \cos(\phi_r - \phi_{2s}) - s_2^2] \right\} \\ &\times \exp \left\{ \frac{-1}{\rho_0^2} [s_1^2 + s_2^2 - 2s_1 s_2 \cos(\phi_{1s} - \phi_{2s})] \right\} \end{aligned} \quad (2)$$

In Eq. (2), the diffraction phenomena is expressed by the first exponential, while the second exponential arises due to turbulence. In this second exponential,  $\rho_0$  is the coherence length of a spherical wave propagating in the turbulent medium and under the conditions of Kolmogorov spectrum and quadratic approximation, given by  $\rho_0 = (0.545 C_n^2 k^2 L)^{-3/5}$ , where  $C_n^2$  refractive index structure constant expressing the turbulence strength. Finally  $r$  and  $\phi_r$  refer to the radial coordinates on the receiver plane.

Upon substituting for  $\Gamma_s(s_1, s_2, \phi_{1s}, \phi_{2s})$  in Eq. (2) from Eq. (1), the integration in Eq. (2) can be solved with respect to  $s_1$  and  $\phi_{1s}$  in the manner described in [12–14], leaving the following double integral

$$\begin{aligned} \langle I_r(r, \phi_r) \rangle &= \frac{0.25k^2}{\pi L^2} \sum_{t_1=1}^2 \sum_{t_2=1}^2 \sum_{t=0}^{\infty} \frac{(0.25)^t}{(t!)^2} C_{t_1} C_{t_2}^* \left( k\alpha_{t_1} - \frac{jk}{2L} + \frac{1}{\rho_0^2} + \frac{0.25}{\sigma_s^2} \right)^{-(t+1)} \sum_{p_1=0}^t \frac{(2t)!!}{2^{p_1} (2t-2p_1)!!} \\ &\times \left\{ \left[ \left( k\alpha_{t_1} - \frac{jk}{2L} + \frac{1}{\rho_0^2} + \frac{0.25}{\sigma_s^2} \right) a^2 \right]^{t-p_1} \exp \left[ - \left( k\alpha_{t_1} - \frac{jk}{2L} + \frac{1}{\rho_0^2} + \frac{0.25}{\sigma_s^2} \right) a^2 \right] \right. \\ &- \left. \left[ \left( k\alpha_{t_1} - \frac{jk}{2L} + \frac{1}{\rho_0^2} + \frac{0.25}{\sigma_s^2} \right) b^2 \right]^{t-p_1} \exp \left[ - \left( k\alpha_{t_1} - \frac{jk}{2L} + \frac{1}{\rho_0^2} + \frac{0.25}{\sigma_s^2} \right) b^2 \right] \right\} \\ &\times \int_a^{b/2} \int_0^{2\pi} ds_2 d\phi_{2s} s_2 \exp \{ - [k\alpha_{t_2}^* s_2^2 - jV_{t_2}^* s_2 (\cos \phi_{2s} + \sin \phi_{2s})] \} \\ &\exp \left\{ \frac{jk}{2L} [2rs_2 \cos(\phi_r - \phi_{2s}) - s_2^2] \right\} \\ &\times \exp \left[ -s_2^2 \left( \frac{1}{\rho_0^2} + \frac{0.25}{\sigma_s^2} \right) \right] \left[ -2V_{t_1}^2 - \frac{k^2 r^2}{L^2} + \frac{4s_2^2}{\rho_0^4} + \frac{0.25s_2^2}{\sigma_s^4} - \frac{2V_{t_1} k r}{L} (\cos \phi_r + \sin \phi_r) \right. \\ &- \left. \left( \frac{4jV_{t_1} s_2}{\rho_0^2} + \frac{jV_{t_1} s_2}{\sigma_s^2} \right) (\cos \phi_{2s} + \sin \phi_{2s}) - \left( \frac{4jkr s_2}{L\rho_0^2} + \frac{jkr s_2}{L\sigma_s^2} \right) \cos(\phi_r - \phi_{2s}) + \frac{2s_2^2}{\rho_0^2 \sigma_s^2} \right]^t \end{aligned} \quad (3)$$

where  $(n)!! = 1 \times 3 \times \dots (n-1)$  or  $(n)!! = 2 \times 4 \times \dots (n-1)$  depending on whether  $k$  is odd or even. As explained in [12, 13], it does not serve much use to continue analytically with Eq. (3), thus it is kept in the present form. Instead the routine mentioned in [12, 13] is employed for relatively rapid evaluation.

### 3. RESULTS AND DISCUSSIONS

Although, the formulation in Eq. (3) can support a variety of beams, here due to space limitations, we restrict our results to cosh-Gaussian, sine-Gaussian and annular beams. Thus, in this section the intensity plots are offered for cosh-Gaussian, sine-Gaussian and annular beams, while they propagate in turbulent atmosphere after having passed through the circular aperture of the source plane. To permit cross-comparisons between the different beam types, for the cosh-Gaussian and sine-Gaussian beams, we use the common settings of,  $\alpha_0 = 1$  cm,  $F_0 \rightarrow \infty$ ,  $V = 200$  m<sup>-1</sup>,  $\sigma_s \rightarrow \infty$ ,

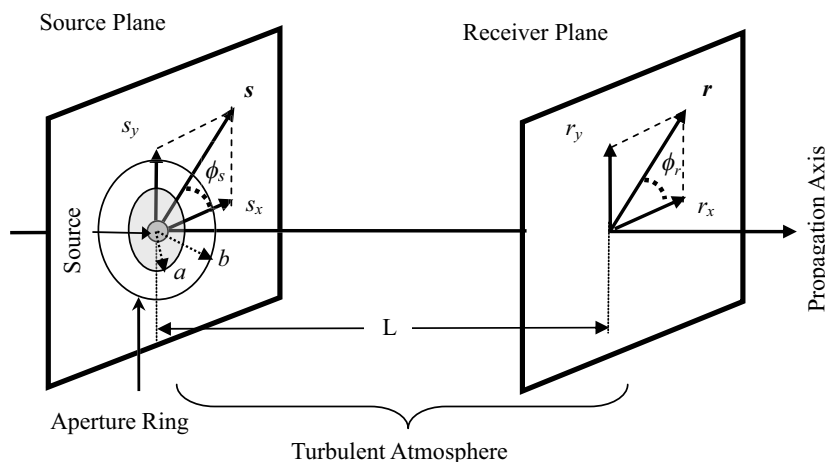


Figure 1: General layout of source and receiver planes and the source ring aperture configuration.

$C_n^2 = 10^{-15} \text{ m}^{-2/3}$ . This means that collimated and coherent beams are examined in this study. For annular beams on the other hand, the above settings are modified in the following way,  $\alpha_{01} = 1 \text{ cm}$ ,  $\alpha_{02} = 0.8 \text{ cm}$ ,  $V = 0$ . Here  $\alpha_{01}$  and  $\alpha_{02}$  consecutively refer to primary and the secondary source sizes. The individual intensity illustrations are arranged to coincide with propagation lengths of  $L = 0, 1, 2, 5 \text{ km}$ . The intensity graphs are drawn on the Cartesian transverse planes, where  $s_x, s_y$  and  $r_x, r_y$  will respectively correspond to the Cartesian counterparts of the source and receiver radial coordinates  $s, \phi_s$  and  $r, \phi_r$  encountered in Eqs. (1) and (3). The vertical axes of the plots are labelled as  $I_{sN}$  or  $\langle I_{rN} \rangle$  meaning that all intensity levels are normalized with respect to the peak value of the source intensity obtained from Eq. (1) by setting  $I_s(s, \phi_s) = \Gamma_s(s, s, \phi_s, \phi_s)$ . It is worth pointing out that in order to obtain a problem-free (or reliable) intensity profile, as many as 26 terms had to be included in the most inner summation appearing in the first line of Eq. (3).

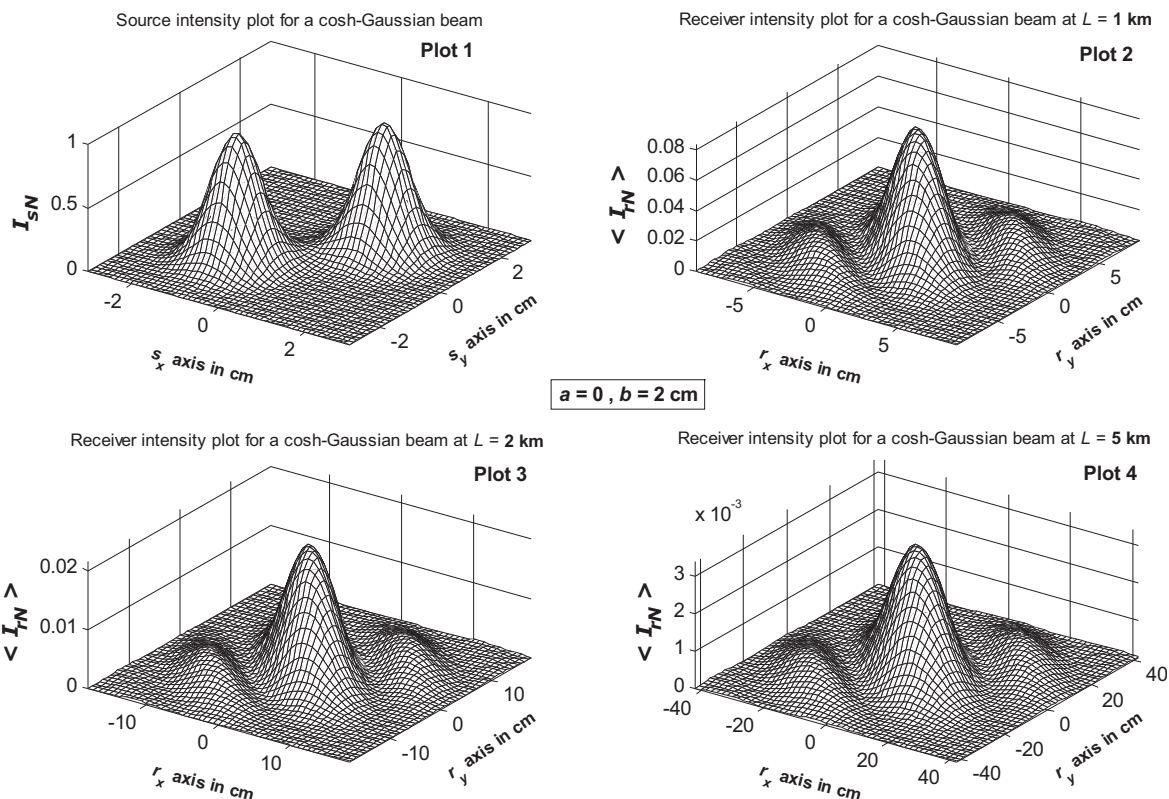


Figure 2: Progress of an cosh-Gaussian beam along propagation axis with aperture ring dimensions of  $a = 0, b = 2 \text{ cm}$ .

Figure 2 shows the progress of a cosh-Gaussian beam along the propagation axis with the radius of interior ring,  $a = 0$ , that of the outer ring,  $b = 2$  cm. Judging by the source intensity plot (Plot 1), it is seen that an outer aperture radius of  $b = 2$  cm allows almost all the source intensity to be emitted from the source plane. In this manner, when Figures 2 and 3 are compared, where the latter shows the propagation of the same cosh-Gaussian beam with the outer radius of the aperture extending to infinity, hardly any noticeable difference is found. A closer joint examination of Figures 2 and 3 will reveal that, the finite aperture (i.e., Figure 2) nevertheless imposes more spreading on the beam, whilst also lowering its peak amplitudes. This is evident from the comparison of Plots 2, 3 and 4 of Figures 2 and 3.

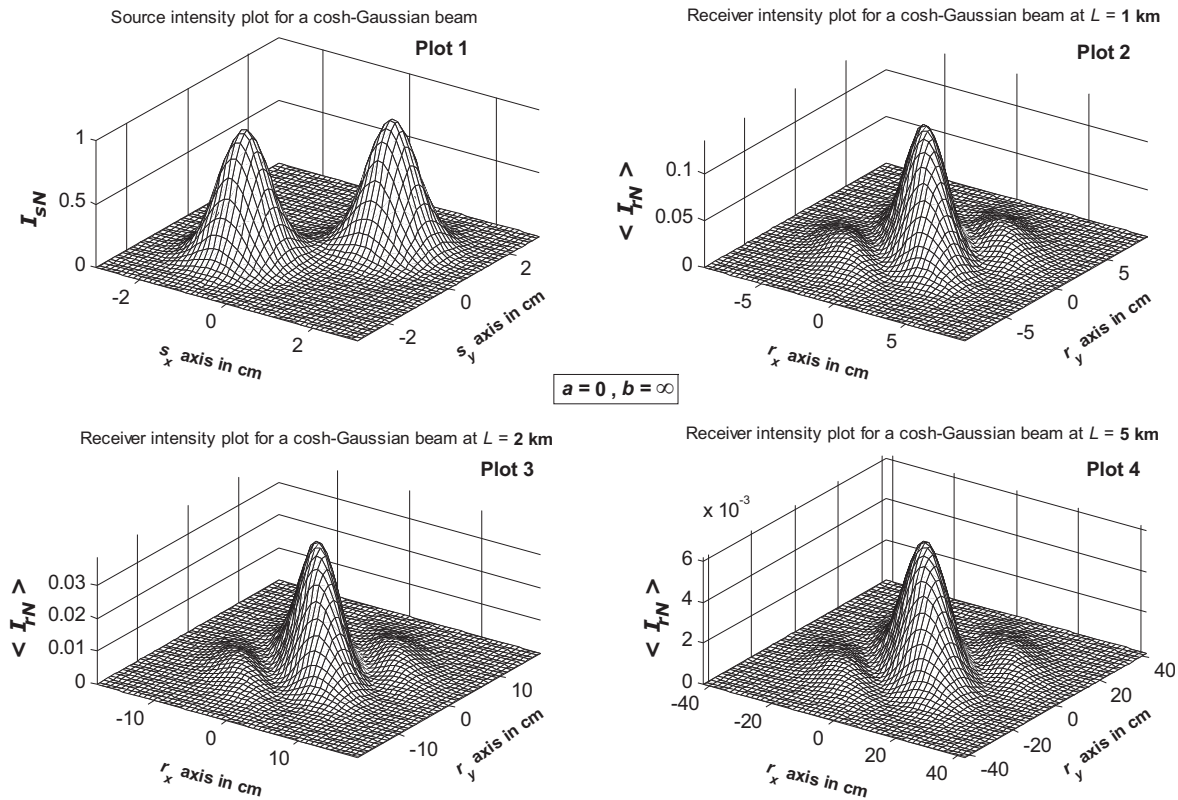


Figure 3: Progress of a cosh-Gaussian beam along propagation axis with aperture ring dimensions of  $a = 0$ ,  $b = \infty$ .

In Figure 4, we introduce a finite interior part, that is  $a = 1$  cm, for the source aperture of the cosh-Gaussian beam. From Figure 4, it is seen that the existence of the nonzero inner part gives rise to the emergence of bigger side lobes, formation of outer rings and more beam spreading. It is interesting to note from Figures 2 and 4 that, the presence of an aperture at the source plane does not hinder the beam evolution phases. That is, the evolutions discussed and demonstrated in [15] for the unapertured propagation of cosh-Gaussian beam are valid here as well. Consequently even with an aperture confinement, as observed from Figures 2 and 4, the cosh-Gaussian beam will still transform into a cos-Gaussian beam upon propagation.

In Figure 5, the progress of the sine-Gaussian beam is displayed for and aperture configuration of  $a = 0$ ,  $b = 1$  cm. Figure 5 proves that, this particular sine-Gaussian beam does not seem to be affected by the presence of the aperture, such that it conveniently transforms into a sinh-Gaussian beam after propagation. Considering the outer aperture size of 1 cm in relation foot-print of source beam from Plot 1 of Figure 5, it easy to see that an aperture opening of 1 cm is able to transmit the whole source beam intensity. Figure 6 shows the sine-Gaussian beam propagation for the case of  $a = 1$  cm,  $b = 2$  cm. According to Figure 6, sine-Gaussian beam will again yield a sinh-Gaussian beam after propagation, but due to the existence of the inner part of the aperture, outer rings will be formed as well.

Finally we provide the illustration of annular beam. To this end, Figure 7 shows that, when a source aperture confinement of  $a = 1$  cm,  $b = 2$  cm is used, annular beam will generate an outer

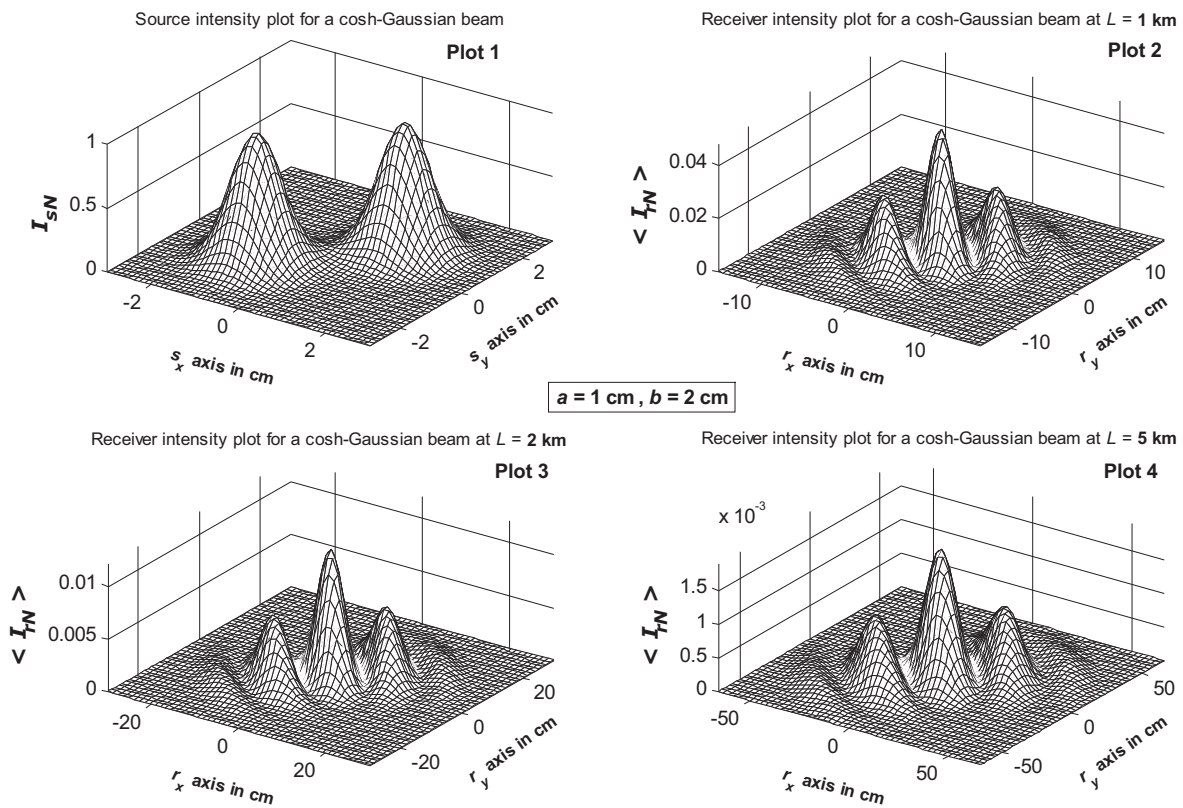


Figure 4: Progress of a cosh-Gaussian beam along propagation axis with aperture ring dimensions of  $a = 1$  cm,  $b = 2$  cm.

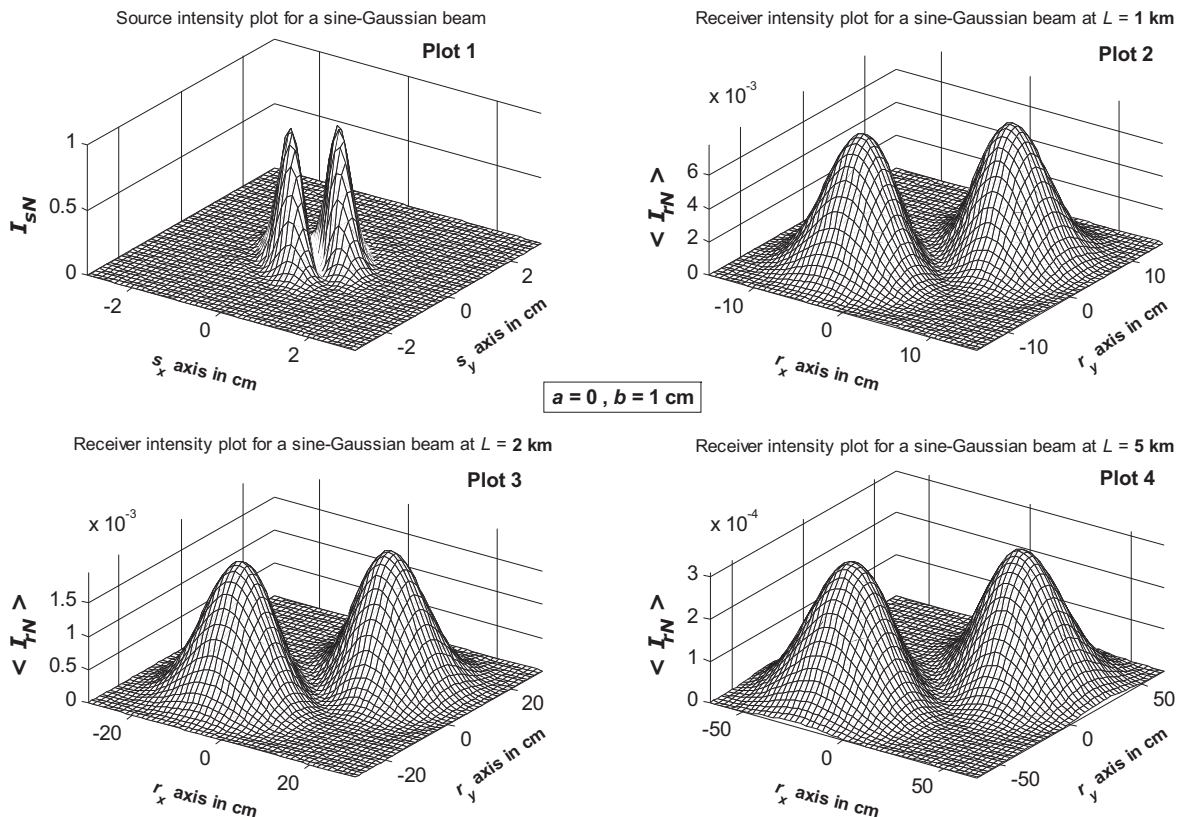


Figure 5: Progress of a sine-Gaussian beam along propagation axis with aperture ring dimensions of  $a = 0$ ,  $b = 1$  cm.

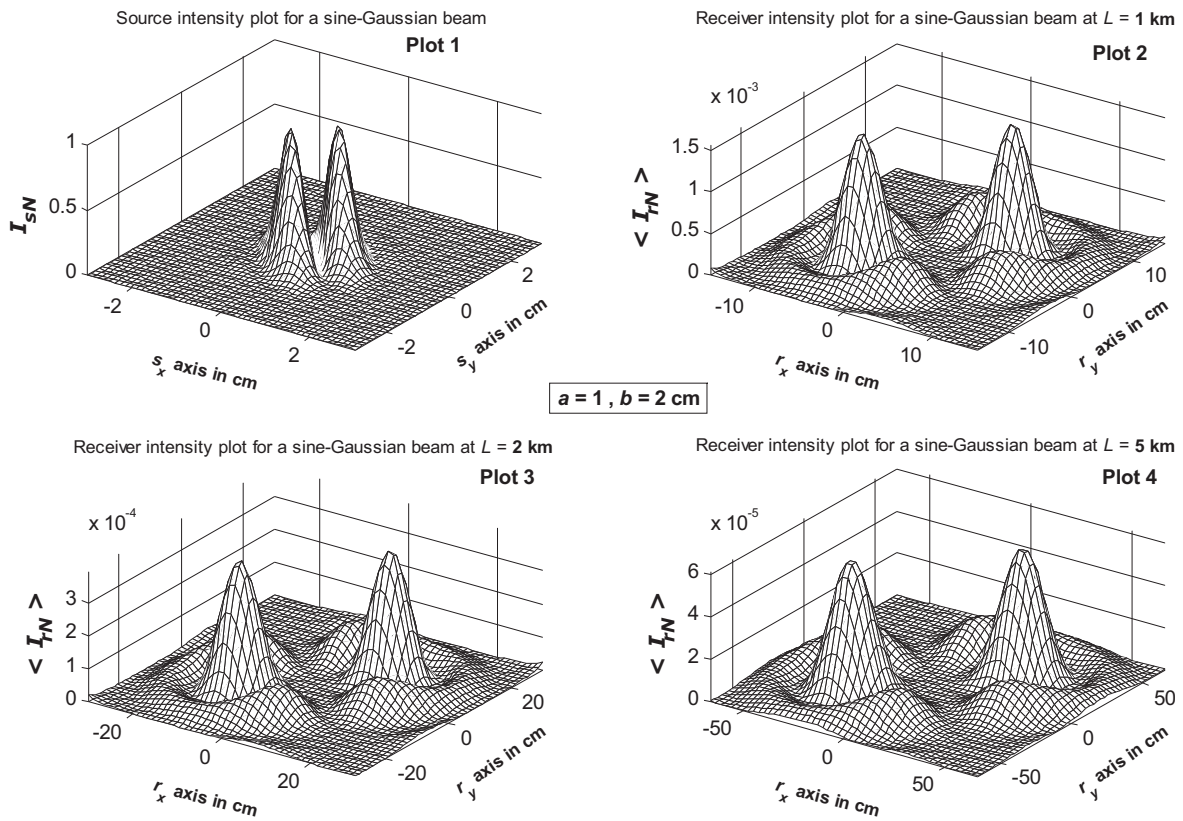


Figure 6: Progress of a sine-Gaussian beam along propagation axis with aperture ring dimensions of  $a = 1$  cm,  $b = 2$  cm.

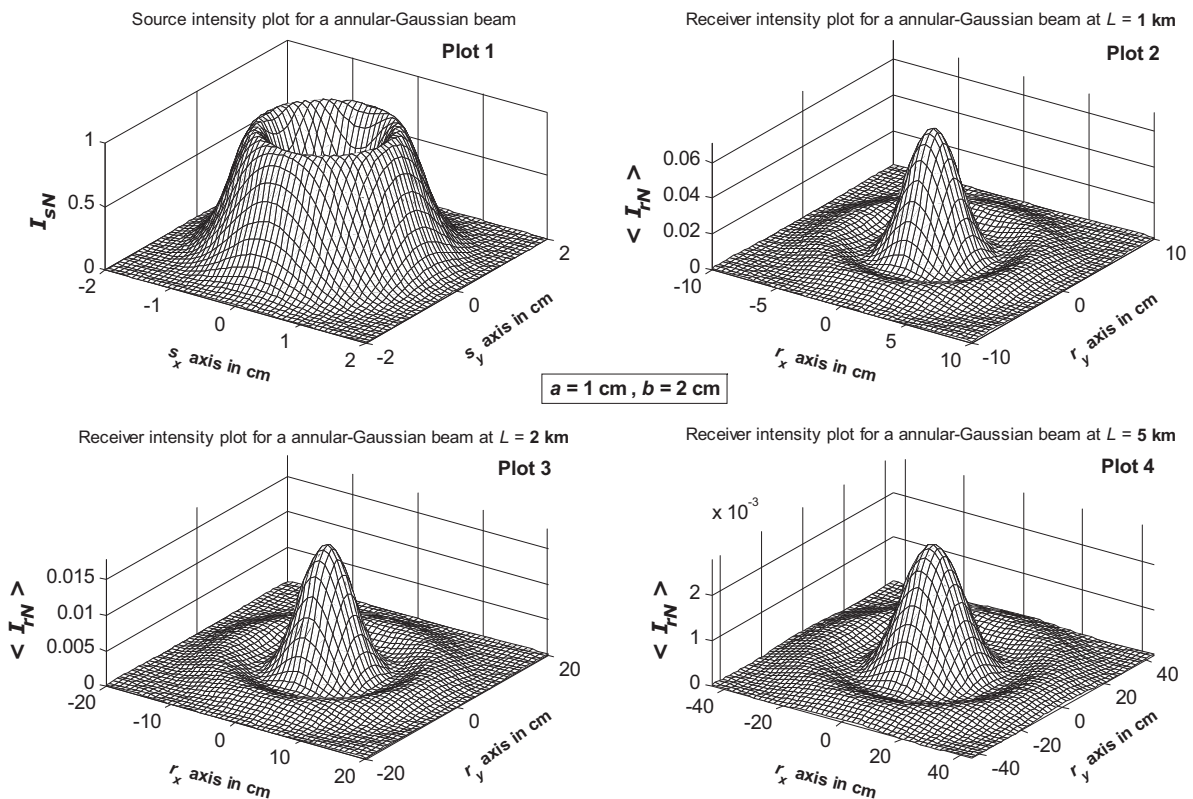


Figure 7: Progress of an annular beam along propagation axis with aperture ring dimensions of  $a = 1$  cm,  $b = 2$  cm.

ring of a complete circle in addition to the central peak. This behaviour is similar to unapertured situations [16], except that the outer ring persists for greater distances.

#### 4. CONCLUSION

We have analyzed the effect of a ring aperture placed on the source plane of the general beam propagating in turbulent atmosphere. From the illustrations presented, it is observed that the aperture does not have a major effect on the beam profile provided that its outer radius is in the range of beam foot-print and has no interior part. When the ring aperture contains an inner part however, it causes somewhat excessive spreading and the formation of outer rings in the received intensity profiles.

#### ACKNOWLEDGMENT

Y. Cai gratefully acknowledges support from the Alexander von Humboldt Foundation.

#### REFERENCES

1. Cai, Y. and Q. Lin, "A partially coherent elliptical flattened Gaussian beam and its propagation," *J. Opt. A: Pure Appl.*, Vol. 6, No. 12, 1061–1066, 2004.
2. Cai, Y. and Q. Lin, "Hollow elliptical Gaussian beam and its propagation through aligned and misaligned paraxial optical systems," *J. Opt. Soc. Am.*, Vol. 21, No. 6, 1058–1065, 2004.
3. Ji, J. and B. Lü, "Matrix formulation of axis-symmetric laser beams through paraxial ABCD system containing hard-edged apertures: A comparative study," *Optik*, Vol. 116, No. 5, 219–225, 2005.
4. Zhang, B., Y. Zhang, and J. Li, "Spectral intensity characteristics of partially coherent flattened multi-Gaussian beams with an axial shadow passing through paraxial ABCD optical systems," *Opt. Commun.*, Vol. 279, No. 1, 7–12, 2007.
5. Du, X. and D. Zhao, "Propagation of decentered elliptical Gaussian beams in apertured and nonsymmetrical optical systems," *J. Opt. Soc. Am.*, Vol. 23, No. 3, 625–631, 2006.
6. Du, X. and D. Zhao, "Propagation of elliptical cosh-Gaussian beams and off-axial elliptical cosh-Gaussian beams in apertured optical systems," *Appl. Phys. B*, Vol. 88, No. 2, 267–272, 2007.
7. Cai, Y. and L. Zhang, "Propagation of a decentered elliptical Gaussian beam through apertured aligned and misaligned paraxial optical systems," *Appl. Opt.*, Vol. 45, No. 22, 5758–5766, 2006.
8. Cai, Y. and L. Hu, "Propagation of partially coherent twisted anisotropic Gaussian Schell-model beams through an apertured astigmatic optical system," *Opt. Lett.*, Vol. 31, No. 6, 685–688, 2006.
9. Chu, X., Y. Ni, and G. Zhou, "Propagation of cosh-Gaussian beams diffracted by a circular aperture in turbulent atmosphere," *Appl. Phys. B*, Vol. 87, No. 3, 547–552, 2007.
10. Eyyuboğlu, H. T. and Y. Baykal, "Transmittance of partially coherent cosh-Gaussian, cosh-Gaussian and annular beams in turbulence," *Opt. Commun.*, Vol. 278, No. 1, 17–22, 2007.
11. Arpali, Ç., C. Yazıcıoğlu, H. T. Eyyuboğlu, S. A. Arpali, and Y. Baykal, "Simulator for general-type beam propagation in turbulent atmosphere," *Opt. Exp.*, Vol. 14, No. 20, 8918–8928, 2006.
12. Eyyuboğlu, H. T., "Propagation of higher order Bessel-Gaussian beams in turbulence," *Appl. Phys. B*, Vol. 88, No. 2, 259–265, 2007.
13. Eyyuboğlu, H. T. and F. Hardalaç, "Propagation of modified Bessel-Gaussian beams in turbulence," *Opt. Laser Technol.*, Vol. 40, No. 2, 343–351, 2008.
14. Eyyuboğlu, H. T., "Hermite hyperbolic/sinusoidal Gaussian beams in ABCD systems," *Optik*, Vol. 118, No. 6, 289–295, 2007.
15. Eyyuboğlu, H. T., "Propagation of Hermite-cosh-Gaussian laser beams in turbulent atmosphere," *Opt. Commun.*, Vol. 245, No. 1–6, 37–47, 2005.
16. Eyyuboğlu, H. T., S. Altay, and Y. Baykal, "Propagation characteristics of higher-order annular Gaussian beams in atmospheric turbulence," *Opt. Commun.*, Vol. 264, No. 1, 25–34, 2006.

# Measurements and Physical Electromagnetic Statistical Modeling of mm Wavelength Propagation

Zaid Muhi-Eldeen<sup>1</sup>, Miqdad Al-Nuaimi<sup>1</sup>, and Leonidas P. Ivrissimtzis<sup>2</sup>

<sup>1</sup>University of Glamorgan, UK

<sup>2</sup>University of Ioannina, Greece

**Abstract**— A Physical statistical model based on GIS terrain incorporation, along with the computationally efficient simulations of the electromagnetic channel and interferences in fixed wireless links at mm-wavelengths, operating within sub-urban channels are presented. The ability for such predictions is highly demanded since it aids in the characterization, design and deployment of the pertinent networks. Massive measurement campaigns were conducted over several paths, for the purposes of modeling assessing. Since both the desired and interference links in a cellular structure attain a dominant signal, knowledge of the Rician and the carrier-to-interference ratio (CIR) distributions becomes an essential principle measure in determining performances of millimetric channels; hence they were used for model evaluation purposes.

## 1. INTRODUCTION

Local Multi-Point Distribution Systems (LMDS) are the main potential applications for mm-wavelength systems. Link design and deployment [1, 2] for such networks requires an understanding of the underlying propagation channel and benefits from a quantitative description of the fundamental mechanisms that affect the integrity of the link, namely attenuation, noise and interference. Development of analytical and numerical modeling tools enables the rationalization and optimization of the system design and its main constraints, such as cost of deployment (cell size, frequency and polarization planning), antenna parameters (positioning and radiation characteristics), and link performance (coverage and outage probability at the receiver), by accounting for the impairments introduced by the wireless channel.

Although the wireless link is fixed, the propagation channel is time-varying, because of the motion of the objects within it, antenna displacements of the order of the wavelength of propagation, as well the variability of the electromagnetic properties of the environment due to varying weather conditions. In addition, at high frequencies, a geometric description of the environment at sub-wavelength scale, including the coordinates of the hub and subscriber antenna locations and orientation, is almost impossible. Hence, due to random errors in the geometrical presentation and the time-varying nature of the channel, the analysis of the propagation mechanisms merits a statistical description, based only on a coarse knowledge of the geometry, where, in essence, the calculated fields and signals are random variables. From such a description, the expected value and probabilistic distributions of the main link parameters can be deduced.

Papazian et al. [3] reported on radio coverage estimates and identified fundamental impairments on the attenuation and its variability, as well as the delay spread, due to obstruction by buildings and vegetation for LMDS with narrow- and broad-band measurements at 27.5–29.5 GHz in small sub-urban cells. Further, Xu et al. [4] investigated the broadband and dispersive channel behavior due to multipath for line-of-sight (LOS) links at 38-GHz under different weather conditions and proposed a Rician model, along with a rain-rate dependent K-factor, for the short term variability of the signal attenuation. The system and co-channel interference characteristics of representative LMDS links were studied analytically and numerically by Gong and Falconer [5]. Their analysis accounted for the subscriber and hub antenna characteristics, site diversity and power control. The behavior and performance analysis of a non-LOS path, particularly benefiting from specular reflection in a multipath environment, were presented by Muhi-Eldeen et al. in [6].

The present work aims at establishing and validating a physical electromagnetic statistical model for an urban propagation channel and its physical representation, with particular consideration of the fading margins of LOS links, which can be either direct or interfering. The frequency of propagation is 40 GHz, according to the bands allocated for future European LMDS systems. In particular, the study focuses on the analysis and measurements of the effects of scattering on the direct and interfering electromagnetic fields in a LMDS link at mm-waves, taking place in urban or sub-urban residential or industrial environments. The propagation environment is statistically modeled from coarse digital GIS data and ad hoc reflectivity measurements. The

electromagnetic (EM) field and signal power at the receiving station are considered random and calculated employing irregular surface scattering methods, augmented by geometrical optics (GO) techniques. The calculations assume realistic transmitting and receiving antenna systems and directive gain patterns. The random nature of the EM fields suggests a presentation in terms of Probabilistic Density Functions (PDF's) and their associated first and higher order moments. Of particular interest is the parameterization of the random simulations and their association with universal statistical models, such as the Rayleigh and Rician distributions, i.e., the description of the received field strength and the characterization of the channel in terms of simple parameters. Such parameterization is useful in the classification of the environment and can be utilized in network design and deployment. Power distribution effects of the environmental scatter, on both the direct LOS hub-subscriber and possible interfering links in the uplink or downlink of the same or adjacent frequency-duplex channels, which can occur in a fully deployed LMDS, are simulated based on the proposed model.

The article is organized as follows: Section 2 outlines the propagation geometry and describes the fundamental geometrical attributes of the model. In Section 3, the theoretical formulation of the elementary scattering mechanism is presented, along with the derivation of the mean and standard deviation of the field quantities, while Section 4 presents the proposed statistical model for the propagation channel in terms of a Rician distribution and pertinent parameters. Finally, representative narrowband measurements and comparisons with the predictions from EM field simulations are presented in Section 5.

## 2. PROPAGATION GEOMETRY

The generic system geometry is illustrated in Fig. 1. A global system of coordinates  $(x, y, z)$  is established, in which  $z = 0$  represents the mean ground. The building surfaces, any site specific GIS data, as well as the location of the antennas, are expressed in this reference system of coordinates. On the other hand, the antenna radiation pattern functions are described and calculated with reference to antenna associated coordinate systems, namely  $(x_1, y_1, z_1)$  and  $(x_2, y_2, z_2)$ . The far-field radiation pattern of the transmitter antenna in free space and in the direction of the unit vector  $\hat{s}_1$  and at a distance  $s_1$  is written as

$$\mathbf{E}^T(\hat{s}_1; s_1) = \mathbf{e}^T(\hat{s}_1) \frac{e^{-jk s_1}}{s_1} \quad (1)$$

where  $\mathbf{e}^T(\hat{s})$  is a pattern vector, depending only on the direction of the observation point with respect to the corresponding antenna-attached coordinate system. A similar spatial dependency applies for the spherical EM wave incident at the receiver antenna from a direction  $\hat{s}_2$  and a distance  $s_2$ . The raw GIS data used are translated and processed to provide polygonal plates, corresponding to building surfaces, as defined by the coordinates of their corners.

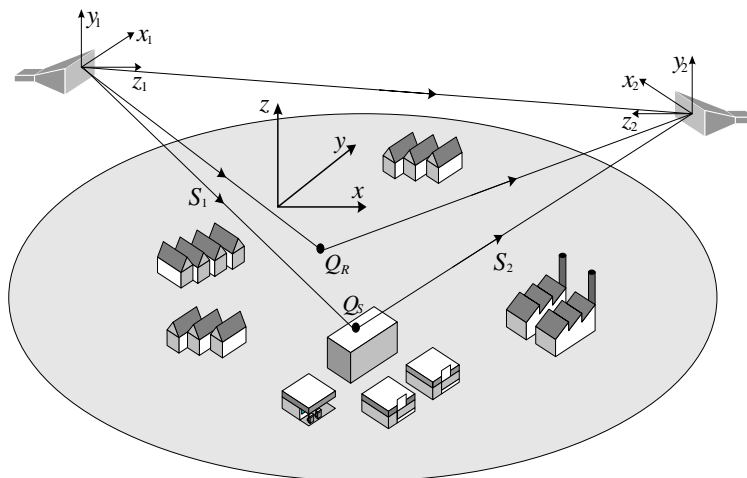


Figure 1: Urban scattering geometry.

### 3. SCATTERING FORMULATION

The surface element in Fig. 2 is considered to be located at the Fraunhofer region of both the transmitting and receiving antennas and, hence, the incident field is considered locally a plane wave. If the total electric and magnetic fields at each point  $\mathbf{r}$  of the surface area, normalized with respect to the incident field wave factor  $\exp(-jk_0 s_1)/s_1$ , are  $\mathbf{e}$  and  $\mathbf{h}$ , respectively, while the corresponding incident fields are denoted by  $\mathbf{e}^T$  and  $\mathbf{h}^T$ , the scattered field  $\mathbf{E}^s$  from the surface can be described in terms of a Stratton-Chu based integral [7]. Accordingly, a two-dimensional representation of the scattered field in terms of the elevation of the  $\zeta(\boldsymbol{\rho})$  above its mean plane  $z = 0$  reads

$$\mathbf{E}^s = \frac{-jk_0 e^{-jk_0(s_1+s_2)}}{4\pi s_1 s_2} \cdot \iint_{\Delta_s} \left\{ \eta_0 \hat{\mathbf{n}} \times (\mathbf{h} - \mathbf{h}^T) - \hat{\mathbf{s}}_2 [\hat{\mathbf{n}} \cdot (\mathbf{e} - \mathbf{e}^T)] + \hat{\mathbf{s}}_2 \times (\hat{\mathbf{n}} \times (\mathbf{e} - \mathbf{e}^T)) \right\} \cdot \exp[jk(\mathbf{q} \cdot \boldsymbol{\rho} + q_z \zeta(\boldsymbol{\rho}))] \cdot \frac{dxdy}{n_z} \quad (2)$$

with  $\boldsymbol{\rho} = x\hat{\mathbf{x}} + y\hat{\mathbf{y}}$  and  $\mathbf{q} = \hat{\mathbf{s}}_2 - \hat{\mathbf{s}}_1$ . A tangent plane approximation is subsequently employed for the approximation of the field on the surface element, with respect of which, the total field at the surface point  $\mathbf{r}$  can be written as

$$\mathbf{e} = \mathbf{e}^T + \mathbf{e}^r, \quad \mathbf{h} = \mathbf{h}^T + \mathbf{h}^r \quad (3)$$

with

$$\mathbf{e}^r = \mathfrak{R}(\hat{\mathbf{s}}_1, \hat{\mathbf{n}}(\boldsymbol{\rho}); \varepsilon(\boldsymbol{\rho})) \cdot \mathbf{e}^T, \quad \mathbf{h}^r = (\hat{\mathbf{s}}_2 \times \mathbf{h}^r) / \eta_0 \quad (4)$$

In the above,  $\mathfrak{R}(\hat{\mathbf{s}}_1, \hat{\mathbf{n}}(\boldsymbol{\rho}); \varepsilon(\boldsymbol{\rho}))$  signifies the local reflection dyadic matrix at the surface point  $(\boldsymbol{\rho}, \zeta(\boldsymbol{\rho}))$  and  $\eta_0$  is the characteristic impedance of free space. Using Eqs. (3) and (4) into Eq. (2) one obtains

$$\mathbf{E}^s \approx \frac{jk_0 e^{-jk_0(s_1+s_2)}}{2\pi s_1 s_2} \frac{(\hat{\mathbf{q}} \cdot \hat{\mathbf{s}}_2) \mathfrak{R}(\hat{\mathbf{s}}_1, \hat{\mathbf{q}}; \varepsilon(\boldsymbol{\rho}_s)) \cdot \mathbf{e}^T}{q_z} I(\hat{\mathbf{q}}) \quad (5)$$

where

$$I(\hat{\mathbf{q}}) = \iint_{\Delta_s} \exp[jk(\hat{\mathbf{q}} \cdot \boldsymbol{\rho} + q_z \zeta(\boldsymbol{\rho}))] \cdot dxdy \quad (6)$$

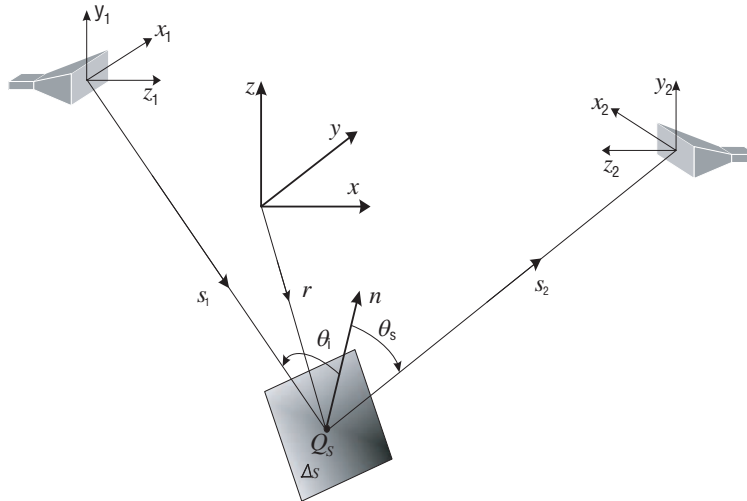


Figure 2: Geometry of a rectangular scattering surface.

#### 3.1. The Mean Field

The variation of the electrical properties of the scattering surface, which are further discussed below, is considered independent of the surface elevation above its mean level. Assuming discrete values of the complex relative dielectric permittivity a relative PDF can be given by

$$p_\varepsilon(\varepsilon) = p_n \delta(\varepsilon - \varepsilon_n) \quad (7)$$

Further, assuming a PDF for the elevation of the surface points, with a characteristic function

$$p(\Psi) = \int p_{\zeta}(\zeta) \cdot e^{j\Psi\zeta} d\zeta, \quad (8)$$

then the mean value of the scattered field over a rectangular surface of dimensions  $S_0 = 2L_x \times 2L_y$  becomes

$$\overline{\mathbf{E}^s} \approx \frac{jkS_0 e^{-jk(s_1+s_2)} (\hat{\mathbf{q}} \cdot \hat{\mathbf{s}}_2) P(kq_z) \sin(ckq_x L_x) \sin(ckq_y L_y) \sum_n p_n \mathfrak{R}(\hat{\mathbf{s}}_1, \hat{\mathbf{q}}; \varepsilon_n) \cdot \mathbf{e}^T}{2\pi s_1 s_2 q_z} \quad (9)$$

### 3.2. Mean Field Power Density

The calculation of the mean power density of the scattered field involves the statistical average of the products

$$\overline{E_u^s (E_v^s)^*} \approx \left( \frac{k\hat{\mathbf{q}} \cdot \hat{\mathbf{s}}_2}{2\pi s_1 s_2 q_z} \right)^2 \cdot \sum_{m,n} \sum_{\kappa,\mu} p_n p_m R_{u\kappa}(\hat{\mathbf{s}}_1, \hat{\mathbf{q}}; \varepsilon_n) R_{v\mu}^*(\hat{\mathbf{s}}_1, \hat{\mathbf{q}}; \varepsilon_m) \left( e_{\kappa}^T (e_{\mu}^T)^* \right) \cdot \overline{J(\hat{\mathbf{q}})} \quad (10)$$

with

$$J(\hat{\mathbf{q}}) = \iiint_{\Delta_s} \iiint_{\Delta_s} \exp \{ jk [\hat{\mathbf{q}} \cdot (\boldsymbol{\rho} - \boldsymbol{\rho}') + q_z (\zeta(\boldsymbol{\rho}) - \zeta(\boldsymbol{\rho}'))] \} \cdot dx dy dx' dy' \quad (11)$$

## 4. STATISTICAL FORMULATION OF THE PROPAGATION CHANNEL

The scattering contribution from the urban propagation environment at the receiver is written as the superposition of randomly distributed scattered components from a set of building surfaces or elevated ground patches, i.e.,

$$\mathbf{e}^s = \sum_{m=1}^N \mathbf{E}_m^s \quad (12)$$

By virtue of the central limit theorem and given the large number of independent scattering surfaces that contribute to the total diffused scatter, the field will be normally distributed, with zero mean real and imaginary parts. The average received scattered power, assuming that contributions from the different scattering surfaces are uncorrelated, equals the sum of the second order moments of the fields, as given by Eq. (9). In particular,

$$(a^s)^2 = \mathbf{e}^s \cdot (\mathbf{e}^s)^* = \sum_{m=1}^N \overline{\mathbf{E}_{(m)}^s \cdot (\mathbf{E}_{(m)}^s)^*} = \sum_{m=1}^N \sum_u \overline{\mathbf{E}_{(m),u}^s \cdot (\mathbf{E}_{(m),u}^s)^*} \quad (13)$$

where the average of can be obtained for each polarization. The random scattered field power intercepted by the receiving antenna is incoherently superimposed to the direct field power

$$p^d = (a^d)^2 = \mathbf{e}^d \cdot (\mathbf{e}^d)^* = \frac{|\mathbf{e}^T(\hat{\mathbf{s}}_0) \cdot \mathbf{e}^R(-\hat{\mathbf{s}}_0)|^2}{s_0^2} \quad (14)$$

as well as that of a Geometrical Optics field reflected from a presumably infinite ground, which is determined from

$$\mathbf{e}^r = \mathfrak{R}(\hat{\mathbf{s}}_1^r, \hat{\mathbf{q}}^r; \varepsilon) \cdot \mathbf{e}^T(\hat{\mathbf{s}}_1^r) \frac{e^{-jk(s_1^r+s_2^r)}}{s_1^r + s_2^r} \quad (15)$$

In summary, the signal at the receiver antenna terminals can be represented by the complex random variable

$$r = a \exp(j\phi) = a^d \exp(j\phi^d) + a^r \exp(j\phi^r) + a^s \exp(j\phi^s). \quad (16)$$

in which the envelope of  $a^r \exp(j\phi^r) + a^s \exp(j\phi^s)$  is Rayleigh distributed, while the relative phases are independent random variables, uniformly distributed in  $(0, 2\pi)$ . Clearly, the envelope of the total received signal, in the presence of a deterministic direct field, will have a Rician distribution, i.e.,

$$f_a(a) = \frac{a}{\sigma^2} \exp\left(-\frac{a^2 + s^2}{2\sigma^2}\right) I_0\left(\frac{as}{\sigma^2}\right) \quad (17)$$

with

$$2\sigma^2 = \mathbf{E} \left[ |a^r \exp(j\phi^r) + a^s \exp(j\phi^s)|^2 \right] = (a^r)^2 + (a^s)^2 \quad (18)$$

and  $s^2 = (a^d)^2$ . Introducing the Rician K-factor

$$K = s^2/(2\sigma^2) \quad (19)$$

where  $\sigma$  signifies the scattered field power, the distribution of the total received power  $p = a^2/2$ , for a normalized direct field ( $s^2 = 1$ ), becomes

$$f_p(p) = 2K \exp[-K(2p + 1)] \cdot I_0 \left( 2K \sqrt{2p} \right) \quad (20)$$

Given a set of random, simulated or measured data, the K-factor can be derived from the mean  $\mu_p = \sigma^2 + s^2/2$  and standard deviation  $\sigma_p^2 = \sigma^4 + s^2\sigma^2$  of received power samples and the formula

$$K = \frac{\sqrt{\mu_p^2 - \sigma_p^2}}{\mu_p - \sqrt{\mu_p^2 - \sigma_p^2}} \quad (21)$$

which is obtained from the definition in Eq. (12). The determination of the K-factor allows the complete narrowband characterization of the flat-fading effects of the wireless propagation channel, namely the effects of building and ground scatter to the received signal, signal-to-noise and signal-to-interference ratio variability. Hence, such a characterization of the wireless channel reduces to an approximate derivation of the Rician K-factor. The latter attains high values for LOS links where the direct boresight field from the transmitter dominates the receiver signal, but it can reduce to smaller values for long interfering links and, eventually, degenerates to a Rayleigh distribution for NLOS or ideal, cross-polarization reception.

Interference studies of the same type of channel are restricted to LOS conditions for both the interfering and useful links. The envelope for both links will follow a Rician distribution with different K-factors, nominally a much higher value for the direct link. It can be shown [10] that the co-channel SIR is distributed according to the PDF

$$f_z(z) = \frac{2zb}{(b+z^2)^2} \exp\left(-\frac{K_I z^2 + Kb}{b+z^2}\right) \cdot \left[ \left(1 + \frac{Kz^2 + K_I b}{b+z^2}\right) I_0(c(z)) + c(z) I_1(c(z)) \right] \quad (22)$$

with

$$c(z) = \frac{\sqrt{4K K_I b z^2}}{b+z^2} \quad (23)$$

and  $b = \sigma^2/\sigma_I^2$  is the ratio of the scattered field power of the direct over the interfering link, and  $K_I$  denotes the K-factor of the Rician distributed interfering link.

## 5. MEASUREMENTS AND DISCUSSION

In addition to fading impairments to the direct link, a number of interference scenarios have been investigated both numerically and experimentally by the authors in [11]. The objective here is the determination of the PDF of a random carrier to co-channel interference ratio (CIR) for different antenna positions, orientations and gains within the environment and, subsequently, the characterization of the wanted link and the cumulative scattered fields standard deviations. A map of one of the several experimental links investigated is shown in Fig. 3.

In all link measurements, a standard 20 dBi horn antenna placed on an elevated position above the highest point within the useful propagation environment, is used as a transmitter of a vertical or horizontal wave. The receiver antennas are placed on top of a mobile platform at approximately 3.5 m above street level. Pyramidal horn antennas with gains of 10, 15 and 20 dBi and lens antennas with 29 dBi and 44 dBi of nominal gains at 40 GHz have been utilized in the measurements. In the simulations, the pyramidal horn antenna radiation patterns are described in terms of the analytical expression in [16].

On the other hand, higher than 20 dBi antennas are represented as circular apertures of uniform field distribution and dimension that provide the same gain and beamwidth in the boresight direction. The transmitter comprises a Gunn diode oscillator, in a temperature controlled environment, that provides a stable reference between 39.75 and 40.25 GHz.



Figure 3: Aerial photo of the industrial link.

The received signal is down-converted to an intermediate frequency, amplified, peak-held and sampled with a resolution bandwidth of 1 MHz. Its associated distribution functions are obtained from the sampling of the received signal, while translating the receiver antenna in directions longitudinal or transversal to the direct link axis, with a maximum displacement of 50 wavelengths from its central position, with approximately 800 signal power samples recorded for each run. Within this displacement window the moving average of the signal power samples is relatively constant. Varying receiver antenna position is equivalent to a fixed link being presented by a stochastically, time-varying scattering environment.

Plots of the PDF of the measured data in most LOS cases observes a Rician distribution, which degenerates to a Rayleigh distribution for cross-polar arrangements and as the receiver recedes towards the edge of the coverage area.

In Figs. 4–5 the PDF of the normalized received signal power, as obtained from either the measurements or the random simulations are shown and compared with the theoretical distribution for a normalized envelope Rician distribution and for the two main links considered (TX1-RX and TX2-RX in Fig. 3).

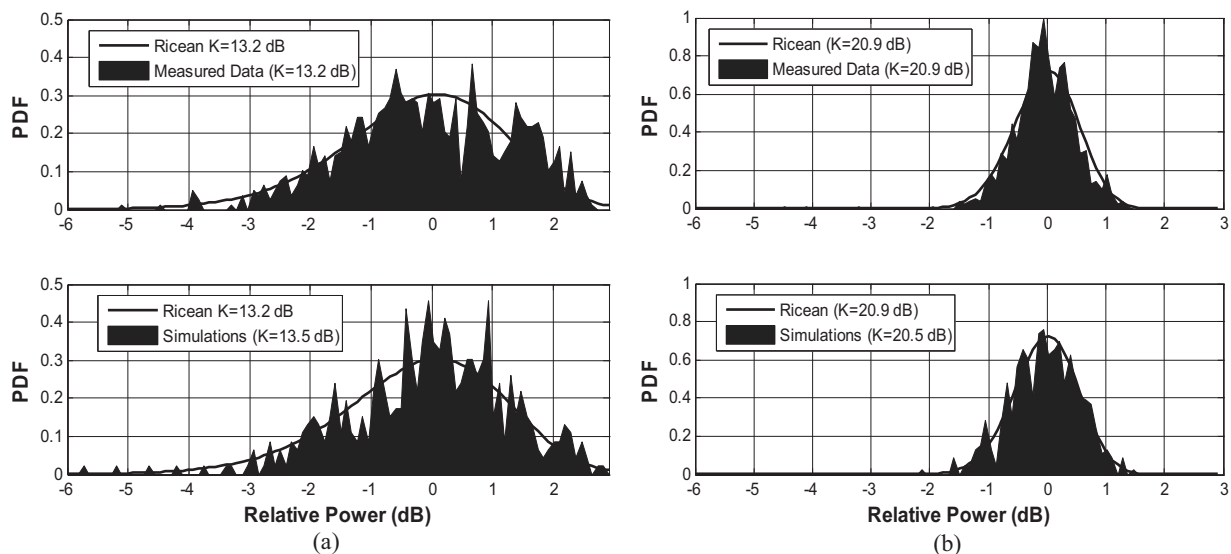


Figure 4: PDF of the received field and comparisons with the theoretical Rician and the distribution obtained from simulations for the vertical polarization: (a) TX1 link; (b) TX2 link.

The horizontal polarization case, not shown here, show a similar probabilistic behavior with that

of the vertical polarization in Fig. 4. Fig. 5 illustrates the cross-polarization case (transmitted field horizontally polarized and vertically polarized receiver antenna) and the comparison is made against the Rayleigh distribution. The minor discrepancy between the measurements and the simulations is due to the assumption of ideal orthogonal patterns in the simulations, which is not the case in practice resulting in higher direct field components.

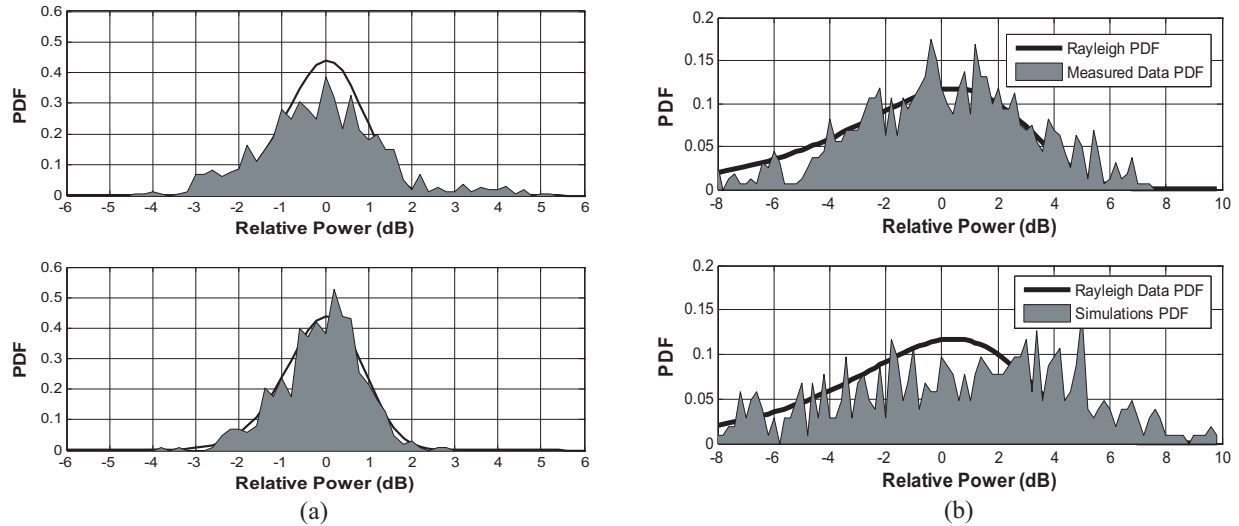


Figure 5: PDF of the received field and comparisons with the theoretical Rician and the distribution obtained from simulations for the cross-polarization case: (a) TX1 link; (b) TX2 link.

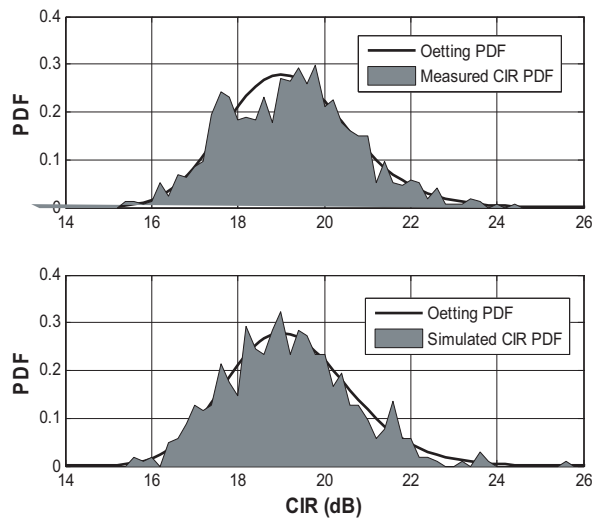


Figure 6: PDF of the co-channel CIR between TX1 and TX2 for a 20 dB receiver and transmitter antenna gains and the vertical polarization case.

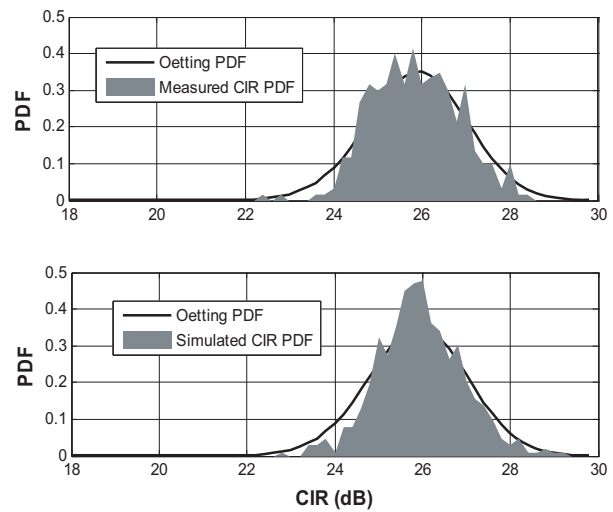


Figure 7: PDF of the co-channel CIR between TX1 and TX2 for a 20 dB receiver and transmitter antenna gains and the horizontal polarization case.

Figures 6–8 illustrate the probabilistic behavior of the CIR, where TX2-RX and TX1-RX are the wanted and interfering links, respectively. It becomes evident from comparisons with the theoretical (solid) curve that the CIR observes the distribution of the ratio of two Rician channels, referred to as the Oetting's distribution. Again, the theoretical distribution is based on the K-factors and ratio of the scattering field powers of the two links, as derived from the statistical analysis of the measured data samples and application of Eqs. (19) and (20). The probabilistic distribution and the underlying statistical parameters of the measured data and signal samples from random simulations shows good agreement, especially for the co-polarization case.

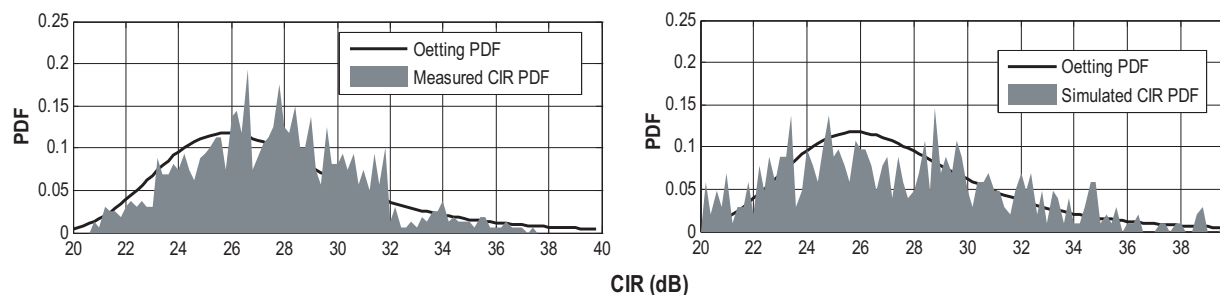


Figure 8: PDF of the co-channel CIR between TX1 and TX2 for a 20 dBi receiver and transmitter antenna gains and the cross-polarization case.

## 6. MODEL APPLICATIONS

The novel physical-statistical model proposed has a number of potential applications, some of which are considered for future and further work. One of the crucial applications of the model is the parameterization of the physical attributes of the channel and the associated electromagnetic mechanisms and, ultimately, the representation of the channel in terms of Rician parameters for a line-of-sight received field power. With those parameters, the model enables the prediction cell SIR statistics and distributions. Furthermore, with typical system values in consideration for BER thresholds (modulation dependent) and capacity factors (outage probabilities and coverage) along with the utilization of digital topographical data, and site-specific information (materials reflection coefficients and roughness factors), any cell plans can be evaluated, enabling the estimating the minimum frequency reuse distances and average cell radii calculations, which in turn, aid in minimizing interference levels for optimum system performances. In an interference limited environment, such predictions incorporating antenna heights and patterns become essential for any millimeter radio system design.

## 7. CONCLUSIONS

A stochastic model for the characterization of fixed wireless links operating in millimeter wave frequencies in urban propagation environments was presented. The model was based on a physical representation of the electromagnetic scatter by irregular surfaces comprising the propagation environment, with large-scales irregularities, augmented with realistic assumptions on the statistical description of the cumulative scattered, ground reflected and direct fields. Random simulations have been conducted and compared with measurements showing good agreement in the prediction of the main statistical parameters and, in particular the K-factor and the relative power of the scattering field contribution, thus verifying the main assumptions relating to the received signal strength and CIR distributions, including the validity of the Rician model in describing the signal envelope variability and outage probability in complex urban environments.

## REFERENCES

1. Acts Project 215, Cellular Radio Access for Broadband Services (CRABS)-Specification of Next Generation of LMDS Architecture, D2P1B, Feb. 1999.
2. Roman, V. I., "Frequency reuse and system deployment in local multipoint distribution system," *IEEE Pers. Comm.*, 20-27, Dec. 1999.
3. Papazian, P. B., et al., "Study of the local multipoint distribution service radio channel," *IEEE Trans. Broad.*, Vol. 43, No. 2, June 1997.
4. Xu, H., T. S. Rappaport, R. J. Boyle, and J. H. Schaffner, "Measurements and models for 38-GHz point-to-multipoint radiowave propagation," *IEEE J. Sel. Areas in Comm.*, Vol. 18, No. 3, 310-321, March 2000.
5. Gong, S. Q. and D. Falconer, "Co-channel interference in cellular fixed broadband access systems with directional antennas," *Wireless Pers. Comm.*, Vol. 10, 103-117, Oct. 1998.
6. Muhi-Eldeen, Z., M. O. Al-Nuaimi, J. Richter, and L. P. Ivriissimtzis, "Performance analysis of reflection paths for millimeter wavelength systems," *IEEE Int. Conf. Computer Systems and Applications*, Amman, Jordan, May 2007.
7. Bass, F. G. and I. M. Fuks, *Wave Scattering from Statistically Rough Surfaces*, Pergamon Press, 1979.

8. Papoulis, A., *Probability, Random Variables, and Stochastic Processes*, McGraw-Hill, 1981.
9. Balanis, C. A., *Advanced Engineering Electromagnetics*, Wiley, 1989.
10. Oetting, J. D., "The effects of fading on antijam performance requirements," *IEEE J. Sel. Areas Comm.*, Vol. 5, 155–161, Feb. 1987.
11. Muhi-Eldeen, Z., M. O. Al-Nuaimi, J. Richter, and L. P. Ivrisimtzis, "Modeling and measurements of mm wavelength propagation in urban environments," *IEEE APS*, Jan. 2007.
12. Balanis, C. A., *Antenna Theory and Design*, Harper & Row, 1981.

# Broadband VCO Using Tunable Metamaterial Transmission Line with Varactor-loaded Split-ring Resonator

Jaewon Choi, Hyoungjun Kim, Chongmin Lee, and Chulhun Seo  
University of Soongsil, Korea

**Abstract**— In this paper, the broadband voltage-controlled oscillator (VCO) using tunable metamaterial transmission line with varactor-loaded split-ring resonator (VLSRR) is presented. It is demonstrated that VLSRR coupled to microstrip line can lead to metamaterial transmission line with tuning capability. The negative effective permeability is provided by the VLSRR in a narrow band above the resonant frequency. The bias of VLSRR is controlled by the varactor diodes. The phase noise of VCO is  $-108.84 \sim -106.84$  dBc/Hz @ 100 kHz in the tuning range, 5.407 ~ 5.84 GHz. The figure of merit (*FOM*) called power-frequency-tuning-normalized (*PFTN*) is 20.144 dB.

## 1. INTRODUCTION

In the last few years, the need for more frequency bands has been increasing in the telecommunications with the emergence of new standards. The implementation of multi-band voltage VCO attracts much attention because a tuning range of VCO is one of the most critical elements for multi-standard frequency synthesizers using frequency fractional-N PLL, for example, in which the resolution frequency is infinite [1].

SRRs are sub-wavelength resonators able to inhibit signal propagation in a narrow band in the vicinity of their resonant frequency, provided the magnetic field is polarized along the axis of the ring. This has been interpreted as a result of the extreme values (positive/negative) of the effective permeability below/above SRRs resonance. Alternatively, this frequency-selective behavior can be explained by the induced current loops in the rings at resonance. These current loops are closed through the distributed capacitance between concentric rings. From this, SRRs can be operated as LC resonant tanks that can be externally driven by a magnetic field and are therefore able to inhibit signal propagation in a certain narrow band if they are properly oriented [2–4].

In the previous papers, it was shown that SRRs loaded with varactor diodes achieved electronic tuning in SRR-based notch filter. This is due to the variable capacitance, which allows for certain control of the resonator's frequency. In this paper, the broadband VCO using this resonance frequency tuning property of VLSRR is presented.

## 2. VARACTOR-LOADED SPLIT-RING RESONATOR DESIGN

Figure 1 shows the two topologies. One is the untunable circular SRR originally proposed by Pendry, and the other is the tunable VLSRR originally proposed by F. Martin, J. G. Garcia. It is similar to the topology originally proposed by Pendry, although the separation  $s$  between rings is no longer uniform in order to connect the varactor diode between the internal and external conductors. Namely, the distance of the region where the varactor diode is placed is increased. Also, a metal pad is added to the center of the particle for easy diode biasing, and square-shaped rings have been considered to enhance the coupling between the microstrip line and the rings. With this structure, the electromagnetic behavior of the VLSRRs does not substantially differ from that of

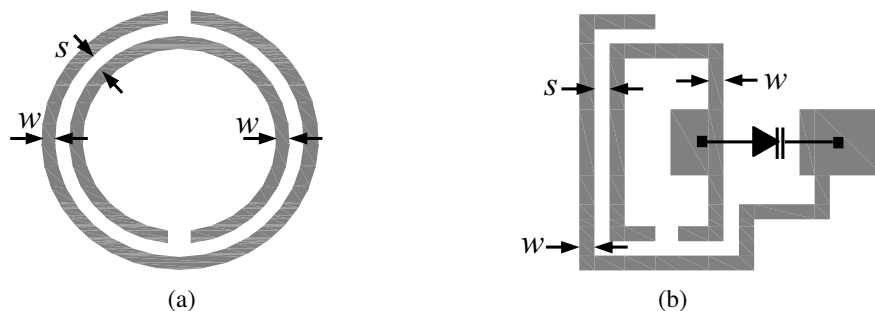


Figure 1: (a) Untunable circular SRR, (b) Tunable varactor-loaded SRR (VLSRR).

the SRRs, except for the fact that certain electronic control of the resonant frequency is possible by the varactor diodes. These are connected between the inner and outer conductors and affect the edge capacitance corresponding to the right half of the structure. Another difference between SRRs and VLSRRs concerns their excitation of current loops at resonance. In the former, these currents are mainly induced by the magnetic field flowing into the inner ring, whereas in VLSRRs, the rings' excitation is mainly obtained by the magnetic field penetrating the inter rings' region where the varactor diodes are placed.

Since the equivalent capacitance is given by the edge capacitance between concentric rings, the resonant frequency can be made very small by decreasing the rings' separation  $s$ . Concerning the line-to-VLSRR coupling, we have a priori assumed that VLSRRs can be driven either by the axial magnetic field generated by the line (inductive coupling) or by the electric field generated between the line and the external ring (capacitive coupling). Both couplings have been properly modeled by means of the mutual inductance and the edge capacitance between the line and the external ring. As shown Figure 1(b), the right-hand arm of the outer ring has been shortened, since no appreciable current flows through it. Namely, the electric current is mostly absorbed by the varactor diodes, preventing it from circulating across the portion of the external ring comprised of the diode junction and the slit [2].

### 3. DESIGN OF TUNABLE METAMATERIAL TRANSMISSION LINE WITH VLSRR

Based on the frequency selective properties of SRRs, we have designed the compact stop band filter in microstrip. Tunability in the metamaterial transmission line has been achieved by replacing the conventional SRRs by VLSRRs. These structures have been optimized to obtain high magnetic coupling between the line and the rings and hence high rejection levels in the forbidden bands. For the coplanar waveguide (CPW) stop band filters, SRRs have been etched in the back substrate side, underneath the slots, while for the microstrip structures, the rings placed in close proximity to the conductor strip have been designed with a square-shaped geometry in order to enhance line-to-VLSRR coupling.

Figure 2 shows the layout of the tunable metamaterial transmission line with a two-stage prototype device. Figure 2(a) and (b) show the top view and the bottom view of the layout, respectively. In this design, the topology of Figure 1(b) has been used, and we have included the inductive chokes between the rings and the voltage source to further prevent an RF path to ground through the series resistance of the voltage source. As shown in Figure 2(b), the rectangular box indicates the inductive chokes. The circular white box indicates the connection between the signal plane and the ground plane as the voltage source biasing. The voltage source is fed at the end of the line for supplying power in the ground plane. The effects of losses associated with the presence of the VLSRRs are reduced by this way. We have used the chip-inductor as the inductive chokes. The designed device consists of a  $50\ \Omega$  microstrip line with two VLSRR pairs placed at both sides of the line. The tunable metamaterial transmission line was fabricated on Taconic substrate with a dielectric constant of 3.2 and a thickness of 31 mils. To tune the rejection position of the resonator, M/A-COM's MA46H202 varactor diodes have been used. These devices exhibit a high capacitance ratio of  $0.6 \sim 7.0\ \text{pF} @ 0 \sim 26\ \text{V}$ . This capacitance range affects the edge capacitance of the rings, and therefore is adequate for our purposes. With regard to VLSRR dimensions, this has been estimated to provide a resonant frequency in the vicinity of 5.4 GHz. The ring strip widths are  $w = 0.2\ \text{mm}$ , while the separation between rings has been set to  $s = 0.2\ \text{mm}$ , except at the right edge of the structure, where this dimension has been increased to provide sufficient space for the

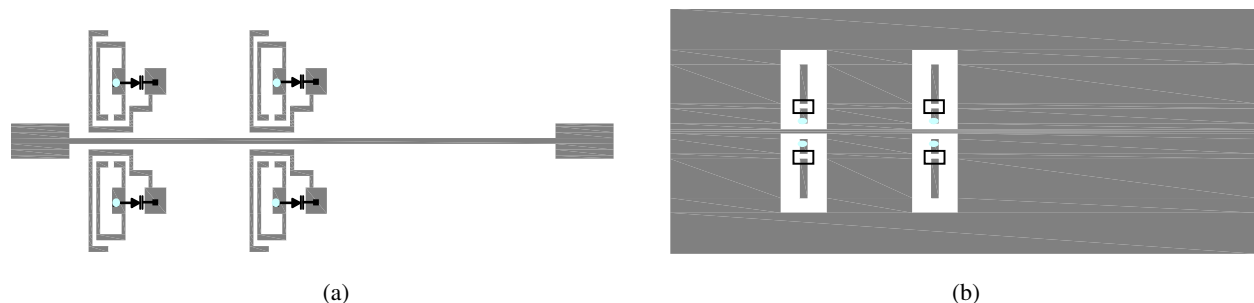


Figure 2: Layout of the two-stage tunable metamaterial transmission line (a) Top view, (b) Bottom view.

varactor diodes. To enhance the coupling between the line and the rings, their separation has been minimized as much as possible.

Figure 3 shows the fabrication of the tunable metamaterial transmission line, and the measured frequency response is depicted in Figure 4. As expected, a stopband behavior with tunable capability is obtained. A wide tuning range has been obtained with rejection levels of  $-31 \sim -8$  dB @ 5.37 ~ 5.87 GHz (about 500 MHz). If the varactor diodes are absent, the current loops do not flow to the inner ring and bias pad, and this resonance is that corresponding to a single ring with an aperture. However, if the varactor diodes are added, the whole current flows through the varactor diodes. The frequency response of the device is decreased, and the bias of the varactor diodes can be controlled by the control voltage. At low varactor diode control voltage, the contribution of the varactor diodes to the whole capacitance is greater, and therefore, the effects of losses decrease. This explains the rejection reduction when the control voltage is increased [2].

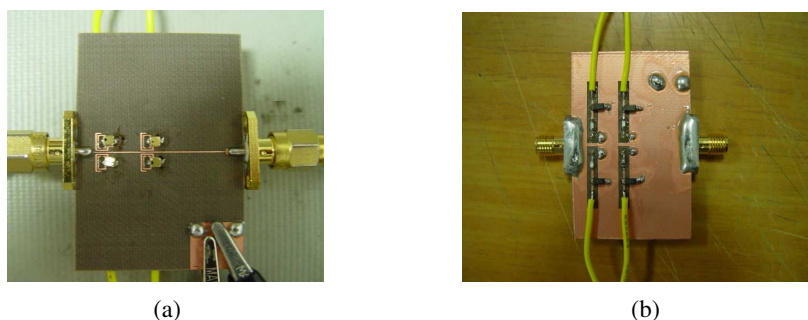


Figure 3: Fabrication of the two-stage tunable metamaterial transmission line (a) Top view, (b) Bottom view.

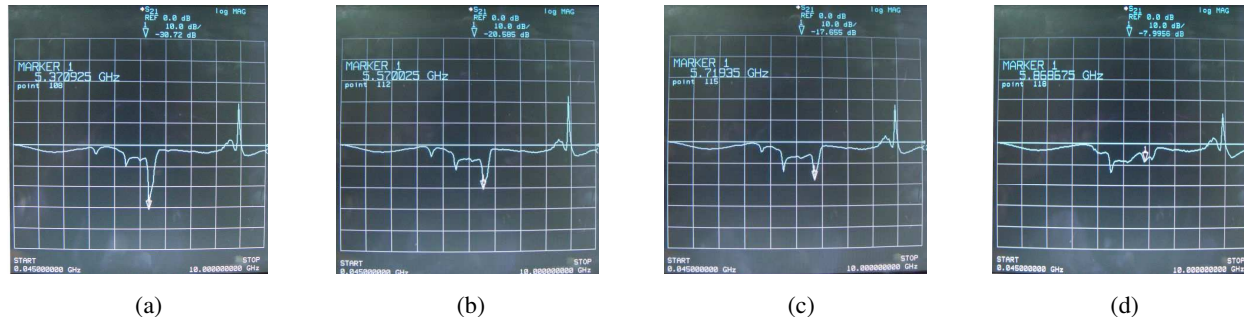


Figure 4: Measured frequency response (a) 5.37 GHz, (b) 5.57 GHz, (c) 5.72 GHz, (d) 5.87 GHz.

#### 4. BROADBAND VCO DESIGN

The proposed broadband VCO using tunable metamaterial transmission line has been fabricated on Taconic substrate with a dielectric constant of 3.2 and a thickness of 31 mils, and designed by using NEC's NE661M04 BJT device and M/A-COM's MA46H202 varactor diodes. Figure 5 shows the fabrication of the proposed VCO.

The proposed VCO's tuning range has been 5.407 ~ 5.84 GHz @ 0 ~ 26 V and the VCO has presented the phase noise which has been  $-108.84 \sim -106.84$  dBc/Hz @ 100 kHz. The output power and the harmonic characteristics of VCO have been obtained 7.0 dBm and  $-16.0$  dBc, respectively. Figure 6 shows the measured output power and the phase noise of the proposed VCO at the lower and upper frequency bands. In order to prove the improvement of the tuning range, the performance of the proposed VCO has been compared with VCO using the conventional SRR. The VCO using the conventional SRR has been fabricated on Taconic substrate with a dielectric constant of 3.2 and a thickness of 31 mils. The tuning range of the proposed VCO and VCO using the conventional SRR has been result in 430 MHz (5.407 ~ 5.84 GHz) and 108 MHz (5.746 ~ 5.854 GHz) at the same varactor diode control voltage range, 0 ~ 26 V, respectively. The widened tuning range has been 322 MHz (four times) compared with VCO using the conventional SRR. The tuning range property

of VCO using the conventional SRR and the proposed VCO is plotted in Figure 7 in the same control voltage, 0 ~ 26 V.

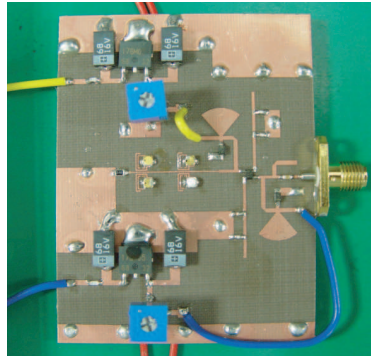


Figure 5: Fabrication of the proposed broadband VCO using tunable metamaterial transmission line with two-stage VLSSRs.

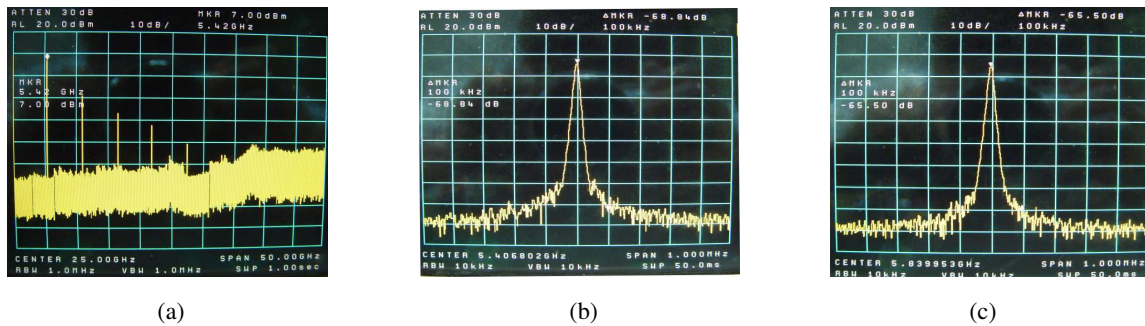


Figure 6: Measured results (a) Output power (full spectrum), (b) Phase noise at lower band (5.407 GHz), (c) Phase noise at upper band (5.84 GHz).

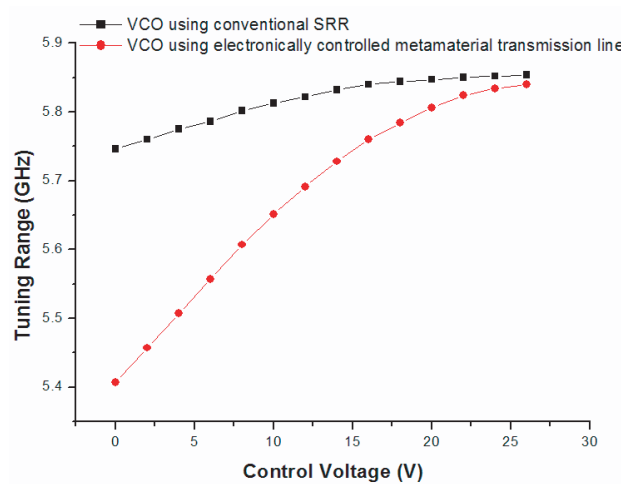


Figure 7: Comparison of the tuning range between the proposed VCO and VCO using the conventional SRR.

To take tuning range into account in the comparison of different VCOs, a figure of merit (*FOM*) called power-frequency-tuning-normalized (*PFTN*) [5]

$$PFTN = 10 \log \left[ \frac{kT}{P_{\text{sup}}} \cdot \left( \frac{f_{\text{tune}}}{f_{\text{off}}} \right)^2 \right] - L \{ f_{\text{off}} \} \quad (1)$$

has been used, where  $L\{f_{off}\}$  is the phase noise at  $f_{off}$  offset from the carrier frequency at  $f_o$  and  $P_{sup}$  is the total dc power dissipated in VCO.  $f_{tune} = f_{max} - f_{min}$ .  $PFTN$  is a unitless figure of merit expressed in dB. A larger  $PFTN$  corresponds to a better VCO. The  $PFTN$  of the proposed VCO is 20.144 dB. Compared with VCO using the conventional SRR, the  $PFTN$  has been improved in 25.607 dB.

## 5. CONCLUSION

In this paper, the broadband VCO using tunable metamaterial transmission line based on two-stages VLSRR is presented. It is demonstrated that VLSRR coupled to microstrip line can lead to metamaterial transmission line with tuning capability. The negative effective permeability is provided by VLSRR in a narrow band above the resonant frequency. The bias of VLSRR is controlled by the varactor diodes. The phase noise of VCO is  $-108.84 \sim -106.84$  dBc/Hz @ 100 kHz in the tuning range, 5.407 ~ 5.84 GHz (about 430 MHz).  $FOM$  called  $PFTN$  is 20.144 dB. Compared with VCO using the conventional SRR, the widened tuning range has been 322 MHz (four times), and  $PFTN$  has been improved in 25.607 dB.

## ACKNOWLEDGMENT

This work was sponsored by MIC/IITA/ETRI SoC Industry Promotion Center, Human Resource Development Project for IT SoC Architect. Our thanks go to MIC/IITA/ETRI, SoC Industry Promotion Center for providing funding for the research work. This work was developed within the scope of Human Resource Development Project for IT SoC Architect.

## REFERENCES

1. Kim, H., S. Ryu, Y. Chung, J. Choi, and B. Kim, "A low phase-noise CMOS VCO with harmonic tuned LC tank," *IEEE Transactions on Microwave Theory and Technique*, Vol. 54, No. 7, 2917–2924, July 2006.
2. Gil, I., J. Bonache, J. G. Garcia, and F. Martin, "Tunable meta-material transmission lines based on varactor-loaded split-ring resonators," *IEEE Transactions on Microwave Theory and Techniques*, Vol. 54, No. 6, June 2006.
3. Falcone, F., T. Lopetegi, J. D. Baena, R. Margues, F. Martin, and M. Sorolla, "Effective negative- $\epsilon$  stopband microstrip lines based on complementary split ring resonators," *IEEE Microwave and Wireless Components Letters*, Vol. 14, No. 6, June 2004.
4. Baena, J. D., J. Bonache, F. Martin, R. M. Sillero, F. Falcone, T. Lopetegi, M. A. G. Laso, J. G. Garcia, I. Gil, M. F. Portillo, and M. Sorolla, "Equivalent-circuit models for split-ring resonators and complementary split-ring resonators coupled to planar transmission lines," *IEEE Transactions on Microwave Theory and Techniques*, Vol. 53, No. 4, April 2005.
5. Ham, D. and A. Hajimiri, "Concepts and methods in optimization of integrated LC VCOs," *IEEE Journal of solid-state circuits*, Vol. 36, No. 6, 896–909, June 2001.

# Design for PCS Antenna Based on WiBro-MIMO

Kyeong-Sik Min, Min-Seong Kim, Chul-Keun Park, and Manh Dat Vu

Radio Sciences and Engineering, Korea Maritime University, Korea

**Abstract**— This paper presents a design of wireless broadband (WiBro)-multi-input multi-output (MIMO) and personal communication service (PCS) antenna for practical mobile phone. To decrease the mutual coupling of WiBro-MIMO antenna, it is considered on the projected ground structure. In addition, two type PCS antennas for multi-function mobile phone are designed. The proposed antennas are well resonated in each operating frequency band. The measured bandwidths of 3-dimensional (3D) and 2-dimensional (2D) PCS antennas are 110 MHz and 130 MHz below  $-10$  dB, respectively. The isolations between WiBro-MIMO and two PCS antenna are below  $-15$  dB by 2D antenna type and  $-20$  dB by 3D antenna type, respectively. The printed IFA has shown a better performance than modified planner IFA with spiral and shorting strip.

## 1. INTRODUCTION

A multi-input multi-output (MIMO) antenna system is a well-known technique to enhance the performance of wireless communication systems. Channel capacity of a MIMO antenna system is much larger than that provided by the conventional wireless system [1, 2]. In order to create a MIMO antenna system on wireless handy device, two or more antenna elements could be placed in a very small space. Due to the complex and narrow structure in the mobile handy terminals, the space which is allowed for antenna is extremely restricted. Thus, in case of a MIMO antenna in mobile handy terminal, the mutual coupling including radiation pattern coupling between closely arrayed antenna elements causes the decrease of a MIMO antenna performance. It means that we must consider not only the antenna size but also the suitable antenna array method to design the MIMO antenna system for mobile handy terminal.

In this research, a 2-channel wireless broadband (WiBro)-MIMO antenna and 1-channel personal communication service (PCS) band antenna are designed for internal type of mobile phone. The antenna elements are employed the planner spiral antenna with shorting strip line antenna and the printed inverted F antenna (IFA), due to its compact size and simple fabrication. All PCS antennas are designed based on modified ground structure for high isolation characteristics.

## 2. WIBRO-MIMO AND PCS BAND ANTENNA

Figure 1 shows the 3-dimension (3D) PCS band antenna with the 2-channel WiBro-MIMO antenna band [3]. The antenna for PCS is designed planar spiral antenna with shorting strip line between

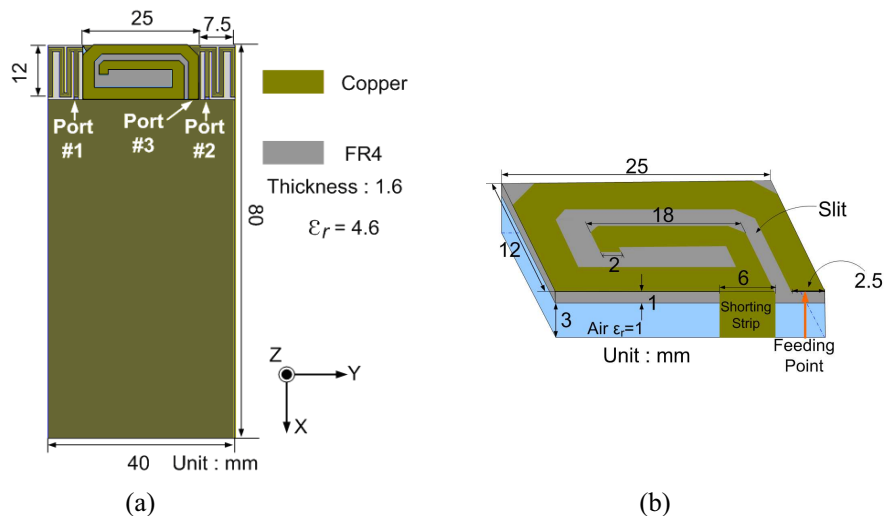


Figure 1: Proposed 3D PCS antenna configuration, (a) Whole antenna configuration, (b) Configuration of 3D PCS band antenna.

two WiBro antenna elements. That structure is considered by conventional planner IFA based. The proposed antenna is designed of 3D structure on the ground between 2-channel WiBro-MIMO antennas. The antenna used an air space to increase the isolation and bent microstrip line like a spiral turned to inner for good isolation in PCS frequency band. Fig. 1(b) shows the antenna structure for PCS band. As shown in the Fig. 1(b), the PCS antenna structure is considered for increase of isolation characteristics. The slit is applied to expand the physical electric length of antenna as shown Fig. 1(b). An air space is employed between PCS band WiBro antennas for good return loss and bandwidth. We examined return loss of PCS antenna with various height of the space. Finally, we decided to 3 mm height because it has a good return loss.

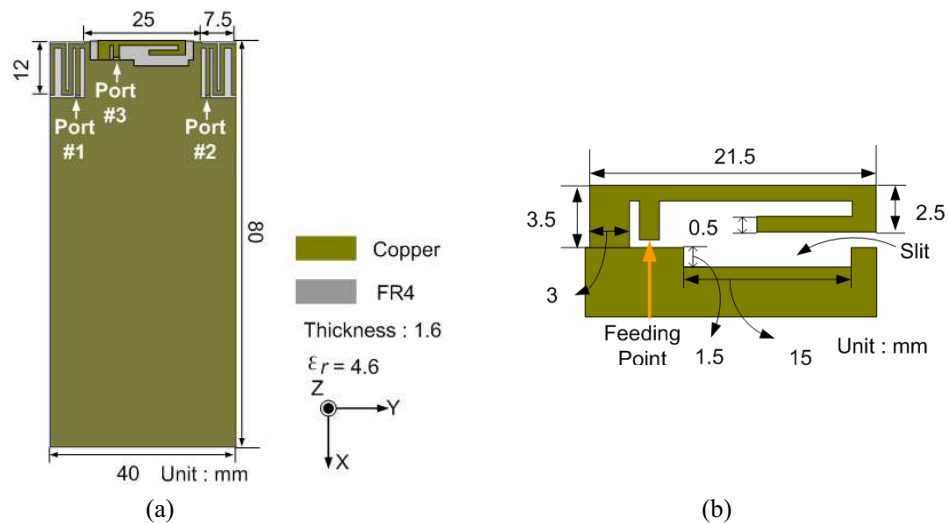


Figure 2: Proposed 2D PCS antenna configuration, (a) Whole antenna configuration, (b) Configuration of 2D PCS band antenna.

Figure 2(a) shows a multi-band antenna configuration which includes the PCS band antenna with a 2-channel WiBro-MIMO antenna band. As shown Fig. 1(b), the proposed antenna has a volume, thus, it is named a 3D PCS antenna. It is designed the printed IFA between two WiBro antenna elements. This antenna is located within a plan, therefore, it is named 2D PCS antenna. Due to the restricted space, it is used a bent microstrip line for good return loss at operating frequency band. Generally, the bandwidth of an IFA antenna is determined by the distance between antenna and ground plane. However, in this design, the distance between antenna and ground plane of the IFA antenna is reduced because of the bent line. Thus, it is used a slit on the ground plane to increase the distance between antenna and ground plane of the IFA antenna. Fig. 2(b) shows the

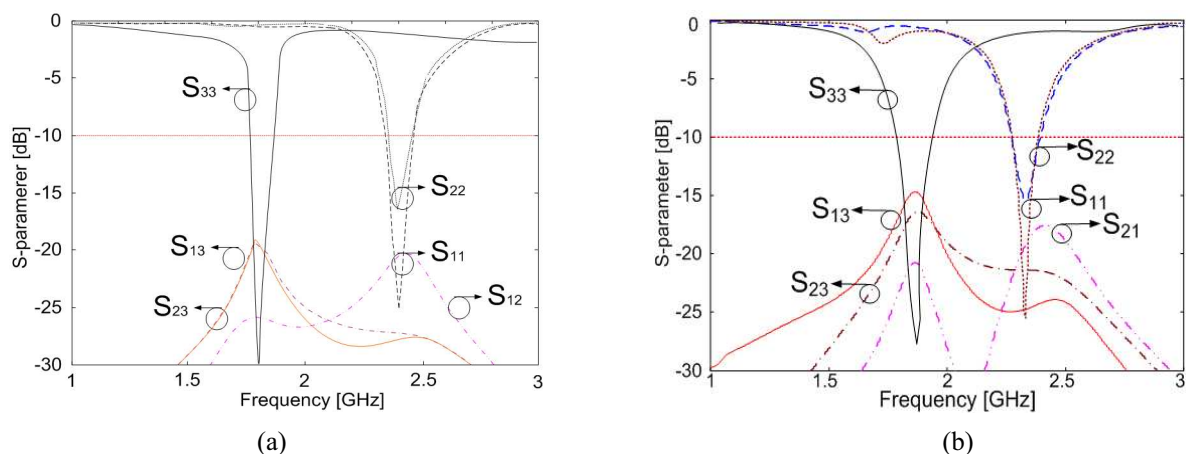


Figure 3: The calculated S-parameters of the proposed antenna, (a) 3D PCS and WiBro-MIMO antenna, (b) 2D PCS and WiBro-MIMO antenna.

IFA for PCS band. As shown in the Fig. 2(b), there is a slit on the ground plane of the IFA for the wide bandwidth of the IFA. In this antenna structure, the antenna bandwidth is determined by the slit height. We examined the antenna bandwidth with various height of the slit and determined with 1.5 mm because it has a good bandwidth.

Figure 3(a) shows the calculated S-parameters of the proposed 3D PCS and WiBro-MIMO antenna. The proposed antenna is well resonated in the PCS and WiBro bands, respectively. The bandwidth of PCS antenna has about 140 MHz which requiring on PCS system. On the other hand, because the isolation between two frequency bands is high, the WiBro antenna characteristic is not much affected by the PCS antenna. The mutual couplings between three antennas are calculated maximum  $-15$  dB below at all frequency bands. Fig. 3(b) shows calculated results of the proposed 2D PCS antenna. The bandwidth of antenna for PCS band is 110 MHz. The 2-channel WiBro antenna is operated at 2.35 GHz. On the other hand, because the isolation between two frequencies bands has a good performance, the WiBro antenna characteristic is not much affected by the PCS antenna. The mutual couplings between three antennas are calculated maximum  $-20$  dB below at all frequency bands. The mutual coupling of 2D PCS antenna is lower than that of 3D PCS antenna. However, that performance shows still good isolation characteristics and the bandwidth is also larger 30 MHz than 3D PCS antenna's one.

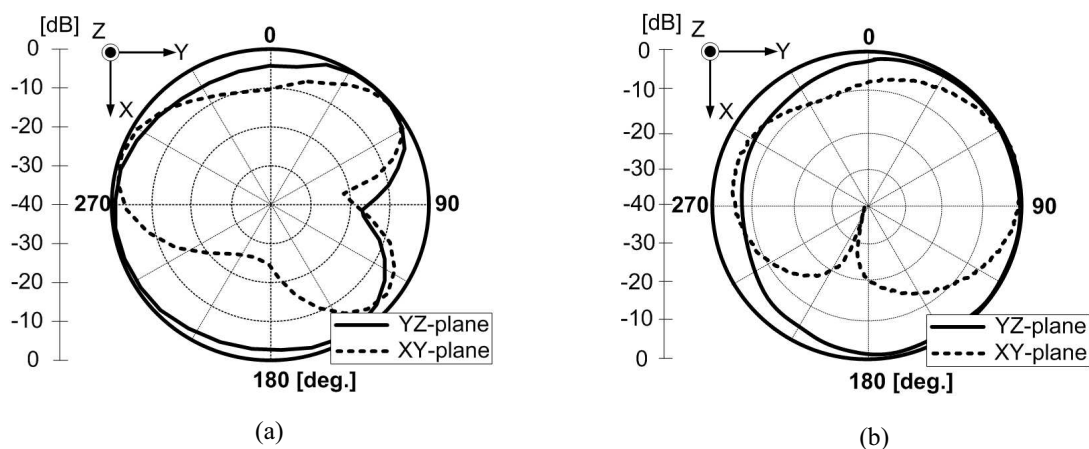


Figure 4: Calculated radiation patterns of PCS band antenna at 1.8 GHz, (a) 3D PCS band antenna, (b) 2D PCS band antenna.

Figure 4 shows the calculated radiation patterns of two proposed PCS antennas. The solid line shows the YZ-plane (H-plane) of the antenna, and it also shows the typical H-plane radiation pattern of the IFA. However, it is tilted to Y direction because the bent of microstrip line leans to the Y direction. The dotted line shows the XY-plane (E-plane) radiation pattern of the antenna,



Figure 5: Photograph of proposed antennas, (a) With 3D PCS antenna, (b) With 2D PCS antenna.

it also shows the typical E-plane radiation pattern of the IFA. Due to the reflection of the PCB board, the main beam of the E-plane is toward to 0 degree. Even though the bent of microstrip line and PCB board effect to the antenna radiation patterns, the PCS band antenna shows a good radiation pattern for communication.

Figure 5 shows the photographs of the proposed antenna for the 2-channel WiBro-MIMO antenna with the PCS antenna. The PCS band antennas are designed using the 2D printed IFA and 3D modified IFA between two WiBro antenna elements.

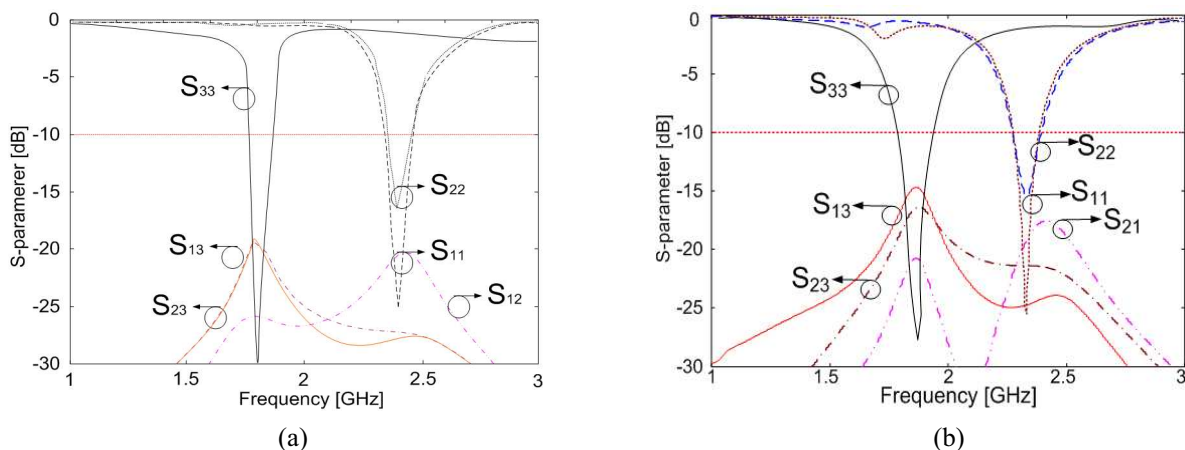


Figure 6: The measured S-parameters of the proposed antenna, (a) 3D PCS and WiBro-MIMO antenna, (b) 2D PCS and WiBro-MIMO antenna.

Figure 6 shows the measured S-parameters of the fabricated multi-channel antenna. As shown in the Fig. 6, the measured S-parameters of the fabricated antenna are shown the good agreement comparing with the calculated results on Fig. 3. Only due to the effect of the connector and coaxial cables of the each antenna for feeding, antenna bandwidth of 2D PCS antenna reduced about 10 MHz. However, it still satisfies the bandwidth requiring in PCS communication.

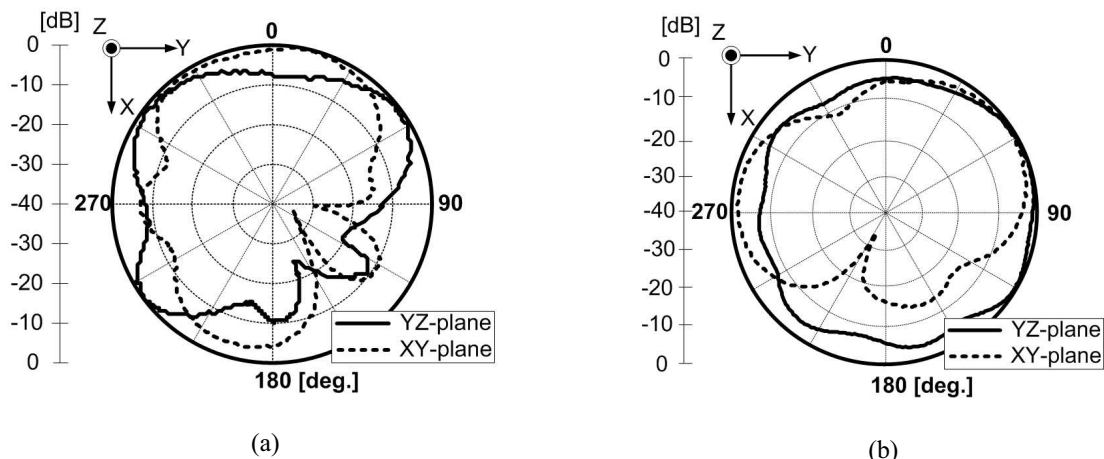


Figure 7: The measured radiation patterns at 1.8 GHz, (a) 3D PCS antenna, (b) 2D PCS antenna.

Figure 7 and Fig. 8 show the measured radiation patterns of the fabricated PCS band antenna and the 2-channel WiBro antenna, respectively. They show the reasonable agreement comparing with calculated ones. The back lobes in Fig. 7(a) and (b) are considered by the effect of the connector and the coaxial cables. Additionally, made lobes to X-direction in Fig. 7(a) is considered by the effect of cable near the shorting-strip line. As shown in Fig. 8, we confirm that the proposed two PCS antenna is not affected to radiation pattern of 2-channel WiBro-MIMO antennas.

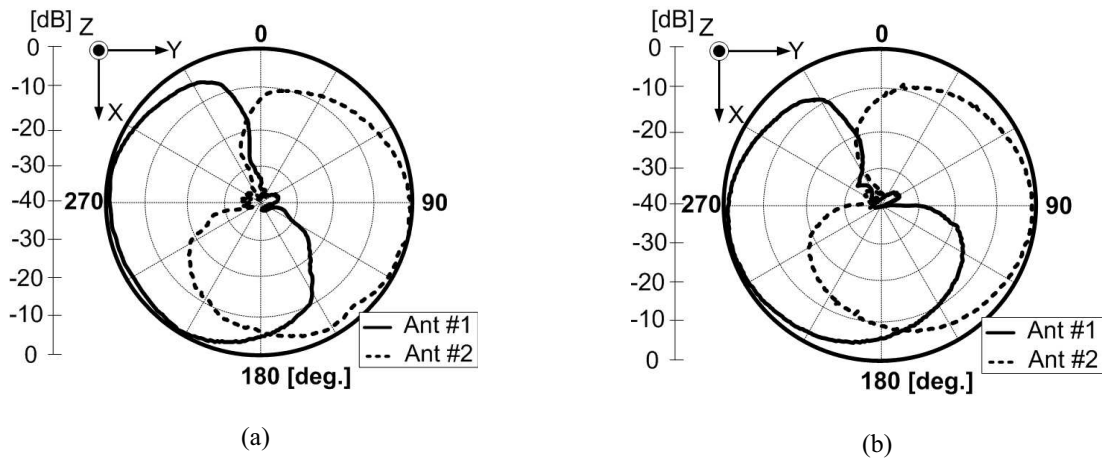


Figure 8: The measured radiation patterns of the WiBro antennas, (a) 2-channel WiBro-MIMO antenna with 3D PCS, (b) 2-channel WiBro-MIMO antenna with 2D PCS.

### 3. CONCLUSION

A compact WiBro-MIMO and two type PCS antenna are proposed. The isolation between each WiBro-MIMO antenna elements is considered using projected ground structure. The S-parameters and radiation patterns are examined and they show reasonable agreements with the simulated results. The characteristics of proposed PCS antennas are satisfied the Korean PCS operating frequency band. The measured bandwidth of 3D and 2D PCS antenna are 110 MHz and 130 MHz, respectively. The isolations between WiBro-MIMO and two PCS antenna are below  $-15$  dB by 2D type and  $-20$  dB by 3D type antenna, respectively. The printed IFA has shown a better performance than modified planner IFA with spiral and shorting strip.

### REFERENCES

1. Foschini, G. J. and M. J. Gans, "On limits of wireless communications in a fading environment when using multiple antennas," *Wireless Personal Comm.*, Vol. 6, No. 3, 311–335, March 1998.
2. Shiu, D.-S., G. J. Foschini, M. J. Gans, and J. M. Kahn, "Fading correlation and its effect on the capacity of multielement antenna systems," *IEEE Trans. on Comm.*, Vol. 48, No. 3, 502–513, Mar. 2000.
3. Kim, D.-J. and K.-S. Min, "Compact 2-channel MIMO antenna for WiBro handy terminal application," *APMC 2006*, Vol. 3, 214–217, Dec. 2006.

# Design of Dual-polarization Stacked Arrays for Wireless Communications

Adel Mohamed Abdin

Department of Communications and Electronics, Shorouk Academy, Cairo, Egypt

**Abstract**— A novel dual-polarized stacked antenna array is designed and built for broadcasting satellite orbital positions. It is working in the 12.43-12.53 GHz band (space-to-Earth). The patches in the bottom layer are fed diagonally by a microstrip line. The upper layer is stacked above the bottom one to increase the operating bandwidth. The design parameters are simulated and optimized using IE3D (Zeland) software to get the suitable S-parameters and radiation performance. The measured and simulated results are very close. The results show that the antenna seems very promising and useful for wireless applications.

## 1. INTRODUCTION

During the last few years there has been an enormous expansion in wireless communication systems and the number of people using these services. The designed antenna is suitable for the 12 GHz Broadcasting Satellite Service (BSS) frequency bands. It is working in the frequency band 12.43-12.53 GHz. In the usage of such antenna, besides having good performance, another main concern is the availability of a simple and low-cost antenna. Single-feed planar antennas can be easily integrated. This antenna has dual polarization. However, in order to reduce the polarization sensitivity of the antenna, the feed-point can be placed on the diagonal of the patch [1–4]. The difficulty in building such an antenna array arises from simultaneously trying to meet two opposing design requirements. The designed array antenna is shown in Figure 1, has a gain of 9.9 dBi, with a minimum half-power beamwidth (HPBW) ( $13.2356^\circ$ ,  $75.3584^\circ$ ) and antenna efficiency is nearly 74%. A simulation is carried out to investigate the effects of varying several physical parameters such as dummy patch size, spacing between the lower and upper patches, and spacing between the patches. The impedance characteristics, radiation pattern, return loss ( $S_{11}$ ), and voltage standing wave ratio (VSWR) for the designed array are simulated and analyzed using IE3D (Zeland) software.  $S_{11}$  and VSWR are measured and compared with the simulated one.

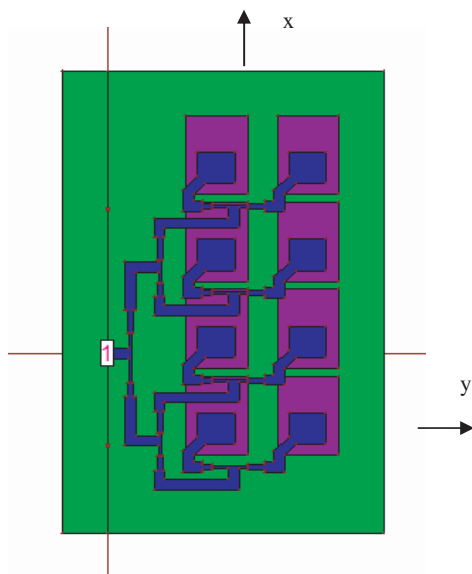


Figure 1: The designed  $2 \times 4$  antenna array.

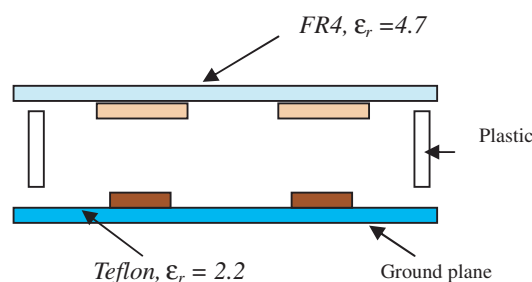


Figure 2: The geometry for the stacked arrays.

## 2. ELEMENT ANTENNA

The antenna has two layers; the lower one is fed by a microstrip line. The upper layer is dummy and stacked above the bottom one. The bottom array was fabricated on a dielectric substrate called

Teflon with  $h_L = 0.787$  mm,  $\epsilon_{rL} = 2.2$ , area of  $62.5 \times 28$  mm, and spacing between patches in  $x$  and  $y$ -directions are 21 and 19.5 mm respectively. The lower patch is a square and its side equal 8 mm. The upper array was fabricated on a dielectric substrate called FR4 with  $h_U = 1.55$  mm,  $\epsilon_{rU} = 4.7$ , area of  $78 \times 33$  mm, and spacing between patches in  $x$  and  $y$ -directions are  $21 \times 21$  mm respectively. The dimensions of the upper patch and the spacing between the excited antenna and the stacked one have been adjusted to minimize the return loss to nearly -35 dB using IE3D (Zeland) software. The optimized values of the spacing between the upper and lower arrays and the dimensions of the upper patch are 6.4, 11, and 9 mm, respectively. The geometry of the stacked arrays is shown in Figure 2. A quarter wavelength microstrip transformer of impedance  $70.7 \Omega$  measuring  $4.2 \times 1.339$  mm is used to match the input impedance of a single antenna ( $50 \Omega$ ) to the transmission line (T.L) of impedance ( $100 \Omega$ ) as shown in Figure 1. The widths of the  $50 \Omega$  and the  $100 \Omega$  T.L are 2.377 and 0.6547 mm respectively.

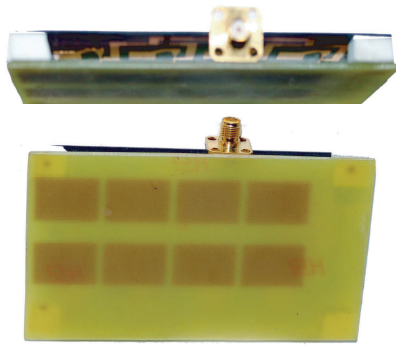


Figure 3: The fabricated  $2 \times 4$  antenna array.

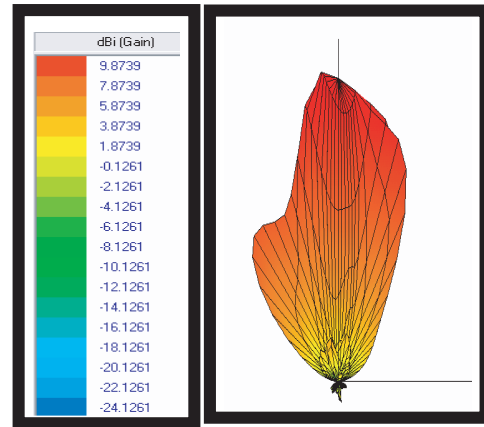


Figure 4: The simulated 3-D radiation pattern of  $2 \times 4$  dual-polarized stacked antenna array at 12.484 GHz.

### 3. ARRAY ANTENNA

The geometry for the stacked antenna arrays is shown in Figure 2. The designed and fabricated  $2 \times 4$  planar antenna arrays are shown in Figure 3. The lower layer consists of 8-elements with corporate feeding network. This feeding was designed to give equal amplitude and phase to each element. The excited array with the upper stacked layer gives  $S_{11} = -35.174$  dB and  $VSWR = 1.03661$  at the center frequency 12.484 GHz.

Table 1: Different parameters for the radiation pattern.

Frequency	12.484 (GHz)
Incident power	0.01 (W)
Input power	0.00989911 (W)
Radiated power	0.00735981 (W)
Average radiated Power	0.000585675 (W/s)
Radiation Efficiency	74.3481%
Antenna Efficiency	73.5981%
Gain	9.8739 dBi
Directivity	11.2052 dBi
3 dB Beam width	(13.2356, 75.3584) deg

The principle simulated radiation pattern of the antenna is shown in Figure 4. The gain, directivity, efficiency, and beamwidth of the dual-polarized  $2 \times 4$  stacked microstrip array antenna are summarized in Table 1.

The simulated and measured return loss ( $S_{11}$ ) and VSWR of  $2 \times 4$  dual-polarized stacked antenna array are shown in Figures 5 and 6 respectively. The simulated and measured results are very close.

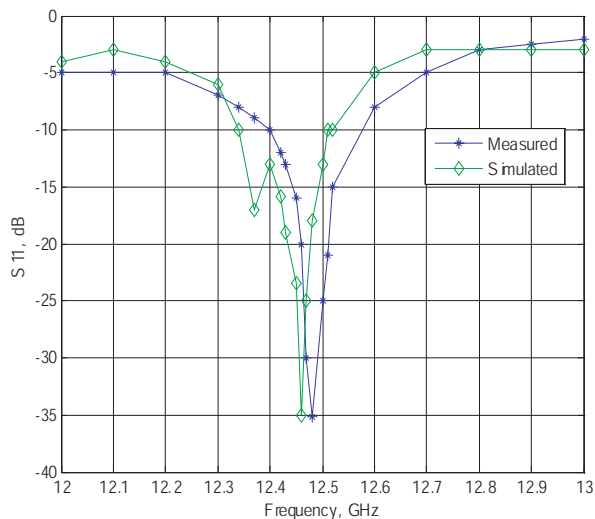


Figure 5: Measured and simulated return loss ( $S_{11}$ ) of  $2 \times 4$  dual-polarized stacked antenna array.

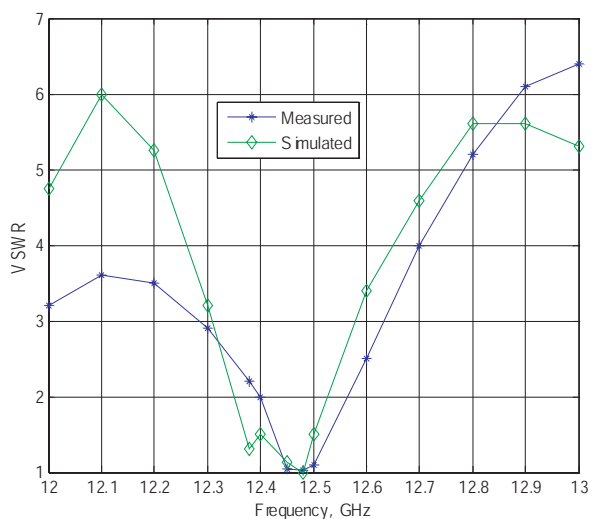


Figure 6: Measured and simulated VSWR of  $2 \times 4$  dual-polarized stacked antenna array.

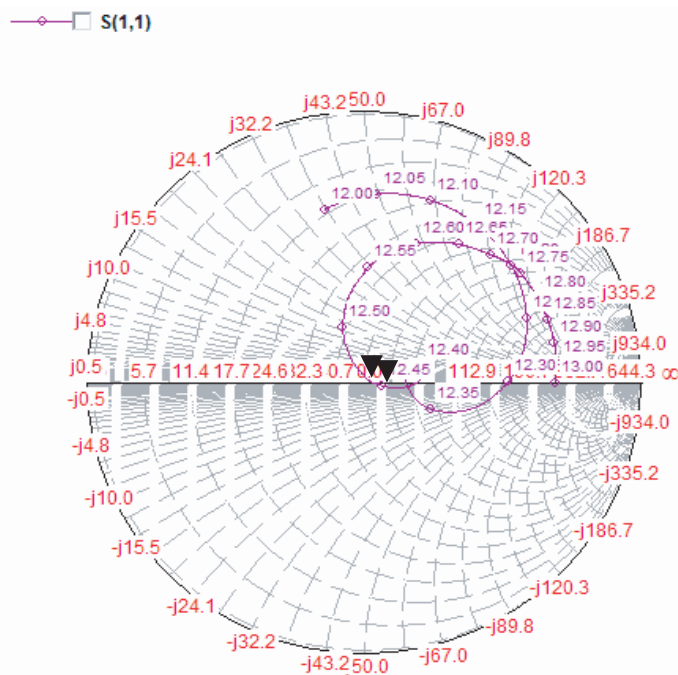


Figure 7: Impedance for variation of frequency.

The impedance smith chart obtained for the designed array is shown in Figure 7. The size of the upper patches and the distance between the upper and the lower layers are adjusted to have good matching. For the plot, it shows that the points are located at the middle of the circle as the frequency becomes nearer to the center frequency. Hence, this indicates that the matching of this antenna is quite good, as the desired location of the points should be in the middle of the circle ( $50 \Omega$ ). Selected points from the impedance smith chart are listed in Table 2.

Table 2: Selected points from the impedance Smith chart obtained for the designed array.

No	F (GHz)	Re (Zs)	Im (Zs)
1	12.46	51.5183	1.01222
2	12.45	56.8377	1.69282

#### 4. CONCLUSIONS

A novel dual-polarized  $2 \times 4$  stacked microstrip array antenna was developed at 12.484 GHz and presented numerically and experimentally. The effects of changing different physical parameters, such as the spacing between the upper and lower layers, the area of the upper patches, and the spacing between elements in upper and lower arrays have been studied through the simulation to optimize the design. The simulated and measured return loss of the designed antenna is  $-35.174$  dB, a VSWR of 1.03661, a gain of 9.9 dBi, and the 3 dB beamwidth is  $13.2356^\circ$ .

#### REFERENCES

1. Cruz, E. M. and J. P. Daniel, "Experimental analysis of corner-fed printed square patch antennas," *Electronics Letters*, Vol. 27, 1410–1412, 1991.
2. See, T. S. P. and Z. N. Chen, "Design of dual-polarization stacked arrays for ISM band applications," *Microwave and Optical Technology Lett.*, Vol. 38, 142–147, 2003.
3. Balanis, C. A., *Antenna Theory: Analysis and Design*, 2nd Ed., John Wiley & Sons, New York, 1997.
4. Lee, R. Q., T. Talty, and K. F. Lee, "Circular polarization characteristics of stacked microstrip antennas," *Electronics Letters*, Vol. 26, 2109–2110, December 1990.
5. *IE3D Software Release 11.5 Developed by Zeland Software, Inc.*

# A High Linearity and Efficiency Doherty Power Amplifier for Retrodirective Communication

Xiaoqun Chen, Yuchun Guo, and Xiaowei Shi

National Key Laboratory of Antennas and Microwave Technology, Xidian University  
Xi'an 710071, China

**Abstract**— This paper presents a Doherty power amplifier with advanced design methods for high efficiency and linearity applied to retrodirective communication system for high peak to average power ratio (PAR). A special inverted Doherty topology is proposed in order to optimize the average efficiency of Doherty amplifier. Also we develop Doherty power amplifier with uneven power drive which is provided more input power to the peak amplifier than carrier amplifier for full power operation and appropriate load modulation. These methods are applied to implement Doherty power amplifier using GaAs FET. The amplifier is optimized at large power back-off. The power added efficiency (PAE) and adjacent channel leakage ratio (ACLR) are 33.1% and  $-47$  dBc, which improves about 3.2% and 5 dB respectively, its third-order intermodulation distortion (IMD3) has 2.5 dB improvement compared with conventional Doherty power amplifier.

## 1. INTRODUCTION

Recently, microwave retrodirective wireless communication has become a hot research area. It shows that the retrodirective array can simultaneously respond to each individual signal proving its usefulness in mobile wireless applications where multiple signal tracking is required [1]. Phase conjugation is a known key technique that applied to retrodirective communication systems [2]. The classical approach to achieve the phase conjugation necessary for these antennas is to use a low noise amplifier, a high linear power amplifier and a mixer arrangement [2]. Highly efficient and linear Power amplifier is a key component in the systems.

However, there is an obstacle in such system makes the use of amplifier difficult, the high peak-to-average power ratio (PAPR) caused by the large number of independent subcarriers with random phase and amplitude added together at the modulator [3]. The communication systems are reduced in both size and cost, but required the quality of communication [4, 5]. According to IEEE 802.11a, so a power amplifier with high linearity and efficiency is great of importance. The simplest method is to back-off signals from the saturation region to the linear region at the cost of power efficiency, usually in an efficiency form 12% to 20%. Another may use predistortion methods or elimination and restoration techniques or feedforward [6]. However, these techniques which need additional components result in an increase in cost, size, and power dissipation [7]. In order to solve these

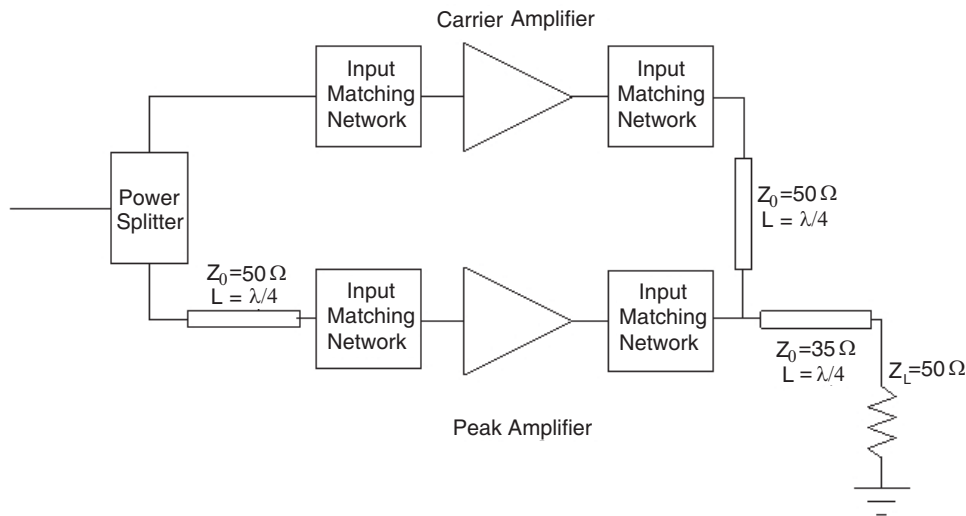


Figure 1: The classical Doherty power amplifier.

problems, a Doherty amplifier is the most promising candidate with simple fabrication and high efficiency for the application, as Fig. 1 shown.

The fundamental operation theory has been well described in [8–11]. The simplest Doherty amplifier operation can be achieved using two cells with a class-AB biased carrier amplifier cell and a class-C biased peak amplifier cell with respective input matching network and output matching network. It has a high linearity and efficiency across the wideband signal has been studied extensively for the application due to its high efficiency. However, the conventional Doherty power amplifier has its limitation. Due to its lower bias point, the current level of the peaking cell is always lower than that of the carrier cell. The load impedances of both cells cannot be fully modulated to the value of the optimum impedance for a high power match. Thus, neither cell can generate full output power. In this paper, two advanced methods are good approaches to solve these problems well. The implementation of the amplifier is simple and results show excellent performance.

## 2. ADVANCE DESIGN METHODS

### 2.1. Inverted Doherty Power Amplifier

As it is mentioned above, carrier amplifier operational theories indicated that the best efficiency at average envelop power actually occurred with load impedance closer to  $25\ \Omega$  than  $100\ \Omega$ . In order to achieve maximum efficiency at  $100\ \Omega$ , approximately one-quarter wavelength of  $50\ \Omega$  line will be applied to the carrier amplifier's output matching network in Fig. 1. Similarly, the off-state impedance presented by the peak amplifier is so low that this also suggests appending  $\lambda/4$  wavelength of  $50\ \Omega$  line to peak amplifier's output matching network to guarantee high impedance at the combining node. Size and loss constraints make this approach undesirable. By reversing the Doherty combining point, a  $25\ \Omega$  maximum efficiency load is provided for the carrier amplifier at average envelop power. The impedance inversion previously accomplished with the  $50\ \Omega$ ,  $\lambda/4$  line is incorporated into peak output matching network, which constrains  $\theta_{S21} = -90$  deg. As the peak cell, a  $50\ \Omega$ ,  $\lambda/4$  line becomes the off-state impedance rotation appended to. Then output is taken from the carrier amplifier side of the combining node as shown in Fig. 2, called "inverted Doherty" topology.

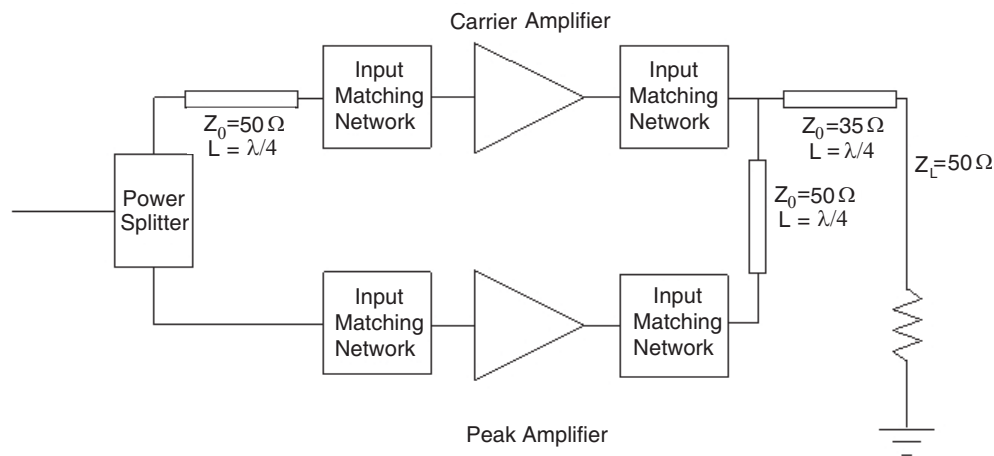


Figure 2: Inverted Doherty power amplifier topology.

This "inverted Doherty" will guarantee the high efficiency at the low drive level. But most challenge of the Doherty design is the carrier amplifier output match. In addition to the  $-90$  degree phase requirement mentioned above, the gain of the carrier amplifier must decrease by 3 dB as its output power transitions between average envelope power and half of peak envelope power. This can be understood by noting the carrier amplifier's input power ranges from average envelope power to peak envelope power, while the required output power range is average envelope power to half of peak envelope power. The gain reduction is necessary to accommodate the half of peak envelope power of the peaking amplifier. With uneven drive, more power will deliver to the peak cell. This creates a constant gain for the composite Doherty amplifier at lower power regain, which is an important linearity consideration. To optimize the Doherty amplifier's average efficiency, the carrier amplifier's output match must be designed for best efficiency performance at average envelope power. For the inverted topology, this occurs at  $25\ \Omega$ . Maximum carrier amplifier

efficiency is limited by the linearity which results when it is operated together with the Class C peaking amplifier. The carrier amplifier design is thus constrained by gain, phase, efficiency, linearity, and absolute power requirements.

When peak amplifier operates at class C, its transfer characteristic must be smooth, without evidence of discontinuities. The adjacent channel leakage and IMD problems are obvious with two tone test. Design of bypassing and decoupling networks as well as the bias circuit are crucial to avoiding this problem with bypassing capacitors. The output contribution of the peaking amplifier is expected to range from zero to half of peak envelope power for the same drive range which causes the carrier amplifier to deliver average envelope power to half of peak envelope power. It is set to provide equal phase lengths in both signal paths. The final phase length is optimized for best linearity and gain flatness.

## 2.2. Uneven Power Drive

The basic operation principle of Doherty power amplifier has been well described in [12, 13]. Fig. 3 depicts the load impedance of both amplifiers versus input voltage.

$$Z_C = \begin{cases} \frac{Z_T^2}{Z_L}, & 0 < V_{in} < V_{in, \max/2} \\ \frac{Z_T^2}{Z_L \left(1 + \frac{I_P}{I_C}\right)}, & V_{in, \max/2} < V_{in} < V_{in, \max} \end{cases} \quad (1)$$

$$Z_P = \begin{cases} \infty, & 0 < V_{in} < V_{in, \max/2} \\ Z_L \left(1 + \frac{I_P}{I_C}\right), & V_{in, \max/2} < V_{in} < V_{in, \max} \end{cases} \quad (2)$$

where  $Z_L$  is the load impedance of the Doherty amplifier;  $I_C$  and  $I_P$  represent the fundamental currents of the carrier and peaking amplifiers, respectively; and  $Z_C$  and  $Z_P$  are the output load impedances of the carrier and peaking amplifiers, respectively, as Fig. 3 shown.

In the low power region, the linearity of the amplifier is entirely determined by the carrier cell. Therefore, the carrier cell should be highly linear for its careful optimized load impedance. In the high-power region, the current level of the peaking cell plays an important role in determining the load modulation of the amplifier. For the asymmetric amplifier with even power drive, the fundamental current of the peaking cell is insufficient to achieve the full load modulation. The load impedances of both cells are larger than the optimum values in the high-power region. As a result, the carrier and peaking cells are driven into saturation without producing full power. Thus, the amplifier is seriously affected by linearity, as well as power level.

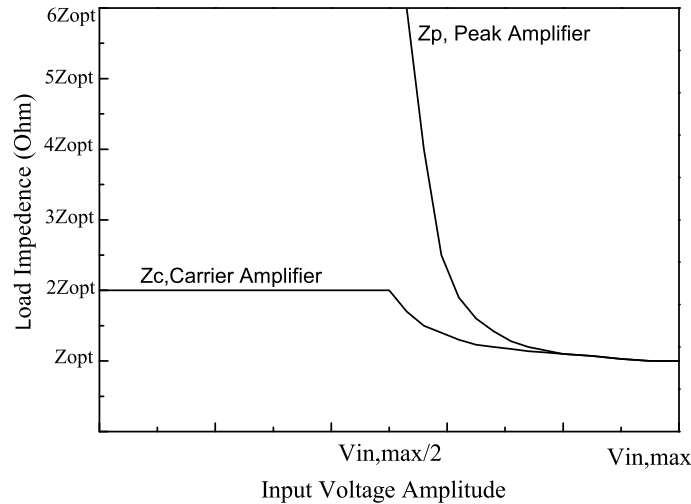


Figure 3: Load impedance versus input drive.

In order to enhance the output power from the peak amplifier, a Doherty amplifier with uneven power drive is proposed, applied more power to the peak cell. As the amplifier with uneven power drive, the linearity of the amplifier is improved due to proper power operation without severe saturation. The linearity is further enhanced by the harmonic cancellation of from the two cells at appropriate gate biases. The carrier cell, which is biased at class AB, has the gain compression at high output power levels, while the class-C biased peak cell has the gain expansion. Hence, the gain expansion of the peak cell can compensate the gain compression of the carrier cell. Specifically, the third-order intermodulation (IM3) level from the carrier cell increases and the phase of IM3 is decreased because the gain of the carrier cell is compressed. On the other hand, when the gain of the peak cell is expanded with uneven drive, both the IM3 level and phase increase. To cancel out IM3s from the two cells, the components must be 180 deg. out-of-phase with the same amplitudes. Therefore, the peak cell should be designed appropriately to cancel the harmonics of the carrier cell.

### 3. AMPLIFIER IMPLEMENTATION AND RESULTS

The proposed Doherty power amplifier is designed with cascaded structure. It consists of three stages pre-driver, driver and final stage, the novel Doherty amplifier. The pre-driver and driver two stages are used to enhance higher output and power gain. They both work in class A, since this method makes the two stages under the small signal situation [14]. We put the emphases on the final stage. Although power amplifiers vary in saturation output power by changing drain dc voltage, this dc-voltage change preserves the power added efficiency (PAE) for the various saturation, and PAE is

$$PAE_{total} = \frac{P_{out} - P_{in}}{P_{DC}} = \frac{P_{out} - P_{in}}{P_{DC1} + P_{DC2} + P_{DC3}} \quad (3)$$

For  $P_{DC}$  is the total power consumption of the DPA

$$P_{DC} = V_{DDC}I_{DQC} + V_{DDP}I_{DQP} \quad (4)$$

In Equation (4),  $V_{DDC}$  and  $V_{DDP}$  represent voltage supply for carrier and peak amplifiers,  $I_{DDC}$  and  $I_{DDP}$  represent current supply for carrier and peak amplifier respectively.

The power amplifier is shown in Fig. 4 and the performance of the Doherty power amplifier not only considers the linearity, but also its efficiency. To satisfy these demands, we use Freescale MFR6S21050L. We also fabricated a conventional Doherty amplifier for comparison.

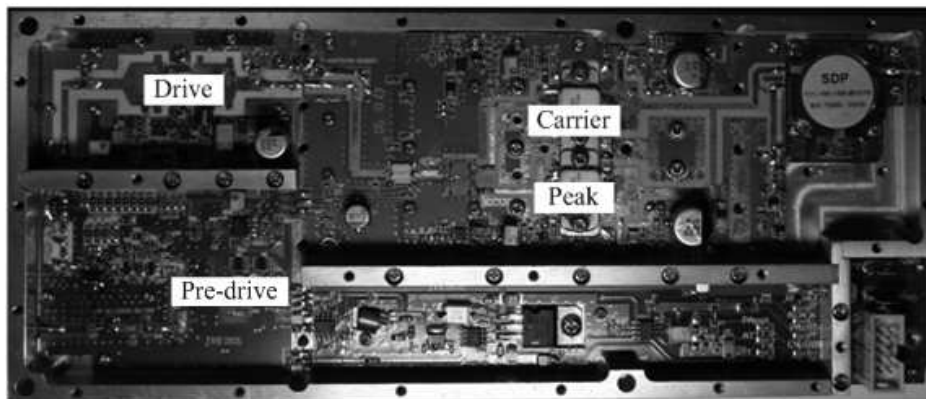


Figure 4: The photograph of cascaded Doherty power amplifier.

Figure 5 depicted the gain and the PAE of the proposed Doherty power amplifier and an ordinarily Doherty power amplifier with even drive. Its gain achieves 44 dB and keeps a good flat performance than the conventional Doherty's. As uneven power drive (1:2.5), the carrier cell is compressed early and the peaking cell expanded early and the region is wider than the usual Doherty amplifier. Therefore, the amplifier with an uneven drive generates more linear power because the early gain expansion of the peaking cell compensates the gain compression of the carrier cell over the wide power range although the power gain of the uneven case keeps a better linearity compared to the even drive case. The PAE of the uneven drive achieves 33.1% at the output of

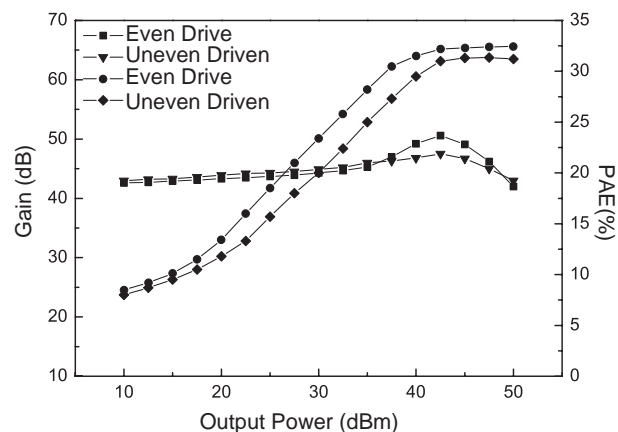


Figure 5: Gain and power added efficiency (PAE) for two types of Doherty power amplifier.

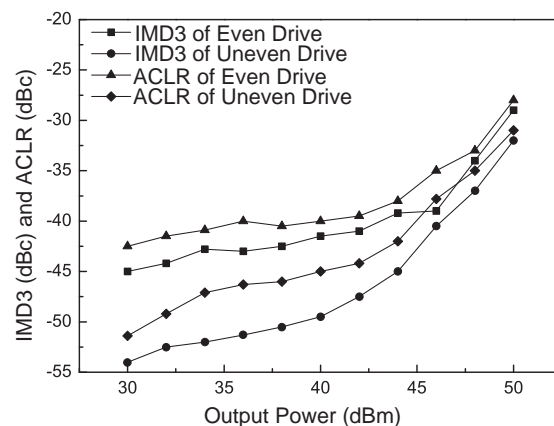


Figure 6: IMD3 and ACLR performances for two-tone signal with 5 MHz tone-spacing.

45 dBm which enhances 3.2% at the average output of 37 dBm with the inverted structure due to load impedance modulation optimum.

Figure 6 shows the measured IMD3 and ACLR of two types Doherty amplifier. In comparison with even case, the uneven case with inverted output structure delivers ACLR performance at  $-47$  dBc at 45 dBm output with 5 dB improvement for two-tone test at 5 MHz. IMD3 has 2.5 dB improvements too. These results that represent the proposed bypassing and decoupling networks in output matching network provides better output with adjacent channel leakage performance.

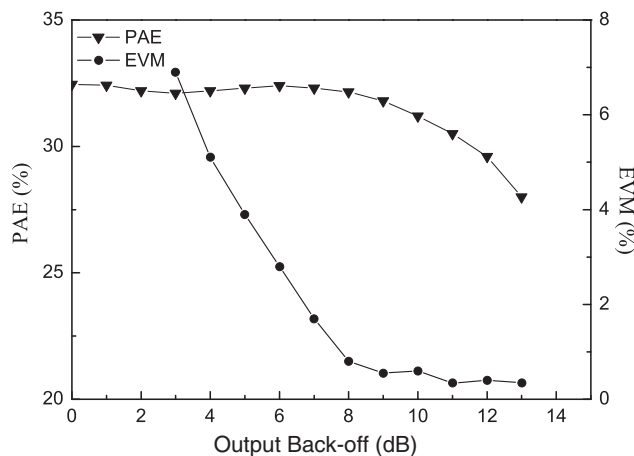


Figure 7: PAE versus EVM with output back-off.

Figure 7 shows that the power added efficiency of the cascaded Doherty power amplifier with different output back-off and error-vector-magnitudes (EVM). According to the specification of the IEEE 802.11a WLAN, which requires an Error Vector Magnitude (EVM) no greater than  $-25$  dB (i.e., less than or equal 5.6%) in order to meet consortium specifications. The efficiency of the inverted Doherty amplifier achieves 32.8% with 5.6% EVM. The PAE maintains 31.5% with 10 dB output power back-off and 30% with 12 dB back-off. The power amplifier performance evident demonstrates an excellent performance than a conventional Doherty power amplifier.

#### 4. CONCLUSIONS

In this paper, a high linearity and efficiency three stages cascaded Doherty power amplifier is proposed and fabricated with uneven power drive and inverted topology. Its PAE achieves 33.1%, which performs 3.2% better in the whole range than even drive case. With the inverted structure and the offset line in output matching network, it performs better in linearity and efficiency than even case. The ACLR presents  $-47$  dBc at 45 dBm output power which has 5 dB improvements at with 5 MHz two-tone test. The proposed amplifier has IMD3 of  $-42$  dBc which presents 2.5 dB

improvements over the even case with appropriately cancellation of the carrier cell harmonics. The PAE maintains 30% while 12 dB Output back-off for low EVM. These experimental results clearly demonstrate the superior performance of the proposed Doherty power amplifier compared to the conventional Doherty power amplifiers. The proposed design methods are suited for retrodirective communication with high efficiency and high linearity operation.

#### ACKNOWLEDGMENT

This work is supported by the National Natural Science Foundation of China under Contract No. 60571057.

#### REFERENCES

1. Karode, S. L. and V. F. Fusco, "Multiple target tracking using retrodirective antenna arrays," *Proceedings of the 1999 IEE National Conference on Antennas and Propagation*, York, UK, 178–181, March 1999.
2. Fusco, V., S. C. Binn, and N. Buchanan, "Analysis and characterization of PLL-based retrodirective array," *IEEE Trans. Microwave Theory Tech.*, Vol. 53, No. 2, 730–8, 2005.
3. Jeong, J. and P. Asbeck, "Efficiency enhancement of W-CDMA base-station envelope tracking power amplifiers via load modulation," *Microwave Opt. Technol. Lett.*, Vol. 49, No. 8, 1954–1957, 2007.
4. Ooi, S. F., S. K. Lee, A. Sambell, E. Korolkiewicz, and P. Butterworth, "Design of a high efficiency power amplifier with input and output harmonic terminations," *Microwave Opt. Technol. Lett.*, Vol. 49, No. 2, 391–395, 2007.
5. Lin, Y.-S., Z.-H. Yang, C.-C. Chen, and T.-C. Chao, "Design and implementation of a miniaturized high-linearity 3–5 GHz ultrawideband CMOS low-noise amplifier," *Microwave Opt. Technol. Lett.*, Vol. 49, No. 3, 524–526, 2007.
6. Yamanouchi, S., K. Kunihiro, and H. Hida, "OFDM error vector magnitude distortion analysis," *IEICE Trans. Electron.*, Vol. E89-C, No. 12, 1836–1842, 2006.
7. Zervas, M. N. and R. I. Laming, "Rayleigh scattering effect on the gain efficiency and noise of erbium-doped fiber amplifiers," *IEEE J. Quantum Electron.*, Vol. 31, No. 3, 468–471, 1995.
8. Kim, W.-J., K.-J. Cho, S. P. Stapleton, and J.-H. Kim, "Doherty feed-forward amplifier performance using a novel crest factor reduction technique," *IEEE Microwave Compon. Lett.*, Vol. 17, No. 1, 82–84, 2007.
9. McMorrow, R. J., D. M. Upton, and P. R. Maloney, "Microwave Doherty amplifier," *IEEE MTT-S Int. Microwave Symp. Dig.*, San Diego, CA, USA, Vol. 3, 1653–1656, May 1994.
10. Raab, F. H., "Efficiency of Doherty RF power-amplifier systems," *IEEE Trans. Broadcast.*, Vol. 33, No. 3, 77–83, 1987.
11. Doherty, M. C., "Applying fluidic operational amplifiers," *ISA-Trans.*, Vol. 8, No. 4, 287–292, 1969.
12. Bumman, K., K. Jangheon, K. Ildu, and C. Jeonghyeon, "The Doherty power amplifier," *IEEE Microwave Mag.*, Vol. 7, No. 5, 42–50, 2006.
13. Doherty, W. H., "A new high efficiency power amplifier for modulated waves," *Proceedings of the IRE*, Vol. 24, 1163–1182, 1936.
14. Yang, Y., J. Yi, Y. Y. Woo, and B. Kim, "Optimum design for linearity and efficiency of a microwave Doherty amplifier using a new load matching technique," *Microwave J.*, Vol. 44, No. 12, 20–22, 2001.

# Effect of the Gap Feeding on the Multi-band Small Antenna Using a Branch Structure

Hyengcheul Choi, Hojeong Kim, Sinhyung Jeon, and Hyeongdong Kim

Department of Electrical and Computer Engineering, Hanyang University  
Haengdang-dong, Seongdong-gu, Seoul, Korea

**Abstract**— This research investigates about the effect an inter-coupling capacitance at small antenna using a branch structure. From the analysis by using an equivalent transmission line model and the comparison with three chip antennas consisted of meandered pattern, it is derived that the large inter-coupling capacitance occurred between two radiating elements leads a very narrow bandwidth. To solve this problem, the branch structure antenna with one gap feeding is proposed in this paper, and this technique is found to be useful for the design of multi-band small antenna.

## 1. INTRODUCTION

In the past several years there has been increasing interest in the design of small multi-band antenna, and many antenna types are developed [1]. Planar Inverted F-Antenna (PIFA) among them is frequently used for a mobile handset because it has small volume and multi-band operations [2]. However, PIFA is not suitable to be installed to the inside of thin mobile handset because it must be installed high from the ground plane of a mobile phone to achieve a broad bandwidth [3].

For this reason, the dual-band small chip antennas were developed in [4]. Because the resonant frequency of these developed antennas is ISM band, higher than PCS band, the chip antenna to operate at GSM, DCS, and PCS bands is studied at [5]. Comparing antenna in [2] with it in [5], the size of chip antenna should be more smaller to be mounted on the thin mobile handset. However, to design small chip antenna for multi-band is very hard work because the extreme size reduction of monopole antenna makes very narrow bandwidth [6] and strong inter-coupling capacitance. Since the narrow bandwidth occurred by size reduction is an avoidable phenomenon [7], this paper concentrate only on the effect of the inter-coupling capacitance between radiating elements, and the gap feeding is introduced to alleviate it.

To examine the inter-coupling capacitance, the multi-band chip antenna having a branch structure is proposed in this paper, and the transmission line model is used as the equivalent model of an antenna. From the circuit analysis and simulation results of chip antennas, it is derived that the bandwidth of an antenna becomes the narrower by the higher value of the inter-coupling capacitance. Also, gap feeding is proposed to decrease the effect of the inter-coupling capacitance, and its effect is proven by comparing two antennas; One is the branch structure antenna having gap feeding, and the other is the branch structure antenna having direct connect feeding.

## 2. THEORY

The branch structure is utilized to achieve a multi-band or a wide bandwidth at the antenna design [8]. When the branch structure is used at small volume antenna, the inter-coupling capacitance become very large. To study about the effect of the inter-coupling capacitance, the antennas and the inter-coupling capacitance at Fig. 1(a) convert into the open lossless transmission line model at Fig. 1(b). This paper assumes that two antennas have no coincident resonant frequencies, a low operation band and high operation band are assigned to a long antenna and a short antenna, respectively, and antenna loss is neglected to focus only the effect of inter-coupling capacitance.

The inter-coupling capacitance in a resonator is utilized to decrease the resonant frequency [9]. Although this technique is very useful in the design of the filter having very narrow bandwidth, it is not suitable for the design of the broadband antenna. Because of the neglect of antenna loss, Eq. (1):

$$Z_{in} = X_{in} = -\frac{j(Y_0 \cos \theta - \omega C_{inter} \sin \theta)}{Y_0(Y_0 \sin \theta - 2\omega C_{inter}(1 - \cos \theta))} \quad (1)$$

expresses the input reactance of Fig. 1(b), and Fig. 2 based on Eq. (1) shows the input reactance as function of frequency when the value of the inter-coupling capacitor is different.

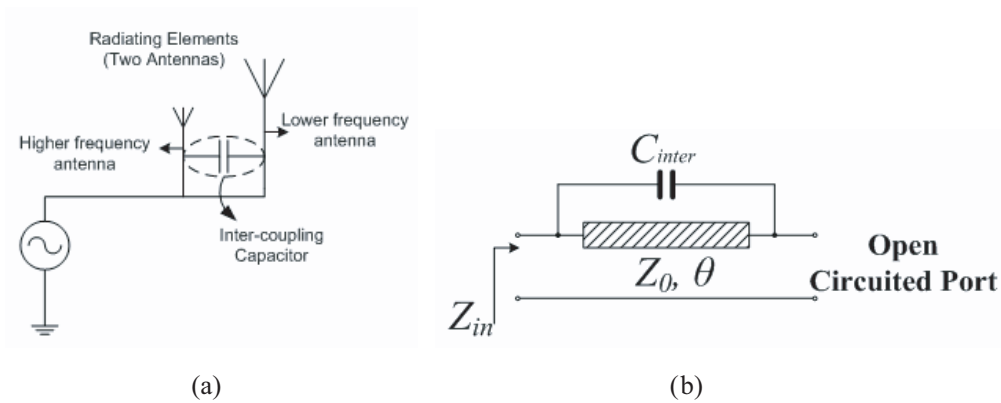


Figure 1: Illustration of small antenna using branch structure. (a) Geometry of small antenna using branch structure. (b) Transmission line model of a branch structure antenna with an inter-coupling capacitor.

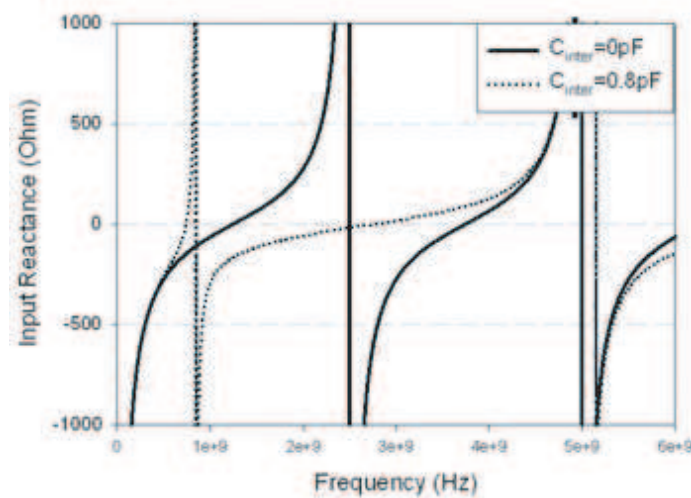


Figure 2: Input reactance with two different inter-coupling capacitors.

From Fig. 2, it is shown that the larger value of the inter-coupling capacitance leads to a steeper slope of input impedance at fundamental resonant frequency. Therefore, a narrow bandwidth appears in conditions where many antenna patterns are near each other in a fixed small volume.

Because it is impossible to reduce significantly the inter-coupling capacitance in a fixed volume, this paper proposes the gap feeding method to decrease the value of capacitance connected with a low frequency antenna. As known well, the value of the total capacitor decreases when two

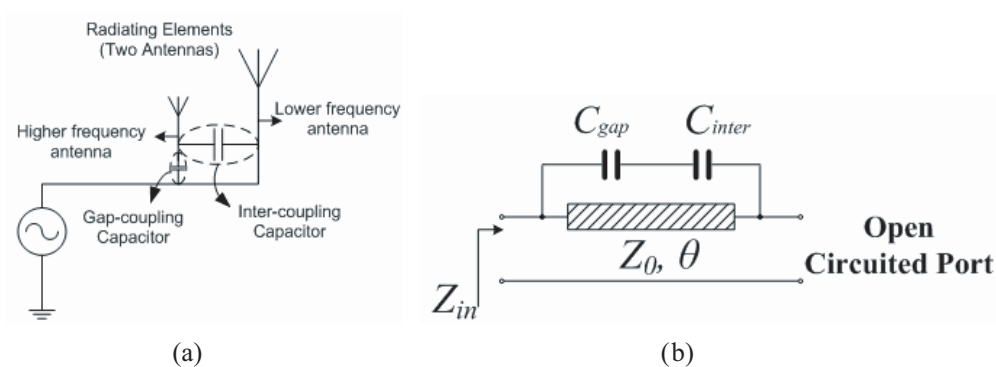


Figure 3: Illustration of small antenna using branch structure with one gap feeding. (a) Geometry of small antenna using branch structure with one gap feeding. (b) Transmission line model of a branch structure antenna with one inter-coupling capacitor with gap feeding.

capacitors are connected in series. Fig. 3 shows the geometry and the equivalent circuit of the branch structure antenna with gap feeding, respectively.

In next chapter, branch structure antennas using meandered patterns will be examined to find the effect of inter-coupling capacitance. Furthermore, the gap feeding antenna is suggested to alleviate narrow bandwidth by the inter-coupling capacitance between radiating elements.

### 3. EXPERIMENTS

Figure 4 shows three antennas for low frequency band, high frequency band, and dual band, separately. Fig. 5 shows the VSWR of each antenna in Fig. 4 when these are installed to  $40 \times 83 \text{ mm}^2$  ground plane. From Fig. 5, it is derived that the inter-coupling capacitance between two meander patterns makes the fundamental resonant bandwidth extremely narrow. To solve this problem, the antenna using gap feeding mentioned in Chapter 2 is proposed as shown in Fig. 6. According to theory in Chapter 2, the bandwidth of the fundamental frequency is broadened by connecting gap feeding with the short antenna in series as illustrated in Fig. 7.

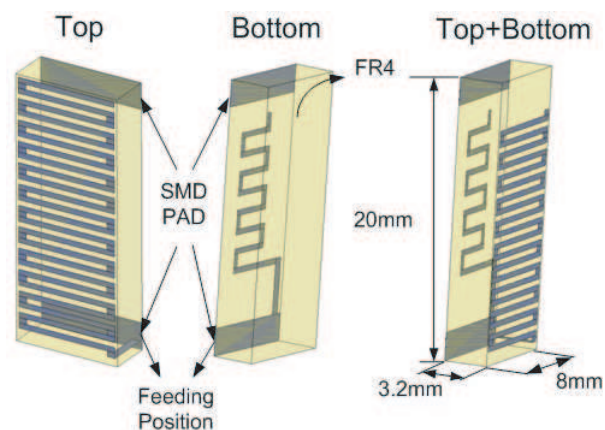


Figure 4: Illustration of the branch structure antenna using two meandered patterns.

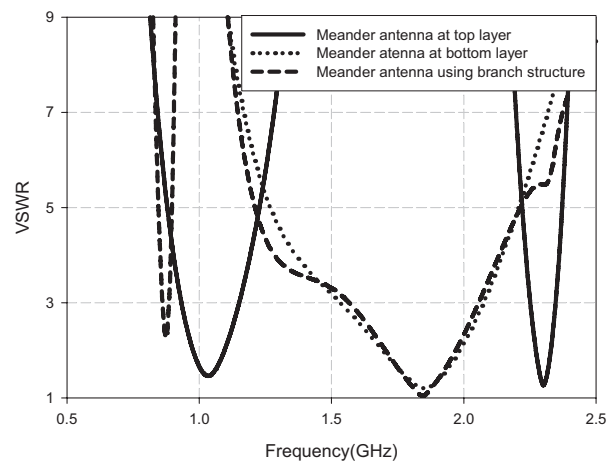


Figure 5: VSWR of each antenna in Fig. 4.

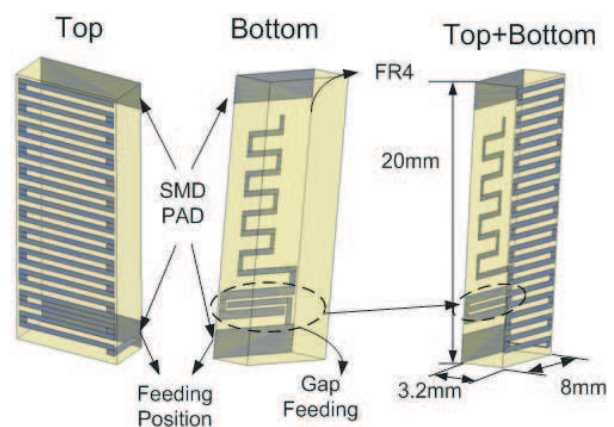


Figure 6: Illustration of the branch structure antenna using two meandered patterns with one gap feeding.

### 4. RESULTS

The measured VSWR graph and radiation pattern of the proposed antenna are illustrated as shown in Fig. 8 and Fig. 9, respectively. From these results, it is shown that the gap feeding is efficient method in small antenna design using branch structure.

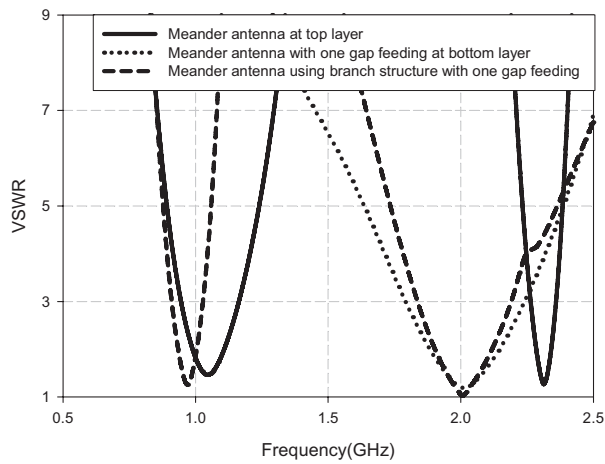


Figure 7: VSWR of each antenna in Fig. 6.

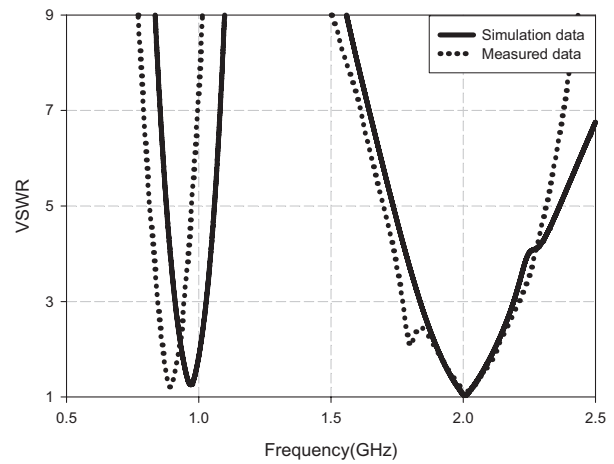


Figure 8: Simulation VSWR and measure VSWR of the proposed antenna.

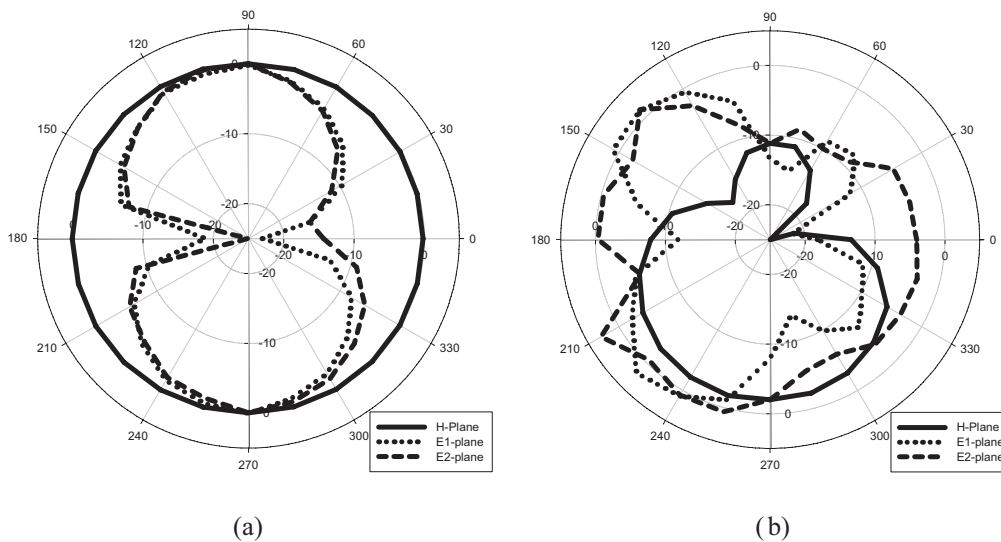


Figure 9: Measured gain of the proposed antenna on three radiation planes: H-plane, E1-plane, E2-plane, (a) at low resonant frequency, (b) at high resonant frequency.

## 5. CONCLUSIONS

To find the effect of inter-coupling capacitance, the small antenna using branch structure is converted into transmission line and a shunt capacitor, and meander antenna using branch structure is designed and manufactured. From the results of these analysis and measured data, it is derived that the inter-coupling capacitance makes the antenna bandwidth very narrow. Therefore, this paper proposes the gap feeding method to solve this problem. As shown in simulation and measured VSWR, the gap feeding is considered as the efficient solution for the multi-band antenna using a branch structure in a fixed small volume.

## ACKNOWLEDGMENT

This research was supported by the MIC (Ministry of Information and Communication), Korea, under the ITRC (Information Technology Research Center) support program supervised by the IITA (Institute of Information Technology Advancement), (IITA-2006-C1090-0602-0011).

## REFERENCES

1. Wong, K. L., *Planar Antennas for Wireless Communications*, Wiley-Interscience, Hoboken, New Jersey, 2003.

2. Guo, Y. X., M. Y. W. Chia, and Z. N. Chen, "Miniature built-in multiband antennas for mobile handsets," *IEEE Transactions on Antennas and Propagation*, Vol. 52, No. 8, 1936–1944, 2004.
3. Nashaat, D. M., H. A. Elsadek, and H. Ghali, "Single feed compact quad-band PIFA antenna for wireless communication applications," *IEEE Transactions on Antennas and Propagation*, Vol. 53, No. 8, 2631–2635, 2005.
4. Moon, J. I. and S. O. Park, "Small chip antenna for 2.4/5.8-GHz dual ISM-band applications," *Antennas and Wireless Propagation Letters*, Vol. 2, No. 1, 313–315, 2003.
5. Chen, H. T., G. Y. Lee, and K. L. Wong, "Surface-mount foam-base chip antenna for dual-band operation," *Proceedings of Antennas and Propagation Society International Symposium*, Vol. 3, 99–102, Columbus, Ohio, USA, June 2003.
6. Best, S. R., "On the resonant properties of the Koch fractal and other wire monopole antennas," *Antennas and Wireless Propagation Letters*, Vol. 1, No. 1, 74–76, 2002.
7. Fante, R., "Quality factor of general ideal antennas," *IEEE Transactions on Antennas and Propagation*, Vol. 17, No. 2, 151–155, 1969.
8. Chen, Z. N. and M. Y. W. Chia, *Broadband Planar Antennas*, John Wiley & Sons, Hoboken, New Jersey, 2005.
9. Makimoto, M. and S. Yamashita, *Microwave Resonators and Filters for Wireless Communication*, Springer, Berlin, New York, 2001.

# Design and Analysis of a 1.2 V, 1.8 GHz, 240.147 $\mu$ w Low Power ASK Transmitter for Wireless Micro Sensor Nodes

T. Sasilatha<sup>1</sup> and J. Raja<sup>2</sup>

<sup>1</sup>Anna University, Chennai, India

<sup>2</sup>SSN College of Engineering, Tamil nadu, India

**Abstract**— A 1.2V, 1.8GHz ASK transmitter for low-rate WPAN is designed and implemented. The performance of the transmitter is analyzed to meet the unique requirements of wireless micro sensor nodes. Emphasis was placed on observing device reliability constraints such as leakage current, short circuit current, switching current, supply voltage and the operating frequency at low power to maximize the life time of the wireless sensor nodes. The power consumption in the design is considerably reduced in this approach. The performance of the ASK transmitter is compared with previously reported low power transmitters operating in similar frequency ranges.

## 1. INTRODUCTION

The wireless sensor networks offer a sophisticated platform for environment observation. The vision of a micro sensor network includes dense, intelligent nodes that are energy autonomous and are deployed in an ad hoc manner. Such networks have broad applications ranging from military surveillance, reconnaissance, and damage assessment to environmental forest fire detection and industrial process monitoring [1]. The main design objective is to maximize the battery life of the sensor nodes while ensuring reliable operations. To achieve this goal, the micro sensor node has to be designed in a highly integrated fashion and optimized across all levels of system abstraction [2]. The block diagram of a core of a micro sensor node is shown in Fig. 1. The sensing unit is composed of a sensor and an analog to digital converter (A/D), which converts the sensed phenomenon to a digital signal that is then fed to the processing unit. A transceiver unit provides communication between the nodes. The processing unit manages the communication between protocols and process the sensed signal. The power in a sensor node is consumed in three processes: Sensing, data communication with other nodes and local data processing. The sensing power varies with applications or the complexity of detecting a certain event [3]. The processing unit is often based on a microcontroller. In micro sensor nodes the transceiver dominates the power consumption since it has major number of analog components in addition to the digital counterparts [3]. The focus of this research is the realization of a high performance, integrated transmitter in CMOS. The chapters are organized as follows. Chapter II reviews the previously reported works. In Chapter III, the transceiver and the necessity of going for ASK modulator and the low power amplifier are discussed. In Chapter IV, the various power reduction techniques are discussed. In Chapter V, the performance of the ASK transmitter along with other previous works is tabulated and results are discussed in the same section.

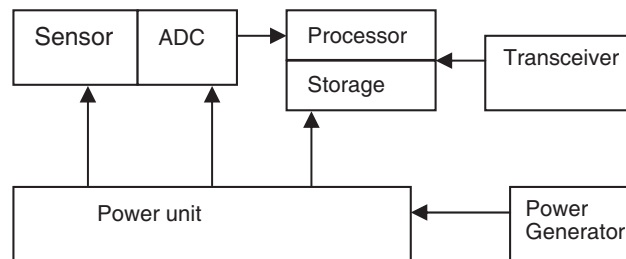


Figure 1: Block diagram of a sensor node.

## 2. RELATED WORKS

A 2.4 GHz, 8.0 mw, ASK transmitter suitable for low power wireless capsule endoscope system is discussed in reference [4]. The transmitter consists of a 20 MHz ASK modulator based on the

constant amplitude phase lock loop (PLL) and a direct up-conversion RF circuit. It was implemented in TSMC 0.25/ $\mu\text{m}$  CMOS process, achieves  $-23.217$  dBm output power with the data rate of 1 Mbps and dissipates 3.17 mA current from 2.5 V power supply. In reference [5], 270 MHz direct-PLL FSK modulator with 500 kHz loop bandwidth is implemented. It consumes a power of 4.9 mW adopting current re-using technique and appropriate divider architecture. A 2.5-GHz/900-MHz dual fractional-N/integer-N frequency synthesizer is implemented in 0.35- $\mu\text{m}$  25-GHz Bi CMOS in discussed in reference [6]. The fractional-N synthesizer offers less than 10-Hz frequency resolution having the in-band noise contribution of  $-88$  dBc/Hz for 2.47-GHz output frequency and  $-98$  dBc/Hz for 1.15-GHz output frequency, both measured at 20-kHz offset frequency. The prototype dual synthesizer consumes 18 mW with 2.6-V supply. In reference [7] an experimental 2.4-GHz CMOS radio composed of RF and digital circuits for the low-power and low-rate preliminary IEEE802.15.4 WPAN is reported, consuming 21 mW in receive mode and 30 mW in transmit mode. In this paper, we propose a low power CMOS ASK modulator based transmitter at 2.4 GHz for wireless sensor networks. It consumes less power when compared to the other circuits operating in similar frequency ranges.

### 3. TRANSCEIVER SECTION

The wireless sensor networks consists of many distributed and disposable sensor nodes that requires a highly integrated, low cost single chip transceiver with high energy efficiency. The radio transceiver has essentially two tasks. They are transmitting and receiving data from a pair of nodes. To consume low power it should be turned off most of the time and only be activated when necessary, that is they work at a low duty cycle. The energy consumed by a transmitter is due to two sources. One part is due to RF signal generation which is mainly due to modulation and the other part is due to the electronic components needed for frequency synthesis, frequency conversions, power amplifiers, filters and so on. These costs are basically constant [8].

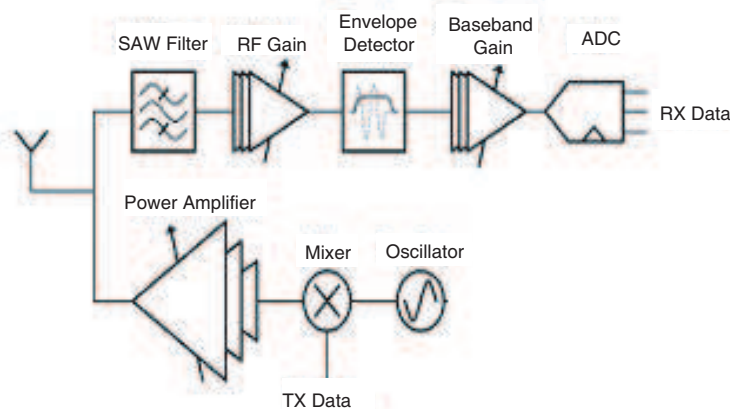


Figure 2: Transceiver in wireless sensor nodes.

#### 3.1. PLL Based Frequency Synthesizer

The role of frequency synthesizer is to provide reference frequency for frequency translation. An ideal frequency synthesizer generates a single frequency tone is shown in Fig. 3. In the receiver case, it mixes with the received RF signal spectrum and shifts it down to base band. In the transmitter case, it mixes with the modulated base band signal and shifts it up to RF. Phase noise and spurious tones are the two key parameters to measure the quality of a frequency synthesizer [9]. Phase noise is specified as the ratio of noise power in 1 Hz bandwidth at a certain offset frequency from carrier to the carrier power. The unit is dBc/Hz [8].

$$\Phi(f) = 10 \log \frac{P_{noise}}{P_{carrier}} \text{ (dBc/Hz)} \quad (1)$$

The direct digital frequency synthesizer takes large power consumption to synthesize very high frequencies directly. So a PLL based frequency synthesizer is used due to its high performance, namely low phase noise and low spurious tones. The performance evaluation of the PLL based frequency synthesizer in the transceiver is considered in this section. Measures are taken to reduce the

power consumption of the synthesizer. A typical PLL based frequency synthesizer [10] is shown in Fig. 4 and contains a reference source oscillating at frequency  $f_r$  and a VCO oscillating at frequency  $f_0$ . The two frequencies are compared in the phase detector. When the two phases are equal (phase locking) then the o/p frequency is locked to the rational fraction of the reference frequency. The synthesizer is capable of generating a large number of highly accurate o/p frequencies. A power hungry circuit is the voltage controlled oscillator. As the gain increases, the VCO output frequency becomes highly sensitive to small variations or noise in the VCO input signal, which results in the increase of VCO phase noise [9]. Fig. 4 depicts the circuit of the typical Ring oscillator type voltage controlled oscillator.

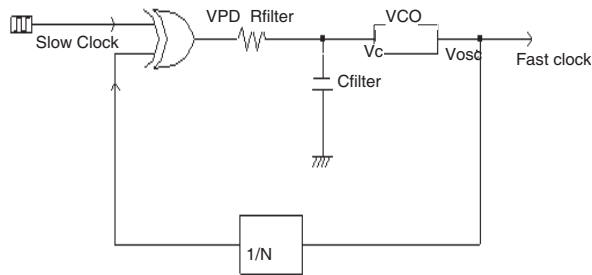


Figure 3: Schematic of PLL based frequency synthesizer.

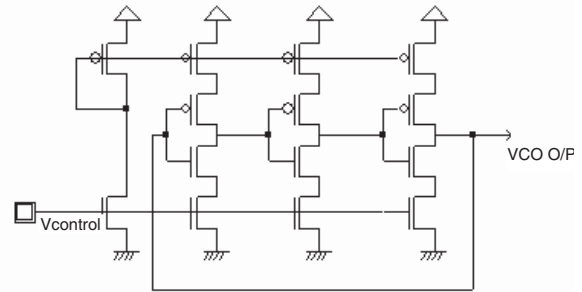


Figure 4: Voltage controlled oscillator.

On the system level the phase noise of the circuit are examined. Though there are a number of VCO categories are available, because of the need for integrability, ring oscillator is very desirable in VLSI environments [11]. This configuration consumes less power of  $0.322 \mu\text{w}$  when compared to other circuits. The structure also employs positive feedback to achieve oscillation. Assuming that  $180^\circ$  phase shift is provided by a chain of  $N$  stages, each stage must provide  $(180^\circ/N)$  of phase shift and sufficient gain at  $\omega_0$ . This usually means that the gain of each individual stage has to be greater than 1 as well.

### 3.2. Modulator

Though the modulation schemes such as QAM and MSK are popular in modern communications and have different filtering requirements and characteristics, BFSK modulators are generally suitable for low power sensor networks. As evidenced by (2), one way to increase the energy of communication is to reduce the transmit ton-time of the radio. This can be accomplished by sending multiple bits per symbol, that is, by using  $M$ -ary modulation. Using  $M$ -ary modulation, the circuit complexity and power consumption of the radio will be increased. In addition, when  $M$ -ary modulation is used, the efficiency of the power amplifier is also reduced. This implies that more power will be needed to obtain reasonable levels of transmit output power. From the references [12, 13], we see that the startup transient plays an important role in choosing a low power modulation scheme. Therefore an ASK modulator is chosen to reduce the power at circuit level. Fig. 5 shows the circuit of an ASK modulator.

### 3.3. Power Amplifier

The schematic of a non-switching power amplifier which operates in class A/B is shown in Fig. 6. Transistor  $M_1$  operates as a trans conductor and converts its input voltage signal  $V_{in}$  into its output drain current  $I_{ds}$ . The RF tank, formed by inductor  $L_1$  and all the capacitances at the drain of the top transistor, filters out the harmonics in the drain current and only allows the fundamental drain current to flow to the load, thus resulting in a sinusoidal drain voltage  $V_{ds}$ . Maximizing the drain efficiency requires the voltage swing  $V_{ds}$  to be maximized. For the output power with a 1.2 V supply and 100 mV knee voltage, a  $500 \Omega$  load resistance at the drain of  $M_2$  is required. To achieve this, the  $50 \Omega$  antenna ( $R_L$ ) is transformed to the required impedance using  $C_1$  and  $C_2$ . Inductor  $L_1$  tunes out the transformed capacitance and the parasitic drain capacitance.

Capacitive transformers are preferred over LC matching networks or inductive transformers because on-chip capacitors have much higher Q ( $>50$ ) than on-chip inductors (Q of 5–10), resulting in less loss. In the current prototype, the required  $L_1$  is 1.2 nH and is implemented using an off-chip

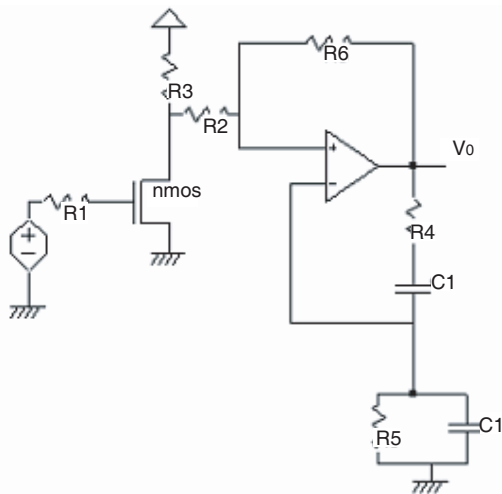


Figure 5: ASK modulator.

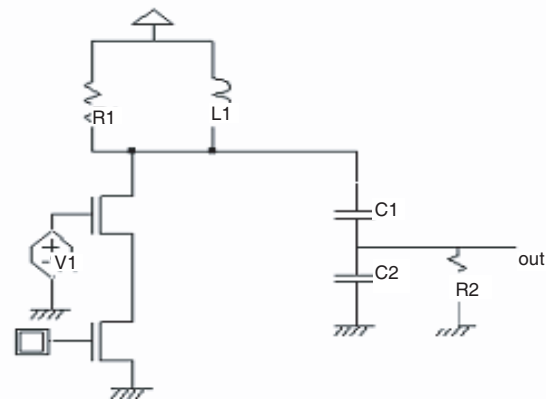


Figure 6: Non switching power amplifier

inductor. However, a short bond wire or an on-chip inductor can be used for a fully integrated solution. Cascode transistor  $M2$  ensures that the drain voltage does not exceed the low gate breakdown voltage for deep sub-micron CMOS [7]. It consumes a power of  $192 \mu\text{w}$ . Usually power amplifier section consumes much power when compared to other analog circuits.

#### 4. LOW POWER DESIGN OF TRANSMITTER

In a typical sensor network, the transmitter sends out sporadic bursts of short data packets to neighboring sensor nodes ( $<10\text{ m}$ ). The transmitter must exhibit fast response time and high efficiency [7, 9]. The power dissipation in CMOS transmitter circuits consists of dynamic and static components. The dynamic power is proportional to  $V_{dd}^2$  and static power is proportional to  $V_{dd}$ , lowering the supply voltage is one of the most effective ways to reduce power dissipation in CMOS circuits. With the scaling of supply voltage and device dimensions, the transistor threshold also has to be scaled to achieve the required performance. But scaling can increase the leakage current. It can be a major component of the total power dissipation in CMOS circuits [14]. Dynamic power dissipation is caused by the switching activities of the circuits. A higher operating frequency leads to more frequent switching activities in the circuits and results in increased power dissipation. Static power dissipation is related to the logical states of the circuits rather than switching activities [11]. From the golden equation [15]  $P = C_L V^2 f$ , if the operating frequency and the supply voltage is reduced, the power dissipation can be reduced much.

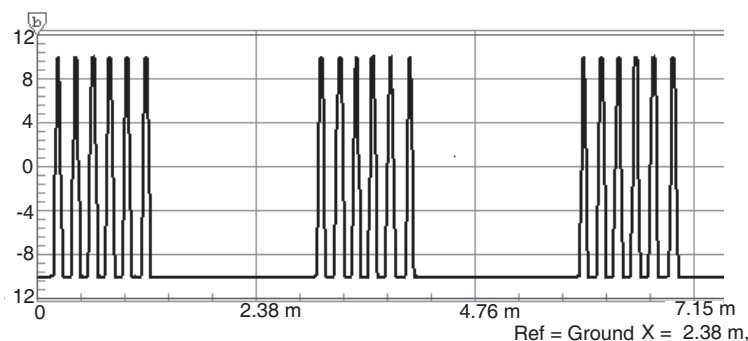


Figure 7: Output of ASK modulator.

##### 4.1. Optimal Supply Voltage

Lowering the supply voltage is an effective way for reducing the power consumption of digital circuits [11, 14, 15]. In the presence of noise, mismatch, finite switch resistance, and distortion, the power consumption of analog circuits is liable to increase with reduced supply. There are many trade-offs to be considered in voltage reduction. Performance is lost because MOS transistors

become slower at lower operating voltages. The main reason is that the threshold voltages of transistors do not scale accordingly with the operating voltage to avoid excessive leakage current. For this study the normalized energies at 1.2 V are based on actual measurements of the layout and these are extrapolated over a range of  $V_{DD}$  using fundamental analytical models.

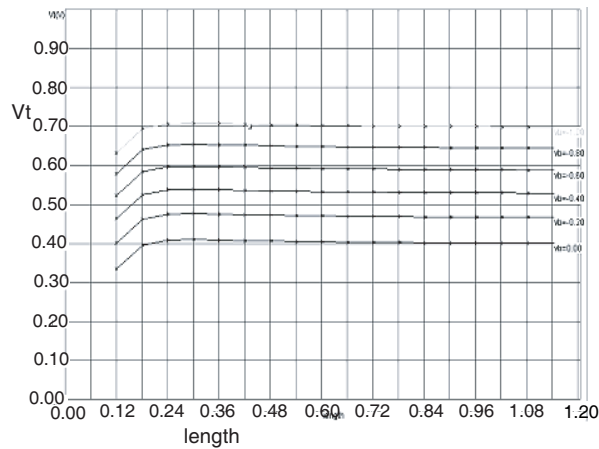


Figure 8: Threshold voltage versus channel length of the N MOS transistor.

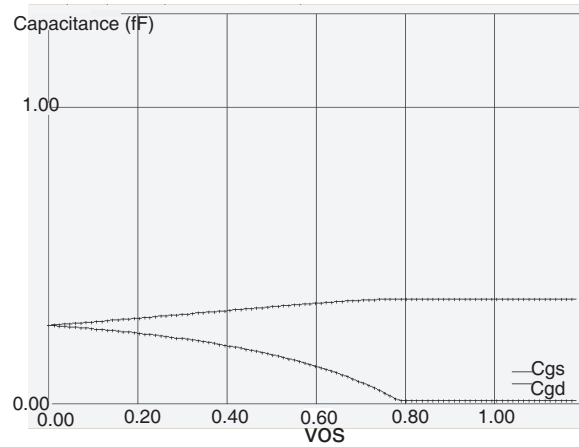


Figure 9: Variation of capacitance with respect to voltage.

#### 4.2. Static Power Dissipation

Leakage current is the only source of static power dissipation. CMOS circuits dissipate significant amount of power even if the input is not changing, called static power dissipation. Scaling of supply voltage and transistor threshold has a large impact on the leakage current. Transistor off state current is the drain current when the gate-source voltage is zero. The off-state leakage in long channel devices is dominated by drain well and well-substrate reverse bias pn junctions. For short channel transistors, the off state current is influenced by threshold voltage, channel physical dimensions, supply voltage, the drain and gate voltages. For long channel transistors, the leakage current is due to pn junction leakage and the weak inversion current [10, 15]. A reverse bias pn junction leakage has two main components. One is the minority carrier drift near the edge of the

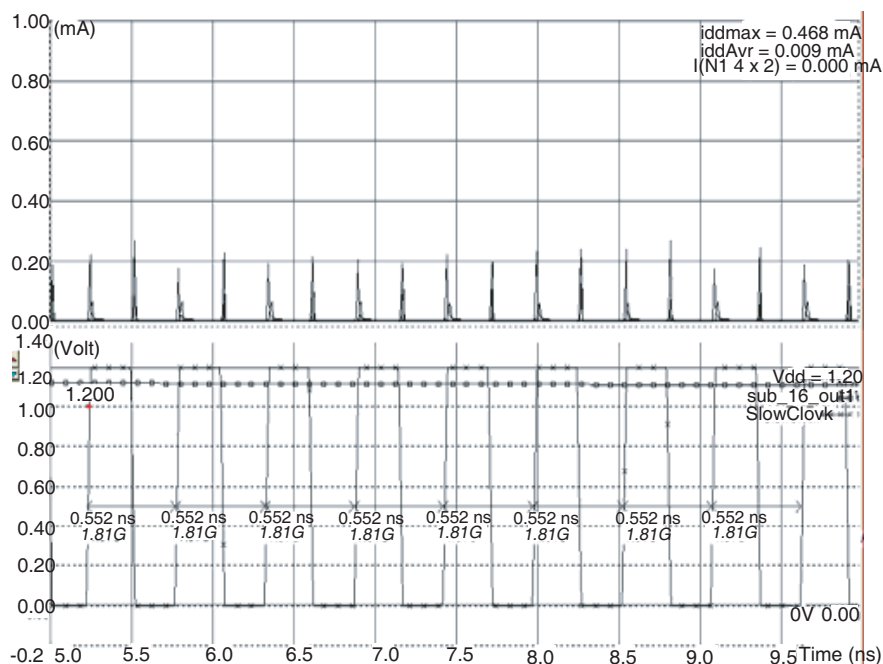


Figure 10: Current flow due to short circuit effects.

depletion region and the other is due to electron hole pair generation in the depletion region of the reverse bias junction [16].

Weak inversion current between source and drain in a MOS transistor occurs when gate voltage is below the threshold voltage  $V_{th}$ . The weak inversion region is shown in Figs. 11(a) and (b) as a linear portion of the curve. It is plotted on a log scale for a 0.12  $\mu\text{m}$  technology. Sub threshold conduction current can be minimized by lowering  $V_{gs}$  and increasing  $V_{th}$  [15]. Short channel effect reduction (includes threshold voltage roll off) has become a major challenge in deep sub micrometer devices and circuits. The relationship between threshold voltage and transistor channel length is shown in Fig. 8. If the channel length is minimum then the threshold voltage required is also minimum. In order to make the device work properly  $dV_{th}/dL$  cannot be too large. This will determine the minimum channel length and is found to be 0.12  $\mu\text{m}$ .

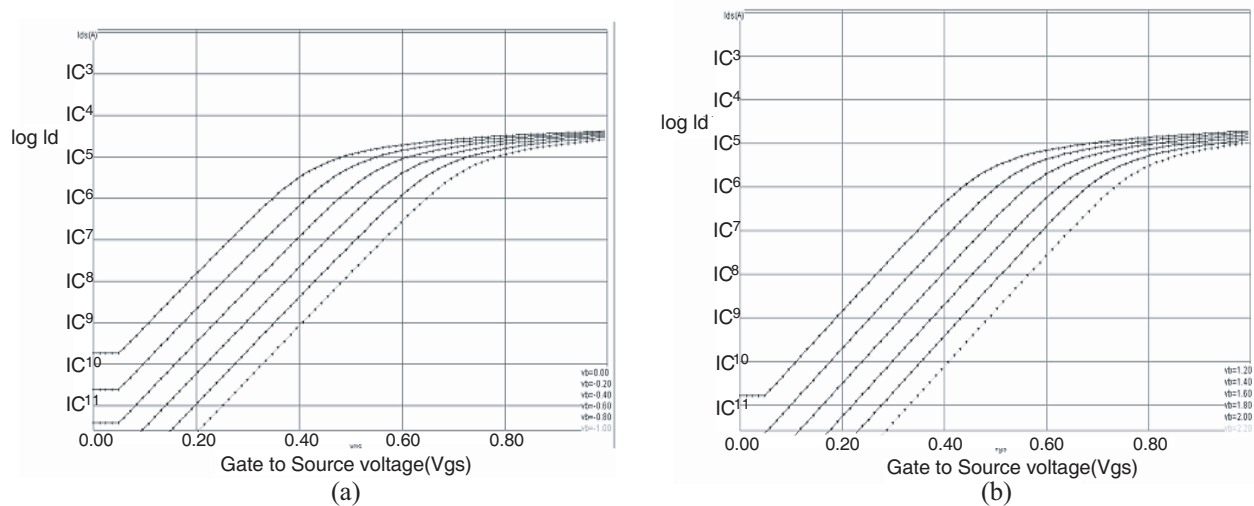


Figure 11: (a)  $V_{gs}$  Versus  $\log (I_d)$  (for NMOS transistor), (b)  $V_{gs}$  versus  $\log (I_d)$  (for PMOS transistor).

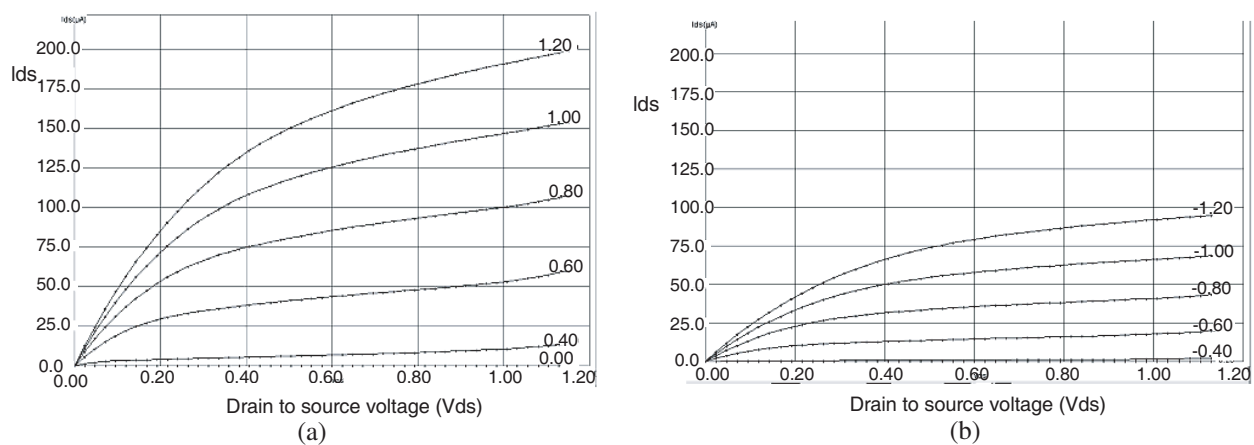


Figure 12: (a) Variation of  $I_{DS}$  with respect to  $V_{DS}$  for the N MOS transistor, (b) Variation of  $I_{DS}$  with respect to  $V_{DS}$  for the P MOS transistor.

### 4.3. Dynamic Power Dissipation

The most significance source of dynamic power dissipation in CMOS circuits is the charging and discharging of capacitance. The capacitance forms due to parasitic effects of interconnection wires and transistors. Reducing parasitic capacitance has been a good way to improve performance as well as power. The real goal to reduce power is to reduce the product of capacitance and its switching frequency [11]. Signals with high switching frequency should be routed with minimum parasitic capacitance to conserve power. From the golden equation [14, 15]  $P = C_L V^2 f$ , we observe

that during charging  $C_L V^2$  energy is drawn from the energy source, half of which is stored in the capacitance. During discharging, the energy stored in the capacitance is dissipated as heat in the discharging resistor  $R_d$ .

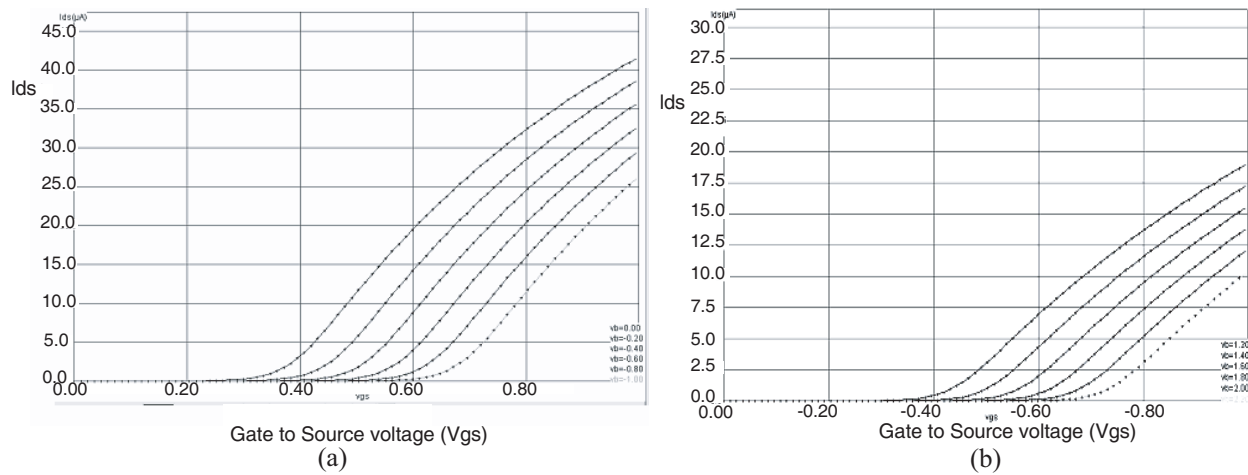


Figure 13: (a) Variation of  $I_{DS}$  with respect to  $V_{gs}$  for the N MOS transistor, (b) Variation of  $I_{DS}$  with respect to  $V_{gs}$  for the P MOS transistor.

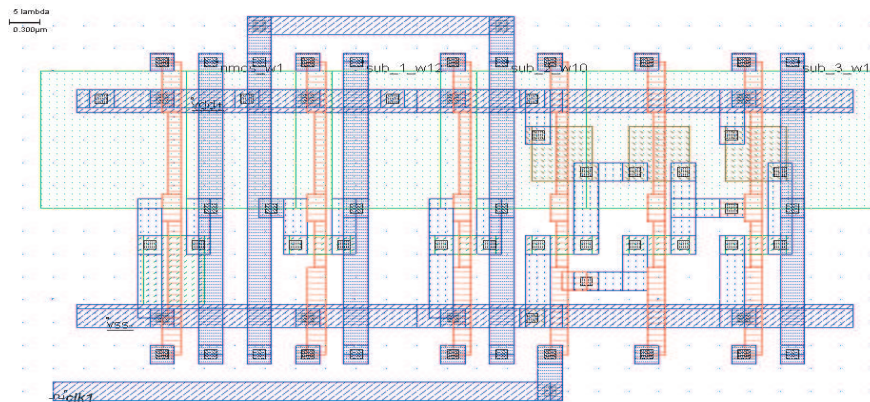


Figure 14: Layout of the proposed FSK transmitter [Width:  $8.3 \mu m$  (138 lambda), Height:  $5.0 \mu m$  (84 lambda), Surf:  $41.7 \mu m^2$  (0.0 mm<sup>2</sup>)].

From the graph (Fig. 9), we observe that if  $V_{ds}$  increases, Capacitance varies till it reaches 0.8 V. After that it remains constant. Short circuit power dissipation is the component of power dissipation due to the flow of current from  $V_{DD}$  to the ground. This current depends on the transition period of the input signal. When the input voltage is between  $V_{tn}$  and  $V_{tp}$  the short circuit current is non zero based on the switching properties of the transistor. This is shown in Fig. 10. Figs. 12(a) and (b) shows the sketch of  $I_{DS}$  versus  $V_{ds}$  for various values of  $V_{gs}$ . Figs. 13(a) and (b) shows the sketch of  $I_{DS}$  versus  $V_{gs}$  for various values of  $V_{ds}$ . The voltage  $V_{DS}$  causes a current  $I_{DS}$  to flow through the induced channel. The magnitude of  $I_{DS}$  depends upon the density of electrons in the channel which in turn depends upon the magnitude of  $V_{GS}$ . For  $V_{GS} = V_t$  the channel is just induced and the current conducted is still negligibly small. As  $V_{GS}$  exceeds  $V_t$  more electrons are attracted into the channel [17].

## 5. SIMULATION RESULTS

A summary of the performance of the ASK transmitter is reported in Table 1. At 27 degree C the evaluation is done and the power consumed in this approach is less when compared to the other approaches [5, 6, 13, 16]. This is tabulated in Table 2.

Table 1: Measured performance at 27 degree C.

Vdd	1.2 V
Technology	0.12 $\mu\text{m}$ technology
Power consumed by the Phase detector with loop filter	14.438 $\mu\text{w}$
Power consumed by the VCO	0.322 $\mu\text{w}$
Power consumed by the frequency Divider	4.283 $\mu\text{w}$
Total power consumed by the frequency synthesizer	19.043 $\mu\text{w}$
Power consumed by the ASK modulator	29 .104 $\mu\text{w}$
Power consumed by the power Amplifier	192 $\mu\text{w}$
Total Power Dissipation of the transmitter at 1.8 GHZ	240.147 $\mu\text{w}$
Tuning Range of the synthesizer	10 MHz to 2 GHz

Table 2: Performance comparison with other works.

Ref	[5]	[6]	[13]	[16]	This work
Tech	0.5 $\mu\text{m}$ CMOS	0.35 $\mu\text{m}$ CMOS	0.35 $\mu\text{m}$ BiCMOS	0.18 $\mu\text{m}$ CMOS	0.12 $\mu\text{m}$ CMOS
$f_{\text{VCO}}$ [MHz]	900	900	2500	540	1.8 GHz
Phase Noise					
[dBc/Hz]	-92	-80	-82	-104	-110
@ 10 kHz					
Power [mW]	29	17.4	16	4.9	240.147 $\mu\text{w}$
Etc	w/o VCO		w/o VCO	w/o DSM	with VCO

## 6. CONCLUSIONS

The proposed ASK transmitter consumes a total power of 240.147  $\mu\text{w}$  from 1.2 V supply at 2.4 GHz frequency. As compared to the previous results [5, 6, 13, 16] a very good reduction in power is reported in this approach by using the low power circuits. The transmitter is implemented in the 0.12  $\mu\text{m}$  technology and the width of the Layout is 8.3  $\mu\text{m}$  and the height is 5.0  $\mu\text{m}$ . Its Surface area is 41.7  $\mu\text{m}^2$ . It is clearly shown in Fig. 14. For Wireless sensor nodes, in order to accommodate large amount of circuitry in a small chip the dimension of the devices should be made smaller. Since the dominant component of power dissipation in CMOS transceiver circuits varies as the square of the supply voltage, the significant saving in power dissipation can be obtained from operation at a reduced supply voltage.

## REFERENCES

1. Verma, N. and A. P. Chandrasekaraan, "An ultra low energy 12 bit rate-resolution scalable for wireless sensor networks," *IEEE Journal of Solid State Circuits*, Vol. 42, No. 6, 1196–1205, June 2007.
2. Shih, E., S. Cho, F. S. Lee, B. H. Calhoun, and A. Chandrakasan, "Design considerations for energy-efficient radios in wireless microsensor networks," *Journal of VLSI Signal Processing*, Vol. 37, 77–94, 2004.
3. Li, L., "Design techniques for high performance integrated frequency synthesizers for multi-standard wireless communication applications," PhD thesis in University Of California, Berkeley.
4. Han, S., et al., "A 8.0 mW 1-Mbps ASK transmitter for wireless capsule endoscope applications," *Radio Frequency Integrated Circuits (RFIC) Symposium*, IEEE, 2006.
5. Choi, H., S. Shin, Y. Ku, M. Jeong, and KwyroLee, "A 4.9 mW 270 MHz CMOS frequency synthesizer/FSK modulator," *Radio Frequency Integrated Circuits (RFIC) Symposium*, 2003 IEEE Volume, Issue 8–10, 443–446, June 2003.

6. Rhee, W., B. Song, and A. Ali, "An 18-mW 2.5-GHz/900-MHz BiCMOS dual frequency synthesizer with <10-Hz RF carrier resolution," *IEEE Journal of Solid-State Circuits*, Vol. 37, Issue 4, 515–520, Apr. 2002.
7. Melly, T., et al., "An ultra low power UHF transceiver integrated in a standard digital CMOS process transmitter," *IEEE J. Solid State Circuits*, Vol. 36, No. 3, Mar. 2001.
8. Karl, H. and A. Willig, *Protocols and Architectures for Wireless Sensor Networks*, John Wiley & Sons, 2005.
9. Kim, W., J. Park., P. Park., and S. Park, "A low-cost, low-power frequency synthesizer for mobile RFID," Korea Advanced Institute of Science and Technology.
10. www.microchip.com
11. Leung, B., *VLSI for Wireless Communication*, first edition, Pearson Education, 2004.
12. Pierret, R., *Semiconductor Device Fundamentals*, Addison-Wesley, Reading, MA, 1996.
13. Rhee, B. and A. A. Song, "A 1.1-GHz CMOS fractional-N frequency synthesizer with a 3-b third-order  $\Delta\Sigma$ -modulator," *IEEE Journal of Solid-State Circuits*, Vol. 35, Issue 10, 1453–1460, Oct. 2000.
14. Roy, K. and S. C. Prasad, *Low Power CMOS VLSI Circuit Design*.
15. Yeap, G. K., *Low Power VLSI Design*.
16. Hegazi, E. and A. A. Abidi, "A 17 mW transmitter and frequency synthesizer for 900 MHz GSM fully integrated in 0.35- $\mu\text{m}$  CMOS," *2002 Symposium On VLSI Circuits Digest of Technical Papers*, 234–237, 2002.
17. Smith, S., *Micro Electronic Circuits*, Fifth Edition, Oxford University press, 2004.

# Wavefront Reconstruction of Breast Microwave Imagery Acquired along Circular Scan Trajectories: A Study on Experimental Feasibility

Daniel Flores-Tapia<sup>1</sup>, Gabriel Thomas<sup>1</sup>, and Stephen Pistorius<sup>2,3,4</sup>

<sup>1</sup>Department of Electrical and Computer Engineering, University of Manitoba, Winnipeg, Canada

<sup>2</sup>Department of Physics and Astronomy, University of Manitoba, Winnipeg, Canada

<sup>3</sup>Department of Radiology, University of Manitoba, Winnipeg, Canada

<sup>4</sup>Department of Medical Physics, CancerCare Manitoba, Winnipeg, Canada

**Abstract**— In recent years, the use radar technology has been proposed in a wide range of subsurface imaging applications. Traditionally, linear scan trajectories are used to acquire data in most subsurface radar applications. However, novel applications, such as breast microwave imaging, require the use of non linear scan trajectories in order to adjust to the geometry of the scanned area. In this paper the experimental feasibility of a 2D wavefront reconstruction algorithm for subsurface radar data acquired along circular scan trajectories is assessed. The proposed algorithm was successfully tested using data collected from phantoms that mimic the dielectric properties contrast present in an average breast microwave imaging scenario, yielding promising results.

## 1. INTRODUCTION

During the last decades, Subsurface Radar (SR) has been extensively used on as a non invasive imaging tool in a wide variety of applications such as archeology, soil humidity estimation and landmine detection. Similarly to conventional radar applications, SR systems irradiate electromagnetic wave into the scan area, which is usually formed by two or more layers with different dielectric properties. The received echoes from different buried objects are recorded [1] and displayed in order to be visualized and interpreted. In recent years, SR technology has been used in imaging scenarios where radar techniques theoretically yield high contrast imagery, like breast cancer detection and wood inspection [2, 3]. The data acquisition process in these novel applications is performed along circular or quasi circular scan trajectories in order to adapt better the geometry of the scan area. Also, due to the short distances between the scan locations and the scattering objects, traditional far field focusing techniques are not suitable to properly reconstruct the recorded data.

Currently, there are two main approaches to reconstruct cylindrical SR data: time domain techniques and wavefront reconstruction methods. Time domain focusing techniques perform a shift-sum process over a set of regions of interest in the scan area. The target responses are delayed according to the location where they were collected and their distance from the regions of interest. Next, the shifted responses are added and the square of the sum is the energy at the region of interest. The same process is repeated for all the regions of interest in the scan area. Some examples of this methodology are the confocal mapping algorithm [2] and the polarimetric parameter based reconstruction performed by Kaestner [3].

Wavefront reconstruction techniques focus the recorded SR data by performing a series of operations in the frequency domain. In general, wavefront reconstruction methods work as follows. First, the spectrum of the collected reflections, both in the signal travel time and the scan trajectory directions, is calculated. Afterwards, the spectrum of the recorded signals is compensated using the frequency response of the imaging trajectory. The compensated spectrum is then mapped from the spatial-temporal frequency space in which was originally collected to the imaging area spatial frequency space. Finally, the inverse Fourier transform is applied to the processed data in order to properly visualize the target signatures. Although wavefront reconstruction methods are traditionally used in SR scenarios where the scan trajectory is linear, their potential application on data acquired along circular scan trajectories was shown by the authors in [4] using simulated data sets.

In this work, the experimental feasibility of the wavefront reconstruction approach for circular trajectories proposed by the authors in [4] is illustrated. An experimental data set was collected from phantoms that mimic the dielectric contrast present on breast cancer detection. The focal quality, signal to noise ratio, and spatial accuracy of the focused images were measured in order to quantitatively and qualitatively assess the performance of the reconstruction method. This paper

is organized as follows. The signal models are described in Section 2. In Section 3, the wavefront reconstruction methodology is explained. The performance assessment of the proposed method using experimental data sets is described in Section 4. Finally, concluding remarks can be found in Section 5.

## 2. SIGNAL MODEL

Consider a circular array formed by  $N$  antennas uniformly positioned in a circle of radius  $Z$ . In this case every antenna element is facing towards the center of the array. A diagram of this model is illustrated in Figure 1.  $T$  point scatterers are assumed to be located inside the area delimited by the array. For the following discussion the center of the antenna array will be considered the origin of the coordinate system. A polar coordinate system will be used in order to simplify the calculations. Then, the location of the  $p$ th scatter will be  $(r_p, \phi_p)$  where  $r = \sqrt{x_p^2 + y_p^2}$  and  $\phi = \tan^{-1}\left(\frac{y_p}{x_p}\right)$ . In this case the distance between the  $n$ th antenna and the  $p$ th scatter is given by  $R' = \sqrt{Z^2 + r_p^2 - 2 \cdot Z \cdot r_p \cos(\phi_p - \theta_n)}$ , where  $(Z, \theta_n)$  are the polar coordinates of the  $n$ th antenna.

A signal  $f(t)$  is irradiated from each array element and the received signal by the  $n$ th antenna can be expressed as:

$$s(t, \theta_n) = \sum_{j=1}^T \sigma_j f \left( t - \frac{2\sqrt{Z^2 + r_j^2 - 2 \cdot Z \cdot r_j \cos(\phi_j - \theta_n)}}{\nu} \right), \quad (1)$$

where  $s(t, \theta_n)$  are the collected responses from the scatterers at the  $n$ th scan location,  $\nu$  is the propagation speed on the medium and  $\sigma_j$  is the reflectivity of the  $j$ th scatter. A diagram of the scan geometry can be seen in Figure 1.

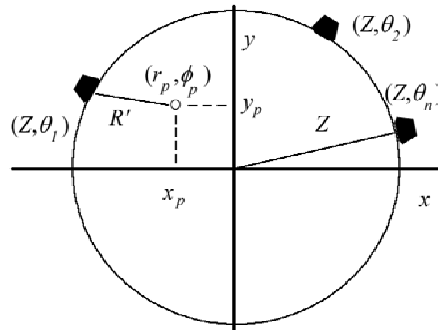


Figure 1: Geometry of the scan trajectory.

## 3. METHODOLOGY

First consider the response from the  $p$ th scatter:

$$s_p(t, \theta_n) = \sigma_p \cdot f \left( t - \frac{2\sqrt{Z^2 + r_{pj}^2 - 2 \cdot Z \cdot r_p \cos(\phi_p - \theta_n)}}{\nu} \right). \quad (2)$$

The frequency counterpart of this signal can be obtained by calculating its Fourier transform, which yields the following expression:

$$s_p(\omega, \theta_n) = \sigma_p F(\omega) \cdot e^{-j(2k\sqrt{Z^2 + r_p^2 - 2 \cdot Z \cdot r_p \cos(\phi_p - \theta_n)})}, \quad (3)$$

where  $k = \frac{\omega}{\nu}$  is often called the wavenumber. As the responses from the  $p$ th scatter are collected by different antennas, a Phase Modulated (PM) signal can be observed. The spectrum of such signal can be obtained by taking the Fourier transform of (4) in the  $\theta$  direction resulting in the following

expression:

$$s_p(\omega, \varepsilon) = \int_0^{2\pi} \sigma_p F(\omega) \cdot e^{-j(2k\sqrt{Z^2+r_p^2-2\cdot Z\cdot r_p \cos(\phi_p-\theta_n)}+\varepsilon\theta)} d\theta, \quad (4)$$

where  $\varepsilon$  is the frequency counterpart of  $\theta$ .

As it can be seen in the previous equation, for large  $k$  values — such as is required by UWB systems — the result of the integral rapidly approaches to 0 [5]. However it is possible to obtain an asymptotic function that describes how fast the angle function approaches zero for large  $k$  values. For this purpose the stationary phase method is used [20]. This method uses the behavior of the rate of change of the frequency, also known as Instantaneous Frequency (IF), of the angle function to determine the asymptotic behavior of the desired function. Using this method, the asymptotic behavior of (4) is given by:

$$s_p(\omega, \varepsilon) = \sigma_p F(\omega, \varepsilon) \cdot e^{-i(\sqrt{4k^2r_p^2-\varepsilon^2}+\sqrt{4k^2Z^2-\varepsilon^2}+\sin^{-1}(\frac{\varepsilon}{2kZ})+\sin^{-1}(\frac{\varepsilon}{2kr_p})+\pi-\varepsilon\phi_p)}, \quad (5)$$

where again  $\varepsilon$  is the frequency counterpart of  $\theta$ .

Note that the  $\pi$  term in the phase of (9) results in the scatter appearing at a location  $180^\circ$  degrees from its original position. The observed position is also farther from the origin than it was supposed to be and these artifacts are related to the term  $\sqrt{4k^2Z^2-\varepsilon^2}$  present in the complex exponential. In order to perform compensation, the double Fourier transform of the scan is obtained and multiplied by the kernel  $e^{-i(\sqrt{4k^2Z^2-\varepsilon^2}+\pi)}$ . Then, the inverse Fourier transform of the compensated data is calculated in the  $\varepsilon$  direction. At this point the data is mapped into a rectangular system of coordinates using the following criteria:

$$(k_x, k_y) = (k \cdot \cos(\theta_n), k \cdot \sin(\theta_n)), \quad (6)$$

where  $n$  goes from 1 to  $N$ , and  $N$  is the total number of locations where the scattered signals were received. If this mapping produces an unevenly sampled space, an interpolation process is performed in order to use the discrete Fourier transform via the Fast Fourier transform. Finally, in order to reconstruct the processed data to its original representation, the 2D inverse Fourier transform is applied to the focused data set.

#### 4. RESULTS

In order to assess the capabilities of the proposed reconstruction technique, a phantom similar to the one used in [6] was employed. This phantom consisted of a PVC pipe filled with air. The PVC pipe has a diameter of 10 cm and its height is 50 cm. PVC and air permittivity values have a similar contrast (see Table 1) to the one exhibited by skin and breast tissue (3:1). Since the signal attenuation in breast tissue is greater than in air, a smaller contrast between air and the simulated cancer tissue is required to recreate this signal loss. For this purpose, wood dowels are used to simulate the malignant tissue. The dowels have a 1.2 cm diameter. The phantom materials present almost no variation in their dielectric permittivity values in the 1–12 GHz frequency range. As it can be seen in Table 1, the contrast between air and wood is 1.7:1. The data acquisition process was performed by rotating the phantom at  $5^\circ$  intervals for a total of 72 positions. At each position, the phantom was irradiated and the collected reflections were recorded. In order to allow

Table 1: Permittivity values of the materials used in the phantoms.

Material	Permittivity Value (6 GHz)
PVC	3
Air	1
Wood	1.55
Cancer tissue	48–52
Breast tissue	9.2
Skin	30

a beamwidth coverage in all the scan positions and reduce undesirable interferences of antenna early time artifacts, the distance between the antenna and the center of the phantom is 70 cm. A zero padding factor of 3 was used to improve the visualization of the reconstructed images. In the following discussion, the center of the phantom will be denoted as the origin.

An experimental setup with two dowels and its reconstructed image are shown in Figures 2(a) and (b) respectively. The reflection of the dowels located at (2, 0) cm and (-2, 0) cm from the origin are however obscured by the surface reflections. Due to the simplicity of the phantom, the reflections of the PVC wall are quasiuniform. The surface reflections were removed using the technique described by the authors in [7]. The red circle denotes the location of the removed PVC reflections. A second experimental setup and its reconstructed image are shown in Figures 3(a) and (b) respectively. In this case, the skin reflection has been already removed from the reconstructed image. The separation between the dowel centers is 2.8 cm. Note that there is no overlapping between the target signatures. Finally, in order to quantitatively assess the performance of the proposed method, the relative strength of the noise present in the image compared to the target signatures magnitude and the focal quality of the reconstructed images were measured. The metrics used for this purpose were the signal to clutter ratio (S/C) and the conditional entropy. The results of this quantitative performance evaluation for each experiment are summarized in Table 2.

Table 2: S/C ratio and conditional entropy values of the reconstructed data for each experiment.

Experiment	S/C Ratio (dB)	Cond. Entropy (bits)
1	10.65	3.4594
2	9.14	3.1699

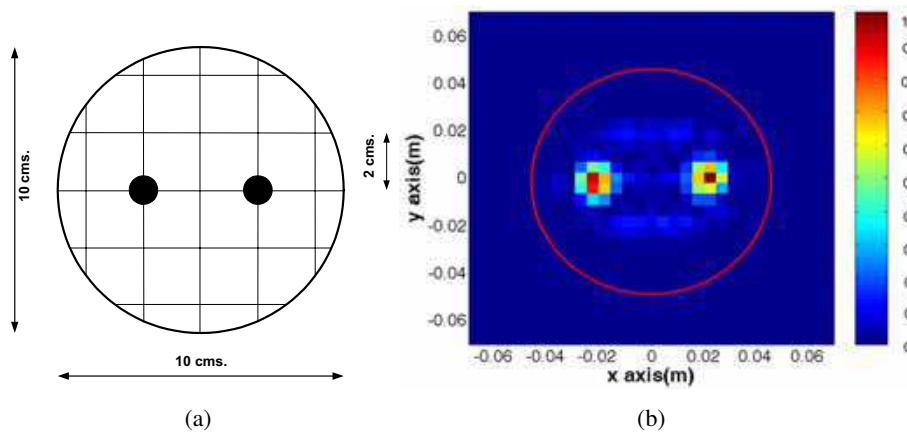


Figure 2: Experiment 1, (a) Experimental setup, (b) Reconstructed image.

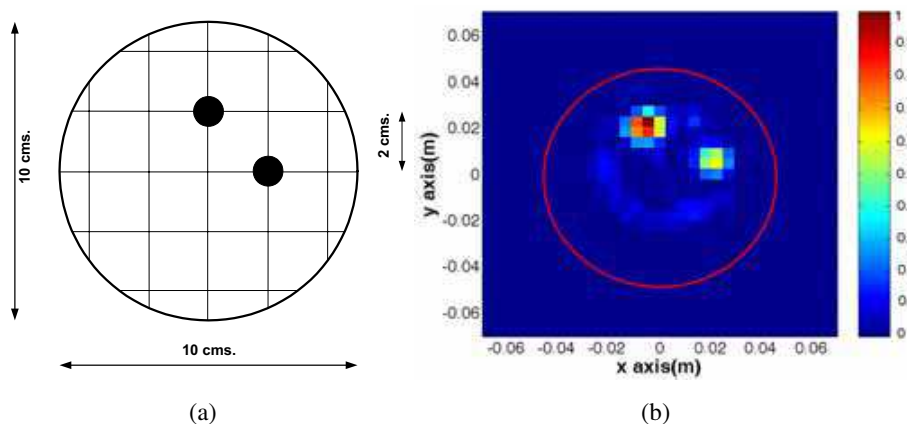


Figure 3: Experiment 2, (a) Experimental setup, (b) Reconstructed image.

## 5. CONCLUSIONS

In this paper, the experimental feasibility of the wavefront reconstruction method for subsurface radar imaging proposed by the authors in [4] was assessed using data sets collected from synthetic phantoms. Although simple in their construction, the phantoms materials exhibit a similar contrast to the one present between breast and cancer tissue. The proposed algorithms yielded accurate results when applied to experimental data.

## ACKNOWLEDGMENT

This work was funded by CancerCare Manitoba and the Natural Sciences and Engineering Research Council of Canada.

## REFERENCES

1. Daniels, D., *Ground Penetrating Radar*, IEE Press, London, UK, 2004.
2. Fear, E. C. and M. A. Stuchly, "Microwave detection of breast cancer," *IEEE Transactions on Microwave Theory and Techniques*, Vol. 48, 1854–1863, Nov. 2000.
3. Kaestner, A. P. and L. B. Baath, "Microwave polarimetry tomography of wood," *IEEE Sensors Journal*, Vol. 5, 209–215, April 2005.
4. Flores-Tapia, D. and G. Thomas, "Breast microwave imaging and focusing based on range migration techniques," *16th Int. Zurich Symposium on Electromagnetic Compatibility, Topical Meeting on Biomedical EMC*, Vol. 1, 75–80, Zurich Switzerland, February 2005.
5. Papoulis, A., *Systems and Transforms with Applications in Optics*, McGraw-Hill, New York, 1968.
6. Fear, E. C., J. Sill, and M. A. Stuchly, "Experimental feasibility study of confocal microwave imaging for breast tumor detection," *IEEE Transactions on Microwave Theory and Techniques*, Vol. 51, 887–892, March 2003.
7. Flores-Tapia, D., G. Thomas, and S. Pistorius, "Skin surface removal on breast microwave imagery," *Proc. SPIE Symposium on Medical Imaging*, February 2006.

# FDTD Analysis in Hyperthermia and Dosimetry for Biomedical Applications

S. Bri<sup>1,2</sup>, A. Saadi<sup>1,2</sup>, A. Nakheli<sup>1</sup>, M. Habibi<sup>2</sup>, L. Zenkour<sup>1</sup>  
L. Bellarbi<sup>1</sup>, and A. Mamouni<sup>3</sup>

<sup>1</sup>Equipe Matériaux et Hyperfréquences, ESTM, B. P. 3103, Route d'agouray, Meknès, Maroc

<sup>2</sup>Laboratoire des Systèmes des Télécommunications et d'Ingénierie de la Décision (LASTID)  
Faculté des Sciences, Département de physique, Université Ibn Tofaïl, Kénitra, Maroc

<sup>3</sup>Groupe CSAM, Institut d'Electronique, de Microélectronique et de Nanotechnologie  
UMR CNRS 8520 IEMN-DHS, Avenue Poincaré, Cité scientifique  
B. P. 60069 59652, Villeneuve d'Ascq Cedex, France

**Abstract**— In this paper, we present the biological effects of the radio-frequency field, and the interaction mode between RF and the tissue. The simulation of this interaction permitted to analysis the absorption of RF energy in the biological tissue. After we describe a technique to heat different sizes of tumors and instantaneous follow up of the thermal diffusion, by microwave applicators realized from coaxial monopole surrounded by an absorbing and thermal conductor dielectric material (ATCDM). The Finite Difference Time Domain method “FDTD” with Perfectly Matched Layers for absorbing boundary conditions is used to model the head, the cell phone, microwave applicator and the “ATCDM” material.

## 1. INTRODUCTION

When electromagnetic waves hit a biological tissue, an interaction takes place. Indeed, the matter becomes like an homogeneous dielectric weakly conductor, then the wave is absorbed, refracted and diffracted. The physical modification of matter after interaction can have a biological effect. Thus, the microwave heating of tissue, constituted in great part of water, causes a damage of the tissue if the temperature elevation is too intense or prolonged. The interaction depends on the dielectric matter properties (conductivity and permittivity) and the rate between the wave-length and tissue dimensions. We distinguish two applications in electromagnetic interaction:

- The dosimetry which is the quantification of the fields and powers in tissue. The theoretical studies and experimental (phantom measure) permit to quantify this interaction in term of electric and magnetic fields. Now, it's very difficult to make a no destructive measure of electromagnetic fields in biological tissue at radio-frequencies, the computer simulation is often required [1–5]. The cellular telecommunication technology advanced quickly, and their users are worry of electromagnetic fields harmful effects emanating from these devices. During these last years, the media are interested to sensitize public at RF field exhibition what dragged more scientific research on the subject. The cellular telephones radiated a power of 0.6 watts (watts), the present works is interested to study the biological effect of this radiated power and the limit in time of cellular telephones uses [4, 5].

- Hyperthermia is a promising technique of microwave heating of the died cells in the biologic tissue, the success of microwave hyperthermia treatment is depending on temperature control [6]. In the literature, the temperature measure is given by a radiometer, who measured only average value in the considered volume [7]. The technique that we propose eliminate the radiometric sensor and it be able to built preciously and an instantaneous thermal profile in the complex tissues who their thermal characteristics are strongly depending on the temperature gradients [8]. Another advantage of this technique, which no mutual electromagnetic influence between applicators and it produces therapeutic heating by microwave hyperthermia of big tumors having different sizes and complex shapes [9].

## 2. THEORY OF FDTD METHOD

### 2.1. Equations Development

The Maxwell's equations described in a tissue having complex permittivity and developed with the Finite Difference method and the distribution of the fields in the YEE cell [10]:

$$\frac{\tilde{D}_x^{n+1/2}(i, j, k) - \tilde{D}_x^{n-1/2}(i, j, k)}{\Delta t} = \frac{1}{\sqrt{\varepsilon_0 \mu_0}} \left( \frac{H_z^n(i, j + 1/2, k) - H_z^n(i, j - 1/2, k)}{\Delta y} - \frac{H_y^n(i, j, k + 1/2) - H_y^n(i, j, k - 1/2)}{\Delta z} \right) \quad (1)$$

We put  $\Delta x = \Delta y = \Delta z$ , then:

$$\tilde{D}_x^{n+1/2}(i, j, k) = \tilde{D}_x^{n-1/2}(i, j, k) + \frac{\Delta t}{\sqrt{\varepsilon_0 \mu_0}} \left( \frac{H_z^n(i, j + 1/2, k) - H_z^n(i, j - 1/2, k)}{\Delta x} - \frac{H_y^n(i, j, k + 1/2) - H_y^n(i, j, k - 1/2)}{\Delta x} \right) \quad (2)$$

And with:  $\Delta t = \frac{\Delta x}{2C_0}$  (will be shown at stability criterion), one has  $\frac{\Delta t}{\Delta x \sqrt{\varepsilon_0 \mu_0}} = \frac{1}{2}$ .

For the calculation of the magnetic field, one takes the second Maxwell equation, and then one clarifies it with a centred differences development.

$$H_x^n(i, j, k) = H_x^n(i, j, k) - \frac{\Delta t}{\Delta x \sqrt{\varepsilon_0 \mu_0}} (E_z^n(i, j + 1, k) - E_z^n(i, j, k) - E_y^n(i, j, k + 1) + E_y^n(i, j, k)) \quad (3)$$

### 2.2. Stability Criterion

The maximum allowable time step must be limited so that the wave does not propagate through more than one cell at a time for the simulation to be stable. This condition lays down the stability to be  $\Delta t_{\max} = \min(\Delta x, \Delta y \Delta z)/c$ . However the maximum allowable cell size is  $\Delta x/c\sqrt{3}$ . For non cubical cells the maximum time step is given by the Courant condition to be  $\Delta t \leq \frac{1}{c\sqrt{(1/\Delta x)^2 + (1/\Delta y)^2 + (1/\Delta z)^2}}$ .

The wave that propagate in the computation region has a variable phase velocity, that is not its physical phase velocity, depending on the wavelength, direction of propagation and grid discretization. This phase velocity, like the physical phase velocity, causes the broadening of pulse, and, in addition, causes spurious anisotropy and pseudo refraction, and is referred to as numerical dispersion. In applying the diagram of the Finite difference to the wave equation, one gets the numeric dispersion equation:

$$\frac{\sin^2(\omega \frac{\Delta t^2}{2})}{c^2 \Delta t^2} = \frac{\sin^2(k_x \frac{\Delta x^2}{2})}{\Delta x^2} + \frac{\sin^2(k_y \frac{\Delta y^2}{2})}{\Delta y^2} + \frac{\sin^2(k_z \frac{\Delta z^2}{2})}{\Delta z^2} \quad (4)$$

While increasing the frequency, the group velocity becomes smaller, what products a distortion of the signal. The most visible consequence of numerical dispersion is that the propagating wave has a phase velocity smaller than the speed of light. This effect is minimal for oblique propagating and maximal for a wave propagating along the  $x$ ,  $y$  or  $z$  axes. Moreover, numerical dispersion sets the minimum allowable wavelength that propagates in the computation region; wavelengths below this minimum do not propagate at all. In other word, the FDTD grid acts as a low-pass filter with cut-off frequency around  $f_{\max} = \frac{c}{2 \cdot \min(\Delta x, \Delta y, \Delta z)}$ .

In practice, however, the effects of this low-pass filtering are left already around to  $\lambda_{\min} = 10 \min(\Delta x, \Delta y, \Delta z)$ .  $\lambda_{\min}$  is the smallest reliable propagating wavelength in the FDTD computation region. The effects of numerical dispersion can be reduced by choosing a small cell size with respect to the size of the simulated structure at the cost of a large computation domain, and, so also, huge computation times.

### 2.3. Perfectly Matched Layer for the Absorption of Electromagnetic Waves

The perfectly matched layers serve for the numeric calculations like numeric absorption walls and permit to delimit the used matrixes dimensions. To really illustrate the effect of the PML layers,

one considers the electromagnetic energy propagation, for example according to the  $OX$  axis, the role of the PML layers is to absorb this energy with no reflection. The energy propagated in the considered domain continuous its propagation in the layers of the PML with no reflection, only if the intrinsic impedance of the studied media and the one of the PML layers is equal. These impedances must be equal to 1. Now, we apply the two criteria's of Berenger [11] to introduce the PML layers in the resolution of the equations propagation in the heterogeneous media. All these equations possess the same writing, in order to simplify the development; we clarify the component only according to  $OX$  direction.  $T$  represents the final simulation time. One puts  $x_n = \frac{\sigma \Delta t}{2\varepsilon_0}$  what gives  $x_n(x) = \frac{\sigma_x(x)\Delta t}{2\varepsilon_0}$ ,  $x_n(y) = \frac{\sigma_y(y)\Delta t}{2\varepsilon_0}$  and  $x_n(z) = \frac{\sigma_x(z)\Delta t}{2\varepsilon_0}$ . The conductivities are determined by Gedney [12, 13], and have for profiles,  $\sigma(z) = \sigma_{\max} \frac{|z-z_0|^m}{length\_pml^m}$ .  $z$  represents the depth of the layer, and  $length\_pml$  represents the number of the layers.  $m$  is a coefficient whose optimal value is situated between 3 and 4. The values of the  $x_n$  are chosen to attenuate the numeric reflection:  $x_n(i) = 0.333(\frac{i}{length\_pml})^3$ . With  $i = 1, 2, 3 \dots length\_pml$ ,  $i$  represents the order of the absorbing layer. It shows that if the layer is far of the studied domain the value of  $x_n$  increases, and on the contrary it decreases when the layer is adjacent to the borders of the domain to study. The coefficient 0.333 is forced the stability of the algorithm, it is found empirically. For a program implantation, one explains the PML with  $X$  direction for example; in the considered media the effect of the electric conductivity must be absent in the three directions, and it will be functional that on the absorbents layers. The adjacent layers to the considered media are:

- Layers of order  $length\_pml$ .
- Layers of order  $IE-length\_pml$ .

Therefore the new writing of  $x_{nx}(i)$  is:  $x_{nx}(i) = 0.333(\frac{length\_pml-i+1}{length\_pml})^3$ .

In considered media  $x_{nx}$ ,  $x_{ny}$  and  $x_{nz}$  are zero. The PML are very efficient absorbing conditions and that, to any incidence angle, what permits to bring closer the absorbing layers to the beaming systems. The borders conditions are then susceptible to be in the field near to the modelled antenna what implies that the PML are optimized to absorb the evanescent components of the field. Indeed, the layers discrediting must be thin enough to take in account the terms some  $1/r^3$  or even  $1/r^5$  of field, the profile of  $\sigma$  must be adapted and finally the thickness of the PML layers must be sufficient to absorb these evanescent waves.

### 3. APPLICATION OF FDTD METHOD TO DOSIMETRY

#### 3.1. Dosimetry

The quantification of absorbed power in biological tissue is determined by the specific absorption rate (SAR). The evaluation of people exhibition level can be making the direct evaluation of the SAR in tissue, or indirectly by the evaluation of field's emaning from basis station. The first approach is the respect of basis restrictions that represents the protective levels. The second approach is based on maximal power absorption; it's bound to the reference levels which guarantee that basis restrictions will never be passed. The approach based on the SAR is recommended when the person is near the antenna. This case represents the human head near cell phone. All groups research work on the field evolution in order to determine the SAR:

$$SAR = \frac{d}{dt} \left( \frac{dw}{dm} \right) = \frac{\sigma |E|^2}{2\rho} \quad (5)$$

where  $w$  represents the energy in joules,  $m$  the mass in Kg,  $t$  the time in s,  $E$  the electric field in V/m,  $\sigma$  the conductivity in S/m and  $\rho$  is the volume density in Kg/m<sup>3</sup>. The reference levels of the SAR are done by ICNIRP and after by CENELEC [14, 15], and are 2 w/Kg for 10 g of cube tissue. The SAR measure within the electric field or the temperature requires the use of a probe. The heterogeneity of tissues and the interstitial probe make difficult the measurement inside. The medical imagery and the electromagnetic numerical methods permit the evaluation of the electric and magnetic fields in tissue. But the computer simulation of cellular phone is very complex.

#### 3.2. Numerical Approach

The numerical model of head is a fundamental element of the simulation. It must be representative of a user's head and must permit an analysis of the absorber power in the different tissues. Often, the numerical model are based on the IRM, one finds ten different tissues such as: (skin, bone, muscle,

cephalo-rachidien liquid, gray matter, white matter, ...). The electromagnetic characteristics of these tissues are those determined by scientific community. This model permitted the evaluation of energy distribution in the main tissues. The cell phone is simulated as a rectangular box with  $\epsilon_r = 2.2$  and the conductivity  $\sigma = 0$ , the inner volume of box is simulated as a metal. The cell phone operated at European GSM (operating at 900 MHz) and radiated two watts, the SAR simulation is 1.1 w/Kg. The dosimetry analysis shows that about 50% of power is absorbed by the head, it's distributed as: 15% absorbed by skin; 10% absorbed by muscle, the cephalo-rachidien liquid 5% and the brain 13%. With this model, the most absorption is localized near the ear: 30% of the energy are absorbed in a volume of  $(5 \times 5 \times 5) \text{ cm}^3$ ; centred on the internal ear. In this reduces volume, skin absorbed an important part about 70%. At the frequency of 1800 MHz, the proportion of the power absorbed by the peripheral tissues is increased. The zone near to the internal ear absorbed the most part of the energy radiated by the cell phone. The experimental approach is necessary to complete the numerical analysis. However, this approach meted the difficulties of the measure inside and the strong heterogeneity of the tissues limited this approach. It's therefore necessary to define a model of homogeneous experimental head. The definition of form and content of phantom are fundamental. The phantom shape must represent the population and its content must have the electromagnetic characteristics that guaranteed the measured SAR in ten grammes is lower than real values [16]. With the international phantom, one gets the following measures:

Table 1: Powers absorbed by the different tissue.

Tissues	Skin	Muscle	Skull	Eyes	LCR	Brain
Power absorbed (mW)	9.3	6.8	2.5	0.009	2.2	8.7

In conclusion, the part of the power absorbed in the head is about 50% of the radiated power (100 mw for GSM 900 MHz). For the head of 3 Kg, the calculate SAR is about 30 mW/Kg. However, the absorbed power decreases exponentially according to the depth, then the local SAR is more important than this calculated in a small volume, for 10 g, it's about 0.4 to 1 w/Kg. The experimental bench of measure is constituted of an absorbing room, where one puts a phantom filled of liquid whose dielectric characteristics are brain characteristics. The cell phone radiated the maximal power is placed at the ear level. In order to measure the electric field into the phantom, a robot piloted by a computer, permits the probe displacement in the liquid and the acquirement of the three electric field component ( $E_x, E_y, E_z$ ). The acquirement process is based on the "NARDA" system [17].

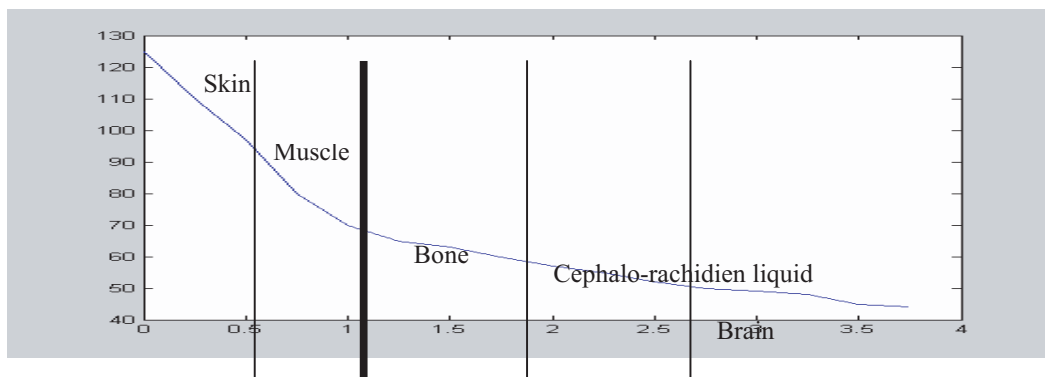


Figure 1: Value of the electric field on the same axis and with the same type of antenna (case of  $\lambda/4$  antenna).

### 3.3. Experimental Results

One presents the first model where the telephone is represented by rectangular box surmounted by a quarter wave antenna. The head model is simplified at concentric spheres. The discretization is constituted by a cube cell of 2.5 mm. All volume possesses 1.16 million of cells. The FDTD simulation shows that electric field decreases quickly (Fig. 1). The tissue conductivity dragged

losses and eliminated all resonance. In conclusion, it seems that some cells of some simple organisms (or modified) can discern the RF, even if their weak level, like a stress.

#### 4. HYPERTHERMIA

##### 4.1. Heating Theory

Every applicator deposits a uniform heat quantity, having a cylindrical shape [6]. This applicator is constituted of a monopole; the inner conductor is surrounded by an absorbing and thermal conductor dielectric material (ATCDM). The position of different applicator permits to generate a deposit of heat quantity that adheres preciously the complex shape of considered tumor, in order to leave normal surrounding tissues at lower temperature.

##### 4.2. Absorbing Thermal Conductor Dielectric Material Model (ATCDM)

The ATCDM is suitable to stock the electromagnetic energy radiated by the inner conductor of coaxial antenna as calorific energy, then to transmit this energy to tissues. In electromagnetic characterisation, the ATCDM possesses two planes: the plane I represents the transition between the inner conductor and the absorbing environment. The plane II represents the reflective plane of the electromagnetic waves.

##### 4.3. Thermal Diffusion

The heat quantity deposited as cylindrical shape can propagate itself in the complex tissue following the bioheat Equation [9]:

$$\rho c \frac{\partial T}{\partial t} = \kappa \nabla^2 T - \rho \rho_b c_b F (T - T_a) + \rho \cdot \text{SAR} \quad (6)$$

$T$  is the temperature ( $^{\circ}\text{C}$ ),  $t$  is the time (s),  $\rho$  is the density of tissue ( $\text{kg}/\text{m}^3$ ),  $c$  is the specific heat ( $\text{J}/\text{kg}\cdot\text{K}$ ),  $\kappa$  is the thermal conductivity ( $\text{W}/\text{mK}$ ),  $\rho_b$  is the blood density ( $\text{kg}/\text{m}^3$ ),  $c_b$  is the blood specific heat ( $\text{J}/\text{kg}\cdot\text{K}$ ),  $F$  is blood flow rate ( $\text{m}^3/\text{kg}\cdot\text{s}$ ),  $T_a$  is the tissue temperature, and SAR is the specific absorption rate ( $\text{w}/\text{kg}$ ). Where  $\sigma_{mc}$  is the complex tissue conductivity,  $E$  is an electric field value ( $\text{v}/\text{m}$ ). The considered medium is a complex tissue where the blood flow rate and the specific heat depend on thermal gradient [8]. Therefore the resolution of the equation must hold account the change of the  $F$  coefficients and  $c_b$  according to the temperature, in order to permit an instantaneous follow-up of the temperature diffusion with an exact reconstruction of the thermal card.

##### 4.4. Control of the Heating Volume

The number of applicators and their positions depend on the tumor shape. They are placed into tumor and they deposited a cylindrical shape of calorific energy [6, 12]. It's possible to mean away one direction of heating by increasing the input power at the considered applicator, and to cut it at the one applicator permits to limit the thermal diffusion in the considered sense. Then, both these two combinations: the applicators positions and the cut or the increase of their input power, we can heat all tumors shape that prove to be complex before and the old techniques tried to assimilate

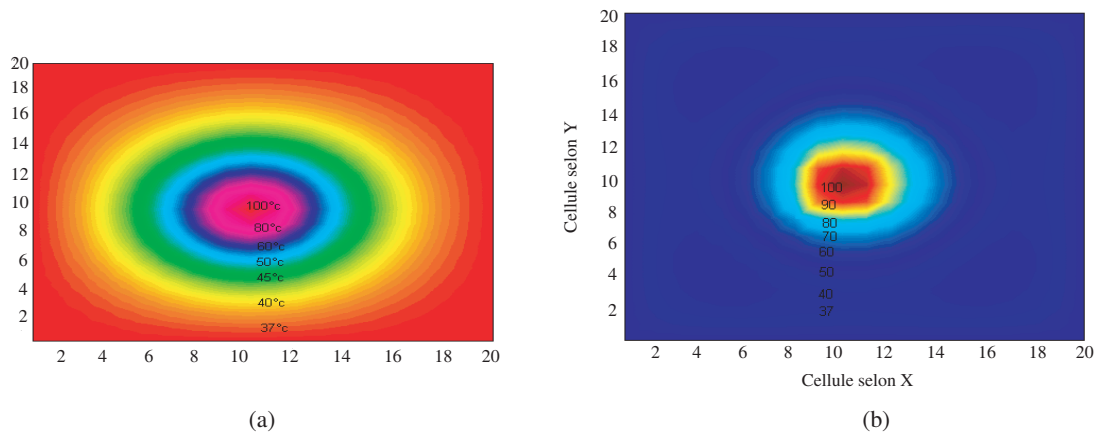


Figure 2: Thermal diffusion after 10 minutes of heating. (a) Plan  $Z = 4$  mm, (b) Plan  $Z = 7$  mm.

it to a known shape as spherical. The proposed technique is very useful if the tumor is finding in high sensitivity zones because to heat after tumor border, causes enormous damages. A primordial advantage of this technique is the reconstruction in real time of the thermal card. The considered tissue has a blood flow rate  $F$  (in  $\text{m}^3/\text{kg}\cdot\text{s}$ ) and the heat specific of blood  $c_b$  (in  $\text{J}/\text{kg}\cdot\text{K}$ ) depend on the thermal gradient [8]. Therefore the bio heat equation becomes an equation with no constant coefficients, and its resolution permits an instantaneous follow-up of the temperature diffusion with an exact reconstruction of the thermal card.

#### 4.5. Results

The used FDTD method for determining the characteristics of ATCDM and the specific absorption rate (SAR). The complex tissue considered has a strong blood circulation. The constant dielectric  $\epsilon_{mcr} = 43.03$  and conductivity  $\sigma = 1.69$  (s/m). The volume is discretized as  $(30 \times 30 \times 30) \text{ mm}^3$ . The Fig. 2 present the reconstruction in real time of the thermal card in the plane ( $Z = 4 \text{ mm}$  and  $Z = 10 \text{ mm}$ ) after 10 minutes of heating.

### 5. CONCLUSION

This paper has presented the FDTD simulation technique. The FDTD implementation has been made adequately flexible to accommodate modelling of a wide variety of antenna and tissue topologies. In this work, we have evaluated the SAR distribution in the head of a human exposed to the electromagnetic field emitted from a hand held cellular phone in a partially closed environment. Particular attention has been devoted to an accurate simulation of the SAR. The results show a sensible dependence of the SAR distribution and of the peak SAR on the type of telephone considered, on the distance between the head and the telephone, and on the type of environment in which the exposure takes place. The SAR peak values, evaluated over any 1g of tissue and for phones radiating 600 mW of power in free space condition, were nearly always below the ANSI limit of 1.6 W/kg, with the exception of the whip phone when used in the proximity of perfectly conducting vertical surfaces or used with the antenna collapsed and in strict contact with the ear. We have pointed out our attention to some selected organs such as the brain, the eyes, the pineal and the parotid glands. The computed SARI values in these critical organs were well below the presently considered safety limit, but their knowledge could be useful, for example, to correlate epidemiological studies to the real conditions of exposure. Among the very numerous studies that have been achieved during these last years on the biological effects of cell phone signals, only some of them revealed biological effects with no serious healthy consequence in our present knowledge. For tumors, the cell phone signals don't provoke the cancer and probably don't accelerate the development of tumors already existing. The research is currently very active, especially in Europe, and in about two years, numerous studies will deliver their results. The international organism such as (WHO, CIRC, ICNIRP, COST 281, etc. . .) takes advantage of these research in order to analysis undesirable effects and protect the users. And we have presented a theoretical study permitting to use a microwave hyperthermia while following a very definite tumor shape. The proposed technique permitted an instantaneous follow-up of thermal diffusion during a microwave hyperthermia treatment, applied to tissue having a very important blood circulation.

Since the biological hazards are mainly due to a temperature rise in tissue for RF exposure, the effect of localized SAR for portable telephones should also be related to the temperature rise in the head. From this point-of-view, the temperature rise in the human head for portable telephones has been computed with an anatomically based human-head model. The SAR in the human head has been determined using the FDTD method, and a bioheat equation has been numerically solved also using the FDTD method. With antenna output powers of 0.6 W at 900 MHz and 0.27 W at 1.5 GHz, respectively, the maximum temperature rises in the head are found to be 0.18 C at 900 MHz and 0.15 C at 1.5 GHz, and the maximum temperature rises in the brain are found to be 0.09 C at 900 MHz and 0.07 C at 1.5 GHz. These results exclude the possibility of thermally induced brain-tissue damage from portable telephones. Further works are required for experimental evaluation.

### REFERENCES

1. Bri, S., A. Mamouni, L. Zenkouar, L. Bellarbi, M. Habibi, and M. ELkadiri, "Control of the temperature-depth profile in biological tissues: medical applications," *International A. Physical Journal*, Vol. 42, No. 2, 29–35, Belgium, 2001.
2. Bri, S., L. Zenkouar, and A. Mamouni, "Experimental microwave radiometry prototype for medical applications," *Proc. Symposium ANTEM'2002, IEEE*, 351–353, Canada, July 31–August 2, 2002.

3. Bri, S., L. Zenkouar, A. Saadi, L. Bellarbi, M. Habibi, and A. Mamouni, "Measure of the temperature-depth profile by an S band radiometric receiver for biomedical applications," *International Journal Annals Telecoms*, Vol. 59, No. 3-4, 467-484, France, Mars-Avril, 2004.
4. Lafkih, A., L. Zenkouar, S. Bri, and A. Kherras, "Conception VHDL du codeur détecteur d'erreurs CRC du GSM pour une réalisation en FPGA," *Proc. Colloque International et Exposition TELECOM & JFMMA '2001*, 46-50, Casa, Maroc, October 17-19, 2001.
5. Bri, S. and L. Zenkouar, "Biological effects of the radiofrequencies," *Proc. International AN-TEM'2004/URSI*, Canada, 2004.
6. Saadi, A., S. Bri, M. Habibi, M. Achour, L. Bellarbi, and A. Mamouni, "Approche de la reconstruction de la carte thermique en temps réel dans une application d'hyperthermie micro-onde," *JFMM*, Marrakech, October 2003.
7. Dubois, L., J. P. Sozanski, V. Tessier, J. C. Camart, J. J. Fabre, J. Pribetich, and M. Chivé, "Temperature control and thermal dosimetry by microwave radiometry in hyperthermia," *IEEE Trans. Microwave Theor. Tech.*, Vol. 44, 1755-1761, 1996.
8. Salcman, M., E. Moriyana, H. J. Elsner, H. Rossman, R. A. Gettleman, G. Neuberth, and G. Corradino, "Cerebral blood flow and the thermal properties of the brain: A preliminary analysis," *Journal of Neurosurg*, 592-597, April 1989.
9. Saito, K., Y. Hayashi, H. Yoshimura, and K. Ito, "Heating characteristics of array applicator composed of two coaxial-slot antennas for microwave coagulation therapy," *IEEE Trans. on MTT.*, Vol. 48. No. 11, 1800-1806, November 2000.
10. Yee, K. S., "Numerical solution of initial boundary problems involving Maxwell's equations in isotropic media," *IEEE Trans. on Ant. and Propagation*, Vol. 14, 302-307, May 1966.
11. Berenger, J. P., "A perfectly matched layer for the absorption of electromagnetic waves," *Journal of Computational Physics*, Vol. 114, No. 2, 185-200, October 1994.
12. Sullivan, D. M., "Electromagnetic simulation using the FDTD method," IEEE Press 2000, NY, USA, 2000.
13. Gedney, S. D., "An anisotropic perfectly matched layer absorbing medium for the truncation of FDTD lattices," *IEEE Trans. on Antennas and Propagation*, Vol. 44, No. 12, 1630-1639, December 1996.
14. Bernardi, P., M. Cavagnaro, and S. Pisa, "Evaluation of the SAR distribution in the human head for cellular phones used in a partially closed environment," *IEEE Trans. on Elec. Comp.*, Vol. 38, No. 3, 357-366, August 1996.
15. CENELEC, "Norme de base relative à la mesure du débit d'absorption spécifique relatif à l'exposition des personnes aux champs électromagnétiques émis par les téléphones mobiles (300 MHz à 3 GHz)," ENV 50361, June 2000.
16. Rivera, T., T. Sarrebourg, D. Lafolie, and J. Wiart, "Etudes de la permittivité des tissus équivalents utilisés dans la mesure du SAR pour les radiotéléphones," *Rapport Interne CNET*, NT/Cnet/6497, Août 1999.
17. Person, C., L. N. Ahlonsou, and C. Grangeat, "New test bench for the characterization of SAR measurement probes used in tissue equivalent liquid," *Proc. of the 22nd World Congress of the BEMS*, Munich, June 2000.

# Technical Equipment for Research of Biological Effects of EM Field

Jan Vrba<sup>1</sup>, Paolo Togni<sup>1</sup>, Lukas Visek<sup>1</sup>, Luca Vannucci<sup>2</sup>, and Peter Peschke<sup>3</sup>

<sup>1</sup>Department of EM Field, Czech Technical University in Prague, Prague, Czech Republic

<sup>2</sup>Institute of Microbiology, Czech Academy of Sciences, University of Pisa, Prague, Czech Republic

<sup>3</sup>German Cancer Research Institute, Heidelberg, Germany

**Abstract**— Research of interactions between EM Field and biological systems is of growing interests elsewhere. Also here in Czech Republic there are several groups working in this field, often in international co-operations. We will describe here mainly basic technical equipment developed for 5 different research projects in the discussed area of interactions of EM field and biological systems.

## 1. INTRODUCTION

In present time four research institutions here in the Czech Republic run research projects focused on studies of interactions between EM field and biological systems. These institutions are technically supported by Dept. of EM Field of the Czech Technical University in Prague. In this contribution we would like to give more details about that projects and obtained technical results (i.e., description of developed exposition systems).

Three of discussed projects (1 in Germany and 2 here in Czech Republic) are basic research for simulation of the microwave hyperthermia treatment. Other two projects (both in Czech Republic) are focused on simulation of the case of exposition by mobile phone.

In the modern view, cancer is intended as a complex illness, involving the cells that undergo to transformation, their environment, and the general responses at biochemical and biological levels induced in the host. Consequently, the anti-cancer treatment protocols need to be multi-modal to reach curative effects. Especially after the technical improvements achieved in the last 15 years by bio-medical engineering, microscopy devices, and molecular biology methods, the combinations of therapeutic procedures are growing in interest in basic and clinical research.



Figure 1: Waveguide applicator for biological experiments.

The combination of applied biological research together to the physical sciences can offer important perspectives in anticancer therapy (e.g., different methodologies and technical devices for application of energies to pathological tissues).

The modern bioengineering knowledge applied to traditional tools, as the microscopy, has largely renewed and expanded the fields of their applications (e.g., *in vivo* imaging), pushing the interest for direct morpho-functional investigations of the biomedical problems.

## 2. WAVEGUIDE APPLICATOR

Very good results of EM field expositions in biological experiments can be obtained by simple but efficient waveguide applicators, see example in Fig. 1.

Waveguide offer a very big advantage — in approximately of fifty percents of its aperture the irradiated electromagnetic field is very near to a plane wave, which is basic assumption for good homogeneity of the heating and optimal treatment penetration.

Here described system is being used (shared) for research projects by two two institutions (Institute of Radiation Oncology in Prague and Institute of Microbiology of the Czech Academy of Sciences).

Aperture of this waveguide is  $4.8 \times 2.4$  cm and it is excited at frequency 2.45 GHz. Effective heating is in the middle of the real aperture — its size is approximately  $2.4 \times 2.4$  cm. Waveguide is filled by teflon to reduce its cut-off frequency. Power from generator is possible to control from 10 to 180 W, in these experiments we work between 10 and 20 W mostly.

### 3. EVALUATION OF WAVEGUIDE APPLICATOR

To evaluate this applicator from technical point of view we made a series of experiments, see e.g., Fig. 2, where you can see example of measurement of temperature distribution by IR camera.

Here you can see temperature distribution obtained on surface of a model of mouse made from agar — with a simulated tumour on mouse back. Experiment has been done by heating phantom during 2 minutes delivering a power of 10 W. Maximum of temperature increase has been found approximately  $10^\circ\text{C}$ . Similar results with different increase in temperature we have got also in other technical experiments on phantom or live mouse when power or heating time was changed.

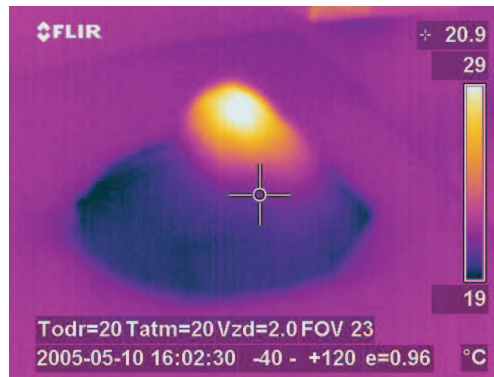


Figure 2: Temperature distribution obtained on surface of a model of mouse.

### 4. ARRAY APPLICATOR

The main goal of the planned biological experiment is a hyperthermia treatment of the experimentally induced pedicle tumours of the rat to verify the feasibility of ultrasound diagnostics and magnetic resonance imaging respectively to map the temperature distribution in the target area of the treatment. That means to heat effective volume of approximately cylindrical shape (diameter approx. 2 cm, height approx. 3 cm). Temperature to be reached is  $41^\circ\text{C}$  or more (i.e., temperature increase of at least  $4^\circ\text{C}$  from starting point  $37^\circ\text{C}$ ), time period of heating is 45 minutes.

Considering the necessary effective heating depth for the planned experiments, we have found 915 MHz to be suitable frequency. As an excellent compatibility of the applicator with non-invasive temperature measurement system (ultrasound or NMR) is a fundamental condition for our project, we should have to use non-magnetic metallic sheets of minimised dimensions to create the conductive elements of the applicator. Therefore the applicator itself (see Figs. 3 and 4) is created by two inductive loops tuned to resonance by capacitive elements [4, 5]. Dimensions of these resonant loops were designed by our software, developed for this purpose. Coupling between coaxial feeder and resonant loops (not shown in Fig. 3) as well as a mutual coupling between resonating loops could be adjusted to optimum by microwave network analyser.

This applicator has been developed for German Cancer Research Institute in Heidelberg. And it is being used there for a series of animal experiments to study effect of hyperthermia on tumours and possibility to combine hyperthermia with chemotherapy etc.

Compatibility of this applicator with a Magnetic resonance unit (MR) has been studied and it has been demonstrated.

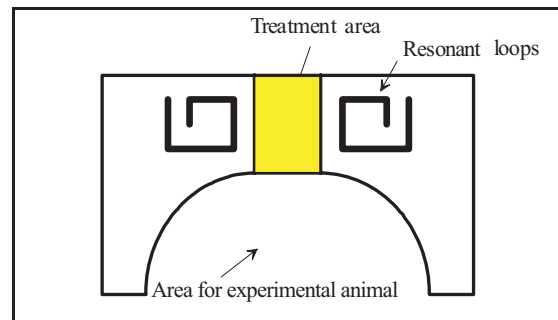


Figure 3: Arrangement of discussed microwave hyperthermia applicator.

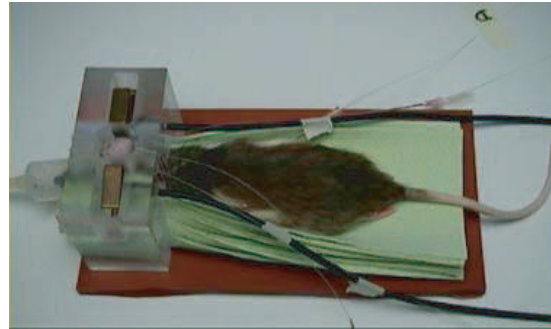


Figure 4: Photograph of the discussed applicator.

#### ACKNOWLEDGMENT

This work was supported by the Czech Academy of Sciences, Institutional Research Concepts No. AV0Z50200510: "Hyperthermia and anticancer immunomodulation, morpho-functional study of micro-environmental interactions in melanoma model".

#### REFERENCES

1. Vrba, J., *Medical Applications of Microwaves*, CTU Press, Prague, In Czech, 2003.
2. Hand, J. and J. R. James (editors), *Physical Techniques in Clinical Hyperthermia*, Wiley, New York, 1986.
3. Franconi, C., J. Vrba, et al., "27 MHz hybrid evanescent-mode applicators," *Int. Journal of Hyperthermia*, Vol. 9, No. 5, 655–674, 1993.
4. Vrba, J., C. Franconi, et al., "Evanescent-mode applicators for hyperthermia," *IEEE Trans. on Biomedical Engineering*, Vol. 40, No. 5, 397–407, May 1993.

# Revisited Implementation of the Spectral Kummer-Poisson's Method for the Efficient Computation of 2-D Periodic Green's Functions in Homogeneous Media

R. R. Boix<sup>1</sup>, A. L. Fructos<sup>1</sup>, F. Mesa<sup>2</sup>, and F. Medina<sup>1</sup>

<sup>1</sup>Department of Electronics and Electromagnetism, College of Physics, University of Seville  
Av. Reina Mercedes, s/n, 41012, Seville, Spain

<sup>2</sup>Department of Applied Physics 1, School of Computer Engineering, University of Seville  
Av. Reina Mercedes, s/n, 41012, Seville, Spain

**Abstract**— This paper presents a new algorithm to accelerate the computation of the series that lead to the determination of the 2-D periodic Green's functions with 1-D and 2-D periodicities in homogeneous media. The algorithm is based on a novel implementation of the spectral Kummer-Poisson's method. In this novel implementation every original series is split into two fast converging series, one with exponential convergence and the other with algebraic convergence of arbitrarily large order. The CPU times required by the new algorithm to obtain the 2-D periodic Green's functions have been compared with those required by Ewald's method, and the new algorithm has been found to be between 2 and 5 times faster than Ewald's method.

## 1. INTRODUCTION

The application of the Method of Moments (MoM) to the solution of periodic electromagnetic problems requires the computation of periodic Green's functions. Thus, the free-space 2-D periodic Green's function with 1-D periodicity (2DPGF-1D) has been used in the determination of the scattering matrix of inductive obstacles in rectangular waveguide [1], and the same 2DPGF-1D has also been used in the analysis of the scattering of plane waves from one-dimensional periodic arrays of lossy strips in free space [2]. In the case of multilayered media, the application of the discrete complex image method makes it possible to express the Green's functions in closed form as linear combinations of spherical and cylindrical waves [3]. According to this, the 3-D periodic Green's functions of multilayered media with 2-D periodicity can be easily obtained in terms of both 3-D periodic Green's functions with 2-D periodicity (3DPGF-2D) in homogeneous media and 2-D periodic Green's functions with 2-D periodicity (2DPGF-2D) in homogeneous media. This approach for the computation of 3-D periodic Green's functions in multilayered media has been followed in [4] as a mean to compute the reflection and transmission properties of frequency selective surfaces embedded in multilayered media. The previous examples show that the development of efficient and accurate algorithms for the computation of the 2DPGF-1D and the 2DPGF-2D in homogeneous media is very useful as an intermediate step for studying the scattering by periodic structures both in homogeneous and multilayered media.

2-D periodic Green's functions in homogeneous media can be written either as spatial infinite series, or as spectral infinite series when Poisson's formula is used [5]. When losses are negligible, both the spatial and the spectral series are slowly converging, and a large number of analytical and numerical methods have been applied to accelerate the convergence of these series. Among the analytical methods, we should mention the spectral Kummer-Poisson's method [6], Veisoglu's transformation method [7], Ewald's method [8] and the lattice sums method [9]. Additional numerical acceleration methods are the Shank's transformation [10], the  $\theta$ -algorithm [11], the Chebyshev-Toeplitz algorithm [12], and the recently developed summation-by-parts algorithm [13]. It should be pointed out that all the mentioned numerical acceleration methods can be directly applied to the spatial and spectral series as well as to the fast converging series resulting from the application of analytical acceleration methods. Linton carries out a comparison among the different acceleration methods that have been used for the computation of 2-D periodic Green's functions in homogeneous media [14], and he concludes that Ewald's method is the best method in most scenarios because of its versatility and good compromise between accuracy and efficiency.

In this paper the authors presents an algorithm for the acceleration of the series involved in the computation of the 2DPGF-1D and the 2DPGF-2D in homogeneous media. The algorithm is based on an original implementation of the spectral Kummer-Poisson's method. In the algorithm any of the series that has to be accelerated is split into two new series containing unknown coefficients.

A judicious choice of these coefficients makes it possible that these two new series converge very fast, one of them with exponential convergence and the other one with algebraic convergence of arbitrarily large order. Whereas other sophisticated algorithms based on Kummer-Poisson's method [15] are heavily dependent on the mathematical expression of the terms of the series that have to be accelerated, the new algorithm presented in this paper is very general and works equally well for 2-D periodic problems with 1-D periodicity and for 2-D periodic problems with 2-D periodicity involving lattices with arbitrarily skewed axes. The CPU times required by the algorithm for the computation of 2-D periodic Green's functions within a predetermined accuracy have been compared with the CPU times required by Ewald's method. The algorithm has been found to be between two and five times faster than Ewald's method in all the cases studied.

## 2. OUTLINE OF THE NUMERICAL PROCEDURES

Figure 1 shows a one-dimensional array of line sources located in a homogeneous medium. If a time dependence of the type  $e^{j\omega t}$  is assumed, the periodic 2-D Green's function with 1-D periodicity (2DPGF-1D) for the array of line sources is given by the spatial series

$$G_{1DP}(\Delta x, \Delta y, k) = \sum_{n=-\infty}^{+\infty} a_n^{1DP}(\Delta x, \Delta y, k) = \frac{1}{4j} \sum_{n=-\infty}^{+\infty} H_0^{(2)}(kR_n) e^{-jk_{x0}nd} \quad (1)$$

where  $k$  is the wavenumber (the wavelength  $\lambda$  is related to  $k$  via  $\lambda = 2\pi/\text{Re}(k)$ ),  $d$  is the period,  $H_0^{(2)}(\cdot)$  is the zeroth-order Hankel function of the second kind [16],  $k_{x0}$  is the phase per period imposed by a plane wave either emitted by the array or incident on the array, and  $R_n$  is defined as

$$R_n = \sqrt{(\Delta x - nd)^2 + \Delta y^2} \quad (2)$$

where  $\Delta x = x - x'$  and  $\Delta y = y - y'$  (see the caption of Fig. 1).

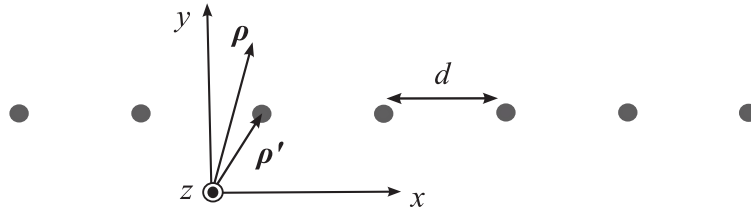


Figure 1: Planar array of line sources with 1-D periodicity along the  $x$  direction in an homogeneous medium.  $\rho' + nd\hat{x} = (x' + nd)\hat{x} + y'\hat{y}$  ( $n = \dots, -1, 0, 1, \dots$ ) is the 2-D vector pointing at the line sources and  $\rho = x\hat{x} + y\hat{y}$  is the 2-D vector for the observation point.

When losses are negligible in the medium of Fig. 1, the  $n$ th term of the series (1) decays like  $|n|^{-1/2}$  as  $|n| \rightarrow \infty$  [5], and therefore, the convergence of (1) is extremely slow. If Poisson's formula is applied to the series of (1), an alternative spectral representation of this series is obtained

$$G_{1DP}(\Delta x, \Delta y, k) = \sum_{n=-\infty}^{+\infty} b_n^{1DP}(\Delta x, \Delta y, k) = \frac{1}{2d} \sum_{n=-\infty}^{+\infty} \frac{e^{-jk_{xn}\Delta x} e^{-\Gamma_n|\Delta y|}}{\Gamma_n} \quad (3)$$

where  $k_{xn} = 2\pi n/d + k_{x0}$  and  $\Gamma_n = \sqrt{k_{xn}^2 - k^2}$ . The  $n$ th term of the series (2) has an exponential decay of the type  $e^{-(2\pi|n||\Delta y|)/d}/|n|$  when  $|\Delta y| \neq 0$ , but has a slow decay of the type  $|n|^{-1}$  when  $|\Delta y| = 0$  [5]. A better alternative to speed up the convergence rate of (1) was reported in [17], where the authors made use of Ewald's method to express the 2DPGF-1D as

$$G_{1DP}(\Delta x, \Delta y) = \frac{1}{4d} \sum_{n=-\infty}^{+\infty} \frac{e^{-jk_{xn}\Delta x}}{\Gamma_n} \left\{ e^{\Gamma_n|\Delta y|} \text{erfc}^+ + e^{-\Gamma_n|\Delta y|} \text{erfc}^- \right\} + \frac{1}{4\pi} \sum_{n=-\infty}^{+\infty} e^{-jk_{x0}nd} \sum_{q=0}^{+\infty} \left( \frac{k}{2E'} \right)^{2q} \frac{1}{q!} E_{q+1} (R_n^2 E'^2) \quad (4)$$

In Eq. (4)  $E_q(\cdot)$  is the  $q$ th-order exponential integral function defined in [16, p228] and

$$\text{erfc}^\pm = \text{erfc} \left( \frac{\Gamma_n}{2E'} \pm |\Delta y|E' \right) \tag{5}$$

where  $\text{erfc}(\cdot)$  stands for the complementary error function [16, p. 297]. The two series of (4) over the integer index  $n$  exhibit extremely fast gaussian convergence [17]. The parameter  $E'$  appearing in (4) is the splitting parameter which must be chosen as shown in [17, Eq. (34)]. The main problem of Eq. (4) is that the  $n$ th term of the second series is another infinite series over the index  $q$  without gaussian convergence, and to the authors' knowledge, no one has been able to find a closed form expression for this series over  $q$ .

In this work, we propose an efficient method for the computation of the 2DPGF-1D, which is based on applying Kummer's transformation to the spectral formula (2), and subsequently applying Poisson's formula to the series containing the asymptotic expression of the  $n$ th term of (2) as  $|n| \rightarrow \infty$  (see [5, Eq. (8)]). Also, when applying Kummer's transformation, we retain several terms in the asymptotic expansion of the  $n$ th term of (2) as  $|n| \rightarrow \infty$  [15] instead of retaining one single term [5], which considerably improves the efficiency of the spectral Kummer-Poisson's method. In particular,  $G_{1\text{DP}}$  is written in this work as a sum of the following two fast converging series

$$G_{1\text{DP}}(\Delta x, \Delta y, k) = \sum_{n=-\infty}^{+\infty} \left[ b_n^{1\text{DP}}(\Delta x, \Delta y, k) - \sum_{i=1}^{M'} B_i b_n^{1\text{DP}}(\Delta x, \Delta y, jC_i) \right] + \sum_{n=-\infty}^{+\infty} \left( \sum_{i=1}^{M'} B_i a_n^{1\text{DP}}(\Delta x, \Delta y, jC_i) \right) \tag{6}$$

where  $B_i$  and  $C_i$  ( $i = 1, \dots, M'$ ) are real coefficients that are judiciously chosen in such a way that the  $n$ th term of the first series of (6) decays like  $|n|^{-(M'+1)}$  as  $|n| \rightarrow \infty$ , and simultaneously the second series of (6) exhibit a fast exponential convergence. Then, if the value of  $M'$  in (6) is chosen to be sufficiently large, the two series of (6) converge very fast.

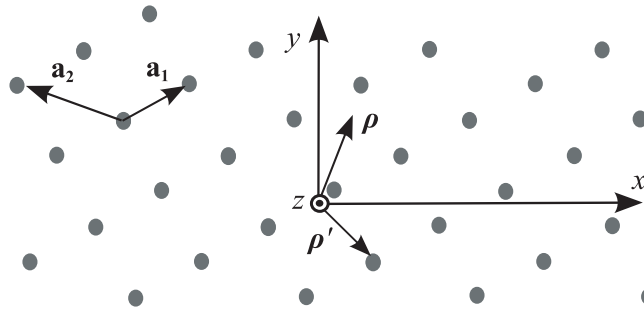


Figure 2: Spatial array of line sources with 2D periodicity.  $\rho' + m\mathbf{a}_1 + n\mathbf{a}_2 = (x' + ma_{1x} + na_{2x})\hat{\mathbf{x}} + (y' + ma_{1y} + na_{2y})\hat{\mathbf{y}}$  ( $m, n = \dots, -1, 0, 1, \dots$ ) is the 2-D vector pointing at the line sources and  $\rho = x\hat{\mathbf{x}} + y\hat{\mathbf{y}}$  is the 2-D vector for the observation point.

Figure 2 shows a two-dimensional array of line sources located in a homogeneous medium. Let  $\mathbf{a}_1$  and  $\mathbf{a}_2$  be the primitive vectors of the periodic 2-D lattice, which are not necessarily orthogonal (i.e., the axes of the periodic array may be skewed). The spatial series for the periodic 2-D Green's function with 2-D periodicity (2DPGF-2D) generated by this 2-D array of line sources is given by

$$G_{2\text{DP}}(\Delta x, \Delta y, k) = \sum_{m=-\infty}^{+\infty} \sum_{n=-\infty}^{+\infty} a_{mn}^{2\text{DP}}(\Delta x, \Delta y, k) = \frac{1}{4j} \sum_{m=-\infty}^{+\infty} \sum_{n=-\infty}^{+\infty} H_0^{(2)}(kS_{mn})e^{-j\mathbf{k}_{\omega 0} \cdot \rho_{mn}} \tag{7}$$

where  $\mathbf{k}_{\omega 0} = k_{x0}\hat{\mathbf{x}} + k_{y0}\hat{\mathbf{y}}$  is a vector in the  $x$ - $y$  plane that accounts for the phase per unit cell introduced by an incident/emitted plane wave and  $S_{mn}$  is given by

$$S_{mn} = |\rho - \rho' - \rho_{mn}| \tag{8}$$

with  $\rho - \rho' = \Delta x\hat{\mathbf{x}} + \Delta y\hat{\mathbf{y}}$  and  $\rho_{mn} = m\mathbf{a}_1 + n\mathbf{a}_2$ .

The series (7) converges slowly in the lossless case since its terms decay like  $|m\mathbf{a}_1 + n\mathbf{a}_2|^{-1/2}$  as both  $|m| \rightarrow \infty$  and  $|n| \rightarrow \infty$ . When the two-dimensional version of Poisson's formula is applied to (7), one obtains a spectral series with a faster convergence rate which is given by

$$G_{2DP}(\Delta x, \Delta y, k) = \sum_{m=-\infty}^{+\infty} \sum_{n=-\infty}^{+\infty} b_{mn}^{2DP}(\Delta x, \Delta y, k) = \frac{1}{A} \sum_{m=-\infty}^{+\infty} \sum_{n=-\infty}^{+\infty} \frac{e^{-j\mathbf{k}_{mn} \cdot (\boldsymbol{\rho} - \boldsymbol{\rho}')}}{|\mathbf{k}_{mn}|^2 - k^2} \quad (9)$$

where  $A = (\mathbf{a}_1 \times \mathbf{a}_2) \cdot \hat{\mathbf{z}}$  is the area of the unit cell of the 2-D lattice and

$$\mathbf{k}_{mn} = \mathbf{k}_{\omega 0} + \frac{2\pi}{A} [m(\mathbf{a}_2 \times \hat{\mathbf{z}}) + n(\hat{\mathbf{z}} \times \mathbf{a}_1)] \quad (10)$$

The terms of the series (9) decay like  $|m(\mathbf{a}_2 \times \hat{\mathbf{z}}) + n(\hat{\mathbf{z}} \times \mathbf{a}_1)|^{-2}$  as both  $|m| \rightarrow \infty$  and  $|n| \rightarrow \infty$ . This indicates that although the convergence of (9) is faster than that of (7), it is still slow.

Ewald's method can also be applied to the computation of the 2DPGF-2D. In fact, if we follow the derivations in Section 4 of [17], Ewald's method leads to the following expression for  $G_{2DP}$

$$G_{2DP}(\Delta x, \Delta y, k) = \frac{1}{A} \sum_{m=-\infty}^{+\infty} \sum_{n=-\infty}^{+\infty} \frac{e^{-j\mathbf{k}_{mn} \cdot (\boldsymbol{\rho} - \boldsymbol{\rho}')}}{|\mathbf{k}_{mn}|^2 - k^2} e^{-\frac{|\mathbf{k}_{mn}|^2 - k^2}{4(E'')^2}} + \frac{1}{4\pi} \sum_{m=-\infty}^{+\infty} \sum_{n=-\infty}^{+\infty} e^{-j\mathbf{k}_{\omega 0} \cdot \boldsymbol{\rho}_{mn}} \sum_{q=0}^{+\infty} \left( \frac{k}{2E''} \right)^{2q} \frac{1}{q!} E_{q+1}(S_{mn}^2 E''^2) \quad (11)$$

where  $E''$  is the splitting parameter (see [17, Eq. (34)]). Although the two series of (11) over the integer indexes  $m$  and  $n$  exhibit extremely fast gaussian convergence, the series over the index  $q$  of (11) does not have gaussian convergence, which causes that Ewald's method for the computation of the 2DPGF-2D is not as efficient as one should expect.

By analogy with Eq. (6), in this work we propose to compute  $G_{2DP}$  by applying the Kummer-Poisson's method to the spectral series (9). Also, we propose to retain several terms in the asymptotic expansion of the terms of (9) as both  $|m| \rightarrow \infty$  and  $|n| \rightarrow \infty$  in order to improve the efficiency of the overall spectral Kummer-Poisson's method. The final expression used in the computation of  $G_{2DP}$  is given by the following sum of two fast converging double series

$$G_{2DP}(\Delta x, \Delta y, k) = \sum_{m=-\infty}^{+\infty} \sum_{n=-\infty}^{+\infty} \left[ b_{mn}^{2DP}(\Delta x, \Delta y, k) - \sum_{i=1}^{M''} D_i b_{mn}^{2DP}(\Delta x, \Delta y, jF_i) \right] + \sum_{m=-\infty}^{+\infty} \sum_{n=-\infty}^{+\infty} \left( \sum_{i=1}^{M''} D_i a_{mn}^{2DP}(\Delta x, \Delta y, jF_i) \right) \quad (12)$$

where  $D_i$  and  $F_i$  ( $i = 1, \dots, M''$ ) are real coefficients that are chosen in such a way that the terms of the first series of (12) decay like  $|\mathbf{k}_{mn}|^{-(2M''+2)}$  as both  $|m| \rightarrow \infty$  and  $|n| \rightarrow \infty$ , and simultaneously the second series of (12) exhibit a fast exponential convergence. This means that Eq. (12) provides a very fast mean for computing  $G_{2DP}$  when  $M''$  is chosen to be large enough.

In order to compare the relative efficiency of Eqs. (4) and (6) in the computation of  $G_{1DP}$ , we have compared the CPU times required by both expressions to obtain  $G_{1DP}$  within an accuracy of eight significant figures. These CPU times have been obtained for a 1-D array of line sources in a lossless homogeneous medium ( $\text{Im}(k) = 0$ ), which is the worst case scenario for the application of Eq. (1). We have found that the CPU times required by the single term Kummer-Poisson's method of [5] (i.e., by Eq. (6) in the case where  $M' = 1$ ) are typically between 2 and 10 times longer than those required by Ewald's method, which agrees with the results plotted in [5, Fig. 3(b)]. However, the CPU times required by the spectral Kummer-Poisson's method of Eq. (6) are comparable to those of Ewald's method when  $M' = 3$ , and are between 2 and 5 times shorter than those of Ewald's method when  $M' = 7$ . This indicates that the spectral Kummer-Poisson's method of Eq. (6) is more efficient than Ewald's method concerning the computation of  $G_{1DP}$ .

Also, we have compared the CPU times required to obtain  $G_{2DP}$  with an accuracy of eight significant figures via Eqs. (11) and (12). In the case where the medium supporting the array of line sources is lossless, the CPU times required by the single term spectral Kummer-Poisson's method

for the computation of  $G_{2DP}$  (i.e., by Eq. (12) in the case where  $M'' = 1$ ) are always significantly longer than those required by Ewald's method. However, the Kummer-Poisson's method of Eq. (12) becomes competitive with Ewald's method when  $M'' = 2$ , and it is between 2.5 and 4 times faster than Ewald's method when  $M'' = 6$ . So, the spectral Kummer-Poisson's method described in this paper is more efficient than Ewald's method not only in the computation of  $G_{1DP}$  but also in the computation of  $G_{2DP}$ .

The comparison between the CPU times provided by Ewald's method and Kummer-Poisson's method will be presented at the Symposium. Additional results showing the fast convergence rate of the series involved in Eqs. (6) and (12) will also be presented at the Symposium.

#### ACKNOWLEDGMENT

This work has been supported by the Spanish Ministerio de Educación y Ciencia and European Union FEDER funds (project TEC2004-03214), and by Junta de Andalucía (project TIC-253).

#### REFERENCES

1. Leviatan, Y., P. G. Li, A. T. Adams, and J. Perini, "Single-post inductive obstacle in rectangular waveguide," *IEEE Trans. Microwave Theory Tech.*, Vol. 31, 806–812, Oct. 1983.
2. Jorgenson, R. E. and R. Mittra, "Oblique scattering from lossy strip structures with onedimensional periodicity," *IEEE Trans. Antennas Propagat.*, Vol. 38, 212–219, Feb. 1990.
3. Chow, Y. L., J. J. Yang, D. G. Fang, and G. E. Howard, "A closed-form spatial Green's function for the thick microstrip substrate," *IEEE Trans. Microwave Theory Tech.*, Vol. 39, 588–592, Mar. 1991.
4. Yu, Y. and C. H. Chan, "Efficient hybrid spatial and spectral techniques in analyzing planar periodic structures with nonuniform discretizations," *IEEE Trans. Microwave Theory Tech.*, Vol. 48, 1623–1627, Oct. 2000.
5. Valerio, G., P. Baccarelli, P. Burghignoli, and A. Galli, "Comparative analysis of acceleration techniques for 2-D and 3-D Green's functions in periodic structures along one and two directions," *IEEE Trans. Antennas Propagat.*, Vol. 55, 1630–1642, June 2007.
6. Jorgenson, R. E. and R. Mittra, "Efficient calculation of the free-space periodic Green's function," *IEEE Trans. Antennas Propagat.*, Vol. 38, 633–642, May 1990.
7. Veysoglu, M. E., H. Yueh, R. Shin, and J. Kong, "Polarimetric passive remote sensing of periodic surfaces," *J. Electromagn. Waves Appl.*, Vol. 5, No. 3, 267–280, Mar. 1991.
8. Mathis, A. W. and A. F. Peterson, "A comparison of acceleration procedures for the twodimensional periodic Green's function," *IEEE Trans. Antennas Propagat.*, Vol. 44, 567–571, Apr. 1996.
9. Nicorovici, N. A. and R. C. McPhedran, "Lattice sums for off-axis electromagnetic scattering by gratings," *Phys. Rev. E*, Vol. 50, No. 4, 3143–3160, Oct. 1994.
10. Singh, S. and R. Singh, "On the use of Shanks's transform to accelerate the summation of slowly converging series," *IEEE Trans. Microwave Theory Tech.*, Vol. 39, 608–610, Mar. 1991.
11. Singh, S. and R. Singh, "A convergence acceleration procedure for computing slowly converging series," *IEEE Trans. Microwave Theory Tech.*, Vol. 40, 168–171, Jan. 1992.
12. Singh, S. and R. Singh, "On the use of Chebyshev-Toeplitz algorithm in accelerating the numerical convergence of infinite series," *IEEE Trans. Microwave Theory Tech.*, Vol. 40, 171–173, Jan. 1992.
13. Mosig, J. R. and A. A. Melcón, "The summation-by-parts algorithm. A new efficient technique for the rapid calculation of certain series arising in shielded planar structures," *IEEE Trans. Microwave Theory Tech.*, Vol. 50, 215–218, Jan. 2002.
14. Linton, C. M., "The Green's function for the two-dimensional Helmholtz equation in periodic domains," *J. Eng. Math.*, Vol. 33, 377–402, May 1998.
15. Baekelandt, B., D. de Zutter, and F. Olyslager, "Arbitrary order asymptotic approximation of a Green's function series," *AEÜ Int. J. Electron. Commun.*, Vol. 51, No. 4, 224–230, 1997.
16. Abramowitz, M. and I. Stegun, *Handbook of Mathematical Functions*, Dover Publications, New York, 9th Edition, 1970.
17. Capolino, F., D. R. Wilton, and W. A. Johnson, "Efficient computation of the 2-D Green's function for 1-D periodic structures using the Ewald method," *IEEE Trans. Antennas Propagat.*, Vol. 53, 2977–2984, Sep. 2005.

# An Improved Matrix Bandwidth and Profile Reduction Algorithm in FEM Problems

Q. Wang, Y. C. Guo, and X. W. Shi

National Key Laboratory of Antenna and Microwave Technology, Xidian University, Xi'an 710071, China

**Abstract**— A Generalized GPS (GGPS) algorithm is proposed to optimize the FEM mesh nodes coding for reducing the bandwidths and profiles of stiffness matrices. The algorithm has three key-points. First, all the endpoints are found, which can be used as the origins for generating the tree structures which all have the same depth, rather than two endpoints in the GPS algorithm. Secondly, a new tree structure is constructed with all the level structures, which is smaller in width than any tree structure. Finally, a new combination rule is used to obtain more sub graphs in order to further reduce the level width. Simulation results show that the bandwidths optimized by the GGPS algorithm are decreased by about 5%, and in most cases, the profiles are reduced by 2%, compared with the results got by the GPS algorithm in relation to the test data in the paper, while the execution time is close to GPS algorithm. It is clear that the GGPS is superior to the GPS in reducing bandwidth and profile.

## 1. INTRODUCTION

The finite element displacement method of analyzing electromagnetic field involves the solution of large systems of linear algebraic equation with sparse, structured, symmetric coefficient matrices [1]. The size of a sparse matrix is determined by its bandwidth and profile [2]. It is obvious that a large-size sparse matrix requires more computer memory which in turn requires more computational time. For example, consider a system of equations

$$AX = B \quad (1)$$

where  $A$  is a positive definite, symmetric, and sparse matrix, called the stiffness matrix. Decreasing bandwidth and profile lowers computational cost. When parallel multiprocessor computers are employed, interprocess communication can be reduced significantly by smaller bandwidth, providing another important reason that reduction in bandwidth is highly desired [3]. The bandwidth and profile of matrix  $A$  in Equation (1) can be reduced by properly permuting the rows and columns, which can be achieved by an appropriate renumbering of vertices of a graph associated with  $A$  [4]. The relationship between  $A$  and the graph is as follows [5, 6]. Let  $A = [a_{ij}]$  be a symmetric and sparse matrix of dimension  $N$ . Let the  $i$ th vertex  $v_i$  be associated with the  $i$ th row. Denote by  $V = \{v_1, v_2, \dots, v_N\}$  the collection of vertices. For  $a_{ij} \neq 0$ , we can define an unordered pair  $\{v_i, v_j\}$ . Denote by  $E$  the collection of such unordered pairs. Then, we can define a graph  $G = \langle V, E \rangle$ , where  $V$  and  $E$  are called *vertices* and *edges*, respectively.

Among existing renumbering schemes, GPS (Gibbs Paul & Stockmeyer) which consists of three algorithms is the most popular and well-known technique [5, 7–9]. GPS uses a pair of endpoints of a pseudo-diameter to find the maximal depth of a level structure [1]. For most classes of graphs, there may be several vertices which produce level structures with same depth but different width [10]. The paper modifies the first algorithm of GPS to get more pairs of endpoints of pseudo-diameter. Then, there may be more than two level structures to combine together to construct a level structure whose width is usually less than the original level structure's width got by the GPS algorithm, so we also modify the second algorithm of GPS to get more sub graphs. In the third part of GPS, we just modify a little to be consistent with the former modifications.

This paper is organized as follows: Section 2 gives the basic procedure of the GGPS algorithm. Section 3 gives the simulation results by GPS and GGPS algorithm respectively and compares the performances of them with some classical models. Section 4 draws up our conclusions.

## 2. PRESENTATION OF GGPS ALGORITHM

In the algorithm based on the graph theory, if the level structure  $L$  is rooted, then we have [7]

$$w(L) \leq \beta \leq 2w(L) - 1 \quad (2)$$

where  $\beta$  is the bandwidth of the stiffness matrix  $A$ ,  $w(L)$  is the width of the level structure  $L$ . From Equation (2), we know that the smaller the level structure is, the smaller the bandwidth

of matrix. In the GPS algorithm, only one pseudo-diameter is found, leading to only two level structures to minimize the level width [7]. However, there may be more than one pseudo-diameter in a graph to generate more level structures for minimizing a smaller level width. If there are more level structures and more sub graphs to partition a graph for us to combine a new level structure, we can probably get a reduction in bandwidth and profile of the corresponding stiffness matrix  $A$ . It is the basic ideas of GGPS algorithm. The description of the new algorithm is divided into three algorithms as well as the GPS algorithm.

### 2.1. Finding a Starting Vertex

For a graph  $G$  with symmetric structure, if  $G$  has  $n$  vertices, there may always be more than one pseudo-diameter with same length. Only two endpoints of a pseudo-diameter are found in the original algorithm. We modify the rule for picking up the endpoints of pseudo-diameters to get endpoints as more as we can.

- A. Pick an arbitrary vertex of minimal degree and call it  $v$ .
- B. Generate a level structure  $L_v$  rooted at vertex  $v$ . Let  $S$  be the set of vertices which are in the last level of  $L_v$  (i.e., those which are farthest away from  $v$ ).
- C. Generate level structures rooted at vertices  $s \in S$  selected in the order of increasing degree. If for some  $s \in S$  the depth of  $L_s$  is greater than the depth of  $L_v$ , then set  $v \leftarrow s$  and return to step B.
- D. Let  $u$  be the vertex of  $S$  whose associated level structure has the smallest width, with ties broken arbitrarily.
- E. If for some  $s \in S$  the depth of  $L_s$  is the same as the depth of  $L_v$  or  $L_u$ , the vertices are picked up with  $u$  as a set of vertices at the “ $u$ ” end of the pseudo-diameter.
- F. If the vertex  $s$  has the same degree as  $v$ , the depth of  $L_s$  is the same as  $L_v$  or  $L_u$ , and it has not been picked up yet, then picked it up to a set of vertices at the “ $v$ ” end of the pseudo-diameter.

### 2.2. Minimizing Level Width

With the set of endpoints found in the first algorithm, we construct a collection of level structures rooted at those endpoints respectively. It is possible to combine these level structures into a new level structure whose width is smaller than any level structure's, while the worst result is the same level width as the level width of the GPS. The problem is that for the discrepancy in location of each pseudo-diameter, when the graph is partitioned to sub graphs, the amount of the sub graphs may be much less than before. We broaden the rules for picking up the partition vertex to get more sub graphs. The partitioning of a graph can be seen as the fractionizing of the graph. The larger the number of sub graphs, the smaller the bandwidth and profile.

Using the rooted level structure  $L_{v_1} = \{L_1^1, L_2^1, \dots, L_k^1\}$ ,  $L_{v_2} = \{L_1^2, L_2^2, \dots, L_k^2\}$ , ..., and  $L_{v_m} = \{L_1^m, L_2^m, \dots, L_k^m\}$  obtained from the first algorithm, associate with each vertex  $w$  of  $G$  the ordered set  $(i_1, \dots, i_{m_1}, i_{m_1+1}, \dots, i_m)$  ( $m_1$  is the number of the vertices at the “ $v$ ” end of the pseudo-diameter, and  $m-m_1$  is the number of the vertices at the “ $u$ ” end of the pseudo-diameter), called the associated level set, where  $i_t$  ( $t = 1, \dots, m_1$ ) is the index of the level in  $L_{v_i}$  ( $i = 1, \dots, m_1$ ) that contains  $w$ , and  $k+1-i_t$  ( $t = m_1+1, \dots, m$ ) is the index of the level in  $L_{v_i}$  ( $i = m_1+1, \dots, m$ ) that contains  $w$ . Thus the set  $(i_1, i_2, \dots, i_m)$  is associated with a vertex  $w$  if and only if  $w \in L_{i_1}^1 \cap \dots \cap L_{i_{m_1}}^{m_1} \cap L_{k+1-i_{(m_1+1)}}^{m_1+1} \cap \dots \cap L_{i_{k+1-m}}^m$ .

- A. Assign the vertices of  $G$  to levels in a new level structure  $L = \{L_1, L_2, \dots, L_k\}$  as follows:
  1. If the associated level set of a vertex  $w$  is of the form  $(i_1, i_2, \dots, i_m)$ , and the absolute difference between  $i_i$  and  $i_j$  ( $i \neq j$ ) is in the required range (the required range varies as the total number of the vertices in graph  $G$ ). The more the number of vertices, the larger the required absolute difference. Then vertex  $w$  is placed in  $L_i$ . The vertex  $w$  and all edges incident to  $w$  are removed from the graph. If  $V(G) = \emptyset$ , stop.
  2. The graph  $G$  now consists of a set of one or more sub graphs  $C_1, C_2, \dots, C_t$  ordered so that  $|V(C_1)| \geq |V(C_2)| \geq \dots \geq |V(C_t)|$ .
  3. For each sub graph  $C_i$ ,  $i = 1, 2, \dots, t$  do the following:
    - a) Compute the vector  $(n_1, n_2, \dots, n_k)$  where  $n_i = |L_i|$ .
    - b) Compute the vectors  $(h_1^1, h_2^1, \dots, h_k^1)$ ,  $(h_1^2, h_2^2, \dots, h_k^2)$ , ..., and  $(h_1^m, h_2^m, \dots, h_k^m)$  where  $h_i^j = n_i +$  (the number of vertices which would be placed in  $L_j$  if the  $j$ th element of the associated level set were used).

- c) Find  $h_0^j = \max_i\{h_i^j : h_i^j - n_i > 0\}$  ( $j = 1, \dots, m$ ). Find  $h_0 = \max\{h_0^1, \dots, h_0^m\}$  and the index  $j$  ( $j = 1, \dots, m$ ), and place all the vertices of the sub graph in the levels indicated by the  $j$ th elements of the associated level set.

### 2.3. Numbering

The numbering procedure is similar to the GPS algorithm in that it assigns consecutive positive integers to the vertices of  $G$  level by level. A new modification were necessary, however, since the level structures obtained by Subsection 2.2 are a more general type than the rooted ones used in the GPS algorithm.

- A. If the degree of  $v$  is not the smallest among all the endpoints, then interchange  $v$  and the vertex with the smallest degree and substitute the level structure obtained in Algorithm 2 by the level structure rooted from vertex with the smallest degree. (This insures that the numbering starts from the endpoint of lower degree.)
- B. Assign consecutive positive integers to the vertices of level  $L_1$  in the following order:
  1. Assign the number 1 to the vertex  $v$  (if this is not the first component of the original graph, then assign the smallest unassigned positive integer to  $v$ ).
  2. Let  $w$  be the lowest numbered vertex of level  $L_1$  which has unnumbered vertices in  $L_1$  adjacent to it. Number the vertices of  $L_1$  adjacent to  $w$ , in the order of increasing degree. Repeat this step until all vertices of  $L_1$  adjacent to numbered vertices are themselves numbered.
  3. If any unnumbered vertices remain in level  $L_1$ , number the one of minimal degree, then go to step B.2. Otherwise proceed to step C.
- C. Number the vertices of level  $L_i$ ,  $i = 2, 3, \dots, k$ , as follows:
  1. Let  $w$  be the lowest numbered vertex of level  $L_{i-1}$  that has unnumbered vertices of level  $L_i$  adjacent to it. Number the vertices of  $L_i$  adjacent to  $w$  in the order of increasing degree. Repeat this step until all vertices of level  $L_i$  adjacent to vertices of level  $L_{i-1}$  are numbered.
  2. Repeat steps B.2 and B.3, replacing 1 with  $i$ .
- D. The numbering is reversed by setting  $i$  to  $n - i + 1$ , for  $i = 1, 2, \dots, m$  if either of the two following conditions holds:

Table 1: Test results (bandwidth, profile and time).

Nodes	Initial		GPS		GGPS		$1 - \beta_{gg}/\beta_g$ %	$T_{gg}/T_g$
	Bandwidth	Profile	Bandwidth	Profile	Bandwidth	Profile		
23	19	218	13	186	11	177	15.38	1.0000
446	419	54319	107	30631	101	30057	5.61	1.2051
1188	1063	338089	186	133542	180	140063	3.23	1.1090
1804	1685	533044	103	119109	98	119034	4.85	0.9707
2457	2334	1320292	230	320592	213	318483	7.39	1.0094
2576	2333	1595263	220	342407	208	337925	5.45	1.0406
2803	2700	2008080	382	624348	368	606821	3.66	1.0000
4184	3855	3882596	355	796828	328	812067	7.61	0.9965
4331	4186	4510009	423	1106248	414	1119011	2.13	1.0090
5420	4905	6518053	465	1421117	430	1499323	7.53	1.0763
7519	7246	14846314	552	2909545	543	2952312	1.63	1.0328
7984	7465	15897809	593	3078711	578	3185422	2.53	1.0360
149610	149180	2012803692	865	94163449	837	93316348	3.24	1.0428

$\beta_{gg}$  — bandwidth after GGPS algorithm  
 $T_{gg}$  — time for GGPS algorithm

$\beta_g$  — bandwidth after GPS algorithm  
 $T_g$  — time for GPS algorithm

1. Step A interchanged vertices  $v$  and the vertex belonging to the set of the “ $v$ ” end of the pseudo-diameter and Algorithm 2 selected the “ $v$ ” end elements of the level set for sub graph  $C_1$ .
2. Step A did not interchange vertices  $v$  and the vertex belonging to the set of “ $v$ ” end of pseudo-diameter and Algorithm 2 selected the “ $u$ ” end elements of the level set for sub graph  $C_1$ .

### 3. DESCRIPTION OF TEST RESULTS

The original and new implementations of the two reordering algorithms were compared on 13 test models meshed in tetrahedron meshes. Table 1 shows the results for 13 volumes with tetrahedron meshes, which are obtained by the GPS and GGPS algorithms. Figure 1 and Figure 2 graphically display the test results with respect to bandwidth, profile and execution time, respectively. From the following table and figures, compared with GPS, the GGPS algorithm reduces the bandwidth by about 5% on average and the profile by 2% in most cases, and it always performs at least as well as the GPS algorithm in time. This improvement was due to the adoption of the increasing of the amount of pseudo-diameter endpoints and sub graphs, which is checked in the GGPS algorithm for additional reduction of bandwidth and profile.

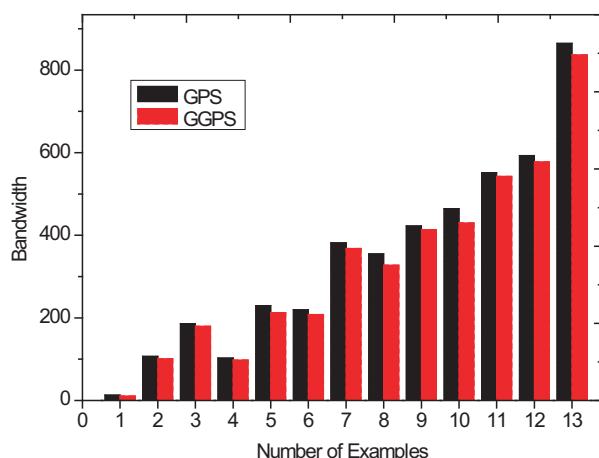


Figure 1: Bandwidths for 13 examples.

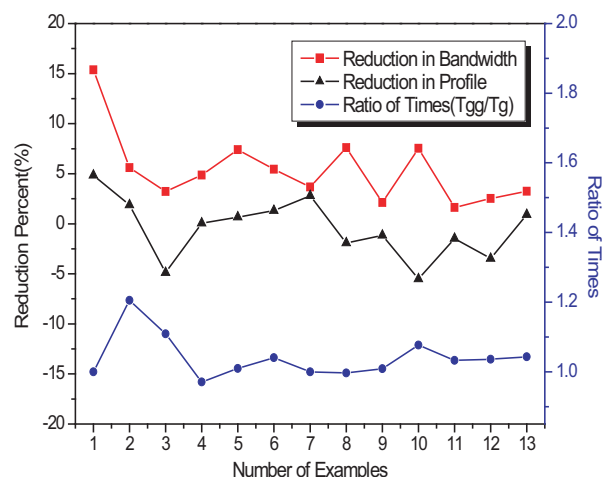


Figure 2: Comparisons of GPS and GGPS algorithms.

### 4. CONCLUSIONS

Optimizing the FEM mesh nodes coding for reducing the bandwidths and profiles of stiffness matrices is a key issue. A Generalized GPS (GGPS) algorithm is proposed in the paper. It increases the amount of pseudo-diameter endpoints and sub graphs, which can be seen as the increasing of the freedom of level structures space, and the bandwidth and profile can be further reduced when the graph is more fractionized. Comparisons of the bandwidth reduced by the well-known GPS and the GGPS had been tested on several classes of graphs. Simulation results show that the bandwidths and profiles optimized by the GGPS algorithm are decreased by about 5% and 2% respectively, compared with the results got by the GPS algorithm, while the execution time is close to GPS algorithm. It is clear that the GGPS is superior to the GPS in reducing bandwidth and profile. Hence, for the reduction of matrix bandwidth and profile, the GGPS algorithm is currently an efficient algorithm which can be used in the projects of FEM applications.

### REFERENCES

1. Lewis, J. G., “Implementation of the Gibbs-Poole-Stockmeyer and Gibbs-King algorithms,” *ACM Transactions on Mathematical Software (TOMS)*, Vol. 8, No. 2, 180–189, 1982.
2. Cuthill, E. and J. McKee, “Reducing the bandwidth of sparse symmetric matrices,” *Proceedings of the 1969 24th National Conference*, 157–172, 1969.
3. Luo, J. C., “Algorithms for reducing the bandwidth and profile of a sparse matrix,” *Computers and Structures*, Vol. 44, No. 3, 535–548, 1992.

4. Armstrong, B. A., "A hybrid algorithm for reducing matrix bandwidth," *International Journal for Numerical Methods in Engineering*, Vol. 20, 1929–1940, 1984.
5. Gibbs, N. E., W. G. Poole Jr., and P. K. Stockmeyer, "A comparison of several bandwidth and profile reduction algorithms," *ACM Transactions on Mathematical Software (TOMS)*, Vol. 2, No. 4, 322–330, 1976.
6. Xinrong, W., L. Yingchun, and W. Xiyang, "The WGPS algorithm to finite element mesh modal number optimization," *Journal of HarBin Institute of Technology*, Vol. 24, No. 4, 99–103, 1992.
7. Gibbs, N. E., W. G. Poole Jr., and P. K. Stockmeyer, "An algorithm for reducing the bandwidth and profile of a sparse matrix," *SIAM Journal on Numerical Analysis*, Vol. 13, No. 2, 236–250, 1976.
8. Lewis, J. G., "Algorithm 582: The Gibbs-Poole-Stockmeyer and Gibbs-King algorithms for reordering sparse matrices," *ACM Transactions on Mathematical Software*, Vol. 8, No. 2, 190–194, 1982.
9. Crane Jr., H. L., N. E. Gibbs, W. G. Poole Jr., and P. K. Stockmeyer, "Algorithm 508: Matrix bandwidth and profile reduction [F1]," *ACM Transactions on Mathematical Software (TOMS)*, Vol. 2, No. 4, 375–377, 1976.
10. Gibbs, N. E., "Algorithm 509: A hybrid profile reduction algorithm [F1]," *ACM Transactions on Mathematical Software*, Vol. 2, No. 4, 378–387, 1976.

# Simulation of Multiple Scattering Scenes for Time Domain Maxwell's Equations by an Hybrid and Parallel Method

V. Mouysset<sup>1</sup>, P. Borderies<sup>2</sup>, X. Ferrières<sup>2</sup>, and P. A. Mazet<sup>1</sup>

<sup>1</sup> Information Modelling and Processing Department, ONERA, Toulouse, France

<sup>2</sup> Electromagnetism and Radar Department, ONERA, Toulouse, France

**Abstract**— This paper deals with the treatment in time-domain of large scattering scenes by a decomposition into disjointed sub-domains. A Finite Volume scheme is introduced in this approach and then hybridized with Finite Differences. The restrictive condition of the smallest time step introduced by CFL from each method employed are then replaced by an inter-domain time step strategy. Comparisons on numerical examples with mono-domain computations show the interest of the method in terms of accuracy and efficiency.

## 1. INTRODUCTION

A relevant problem of the electromagnetic compatibility (EMC) is to take properly account for coupling between sources and scatterers. When dealing with large scattering scenes, the tradeoff between accuracy and efficiency of the scheme is very sensible.

From the accuracy point of view, geometrical details are crucial and can lead to extra-refinements on the meshing, or need to be solved using conformal scheme such as Finite Volume in Time Domain (FVTD) [1, 2]. From the efficiency point of view, extra-refinements or free-space meshing can be significantly penalizing. Hence, Finite Differences in Time Domain (FDTD) [3] are often involved. An interesting approach from both points of view is to hybridize FDTD with FVTD close to the scatterers (e.g., [4, 5]). However, this method does not appear to be optimal as free space regions between sources and scatterers are still meshed and then dissipative and/or dispersive errors are, *a priori*, propagated and amplified from a cell to another one.

In this paper, we are going to investigate an alternative way by introducing (Section 3) FVTD in a multi-domain method based on a disjointed decomposition of the scene [6] (previously recalled in Section 2). Moreover, its hybridization with FDTD is presented in order to take the better part of each method (Section 4). The last part is devoted to present an *inter-domain* time step strategy freeing from applying a global CFL condition (Section 5) and enhancing the global efficiency.

## 2. PRINCIPLE OF THE MULTI-DOMAIN DECOMPOSITION

Let us first recall the principle of the method as it was introduced into [6]. Considering multiple scatterers and sources, we group them into disjointed domains named  $D^i$ ,  $i = 1, \dots, n$  and we surround each group respectively by a Huygens and a Pick up surface, noted  $\mathcal{H}^i$  and  $\mathcal{P}^i$  (see Figure 1).

Now, multi-domain method consists in solving the coupled system of  $n$  Maxwell's equations

$$\begin{cases} \varepsilon(x)\partial_t E^i - \text{rot}H^i + \sigma(x)E^i = E^{src} + \mathbf{n}^{\mathcal{H}} \times \left( \sum_{j \neq i} H^j \right), \\ \mu(x)\partial_t H^i + \text{rot}E^i = H^{src} - \mathbf{n}^{\mathcal{H}} \times \left( \sum_{j \neq i} E^j \right), \end{cases} \quad (1)$$

where  $(E^j, H^j)$ -fields provided by other  $D^j$ ,  $j \neq i$  are evaluated according to a specific integral formula

$$\begin{aligned} E^i(t, X) \approx & \sum_k \int_{\mathcal{P}_k^i} \left[ \frac{1}{c_0 d_k} (Z_0 \mathbf{T}_k \partial_t J_i - \mathbf{t}_k \times \partial_t M_i) + \frac{Z_0}{d_k^2} \left( 3\mathbf{T}_k J_i - 2\mathbf{N}_k J_i - \frac{1}{Z_0} \mathbf{t}_k \times M_k \right) \right. \\ & \left. + \frac{c_0 Z_0}{d_k^3} \int_t (3\mathbf{T}_k J_i - 2\mathbf{N}_k J_i) \right] (t - T_k, y) \frac{dy}{4\pi}, \end{aligned} \quad (2)$$

$$\begin{aligned} H^i(t, X) \approx & \sum_k \int_{\mathcal{P}_k^i} \left[ \frac{1}{c_0 d_k} (Z_0^{-1} \mathbf{T}_k \partial_t M_i + \mathbf{t}_k \times \partial_t J_i) + \frac{Z_0^{-1}}{d_k^2} (3\mathbf{T}_k M_i - 2\mathbf{N}_k M_i + Z_0 \mathbf{t}_k \times J_i) \right. \\ & \left. + \frac{c_0 Z_0^{-1}}{d_k^3} \int_t (3\mathbf{T}_k M_i - 2\mathbf{N}_k M_i) \right] (t_0 - T_k, y) \frac{dy}{4\pi}, \end{aligned} \quad (3)$$

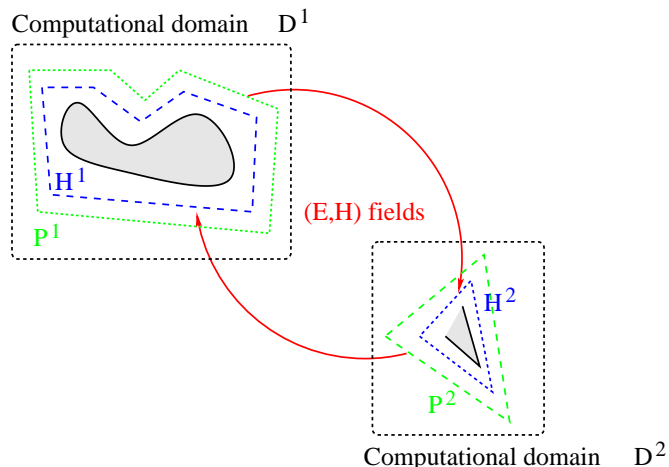


Figure 1: Principle of the multi-domain decomposition.

where  $\mathbf{T}_k v = \mathbf{t}_k \times (\mathbf{t}_k \times v)$ ,  $\mathbf{N}_k v = \mathbf{n}_k \times (\mathbf{n}_k \times v)$ ,  $Z_0 = \sqrt{\mu_0 \varepsilon_0^{-1}}$  and  $c_0 = (\mu_0 \varepsilon_0)^{-1/2}$ ,  $d_k = |X_k - X|$ ;  $T_k = d_k/c_0$  stands for the time for the signal to travel from  $X_k$  to point  $X$ . Formulas (2–3) are constructed with an arbitrary cutting out of  $\mathcal{P}^i$  into a set of small “sub-faces”  $(\mathcal{P}_k^i)_k$ , and choosing points  $X_k \in \mathcal{P}_k^i$ . At last,  $\mathbf{n}_k$  is the outward unitary normal vector to  $\mathcal{P}_k^i$ , and  $\mathbf{t}_k$  is the normalized vector  $\mathbf{t}_k = (d_k)^{-1} \overrightarrow{X X_k}$ .

These approximations are established under the following assumption [7]

$$\delta/d \ll 1, \quad (4)$$

where  $\delta$  is a characteristic length describing a reference sub-face  $\mathcal{S}$  ( $\mathcal{S} = C\delta^2$  with  $C > 0$ ) such that each sub-face of  $\mathcal{P}^i$  is smaller than  $\mathcal{S}$ ; and  $d$  stands for the smallest value of all  $d_k, k$ .

At last, for each  $j \neq i$ , the right-hand-side terms  $\mathbf{n}^{\mathcal{H}} \times H^j$  and  $\mathbf{n}^{\mathcal{H}} \times E^j$  in (1) are given as piecewise functions of  $(E^j, H^j)(t, x)$ , onto the Huygens’ surface  $\mathcal{H}^i$ . These functions are obtained from (2–3) performing a cut-off of the Huygens’ surface  $\mathcal{H}^i$  into small patches whose characteristic lengths are given by  $\delta$ , and then assuming  $(E^j, H^j)$ -fields to be constant on each considered patch.

Performing this elementary steps, we show [6] that error of the so-introduced approximations are given in  $O(\delta/d)$  where the local parameter  $\delta$  is free. In [8] we have shown that playing on the admissible global error on the grouping parameter  $\delta/d$  permits to significantly lower the computational effort while we control the global error on the solution.

### 3. MULTI-DOMAIN WITH FINITE VOLUME IN TIME DOMAIN

In [6], we were interested in numerically perform the multi-domain decomposition by involving the FDTD [3]. However, for some obvious cases, one should prefer conformal schemes instead of FDTD. Hence, in this section, we will deal with the interest of performing the multi-domain decomposition with a FVTD scheme to take account for fine geometrical specificities. The FVTD scheme we consider has been introduced in [2] and lies onto a MUSCL approximation in time domain.

We consider the scattering scene composed of two identical metallic spheres of radius  $R = 1$  m and centered respectively at  $O_1 = (0, 0, 0)$  and  $O_2 = (4.5, 4.5, 4.5)$ , and excited by a plane wave with characteristics  $(E_x = 377f(t), H_y = -f(t), k_z = -1)$  where  $f(t) = 3 \cdot 10^8 \sqrt{2} e^{-(t-6+z)^2}$ .

A well known characteristic of this kind of FVTD schemes is the dissipative error they introduce. From a numerically point of view, it implies the global stability of the method whence a good accuracy on the computed  $(E, H)$ -field requires mesh refinements. Hence, we have performed several numerical experimentations with coarse and fine meshes, and we compare these to the one obtained for the multi-domain method using a mesh close to the coarsest mono-domain one. Results obtained for a test-point located at  $A = (3, 3, 3)$  are drawn on Figure 2.

We can straightforwardly observe that the multi-domain solution with a coarse mesh is almost as accurate as the mono-domain one with the finest mesh. Thus, the multi-domain strategy sig-

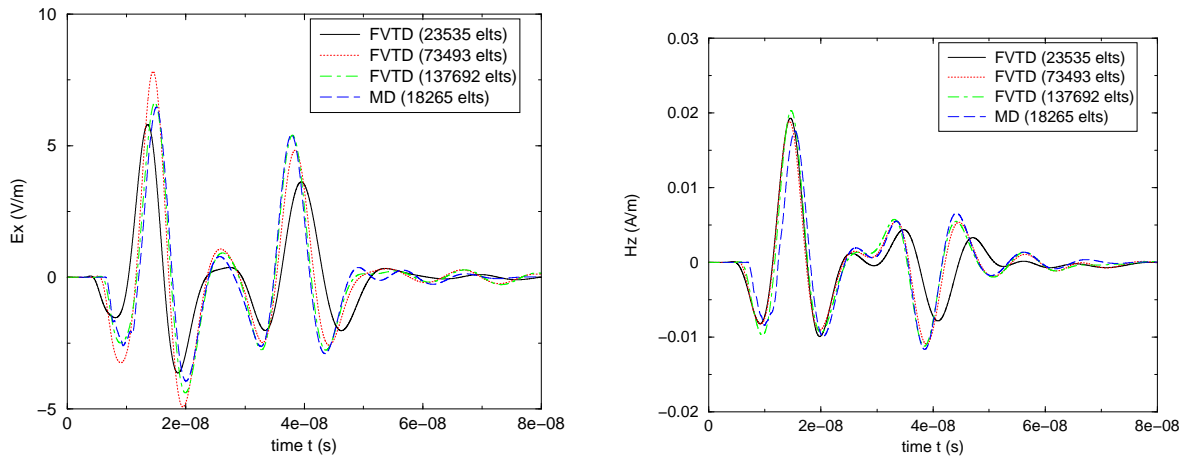


Figure 2: Comparison on  $E_x$  (left) and  $H_z$  (right) fields of the mono- and multi-domain FVTD methods.

nificantly reduces the dissipative effects cumulated by the FVTD on free-space cells. Moreover, if we look at the global costs of these experiments (see Table 1), we see an appreciable gain on the computational effort when involving the multi-domain FVTD instead of the mono-domain FVTD in order to obtain the same accuracy.

Table 1: CPU and memory costs for the different mono and multi-domain computations.

Method:	CPU time:	Memory cost:
FVTD (23535 elts)	$\times 1$	$\times 1$
FVTD (73493 elts)	$\times 4$	$\times 3$
FVTD (137692 elts)	$\times 6.7$	$\times 5.7$
FVTD multi-domain (18265 elts) [per domain]	$\times 3.7$	$\times 1.3$

#### 4. HYBRIDIZATION: FINITE DIFFERENCE / FINITE VOLUME

As the multi-domain system described in (1) does not pay attention to the numerical scheme used, and as we can prove the global stability of this system, then separated choices for the numerical schemes to use can be planned. Thus we study the coupling between a wide-band antenna (20 Mhz–1 Ghz) with the previous metallic sphere (see Figure 3 left). Such a test case needs to be accurate on the geometrical properties of the sphere because of small wave-length signals. On the other hand, these refinements induce a huge decrease on the global efficiency of the simulation. Hence, it appears to be a relevant experiment for our method.

So, to take account of the geometry of the sphere we will use a FVTD sub-domain on it, and then to give fast evaluations with the antenna we will choose the FDTD. As a comparison, we compute the global solution with mono-domain FDTD simulations with 3 successive refinements noted FDTD (same mesh as for multi-domain simulation), FDTD/2 and FDTD/3. When plotting the different fields obtained from the scattering at half-distance between the sphere and the antenna (see Figure 3 right), we can observe the influence of both a good geometrical description of the sphere on the FDTD results, and a decrease of the dispersive effects linked to the FDTD. However, from a quality point of view, the hybridized multi-domain FDTD-FVTD scheme gives as good results as the finest FDTD one because of its better description of the sphere and the break introduced on the cumulative process for the dispersive error over the free space parts of the global domain.

According to the performance criterium, the hybridized multi-domain scheme appears to be cheaper in terms of memory storages (see Table 2) but as long to process as the finest FDTD simulation. Its main restriction comes from the very low CFL condition imposed by the FVTD domain onto the FDTD one. This leads to extra and useless time computations. To bypass this problem we introduce an *inter-domain local time step* strategy in the next paragraph.

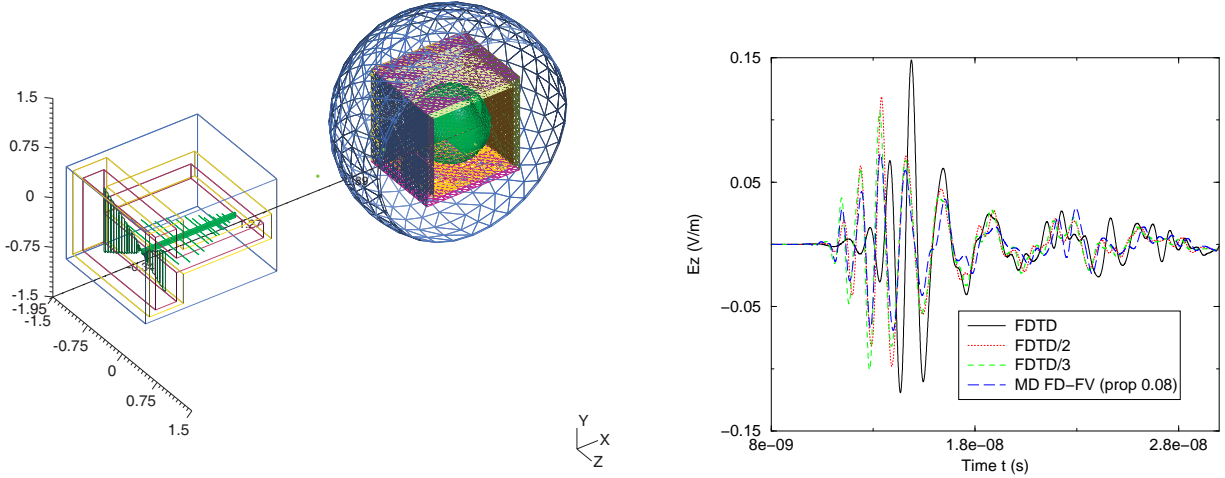


Figure 3: Coupling between a sphere and an antenna: FDTD-FVTD multi-domain mesh (left),  $E_z$  field at half-distance between domains.

Table 2: Comparison of costs for the FDTD, FDTD/2, FDTD/3 and multi-domain FDTD-FVTD simulations.

Method:	CPU time:	Memory cost:
Mono-domain FDTD	$\times 1$	$\times 1$
Mono-domain FDTD/2	$\times 10.52$	$\times 6.30$
Mono-domain FDTD/3	$\times 22.48$	$\times 11.84$
MD (prop. 0.08) [sphere / FVTD]	$\times 6.49$	$\times 0.82$
MD (prop. 0.08) [antenna / FDTD]	$\times 22.02$	$\times 1$

## 5. INTER-DOMAIN LOCAL TIME STEP STRATEGY

First, we start by computing the minimal distance  $\underline{d}$  between all domains. For each domain  $\mathcal{D}^i$ , this provides a global time delay  $T_{sync}^i = [\underline{d}/(c\Delta t_i)]\Delta t_i$ , where  $[x]$  stands for the integer part of  $x$ , and  $\Delta t_i$  is the time step used on  $\mathcal{D}^i$ . Then we note  $T_{sync}$ , the biggest value of  $T$  such that for all  $i$  we have  $T < T_{sync}^i$  and  $\exists n_i \in \mathbb{N}$ ,  $T_{sync} = n_i \Delta t_i$ . Hence, for each domain  $\mathcal{D}^i$ , the time scheme chosen introduces weights  $(\omega_k^i(t))_k$  such that any time function  $f$  is approximated by

$$f(t) \approx \sum_{k=1}^{n_i} \omega_k^i(t) f(k\Delta t_i), \quad t \in [0, T_{sync}], \text{ on } \mathcal{D}^i. \quad (5)$$

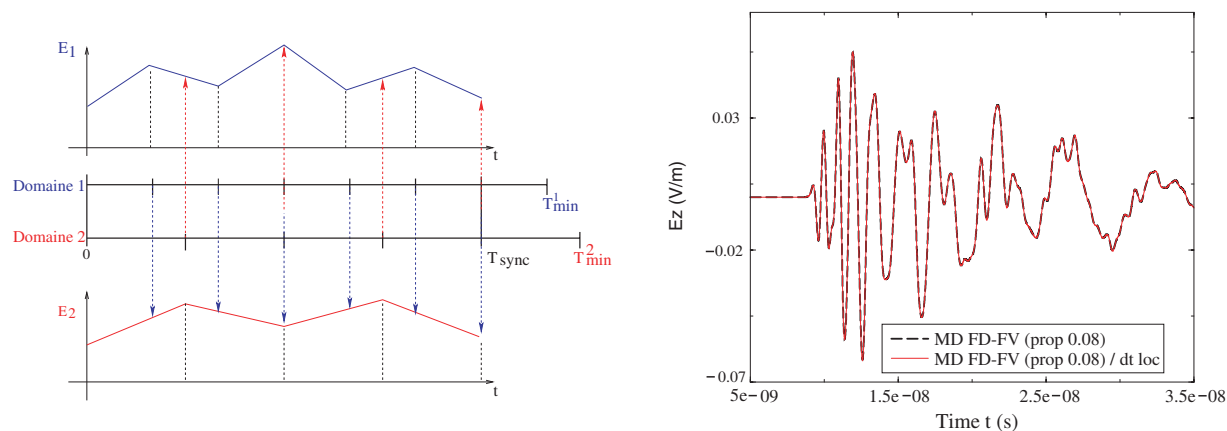
We now split the global study time  $[0, T]$  into small intervals  $I_p = [pT_{sync}, (p+1)T_{sync}]$ , and then our local time step strategy can be summed up, for each domain  $\mathcal{D}^i$  and for each  $I_p$  in: (a) compute  $(E^i, H^i)$  contributions to other domains  $\mathcal{D}^j$ ,  $j \neq i$  with (2-3) at times  $pT_{sync} + k\Delta t_i$ ; (b) from (5) and these values evaluate (see Figure 4 left)

$$\begin{pmatrix} E^j \\ H^j \end{pmatrix} (pT_{sync} + q\Delta t_j) \approx \sum_{k=1}^{n_i} \omega_k^i(q\Delta t_j) \begin{pmatrix} E^j \\ H^j \end{pmatrix} (pT_{sync} + k\Delta t_i), \quad \forall q \in [1, n_j]. \quad (6)$$

This inter-domain local time step appears not to penalize the accuracy on the solution of the multi-domain computations (see Figure 4 right), whence significant gains on the computational time are introduced, as shown on Table 3.

Table 3: Comparison of costs for solving with hybrid FDTD-FVTD scheme with and without inter-domain time step.

Method:	CPU time:	Memory cost:	Time step:
MD FD-FV (prop. 0.08) [sphere / FVTD]	$\times 1$	$\times 1$	$\times 1$
MD FD-FV (prop. 0.08) [antenna / FDTD]	$\times 3.47$	$\times 1.22$	$\times 1$
MD FD-FV (prop. 0.08) [sphere / FVTD] dt loc	$\times 1$	$\times 1$	$\times 1$
MD FD-FV (prop. 0.08) [antenna / FDTD] dt loc	$\times 1.81$	$\times 0.89$	$\times 0.5$

Figure 4: Principle of the *inter-domain time step* (left) and comparisons of results with *inter-domain time step* for the last test case (right).

Even if we have not yet proved the global stability of this strategy, all numerical tests using very important differences on  $\Delta t$  between domains (from 1 to 20) revealed to be stable and did not penalize the accuracy.

## 6. CONCLUSION

In this paper we have presented numerical simulations on finite volume scheme within the multi-domain method previously introduced in [6].

They have first enlightened the efficiency of this method in terms of accuracy and reduction of computational effort. In a second time, its hybridization with finite differences and finite volumes has been explored on significant examples relevant of the EMC and showing the interest of this hybridized approach. At last, by a strategy of inter-domain time steps, we have freed the hybrid approach of a global CFL condition and again obtained significant lowering on the computational time.

The method presented here hence appears as an adequate tool to study efficiently and with low costs various kind of coupling problems for the EMC and fully adequate for hybridizing different resolution methodes over disjointed zones.

## REFERENCES

1. Rao, S. M., *Time Domain Electromagnetics*, Academic Press, J. D. Irwin, Auburn University, 1999.
2. Bonnet, P. and X. Ferrieres, "Numerical modelling of scattering problems using a time domain finite volume method," *Journal of Electromagnetic Waves and Applications*, Vol. 11, 1165–1189, 1997.
3. Yee, K. S., "Numerical solution of initial boundary value problems involving Maxwell's equations in isotropic media," *IEEE Trans. on Ant. and Prop.*, Vol. 14, 302–307, 1966.
4. Edelvik, S. and G. Ledfelt, "Explicit hybrid time-domain solver for the Maxwell's equations in 3D," *Journal of Scientific Computing*, Vol. 15, No. 1, 61–78, 2000.
5. Ferrieres, X., J. P. Parmentier, S. Bertuol, and A. Ruddle, "Application of an hybrid finite difference/finite volume method to solve an automotive EMC problem," *IEEE Trans. EMC*, Vol. 46, 624–634, 2005.

6. Mouysset, V., P. A. Mazet, and P. Borderies, "Efficient treatment of 3D time-domain electromagnetic scattering scenes by disjointing sub-domains and with consistent approximations," *Progress In Electromagnetics Research*, Vol. 71, 41–57, 2007.
7. Mouysset, V., P. A. Mazet, and P. Borderies, "A new approach to evaluate accurately and efficiently electromagnetic fields outside a bounded zone with time-domain volumic methods," *Journal of Electromagnetic Waves and Applications*, Vol. 20, 803–817, 2006.
8. Mouysset, V., P. A. Mazet, and P. Borderies, "A multi-domain decomposition method to solve electromagnetic scattering problems in time domain," *Radio Science*, Vol. 42, RS4009, 2007.

# Tailoring Particles for Optical Trapping and Micromanipulation: An Overview

T. A. Nieminen<sup>1</sup>, T. Asavei<sup>1</sup>, Y. Hu<sup>1,2</sup>, M. Persson<sup>1</sup>, R. Vogel<sup>1</sup>  
V. L. Y. Loke<sup>1</sup>, S. J. Parkin<sup>1</sup>, N. R. Heckenberg<sup>1</sup>, and H. Rubinsztein-Dunlop<sup>1</sup>

<sup>1</sup>The University of Queensland, Australia

<sup>2</sup>Rice University, USA

**Abstract**— Optical trapping and micromanipulation has developed from an interesting novelty to a powerful and widely used tool, with the capability to move or trap microscopic live biological specimens and measure forces on the order of piconewtons, typical of forces in microbiological systems. Despite this, the range of particles typically trapped or manipulated is quite small, and it is unusual to see applications involving objects other than biological specimens or homogeneous isotropic microspheres, typically polymer or silica.

However, particles can be modified or specially fabricated to expand the possible applications of optical tweezers. For example, while non-absorbing homogeneous isotropic spheres cannot be rotated, optically anisotropic spheres can, and can therefore function as microscopic torque sensors, extending the usual translational micromanipulation and force measurement to rotational manipulation and torque sensing. The development of such particles has led to applications in microscale metrology and biophysics, along with potential deployment of optically-driven micromachines in lab-on-a-chip devices.

We present an overview of our work on the tailoring of microparticles for versatile optical trapping and micromanipulation. This includes approaches based on controlled chemistry — nano-assembly — and optical microfabrication. Beginning with the production of anisotropic vaterite microspheres, we review some of the applications, and difficulties encountered along the way. Some of these difficulties can be overcome by coating of the vaterite microspheres. We also discuss the use of anti-reflection coating to allow strong trapping of high refractive index particles. The alternative strategy of producing arbitrarily shaped polymer microstructures through two-photon photopolymerization is also discussed. This can be used to produce optically-driven microrotors or structurally anisotropic microspheres to replace vaterites for particular applications.

## 1. INTRODUCTION

Optical tweezers have developed from an interesting novelty of physics, directly demonstrating the transport of momentum by light, to a versatile and widely-used tool, especially for biological applications. A key element in this growth has been the ability to measure forces on the order of piconewtons—an optical tweezers trap can be approximated as a harmonic potential and measurement of displacement within the trap yields the optical restoring force. Optical tweezers are also useful for capturing, holding, and moving biological specimens. Despite this, the typical application usually involves the trapping of polymer or silica microspheres. Notably, this immediately removes the possibility of angular or rotational manipulation or torque detection, as the rotational symmetry of a sphere means that no optical torque can be exerted in the absence of absorption. Furthermore, trapping is limited by competition between the gradient force acting to trap particles, and the scattering force acting to push particles out of the trap in the direction of propagation of the trapping beam. Since the reflectivity of the particle increases as the relative refractive index increases, this restricts the range of particles that can be effectively trapped.

However, particles can be specially fabricated to extend the potential of optical tweezers, especially with regard to optical measurements of torque and rotational micromanipulation. We provide an overview of work carried out by ourselves and others in this field. Two different strategies have been applied: chemistry, and optical microfabrication. The first has yielded vaterite microspheres as the most promising tool for high-torque rotation in optical tweezers developed so far, and the latter allows the production of arbitrary structures, including a diverse range of optically-driven rotors.

For rotational manipulation, a key element is that the particle must not be rotationally symmetric. Rotational symmetry can be broken either on the microscopic scale, through the use of an optically anisotropic material, such as birefringent crystals or polymers, or on a larger scale,

by a non-rotationally symmetric shape. Depending on the shape, the effect can be predominantly form-birefringence, optically identical to material birefringence in effect, or can involve coupling to modes of light carrying orbital angular momentum. The latter type of particle can be thought of as microscopic versions of the holograms often used to generate orbital angular momentum carrying beams.

When the torque is a result of birefringence, there is an accompanying change in the degree of circular polarization of the trapping beam. This can be measured optically, giving an all-optical determination of the applied torque [1]. This is the case for both material birefringence and form-birefringence [2]. This allows the rotational equivalent of the force-sensing applications that have become a standard application of optical tweezers, and has been a major motivation for the production of birefringent particles for optical trapping.

## 2. VATERITE MICROSPHERES

Although it was realised many years ago that optical measurement of the torque exerted on birefringent particles by the trapping beam offered the potential to measure other external microscale torques, such as the viscous or visco-elastic resistance of the surrounding medium, it was clear that spherical birefringent particles would be best for such purposes, since the surrounding fluid flow field is given by a simple analytical formula. The lack of a readily available spherical birefringent particle made metrological applications difficult — generally, there would be unknown viscous drag torques.

The synthesis and optical rotation of vaterite microspheres proved to be a decisive advance in rotational micromanipulation [3]. Vaterite is a semistable calcium carbonate ( $\text{CaCO}_3$ ) mineral that rarely occurs in nature, and is a positive uniaxial birefringent crystal. It may, however, be grown in the laboratory, and under certain conditions, it forms polycrystalline spheres with radii on the order of microns. It is important that the material be positive uniaxial, since in that case, the optic axis will align with the electric field of a plane-polarized trapping beam, or will lie normal to the beam axis of a circularly polarized beam. Thus, the particle retains its deviation from rotational symmetry about the beam axis, whereas a negative uniaxial material will tend to align such that the optic axis lies on the beam axis, presenting a rotationally symmetric aspect to the trapping beam, which means that no optical torque can be exerted.

Vaterite microspheres have proved useful for microscale viscometry [3, 4], and have also seen use as optically-driven micromachines in lab-on-a-chip devices [5].

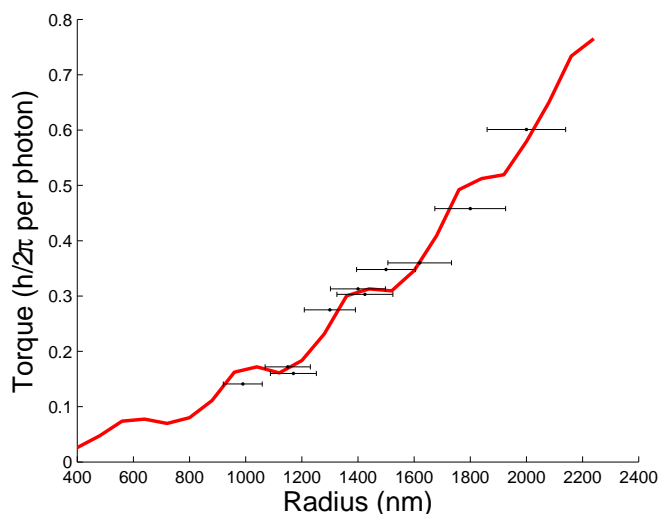


Figure 1: Calculated (solid line) and measured (points) optical torque on vaterite microspheres.

Interestingly, the vaterite microspheres appear to have a “sheaf-of-wheat” internal structure [6]. Modelling the optical trapping vaterites as inhomogeneous particles with a local optic axis given by this model closely matches the observed torque, as shown in Figure 1, supporting this model [7].

However, the application of vaterite to the study of biological systems such as rotational molecular motors and the rotational mechanics of biomolecules has been seriously hampered by the

chemistry of vaterite. Firstly, as a calcium carbonate crystal, vaterites have a very short lifetime in many solutions of interest, such as commonly used buffer solutions for biological specimens, such as phosphate buffered saline (PBS). Secondly, specific attachment of molecules such as DNA to vaterite is difficult.

In an attempt to solve these problems, we have coated vaterite microspheres with silica. The coating is formed by condensation of tetraethoxysilane (TEOS) in ethanol-water solution according to the Stöber method [8]. The thickness of the coating can easily be adjusted by varying the amount of TEOS used, and multiple coatings may be applied to achieve any desired thickness. The coating allows attachment of a greater range of biomolecules, and affords the underlying vaterite some protection from the environment.

### 3. ANTI-REFLECTION COATING

The ability to coat vaterites with silica — and the process will also work for other types of particles — suggests a further use for this type of modification of microparticles: anti-reflection coating for improved trapping. High refractive index particles are usually difficult to trap, because their high reflectivity results in a significant fraction of the trapping beam being back-scattered, with a resultant optical force, the so-called “scattering force”, acting to push the particle out of the trap in the direction of propagation of the beam. Since anti-reflection coating of optical components is a standard practice to reduce reflection, a similar strategy would appear to be feasible for microparticles.

Since, ideally, the coating should have a refractive index of  $n_{\text{coating}} = (n_{\text{medium}}n_{\text{particle}})^{1/2}$ , it would be very useful to be able to control the refractive index of the silica coating. This is generally done by changing the porosity of the silica which, in turn, can be done in several ways. To some extent, the porosity of a TEOS coating may be varied by simply changing the ethanol/water ratio in base catalyzed reactions [9] or the water/TEOS ratio in acid catalyzed reactions [10]. High porosity may also be induced by the addition of surfactants such as octadecyltrimethoxysilane (C18TMS) [11, 12] or alkyltrimethylammonium bromide (CnTAB) [13] to the polymerization process followed by removal of the organic group by calcination. Interestingly, by using a multiple-coating approach, with variation of the refractive index, it should be possible to produce gradient-index coated particles. The improvement in trapping resulting from coating is shown in Figure 2.

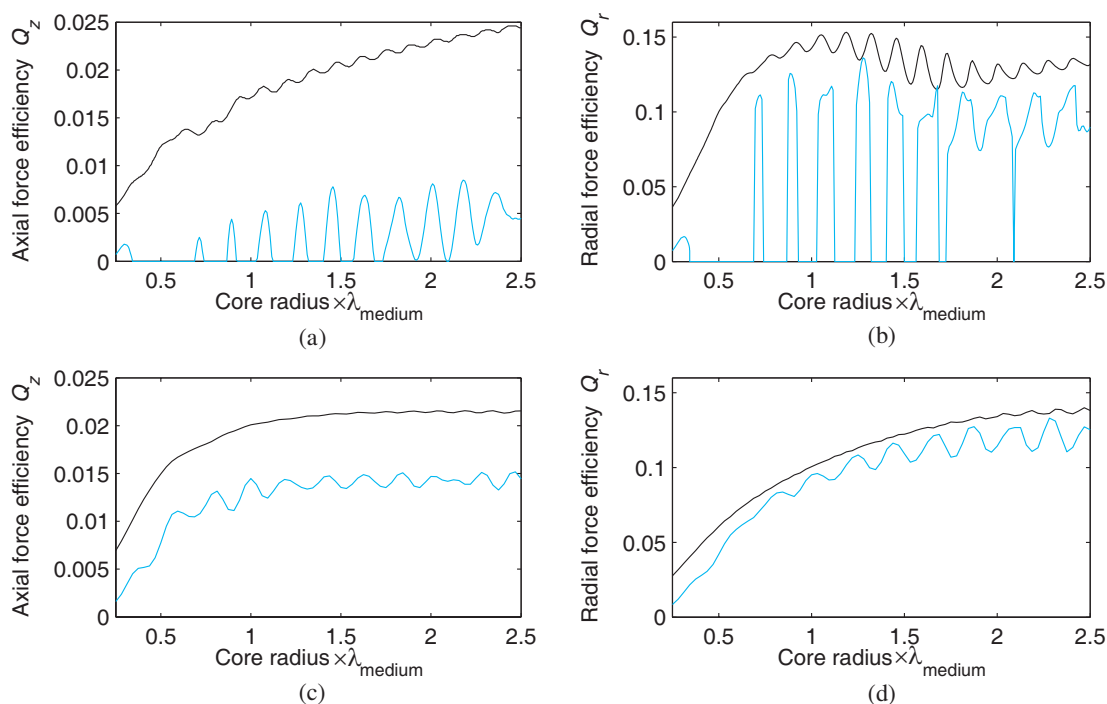


Figure 2: Axial and radial trapping efficiencies for coated (black) and uncoated (cyan/gray) particles with (a), (b)  $n = 1.8$  and (c), (d)  $n = 1.6$ .

#### 4. MICROFABRICATION BY TWO-PHOTON PHOTOPOLYMERIZATION

Another strategy for the production of specially-designed particles is to use optical microfabrication, based on two-photon photopolymerization. This technique was pioneered by Strickler and Webb in 1991 [14], following the application of two-photon excitation in two-photon laser scanning fluorescence microscopy [15]. The first 3D structures microfabricated using two-photon polymerization were reported in 1997 [16], spiral structures with a diameter of  $6\ \mu\text{m}$  and a wire width of  $1.3\ \mu\text{m}$ . Since then, various micromachines have been produced (micropumps, microgears, microneedles) with high resolution [17–19].

We use the NOA series of UV curing resins from Norland Products for the fabrication of our devices. They are based on a mixture of photoinitiator molecules and thiol-ene monomers. These resins are photopolymerized when exposed to light with wavelengths shorter than  $400\ \text{nm}$  and require an energy flux of  $2\text{--}4.5\ \text{J}/\text{cm}^2$  for full curing. We use a femtosecond laser at  $780\ \text{nm}$ , with an  $80\ \text{fs}$  pulse length and an  $80\ \text{MHz}$  repetition rate. A computer-controlled shutter is used to control the beam, which is turned on or off as needed as the stage is moved, building up a three-dimensional structure voxel-by-voxel by layer-by-layer raster scanning (see Figure 3). Lateral steps are  $100\ \text{nm}$ , and steps in the  $z$  direction are  $200\ \text{nm}$ . The structures are grown upside down on the upper coverslip in an inverted microscope, with an objective of numerical aperture of 1.3. This top-down scanning method has the advantage that the laser beam does not pass through already exposed resin on the way to the focus, reducing the possibility of distortion of the focal spot.

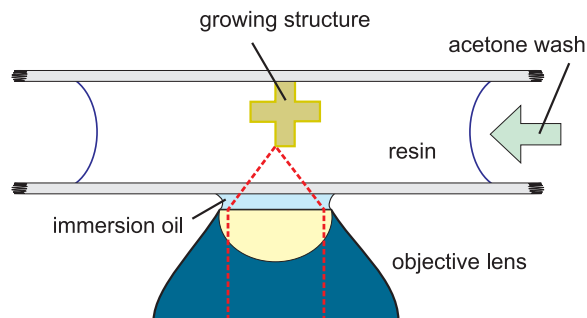


Figure 3: Two-photon photopolymerization.

After the polymerization, the unexposed resin is washed off with acetone, leaving the 3D structure attached to the coverslip. The first structures we produced were 3D chiral objects with 4-fold rotational symmetry (off-set crosses) which are ideal as optically driven microrotors [20, 21].

#### 5. CONCLUSION

We have described some of the possibilities of, and existing applications of, the fabrication of particles specially tailored for specific applications in optical trapping. In particular, such particles can be electromagnetically or structurally anisotropic, allowing optical torques to be exerted. This greatly expands the manipulation possible with optical tweezers, introducing rotation and spinning, and allowing the measurement of microscale torques.

Optically microfabricated particles, produced using two-photon photopolymerization, have potential for use as optically-driven micromachines. Space does not permit a full coverage of this interesting field, but a recent review is available [22].

Finally, even simple modification of microspheres by coating offers improved trapping, the trapping of otherwise untrappable high-index particles, and permits the use of lower numerical aperture optical systems.

#### REFERENCES

1. Nieminen, T. A., N. R. Heckenberg, and H. Rubinsztein-Dunlop, "Optical measurement of microscopic torques," *Journal of Modern Optics*, Vol. 48, 405–413, 2001.
2. Bishop, A. I., T. A. Nieminen, N. R. Heckenberg, and H. Rubinsztein-Dunlop, "Optical application and measurement of torque on microparticles of isotropic nonabsorbing material," *Physical Review A*, Vol. 68, 033802, 2003.

3. Bishop, A. I., T. A. Nieminen, N. R. Heckenberg, and H. Rubinsztein-Dunlop, "Optical microrheology using rotating laser-trapped particles," *Physical Review Letters*, Vol. 92, 198104, 2004.
4. Parkin, S. J., G. Knöner, T. A. Nieminen, N. R. Heckenberg, and H. Rubinsztein-Dunlop, "Picoliter viscometry using optically rotated particles," *Physical Review E*, Vol. 76, 041507, 2007.
5. Leach, J., H. Mushfique, R. di Leonardo, M. Padgett, and J. Cooper, "An optically driven pump for microfluidics," *Lab on a Chip*, Vol. 6, 735–739, 2006.
6. Morse, H. W. and J. D. H. Donnay, "Optics and structure of three-dimensional spherulites," *American Mineralogist*, Vol. 21, 391–427, 1936.
7. Loke, V. L. Y., T. A. Nieminen, S. J. Parkin, N. R. Heckenberg, and H. Rubinsztein-Dunlop, "FDFD/T-matrix hybrid method," *Journal of Quantitative Spectroscopy and Radiative Transfer*, Vol. 106, 274–284, 2007.
8. Stober, W., A. Fink, and E. Bohn, "Controlled growth of monodisperse silica spheres in micron size range," *Journal of Colloid and Interface Science*, Vol. 26, 62–69, 1968.
9. Vasconcelos, D. C. L., W. R. Campos, V. Vasconcelos, and W. L. Vasconcelos, "Influence of process parameters on the morphological evolution and fractal dimension of sol-gel colloidal silica particles," *Materials Science and Engineering A*, Vol. 334, 53–58, 2002.
10. Meixner, D. L. and P. N. Dyer, "Influence of sol-gel synthesis parameters on the microstructure of particulate silica xerogels," *Journal of Sol-Gel Science and Technology*, Vol. 14, 223–232, 1999.
11. Büchel, G., K. K. Unger, A. Matsumoto, and K. Tsutsumi, "A novel pathway for synthesis of submicrometer-size solid core/mesoporous shell silica spheres," *Advanced Materials*, Vol. 10, 1036–1038, 1998.
12. Zhao, W., J. Shi, H. Chen, and L. Zhang, "Particle size, uniformity, and mesostructure control of magnetic core/mesoporous silica shell nanocomposite spheres," *Journal of Materials Research*, Vol. 21, 3080–3089, 2006.
13. Yoon, S. B., J.-Y. Kim, J. H. Kim, Y. J. Park, K. R. Yoon, S.-K. Park, and J.-S. Yu, "Synthesis of monodisperse spherical silica particles with solid core and mesoporous shell: Mesopore channels perpendicular to the surface," *Journal of Materials Chemistry*, Vol. 17, 1758–1761, 2007.
14. Strickler, J. H. and W. W. Webb, "Three-dimensional optical data storage in refractive media by two-photon point excitation," *Optics Letters*, Vol. 16, 1780–1782, 1991.
15. Denk, W., J. H. Strickler, and W. W. Webb, "Two-photon laser scanning fluorescence microscopy," *Science*, Vol. 248, 73–76, 1990.
16. Maruo, S., O. Nakamura, and S. Kawata, "Three-dimensional microfabrication with two-photon-absorbed photopolymerization," *Optics Letters*, Vol. 22, 132–134, 1997.
17. Maruo, S. and H. Inoue, "Optically driven micropump produced by three-dimensional two-photon microfabrication," *Applied Physics Letters*, Vol. 89, 144101, 2006.
18. Maruo, S., K. Ikuta, and H. Korogi, "Submicron manipulation tools driven by light in a liquid," *Applied Physics Letters*, Vol. 82, 133–135, 2003.
19. Galajda, P. and P. Ormos, "Complex micromachines produced and driven by light," *Applied Physics Letters*, Vol. 78, 249–251, 2001.
20. Nieminen, T. A., S. J. Parkin, N. R. Heckenberg, and H. Rubinsztein-Dunlop, "Optical torque and symmetry," *Proceedings of SPIE*, Vol. 5514, 254–263, 2004.
21. Knöner, G., S. Parkin, T. A. Nieminen, V. L. Y. Loke, N. R. Heckenberg, and H. Rubinsztein-Dunlop, "Integrated optomechanical microelements," *Optics Express*, Vol. 15, 5521–5530, 2007.
22. Nieminen, T. A., J. Higuette, G. Knöner, V. L. Y. Loke, S. Parkin, W. Singer, N. R. Heckenberg, and H. Rubinsztein-Dunlop, "Optically driven micromachines: Progress and prospects," *Proceedings of SPIE*, Vol. 6038, 237–245, 2006.

# Wide-angle Absorption by the Use of a Metamaterial Plate

A. N. Lagarkov, V. N. Kisel, and V. N. Semenenko

Institute for Theoretical and Applied Electromagnetics, Izhorskaya 13, Moscow 125412, Russia

**Abstract**— The problem regarding top possible (hopefully, total) field suppression of a filamentary source placed above nonuniform impedance plane is discussed. New designs of the electromagnetic field absorbers and resonators are suggested which may be engineered with the use of metamaterials.

## 1. INTRODUCTION — ABSORPTION OF THE ENERGY OF A POINT SOURCE BY A HALF-SPACE

Interest to the field propagation along the imperfect surface has about century-old history, the beginnings of which trace back to the Sommerfeld's solution of the classical problem for the dipole radiating above the plane with finite conductivity. Later, as the radio broadcasting evolved, a lot of publications appeared which dealt with electromagnetic field propagation in the presence of an absorbing half-space with the aim to *minimize* the signal losses.

Now certain practical needs [1] set questions about what value of impedance of a plane should be chosen to absorb the *maximum* portion of energy radiated by a point source (say, filamentary current), how much the amount of the absorbed energy is and how to create such an impedance. Note, in view of the symmetry of the radiation pattern of the filament, at the absence of the plate (in the free space) equal power fluxes are radiated into upper and lower half-spaces, and exactly one half of the radiated energy penetrates through the plane  $y = 0$ , see Fig. 1.

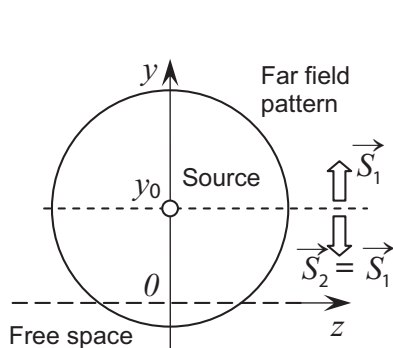


Figure 1.

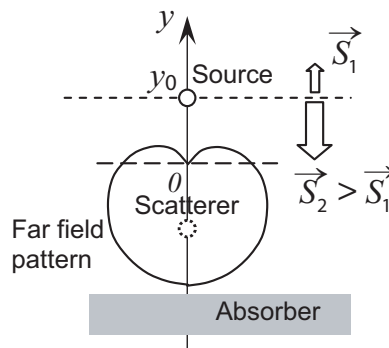


Figure 2.

Calculations showed that even at some “optimal” but constant value of  $Z$  the integral of the real part of the Poynting vector taken over the surface  $y = 0$  (that is,  $z_0 = -\infty, \dots, +\infty$ ) does not exceed a half of radiated power. However it is evident that the lower half-space can absorb more than one half of radiated power provided the impedance distribution is inhomogeneous. For example, let place a specially designed scatterer in the region  $y < 0$ . Then an asymmetric radiation pattern with respect to the  $y = 0$  plane can be formed with its main lobe directed downward, see Fig. 2 (similar trick is used in the Uda-Yagi dipole antennas). In doing so, the major portion of energy is directed into lower half-space. Further, it may be absorbed in an ordinary way. Once the tangential components of the electric and magnetic fields are calculated in the plane  $y = 0$ , one can evaluate the desired distribution of the equivalent surface impedance of such a system.

## 2. TOTAL TRANSMISSION OF THE POINT SOURCE RADIATION INTO A HALF-SPACE

The system shown in Fig. 2 may be further complicated. Evidently, it is possible to make the field cancellation in the upper half-space more complete and, correspondingly, to increase the portion of the energy absorbed in the lower half-space by increasing a number of auxiliary scatterers. The question arises: what *maximum* portion of energy emitted by source can be directed into lower half-space without using any additional devices (say, mirrors) in the upper half-space, at  $y > y_0$ .

It will be shown below that one can create such a passive system which secures *total* cancellation of the source field in the upper half-space and, correspondingly, transfers the whole of the emitted energy into the lower half-space.

Consider an example of designing such a system, firstly, on a qualitative level. Let a filamentary source with a single  $x$ -directed component of the electrical current be placed in the point  $y_0$  over the conducting half-plane  $y = 0$ , Fig. 3. As known, in this case the secondary field can be interpreted as produced by the mirror source, the currents in filament and in its image are of the same magnitude but opposite to each other. In other words, the sign of the wave is reversed when reflection from the conductor occurs. Let a focusing flat plate (Veselago's lens [2]) with a thickness of  $d = y_0/2$  made of the metamaterial with  $\varepsilon = -1$ ,  $\mu = -1$  be inserted between the source and the plane at the altitude  $h$  so as  $0 < h < y_0/2$ . Then the focusing occurs right at the surface of the conducting plate (see, for example, the ray picture in Fig. 4).

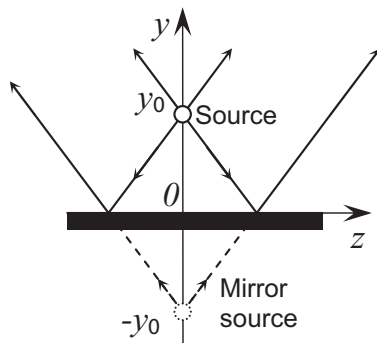


Figure 3.

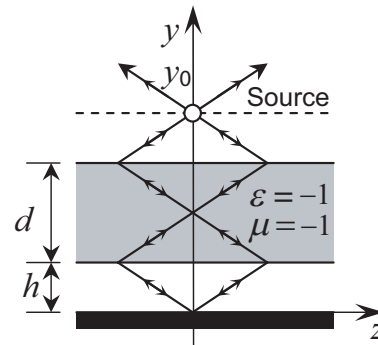


Figure 4.

Once the total phase advance along ray paths is calculated bearing in mind the negative phase velocity of the wave traveling through the plate and the field reversal due to the reflection from the conducting plane, one can discover that in the region  $y > y_0$  the incident and secondary fields mutually cancel each other. In an ideal case, when electromagnetic losses in the plate are infinitesimally small, the total field in the upper half-space tends to zero.

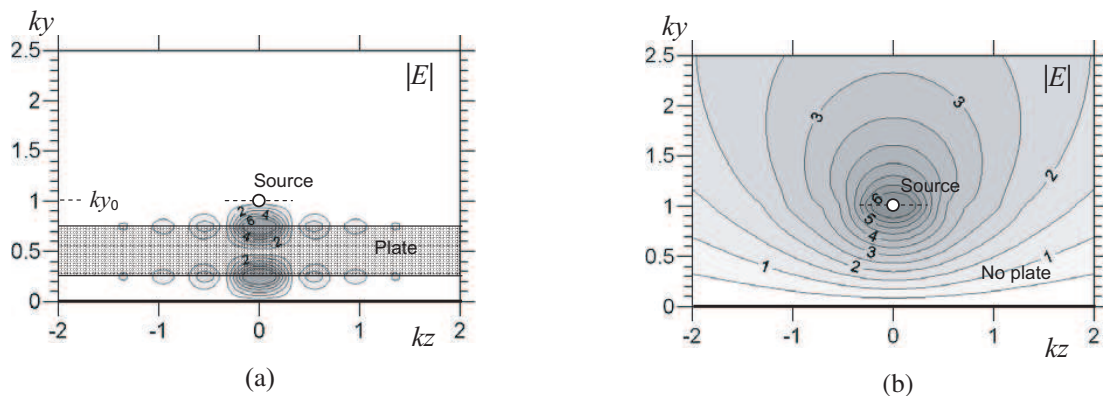


Figure 5.

Rigorous solution of the corresponding boundary problem results in the same conclusion. This is illustrated by Fig. 5 and Fig. 6, which show the absolute values of the total field in the vicinity of the source (in the plane perpendicular to the filament of electrical current). Contour plots are given in Fig. 5, and corresponding 3D images of the field distribution are shown in Fig. 6.

Figures (a) depict the results obtained at  $ky_0 = 1$ ,  $d = 2h = y_0/2$ ,  $\varepsilon = \mu = -1 - i0.001$  (time dependence is chosen as  $\exp(i\omega t)$ ), geometry of the problem corresponds to Fig. 4. Figs. (b) refer to the case of plate absence, when  $\varepsilon = \mu = 1$ . They are given for reference purposes. Note, in the presence of the metamaterial plate the field in the region  $y > y_0$  is almost equal to zero in contrast to the second case, when the field of the filamentary source does not attenuate.

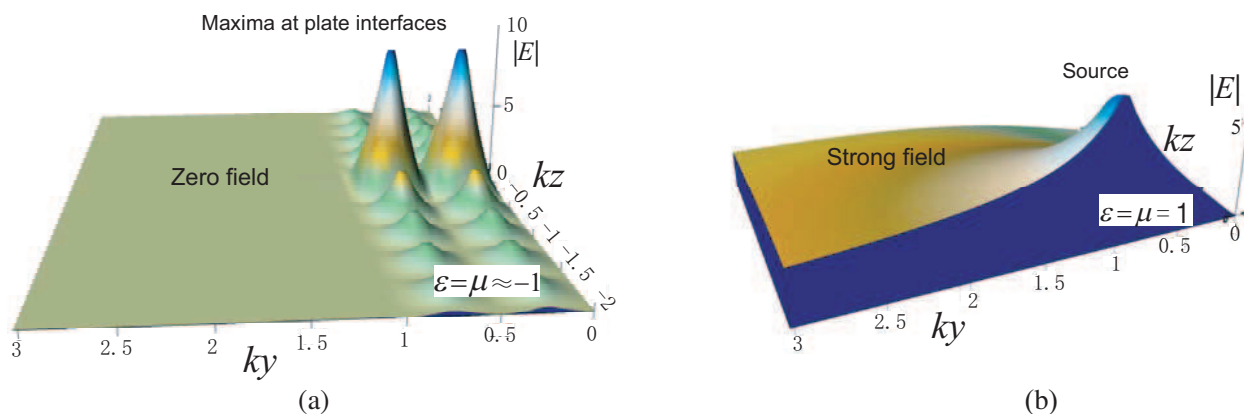


Figure 6.

Of course, microwave experiments on the discussed phenomena with a linear antenna operating as a source should indicate a strong reflected wave in the antenna feeder. This wave can be easily suppressed by a number of techniques commonly used in microwave engineering. Moreover, in a realistic case of easy to manufacture metamaterial plate with a rather high losses, say,  $\epsilon = \mu = -1 - i0.1$ , matching the antenna to a feeder is better while the conclusions remain the same. As calculations show, the major portion of energy, as much as 99.4% is transferred into the lower half-space and dissipates there.

### 3. OPEN RESONATOR

The regions with high field concentration due to accumulating reactive energy are worth noting in the figures (see Fig. 5(a), Fig. 6(a)). They arise next to the metamaterial plate faces while field compensation in upper half-space occurs. These maxima reach especially great values in the case of the plate arrangement side-by-side to the conducting surface,  $h = 0$ , Fig. 7. Thus, the structures shown in Fig. 4 and Fig. 7(a) may serve as prototypes for designing *novel open resonators* without usual restrictions on the thickness of the system in terms of wavelength. Note, previously a different idea of a “thin” metamaterial-based resonator of “closed” type was suggested [3] (the metamaterial

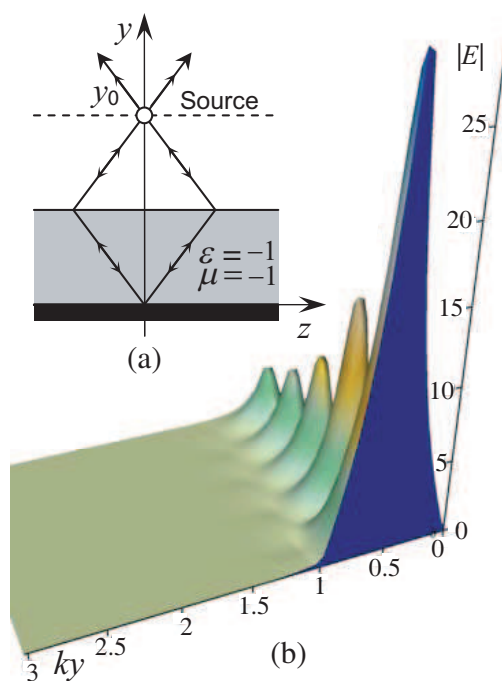


Figure 7.

sheet was sandwiched between a pair of conducting plates). Other design of an open resonator is also known [4], it is based on the negative refraction property of photonic crystal or metamaterial prisms.

#### 4. CORRESPONDENCE TO THE “SUPERRESOLUTION” PHENOMENON. EFFECT OF LOSSES

One of the specific features of the Veselago’s lens is the ability to produce an image with extremely fine details as its resolution is not restricted with so called “diffraction limit”. This surprising fact was firstly pointed out by Prof. Pendry [5]. Later it was shown that the absorption in metamaterial plays a crucial role in view of achieving superresolution in practice. And the smaller the plate thickness (in wavelengths), the higher is the upper level of losses to secure desired resolution (see, e.g., [6]).

Similar conclusions can be made regarding the performance of the systems under consideration. Even if one tends to compensate only propagating modes of the far field in upper half-space, rather strict requirements should be placed to the quality of metamaterial. But to attain the *near field* compensation in the vicinity of the source (around  $y_0$  point), the mirror image should be developed with “superresolution”, which is achievable only with extremely low losses in the plate. Though, at small  $ky_0$  and  $kd$  one may expect rather good results even using existing metamaterials with noticeable absorption, as was in the case of electrically thin focusing plate [6]. Passing on to the greater values of  $ky_0$ , the near field is much more difficult to compensate, and this was proven by calculations.

#### 5. ELECTROMAGNETIC WAVE ABSORBER WITH SPECIAL ANGULAR PROPERTIES

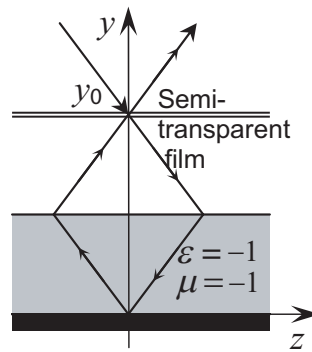


Figure 8.

Finally, note that metamaterials may be efficiently used to create *novel absorbers* of the electromagnetic energy of a plane wave. Their special properties may be achieved, particularly, due to arranging a wave path so as to cross the metamaterial structure with the result of phase advance compensation. An example of the RAM design usable under the incidence of perpendicularly polarized (TM) plane wave is shown in Fig. 8. Provided the electromagnetic response of the semi-transparent film, particularly, its transmission and reflection coefficients were properly chosen, the wave reflected from the film cancels the wave penetrated into and returned back from the region  $y < y_0$ . This latter wave got a negative phase correction when propagated in the metamaterial plate and additional reversal because of the reflection from the conducting plane. It is interesting that total phase advance of that wave is equal to  $\pi$  independently on the incidence angle. Therefore, it is possible to achieve a very broad angular range in which such an absorber should operate efficiently, in contrast to classical designs, like Salisbury screen [1]. In fact, only deviations of semi-transparent film properties impose certain limits to the angular performance. Finally, as there are no fundamental physical restrictions on the thickness of the described absorber, it can be made electrically thin (at least, in principle), as well as earlier suggested system of complementary metamaterials [7].

Our experimental investigations (Fig. 9) support these theoretical suggestions.

The experimental setup is schematically shown in Fig. 9(a). By means of a dihedral corner one face of which is lined with a tested coating the angular dependency of its reflection coefficient can be measured via registering the power of the reflected wave in the course of the corner rotation.

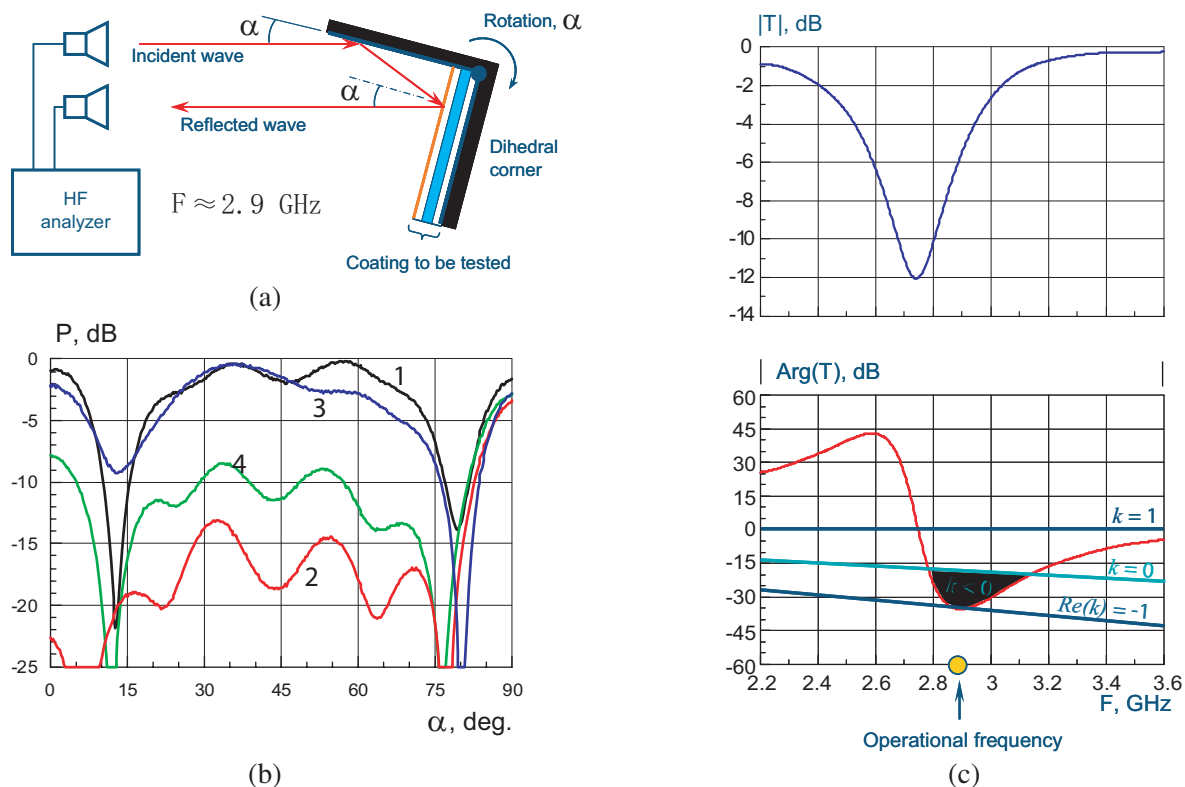


Figure 9.

An example of the measured reflected power (in dB) is depicted in Fig. 9(b), curve 1 corresponds to the uncoated corner, curve 2: metamaterial-based multilayer coating is arranged as suggested in this section, curve 3: only semi-transparent film is placed parallel to the corner face, curve 4: only metamaterial layer is present on the face. The metamaterial sample was prepared using right- and left-handed helices as resonant inclusions, the details of the design are given in [8]. The superiority of the sandwiched structure (curve 2) is clearly seen, one can observe a broad angular range of the efficient absorption. Note, the operational frequency was chosen in such a way as to secure the negative phase advance of the wave penetrated into the metamaterial. To that purpose, the transmission coefficient of the metamaterial slab was measured beforehand; the results are shown in Fig. 9(c).

## 6. CONCLUSION

Thus, the obtained results show that the energy radiated by an omnidirectional (point) source can be completely absorbed by a flat surface with special equivalent impedance. In order to suppress both propagating and evanescent components such a surface should be engineered with the use of metamaterials. However, partial compensating and absorbing essentially propagating modes may be achieved by some other means, for example, using a system of auxiliary scatterers combined with a suitable absorber. Photonic crystals or stacked frequency selective surfaces are also good candidates for that purposes.

Some new opportunities originating from the discussed phenomenon are presented as well. Besides the evident option to use metamaterial layer in order to solve the electromagnetic compatibility problems, we suggest a new design of an open resonator excited by a point source. A new approach to design radio absorbing interference coatings to operate under a plane wave illumination is also introduced. The approach enables one to obtain some specific features of the absorber, e.g., wide angular operational range at small electrical thickness. The latter becomes possible thanks to the fact that the required (e.g., effective negative) phase advance for mutual compensation of the waves reflected from the media interfaces is achieved by the application of a backward wave medium (metamaterial) instead of arranging thick layers of ordinary coating with a subsequent narrowing the angular range. Finally, a possible design of a wide-angle metamaterial-based microwave absorber is shown and experimentally tested.

**REFERENCES**

1. Knott, E. F., J. F. Shaeffer, and M. T. Tuley, *Radar Cross Section*, Artech House, Boston-London, 1993.
2. Veselago, V. G., "The electrodynamics of substances with simultaneously negative values of  $\epsilon$  and  $\mu$ ," *Sov. Phys. Usp.*, Vol. 10, 509, 1968.
3. Engheta, N., "An idea for thin subwavelength cavity resonators using metamaterials with negative permittivity and permeability," *IEEE Antennas and Wireless Propag. Lett.*, Vol. 1, 10–13, 2002.
4. He, S., Y. Jin, Z. Ruan, and J. Kuang, "On subwavelength and open resonators involving metamaterials of negative refraction index," *New Journal of Physics*, Vol. 7, 210, 2005.
5. Pendry, J. B., "Negative refraction makes a perfect lens," *Phys. Rev. Lett.*, Vol. 85, No. 18, 3966–3969, 2000.
6. Lagarkov, A. N. and V. N. Kissel, "Near-perfect imaging in a focusing system based on a left-handed-material plate," *Phys. Rev. Lett.*, Vol. 92, 077401, 2004.
7. Alu, A., F. Bilotti, N. Engheta, and L. Vegni, "A thin absorbing screen using metamaterial complementary pairs," *Proc. of Joint 9th International Conference on Electromagnetics in Advanced Applications (ICEAA 2005) + 11th European Electromagnetic Structures Conference (EESC 2005)*, 229–232, Torino, Italy, September 2005.
8. Lagarkov, A. N., V. N. Semenenko, V. N. Kisel, and V. A. Chistyayev, "Development and simulation of microwave artificial magnetic composites utilizing nonmagnetic inclusions," *J. Magn. Magn. Mater.*, Vols. 258–259, 161–166, 2003.

# Design of Double-frequency Coaxial CTS Antenna

Bo Sun, Jinghui Qiu, Lingling Zhong, and Xiaohang Xing

School of Electronics and Information Technology  
Harbin Institute of Technology, Harbin 150001, China

**Abstract**— Continuous Transverse Stub (CTS) technology is suitable to use with coaxial lines to produce effective microwave antenna structures that radiate omnidirectionally, with high efficiency, low reflection, and useful radiation patterns. In this paper, a new coaxial CTS antenna structure working at double frequency is presented, which reduces the size of antenna without performances changing much. Coaxial CTS antenna consists of several stub elements, and each stub element includes cascade sections of standard coaxial transmission line and open-ended radiating stubs. The proposed antenna consists of five open-ended radiating stubs. Two of the stubs are designed as the low frequency array to operate at 2.45GHz, while the other three stubs are designed as the high frequency array to operate at 12GHz. The basic theory and design method are analyzed, and simulation using CST Microwave Studio<sup>®</sup> commercial software is employed to optimize the antenna's properties. Simulation results shows that the radiant efficiency at 2.45 GHz got to be 78.9%, while the  $-10$  dB bandwidth ( $S_{11} < -10$  dB) was 60 MHz. And at 12 GHz, the bandwidth was about 10% which was 1.2 GHz, and within the bandwidth the radiant efficiency was about 98%. At the upper and lower frequency, the radiating patterns in horizon plane were omnidirectional, the gains were 2.8 dB and 4.6 dB, respectively. The proposed coaxial CTS antenna reduces 40% in size, while the radiation efficiency does not become worse obviously. These simple and low cost coaxial CTS structures could be adapted for base station applications in wireless communication, for satellite communication systems, and for personal communication systems.

## 1. INTRODUCTION

The planar Continuous Transverse Stub (CTS), which was originally invented by W. Milroy at Hughes Aircraft Company in 1991, represents a new category of low-cost antenna array [1]. It is exploiting the low-loss, low-dispersion, dimensional robustness, and design flexibility of an open parallel-plate structure as both its transmission line and radiator bases [2–4]. The planar CTS is composed of cascade CTS elements for high radiation efficiency, and fed by rectangular wave guide expediently. In 2001, based on planar CTS, Magdy F. Iskander and Zhijun Zhang devised coaxial CTS antenna [5].

Besides characteristics of planar CTS antenna, coaxial CTS antenna has some others: (1) It is fed by coaxial line, and it can reduce the reflection loss due to good input impedance; (2) It is convenient to work at multi-frequency; (3) The radiation pattern in horizon plan is omnidirectional; (4) Compared with dipole, electromagnetic wave radiated from slot could transmit better in close space. For these characteristics, coaxial CTS antenna could be widely used in personal communication systems.

## 2. STRUCTURE AND PARAMETERS

Figure 1 shows the structure of double-frequency coaxial CTS antenna. Generally, coaxial CTS antenna consists of several stub elements, and each stub element includes cascade sections of standard coaxial transmission line and open-ended radiating stubs. This double-frequency coaxial CTS antenna includes two CTS arrays, low frequency array and high frequency array. The end near high frequency array is fed by coaxial line, and the other end is connected with a matching load. There are some important parameters for coaxial CTS antenna: (1) width of stub segment  $L_1$ ; (2) length of transmission line segment between stubs  $L_2$ ; (3) diameter of inner conductor  $D_1$ ; (4) diameter of outer conductor  $D_2$ ; (5) diameter of stub  $D_3$ ; and (6) dielectric constant of fill material  $\epsilon_r$ . Customarily, dielectric loading is used to improve the performance and reduce the size of the antenna.

Diameters of inner and outer conductors of the coaxial transmission line could be adjusted to obtain the desired impedance. According to transmission line theory, the impedance of coaxial line is

$$Z_0 = \frac{60}{\sqrt{\epsilon_r}} \ln \frac{D_2}{D_1}$$

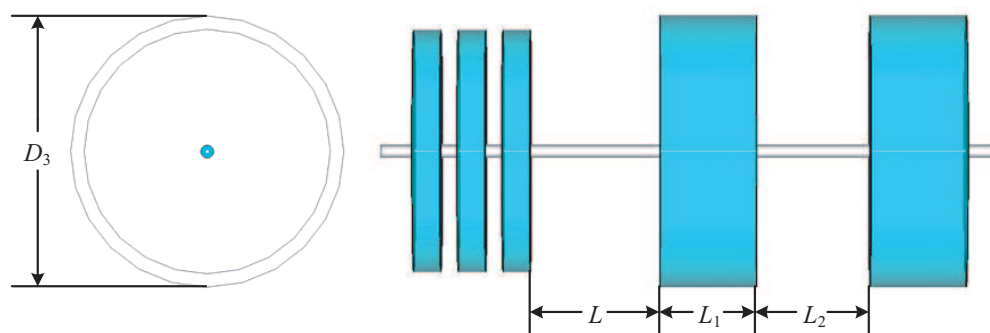


Figure 1: The structure of double-frequency coaxial CTS antenna.

Once the dielectric is selected, the impedance can be determined by the ratio between  $D_1$  and  $D_2$ . In most design,  $50 \Omega$  or  $75 \Omega$  coaxial line is required because of the extensive use in engineering, therefore the antenna design could be predigest. Usually, the width of stubs  $L_1$  is selected to be approximately half wave length in dielectric that fills the stub. The length of transmission line between two stubs  $L_2$  is chosen to fulfill the phase difference so that the interference of waves radiated from stubs is rational to generate expected radiation pattern and gain.

### 3. DESIGN AND ANALYSIS

CST Microwave Studio<sup>®</sup> is used to analyze coaxial CTS antenna, which is electromagnetic simulation software based on finite integral method. Double-frequency coaxial CTS antenna is shown in Figure 1. The proposed antenna consists of five open-ended radiating stubs. Two of the stubs are designed as the low frequency array to operate at 2.45 GHz, while the other three stubs are designed as the high frequency array to operate at 12 GHz. The dielectric filled in the stubs is Teflon, whose relative dielectric constant is 2.2. After calculation and optimization, a series of parameters is selected, shown in the table below.

Table 1: Parameters of double-frequency coaxial CTS antenna.

	$D_1$	$D_2$	$D_3$	$L$	$L_1$	$L_2$
Upper Frequency	1.12 mm	3.6 mm	74.5 mm	40 mm	8.2 mm	5.5 mm
Lower Frequency			83.8 mm		29.3 mm	35 mm

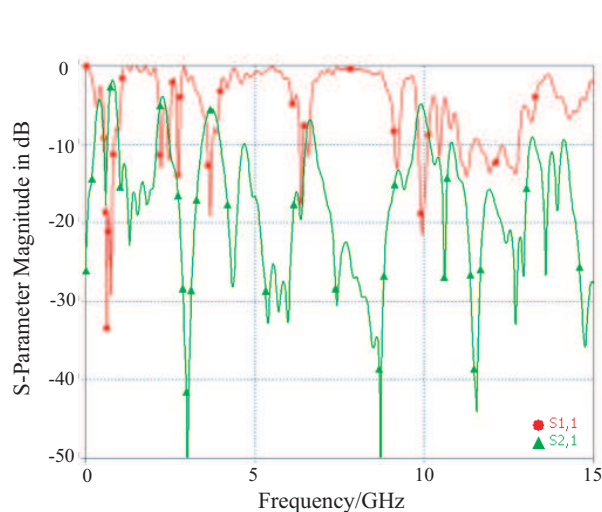


Figure 2: Simulated reflection loss and transmission coefficient.

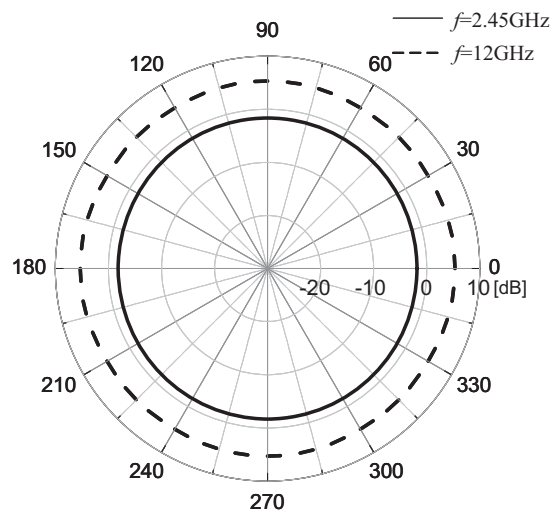


Figure 3: Simulated radiation pattern.

The total length of CTS antenna is sum of length of low-frequency array, high-frequency array and the distance between two arrays. And the length of each array may be calculated by formula

$$\text{length} = L_1 \times n + L_2 \times (n - 1)$$

where  $n$  is number of elements in array. According to the formula above, lengths of arrays can be obtained as follow: the length of HF array is 34.6 mm; the length of LF array is 93.6 mm. Added the distance between two arrays, the total length of antenna is 168.2 mm. The wavelength of 2.45 GHz electromagnetic wave is 122.5 mm, therefore the antenna length is  $1.37\lambda$ . Using the same method, another CTS antenna working at 4.2 GHz and 19.4 GHz has been published, and its length is  $2.25\lambda$  [6].

Because the relative dielectric constant of Teflon is 2.2 and the ratio of the inner and outer diameters is 3.1, the impedance of transmission line is  $50\Omega$ . The reflection loss  $S_{11}$  and the transmission coefficient  $S_{21}$  of the CTS antenna are shown in Figure 2. When the reflection loss  $S_{11}$  reaches the minimum, an expectant transmission appears at the input port, for most energy runs into the coaxial line. At the time when the transmission coefficient  $S_{21}$  arrives at minimum point, the least energy is received at the matching load. The situation that  $S_{11}$  and  $S_{21}$  reach minimum simultaneously may be expected. At that time, most energy comes into the antenna, but the least runs through it. It means that most energy running into the antenna is radiated, and the radiating efficient is the highest. The radiating efficient can be calculated.

Simulation results shows that the radiant efficiency at 2.45 GHz got to be 78.9%, while the -10dB bandwidth ( $S_{11} < -10$  dB) was 60 MHz. And at 12 GHz, the bandwidth was about 10% which was 1.2 GHz, and within the bandwidth the radiant efficiency was about 98%. At the upper and lower frequency, the radiating patterns in horizon plate were omnidirectional, the gains were 2.8 dB and 4.6 dB, respectively. The proposed coaxial CTS antenna reduces 40% in size, while the radiation efficiency does not become worse obviously.

#### 4. CONCLUSIONS

In this paper, a new coaxial CTS antenna structure working at double frequency is presented, which reduces the size of antenna without performances changing much. The basic theory and design method are analyzed, and simulation using CST Microwave Studio® commercial software is employed to optimize the antenna's properties. The proposed antenna only has two elements in lower frequency, and simulation result shows it reduces 40% in size while the radiation efficiency does not become worse obviously. Further more, there is a wide bandwidth in upper frequency. This coaxial CTS antenna could be adapted for base station applications in wireless communication, for satellite communication systems, and for personal communication systems.

#### ACKNOWLEDGMENT

The authors would like to express their sincere gratitude to CST Ltd., Germany, for providing the CST Training Center (North East China Region) at our university with a free package of CST MWS software.

#### REFERENCES

1. Milroy, W. W., "The continuous transverse stub (CTS) array: Basic theory, experiment, and application," *Proc. Antenna Applications Symp.*, Sept. 25-27, 1991.
2. Iskander, M. F., Z. Yun, Z. Zhang, R. Jensen, and S. Redd, "Design of a low-cost 2-D beam-steering antenna using ferroelectric material and the CTS technology," *IEEE Trans. Microwave Theory Tech.*, Vol. 49, 1000-1003, 2001.
3. Matterer, V. P., "Phase tuning technique for a continuous transverse stub antenna arrays," U.S. Patent 5604505.
4. Chu, R.-S., "Analysis of continuous transverse stub (CTS) array by floquet mode method," *1998 IEEE International Antennas and Propagation Symposium and USNC/URSI National Radio Science Meeting*, Vol. 2, June 21-26, 1998.
5. Iskander, M. F., Z. Zhang, Z. Yun, and R. Isom, "Coaxial continuous transverse stub (CTS) array," *IEEE Microwave and Wireless Components Letters*, Vol. 11, No. 12, 489-491, December 2001.
6. Isom, R., M. F. Iskander, Z. Yun, and Z. Zhang, "Design and development of multiband coaxial continuous transverse stub (CTS) antenna arrays," *IEEE Transactions on Antennas and Propagation*, Vol. 52, No. 8, 2180-2184, 2004.

# Frequency Scanning Using Micro-strip Array Antenna

Alireza Bayat<sup>1</sup> and Mitra Torabipour Banadkok<sup>2</sup>

<sup>1</sup>Department of Communication Engg., Imam Khomeini International University, Iran

<sup>2</sup>Ministry of TCI, Iran

**Abstract**— Micro-strip antennas are ideally suited for arrays which can be used to electronically scan the radiation beam essentially needed for longer detection range and faster data rate (short reaction time). In the present study the micro strip array antenna consists of two series of array which are parallel to each other and each series consists of nineteen elements which is rectangular in shape. Each element functions as a radiator and phase shifter. Unlike a conventional planar array, however, the elements on the array surface are spatially fed using a quarter wave transformers, which is cascade, coupled to each other. With electronic scanning it is possible to obtain practically instantaneous slewing of an antenna radiation beam to any position in the designated sector. Other features, such as scanning exhibited by the proposed antenna is  $120^\circ$  in azimuth as in Fig. 3 which is just, double the scanning reported by Danielson [1]. The scanning rate of 0.117 deg/MHz is observed which is better than the earlier reported rate of 0.1 deg/MHz Fig. 4.

## 1. INTRODUCTION

Now a day the radar technology has developed to such an extent that it plays an important role in communication field. However, radar needs some cyclic modification of radiation beam or pattern of the antenna such that it can be suitable for practical requirements which are called beam scanning. Searching of the target requires the scanning of the large volume of space. In past the mechanism by which radar beam was used for searching through space was mechanical. Where a motor rotates the antenna. However, such a bodily movement is difficult for large antenna. Moreover, this method is obviously is costly, heavy and complex. Due to growing needs for radars such as longer detection ranges, faster data rates and accommodate increased target densities, it is necessary to have some new design concept in radars. Most promising of these approaches is electronic scanning. With electronic scanning it is possible to obtain practically instantaneous slewing of an antenna beam to any position in a designated sector. Electronic scanning can be defined as method of slewing or positioning of EM beam of an antenna in large volume of space by electronic means with the antenna aperture remaining fixed in space and no mechanical mechanism is involved in the scanning process. Thus, the electronic scanning systems avoid such complexity and hence are found to be lighter and may be cheaper. Because of the above-mentioned advantages of the electronic scanning, it was thought useful to design and develop some new electronic scanning antennas. Initially the analysis of micro strip patch is considered which is used to design and developed the new series parallel array antenna. The entire investigations both theoretical and experimental are given in the following section.

## 2. MECHANISM OF RADIATION

The mechanism of radiation from micro-strip antenna can be understood by defining the radiation from discontinuities. The radiation field in micro strip antennas occurs from the fringing fields between the edge of the micro strip antenna and the ground plane. The simplest case of micro strip antenna is a rectangular micro strip patch spaced a small fraction of a wavelength above a ground plane, as shown in Fig. 1. The fields vary along the patch length, which is about half a wavelength ( $\lambda/2$ ). Radiation may be described to mostly to the fringing fields at the open circuited edge of the patch. The field at the edge can be resolved into normal and tangential components with respect to the ground plane. The normal components are out of phase due to the length of patch, which is equal to the ( $\lambda/2$ ). Therefore, the far field produced by them cancels in the broad side direction. The tangential components (which are parallel to the antenna patch) are in phase, and these fields combine to give maximum radiation normal to the surface of the antenna. Therefore, the patch may be represented by two slots ( $\lambda/2$ ) apart.

### 3. METHOD OF EXCITATION

In this theory source is derived with the help of fringing capacitance, which is due to the fringing field at the edges of the patch [1]. The following assumptions are made while analyzing the radiation from patch.

- 1- Radiation is proportional to the length of the radiating slot, i.e., ( $w$ ).
- 2- There, is negligibility small coupling between the two radiating slots?
- 3- The radiating patch and ground plane with the dielectric material is treated as capacitor. As per transmission line model, the radiation is due to the fringing field at the edge of the patch,  $w$  to calculate the radiation patterns, source that is due to the fringing field on the two edge of patch must be found out as shown in Fig. 1.

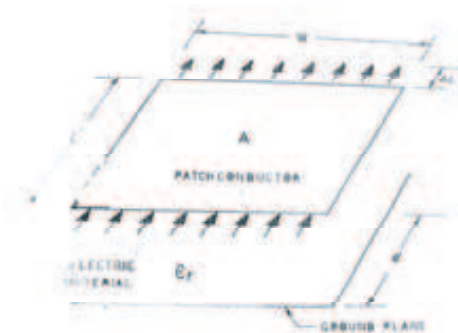


Figure 1: Capacitor model micro-strip patch.

The capacitance “ $C$ ” formed by the patch and the ground plane may be defined as  $C = \frac{\epsilon(L \cdot W)}{d}$ , where  $L$ ,  $W$ , are length and width of the patch respectively,  $d$  is separation between plates.

### 4. PHASE SCANNING ARRAY

It is therefore, logical to assure that the maximum radiation beam can be positioned in any direction to form a scanning array. Let us assure that the maximum radiation of the array is required  $\theta_m$  such that ( $0 < \theta_m < 180^\circ$ ). To get this condition the phase excitation  $\alpha$  between the elements must be adjusted in such a manner that ( $\psi = kd \cos \phi + \alpha$ , where,  $k = \frac{2\pi}{\lambda_0}$  and  $\alpha$  is equal to progressive phase shift between elements.)  $\psi$  becomes  $\psi = kd \cos \phi + \alpha|_{\phi=\phi_m} = kd \cos \theta_m + \alpha = 0$ . Therefore,  $\alpha = -kd \cos \phi_m$ . Thus, the beam of an array may be steered rapidly in space by properly controlling the progressive phase difference between the elements. This is the basic principle of electronic scanning by phased array operation.

### 5. TIME DELAY SCANNING

It is special case of phase scanning [3]. It differs from phase scanning that time delay is used instead of phase delay to form a beam in the specified direction. A time delay device may easily be realized by switching different lengths of transmission line from one element to another providing an incremental delay from element to element of  $t = \frac{d}{v} \sin \theta$ . Where  $v$  is velocity of propagation &  $d$  is spacing between two elements. In practice, individual time delay circuits are too complex and hence a reasonable representation may be reached by adding one-time delay network to a group of elements that have phase shifter.

#### 5.1. Frequency Scanning Array

An electromagnetic wave while propagating through a transmission line of length  $L$  will encounter a phase change and is given as:

$$\phi = \frac{2\pi fl}{v}$$

where,  $L$  is the length of line.

According to above formula by changing in frequency, some change in phase will occur & this can be used for electronically scanning the beam. Let consider a set of radiator spaced a distance

apart, the above equation expresses the phase difference between two adjacent elements in the series fed array and hence

$$\phi = \frac{2\pi L}{\lambda}$$

For beam to be pointed in a direction  $\phi$ , the phase difference between elements must be given as:

$$\psi = 2\frac{\pi d}{\lambda} \sin \phi.$$

It may be mentioned that the addition of an integral of  $2\pi$ -radian relative phase difference per unit, a required scan angle can be obtained with smaller frequency variation. If “ $m$ ” be the integer number of  $2\pi$  radius that is added then. Therefore,

$$\sin \phi = \frac{L}{d} - \frac{m}{d}\lambda$$

As the frequency changes one beam after another will appear and disappear, each beam corresponding to a different value of  $m$ .

## 6. PARALLEL & SERIES FED MICRO-STRIP SCANNING ARRAY

One of the most important factors of the micro-strip array antenna is the feeding network, which should be designed to occupy less space and provide perfect matching, resulting in more efficient array [4].

Series array configurations have advantages to the micro-strip antenna designer. First, feed line lengths are inherently minimized, thus reducing line decrease array efficiency. Second, in large array high power feed lines are decoupled from elements radiating low-power level. This control aperture distribution to synthesize accurately shaped patterns with low side lobes level [5] & finally steered beam can be easily achieved.

### 6.1. Single Micro-strip Resonator

The basic elements in the antenna array are micro-strip transmission resonator with a common conducting ground plain. The phase shift through the resonator is fixed to the same value for all elements in the array. With the purpose to calculate the phase shift through the resonator from reference plane  $B$  to  $C$  in Fig. 2 the resonator is connected to equivalent input and output lines with the characteristic admittances  $Y_0'^2/Y_0$  and  $Y_{00}'^2/Y_{00}$ , respectively, obtained by the transformation and the real transmission line characteristic admittances through the quarter wave length transformers. The field transmission coefficient from point  $B$  to  $B'$  is given by:

$$\eta_1 = 1 - \rho_1' = \frac{\frac{2Y_0'^2}{Y_0}}{\frac{Y_0'^2}{Y_0} + Y + G}$$

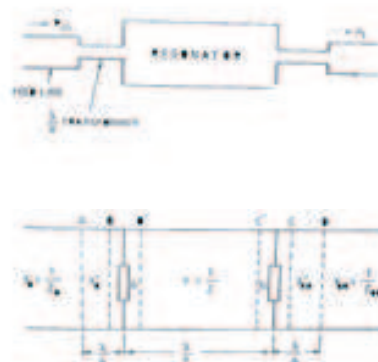


Figure 2: Transmission micro-strip resonator and its equivalent network.

Similarly the field transmission coefficient from point  $C'$  to  $C$  is

$$\eta_2 = 1 + \rho'_2 = 2Y/Y_0'^2/Y_0 + Y + G$$

Mutual coupling between elements has been neglected. The excitation of the element is then given by:

$$I_m = I_0 \sqrt{P_n} \quad 1 < m < N$$

where  $I_0$  is the normalization constant.

## 7. DESIGN OF PATCH RADIATOR

These arrays are connected in parallel to provide an equal power and phase excitations. The distance between elements are kept  $P$  free space wavelength ( $P\lambda$ ), while the distance between the arrays nearly equal to  $0.75\lambda_0$ , to avoid formation of grating lobes. Glass epoxy is used as a substrate material and the operating frequency is 9.00 GHz. Two identical arrays are used to increase radiated power level and get wider scanning angle with wide bandwidth. The practical width of the patch may be given by:

$$W = \frac{c}{2f_r} \left( \frac{\epsilon_{r+1}}{2} \right)^{-1/2}$$

Hence, the length of the patch can be given as:

$$L = \frac{C}{2f_r \sqrt{\epsilon_r}} - 2\Delta L$$

The input resistance of the patch is given by  $R_L = \frac{1}{20} \Omega$ , form which quarter wave transformer can be designed. The patch impedance is given by  $Z = 1/Y_{in}$ .

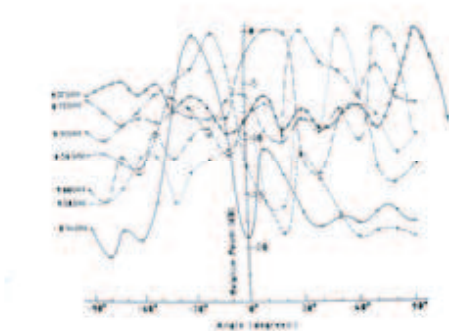


Figure 3: H-plane radiation pattern.

## 8. DISCUSSION OF RESULT

The examination of the H-plane patterns Fig. 3 reveals that there is a beam scanning of  $\pm 60^\circ$  with a 3 dB beam width less than  $15^\circ$  for a sweep interval of  $\pm 515$  MHz. The scanning exhibited by the proposed antenna is  $120^\circ$  which is just double the scanning reported by Danielson [1]. All patterns are combined in Fig. 3, just to indicate the scanning characteristics. The scanning rate of  $0.117$  deg/MHz is observed which is better than the earlier reported rate of  $0.1$  deg/MHz Fig. 4. However, there is appreciable increase in the beam width which is shown in Fig. 6, when antenna is operated in the off-resonance region toward lower frequency side. It has been observed that scanning range, scanning rate and radiated power improve when number of elements in the array is increased. Further the radiated power increases with frequency Fig. 5. The variation of VSWR with frequency Fig. 7 shows that the value of VSWR is considerably high for lower range of frequency. This is why the radiated power is substantially low in this range of frequency.

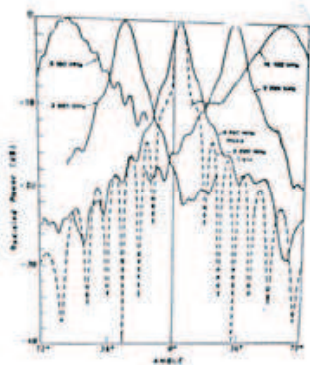


Figure 4: Radiation pattern for antennas with parameters  $T = 0.6$ ,  $k = 0.65$ ,  $r = 0.95$  full lines: measured patterns Dotted line theoretical pattern 9.6 GHz.

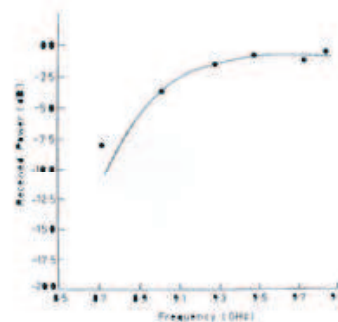


Figure 5: Received power vs. frequency for H-plane.

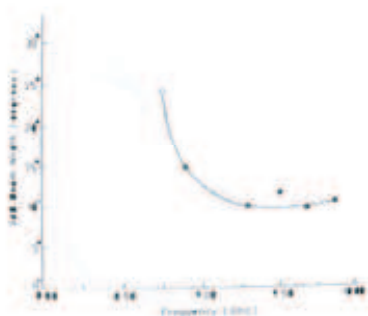


Figure 6: 3dB-beam width vs. frequency for H-plane.

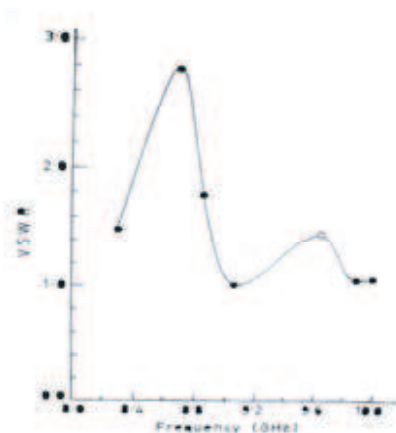


Figure 7: VSWR vs. frequency.

## 9. SUMMARY

With electronic scanning it is possible to obtain practically instantaneous slewing of an antenna radiation beam to any position in the designated sector. In the present endeavor therefore both theoretical and experimental investigations were carried out on frequency scanning micro strip array antenna the results of which embody the present paper. The scanning rate of 0.117 deg/MGH is observed which is better than the earlier report rate of 0.1 deg/MGH. The 3 db beam width of the antenna is less than  $15^\circ$  around the center frequency. The variations of VSWR with frequency Fig. 7 show that the value of VSWR is considerably high for lower range of frequency. This is why the radiated power is substantially low in this range of frequency and much of the input power to the antenna is lost as reflected power [5].

## REFERENCES

1. Danielson, M. and R. Jorgensen, "Frequency scanning micro strip antenna," *IEE-I*, Vol. 27, No. 2, 1979.
2. Arif-Ahmad Al-Fitianl, "Radiation and scanning characteristics of micro strip antennas," BHU, India, Jan. 1989.
3. Byron, E. V., "A new flash mounted antenna element for phased array application," *Proc. Phased Array Antenna Symp.*, 187-192, 1970.
4. Mrstik, A. V. and P. G. Smith, "Scanning capabilities of large parabolic cylinder reflector antenna with phased-array feeds," *IEEE Trans. Antennas Propagat.*, Vol. 29, No. 3, 455-462, May 1981.
5. Spradley, J. L., "A volumetric electrically scanned two-dimensional microwave antenna array," 204-218.

# Cluster Head Selection Using Evolutionary Computing in Wireless Sensor Networks

G. Ahmed<sup>1</sup>, N. M. Khan<sup>1</sup>, and R. Ramer<sup>2</sup>

<sup>1</sup>Mohammad Ali Jinnah University, Pakistan

<sup>2</sup>University of New South Wales, Australia

**Abstract**— Wireless Sensor Network (WSN) comprises of micro sensor nodes with limited energy and processing ability. It is used in military as well as civil applications. In order to enhance the network life time by the period of a particular mission, many routing protocols have been devised. One of these are network clustering, in which network is partitioned into small clusters and each cluster is monitored and controlled by a node, called Cluster Head (CH). The CH should be powerful, closer to the cluster-centroid, less vulnerable and has low mobility, so that it can aggregate the data from its own cluster nodes and then send it directly to the Base Station (BS). In this paper, we are using the method of evolutionary computing for the selection of the CHs. The BS periodically runs the proposed algorithm to select new CHs after a certain period of time. Results show that network life time is drastically increases by the help of evolutionary computing.

## 1. INTRODUCTION

Wireless Sensor Network (WSN) comprises of micro sensor nodes with limited energy and processing ability. It is used in military as well as civil applications. In order to enhance the network life time by the period of a particular mission, many routing protocols have been devised. One of these is network clustering, in which network is partitioned into small clusters and each cluster is monitored and controlled by a node, called Cluster Head (CH). These cluster heads can communicate directly with the base station (BS). Other nodes send the data, sensed from the environment to these CHs. CHs first aggregates the data from the multiple sensor nodes, and then finally send it directly to the BS. Hence the CH should be powerful, closer to the cluster-centroid, less vulnerable [5] and has to have low mobility. These factors on which CH selection should depend, are described in Section 2.

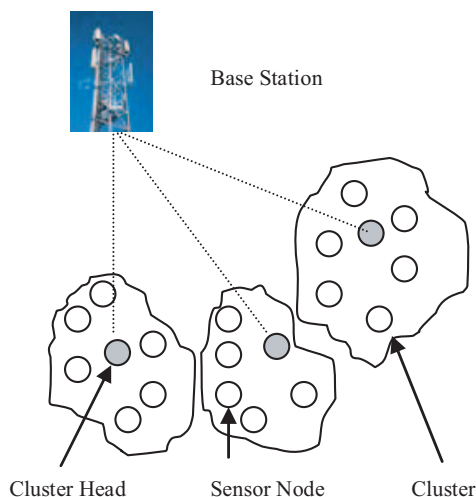


Figure 1: Wireless Sensor Network.

Several analyses of energy efficiency of sensor networks have been realized [2, 3, 7, 8] and several algorithms that lead to optimal connectivity topologies for power conservation have been proposed [1, 6, 9–12]. But most of them do not provide long lifetime system in a dynamic environment, where the sensors are unattended and it is very difficult to recharge their battery. Therefore we need more energy-efficient solution. In this paper, we are using Evolutionary Computing (EC), also called Genetic Algorithm (GA) for CH selection in a cluster-based WSN. Many aspects of such an evolutionary process are stochastic [4].

The rest of the paper is organized as follows: Section 2 describes the four factors that influence the network lifetime; Section 3 describes our approach to CH selection in a sensor network. Finally, Section 4 concludes the paper.

## 2. FOUR FACTORS THAT INFLUENCE NETWORK LIFETIME

A brief discussion of four factors is given below:

1. Distance of a node from the cluster centroid: The BS calculates the distance of each node to its cluster centroid. The lesser the distance, the higher the probability that the node will become CH.
2. Remaining battery power: Obviously, the higher the battery power, the higher the probability that the node will become CH.
3. Degree of mobility: The mobility of the node has great impact on the network lifetime. The topology of the network will be change very frequently due to the high mobility of nodes, which leads to reselection of CHs rapidly.
4. Vulnerability index: This factor tells us how much vulnerable a node is. If it is high, then the node will not be selected as the CH. A detail discussion of this factor can be found in [5].

## 3. CLUSTER HEAD SELECTION USING GA

Our goal is to search best sensor nodes among hundreds of nodes, so that they can act as CHs. Conventional search methods are not robust, while the GA is a search procedure that uses random choice as a tool to guide a highly exploitative search through a coding of a parameter space. According to Goldberg in [4], the GA has 4 major characteristics:

1. GAs with a coding of the parameter set, not the parameters themselves.
2. GAs search from a population of points, not a single point.
3. GAs use payoff (objective function) information, not derivatives or other auxiliary knowledge.
4. GAs use probabilistic transition rules, not deterministic rules.

In many optimization methods, we move carefully from a single point in the decision space to the next using some transition rule to determine the next point. This point-to-point method is dangerous because it is a perfect prescription for locating false peaks in multi modal (many peaked) search spaces. By contrast, GA works from a rich database of points simultaneously (a population of strings), climbing many peaks in parallel; thus, the probability of finding a false peak is reduced over methods that go point-to-point [4].

A GA starts with a population of strings and thereafter generates successive populations of strings. A simple GA consists of three operators:

1. Reproduction
2. Crossover
3. Mutation

The chromosome of the GA contains all the building blocks to a solution of the problem at hand in a form that is suitable for the genetic operators and the fitness function. Each individual sensor node is represented by a 4-bit binary number called ‘gene’. These four-bit genes which define the feature of the node are called “allele” and are represented as follows:

**X1X2X3X4**

**X1:** distance of a node from the cluster centroid,

**X2:** its vulnerability index,

**X3:** its degree of mobility, and

**X4:** its remaining battery power.

The possible values of these 4 attributes are shown in Table 1.

Let’s take an example. To start off, select an initial population at random. Here, we select a population of size 4. Each string (node) has some fitness value. This value can be evaluated from a fitness function,  $f(x) = f(x_1, x_2, x_3, x_4)$ . In the case of WSN, the fitness function depends upon the four factors, discussed in Section 2. Nodes with higher energy, low mobility, closer to the cluster centroid and low in vulnerability have high fitness values and can be declared as CHs. For our example, let  $f(x) = x^2$ .

A generation of the GA begins with reproduction. We select the mating pool of the next generation by spinning the weighted roulette wheel four times. From this, the best string get more copies, the average stay even, and the worst die off.

Table 1: Possible values for the attributes.

<b>X1</b>	Near	Far
<b>X2</b>	Low	High
<b>X3</b>	Low	High
<b>X4</b>	High	Low
<b>Digital Value</b>	<b>1</b>	<b>0</b>

Table 2: CH selection through GA.

No.	Node*	x	f(x) =x <sup>2</sup>	Pselect <sub>i</sub> (f <sub>i</sub> /Σf)	Expected Count (f <sub>i</sub> /avg(f))	Actual Count**	Mating Pool***	Mate ****	Cross- Over Site*****	New Nodes	X	f(x)=x <sup>2</sup>
1	0110	6	36	0.12	0.51	1	011 0	2	3	0110	6	36
2	1100	12	144	0.51	2.07	2	110 0	1	3	1100	12	144
3	0100	4	16	0.05	0.23	0	11 00	4	2	1101	13	169
4	1001	9	81	0.29	1.16	1	10 01	2	2	1000	8	64
<b>Sum</b>			277	1.00	4.00	4.0						413
<b>Avg.</b>			69.25	0.25	1.00	1.0						103.25

\*Initial population (Randomly Generated)

\*\*From Roulette Wheel

\*\*\*After Reproduction (Cross site shown)

\*\*\*\*Randomly selected

From Table 2, we can see that the CHs have improved in the new population. Nodes which are not copying in the next generation will not be elected for CH in the future. In case if the new nodes (offspring) are not present in current WSN setup (have become die off), then we will exclude it for further processing.

#### 4. CONCLUSIONS

The improvement that is provided by GA is not a fluke (a lucky or unusual thing that happens by accident). In our example Table 2, the best string of the first generation (1100) receives two copies because of its high, above average performance. When this combines at random with the next highest string (1001) and is crossed at location 2 (again at random), one of the resulting strings (1101) proves to be a very good choice for CH indeed.

#### ACKNOWLEDGMENT

The authors would like to thanks to Mr. Badaruddin, PhD Scholar at Institute of Business Administration (IBA), Karachi for his help and guidance.

#### REFERENCES

1. Chmielewski, D. J., T. Palmer, and V. Manousiouthakis, "On the theory of optimal sensor placement," *AIChE J.*, Vol. 48, No. 5, 1001–1012, 2002.
2. Slijepcevic, S. and M. Potkonjak, "Power efficient organization of wireless sensor networks," *Proc. IEEE Int. Conf. on Communications*, 472–476, Helsinki, Finland, 2001.
3. Krishnamachari, B. and F. Ordoñez, "Analysis of energy-efficient, fair routing in wireless sensor networks through non-linear optimization," *Proc. IEEE Vehicular Technology Conference — Fall*, 2844–2848, Orlando, FL, 2003.
4. Goldberg, D., *Genetic Algorithm in Search, Optimization and Machine Learning*, Addison-Wesley Publishing Company, Inc, 1989.
5. Khalid, Z., G. Ahmed, N. M. Khan, and P. Vigneras, "A real-time energy-aware routing strategy for wireless sensor networks," accepted for presentation in *The 2007 Asia-Pacific Conference on Communications*, Bangkok, Thailand, 2007.
6. Zhou, C. and B. Krishnamachari, "Localized topology generation mechanisms for wireless sensor networks," *IEEE GLOBECOM'03*, San Francisco, CA, December 2003.

7. Trigoni, A., Y. Yao, A. Demers, J. Gehrke, and R. Rajaraman, "Wave Scheduling: energy-efficient data dissemination for sensor networks," *Proc. Int. Workshop on Data Management for Sensor Networks (DMSN)*, in conjunction with *VLDB*, 2004.
8. Mhatre, V., C. Rosenberg, D. Kofman, R. Mazumdar, and N. Shroff, "A minimum cost heterogeneous sensor network with a lifetime constraint," *IEEE Trans. Mobile Comput.*, Vol. 4, No. 1, 4–15, 2005.
9. Ghiasi, S., A. Srivastava, X. Yang, and M. Sarrafzadeh, "Optimal energy aware clustering in sensor networks," *Sensors*, Vol. 2, 258–269, 2002.
10. Rodoplu, V. and T. H. Meng, "Minimum energy mobile wireless networks," *IEEE J. Select. Areas Commun.*, Vol. 17, No. 8, 1333–1344, 1999.
11. Heinzelman, W. R., A. Chandrakasan, and H. Balakrishnan, "Energy-efficient communication protocol for wireless microsensor networks," *Proc. 33rd Hawaii Int. Conf. on System Sciences*, Maui, Hawaii, 2000.
12. Chang, J.-H. and L. Tassiulas, "Energy conserving routing in wireless ad-hoc networks," *Proc. IEEE INFOCOM'00*, 22–31, Tel Aviv, Israel, 2000.

# A Robust Transmission Technique for Arbitrary 3D Images in Wireless Multimedia Sensor Networks

G. Ahmed<sup>1</sup>, N. M. Khan<sup>1</sup>, and R. Ramer<sup>2</sup>

<sup>1</sup>Mohammad Ali Jinnah University, Pakistan

<sup>2</sup>University of New South Wales, Australia

**Abstract**— Wireless Multimedia Sensor Networks (WMSNs) are networks of wirelessly interconnected devices that are able to ubiquitously retrieve multimedia content such as video and audio streams, still images, and scalar sensor data from the environment. Transmission of 3D objects over unreliable wireless medium is a challenging issue. In this paper, we are focusing on this issue and describe a perceptually motivated strategy for transmission of 3D objects represented by texture and mesh over unreliable WMSNs. The proposed approach can also be used for scalable transmission as well, allowing graceful degradation of a 3D model under limited bandwidth.

## 1. INTRODUCTION

Wireless Multimedia Sensor Networks (WMSNs) are networks of wirelessly interconnected devices that are able to ubiquitously retrieve multimedia content such as video and audio streams, still images, and scalar sensor data from the environment. With rapid improvements and miniaturization in hardware, a single sensor device can be equipped with audio and visual information collection modules. In addition to the ability to retrieve multimedia data, WMSNs will also be able to store, process in real-time, correlate and fuse multimedia data originated from heterogeneous sources. Potential applications of WMSNs include remote video-based surveillance, traffic monitoring, virtual reality, tracking, home automation, and environmental monitoring.

The wireless medium used in WMSNs is characterized by highly unreliable, mostly caused by multi-path channel fading, and shadowing at the physical layer, collisions or co-channel interference at the MAC layer, high path loss, noise disturbances, and bit error rate (BER), these result in the wireless channel having much lesser capacity than wired channels [3]. Thus, streaming of real-time multimedia data over a wireless sensor network is particularly challenging due to the QoS requirements of a video/audio stream and the unreliability of the wireless medium.

In this paper, we describe a perceptually motivated strategy for transmission of 3D objects represented by texture and mesh over unreliable WMSNs. The rest of the paper is organized as follows: Section 2 describes the proposed strategy; and Section 3 concludes the paper.

## 2. PROPOSED STRATEGY

When transmitting 3D object especially irregular mesh data, not only vertex information but also connectivity information plays a crucial role in 3D reconstruction at the client site. In order to preserve the original geometry of the object, many transmission algorithms suggest retransmission [4] of the base layers to safeguard the successful transmission of important features of the object [1, 2]. Retransmission adds an overhead on bandwidth limited connections, in particular on wireless and mobile networks. Without the need to retransmit the base layer, our goal is to find a robust approach for 3D transmission of arbitrary meshes. Our approach to arbitrary meshes considers stripification of the mesh and distributing nearby vertices into different packets, combined with a strategy that does not need texture or mesh packets to be re-transmitted. Only the valence (connectivity) packets need to be re-transmitted; however, storage of valence information requires only 10% space compared to vertices and even less compared to photo-realistic texture. Thus, less than 5% of the packets may need to be re-transmitted in the worst case to allow our algorithm to successfully reconstruct an acceptable object under severe packet loss.

We can also transmit real-time data through this approach. In this case, to avoid the delays in requesting re-transmission of packets, it may be wiser to send duplicate packets containing the connectivity information so that real-time visualization of photo-realistic texture mapped 3D objects at high packet loss can be facilitated. The proposed approach can also be used for scalable transmission as well, allowing graceful degradation of a 3D model under limited bandwidth [5].

Our approach focuses on following two factors:

1. Efficient compression based on stripification [5]
2. Robustness to packet loss based on distribution of neighboring vertices into different packets [6]

The sensor nodes encode and group the data (vertices) into different packets and transmit them to sink or base station (BS). After all the packets are received by the BS, first, the mesh is partially reconstructed based on the partial geometry packets and connectivity; following the same order as in the encoding process. Then, the vertices are traversed in the reconstruction order of the valence-driven decoding algorithm [7]. When a vertex with lost geometry,  $L$ , is encountered, the adjacent reconstructed vertices with an edge connected to  $L$ , whose geometry is either not lost or is interpolated previously, are used to interpolate the geometry of  $L$ . A linear interpolation algorithm can be used for the interpolation of the missing vertices.

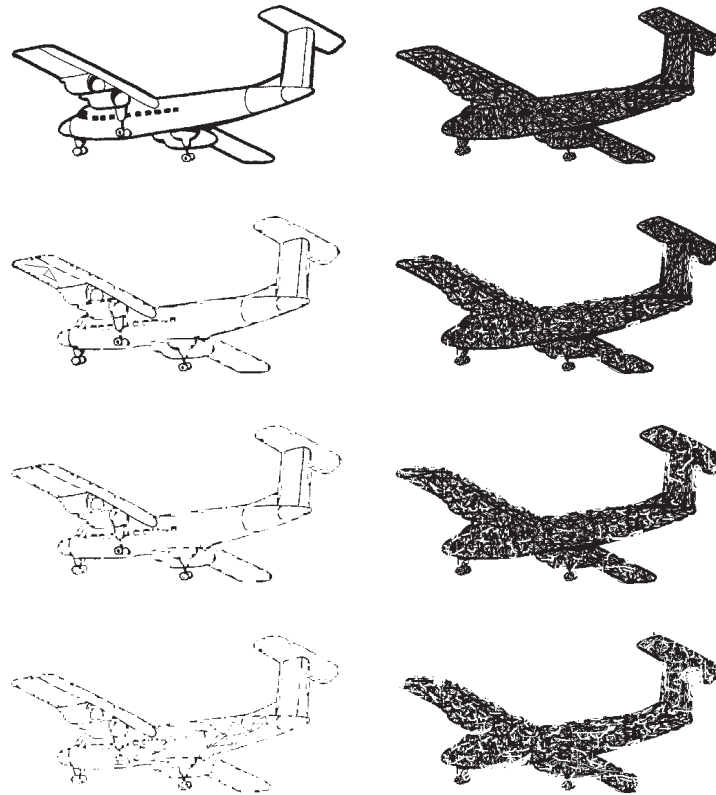


Figure 1: An airplane meshes in left column highlighting the packet loss region before interpolation, while the same airplane mesh after the interpolation is shown in the left column. From top to bottom: 0%, 30%, 60% and 80% packet loss.

### 3. CONCLUSIONS

In Figure 1, 30%, 50%, 60%, and 80% randomly selected vertices were lost for an airplane meshes. However, the lost geometry was interpolated based on neighboring vertices and valence information, which is transmitted without error. It can be seen that smoothness on the object surface begins to deteriorate at about 60% loss. Visual degradation becomes more obvious at 80% loss; still the object is recognizable as airplane.

### ACKNOWLEDGMENT

The authors would like to thanks to Mr. Zubair Khalid, MS Scholar at GIK Institute of Engineering, Sciences & Technology, Topi, Pakistan, for his help and guidance.

### REFERENCES

1. Misra, S., M. Reisslein, and G. Xue, "A survey of multimedia streaming in wireless sensor networks," submitted work, [www.fulton.asu.edu/~mre/WSNstreaming.pdf](http://www.fulton.asu.edu/~mre/WSNstreaming.pdf).

2. Limb, J. O., "Distortion criteria of the human viewer," *IEEE Trans. Systems, Man and Cybernetics*, Vol. 9, No. 12, 778–793, 1979.
3. Jakes, W., *Microwave Mobile Communications*, John Wiley and Sons, New York, 1974.
4. Wittenburg, G. and J. Schiller, "A quantitative evaluation of the simulation accuracy of wireless sensor networks," *Proceedings of 6. Fachgesprach "Drahtlose Sensornetze" der GI/ITG-Fachgruppe "Kommunikation und Verteilte Systeme"*, Aachen, Germany, July 2007.
5. <http://www.cosy.sbg.ac.at/~held/projects/strips/strips.html>.
6. Cheng, I., L. Ying, and A. Basu, "A perceptually driven model for transmission of arbitrary 3D models over unreliable networks," *Proc. 3rd International Symp. 3D Data Processing, Visualization and Transmission (3D PVT'06)*, 421–428, Washington, USA, June 2006.
7. Touma, C. and C. Gotsman, "Triangle mesh compression," *Proc. Graphics Interface Conference*, 26–34, 1998.

# Medical Imaging and Diagnostics Based on Microwaves

**Jan Vrba, Ladislav Oppl, Radim Zajicek, Katerina Novotna, and David Vrba**  
Department of EM Field, Czech Technical University in Prague, Prague, Czech Republic

**Abstract**— Future trends in medical applications of microwave technique and technology can be seen in development of new diagnostic and imaging methods based on high frequency EM field. A significant importance for the future can be identified for the following methods: Microwave tomography, Microwave radiometry, Measurement of complex permittivity, Imaging in the Terahertz waves band and Microwave diagnostic radars.

## 1. INTRODUCTION

Interactions of EM field with biological systems are utilised in the area of therapy (oncology, physiotherapy, urology atp.) from late seventieth of last century. Wideutilization of microwave thermotherapy can be observed in the countries of EU, USA and Japan. Our activities in microwave thermotherapy in former Czechoslovakia started in the year 1981. Since 1990 we are member of ESHO (European Society for Hyprthermia Oncology), which co-operates with NAHS (North American Hyperthermia Society) and ASHO (Asian Society of Hyperthermia Oncology).

Recent trends in microwave medical applications are to study the possibilities to develop new diagnostics based on EM field resp. on microwace technique. A significant importance for the future can be identified for the next methods:

- Magnetic resonance,
- Microwave tomography,
- Microwave radiometry,
- Measurement of complex permittivity,
- Imaging with terahertz waves,
- Microwave diagnostic radar.

We will not talk here about magnetic resonance, as it is just well known and broadly used application of EM field in medical diagnostics. We will focus here on other above mentioned methods (excluding microwave diagnostics radars).

## 2. MICROWAVE APPLICATORS FOR MEDICAL IMAGING AND DIGNOSTICS

Since 1981 we develop waveguide applicators working in frequency band from 27 MHz up to 2450 MHz. These applicators were used for the treatment of more then 1000 patients with superficial or sub-cutaneous tumors (up to the depth cca 4–6 cm). Now, following new trends in this field, we continue our research in the important directions of deep local and regional applicators. We have found, that quite similar applicators are optimal to be used for medical imaging and diagnostics.

Examples of mentioned applicators are given in the F

## 3. MICROWAVE TOMOGRAPHY

Microwave tomography [1] is in general application of basic CT principals but by utilization of microwave band. Scattering of EM waves in non-homogeneous human body is however much more complicated than simple attenuation of ionising radiation. Therefore development of microwave tomography is conditioned by new theoretical approach, optimization of evaluation algorithms and more efficient computer technique.

An experimental setup is schematically shown on next figer. Studied object will be placed in water phantom. It will be irradiated by transmitting antenna while scattered EM field will be monitored by receiving antenna and evaluated by a network analyser. Receieving antenna will be scanning around studied object and/or it will be possible to move/rotate the studied object.

Microwave tomography represents applications of CT known principals to microwave frequency band, where in general situation is more complicated because of much more complicated propagation of EM waves. Therefore mathematical model should be created and optimized evaluation algorithms are needed and last but not least — powerful computers are necessary for the calculations.

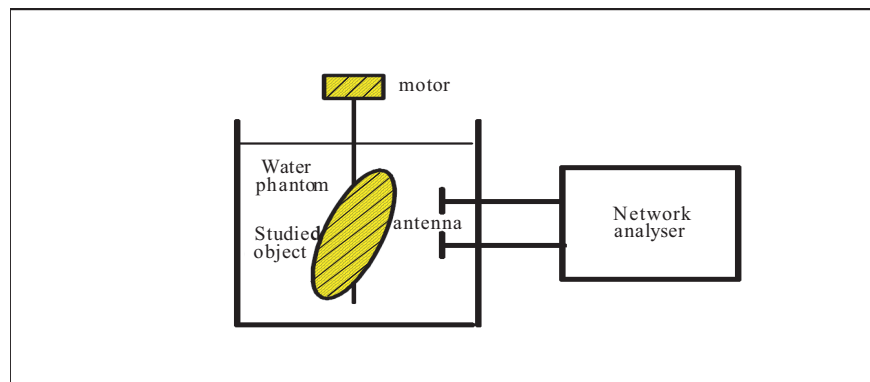


Figure 1: Schematics of experimental setup of microwave tomograph for biomedical imaging.

#### 4. MICROWAVE RADIOMETRY

Microwave radiometry is based on measurement of a very weak EM signal, which radiate any object (e.g., people), whose temperature is superior to absolute zero [1]. It is based on utilization of so-called Planck radiation law. Interest in microwave radiometry is given by possibility of its utilization at diagnostics of cancer and also of inflammatory disorder (e.g., appendicitis, arthritis, atp.) because tumors and inflammatory processes causes temperature rise. Microwave radiometer as a tool for biomedical imaging applications has the possibility to “monitor” a thermal noise produced by objects with the temperature over absolute zero. Next figure gives a basic idea about experimental setup. Advantage of microwave radiometer is ability to “see” the temperature increase under the surface of human body. Therefore we need to scan studied area of the tissue with a sensor and to evaluate the results of temperature measurements.

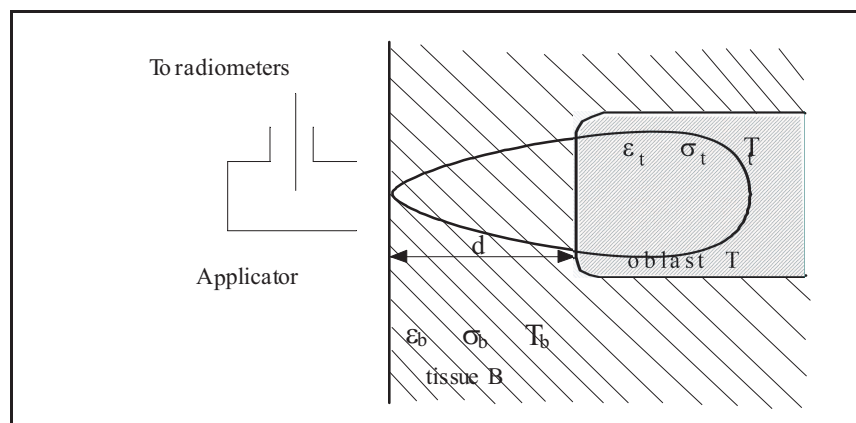


Figure 2: Principals of imaging by a microwave radiometer.

Let us suppose, that applicator (antenna of the radiometer) is situated on the layer B of the monitored biological tissue. Thickness of this layer is  $d$  and its temperature  $T_b$ . Its dielectric parameters will be  $\epsilon_b$  and  $\sigma_b$ .

#### 5. MEASUREMENTS OF COMPLEX PERMITTIVITY

Measurements of complex permittivity “in vivo” could be a suitable for biomedical imaging applications [1]. Usually an open end of coaxial line is used as a very suitable sensor for this measurement. Scanning the studied object by a such probe can bring us a map of the permittivity — we can then evaluate symmetry resp. unsymmetry of the measurement results and from this information we can make hypothesis about possible medical problems.

Characteristic impedance is  $Z_o$ ,  $C_o$  and  $C_f$  are fringing.

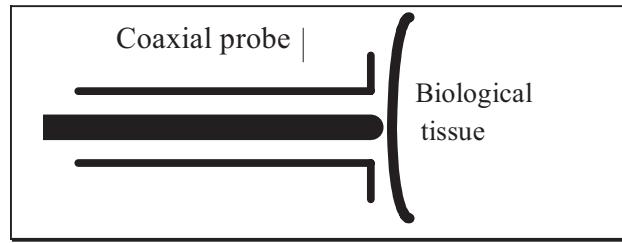


Figure 3: Coaxial probe for measurement of.

#### ACKNOWLEDGMENT

This research is supported by Grant Agency of the Czech Republic, project: “Microwave Imaging for Biomedical Applications” (102/05/0959) and by the research program MSM6840770012 “Trans-disciplinary Research in the Area of Biomedical Engineering II” of the CTU in Prague, sponsored by the Ministry of Education, Youth and Sports of the Czech Republic.

#### REFERENCES

1. Vrba, J., *Medical Applications of Microwaves*, 168, 1 ed., CTU, ISBN 80-01-02705-8, Prague, 2003.
2. Semenov, S. Y., et al., “Three-dimensional microwave tomography, initial experimental imaging of animals,” *IEEE Transactions on BME*, Vol. 49, No. 1, 55–63, Jan. 2002.
3. Gabriel, S., R. W. Lau, and C. Gabriel, “The dielectric properties of biological tissue–II. measurements in the frequency range 10 Hz to 20 GHz,” *Phys. Med. Biol.*, Vol. 41, 2251–2269, 1996.
4. Fear, E. C. and M. A. Stuchly, “Microwave detection of breast cancer,” *IEEE Trans. Microwave Theory Tech.*, Vol. 48, 1854–1863, 2000.
5. Vrba, J., et al., “Technical aspects of microwave thermotherapy,” *RF Interaction with Humans: Mechanisms, Exposures and Medical Applications*, IPEM Meeting, Institute of Physics, London, February 2003.
6. Vrba, J., C. Franconi, F. Montecchia, and I. Vanucci, “Evanescent mode applicators for sub-cutaneous hyperthermia,” *IEEE Trans. on Biomedical Engineering*, Vol. 40, No. 5, 397–407, May 1993.
7. Franconi, C., J. Vrba, and F. Montecchia, “27 MHz hybrid evanescent-mode applicators with flexible heating field for deep hyperthermia,” *International Journal of Hyperthermia*, Vol. 9, No. 5, 655–673, 1993.

# Electromagnetic Radiation from Ingested Sources in the Human Intestine at the Frequency of 2.4 GHz

L. S. Xu, Max Q.-H. Meng, and H. L. Ren

Department of Electronic Engineering, The Chinese University of Hong Kong, Shatin, Hong Kong, China

**Abstract**— The radiation effects and the link performance of the 2.4 GHz ingested wireless devices in the realistic human body model are studied by using the finite-difference time-domain (FDTD) method. Simulations are carried out for three orientations at seven source positions. Results show that all the temperature-rises, peaks of Specific Absorption Rate (SAR) and averaged SARs inside the realistic human body exposed to a realistic 2.4 GHz capsule antenna model are under the safety limits when the delivered power is no more than 26.16 mW, although its radiation effect and link performance greatly depend on the orientation and position.

## 1. INTRODUCTION

The widespread use of ingested wireless devices during the last few years has attracted lots of social and scientific concern about the possible harmful effects of radiation [1–3]. Among these capsule endoscopes that we can find, the 300–500 MHz is the most often used frequency band [3]. However, higher resolution information of the gastrointestinal (GI) tract and higher speeds of transmission are required for more accurate diagnosis. The compact antenna in the ingested device is electrically small. The bandwidths of these compact antennas working at low frequency cannot be wide enough and its radiation efficiency cannot be very high. Thus, higher transmission frequencies need to be employed as their electrical sizes increase.

Among the industrial, scientific, and medical (ISM) frequencies, 2.4 GHz that is usually used in commercial applications can be a good choice. Unfortunately, the antenna with a higher frequency may cause higher radiation absorption and worse communication link performance in human body. Since more energy will be absorbed by human tissues for higher frequency, many questions are posed such as whether a battery can provide enough power for the capsule endoscope, whether it is safe for clinic use, and how the positions and orientations of the radiation source influence its radiation characteristics such as temperature rise, link performance and so on. Chirwa et al. studied the radiation of ingested radio frequency (RF) sources in human body between 150 MHz and 1.2 GHz and suggested that the design for sources in the GI tract should be optimized for a higher efficiency [4]. However, only five positions were selected. They did not analyze the condition when the ingested sources were at the backmost of the intestine, which is the worst condition for RF communication than in other positions. Furthermore, the biological effects of the ingested RF devices were not studied in detail. In this paper, we analyzed the temperature rises, peaks of SAR, maximums of averaged SAR and link performance of the ingested RF source at seven positions spread nearly evenly in the abdomen (added forefront and backmost of the intestine) at 2.4 GHz.

## 2. HUMAN BODY AND SOURCE MODELS

The female model, the capsule antenna model and the seven locations are illustrated in Fig. 1. The high-fidelity 5 mm resolution female body model employed in this paper was created by Remcom Inc. [5]. This female body mesh, whose height is 173 cm, includes 34 groups of tissue types. Due to the ingested wireless device can move and rotate in the GI tract, the ingested antenna must be omni-directive for assuring that the data can be transmitted reliably to the outside receiver. Therefore, we selected a helix antenna and analyzed its three possible orientations, i.e., parallel to  $x$ -axis,  $y$ -axis and  $z$ -axis. The mesh step size of 1 mm is used in the area around the ingested capsule device and the mesh step size of the other area is 5 mm. Thus, the stability and the accuracy of the input impedance are assured.

## 3. COMPUTATION METHODS

In this paper, we analyzed the radiation effects and wireless link performance of an ingested source in a realistic human body model at the frequency of 2.4 GHz in 21 scenarios to verify whether 2.4 GHz can be used in ingested devices. We assume the signals transmitted from the helix antenna at the seven locations with three orientations are received by an antenna put at the center position of

the surface of the abdomen as illustrated in Fig. 1. The FDTD method [6] was applied to analyzing the electromagnetic interaction with human body and the Penns bio-heat equation [7] was applied to calculating the temperature rise due to the SAR deposition. We suppose the immersive medium is air, whose temperature and thermal conductivity are  $23.0^{\circ}\text{C}$  and  $0.026\text{ W/m}^{\circ}\text{C}$ , respectively. The perfusive medium is blood and the body temperature is  $37.0^{\circ}\text{C}$ .

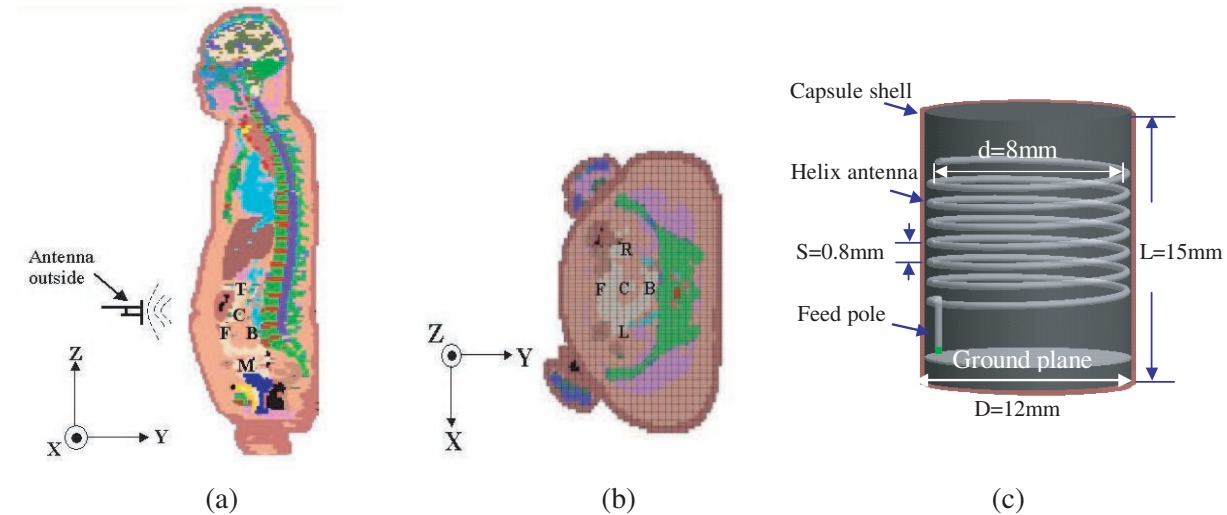


Figure 1: Simulation configuration. (a) Sagittal slice of the human model; (b) Transverse slice of the human model; (c) The Capsule model of the ingested wireless device. The 7-turn thin single component helix antenna, whose radius and length are 4 mm and 5.6 mm respectively, works at normal mode. The thickness of the plastic capsule shell is 1 mm. The length and radius of the feed pole are 2 mm and 1 mm, respectively. The radius and the length of the capsule wireless ingested device are 6 mm and 15 mm, respectively. C is the center of the abdomen area that includes small intestine; F and B are the front and back positions of the small intestine in the human abdomen; T and M are the top and bottom positions of the small intestine; L and R are the left and right positions of the small intestine.

#### 4. RESULTS AND DISCUSSION

The port impedances and the radiation efficiencies of these simulations vary greatly with the locations and orientations as demonstrated in Table 1. The impedances of the  $X$  and  $Y$  orientations are similar, while the impedances of the  $Z$  orientation are higher than those of the  $X$  and  $Y$  orientations. When the ingested device is positioned at B, the tissues reflect too much power. On the other hand, when the ingested device is positioned at F, less power is reflected by human tissues than in the other six positions due to the impedance is matched better than the others. The simulation results indicate that most of the radiation power was dissipated in the tissues. When the ingested source is  $X$  oriented and located in position C, the temperature rise is maximal (maximum is  $0.029^{\circ}\text{C}$ ) because its SAR is bigger than the others too. The maximums of SAR and temperature rise all occurred at the positions of the imbedded antennas and then these values attenuate 40 dB at the distance of 5 cm. The peak of SAR for the antenna in  $X$  orientation is more than twice of those in  $Y$  and  $Z$  orientations, whereas their local temperature-rise maxima have less difference.

Figures 2–3 demonstrate the electric fields of the  $XY$  planar slice where  $Z$  is 100 cm, including the electric fields inside and outside the human body. In these figures, we can find that the near fields of the antenna at the  $X$ ,  $Y$  and  $Z$  orientations are differently distributed. The electric fields in the anterior part of the human body are bigger than those in the posterior, which is in accordance with [4]. All the distributions of the electric fields outside the human body are irregular and asymmetrical due to the irregular distribution of human tissues. When the ingested antenna is located in position F, the near fields is larger than those of the other six positions; while when the ingested antenna is in position B, the near fields is less than those in the other six positions. Usually, the near fields in the  $X$  and  $Y$  orientations are bigger than those in the  $Z$  orientation. In these 21 scenarios, the minimal electrical field is  $-29\text{ dB}$ , which demonstrates that the 2.4 GHz can be applied to the efficient transmission of video signal in wireless capsule endoscope.

In these simulations, the SAR maximum at  $X$  orientation attenuates more than those at  $Y$  and

Table 1: The Peak of SAR, maximums of 1-g and 10-g averaged SAR, maximum values of temperature rise, and impedances for the ingested source in the seven positions and three orientations. In these simulations, all the delivered powers are normalized to 25 mW.

Orientations & Locations		Maximum SAR [W/kg]			Max Trise [°C]	Impedance [Ohms]	Radiation Efficiency [%]
		Peak	SAR1g	SAR10g			
<b>X</b>	<b>C</b>	12.871	1.529	0.564	2.9e-2	25+j28	3.76
	<b>T</b>	9.312	0.796	0.338	2.0e-2	26+j34	3.53e-3
	<b>M</b>	4.569	0.986	0.458	3.1e-3	32+j37	0.84
	<b>F</b>	5.733	0.873	0.281	1.7e-2	24+j16	1.39
	<b>B</b>	3.507	0.904	0.303	6.3e-3	28+j60	1.19e-3
	<b>L</b>	6.199	0.819	0.351	1.7e-2	15+j20	1.81
	<b>R</b>	5.328	0.768	0.352	1.9e-2	28+j32	1.06
<b>Y</b>	<b>C</b>	5.111	0.838	0.4	3.1e-3	26+j7	2.67
	<b>T</b>	9.491	1.017	0.482	1.9e-2	16+j9	2.24e-3
	<b>M</b>	5.699	0.813	0.263	1.6e-2	21-j20	0.40
	<b>F</b>	5.774	0.842	0.257	2.2e-2	18-j7	5.59
	<b>B</b>	6.672	1.101	0.43	9.4e-3	18+j26	1.68e-2
	<b>L</b>	6.192	1.082	0.468	2.1e-2	19-j8	3.25
	<b>R</b>	4.749	1.344	0.485	2.3e-3	21+j25	0.16
<b>Z</b>	<b>C</b>	5.037	1.223	0.329	2.1e-2	43+j74	3.61
	<b>T</b>	4.07	0.564	0.175	1.5e-2	60+j86	1.75
	<b>M</b>	2.073	0.311	0.17	1.4e-2	43+j93	1.16e-1
	<b>F</b>	2.564	0.402	0.143	8.1e-3	40+j64	0.70
	<b>B</b>	2.109	0.523	0.147	9.1e-3	48+j99	2.96e-3
	<b>L</b>	3.026	0.544	0.236	3.0e-2	26+j74	1.18
	<b>R</b>	2.18	0.478	0.119	9.3e-3	43+j85	5.32

Z orientations. The orientations have less influence on the distributions of temperature rise than that of SAR. The temperature rise of Y orientation is less than those of X and Z orientations due to the dimension of the human model in Y axis is smaller than those in X and Z axes. The maximums of temperature rise, 1-g and 10-g averaged SAR are  $0.029^{\circ}\text{C}$ ,  $1.529\text{ W/kg}$  and  $0.564\text{ W/kg}$ , respectively. When the delivered power is  $100\text{ mW}$ , the maximal temperature rise is  $0.078^{\circ}\text{C}$ . According to the guideline of 1-g and 10-g averaged SAR limits [8], the maximum allowable input power of the ingested wireless device can be  $26.16\text{ mW}$  and  $88.62\text{ mW}$ , demonstrating that

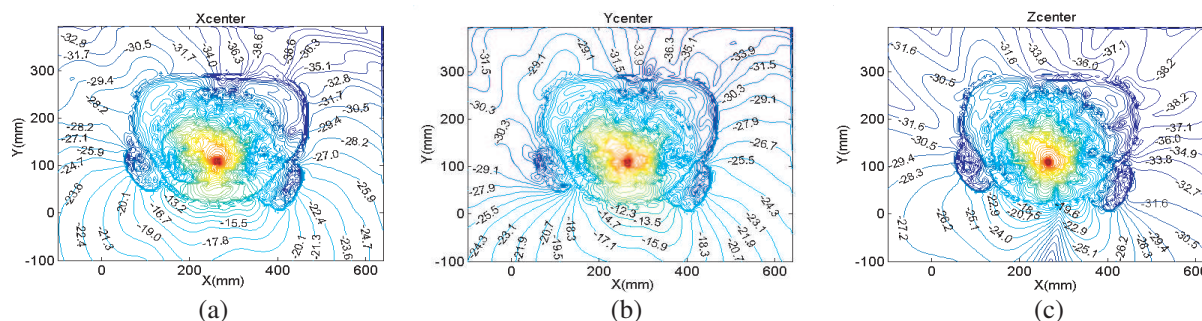


Figure 2: Near fields of the XY planar slice where  $Z = 100\text{ cm}$  in decibels for ingested  $2450\text{ MHz}$  source in position C. (a) X orientation; (b) Y orientation; (c) Z orientation.

the 2.4 GHz ingested antenna is safe and stable to be applied in the capsule endoscope at the input power of 26.16 mW. Furthermore, with the development of low power technology, the ingested wireless device can consume less power [9]. The energy in the battery of an ingested device is enough to work for more than 8 hours. In another word, 2.4 GHz can be safely and efficiently applied to transmit the video signal and command safely in wireless capsule endoscope.

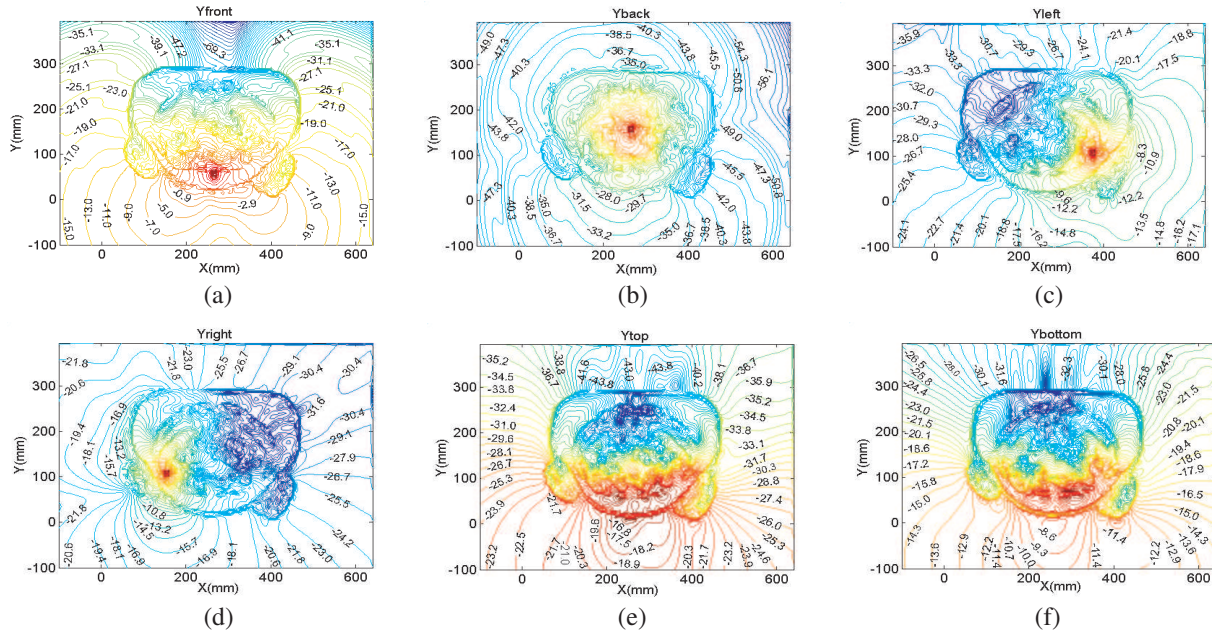


Figure 3: Near fields of the  $XY$  planar slice where  $Z = 100$  cm in decibels for ingested 2450 MHz source at  $Y$  orientation. (a) in position F; (b) in position B; (c) in position L; (d) in position R; (e) in position T; (f) in position M.

## 5. CONCLUSIONS

This paper analyzed the radiation effects and link performance of the 2.4 GHz ingested wireless devices in a realistic human body model in 21 scenarios. The power flow from the ingested antenna is mainly absorbed in the surrounding tissues. The orientation and the location of the wireless device greatly influenced the radiation characteristics of ingested wireless devices. The results showed that the frequency of 2.4 GHz could be employed safely and efficiently in the ingested wireless device when its input power is no more than 26.16 mW. Battery can provide enough power for the capsule endoscope at the frequency of 2.4 GHz.

## ACKNOWLEDGMENT

This research is supported via SHIAE project #BME4/06 of the Shun Hing Institute of Advanced Engineering of The Chinese University of Hong Kong, awarded to Max Meng.

## REFERENCES

1. Iddan, G., et al., "Wireless capsule endoscopy," *Nature*, Vol. 405, 417–420, 2000.
2. Werber, D., A. Schwentner, and E. M. Biebl, "Investigation of RF transmission properties of human tissues," *Advance in Radio Science*, Vol. 4, 357–360, 2006.
3. Yoon, K. W., et al., "Telemetry capsule for pressure monitoring in the gastrointestinal tract," *IEICE Trans. Fundamentals*, Vol. E89-A, No. 6, 1699–1670, 2006.
4. Chirwa, L.C., P. A. Hammond, S. Roy, and D. R. S. Cumming, "Electromagnetic radiation from ingested sources in the human intestine between 150 MHz and 1.2 GHz," *IEEE Transactions on Biomedical Engineering*, Vol. 50, No. 4, 484–492, 2003.
5. *XFDTD Reference Manual*, REMCOM Inc, 2005.
6. Taflove, A. and S. C. Hagness, *Computational Electromagnetics: The Finite-difference Time-domain Method*, Artech House, Boston, MA, 2000.

7. Pennes, H. H., "Analysis of tissue and arterial blood temperature in resting forearm," *J. Appl. Physiol.*, No. 1, 93–122, 1948.
8. "IEEE standard for safety levels with respect to human exposure to radio frequency electromagnetic fields, 3 KHz to 300 GHz," *IEEE Standard C95.1-1999*, Apr. 16, 1999.
9. Arshak, K., E. Jafer, G. Lyons, D. Morris, and O. Korostynska, "A review of low-power wireless sensor microsystems for biomedical capsule diagnosis," *International Microelectronics*, Vol. 21, No. 3, 8–19, 2004.

# Microwave Thermotherapy — Technical and Clinical Aspects

Jan Vrba

Department of EM Field, Czech Technical University, Technická 2, Prague 16627, Czech Republic

**Abstract**— Paper deals with our new results in the field of waveguide and intracavitary applicators used for microwave thermotherapy, like e.g., cancer treatment, physiotherapy, benign prostatic hyperplasia (BPH) treatment, etc.

## 1. INTRODUCTION

In our contribution we describe waveguide and intracavitary applicators working at 70, 434 and 2450 MHz see Ref. [1–6]. These applicators were used here in Prague for the treatment of more than 500 cancer patients with superficial or subcutaneous tumors (up to the depth of approximately 4 cm). Now, following new trends in this field, we continue our research in important direction of deep local and regional applicators.

## 2. WAVEGUIDE APPLICATORS

For the deep local thermotherapy treatment we develop above all waveguide type applicators based on the principle of evanescent mode waveguide, which is our specific solution and original contribution to the theory of microwave hyperthermia applicators, see Ref. [5, 6]. This technology enable us:

- to design applicators with as small aperture as necessary also for the optimum frequency range for deep local and/or for regional thermotherapy treatment (the frequency band between 27 and 70 MHz).
- using our technology we need not to fill the applicator by dielectric (necessary for deep penetration into the biological tissue — i.e., up to 10 centimetres under the body surface).
- two to four of such applicators can be also used for regional treatment.

Waveguide type applicators are often used in the local external hyperthermia treatment of cancer and other modifications of microwave thermotherapy as they offer very advantageous properties, above all:

- depth of penetration of the EM energy approaching the ideal case of plane wave,
- low irradiation of the energy in the vicinity of the hyperthermia apparatus,
- very good impedance matching, i.e., perfect energy transfer to the biological tissue.

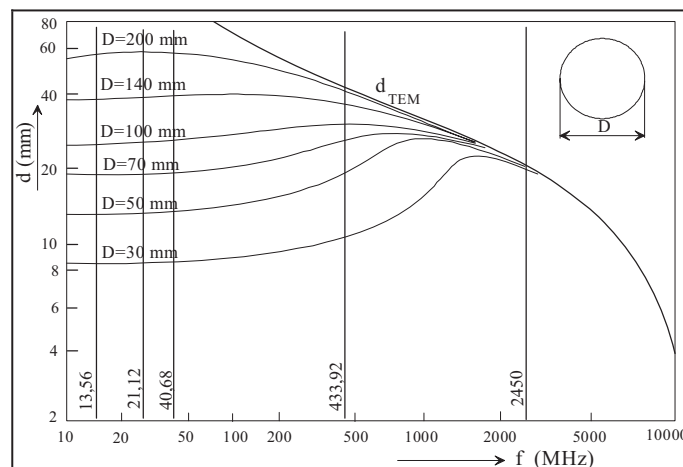


Figure 1: Effective depth of heating  $d$  for external waveguide applicator with respect to frequency  $f$  [MHz] and diameter of aperture  $D$  [mm].

We have studied waveguide applicators heating pattern for the aperture excitation at above and at under the cut-off frequency. It has helped us to get analytical approximations of the electromagnetic field distribution in the treated area of the biological tissue. In the Fig. 1. there is one of very important results - diagram showing the theoretical depth of heating  $d$  as a function of the used frequency  $f$  and of the aperture diameter  $D$  of the applicator. The most important results for the effective heating depth  $d$  can be characterised as follows:

- at high frequencies (above approx. 1000 MHz) the depth of effective heating  $d$  is above all a function of frequency  $f$  (skin effect),
- below approx. 100 MHz  $d$  is the dominantly function of the diameter  $D$  of applicator aperture ( $d = 0.386D$ ).

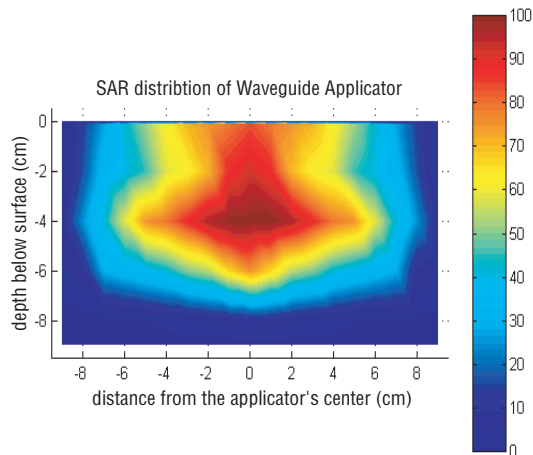


Figure 2: Measured SAR distribution of a passband Waveguide Applicator.

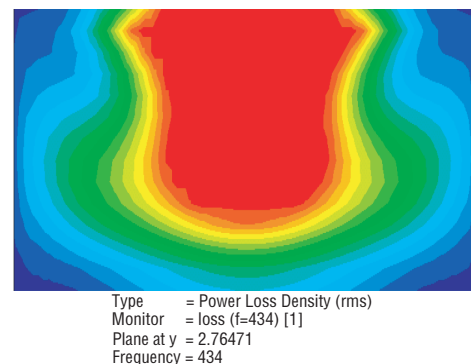


Figure 3: Calculated SAR distribution of a passband Waveguide Applicator.

One of our project was comparison of Evanescent Mode Waveguide Applicator with a reference Waveguide Applicator. The both applicators have aperture dimensions of  $18 \times 12$  cm and are operating at 434 MHz. Evanescent Mode Applicator is a waveguide, which is excited under cut off frequency. Inserting a capacity and inductive element + inductive wave admittance of TE mode we can build up band pass filter for operating frequency. Reference Waveguide Applicator is filled by dielectric with for decreasing the cut off frequency. For good knowledge of SAR distribution is necessary to measure thermal increments in high enough number of points in front of applicator aperture. Figs. 2 and 3 give results of measurements resp. calculations of SAR for the case of reference wave guide applicator, Fig. 4 then shows SAR distribution for the case of Evanescent mode applicator.

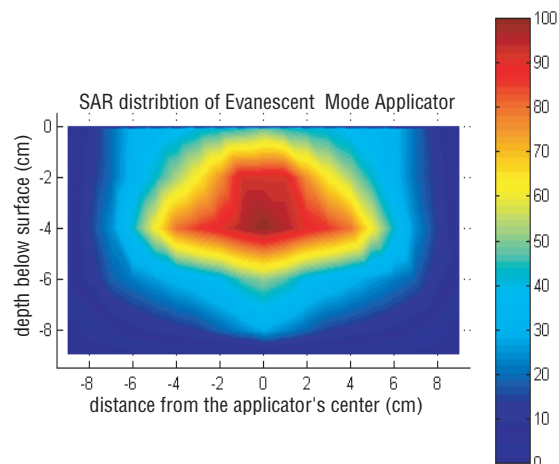


Figure 4: Measured SAR distribution of Evanescent Waveguide Applicator.

Another of our research interests is to study what happens, when the frequency  $f$  of hyperthermia apparatus is either very different (much higher or much lower) from the cut-off frequency  $f_c$  of the used waveguide applicator or very near (even equal) to this cut-off frequency  $f_c$ . This happens when either the hyperthermia apparatus is tunable in broader frequency range or the cut-off frequency  $f_c$  of the applicator is changed by different dielectric parameters of various types of biological tissues near to heated locality.

Let us take into account the area of biological tissue surrounded by electric and magnetic walls. Then the hybrid waveguide mode  $HE_{11}$  (i.e., the lowest possible one) can be defined and excited in the biological tissue in front of applicator aperture (it is a linear superposition of the modes  $TE_{11}$  and  $TM_{11}$ ). Higher order modes can be suppressed by the design of the applicator. Following 3 cases describe the change of the SAR in front of the applicator aperture as a function of working frequency  $f$  of the hyperthermia apparatus with respect to the  $f_c$ :

- if there is enough big difference between  $f$  and  $f_c$ , then homogeneous heating of the treated area can be expected — see Figs. 5(a) and (b).
- if the both frequencies are very near each to other (difference between  $f$  and  $f_c$  is going down), then overheating (hot-spots) out of the treated area can arise — see Fig. 6.

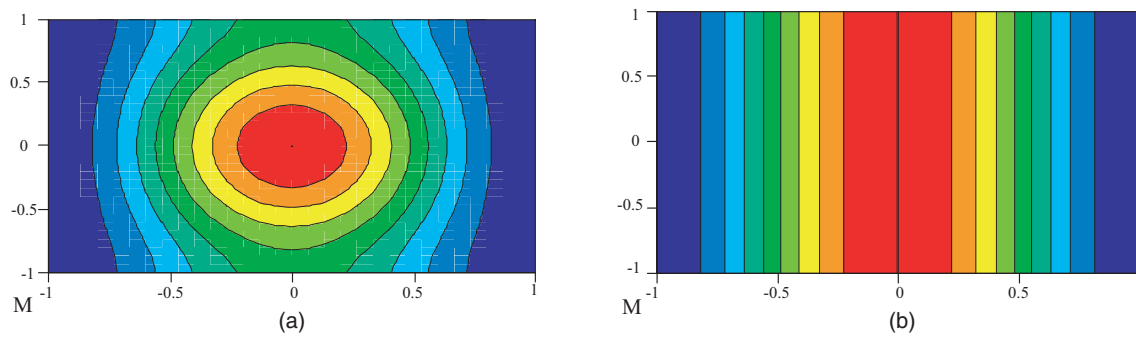


Figure 5: SAR in the aperture of applicator.

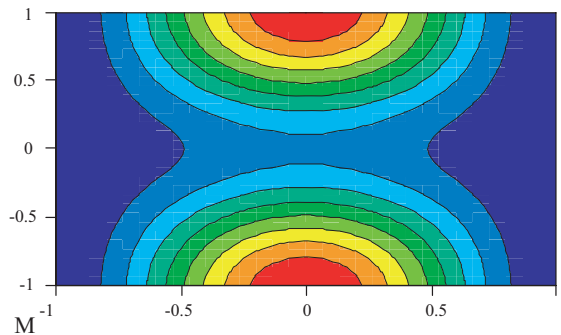


Figure 6: Calculated SAR in the waveguide aperture.

Evaluation of hyperthermia applicators in the water phantom means to measure the electromagnetic field power distribution in front of the aperture of this applicator. The E-field distribution can be measured by the dipole antenna. The length of this antenna must be smaller than  $\lambda/4$  ( $\lambda$  is the wavelength of measured field in this media). The voltage induced in this antenna supply the LED. The optical signal from the LED is leaded by the optical fiber outside the phantom to the optical detector. The scheme of the described system for microwave applicators evaluation is shown in the Fig. 7.

The output voltage from the optical detector is measured by the voltmeter or is converted by the ADC to the digital form and processed by the computer.

### 3. INTRACAVITARY APPLICATORS

Costs and risks associated with classical BPH treatment (TURP and open surgery) have promoted the development of minimally invasive methods. Microwave thermotherapy, varying forms of laser treatment, transurethral needle ablation, etc. have all been developed in the 1990s. The underlying

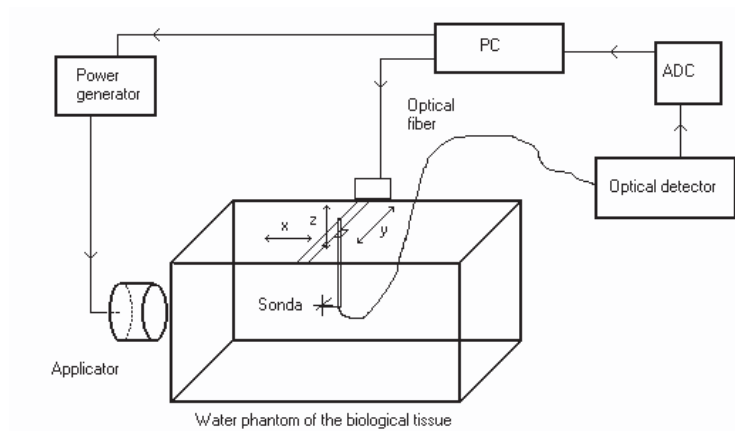


Figure 7: Apparatus for evaluation of applicators.

principle behind these methods is to coagulate prostatic adenomatous tissue by means of heat. Of all the available minimal invasive treatment modalities, transurethral microwave is one of the most wide spread at present [1].

We have investigated basic types of microwave intracavitary applicators suitable for BPH treatment, i.e., monopole, dipole and a helical coil structures. These applicators are designed to work at 915 MHz. In the conference contribution we would like to discuss it's effective heating depth, based on the comparison of the theoretical and experimental results. Basic mechanisms and parameters influencing (limiting) heating effective depth are described and explained in Ref. [2, 3].

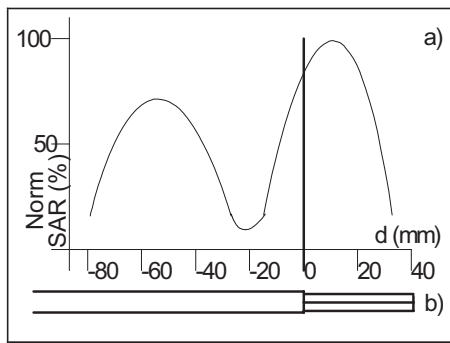


Figure 8: Monopole applicator.

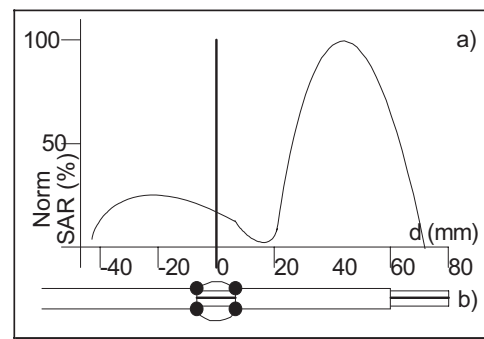


Figure 9: Dipole applicator.

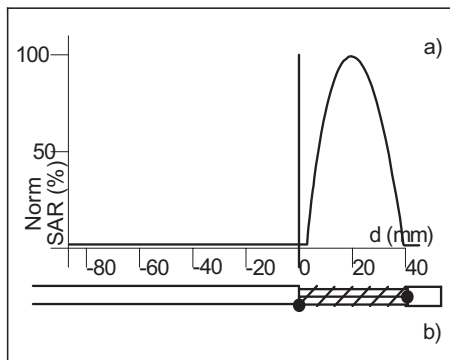


Figure 10: Helical coil applicator.

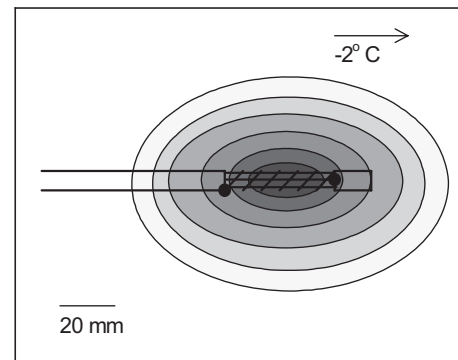


Figure 11: Temperature field around the helix.

The basic type of intracavitary applicator is a monopole applicator. The construction of this applicator is very simple, but calculated and measured “Specific Absorption Rate” (“SAR”) distribution along the applicator is more complicated, than has been the first idea. “SAR” can be measured either in water phantom or by infrared camera. During measurements of SAR along the

applicator we have found, that typically there is not only a one main “SAR” maximum (first from the right side), but also a second and/or higher order maximas can be created, being produced by outside back wave propagating along the coaxial cable, see Fig. 8.

In Fig. 9, the “SAR” distribution improvement (i.e., reduction of second maximum) can be noticed for the case of dipole like applicator. To eliminate this second maximum and optimise the focusing of “SAR” in predetermined area of biological tissue needs to use the helical coil antenna structure. After coil radius and length optimisation we have obtained very good results of “SAR” distribution, see Figs. 10 and 11. Some problems can be with the antenna self-heating, but it can be reduced by cooler at the end of applicator tip.

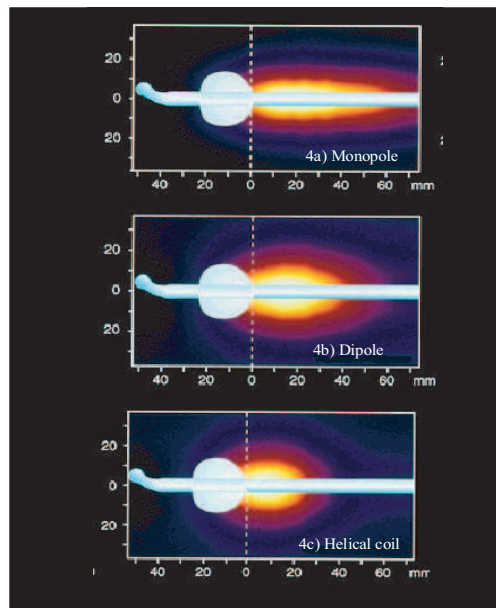


Figure 12: The heating pattern obtained for different antennas: the monopole (a), the dipole (b), the helical coil (c).

In Fig. 12 there is the typical measured heating pattern of monopole (a), dipole (b), and helical coil antennas (c). Note the long back heating tails with a monopole antenna (Fig. 12(a)) which is caused by microwave currents that flow backwards along the cable and cause the feeding cable to radiate. The radiation pattern from a dipole antenna (Fig. 12(b)) is generally well confined without any excessive backheating. The dipole antenna is suitable for prostates with axial length  $> 40$  mm. The helical coil antenna (Fig. 12(c)) has the shortest and most focussed heating and would be the choice for small prostates, 25–40 mm in length.

The pattern is colour-coded according to a linearly decreasing scale of white-yellow-red, where white is the maximum temperature. A diagrammatic catheter is inserted in each figure; the orientation of the bladder neck in a patient is indicated by a dashed line.

#### 4. CONCLUSIONS

Microwave thermotherapy is successfully applied in clinics in the Czech Republic. Technical support is at present from the Czech Technical University in Prague. Our goal for the next technical development is:

- improve the theory of the local and intracavitary applicator design and optimisation,
- innovate the system for the applicator evaluation (mathematical modelling and measurements),
- develop system for regional treatment.

#### ACKNOWLEDGMENT

This research is supported by Czech Research Programme: “Transdisciplinary Research in the Area of Biomedical Engineering II” and by Grant Agency of the Czech Republic, project: “Microwave Imaging for Biomedical Applications” (102/05/0959).

**REFERENCES**

1. De la Rosette, J., F. D'Ancona, and F. Debruyne, "Current status of thermotherapy of the prostate," *J. Urol.*, Vol. 157, 430–438, 1997.
2. Vrba, J., C. Franconi, and M. Lapeš, "Theoretical limits for the penetration depth of intracavitary applicat.," *Int. J. of Hyperthermia*, No. 6, 737–742, 1996.
3. Vrba, J., M. Lapeš, and L. Oppl, "Technical aspects of microwave thermotherapy," *Bioelectrochemistry and Bioenergetics*, Vol. 48, 305–309, 1999.
4. Bolmsjö, M., L. Wagrell, A. Hallin, T. Eliasson, B.-E. Erlandsson, and A. Mattiasson, "The heat is on — but how? A comparison of TUMT devices," *Br. J. Urol.*, Vol. 78, 564–572, 1996.
5. Franconi, C., J. Vrba, and F. Montecchia, "27 MHz Hybrid Evanescent-mode Applicator," *Int. J. Hyperthermia*, Vol. 9, No. 5, 655–674, 1993.
6. Vrba, J. and C. Franconi, "Evanescent-mode applicators for subcutaneous hyperthermia," *IEEE Trans. on BME*, Vol. 40, No. 5, 397–407, May 1993.

# A Physical Model for Study of Electromagnetic Field Interaction with Cancer Cell

D. Sardari<sup>1</sup> and N. Verga<sup>2</sup>

<sup>1</sup>Faculty of Engineering, Science and Research Campus, Azad University, Tehran, Iran

<sup>2</sup>Carol Davila University, Bucharest, Romania

**Abstract**— It has been known that electromagnetic fields are helpful in treatment of disease. It is already shown that electrostatic, magnetostatic, extremely low frequency electromagnetic fields, and pulsed electromagnetic radiation could be utilized in cancer treatment. These radiations alone or in combination with gamma or X-ray improve the healing of cancer tumors. The healing effect depends on frequency and amplitude of electromagnetic radiation. In the present work a physical model is developed to facilitate study the interaction of electromagnetic fields with the living cell. This model consists of an insulating layer as the cell membrane and a conducting colloid inside as the cytoplasm. In this model, electrical properties of a colloidal liquid are specified. This includes charge mobility and electric conductance. The electric field distribution inside and around the cell is studied.

## 1. INTRODUCTION

Combined effect of electromagnetic field and X-ray for treatment of cancer tumors has recently gained interest [8,10]. For the purpose of studying the interaction of electromagnetic field with the living cell, a physical model is required. A comprehensive model for the cell might include electrical [3] and rheological [7] aspects.

A lot of work has been accomplished to develop the treatment methods with electric field [5,7]. Electric properties of cell are known [3]. More work is needed to obtain the distribution of electric field strength in the cell precisely. In the present work, the direct ionization of a hydrogen atom by a DC electric field is considered. In what follows, the electric field intensity required to separate an electron from atom is estimated.

## 2. CELL DIMENSIONS

In the present work, the nucleus of the cell is not included in the model. The cell is considered being made up of two concentric spheres, producing the cytoplasm membrane. The thickness of membrane is in order of 5 nm. The radius of such spherical cell is about 10 micron. Inside the inner sphere is filled with a gel-like liquid, called cytoplasm.

## 3. ELECTRIC FIELD CALCULATION

When a cell undergoes dividing process, the curvature radius in the region connecting the two parts is much smaller than the radius of the original cell. Thus the electric field is supposed to be stronger. Electric field strength is proportional to inverse-square of the curvature radius [4]:

$$E \propto \left(\frac{1}{r}\right)^2 \quad (1)$$

As a rough estimate we consider:

$$r = 2d$$

where  $d$  is the membrane thickness and  $r$  the curvature radius in the junction between two newly produced cells.

Hydrogen ionization energy is 13.6 eV, and the electric potential produced by the hydrogen nucleus (proton) in a distance  $r$  is:

$$V = \frac{kq}{r} \quad (2)$$

In the above equation  $k$  is  $1/4\pi\epsilon$  and  $q$  being the electric charge of a single electron or proton.

The energy required overcoming the attraction force between electron and proton is:

$$W = Vq = \frac{kq^2}{r} = 13.6 \text{ eV} \quad (3)$$

Thus we can estimate the radius of orbit for electron:

$$r = 1.1 \text{ \AA}$$

Electric field strength at such distance produced by the nucleus is

$$E = \frac{kq}{r^2} \quad (4)$$

This leads to:

$$E = \frac{9 \times 10^9 \times (1.6 \times 10^{-19})}{(1.1 \times 10^{-10})^2} = 10^8 \frac{\text{v}}{\text{cm}}$$

As a general rule, the electric field is intensified over sharp objects. This must be considered in microscopic scale. Thus the applied electric field is much lower than what is computed above. According to Equation (1), one can write:

$$\frac{E_{joint}}{E_{app}} = \left( \frac{R_{cell}}{r_{joint}} \right)^2 \quad (5)$$

where:

$E_{app}$  = Applied electric field

$E_{junct}$  = Intensified electric field at the junction between two cells

$R_{cell}$  = Radius of cell

$r_{joint}$  = Curvature radius of the junction between two cells

The applied field is approximately amplified by a factor of  $\left( \frac{R_{cell}}{r_{joint}} \right)^2$  and appears in the pore of the dividing cell. This field should be strong enough to damage the cancer cell by ionizing essential molecules. The amplification factor might be calculated using the typical dimensional data of cell given in the introduction section above. This is in the order of  $10^3$ – $10^4$ . Thus applied electric field could be about  $10^4$  v/cm. Considering carbon atom instead of hydrogen and taking into account other technical factors, will result an estimate of  $10^3$  v/cm. As a whole, there might be one order of magnitude variation in our calculations, especially in cell dimensions and the thickness of junction connecting two young cells. The computed electric field strength in the present work is in agreement with the result of experiments [1–3, 5–9]. Electromagnetic fields are known as non-ionizing radiation, but strong electrostatic fields can separate electrons from the atom directly. This phenomena is called “field emission”.

## REFERENCES

1. Chen, G., N. Chen, A. L. Garner, J. Kolb, R. J. Swanson, S. Beebe, R. P. Joshi, and K. H. Schoenbach, “Conductivity in Jurkat cell suspension after ultrashort electric pulsing,” *3rd Int. Workshop on Biological Effect of EMFs*, Greece, Oct. 4–8, 2004.
2. Fan, J., G. Yu, and J. Tan, “Modeling and analysis of biological cells in DRAM implementation,” *IEEE*, 2007.
3. Gowrishankar, T. R. and J. C. Weaver, “An approach to electrical modeling of single and multiple cells,” *PNAS*, Vol. 100, No. 6, 3203–3208, March 18, 2003.
4. Haliday, D., R. Resnick, and J. Walker, *Fundamentals of Physics*, 7th ed., John Wiley, 1986.
5. Kirson, E. D., Z. Gurvich, R. Schneiderman, E. Dekel, A. Itzhaki, and W. Wasserman, “Disruption of cancer cell replication by alternating electric fields,” *Cancer Research* 64, 3288–3295, May 1, 2004.
6. Kirson, E. D., “Alternating electric fields arrest cell proliferation in animal tumor models and human brain tumors,” *PNAS*, Vol. 104, No. 24, 10152–10157, June 12, 2007.
7. Pawlowski, P., I. Szutowicz, S. Rozycki, J. Zielinski, and M. Fikus, “Bioelectrorheological model of the cell. VI. experimental verification of the rheological model of cytoplasmic membrane,” *Biophysical Journal*, Vol. 70, 1024–1026, February 1996.

8. Persson, B. R., C. B. Koch, G. Grafstrom, E. P. Engstrom, and L. G. Salford, "A model for evaluating therapeutic response of combined cancer treatment modalities: applied to treatment of subcutaneously implanted brain tumors (N32 and N29) in fischer rats with pulsed electric fields (PEF) and  $^{60}\text{Co}$ -gamma radiation (RT)," *Technology in Cancer Research & Treatment*, Vol. 2, No. 5, 459–470, October 2003.
9. Vernier, P. T., A. Li, L. Marcu, C. M. Craft, and M. A. Gundersen, "Ultrashort pulsed electric fields induce membrane phospholipid translocation and caspase activation: differential sensitivities of Jurkat T lymphoblasts and rat glioma C6 cells," *IEEE Transactions on Dielectrics and Electrical Insulation*, Vol. 10, No. 5, October 2003.
10. Verga, N., private communication.

# Method of Integral Equations for Solving 3D Electromagnetic Diffraction Problems in a Perturbed Layer Using Parallel Computations

Y. V. Shestopalov<sup>1</sup> and Y. G. Smirnov<sup>2</sup>

<sup>1</sup>Karlstad University, Karlstad, Sweden

<sup>2</sup>Penza State University, Penza, Russia

**Abstract**— We consider a Dirichlet boundary value problem for the Helmholtz equation in a three-dimensional layer with a local perturbation  $S$  of the boundary and apply the solution technique based on equivalent reduction to a boundary integral equation (IE). We prove the unique solvability of the IE and its Fredholm property, the convergence of the Galerkin method applied for its numerical solution, and describe parallel algorithms and computational techniques developed specifically when  $S$  is a set of many disjoint irregularities.

## 1. INTRODUCTION

Boundary value problems (BVPs) for the Maxwell and Helmholtz equations in dielectric or magnetic layers with perturbed boundaries arise in mathematical models of electromagnetic wave propagation in irregular waveguides; some typical statements are surveyed in [1, 2]. We develop the solution techniques set forth in [2, 3] considering BVPs in a layer with perturbed boundaries in Sobolev spaces and applying the reduction to surface integral equations (IEs) developed in [2] for electromagnetic diffraction problems. The IE method enables one to decrease the dimension of the problem and offers an approach applicable in unbounded domains with complicated irregularities where the methods based on discretization fail or meet substantial difficulties. IEs are solved numerically by the Galerkin method [4, 5] using algorithms of parallel computations [6].

## 2. FORMULATION

Consider a Dirichlet problem for the Helmholtz equation

$$\Delta u + k^2 u = 0, \quad x \in U, \quad u|_{\Omega} = \mu, \quad u|_{\partial U \setminus \Omega} = 0, \quad (1)$$

where  $U = \{x : 0 < x_3 < 1 - \varphi(x_1, x_2)\}$  denotes the layer bounded by two planes  $x_3 = 0$  and  $x_3 = 1$  with a local perturbation of the boundary specified by  $x_3 = \varphi(x_1, x_2)$ . We assume that the function  $\varphi(x_1, x_2)$  is compactly supported, so that  $\text{supp } \varphi = \Omega_0$ , where  $\Omega_0$  is a bounded domain on the plane of variables  $x_1, x_2$  with a piecewise smooth boundary. Assume also that  $0 \leq \varphi(x_1, x_2) < 1$  and  $\varphi \in C^1(\mathbb{R}^2)$  (once continuously differentiable).  $\Omega = \{x : (x_1, x_2) \in \Omega_0, x_3 = \varphi(x_1, x_2)\}$  denotes the perturbed part of the boundary of  $U$ . Function  $u$  simulates a component of the scattered electromagnetic field in the layer between two perfectly conducting planes (perturbed and unperturbed) under the influence of the boundary sources  $\mu$ .  $k$  is the wavenumber of the medium filling the layer; we assume that  $\Im k \geq 0$  and  $k \neq 0$ .

Let us formulate the conditions at infinity. Set  $x' := (x_1, x_2)$  and assume that

$$u = O(\rho^{-1/2}), \quad \rho := |x'| \rightarrow \infty, \quad (2)$$

for  $\text{Im} k > 0$ , uniformly along all directions  $x'/\rho$  and with respect to  $x_3$ . Assume that for  $\text{Im} k = 0$ , the Fourier coefficients

$$u_n(x') = 2 \int_0^1 u(x) \sin \pi n x_3 dx_3, \quad n \geq 0, \quad (3)$$

satisfy the conditions

$$\frac{\partial}{\partial \rho} u_n - i k_n u_n = O(\rho^{-1/2}), \quad u_n = O(\rho^{-1/2}), \quad \rho \rightarrow \infty, \quad (4)$$

for  $k_n^2 := k^2 - \pi^2 n^2 > 0$  (where  $k_n > 0$  if  $k > \pi n$  and  $k_n < 0$  if  $k < -\pi n$ ),

$$u_n = O(1), \quad \rho \rightarrow \infty, \tag{5}$$

for  $k_n = 0$ , and

$$u_n = O(\rho^{-1/2}), \quad \partial u_n / \partial \rho = O(\rho^{-1/2}), \quad \rho \rightarrow \infty, \tag{6}$$

for  $\text{Im}k_n > 0$ , uniformly along all directions  $x'/\rho$  and with respect to  $n$ .

Let us formulate the boundary value problem to be considered: determine the function  $u = u(x_1, x_2, x_3)$  satisfying (i) the Helmholtz equation  $\Delta u + k^2 u = 0$  in an unbounded domain  $U$ ; (ii) the boundary conditions

$$u|_{\Omega} = \mu(x_1, x_2, x_3),$$

where  $\mu(x_1, x_2, x_3)$  is given on the perturbed part of the boundary  $\Omega$  (and  $u = 0$  everywhere on the boundary of  $U$  outside  $\Omega$ ); and (iii) the conditions at infinity (2)–(6).

### 3. BOUNDARY INTEGRAL EQUATION

Define Green's function  $G^U = G^U(x, y)$ ,  $x, y \in U_0$ , for the layer  $U_0 = \{x : 0 < x_3 < 1\}$  using the series representation [3]

$$G^U(x, y) = \frac{1}{4\pi} \sum_{j=-\infty}^{\infty} \left( \frac{\exp(ikr_j)}{r_j} - \frac{\exp(ikr'_j)}{r'_j} \right), \tag{7}$$

where

$$r_j = \sqrt{r' + (x_3 - y_3 - 2j)^2}, \quad r'_j = \sqrt{r' + (x_3 + y_3 - 2j)^2}, \quad r' = (x_1 - y_1)^2 + (x_2 - y_2)^2.$$

Green's function satisfies the Dirichlet boundary conditions  $G^U|_{x_3=0} = G^U|_{x_3=1} = 0$ .

Applying Green's formula to  $G^U$  and a solution  $u$  of problem (1)–(6) we obtain an integral representation

$$u(y) = \iint_{\Omega} G^U \frac{\partial u}{\partial n} d\sigma - \iint_{\Omega} \mu \frac{\partial G^U}{\partial n} d\sigma. \tag{8}$$

Here  $n$  is the external normal;  $\frac{\partial}{\partial n} = \cos \alpha_1 \frac{\partial}{\partial x_1} + \cos \alpha_2 \frac{\partial}{\partial x_2} + \cos \alpha_3 \frac{\partial}{\partial x_3}$  is the derivative in the direction of  $n$ ;  $\alpha_j$  are the angles between  $n$  and axes  $Ox_j$ ,  $j = 1, 2, 3$ ;

$$\cos \alpha_j = \frac{\partial \varphi}{\partial x_j} / \sqrt{1 + \left(\frac{\partial \varphi}{\partial x_1}\right)^2 + \left(\frac{\partial \varphi}{\partial x_2}\right)^2} \quad (j = 1, 2), \quad \cos \alpha_3 = 1 / \sqrt{1 + \left(\frac{\partial \varphi}{\partial x_1}\right)^2 + \left(\frac{\partial \varphi}{\partial x_2}\right)^2};$$

and  $\mu$  and  $G^U$  are known. The only unknown function  $\psi := \frac{\partial u}{\partial n}$  enters the first integral of representation (8), while the second integrand is a product of known functions; we denote the second integral by

$$F = \iint_{\Omega} \mu \frac{\partial G^U}{\partial n} d\sigma.$$

The latter integral undergoes a break on the boundary of the domain according to the properties of double-layer potentials [1]. Therefore when performing a transition to the limit  $x \rightarrow y \in \Omega$  in the second integral (8) the quantity  $\frac{1}{2}\mu(y)$  is added,

$$\mu(y) = \iint_{\Omega} G^U \psi d\sigma - F(y) + \frac{1}{2}\mu(y), \quad y \in \Omega.$$

Thus function  $\psi$  can be determined as a solution to the IE

$$\iint_{\Omega} G^U \psi d\sigma = \frac{1}{2}\mu(y) + F(y), \quad y \in \Omega. \tag{9}$$

Write IE (9) in the operator form

$$S\psi + K\psi = f, \quad f = \frac{1}{2}\mu + F, \tag{10}$$

where

$$S\psi = \frac{1}{4\pi} \iint_{\Omega} \frac{1}{|x - y|} \psi d\sigma, \tag{11}$$

$$K\psi := K_1\psi + K_2\psi, \quad K_1\psi = \iint_{\Omega} G_K^U \psi d\sigma, \quad K_2\psi = \frac{1}{4\pi} \iint_{\Omega} \frac{\exp(ik|x - y|) - 1}{|x - y|} \psi d\sigma, \tag{12}$$

$$G_K^U(x, y) = \frac{1}{4\pi} \sum_{j=-\infty}^{-1} \left( \frac{\exp(ik|x - y - 2je_3|)}{|x - y - 2je_3|} - \frac{\exp(ik|x - y^* + 2je_3|)}{|x - y^* + 2je_3|} \right) + \frac{1}{4\pi} \sum_{j=1}^{\infty} \left( \frac{\exp(ik|x - y - 2je_3|)}{|x - y - 2je_3|} - \frac{\exp(ik|x - y^* + 2je_3|)}{|x - y^* + 2je_3|} \right), \tag{13}$$

$e_3 = (0, 0, 1)$ , and  $y^* = (y_1, y_2, -y_3)$ . Look for the solution to Equation (9) in the Sobolev space  $\psi \in H^{-1/2}(\bar{\Omega})$ ; the right hand side  $f \in H^{1/2}(\Omega)$ ; and the integral operators  $S$  and  $K$  are defined appropriately

$$S : \tilde{H}^{-1/2}(\bar{\Omega}) \rightarrow H^{1/2}(\Omega), \quad K : \tilde{H}^{-1/2}(\bar{\Omega}) \rightarrow H^{1/2}(\Omega).$$

Operator  $S$  is bounded and has a bounded inverse [4] in the chosen spaces. Since Green's function  $G_K^U(x, y)$  is continuous in  $\bar{\Omega} \times \bar{\Omega}$  (and has no singularity at  $x = y$ ), operator  $K$  is compact in these spaces. Thus  $S + K : \tilde{H}^{-1/2}(\bar{\Omega}) \rightarrow H^{1/2}(\Omega)$  is a Fredholm operator (with the zero index). We have proved the following statement: the solution  $\psi \in \tilde{H}^{-1/2}(\bar{\Omega})$  to IE  $S\psi + K\psi = f$  (and to Equation (9)) exists and is unique for every right-hand side  $f \in H^{1/2}(\Omega)$  if corresponding homogeneous equations (with  $f = 0$ ) have only trivial solutions.

Consider IE (9) to which problem (1)–(3) has been reduced. Transform the surface integral over  $\Omega$  to a double integral over  $\Omega_0$ :

$$\iint_{\Omega_0} \tilde{G}^U(x, y) \tilde{\psi}(x) dx_1 dx_2 = \tilde{F}(y), \quad y = (y_1, y_2) \in \Omega_0, \tag{14}$$

$$\tilde{F}(y_1, y_2) = 1/2\mu(y_1, y_2, 1 - \varphi(y_1, y_2)) + F(y_1, y_2, 1 - \varphi(y_1, y_2)), \tag{15}$$

$$\tilde{G}^U(x_1, x_2; y_1, y_2) = G^U(x_1, x_2, 1 - \varphi(x_1, x_2); y_1, y_2, 1 - \varphi(y_1, y_2)), \tag{16}$$

$$\tilde{\psi}(x_1, x_2) = \psi(x_1, x_2, 1 - \varphi(x_1, x_2)) \sqrt{1 + \left(\frac{\partial\varphi}{\partial x_1}\right)^2 + \left(\frac{\partial\varphi}{\partial x_2}\right)^2}. \tag{17}$$

IE in the form (14)–(17) will be solved numerically by the Galerkin method.

#### 4. NUMERICAL

Consider the scheme of the Galerkin method [4, 5] for the numerical solution of IE (10)

$$\langle (S + K)\psi_N, u_k \rangle = \langle f, u_k \rangle, \quad k = 1, \dots, N. \tag{18}$$

Here  $\psi_N \in H_N$  is the approximate solution,  $u_k \in H_N$  are basis functions, and  $H_N \in H$  finite-dimensional spaces. Brackets  $\langle \cdot, \cdot \rangle$  denote the duality relation on the pair of dual spaces  $H'$  and  $H$ , where  $H' = H^{1/2}(\Omega)$  and  $H = \tilde{H}^{-1/2}(\bar{\Omega})$ , with respect to the sesquilinear form  $\langle \psi, f \rangle = \iint_{\Omega} \psi f d\sigma$ .

Galerkin method (18) converges [4, 5] if the following conditions of approximation are fulfilled

$$\inf_{u_N \in H_N} \|u_N - \psi\| \rightarrow 0, \quad N \rightarrow \infty, \quad \forall \psi \in H. \tag{19}$$

Describe numerical solution of IE (14) by the Galerkin method. Let  $\Omega_0 = \Pi$ , where  $\Pi := \{x : 0 < x_1 < a_1, 0 < x_2 < a_2\}$  is a rectangle. Choose in  $\Pi$  a uniform rectangular grid with the nodes  $(x_1^i, x_2^j)$ ,  $x_1^i = ih_1$ ,  $x_2^j = jh_2$ , where  $h_1 = \frac{a_1}{N_1}$ ,  $h_2 = \frac{a_2}{N_2}$ ,  $N_1 \geq 1$ ,  $N_2 \geq 1$ ,  $i = 0, \dots, N_1$ ,  $j = 0, \dots, N_2$ . Define the basis functions

$$u_{ij} = (\chi(x_1 - x_1^i) - \chi(x_1 - x_1^{i+1}))(\chi(x_2 - x_2^j) - \chi(x_2 - x_2^{j+1})),$$

where  $\chi(t) = 0$  for  $t < 0$  and  $\chi(t) = 1$  for  $t \geq 0$ . Thus every basis function has a compact support  $\Pi_{ij} := \{x : x_1^i \leq x_1 \leq x_1^{i+1}, x_2^j \leq x_2 \leq x_2^{j+1}\}$ . Applying the Galerkin method we obtain a linear equation system

$$\sum_{i=0}^{N_1-1} \sum_{j=0}^{N_2-1} a_{ijkl} c_{ij} = f_{kl}, \quad k = 0, \dots, N_1 - 1, \quad l = 0, \dots, N_2 - 1, \quad (20)$$

where entries  $a_{ijkl}$  and components of the right-hand side  $f_{kl}$  are calculated as multiple integrals:

$$a_{ijkl} = \iiint_{\Pi_{ij}} \iiint_{\Pi_{kl}} \tilde{G}^U(x_1, x_2; y_1, y_2) dx_1 dx_2 dy_1 dy_2, \quad f_{kl} = \iint_{\Pi_{kl}} \tilde{F}(y_1, y_2) dy_1 dy_2. \quad (21)$$

Approximate solution  $\tilde{\psi}_{N_1, N_2}$  is represented as

$$\tilde{\psi}_{N_1, N_2} = \sum_{i=0}^{N_1-1} \sum_{j=0}^{N_2-1} c_{ij} u_{ij}. \quad (22)$$

An advantage of the proposed method in comparison with the existing techniques is that a 2D equation is solved in the domain occupied by the inhomogeneity rather than a 3D problem in the unbounded domain. If the perturbation of the boundary is sufficiently complicated, the only possibility to solve such problems efficiently is application of parallel computations using multiprocessor systems (clusters), or supercomputers. However, they require creation of the specific problem-oriented algorithms of parallel computations. We propose the following algorithms of parallel computations for the solution of the problem under study.

1. Integrals forming the entries of the matrix of the linear algebraic system are calculated in parallel using several ( $M$ ) different processors. Since the data exchange between the processors in the course of computations is not necessary, the rate of computations increases by a factor of  $M$ .
2. If the given function  $\mu$  is a superposition of a big number of functions with nonoverlapping supports, then the problem can be solved separately for every such function on a separate processor and the general solution can be obtained then as a superposition of particular solutions of separate problems. An advantage here is in the following: Denote by  $k$  (e.g., equal to  $10^{-m}$ ,  $m \geq 3$ ) the ratio of the diameter of the support of a separate small subdomain to that of the whole inhomogeneity. Then the ratio of the respective computation times is proportional to  $k$ .
3. The linear algebraic system of the Galerkin method can be solved using algorithms of parallel computations and clusters if we apply iteration techniques (e.g., a parallel version of the conjugate gradient method) when the most time-consuming matrix-vector multiplications are performed in parallel on different processors.

Such problems are solved at the Penza Supercomputer Center (PSC) since 2000. The PSC team (head Prof. Yury Smirnov) elaborated several algorithms and software for parallel computations using multiprocessor systems (clusters) or supercomputers.

#### ACKNOWLEDGMENT

This work is supported by Russian Foundation of Basic Research, grant 06-07-89063.

**REFERENCES**

1. Tikhonov, A. N. and A. A. Samarskii, *Equations of Mathematical Physics*, Nauka, Moscow, 1972.
2. Ilinskii, A. S. and Y. G. Smirnov, *Electromagnetic Wave Diffraction by Conducting Screens*, VSP Int. Sci. Publ., Utrecht, 1997.
3. Morgenröther, K. and P. Werner, "On the instability of resonances in parallel-plane waveguides," *Mathematical Methods in the Applied Sciences*, Vol. 11, 279–315, 1989.
4. Stephan, E. P., "Boundary integral equations for screen problems in  $\mathbb{R}^3$ ," *Journal of Integral Equations and Operator Theory*, Vol. 10, 236–257, 1987.
5. Kress, R., *Linear Integral Equations*, Applied Mathematical Science 82, Springer-Verlag, New York, 1989.
6. Smirnov, Y. G., "Theoretical analysis of volume integral equation method and subhierarchical parallel algorithm for solving electromagnetic diffraction problem on a dielectric body in a layer," *Proceedings of Progress In Electromagnetics Research Symposium*, 320, Tokyo, Japan, August 2006.

# A Specific Architectures of CMOS Readout for Resonant-cavity-enhanced Devices

G. Z. Zhan, F. M. Guo, W. Lei, J. Huang, Z. Q. Zhu, and J. H. Chu

College of Information Science and Technology, East China Normal University, Shanghai 200062, China

**Abstract**— Application-specific architectures of CMOS readout circuit (ROIC) for the processing of signals from the resonant-cavity-enhanced (RCE) devices is proposed in this paper. The capacitor feedback transimpedance amplifier (CTIA) used for the amplifying small signals is implemented by means of a low-noise preamplifier and a feedback capacitor. The multiple analog channels of the chip are multiplexed to a single analog output. A suitable digital section provides self-resetting of each channel and trigger output. In this work, the main features of the circuit are presented along with the experimental results of its characterization.

## 1. INTRODUCTION

The increasing need for high-speed commutation and data transfer has brought about intensive research in resonant-cavity-enhanced devices [1, 2]. Such devices require the integration of readout electronics. For the optimization of the readout electronics, it is necessary to simulate the circuit along with the RCE devices. The ROIC is used to amplify, transact and output the signals, so it is important to photo-detection and imaging [3]. To improve the efficiency of RCE, a high performance ROIC is needed. The CTIA is one of several preamplifier structures for ROIC [4]. It provides a highly stable voltage level bias, high efficiency, high gain and low noise. Besides, a correlated double sampling (CDS) circuit is on the output of the CTIA. CDS is used to eliminate the effect of the background level noise by means of two peak stretchers. This approach also improves the signal-to-noise ratio without worsening the noise characteristic.

## 2. DEVICES MODELING

RCE devices grown on GaAs substrates have been attracting much interest because there are advantages that they can be grown monolithically on a GaAs/AlGaAs distributed Bragg reflector (DBR) mirror with high reflectivity. Fig. 1 shows the structures of RCE devices [5]. At the peak wavelength 1056 nm, for the RCE devices, the peak quantum efficiency reaches 30%, and FWHM is less than 5 nm.

The operation of RCE devices can be represented by two equations as functions of bias across the device and operating temperature. Fig. 2 is an assumed circuit model for RCE devices. These voltages can be varied in the simulation to analyses the effects of temperature and the detector performance.

## 3. CITCUIT STRUCTURE AND IMPLEMENTATION

The timing pattern for a general readout circuit is shown in Fig. 3. The operation is divided into two phases: the integration process and the readout process [6]. The integration time  $T_{\text{int}}$  can be tuned to avoid saturation of the limited integration capacitance and operating voltage, especially in the operation of a high background flux. ROIC concludes unit cells, row multiplexer, column multiplexer and output buffers.

Figure 4 shows the structure of the unit cell. It concludes the CTIA and CDS. The photocurrent generated by photodetectors run into CTIA through the row multiplexer. After integration process, CTIA transmits the current to voltage. Then CDS samples and holds the voltage levels at the beginning of integration ( $V_1$ ) and the end of integration ( $V_2$ ), respectively. Finally, these voltages are outputted by output buffers through column multiplexer. We can get the voltage level ( $\Delta V$ ) from  $V_2$  minus  $V_1$ , which depends on the intensity of photocurrent.

The photocurrent runs into the integrator. After integration, the output voltage level is given by

$$V_{\text{out}} = \frac{\int_0^{T_{\text{int}}} I_{\text{det}} dt}{C_{\text{int}}} - V_{\text{ref}} \quad (1)$$

where  $T_{\text{int}}$  is the integration time,  $I_{\text{det}}$  is photocurrent,  $C_{\text{int}}$  is a feedback capacitor and  $V_{\text{ref}}$  is the reference voltage. The output voltage level and corresponding integration times are used to

	GaAs	76.15nm	$p^+ 1 \times 10^{18} \text{cm}^{-3}$
14 ×	AlAs	90.14nm	$p^+ 1 \times 10^{18} \text{cm}^{-3}$
	GaAs	5nm	$p^+ 1 \times 10^{18} \text{cm}^{-3}$
	GaAs	123.3nm	i
	InGaAs QD	6MLs	i
4 ×	GaAs	12nm	i
	InGaAs QD	6MLs	i
	GaAs	104.3nm	i
	InGaAs QD	6MLs	i
4 ×	GaAs	12nm	i
	InGaAs QD	6MLs	i
	GaAs	123.3nm	i
	GaAs	5nm	$n^+ 1 \times 10^{18} \text{cm}^{-3}$
	AlAs		$n^+ 1 \times 10^{18} \text{cm}^{-3}$
19 ×	GaAs		$n^+ 1 \times 10^{18} \text{cm}^{-3}$
	GaAs buffer		$n^+ 1 \times 10^{18} \text{cm}^{-3}$
	n	GaAs substrate	

Figure 1: RCE device structures.

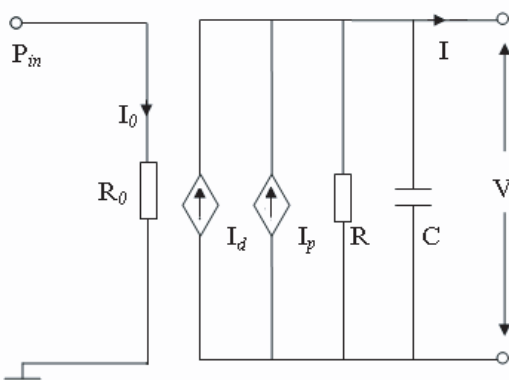


Figure 2: Circuit model for RCE devices.

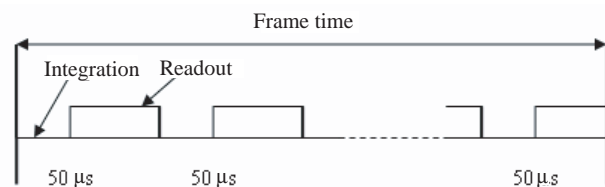


Figure 3: Timing diagram of the readout circuit.

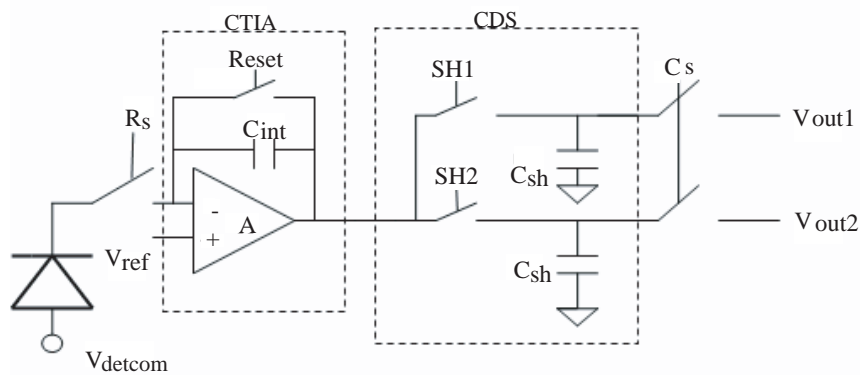


Figure 4: Single unit cell structure.

estimate the photocurrent. Besides, the changed voltage level at the input port of operational amplifier is given by

$$\Delta V_{in} = \frac{I_{det} T_{int}}{C_{int}(1 + A_v)} \quad (2)$$

where  $A_v$  is the open gain of operational amplifier,  $A_v \gg 1$ . So the  $\Delta V_{in}$  is very small. This is why CTIA can provide a highly stable detector bias, high photon current injection efficiency, high gain and low noise. Then the noise in CTIA is KTC noise and a simplified Signal-to-Noise ratio (SNR) of the integrated photocurrent is given by [7]

$$V_n = \left( \frac{KT}{C_{int}} \right)^{1/2} \quad (3)$$

$$SNR(i_p) = \frac{(i_p T_{int})^2}{q i_p T_{int} + q^2 \sigma_{Readout}^2}, \quad for \quad i_p \leq \frac{q Q_{max}}{T_{int}} \quad (4)$$

where  $K$  is Bolt Mann's constant ( $1.38 \times 10^{-23} J/K$ ),  $q$  is the charge of an electron,  $Q_{max} = C_{int} \times V_{max}$  is the saturation charge or well capacity,  $V_{max}$  is the maximum voltage on the  $C_{int}$ , and  $\sigma_{Readout}$  is the readout noise. This SNR only considers integrated shot noise and readout noise. The reset noise and offset contributions is eliminated by CDS. Fig. 5 shows the relationship between  $V_n$  and temperature. For the thermal noise of MOS channel is random, the voltage level on feedback capacitor after reset is random. Fig. 6 shows the wave of  $V_{int}$  gone with noise. It indicates that the noise existed with Gauss function.

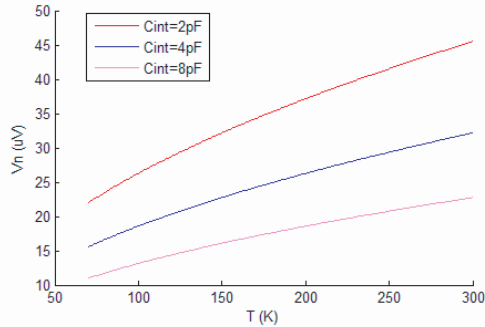


Figure 5:  $V_n$  vs temperature with different  $C_{int}$ .

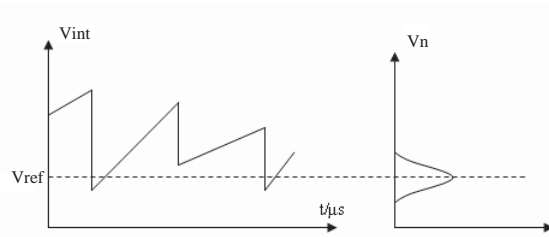


Figure 6: The wave of  $V_{int}$  gone with noise.

Table 1: Key parameters of the readout circuit.

Chip size	2 mm × 2 mm
Operating temp	>77 K
Process	0.6 μm CMOS
Unit-cell design	CTIA
Test cp	1 MHz
Power supply	5 V
Dynamic range	100 dB
Gain uniformity	>90%
Power dissipation	<200 μw
Readout speed	< 56 μs per frame

#### 4. EXPERIMENTAL RESULTS

A RCE device is used for testing. The chip digital signal SH1 and SH2 are tuned to fit corresponding effective integration time. The integration time is used to estimate small signals from the RCE

device. Read noise is expected to be lower with test setup improvements.

The test results show that the readout circuits have a near 100 dB dynamic range and over 90% gain uniformity. The power dissipation is 200  $\mu$ W when power supply is 5 V. The frame frequency is very high, which makes it possible to gain an availability frame frequency at large array condition. Table 1 tabulates the readout circuit's salient parameters.

## 5. CONCLUSION

A complete readout chip for low dimensional device has been developed. The CTIA provides a highly stable detector bias, high photon current injection efficiency, high gain and low noise. CDS is used to eliminate the effect of the background level while pre-amplifying the signal. The readout architecture is also tolerant to undesirable scene disturbances that generate transient spikes of photocurrent.

## ACKNOWLEDGMENT

The work supported by National Scientific Research Plan (2006CB932802), National Science Foundation Grant (No. 10374095) and Shanghai Leading Academic Discipline Project(No. B411).

## REFERENCES

1. Baklenov, O., H. Nie, K. A. Anselm, et al, "Multi-stacked quantum dot resonate-cavity photodetector operating at 1.06  $\mu$ m," *Electron Lett.*, Vol. 34, No. 7, 694, 1998.
2. Liang, K., X. Yang, Y. Du, et al, "RCE photodiodes at wavelength band of 1.06  $\mu$ m," *Chinese Optics Letters*, Vol. 1, No. 6, 223, 2003.
3. Sugg, A. R., M. J. Cohen, M. J. Lange, P. Dixon, and G. H. Olsen, "Photodiode array spectroscopy for wavelength division multiplexing," *Proc. 13th IEEE Lasers and Electro-optics Soc. Annu. Meeting*, Vol. 1, 346–347, 2000.
4. Masaki, S., K. Shoji, H. Dwi, N. Mobuo, and H. Mizuho, "A high-sensitivity CMOS image sensor with gain-adaptive column amplifiers," *IEEE Journal of Solid-state Circuit*, Vol. 40, No. 5, 1147–1156, May 2005.
5. Kozlowski, L. J., "Low noise capacitive transimpedance amplifier performance vs. alternative IR detector interface schemes in submicron CMOS," *Proc. SPIE Infrared Readout Electronics III*, Vol. 2745, 2–11, April 1996.
6. Kang, S. G., D. H. Woo, and H. C. Lee, *IEEE Transactions on Circuits and Systems-II: Express Briefs.*, Vol. 52, No. 9, 553–557, September 2005.
7. Kavusi, S., K. Ghosh, and A. E. Gamal, "Architectures for high dynamic range, high speed image sensor readout circuits," to appear, *IEEE Custom Integrated Circuits Conference*, September 2006.

# Design of Reusable and Flexible Test Access Mechanism Architecture for System-on-Chip

G. Rohini<sup>1</sup> and S. Salivahanan<sup>2</sup>

<sup>1</sup>St. Joseph's College of Engineering, Chennai 600 119, India

<sup>2</sup>SSN College of Engineering, Kalavakkam 603 110, India

**Abstract**— Recent advances in IC design methods and manufacturing technologies have led to the integration of a complete system onto a single IC, called system on chip (SoC). These system chips offer advantages such as higher performances, lower power consumption, and decreased size and weight, when compared to their traditional multichip equivalents. However, testing such core-based SoCs poses a major challenge for system integrators. Modular testing of embedded cores in a system-on-chip (SoC) is now recognized as an effective method to tackle the SoC testing problem. In this paper we present an approach to design a TAM architecture and its associated test schedule using a fast and efficient heuristic. The test access mechanism architecture is responsible for the transportation of the test data from the system inputs to the core inputs and from the core outputs to the system outputs and also it could be very useful testing multi-frequency cores in SoC.

## 1. INTRODUCTION

A hierarchical system-on-chip (SoC) is designed by integrating heterogeneous technology cores at several layers of hierarchy. The ability to re-use embedded functionality has led to the paradigm of “today’s SoC is tomorrow’s embedded core”. Two broad design transfer models are emerging in hierarchical SoC design flows.

**Non-interactive:** In this model, there is limited communication between the core vendor and the SoC integrator. The cores are taken off-the-shelf and integrated into designs “as is”.

**Interactive:** Here, there is a certain amount of communication between the core vendor and core user during system integration. While hierarchical SoCs offer reduced cost and rapid system implementation, they pose several difficult test challenges. Modular testing of the embedded cores [7] in an SoC can simplify the complex problems of test access and application. For modular testing, an embedded core is isolated from surrounding logic and a test access mechanism (TAM) is designed to deliver test data from the I/O pins of the SoC. This facilitates the reuse of precomputed tests for individual cores and partitions the SoC for test; thus the test methodology follows the modular design process. The problem of multi-level TAM design and optimization for hierarchical SoCs has not been systematically addressed. However, when older-generation SoCs are themselves used as embedded cores in new SoC designs. In such cases, the core vendor may have already designed a TAM, as in Fig. 1. within the “mega-core” that is provided to the SoC integrator. A mega-core is defined as a design that contains non-mergeable embedded cores. In order to ensure effective testing of an SoC based on mega-cores, the top-level TAM [3] must communicate with lower level TAMs within mega-cores. The top-level TAMs must also be wide enough to fork out to the pre-designed lower-level TAMs.

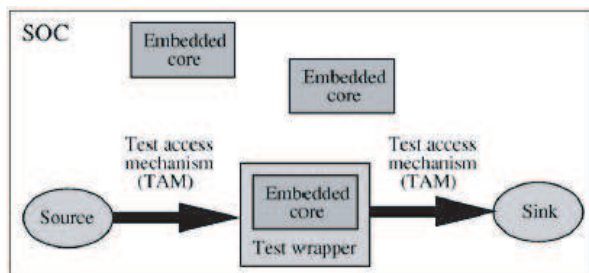


Figure 1: SOC testing using test wrappers and TAMs.

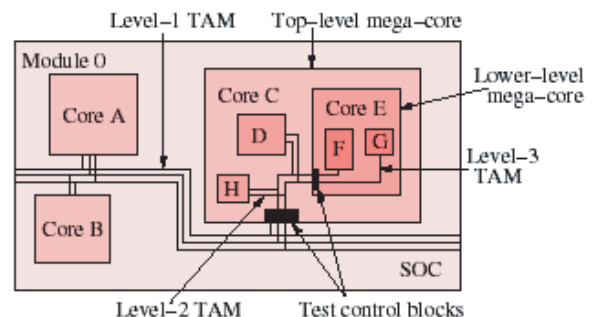


Figure 2: Illustration of a multi-level TAM architecture for a hierarchical SoC.

Moreover, the system level test architecture must be able to reuse the existing test architecture within cores; redesign of core test structures must be kept to a minimum and must be consistent with the design transfer model between the core designer and the core user. Fig. 2 illustrates a hierarchical SoC having two top-level cores A and B, and one top-level megacore C. Core C contains Cores D and H, and a lower-level megacore E, which in turn contains Cores F and G. A Level-1 TAM is connected to Cores A, B, and C. This TAM connects to a Level-2 TAM within Core C for the testing of Cores C, D, H, and E. The Level-2 TAM connects to a Level-3 TAM within Core E. The Level-3 TAM is used to test Cores F and G. Three proposals for test access to hierarchical embedded cores. A TAM design methodology that closely follows the design transfer model in use is critical because if the core vendor has implemented “hard” (i.e., non-alterable) TAMs within mega-cores, the SoC integrator must take into account these lower-level TAM widths while optimizing the widths and core assignment for higher-level TAMs. On the other hand, if the core vendor designs TAMs within mega-cores in consultation with the SoC integrator, the system designer’s TAM optimization method must be flexible [1] enough to include parameters for lower-level cores. Finally, multilevel TAM design for SoCs that include reused cores at multiple levels is needed to exploit “TAM reuse” in the test development process. In this paper, we describe the optimization of multi-level TAMs for the “cores within cores” design paradigm. We do not present new algorithms for TAM optimization here; instead, we show how known methods for flattened SoCs can be used for multi-level TAM optimization in hierarchical SoCs.

TAM widths are calculated for higher- and lower-level TAMs using a combination of integer linear programming (ILP) and enumeration, and efficient heuristics. The method presented here, unlike prior methods, time division multiplexing (TDM) is a technique used for transmission of several pieces of data (either digital or analog signals) over a communication channel by dividing the time frame into slots, one slot for each piece of data. We use this approach to end/collect test data across a test bus.

## 2. TAM DESIGN ANALYSIS

The advantage in design methodologies and semiconductor process technologies has led to the development of systems with excessive functionality implemented on a single die, called system-on-chip (SoC). In a core-based design approach, a set of cores, i.e., predefined and preverified design modules, is integrated into a system using user-defined logic (UDL) and interconnections. In this way, complex systems can be efficiently developed. However, the complexity in the systems leads to high test data volumes and the development of a test solution must therefore consider the following interdependent problems:

- to design an infrastructure for the transportation of test data in the system, a test access mechanism.
- to design a test schedule to minimize test time, considering test conflicts and power constraints.

The testable units in a SoC design are the cores, the UDL, and the interconnections. The cores are usually delivered with predefined test methods and test sets, while the test sets for UDL and interconnections are to be generated prior to test scheduling and TAM design [6]. The test vectors, forming the test sets for each testable unit, are stored or created in some test source, and their test responses are stored or analyzed in some test sink. The TAM is the connection between the test sources, the testable units and the test sinks. The test-application time can be minimized by applying several test sets concurrently; however, test conflicts, limitations, and test-power consumption must be considered. The workflow when developing a SoC test solution can mainly be divided into two consecutive parts: an early design space exploration followed by an extensive optimization for the final solution. For the former, we have proposed a technique for integrated test scheduling and TAM design to minimize test time and TAM cost. The advantage of the technique is its low computational cost making it useful for iteratively use in the early design space exploration. In this paper, we propose a technique to integrate test scheduling and TAM design with the objective to minimize the test application time and the TAM routing cost while considering test conflicts and power constraints. The aim with our approach is to reduce the gap between the design space exploration and the extensive optimization, i.e., to produce a high quality solution in respect to test time and TAM cost at a relatively low computational cost. The features of our proposed approach are that we support:

- testing of interconnections;

- testing of UDL;
- testing of unwrapped cores;
- consideration of memory limitations at test sources;
- consideration of bandwidth limitations on test sources and test sinks;
- embedding cores in core.

### 2.1. Test Access Mechanism (TAM) Switch

The TAM Switch is a synthesizable RTL core that can be instantiated in an ASIC design to provide test data access to embedded cores. As shown in Fig. 3. TAM is a programmable crossbar switch that allows efficient delivery of test vectors to embedded cores at varying bandwidth. It consists of an  $N \times N$  switch matrix where  $N$  is the number of input and output lines. modified.

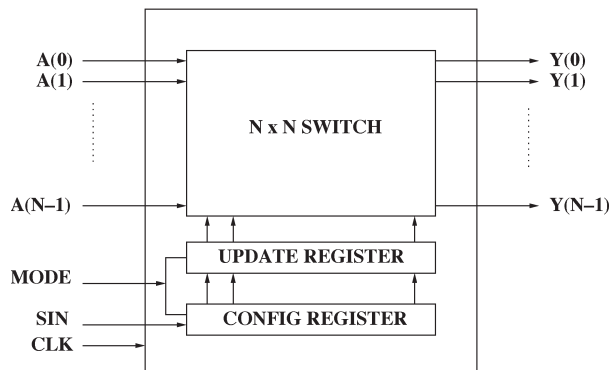


Figure 3: Test access mechanism switch.

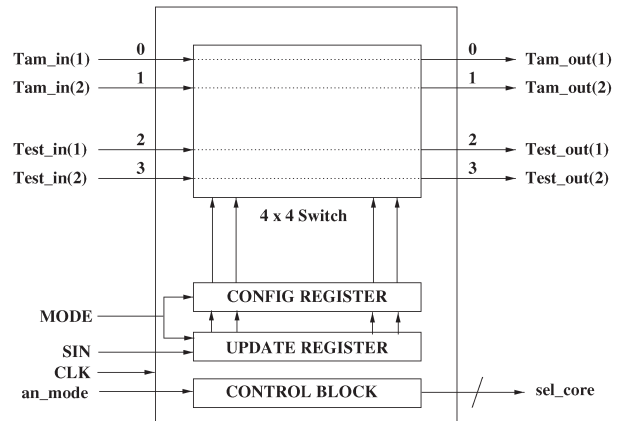


Figure 4: The MTAM switch.

In order to check the proper functionality of the analog core a strategy has been found in which TAM switch has been used. To make the testing scheme digitally compliant mixed signal test access mechanism (MTAM) switches has been used as shown in Fig. 4 [2, 4] describes the basic architecture of the proposed testing scheme. To test the digital cores the TAM switches are used to provide I/O access to the cores. The analog cores have been accessed through a separate analog test bus, according to IEEE P1149.4 [2] standard. The analog test bus is a wire carrying the voltage input signal to the core under test (CUT). The test rail carries out the response from the analog CUT to an ADC [5]. The digital TAM switches are placed on the digital test bus to test the digital cores. MTAM switches are placed along with the digital TAM switches. The MTAM is termed as the mixed TAM switch because it simultaneously probes digital core and also passes signals for the testing of the analog core. The MTAM is activated by the mode signal and the MTAM responds with a sel core signal which selects the core under test by activating the sel signal of the individual cores.

### 2.2. Timing Model

In this section, a model for test time with the TDM-TAM is developed. A core's test time  $T$  (in clock cycles) is determined by the scan-in cycles,  $s_i$ , the scan-out cycles,  $s_o$ , and the number of test patterns,  $N_p$ , according to the following

$$T = (1 + \max(s_i, s_o))N_p + \min(s_i, s_o) \quad (1)$$

The Equation (1) assumes that a scan-out operation is done concurrently with the scanning in of the subsequent test pattern, and that the application of one scan test pattern requires one system clock cycle.

### 2.3. Operation with Multi-frequency SoC

Today's SoC could have cores with different frequencies. None of the existing TAMs are suitable for multi-frequency SoC testing. The proposed TDM-TAM can handle the multi-frequency SoC, because with the TDM technique, we can manipulate frequency. Consider the example in Fig. 6. where data fed is to core A and core C is a one-fourth of the frequency of the branch. Core B is fed by a half of the frequency of the branch. Also, with  $n$ -lines and multiplexers, we can have

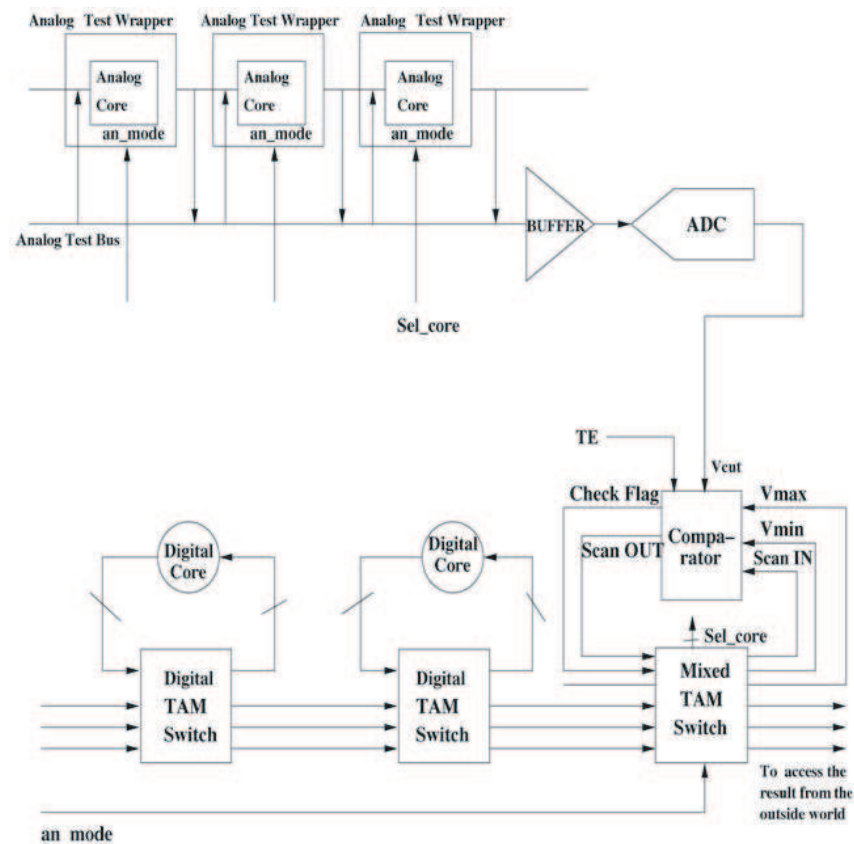


Figure 5: Basic architecture of the testing scheme.

a line with frequency,  $n$  times of the frequency of a single line. Fig. 6 shows a SoC with 3 cores, working at two different frequencies. Assume that the ATE can send data at 1 GHz. One-branch configuration that can test each core at its own speed is shown in Fig. 7. The mask of core A, B and C should be “1000”, “0101” and “0010”, respectively [1]. This way, if the frequency of the branch is  $F$ , the frequency of buses going to cores A, B and C is  $F/4$ ,  $F/2$  and  $F/4$ , respectively.

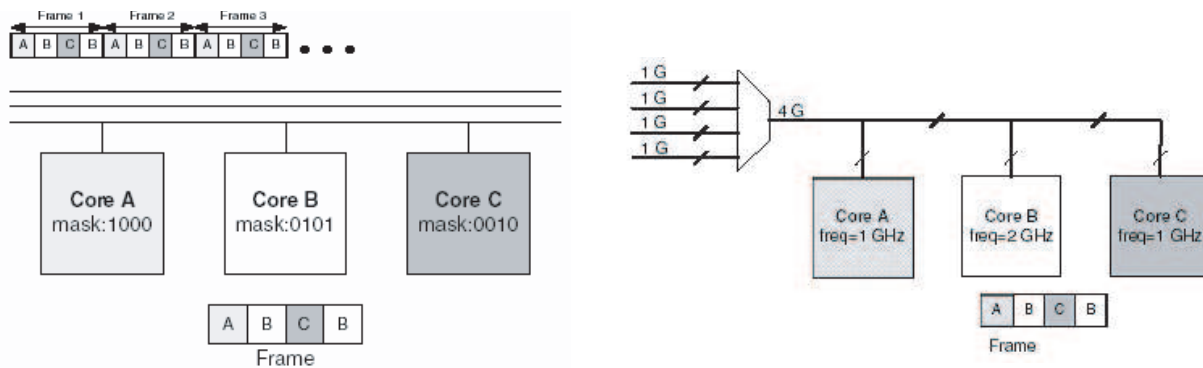


Figure 6: Example illustrating TDM-TAM concept. Figure 7: Using TDM-TAM for multi-frequency SoC.

Based on this formulation,  $F$  should be 4 GHz, but the maximum frequency of the ATE machine is 1 GHz. Using 4 lines and a multiplexer, we can generate a 4 GHz line. With this configuration, we can test each core at its own speed of  $N$  cores is assigned to  $N$  branches; determine the optimal core-branch pairing for each core. The goal in both cases is minimization of test time. These problems are in fact revised from earlier TAM optimization work, where the objective is to find the optimum configuration for a specific TAM, to achieve a minimum test time. In our case (TDM-TAM), the problem is finding the best assignment of cores to buses, and finding the

best mask assignments for each core. We use a genetic algorithm (GA) [8] for optimization. Our program requires the following information as input: number of cores, number of branches, the test strategy for each core, and whether any functional (non-scan) test patterns need to be applied, the number and length of the core scan chains, and the number of core input/outputs. Our program outputs an optimal branch configuration and core mask assignments.

### 3. ALGORITHM DFT TECHNIQUE FOR MIXED SIGNAL SOC DESIGNS

```

Create_graph
For all bandwidth divisions
{
do initial allotment of cores
/*allot one switch per core*/
while(deficiency > 0 or cores in the
neighborhood of the cluster > 0)
{
procedure_clustering(); /*Create clusters*/
if(deficiency < 0)
{

find_deficiency_new_cluster;
/*Recalculate the deficiency*/
break
}
}
while(deficiency < 0)
{
if(core==digital)
procedure_stitching();
/*Stitches the scan chains*/

procedure_partitions();
/*Computes the number of partitions*/
}
}
integrate_SoC_dft();
/*develop the RTL for the DFT of the SOC*/
reformat_test_patterns();
generate_reports();
/*time, area and objective function*/
}
integrate_SoC_dft()
{
For digital cores assign TAM switches;
For analog cores assign MTAM switches;
}

```

### 4. CONCLUSIONS

The present paper develops an integrated test methodology for mixed signal SoCs. A new DFT strategy has been developed so that the scheduling algorithms for the digital cores can also be employed for the analog cores to make the mixed signal DFT digitally compliant. Extensive experiments have been performed on Mixed Signal SoCs and the results show the DFT solution is hardware efficient. The proposed TAM uses the concept of time-division multiplexing (TDM) to effectively reduce TAM area requirements while still achieving good test time performance. This is possible by making optimal assignments of cores to buses and optimal assignment of time slots in the TDM scheme.

**REFERENCES**

1. Ebadi, Z., A. Ivanov, A. N. Avanaki, and R. Saleh, "Design and implementation of reconfigurable and exible test access mechanism for system-on-chip," *Integration, the VLSI Journal*, Vol. 40, 149–160, 2007.
2. Ozev, S., A. Sehgal, and K. Chakrabarty, "TAM optimization for mixed-signal SoCs using analog test wrappers," *ICCAD'03*, 95–99, San Jose, California, USA, November 2003.
3. Basu, S., I. Sengupta, D. R. Chowdhury, and S. Bhowmik, "An integrated approach to testing embedded core and interconnects using test access mechanism (TAM) switch," *Journal of Electronic Testing: Theory and Applications (JETTA), Special Issue on Plug-and-play Test Automation for System-on-a-chip*, Vol. 18, 475–485, Aug. 2002.
4. Mukhopadhyay, D., C. V. G. Rao, and D. R. Chowdhury, "A new strategy and design for mixed signal SoC testing," *Proceedings of International Workshop on RTL and High Level Testing (WRTL'03)*, Nov. 2003.
5. Banerjee, S., D. Mukhopadhyay, and D. R. Chowdhury, "Testing of ADC embedded in mixed signal SoC," *Proceedings of International Conference On Communications, Devices And Intelligent Systems*, Jadavpur University, Calcutta (Kolkata), India, January 2004.
6. Ghosh, I., N. Jha, and S. Dey, "A low overhead design for testability and test generation technique for core-based systems," *Proceedings of the International Test Conference*, 50–59, 1999.
7. Toubia, N. and B. Pouya, "Testing embedded cores using partial isolation rings," *Proceedings of the International Test Conference*, 10–16, 1997.
8. Chattopadhyay, S. and N. Choudhary, "Genetic algorithm based approach for low power combinational circuit testing," *Proceedings of the IEEE International Conference on VLSI Design*, 2003.

## Design and Simulation of Modified 1-D Electrostatic Torsional Micromirrors with $z$ -axis Displacement

Lijie Li, Deepak Uttamchandani, and Mark Begbie

The Institute for System Level Integration, Alba Campus

Livingston, Scotland EH54 7EG, UK

### Abstract—

Micromirrors based on Micromechanical systems (MEMS) have been essential components in many applications, such as micro confocal microscopy, optical data storage and biomedical imaging [1–3]. A variety of microfabrication and actuation technologies have been used to realize micromirrors, including electrothermal [3], electrostatic [1], etc., of which electrostatic torsional drive has been thought to be the most popular driving mechanism. K. E. Peterson [4] has developed the world first 1-D electrostatic driven torsional micromirror. The Lucent [5] Lambdrouator is one of famous and successful examples of 2-D electrostatic torsional micromirrors. For design improvement of this type of 2-D micromirror, Toshiyoshi et al. [6] have proposed a linearization method based on applying a small control voltage over a large bias voltage. Chiou et al. [7] have presented improved design to demonstrate linear stepping angles of 1-D micromirrors based on multiple electrodes. These developments are focus on realizing linear steps in angle. As mentioned by above articles, there are also displacements in  $z$ -axis as the micromirror is actuated, which have been ignored. The  $z$ -axis displacements have become a significant problem when the micromirrors are used on high resolution spatial scanning. Krishnamoorthy et al. [8] presents a dual-mode 1-D micromirror utilizing stacked multilayer vertical comb drive actuators, which can provide both piston and tilt motion. We have developed a  $z$ -axis displacement compensation concept for 2-D electrostatic torsional micromirrors previously [9].

In this paper, we expand the novel compensation concept into 1-D electrostatic torsional micromirror design. Modified 1-D electrostatic torsional micromirrors with fine control in  $z$ -axis displacement are presented in this paper. Here  $z$ -displacement is the mirror centre position changing in  $-z$  direction. The compensation concept is to add a separate electrode exactly centred with respect to the micromirror to control the  $z$ -displacements. The voltages applied on the central electrode are closely related to voltages applied on the side electrodes. When the  $z$ -displacement has a large value due to voltages applied on the side electrodes, the centre electrode will be given a small value voltage to compensate  $z$ -displacement to the constant value of  $z_m$ . In contrast, a large voltage applied on centre electrode will compensate a small  $z$ -displacement to  $z_m$ . Therefore, the angle-voltage transfer curves remain nearly unchanged, but  $z$ -axis displacement - voltage transfer

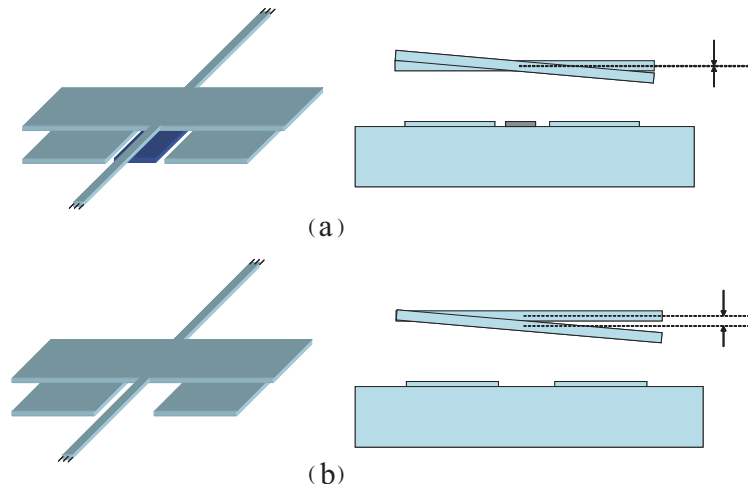


Figure 1: Schematic of the 1-D torsion micromirror with central electrode. Figure 1(a) shows the new design, and Figure 1(a) shows the traditional design.

curve is completely compensated. Furthermore, the displacements can be controlled precisely by turning the voltages applied on the centre electrode. Figure 1 shows the comparison of the classical and modified designs for 1-D micromirror.

The governing equations for the modified 1-D electrostatic micromirrors have been derived and listed as follows:

$$\begin{aligned} & \frac{1}{2}\varepsilon_0 V_s^2 \iint_{\text{side electrode}} x \left( \frac{\sin \theta}{\theta} \frac{1}{g - z - x \sin \theta} \right)^2 dA_s \\ & + \frac{1}{2}\varepsilon_0 V_c^2 \iint_{\text{central electrode}} x \left( \frac{\sin \theta}{\theta} \frac{1}{g - z - x \sin \theta} \right)^2 dA_c = \frac{2Gwt^3}{3l} \left( 1 - \frac{192t}{\pi^5 w} \tanh \frac{\pi w}{2t} \right) \theta \end{aligned} \quad (1)$$

$$\begin{aligned} & \frac{1}{2}\varepsilon_0 V_s^2 \cos \theta \iint_{\text{side electrode}} \left( \frac{\sin \theta}{\theta} \frac{1}{g - z - x \sin \theta} \right)^2 dA_s \\ & + \frac{1}{2}\varepsilon_0 V_c^2 \cos \theta \iint_{\text{central electrode}} \left( \frac{\sin \theta}{\theta} \frac{1}{g - z - x \sin \theta} \right)^2 dA_c = \frac{192EI}{(2l)^3} z \end{aligned} \quad (2)$$

Above equations have been numerically solved taking all the parameters and material properties listed in Table 1. Figure 2 shows the comparison of the traditional and modified micromirrors' performances, in which we can conclude that the modified electrostatic micromirrors have compensated, constant  $z$ -displacement, which is useful for precise spatial optical scanning. Figure 3 shows the calculated voltage values for the centre electrode.

Table 1: Material properties and parameters used in simulation.

Young's modulus	169 GPa
Shear modulus, $G$	73 GPa
Micromirror dimension	600 $\mu\text{m}$ $\times$ 300 $\mu\text{m}$
Torsion Beam ( $l, w, t$ )	200 $\mu\text{m}$ $\times$ 2 $\mu\text{m}$ $\times$ 2 $\mu\text{m}$
Gap ( $g$ )	70 $\mu\text{m}$

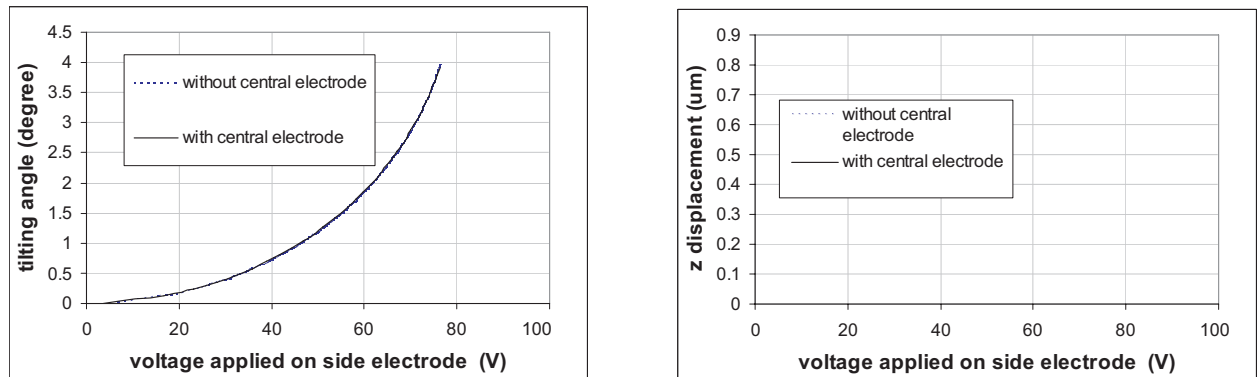


Figure 2: Simulation results. Top picture shows angle-voltage curve of 1-D torsion micromirror with and without control electrode. Bottom picture shows displacement-voltage curve of 1-D torsion micromirror with and without control electrode.

FEM modeling has also been performed to verify the analytical models. Table 2 shows both the analytical and FEM results, from which we can see that they are very close.

Table 2: Comparison of the analytical and FEM results.

Applied voltages		Mathematical		FEM	
$V_s(V)$	$V_c(V)$	$\theta(^{\circ})$	$z(\mu\text{m})$	$\theta(^{\circ})$	$z(\mu\text{m})$
4	146	0.05	0.78	0.04	0.77
45	127	0.92	0.78	0.93	0.79
61	101	1.95	0.78	1.96	0.78
71	67	2.98	0.78	2.94	0.77
76	15	3.90	0.78	3.88	0.78

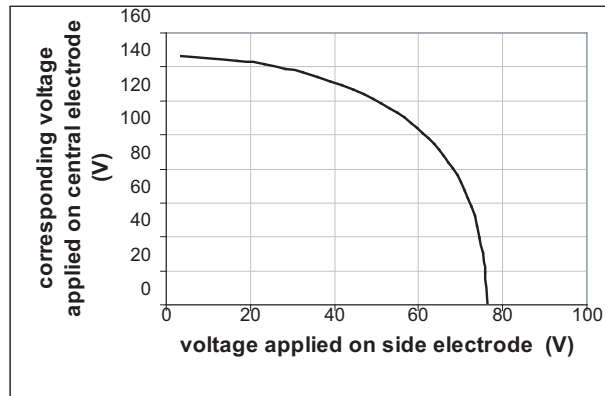


Figure 3: Calculated voltage value for centre electrode.

In conclusion, we present a novel concept to compensate the  $z$ -displacement of the 1-D electrostatic torsional micromirrors. Analytical and FEM model has been developed to verify the idea.

#### REFERENCES

1. Dickensheets, D. L. and G. S. Kino, "Silicon-micromachined scanning confocal optical microscope," *Journal of Microelectromechanical Systems*, Vol. 7, No. 1, 38–47, March 1998.
2. Yee, Y., H.-J. Nam, S.-H. Lee, J. U. Bu, and J.-W. Lee, "PZT actuated micromirror for fine-tracking mechanism of high-density optical data storage," *Sensors and Actuators A*, Vol. 89, 166–173, 2001.
3. Jain, A., A. Kopa, Y. Pan, G. K. Fedder, and H. Xie, "A two-axis electrothermal micromirror for endoscopic optical coherence tomography," *IEEE Journal of Selected Topic in Quantum Electronics*, Vol. 10, No. 3, 636–642, May/June 2004.
4. Petersen, K. E., "Silicon torsional scanning mirror," *IBM J. Res. Develop.*, Vol. 24, No. 5, 631–637, Sep. 1980.
5. Bishop, D. J., C. R. Giles, and G. P. Austin, "The lucent lambdarouter: MEMS technology of the future here today," *IEEE Commun. Mag.*, Vol. 40, No. 3, 75–79, Mar. 2002.
6. Toshiyoshi, H., C.-T. Chan, and M. C. Wu, "Linearization of electrostatically actuated surface micromachined 2-D optical scanner," *J. Microelectromech. Syst.*, Vol. 10, No. 2, 205–213, Jun. 2001.
7. Chiou, J. C. and Y. C. Lin, "A multiple electrostatic electrodes torsion micromirror device with linear stepping angle effect," *J. Microelectromech. Syst.*, Vol. 12, No. 6, 913–920, Dec. 2003.
8. Krishnamoorthy, U., K. Li, K. Yu, D. Lee, J. P. Heritage, and O. olgaard, "Dual-mode micromirrors for optical phased array applications," *Sensors and Actuators A*, Vol. 97–98, 21–26, 2002.
9. Li, L. and M. Begbie, "A design approach to 2-D electrostatic torsional micromirrors with  $z$ -axis displacement compensation," *IEEE Photonics Technology Letters*, Vol. 18, No. 22, 2422–2424, November 2006.

# Design and Characterization of a Radio Frequency MEMS Inductor Using Silicon MEMS Foundry Process

Deepak Uttamchandani and Lijie Li

Department of Electronic and Electrical Engineering  
University of Strathclyde, Glasgow G1 1XW, UK

**Abstract**— A successful design of RF inductor based on a silicon MEMS foundry process is presented. The suspended inductor has been realized in electroplated thick nickel with front side bulk micromachining of the substrate. The overall size of the inductor is about  $1\text{ mm} \times 1\text{ mm}$ . The inductors have been experimentally characterized and inductances around  $2\text{ nH}$  in the frequency range of  $200\text{ MHz}$ – $7\text{ GHz}$  have been measured with self resonant frequency of  $9.8\text{ GHz}$ . The peak measured value of the  $Q$  factor is 12 at a frequency of  $4\text{ GHz}$ . After de-embedding, the  $Q$  factor reaches 13 at a frequency of  $4.8\text{ GHz}$ . Simulation based on a parameter extraction method has been carried out for the inductor. There is a good agreement between simulated and experimental results.

## 1. INTRODUCTION

High performance monolithic inductors are widely used in wireless communication systems. They are key elements in RF integrated circuits, filters, amplifiers and baluns. Achievement of high performance micromachined inductors on silicon substrates is one of the major challenges in the move towards monolithic solutions [1]. The performance of silicon based inductors is limited by substrate parasitics and the conductivity of the silicon substrate. The solution to overcome these limitations involves separating the micromachined inductor from the proximity of the substrate. Several approaches have been employed to lift or suspend the micromachined inductors as far as possible from the silicon substrate. Mechanically orientated techniques such as surface tension based self-assembly [2], plastic deformation magnetic assembly (PDMA) [3], bimorph based self-lifting structures [4], and flip chip bonding [5] are amongst those that have been applied in microfabricating 3D vertical inductors or inductors which overhang the silicon substrate. Another approach has been to use material orientated techniques such as the introduction of a thick, low-loss dielectric layer (such as  $\text{SiO}_2$ ) between the inductor structure and the silicon substrate [6]. However, all of these methods involve material processing or post-processing of the silicon substrates. Glass substrates have also been used in the microfabrication of inductors [7], but this material does not lend itself to monolithic integration of RF devices. In this Letter, we report a new implementation of low-loss microfabricated RF inductors based on a commercial MEMS foundry process — MetalMUMPs [8]. Using this process, RF inductors have been achieved directly on a silicon substrate without further post-processing, and their performance is shown to be comparable to MEMS inductors fabricated by other more complex microfabrication processes. The foundry approach described here offers an excellent platform for the integration of microactuators and RF components onto silicon substrates that can be used to achieve monolithic systems, as the MetalMUMPs process is also capable of yielding MEMS microactuators.

## 2. DESIGN AND FABRICATION

MetalMUMPs is a silicon based MEMS process provided by the commercial MEMS foundry MEM-SCAP, Inc. Full details of the MetalMUMPs process, together with Design Rules can be obtained from [8]. Figure 1 illustrates the cross section of the inductor fabricated using MetalMUMPs. The process involves a high resistivity ( $\sim 5000\text{ Ohm-cm}$ ) silicon wafer as substrate. First, a layer of silicon oxide is deposited and patterned. This oxide layer outlines the area that will be used to etch a trench in the silicon substrate. The first nitride layer of  $0.35\text{ micron}$  thickness is then deposited and patterned. On top of the first nitride layer, a  $0.7\text{ micron}$  layer of polysilicon is deposited and patterned. A second nitride layer of  $0.35\text{ micron}$  thickness is then deposited and patterned. A second layer of oxide  $1\text{ micron}$  thick is then deposited. The second oxide layer is patterned and etched so that the metal layer, which is the last layer deposited in the process, is anchored to the nitride. This metal layer consists of  $20\text{ microns}$  of nickel with  $0.5\text{ micron}$  of gold deposited on top of the nickel layer. The last step in the process is to etch out the sacrificial layers as well as to etch

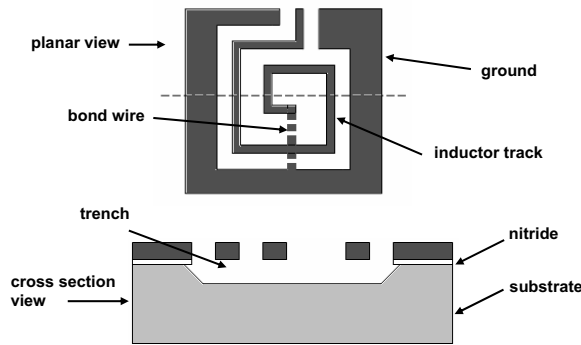


Figure 1: Schematic diagram of the inductor, the top picture is planar view and bottom picture is cross section view.

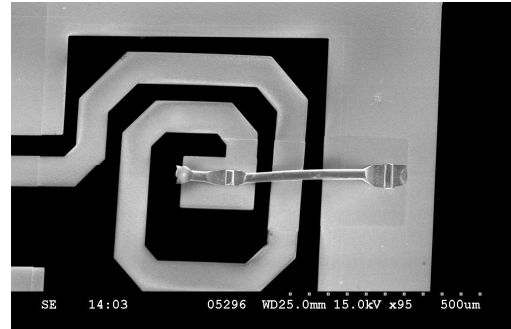


Figure 2: SEM photograph of fabricated inductor.

a 25 micron trench in the silicon substrate. The trench etch of the substrate is determined by the first oxide layer.

The inductor consists of a square coil of 1.5 turns, as shown in Figure 2. The width of the track forming the inductor is 80 microns while the spacing between the tracks is 40 microns. The inductor is based on a coplanar waveguide (CPW) design for the convenience of RF characterization which makes use of waveguide probes of ground-signal-ground (G-S-G) configuration. In the CPW design, the width of the signal line and the spacing between the signal line and ground plane are 80 microns and 22 microns respectively in order to produce a waveguide of 50 Ohm characteristic impedance. A K&S 4526 wire bonding machine has been used to bond 25 micron diameter gold wire between the centre of the inductor and the ground plane. There is a further 25 micron air gap between the bottom of the inductor structure and the high resistivity silicon substrate. This gap is formed by front side bulk micromachining which, as stated earlier, is a feature of the MetalMUMPs fabrication process. This air-gap significantly helps reduce the substrate induced loss in the device. Figure 2 shows a scanning electron microscope image of the inductor.

### 3. MEASUREMENTS

The performances of the RF inductor was measured using a vector network analyzer, Agilent N5230A and a Cascade Microtech 9000 probe station with on-wafer G-S-G probes. Before measuring the RF MEMS inductor, a Line-Reflect-Reflect-Match (LRRM) impedance standard substrate (ISS) was used to calibrate the probe station and VNA. The calibrated 1-port measurement result of the inductor was then imported from the VNA to WinCal software. The inductance  $L$  and the  $Q$  factor derived from the measured  $S$  parameters are given by

$$L = \frac{\text{imag}(1/Y_{11})}{\omega}, \quad Q = -\frac{\text{imag}(Y_{11})}{\text{real}(Y_{11})} \quad (1)$$

where  $\omega$  is angular frequency. Both inductance and  $Q$  factor were obtained over a frequency range of 200 MHz to 10 GHz. A set of simple open coplanar pads was also designed and fabricated adjacent to the inductor in order to de-embed the effect of the inductor pads. The de-embedding process followed the methodology described in detail in [5]. The measured results are shown in Figure 3.

### 4. ANALYSIS OF THE INDUCTOR

Analysis of the MEMS inductor is based on a parameter extraction method. The on-chip inductor can be represented by a nine-element equivalent circuit as shown in Figure 4 [9].  $L_s$  represents the series inductance of the structure,  $R_s$  represents the series resistance of the metallization and includes the frequency dependent term to model skin effect and other high frequency effects,  $C_s$  represents the fringing capacitance between the metal lines,  $C_{sub1}$  represents the capacitance from the metal layer to the substrate,  $R_{sub}$  represents the substrate resistance, and  $C_{sub2}$  represent the capacitance into the substrate. The values of the equivalent circuit elements of Figure 4 can be obtained from the measured  $S$  parameter of the inductor following the method described in [10].

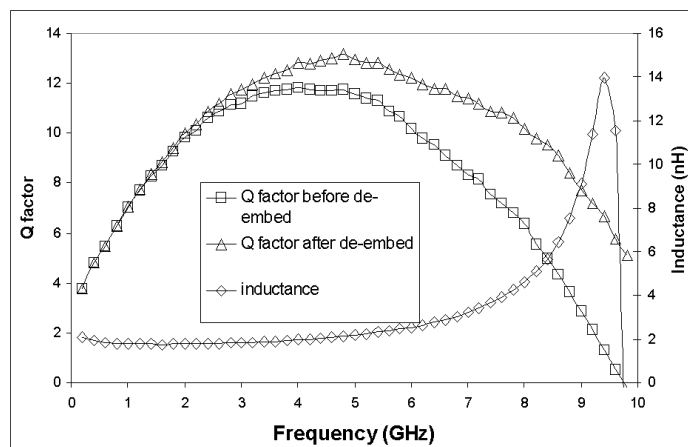


Figure 3: RF Measurement results of the inductor.

The series components can be obtained using Equations (2) and (3):

$$\frac{1}{\text{real}(Y_s)} = R_s + \omega^2 \frac{L_s^2}{R_s} \quad (2)$$

$$\frac{\text{imag}(Y_s)}{\omega} = C_s - \frac{L_s}{R_s} \text{real}(Y_s) \quad (3)$$

Here  $Y_s = -Y_{12}$ , where  $Y_{12}$  can be derived from measured  $S$  parameters. In order to include the substrate loss, the shunt branch ( $C_{sub1}$ ,  $C_{sub2}$ ,  $R_{sub}$ ) should be considered and can be extracted using Equations (4) and (5):

$$\frac{\omega^2}{\text{real}(Y_{sub})} = \frac{1}{R_{sub} C_{sub1}^2} + \frac{R_{sub}^2 (C_{sub1} + C_{sub2})^2}{R_{sub} C_{sub1}^2} \omega^2 \quad (4)$$

$$\frac{\text{imag}(Y_{sub})\omega}{\text{real}(Y_{sub})} = \frac{C_{sub1}}{R_{sub} C_{sub1}^2} + \frac{R_{sub}^2 C_{sub1} C_{sub2} (C_{sub1} + C_{sub2})}{R_{sub} C_{sub1}^2} \omega^2 \quad (5)$$

Here  $Y_{sub} = Y_{11} + Y_{12}$ . Using Equations (2)–(5), the equivalent circuit values have been calculated as follows:  $L_s = 1.8$  nH,  $R_s = 2.1$  Ohm,  $C_s = 85$  fF,  $C_{sub1} = 95$  fF,  $C_{sub2} = 0.16$  pF,  $R_{sub} = 350$  Ohm.

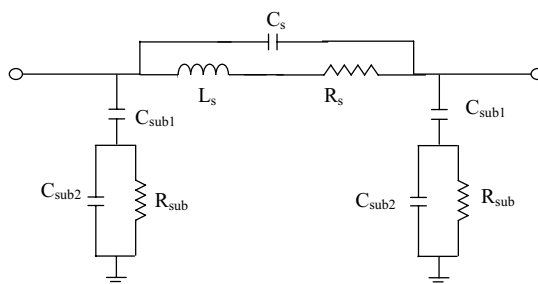


Figure 4: Equivalent circuit of the inductor.

## 5. DISCUSSION

The measured  $Q$  factor, de-embedded  $Q$  factor, and the measured inductance plotted against frequency are shown in Figure 3. The inductance and the self-resonance frequency of the device are 2 nH and 9.8 GHz respectively. The  $Q$  factor is measured to have a value of 12 at the peak frequency of 4 GHz frequency, while the  $Q$  factor after de-embedding is 13 at a peak frequency of 4.8 GHz. The inductance and  $Q$  factor of the device are comparable to the values of devices reported previously [2–6] which were fabricated by more elaborate processes or on materials of inherently low RF loss. Analysis of the equivalent circuit of the inductor has been accomplished by

a parameter extraction method. The comparison between measured and modelled results is shown in Figure 5. The fit between measurement and modelled inductance is within 5% root-mean-square (RMS) deviation over the frequency range of 0.2–10 GHz. The fit between measurement and modelled  $Q$  factor is within 10% RMS deviation over the same frequency range. It can be seen that the modelled results are closely matched to the measurements.

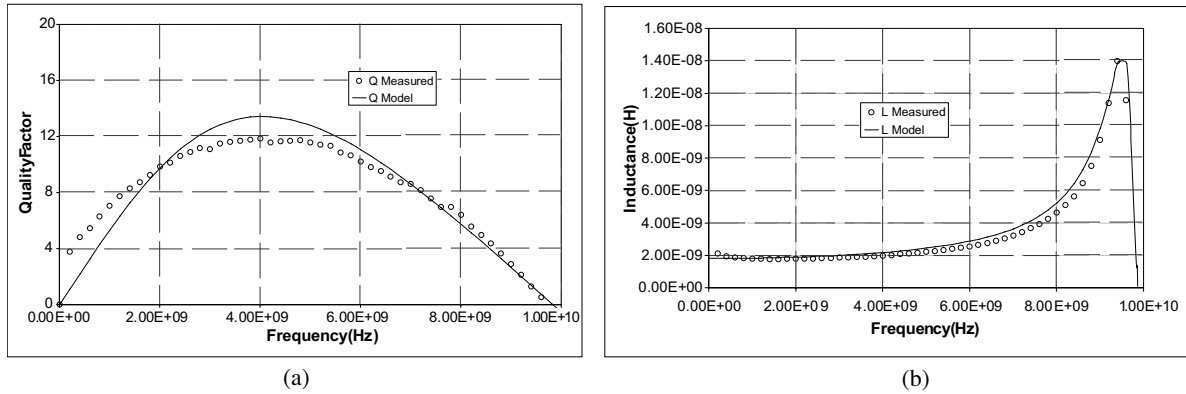


Figure 5: Comparison of measured and simulated  $L$  and  $Q$ .

## 6. CONCLUSION

Modelling and characterization of a high performance RF MEMS inductor fabricated using a commercial MEMS foundry process (MetalMUMPs) is reported. The overall size of the inductor is about  $1\text{ mm} \times 1\text{ mm}$ , and the inductor is formed in electroplated nickel of 20 microns thickness. To reduce parasitic effects of the substrate, bulk micromachining has been used to etch a 25 microns deep trench directly below the inductor, leaving behind a suspended inductor. The inductance is around 2 nH over the frequency range of 200 MHz–7 GHz. The self resonance frequency is 9.8 GHz. The de-embedded  $Q$  factor reaches 13 at a frequency of 4.8 GHz. Modelling based on parameter extraction was performed, and the results fit very well with the measurements.

## REFERENCES

- Burghartz, J. N., "Progress in RF inductors on silicon-understanding substrate losses," *IEDM Tech. Dig.*, 523–526, 1998.
- Dahlmann, G. W. and E. M. Yeatman, "High Q microwave inductors on silicon by surface tension self-assembly," *Electron. Lett.*, Vol. 36, 1707–1708, 2000.
- Zou, J., C. Liu, D. R. Trainor, J. Chen, J. E. Schutt-Aine, and P. L. Chapman, "Development of three-dimensional inductors using plastic deformation magnetic assembly (PDMA)," *IEEE Trans. Microw. Theory Tech.*, Vol. 51, 1067–1075, 2003.
- Lubecke, V. M., B. Barber, E. Chan, D. Lopez, M. E. Gross, and P. Gammel, "Self-assembling MEMS variable and fixed RF inductors," *IEEE Trans. Microw. Theory Tech.*, Vol. 49, 2093–2098, 2001.
- Zeng, J., A. J. Pang, C. H. Wang, and A. J. Sangster, "Flip chip assembled MEMS inductors," *Electron. Lett.*, Vol. 41, 480–481, 2005.
- Sun, J. and J. Miao, "High performance MEMS inductors fabricated on localized and planar thick  $\text{SiO}_2$  layer," *Electron. Lett.*, Vol. 41, 446–447, 2005.
- Wu, W., F. Huang, Y. Li, S. Zhang, X. Han, Z. Li, Y. Hao, and Y. Wang, "RF inductors with suspended and copper coated thick crystalline silicon spirals for monolithic MEMS LC circuits," *IEEE Microw. Wireless Compon. Lett.*, Vol. 15, 853–855, 2005.
- Cowen, A., B. Dudley, E. Hill, M. Walters, R. Wood, S. Johnson, H. Wynands, and B. Hardy, *MetalMUMPs Design Handbook*, MEMSCAP Inc. <http://memsrus.com/documents/MetalMUMPs.dr.v1.pdf>.
- Ashby, K. B., I. A. Koullias, W. C. Finley, J. J. Bastek, and S. Moinian, "High Q inductors for wireless applications in a complementary silicon bipolar process," *IEEE J. Solid-State Circuits*, Vol. 31, No. 1, 4–9, 1996.
- Huang, F. Y., N. Jiang, and E. L. Bian, "Modeling of single-pi equivalent circuit for on-chip spiral inductors," *Solid-State Electron.*, Vol. 49, 473–478, 2005.

## A Concept of Moving Dielectrophoresis Electrodes Based on Microelectromechanical Systems (MEMS) Actuators

Lijie Li and Deepak Uttamchandani

Department of Electronic and Electrical Engineering  
University of Strathclyde, Royal College Building, G1 1XW, UK

**Abstract**— A concept of moving dielectrophoresis electrodes (MDEP) based on Microelectromechanical Systems (MEMS) actuators is introduced in this letter. An example design of tuneable dielectrophoresis filter is presented. Finite Element Analysis of the electrostatic field of the tuneable filter has been conducted. Results show that the trapping force can be adjusted by actuating the MEMS actuators.

The principle of the dielectrophoresis (DEP) is based on polarization of the dielectric particles under electrostatic field. Polarized dielectric particles can be moved toward the direction of the electric field gradient. Examples of polarized objects include dielectric materials, metallic particles, and many biological objects, such as nucleic acids, proteins, cells, and virus. DEP has been proven to be a powerful technique to perform sample sorting, trapping, manipulation, and concentration [1]. The classical DEP has been expanded to travelling wave DEP in order to get high throughput cell manipulation without external liquid pumping [2], CMOS DEP in order to achieve parallel manipulation of large number of cells [3], and laser induced DEP by optically programmable electrodes [4]. Microfabricated interdigitated electrode array was introduced previously [5] for application of separating two populations of particles pumped across the electrode array, one population of particles having positive dielectrophoresis and another having negative dielectrophoresis.

The above approaches are all based on fixed electrodes arrangement. A concept of moving dielectrophoresis electrode (MDEP) is introduced based on microelectromechanical systems (MEMS) electrostatic or electrode thermal actuators in this letter. The electrostatic or electrothermal actuators were previously operated under the water [6], which proves the idea of MDEP very feasible. Previous research on interdigitated electrodes [7] shows that the DEP force changes with electrode dimensions (electrode width and gap) at a given voltage. If for example, the gap of the electrodes changes, the trapping force will also changes accordingly. A tuneable DEP filter as an example of MDEP is therefore generated, which is schematically shown in Figure 1. The interdigitated comb

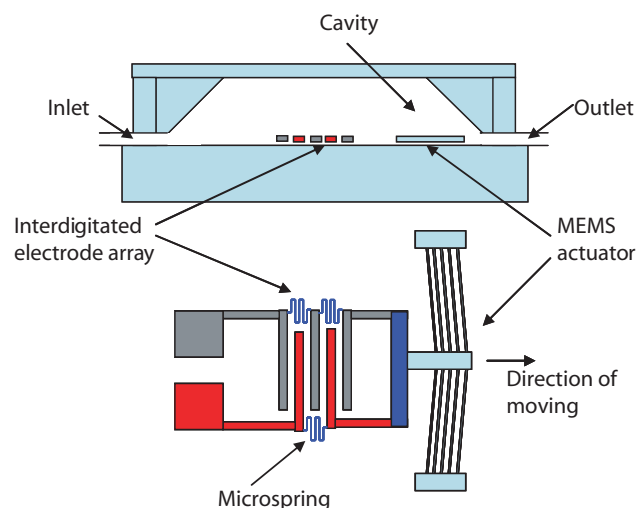


Figure 1: Schematic picture of a moving dielectrophoresis electrode (MDEP) filter.

fingers act as two opposite electrodes of DEP, which can be stretched by either electrothermal or electrostatic actuators. There are microsprings connecting two adjacent comb fingers to allow uniform gap changing. Microelectrodes are electrically separated and mechanically connected with the microactuators, so that the driving signal for the microactuators does not affect the DEP electrodes.

The microactuated electrodes can be fabricated easily using relevant MEMS foundries. The cavity contains micro particles such as cells can be manufactured using transparent dielectric materials, such as glass or sapphire. The two chips will be then flip-chip bonded to form a tuneable DEP filter.

Theoretical analysis of the DEP force of the tuneable filter is conducted in this letter to show the scale of the tenability. The expression of the DEP force  $F$  for spherical particles is well known and given as [8]:

$$F = 2\pi r^3 \varepsilon_m R_e[K] \nabla E^2 \quad (1)$$

where  $r$  is the particle radius,  $E$  is electrical field,  $\varepsilon_m$  is the absolute permittivity of the suspending medium.  $R_e[K]$  is the real part of the polarization factor, defined as:

$$K = \frac{\varepsilon_p^* - \varepsilon_m^*}{\varepsilon_p^* + 2\varepsilon_m^*} \quad (2)$$

where  $\varepsilon_m$  and  $\varepsilon_p$  are the complex permittivity of the particle and medium respectively. The complex permittivity for a dielectric material  $\varepsilon^*$  can be described by its permittivity  $\varepsilon$  and conductivity  $\sigma$ ,  $\varepsilon^* = \varepsilon - j\frac{\sigma}{\omega}$ , here  $\omega$  is the angular frequency of the applied electrical field  $E$ . From the Equation (1), the dimensions of the electrode (width and gap) determine the electrical field  $E$  at a given AC voltage. In the tuneable DEP filter design, the interdigitated electrode finger width is designed to be  $20 \mu\text{m}$ , and the gap can be varied from  $5 \mu\text{m}$  to  $20 \mu\text{m}$  using MEMS actuators. The electrical field  $E$  of  $5 \mu\text{m}$ ,  $6 \mu\text{m}$ ,  $7 \mu\text{m}$ ,  $10 \mu\text{m}$ ,  $15 \mu\text{m}$ ,  $20 \mu\text{m}$  gap electrodes array have been analyzed using Finite Element Method (FEM) with the CoventorWare NetFlow package [9]. The conductivity and permittivity of surrounding medium is taken to be xxx and xxx respectively. The thickness of the cavity is designed to be  $20 \mu\text{m}$ . AC RMS voltage of  $30 \text{V}$  has been applied to the electrodes. Figures 2–4 show the simulation results of the electrical field  $E$  generated by  $5 \mu\text{m}$ ,  $10 \mu\text{m}$ , and  $15 \mu\text{m}$  gap electrodes arrays. From the results, we can see that the electrical fields are symmetrical about the vertical line of electrode edge. As the gap become wider, the electrical field between the electrodes becomes weaker. The maximum electrical field is located in the corner of the electrodes. The maximum electrical field  $E_m$  of  $5 \mu\text{m}$  is around  $5.5 \text{V}/\mu\text{m}$ , the  $E_m$  of  $10 \mu\text{m}$  is around  $3.2 \text{V}/\mu\text{m}$ , the  $E_m$  of  $15 \mu\text{m}$  gap is about  $2.6 \text{V}/\mu\text{m}$ .

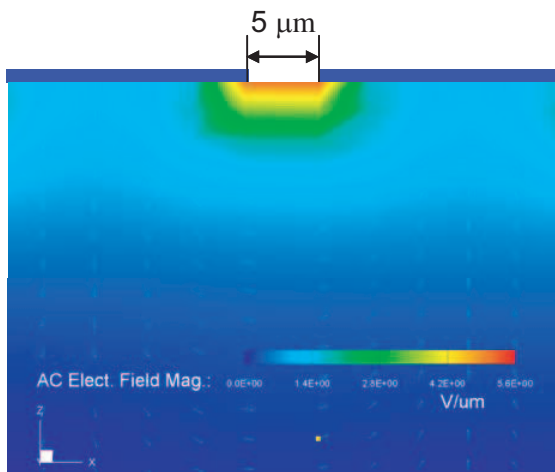


Figure 2: Electrical filed  $E$  of  $5 \mu\text{m}$  gap.

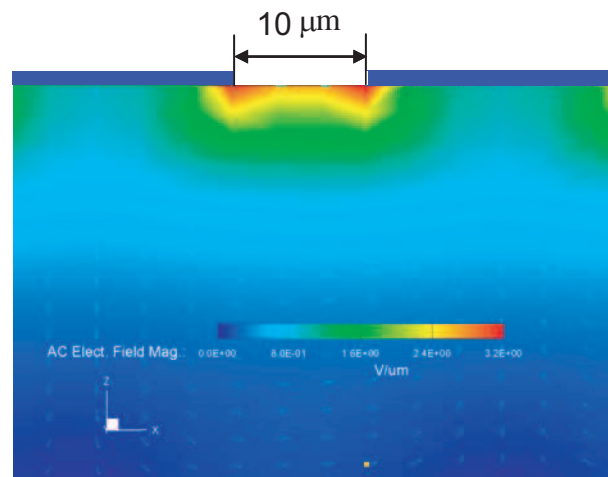
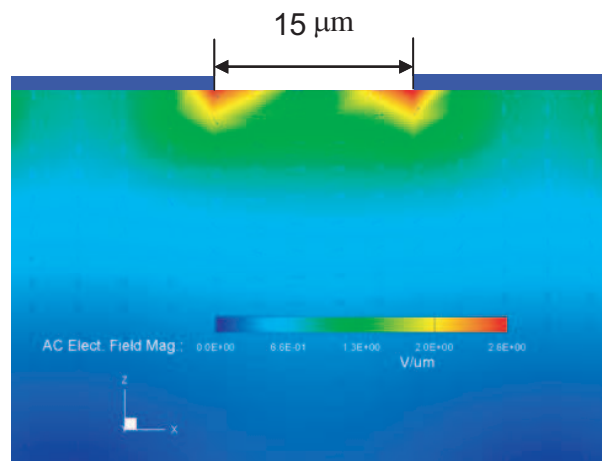
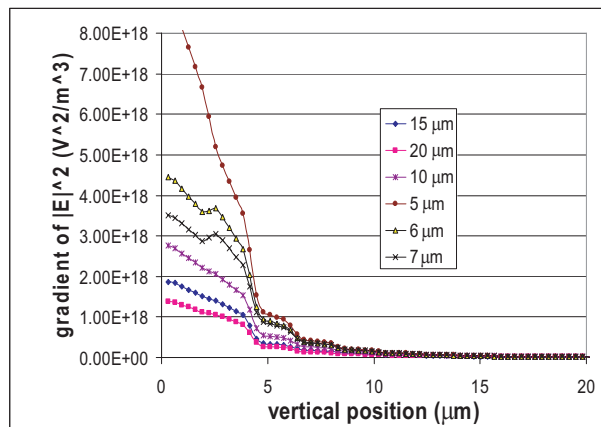


Figure 3: Electrical filed  $E$  of  $10 \mu\text{m}$  gap.

The  $\nabla E^2$  along the vertical line of the electrode edge has been extracted from the FEM results, which is shown in Figure 3. It is clear shown that as the spacing of the electrodes increases, the  $\nabla E^2$  reduces, therefore the trapping force reduces. By adjusting the gap between the electrodes using MEMS actuators, the tuneable DEP filter can be realized.

In conclusion, a design concept of the tuneable DEP filter using MEMS actuators have been presented. FEM modelling of the electrical fields of different electrode gaps have conducted in order to validate the concept. The simulation results show that with adjustable gap electrode array, tuneable trapping force can be achieved. The MEMS actuators operated in the water [ ]

Figure 4: Electrical field  $E$  of 15  $\mu\text{m}$  gap.Figure 5: Electrical field  $E$  of 15  $\mu\text{m}$  gap.

proves this idea is feasible from the MEMS point of view. Device manufacture is being pursued and will be reported in the future.

The project was supported by the Scottish Funding Council under the Scottish Consortium in Integrated Micro-Photonics Systems.

#### REFERENCES

1. Hughes, M. P., *Nanoelectromechanics in Engineering and Biology*, FL: CRC Press, Boca Raton, 2003.
2. Masuda, S., et al., "Separation of small particles suspended in liquid by non-uniform travelling field," *IEEE Trans. Ind. Appl.*, Vol. 23, 474–480, 1987.
3. Manaresi, N., et al., "A CMOS chip for individual cell manipulation and detection," *IEEE J. Solid-state Circuits*, Vol. 38, 2297–2305, 2003.
4. Chiou, P., A. Ohta, and M. C. Wu, "Massively parallel manipulation of single cells and microparticles using optical images," *Nature*, Vol. 436, 370–372, 2005.
5. Li, H., Y. Zheng, D. Akin, and R. Bashir, "Characterization and modelling of a microfluidic dielectrophoresis filter for biological species," *Journal of Microelectromechanical Systems*, Vol. 14, No. 1, 103–112, Feb. 2005.
6. Sameoto, D., T. Hubbard, and M. Kujath, "Operation of electrothermal and electrostatic MUMPs microactuators underwater," *Journal of Micromechanics and Microengineering*, Vol. 14, 1359–1366, 2004.
7. Gadish, N. and J. Voldman, "High-throughput positive-dielectrophoretic bioparticle microconcentrator," *Analytical Chemistry*, Vol. 78, No. 22, 7870–7876, 2006.
8. Jones, T. B., *Electromechanics of Particles*, Cambridge, U.K.: Cambridge Univ. Press, 1995.
9. CoventorWare, Coventor Inc., <http://www.coventor.com/>.

# Holographic Femtosecond Laser Processing and Three-dimensional Recording in Biological Tissues

Yoshio Hayasaki

Department of Optical Science and Technology, Faculty of Engineering  
The University of Tokushima, Japan

**Abstract**— Data recording on biological tissues and prostheses with femtosecond laser processing for personal identification is demonstrated. The target materials are human fingernails (fingernail memory) and dental prostheses (dental memory). Because they have unexpected movements and individual three-dimensional shapes, the processing system is required an adaptive focusing and high-throughput recording capability. The adaptive focusing is performed with a target surface detection. The high throughput is realized by parallel laser processing based on a computer-generated hologram displayed on a spatial light modulator. Two-dimensional and three-dimensional parallel laser processing of glass is demonstrated.

## 1. INTRODUCTION

Femtosecond lasers are powerful tools for micro- and nano-structuring of transparent materials because they can process with high spatial resolution resulting from multiple photon absorption, and reduced thermal damage due to the ultra-short interaction time between the laser pulse and the material, as well as various physical phenomena caused by the ultra-high intensity of the laser pulse. The high three-dimensional (3-D) spatial resolution requires a precise control of the focus position. Femtosecond laser processing with an axial focus position control is commercially available at present. To realize data recording on biological tissues and prostheses for personal identification [1–4], a femtosecond laser processing system with a lateral focus position in addition with the axial focus position control is developed [5] because the biological tissues and the prostheses have unexpected movements and individual three-dimensional shapes. Another approach of processing of biological tissue is to develop femtosecond laser processing system with a high-throughput. The high-throughput is realized by parallel laser processing based on a computer-generated hologram (CGH) displayed on a liquid crystal spatial light modulator (LCSLM). This is called as holographic femtosecond laser processing [6–10]. The use of a LCSLM enables to perform an arbitrary and variable patterning.

In this paper, we demonstrate the data recordings in fingernail (fingernail memory) and dental prostheses (dental memory). We also demonstrate two-dimensional and three-dimensional parallel laser processing of glass using the holographic femtosecond laser processing.

## 2. FINGERNAIL MEMORY

Our goal is to realize optical memory in a human fingernail for highly secure data transportation that does not suffer from problems such as theft, forgery, or loss of recording media. In this section, we demonstrate to record a 3-D arranged bit data inside fingernail by a femtosecond laser pulse and demonstrate the fluorescence readout.

An optical system for recording is composed of an amplified femtosecond laser system and an optical microscope. The femtosecond laser system is composed of a mode-locked Ti:sapphire laser (Spectra Physics, Tsunami) pumped by a diode-pumped solid-state cw green laser (Spectra Physics, Millennia), and a multikilohertz pulsed Ti:sapphire regenerative amplifier (Spectra Physics, Spitfire) pumped by a diode-pumped, Q-switched Nd:YLF laser (Spectra Physics, Merlin). The femtosecond laser system generates pulses with a central wavelength of 800 nm and a pulse width of  $\sim 150$  fs. The optical microscope system having a  $40\times$  objective lens (OL) (numerical aperture (NA) = 0.55) has a computer-controlled three-axis motorized stage. The read out of the bit data is performed with an ordinary fluorescence microscope.

Figure 1 shows transmission-illumination microscope observations of three bit layers recorded inside a human fingernail. These bit arrays were recorded with  $E_p = 0.49 \mu\text{J}$  at the depths of (a)  $Z = 40 \mu\text{m}$ , (b)  $60 \mu\text{m}$ , and (c)  $80 \mu\text{m}$ . The bit spacing was  $5 \mu\text{m}$  in the transverse direction and  $20 \mu\text{m}$  in the axial direction, the corresponding recording density was  $2 \text{ Gbit}/\text{cm}^3$ .

In investigating a suitable readout method of the recorded bit data inside a human fingernail, we discovered increased fluorescence at the structural changes formed in the fingernail compared with

the auto-fluorescence of the fingernail [3]. Figure 2 shows the fluorescence readout observed with a fluorescence microscope. Each bit layer was read out without crosstalk. The increased fluorescent effect had been continued over 180 days, which is the time a fingernail is replaced by growing in about 6 months.

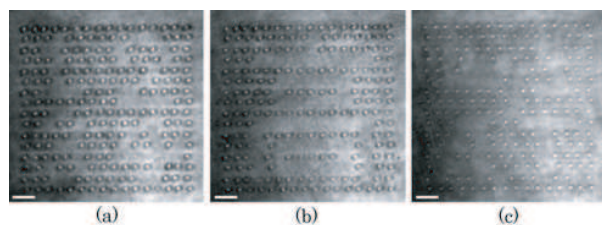


Figure 1: Three bit planes at (a)  $Z = 40 \mu\text{m}$ , (b)  $60 \mu\text{m}$ , and (c)  $80 \mu\text{m}$ . The scale bar indicates  $10 \mu\text{m}$ .

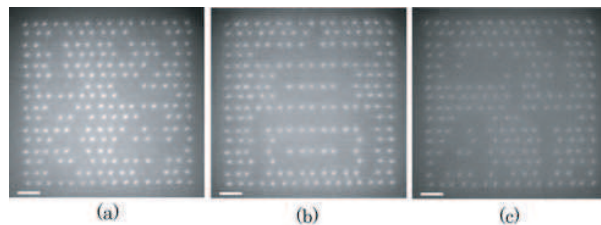


Figure 2: Fluorescence images of three bit planes at (a)  $Z = 40 \mu\text{m}$ , (b)  $60 \mu\text{m}$ , and (c)  $80 \mu\text{m}$ .

### 3. DENTAL MEMORY

In mass natural disasters such as earthquakes and tsunamis, personal identification of victims is an important problem. Forensic dentistry and fingerprints have been used for personal identification. These methods, however, require a lot of time and are expensive when identifying a large number of victims, because they involve comparing personal information about the victim with pre-registered information. If information for identifying the victim could be obtained from the victim himself, the time and cost involved could be substantially reduced.

As a method for realizing this scheme, we proposed to record personal information on a dental prosthesis. Dental prostheses are good information storage media because it is resistant to thermal and putrefactive changes. The method has some advantages, including ease of data access, low risk of theft of the recorded information, and high data storage capacity. Furthermore, combining the method with forensic dentistry could improve the accuracy of personal identification, as well as reducing the time required.

Figure 3 shows the experimental setup composed of an amplified femtosecond laser and a confocal surface detection system. The processing was performed by single pulse irradiation. The confocal optical system consisting of a laser diode ( $\lambda = 650 \text{ nm}$ ), a  $20\times$  OL ( $\text{NA} = 0.40$ ), a pinhole, and a photodetector was used to control the focus position of the femtosecond laser pulses. Samples are made of a Au-Ag-Pd dental alloy (Castwel MC<sup>®</sup>, GC, Tokyo, Japan). The processed structures were observed with a scanning electron microscope (SEM; S-4700, Hitachi).

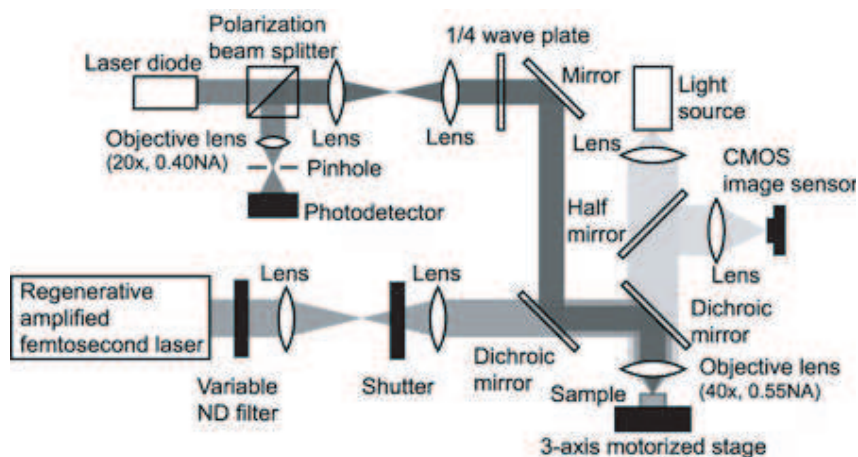


Figure 3: Experimental setup.

Figure 4 shows the SEM images of two-dimensional data recorded on the alloy plate surface without and with surface detection. Femtosecond laser pulses with an energy of  $0.06 \mu\text{J}$  were irradiated at  $2 \text{ Hz}$ . Around the upper left area where the processing was started with manual

correction of the focus position, the structures were ablated depressions surrounded with melted and scattered debris. Around the lower right area where the processing ended, the surface morphologies processed without and with the surface detection were quite different. When the surface detection was used, the morphologies of the processed areas were the same ablated structures over a wide area and a wide axial range. The spacing between the recording points was  $2.0\ \mu\text{m}$ , resulting in a recording density of  $250\ \text{kbit}/\text{mm}^2$ .

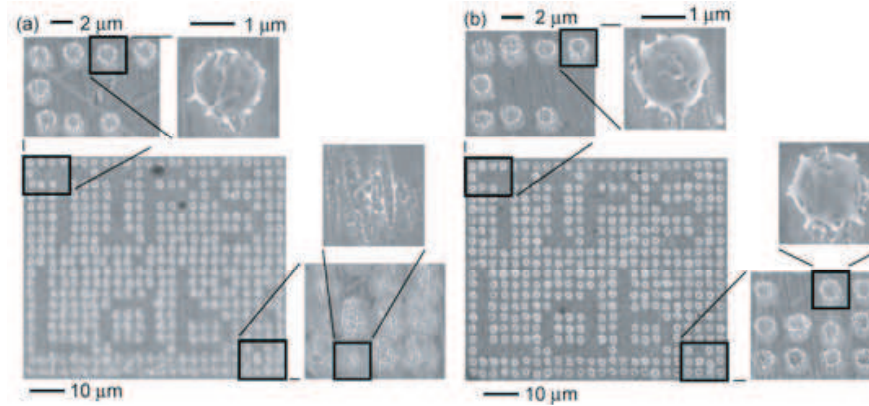


Figure 4: SEM images of the recording data on sample surface (a) without and (b) with the surface detection.

#### 4. HOLOGRAPHIC FEMTOSECOND LASER PROCESSING

Holographic femtosecond laser processing is classified three types according to a positional relationship between a hologram and a target. (1) When the target is put on the image plane of the hologram, the irradiation beam is divided to multiple-beams by a diffractive beam splitter, which is a kind of holograms. The diffractive beams form the interference pattern on the target through a 4f-imaging optical system. An advantage of this method is suitable for processing of a periodic structure to a large area. (2) When the target is put on the Fourier plane of the hologram, the Fourier transform hologram is used [6, 9, 10]. The hologram with a high quality is designed with a low computational cost by optimization techniques. The reconstructed diffraction has little dependence on an undesired beam intensity distribution. (3) When the target is put on the Fresnel plane of the hologram [7, 8], the Fresnel transform hologram is used. Because the femtosecond laser processing is based on the multiphoton process, the 0th-order beam doesn't contribute to the processing. The Fresnel transform hologram enable us to perform a three-dimensional processing without any mechanical movements.

Figure 5 shows the experimental setup of the holographic femtosecond laser processing system using a Fourier hologram. The system mainly consisted of an amplified femtosecond laser system and an LCSLM (Hamamatsu Photonics, PPM). The collimated laser pulse was diffracted by the CGH displayed on the LCSLM to form a processing pattern at the plane P. The 0-th order light was obstructed at plane P. The processing pattern was reduced with Lens 4 and a  $60\times$  OL (NA = 0.85) and was applied to a sample. The processing was performed with single-pulse irradiation. A halogen lamp (HL) and a charge-coupled device (CCD) image sensor were used to observe the processing. The sample was an ordinary glass microscope cover slip (Matsunami), subjected to ultrasonic cleaning in ethanol and pure water.

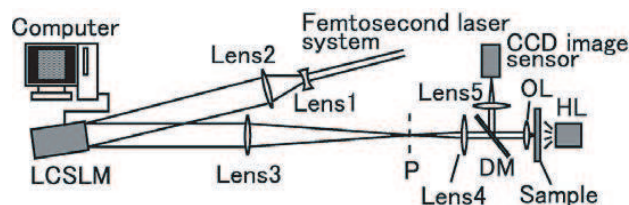


Figure 5: Experimental setup.

Figure 6 shows the results of 3-D processing using three CGHs without an axial translation of the sample. The processing for each CGH performed with single-pulse irradiation. Figure 6(a)

shows the CGHs designed to generate 12, 12, and 8 diffraction peaks, and having focal lengths of 1800, 2000, and 2400 mm, respectively. Figure 6(b) shows the optical reconstructions of the CGHs. The respective uniformities  $U$  were 92%, 93%, and 83%, and the diffraction efficiencies  $\eta$  were 73%, 71%, and 68%. The uniformity is defined as  $U = I_{\min}/I_{\max}$ , where  $I_{\min}$  and  $I_{\max}$  are the minimum and maximum peak intensities, respectively. In the transmitted optical microscope observation of the fabricated area, when the axial positions were 9, 17, and 30  $\mu\text{m}$  inside the glass from the sample surface was focused, the structures were observed as the dark spots, as shown in Figure 6(c). The irradiation energies were 7.3, 7.0, and 6.9  $\mu\text{J}$ , respectively.

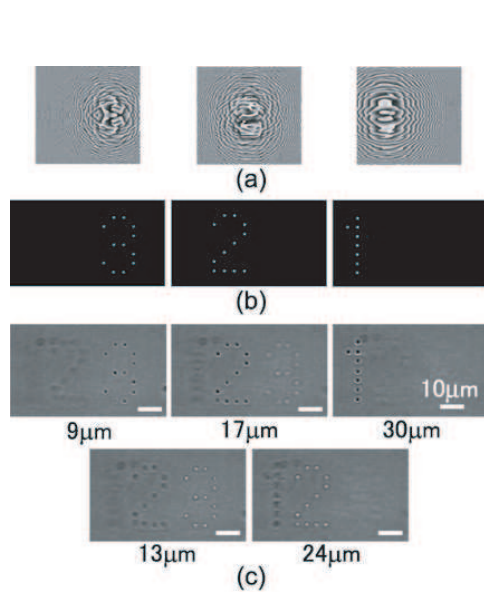


Figure 6: (a) Three CGHs having focal lengths of 1800, 2000, and 2400 mm, (b) optical reconstructions of the CGHs, (c) and microscope images of 3-D fabrications.

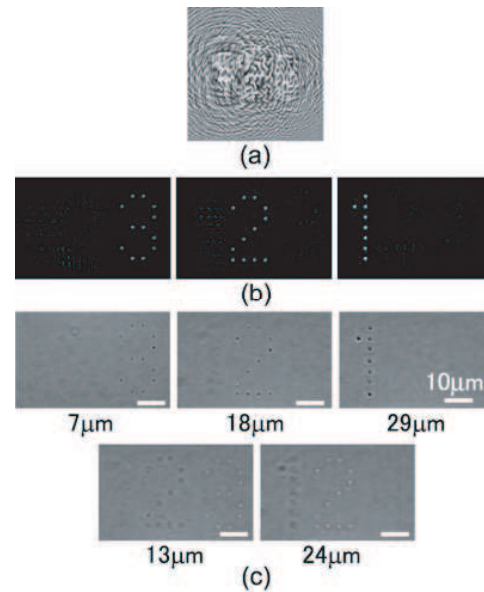


Figure 7: (a) A CGH having focal lengths of 1800, 2000, and 2400 mm, (b) optical reconstructions of the CGH, and (c) microscope images of 3-D fabrication.

Figure 7 shows the results of 3-D processing with a single pulse. Figure 7(a) shows CGH designed to generate 32 diffraction peaks, and having focal lengths of 1800, 2000, and 2400 mm, respectively. Figure 7(b) shows the optical reconstructions of the CGH. The respective uniformities  $U$  were 89%, 88%, and 83%. The total diffraction efficiency  $\eta$  was 68%. The upper three images in Figure 7(c) show the transmitted optical microscope observation of the fabrication area, when the axial positions were 7, 18, and 29  $\mu\text{m}$  was focused, the structures were observed as the dark spots. The irradiation energy was 18  $\mu\text{J}$ .

## 5. CONCLUSIONS

We have demonstrated the fingernail memory. The data recording is implemented with a focused femtosecond laser pulse and the readout is performed with an increased fluorescence intensity. Three bit planes read out with little cross-talk with the fluorescence readout. We have also data recording on a dental prosthesis for personal identification using a femtosecond laser processing system with a surface detection function. We have demonstrated holographic femtosecond laser processing with three-dimensional parallelism. The next stage of our study is integrated the focus control technique and holographic technique.

## ACKNOWLEDGMENT

This work was supported by the Venture Business Incubation Laboratory of The University of Tokushima, The Murata Science Foundation, The Asahi Glass Foundation, Research for Promoting Technological Seeds program of the Japan Science and Technology Agency, and a Grant-in-Aid for Scientific Research (B) from the Ministry of Education, Culture, Sports, Science, Japan.

## REFERENCES

1. Takita, A., M. Watanabe, H. Yamamoto, S. Matsuo, H. Misawa, Y. Hayasaki, and N. Nishida, "Optical bit recording in a human fingernail," *Jpn. J. Appl. Phys.*, Vol. 43, No. 1, 168–171, 2004.
2. Hayasaki, Y., H. Takagi, A. Takita, H. Yamamoto, N. Nishida, and H. Misawa, "Processing structures on human fingernail surface by a focused near-infrared femtosecond laser pulse," *Jpn. J. Appl. Phys.*, Vol. 43, No. 12, 8089–8093, 2004.
3. Takita, A., H. Yamamoto, Y. Hayasaki, N. Nishida, and H. Misawa, "Three-dimensional optical memory using a human fingernail," *Optics Express*, Vol. 13, No. 12, 4560–4567, 2005.
4. Ichikawa, T., Y. Hayasaki, K. Fujita, K. Nagano, M. Murata, T. Kawano, and J. R. Chen, "Femtosecond pulse laser-oriented recording on dental prostheses," *Dental Materials J.*, Vol. 25, No. 4, 733–736, 2006.
5. Takita, A., Y. Hayasaki, and N. Nishida, "Femtosecond laser processing system with target tracking feature," *Journal of Laser Micro/Nanoengineering*, Vol. 1, No. 3, 288–291, 2006.
6. Hayasaki, Y., T. Sugimoto, A. Takita, and N. Nishida, "Variable holographic femtosecond laser processing by use of spatial light modulator," *Appl. Phys. Lett.*, Vol. 87, No. 3, 031101, 2005.
7. Hasegawa, S., Y. Hayasaki, and N. Nishida, "Holographic femtosecond laser processing with multiplexed phase Fresnel lenses," *Opt. Lett.*, Vol. 31, No. 11, 1705–1707, 2006.
8. Hasegawa, S. and Y. Hayasaki, "Holographic femtosecond laser processing with multiplexed phase fresnel lenses displayed on the liquid crystal spatial light modulator," *Opt. Rev.*, Vol. 14, No. 4, 208–213, 2007.
9. Takahashi, H., S. Hasegawa, and Y. Hayasaki, "Holographic femtosecond laser processing using optimal-rotation-angle method with compensation of spatial frequency response of liquid crystal spatial light modulator," *Appl. Opt.*, Vol. 46, No. 23, 5917–5923, 2007.
10. Chaen, K., H. Takahashi, S. Hasegawa, and Y. Hayasaki, "Display method with compensation of the spatial frequency response of a liquid crystal spatial light modulator for holographic femtosecond laser processing," *Opt. Commun.*, Vol. 280, No. 1, 165–172, 2007.

# Photonic Waveguide Devices Directly Written into Dielectric Materials Using Femtosecond Laser Pulses

M. Ams, G. D. Marshall, P. Dekker, and M. J. Withford  
Centre for Ultra-high bandwidth Devices for Optical Systems (CUDOS)  
Centre for Lasers and Applications (CLA)  
Department of Physics, Macquarie University, NSW 2109, Australia

**Abstract**— In this paper we will present our most recent contributions to the field of femtosecond laser direct written waveguides. In particular, at the CUDOS at Macquarie we employed novel femtosecond laser beam delivery techniques in order to fabricate low-loss photonic waveguide devices for application in technologies such as telecommunications. After trialling various passive devices including waveguides, 1-N splitters and waveguide-Bragg gratings in non-doped glasses, we transferred our technologies into Erbium/Ytterbium co-doped media resulting in active Photonic devices.

## 1. INTRODUCTION

Significant attention has been directed to the use of laser pulses for fabricating optical components on or inside various materials since the introduction of ultrashort pulsed lasers in the 1980s. In particular, it was demonstrated in 1996 that tightly focussed femtosecond ( $10^{-15}$  s) Ti: Sapphire laser pulses can induce a local internal increase in the refractive index of bulk transparent glasses [1]. Although not fully understood, the index change is most likely due to electrons of the material locally absorbing energy from the radiation field via various nonlinear mechanisms, namely multi-photon ionisation. When the electrons transfer their energy to the surrounding lattice, structural changes including the formation of colour centres [2–4], densification [5–7] and refractive index changes [1–5] occur. Index changes on the order of  $10^{-3}$  are typically observed.

This discovery offers unique opportunities for the fabrication of arbitrary 3D photonic waveguide devices inside a wide range of materials simply by translating a sample through the focal point of a focussed femtosecond laser beam. From the first report of simple linear waveguides created in fused silica [1], the unique capabilities of the direct-write technique have been used to create monolithic photonic devices such as waveguide power splitters [8], waveguide couplers [9] and waveguide amplifiers [10]. Not only can this direct-write technique be carried out rapidly, it is readily compatible with existing fibre systems, it does not require a lithographic mask and it can be conducted in a regular laboratory environment with the minimum of sample preparation.

In this paper we will discuss the development of this fabrication technique and review advances leading to the generation of embedded low-loss waveguides in bulk glasses. The performance of photonic components, including splitters, gratings and amplifiers, based on this technology and opportunities for 3D fabrication will also be highlighted.

## 2. EXPERIMENT

Optical waveguide devices were manufactured using a regeneratively amplified Ti: Sapphire Spectra Physics Hurricane laser (pulse length  $<120$  fs, wavelength 800 nm, repetition rate 1 kHz) in a system similar to that described in [11] and [12]. Structures were formed by translating a glass sample through the focused laser beam, transverse to the direction of beam propagation, at  $25 \mu\text{m/s}$  with laser power (measured after the slit, see Figure 1) typically in the range 0.5–3.0 mW.

In order to characterise the fabricated devices, a fibre alignment stage was used to position a single mode fibre on the entry port of the structure of interest. Near-field optical mode profiles exiting waveguide structures were captured using a lens coupled to an optical beam profiler. A computational method [13] was performed on these profiles in order to estimate the peak refractive index change between the bulk material and the waveguide structures. Transmitted radiation was collected using an aligned single mode fibre (at the structure's exit ports) coupled to a power meter. Images of fabricated waveguide devices were taken with an Olympus differential interference contrast (DIC) microscope.

### 3. RESULTS & DISCUSSION

To date our research program has focused on the development of processing methodologies enabling the fabrication of the key building blocks of photonic circuitry, namely low-loss waveguides, splitters, gratings and amplifiers for use in optical telecommunication systems.

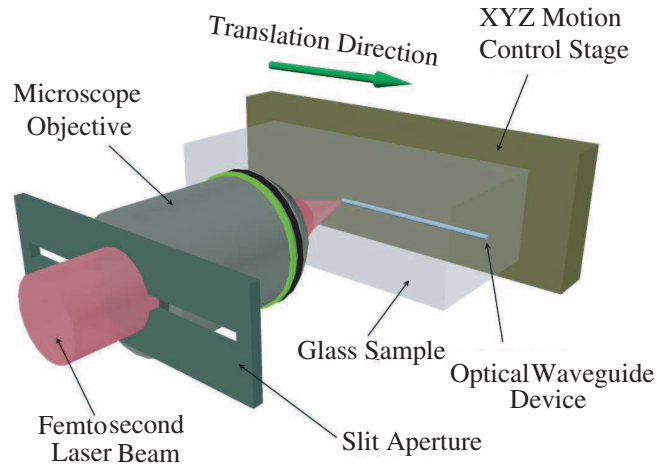


Figure 1: Writing setup used to fabricate optical waveguide devices.

Most notably, we developed a writing technique whereby a slit aperture was positioned before the focussing objective aligned parallel to the direction of sample translation. The slit aperture served to expand the laser focus in the direction normal to the laser beam propagation and sample translation enabling waveguides with circular cross-sections (Figure 2) to be written using a low magnification, long working distance objective [11]. This in turn greatly increased the fibre-to-waveguide coupling efficiency whilst also reducing the propagation loss associated with the waveguide itself to approximately 1.75 dB/cm.



Figure 2: Top-view DIC microscope images of waveguides fabricated in fused silica. (a) without a slit and (b) with a 500  $\mu\text{m}$  slit positioned before the focussing objective. The insets show end-on white light transmission images of the respective waveguides.

We also compared and contrasted, for the first time, the optical transmission properties of straight and curved waveguides written with linearly and circularly polarised light, and showed an increase in transmission through waveguides written using circularly polarised light [12]. This increase in light transmission is still under investigation but may be explained by a modification of the periodic aligned nanostructures that accompany devices fabricated with linearly polarised radiation [14, 15]. Linear waveguides fabricated using the slit method and a circularly polarised writing beam possess a propagation loss of approximately 0.83 dB/cm.

It has been shown that the refractive index contrast could be increased by overwriting a waveguide with more than one pass of the laser beam in a multiple fabrication scan fashion [1, 5, 16]. We conducted a study of this proposition and found that waveguides written in fused silica with

8 multiple passes exhibit a propagation loss of approximately 0.36 dB/cm. As the diameter of the waveguides do not change with increasing laser scans, we also concluded that the reduction in propagation loss is due to an increase in the refractive index contrast associated with the laser irradiated region.

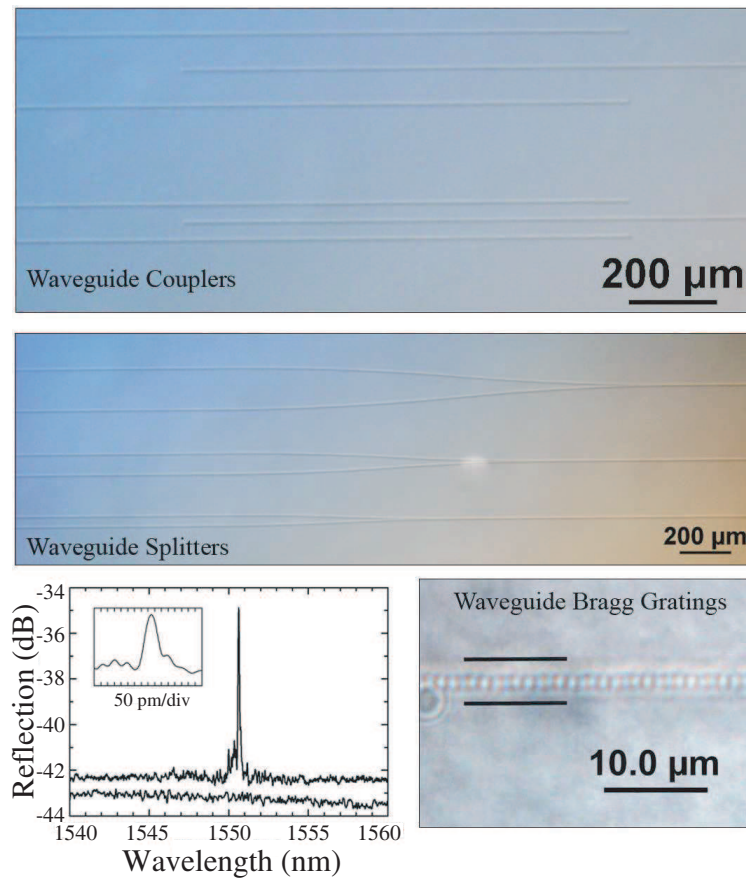


Figure 3: Passive devices fabricated in fused silica at the CUDOS at Macquarie using the femtosecond laser direct-write technique.

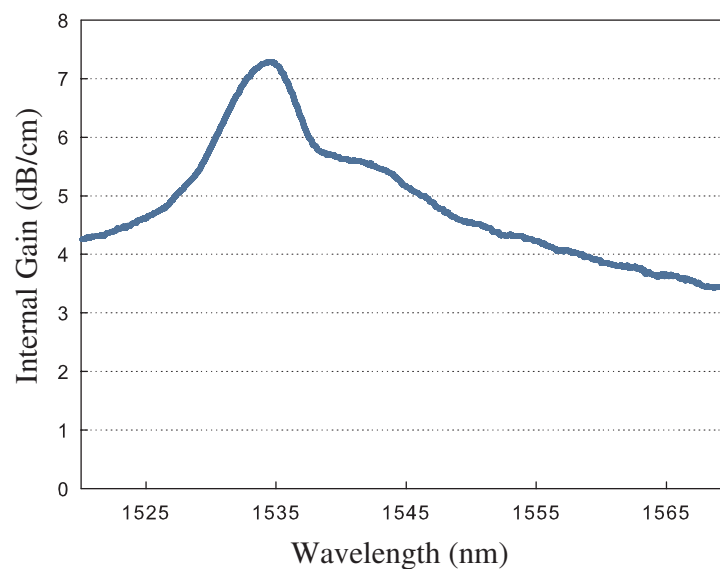


Figure 4: Internal gain as a function of wavelength for a waveguide written in Er-doped phosphate glass. This result shows amplification across the whole C-band comparing well with current literature [18].

Equipped with a recipe for fabricating low-loss symmetric waveguides in fused silica, a suite of passive devices were then able to be generated. Figure 3 shows a range of photonic devices we fabricated in fused silica using the femtosecond laser direct-write technique.

The current thrust of our research program is directed towards optimisation and integration of these photonic components onto a monolithic optical chip. Furthermore we plan to fabricate similar structures in doped glasses resulting in active devices. Recent results include demonstrations of high gain, 7 dB/cm (Figure 4), Er-doped waveguide amplifiers (EDWAs), and narrow linewidth waveguide Bragg gratings (WBGs) [17] in phosphate glass. This combination of device potential, genuine 3D capability and ease of manufacturing significantly expands the range of devices and applications that the femtosecond laser direct-write technique can enable.

#### 4. CONCLUSION

Optical waveguide devices were fabricated in fused silica and doped phosphate glasses using the femtosecond laser direct-write technique. These devices exhibited low-loss due to various writing techniques developed at the CUDOS at Macquarie. Demonstrations of low-loss waveguides, splitters and couplers were shown. Finally, the performance of working photonic devices such as EDWAs and WBGs, and the future implications for this technology were discussed.

#### ACKNOWLEDGMENT

This work was produced with the assistance of the Australian Research Council under the ARC Centres of Excellence & LIEF programs.

#### REFERENCES

1. Davis, K. M., K. Miura, N. Sugimoto, and K. Hirao, "Writing waveguides in glass with a femtosecond laser," *Opt. Lett.*, Vol. 21, No. 21, 1729–1731, 1996.
2. Efimov, O. M., L. B. Glebov, K. A. Richardson, et al., "Waveguide writing in chalcogenide glasses by a train of femtosecond laser pulses," *Opt. Mat.*, Vol. 17, 379–386, 2001.
3. Chan, J. W., T. R. Huser, S. H. Risbud, et al., "Waveguide fabrication in phosphate glasses using femtosecond laser pulses," *Appl. Phys. Lett.*, Vol. 82, No. 15, 2371–2373, 2003.
4. Chan, J. W., T. R. Huser, S. H. Risbud, et al., "Modification of the fused silica glass network associated with waveguide fabrication using femtosecond laser pulses," *Appl. Phys. A*, Vol. 76, 367–372, 2003.
5. Hirao, K. and K. Miura, "Writing waveguides and gratings in silica and related materials by a femtosecond laser," *J. Non-Crys. Sol.*, Vol. 239, 91–95, 1998.
6. Kawamura, K., N. Sarukura, M. Hirano, and H. Hosono, "Holographic encoding of fine-pitched micrograting structures in amorphous SiO<sub>2</sub> thin films on silicon by a single femtosecond laser pulse," *Appl. Phys. Lett.*, Vol. 78, No. 8, 1038–1040, 2001.
7. Chan, J. W., T. R. Huser, S. H. Risbud, et al., "Structural changes in fused silica after exposure to focused femtosecond laser pulses," *Opt. Lett.*, Vol. 26, No. 21, 1726–1728, 2001.
8. Liu, J., Z. Zhang, S. Chang, et al., "Directly writing of 1-to-N optical waveguide power splitters in fused silica glass using a femtosecond laser," *Opt. Comm.*, Vol. 253, 315–319, 2005.
9. Minoshima, K., A. M. Kowalevich, E. P. Ippen, and J. G. Fujimoto, "Fabrication of coupled mode photonic devices in glass by nonlinear femtosecond laser materials processing," *Opt. Exp.*, Vol. 10, No. 15, 645–652, 2002.
10. Osellame, R., S. Taccheo, G. Cerullo, et al., "Optical gain in Er-Yb doped waveguides fabricated by femtosecond laser pulses," *Elec. Lett.*, Vol. 38, No. 17, 964–965, 2002.
11. Ams, M., G. D. Marshall, D. J. Spence, and M. J. Withford, "Slit beam shaping method for femtosecond laser direct-write fabrication of symmetric waveguides in bulk glasses," *Opt. Exp.*, Vol. 13, No. 15, 5676–5681, 2005.
12. Ams, M., G. D. Marshall, and M. J. Withford, "Study of the influence of femtosecond laser polarisation on direct writing of waveguides," *Opt. Exp.*, Vol. 14, No. 26, 13158–13163, 2006.
13. Mansour, I. and F. Caccavale, "An improved procedure to calculate the refractive index profile from the measured near-field intensity," *J. Lightwave Tech.*, Vol. 14, No. 3, 423–428, 1996.
14. Shimotsuma, Y., P. G. Kazansky, J. Qiu, and K. Hirao, "Self-organized nanogratings in glass irradiated by ultrashort light pulses," *Phys. Rev. Lett.*, Vol. 91, No. 24, 247405, 2003.
15. Hnatovsky, C., R. S. Taylor, E. Simova, et al., "Fabrication of microchannels in glass using focused femtosecond laser radiation and selective chemical etching," *Appl. Phys. A*, Vol. 84, 47–61, 2006.

16. Low, D. K. Y., H. Xie, Z. Xiong, and G. C. Lim, "Femtosecond laser direct writing of embedded optical waveguides in aluminosilicate glass," *Appl. Phys. A*, Vol. 81, 1633–1638, 2005.
17. Marshall, G. D., M. Ams, and M. J. Withford, "Direct laser written waveguide Bragg gratings in bulk fused silica," *Opt. Lett.*, Vol. 31, No. 18, 2690–2691, 2006.
18. Osellame, R., N. Chiodo, G. Della Valle, et al., "Waveguide lasers in the C-Band fabricated by laser inscription with a compact femtosecond oscillator," *IEEE J. Sel. Topics in Q. Elec.*, Vol. 12, No. 2, 277–285, 2006.

# 3D Microstructuring of Glass by Femtosecond Laser Direct Writing and Application to Biophotonic Microchips

Koji Sugioka, Yasutaka Hanada, and Katsumi Midorikawa

The Institute of Physical and Chemical Research, RIKEN

Wako, Saitama 351-0198, Japan

**Abstract**— Three-dimensional (3D) microfabrication of photostructurable glass by femtosecond (fs) laser direct writing is demonstrated for manufacture of biophotonic microchips. The fs laser direct writing followed by annealing and successive wet etching can fabricate the hollow microstructures, achieving a variety of microfluidic components and microoptical components in a glass chip. One of the interesting and important applications of the 3D microfluidic structures fabricated by the present technique is inspection of living microorganisms. The microchips used for this application are referred to as nanoaquarium. Furthermore, the optical waveguide is written inside the glass by the fs laser direct writing without the annealing and the successive etching. It is revealed that integration of the microfluidic and microoptical components with the optical waveguides in a single glass chip is of great use for biochemical analysis and medical inspection based on optical sensing.

## 1. INTRODUCTION

In the last decade, it has been realized that miniaturization of the “field” is urgently demanded in chemical reaction, biological analysis and medical inspection, which emphasizes the use of micro-components three-dimensionally (3D) integrated in the microchips. Examples of the miniaturized microchip devices are the so-called Lab-on-a-chip devices and micro total analysis system ( $\mu$ -TAS). By shrinking a roomful of laboratory equipments and packing them into a palm-size chip, such microchip devices are capable of performing chemical and biological analyses with great reduction of reagent consumption, waste production, analysis time and labor cost. It has been shown that femtosecond (fs) laser is a promising tool for manufacture of integrated microcomponents in glass due to its ability of internal modification of transparent materials using multiphoton absorption. So far, a broad variety of photonic micrcomponents, such as waveguides, couplers, gratings, and Fresnel zone plates have been fabricated inside the glass [1–3]. In addition, fs laser is also a good tool for fabrication of microfluidic structures embedded in the glass, like 3D microfluidic channels [4, 5]. Recently, we developed the technique that directly forms 3D hollow microstructures with smooth internal surfaces inside glass by fs laser direct writing followed by post annealing and successive wet etching [6–13]. This technique can fabricate both 3D microfluidic and microoptic components in a single glass chip by a single procedure. In the present paper, fabrication of 3D hollow microstructures embedded in the glass is demonstrated by the fs laser direct writing followed by the annealing and the successive wet etching. The microchips with 3D microfluidic structures fabricated by this technique, that are referred to as nanoaquarium, are applied for dynamic observation of microorganisms. More recently, we also succeeded in forming optical waveguides inside the same glass chip by the fs laser direct writing [14]. Then, microfluids, microoptics, and optical waveguides are integrated in a single glass chip for photonic biosensing.

## 2. EXPERIMENTAL

Experiments were carried out by a commercial fs laser workstation [6]. The laser wavelength, pulse width and repetition rate were 775 nm, 150 fs and 1 kHz, respectively. The focusing system was a 20 $\times$  microscope objective with a numerical aperture (N. A.) of 0.46. The substrate used in this study for 3D microstructuring is photostructurable glass that is commercially available under the trade name of Foturan from Schott Glass Corporation [15]. Samples under fabrication were translated by a PC controlled xyz stage for 3D microstructuring. For fabrication of the 3D hollow microstructures, the typical irradiation condition of fs laser was a fluence of 78 mJ/cm<sup>2</sup> and a scanning speed of 510 mm/s. After the fs laser exposure step, the sample was subjected to a programmed annealing, and then soaked in a 10% HF solution with an ultrasonic bath at variable period of etching time, depending on the size of the hollow structures. The laser-exposed regions can be preferentially etched away with a contrast ratio of ca. 50 in etching selectivity. Lastly we baked the photostructurable glass sample again to smooth the etched surfaces. The

details of procedures and mechanism of selective etching of photostructurable glass are described elsewhere [6, 8, 16–18]. In the meanwhile, for the optical waveguide writing, the tightly focused fs laser beam was scanned inside the samples by moving the samples perpendicularly to the laser beam axis using a PC-controlled xyz stage without the annealing and the successive wet etching [14]. The typical writing condition is  $0.5 \mu\text{J}/\text{pulse}$  of laser power and  $200 \mu\text{m}/\text{s}$  of scanning speed.

### 3. INSPECTION OF MICROORGANISMS

One of the interesting and important applications of 3D microchips, that are referred to as nanoaquarium, fabricated by the present technique is inspection of microorganisms. To inspect movement of *Euglena's* flagellum is of great interest for biologists due to application to biomotors and clarification of the fertilization process. Currently, many biologists are trying to observe microorganisms placed in a Petri dish by an optical microscope with high-speed camera. However, the high numerical aperture objective lens used for the observation limits the field of view to a very narrow region and also limits the depth of focus to a very shallow region, thereby making it difficult to capture images of moving microorganisms. Consequently, it takes very long time to take significant images. To shorten the observation time is strongly demanded for biologists due to not only cost-effectiveness and time-effectiveness but also due to limited PC memory for taking movies using the high-speed camera. To overcome these problems, we propose to use the microchip for the observation of microorganisms. The microchip can scale down the observation site, namely, it can 3D encapsulate microorganisms in a limited area, so that it makes much easier to capture the images of moving microorganisms.

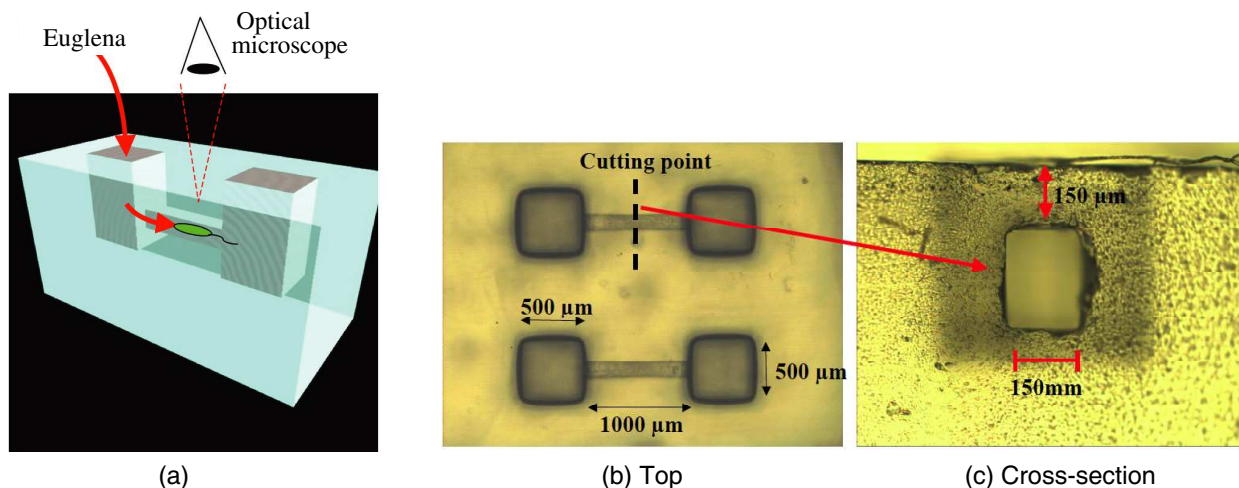


Figure 1: (a) 3D schematic illustration and (b) a top view and (c) a cross-sectional view of optical microscope images of a microchip fabricated for the inspection of *Euglena*.

Figure 1 shows (a) a 3D schematic illustration and (b) a top view and (c) a cross-sectional view of optical microscope images of a microchip fabricated for the inspection of *Euglena*. The top wall of the channel is flat and parallel to the glass surface. Such a flat surface was achieved by multiple scanning of the laser beam with lateral shifts. In addition, post thermal treatment after wet etching realized very smooth surfaces [7]. These results are important for taking clear images. For the observation, *Euglenas* are introduced into one of reservoirs filled with water and then *Euglenas* swim into the channel. At this moment, we can see the movement of *Euglena* using a microscope from the top of the glass surface.

Figure 2 shows a picture of living *Euglena* taken using the microchip. We also succeeded in taking a movie that revealed that *Euglena* coils his flagellum around his body and rotates it with high-speed to get a driving force when he moves straight. The observation using the microchip has several advantages over the conventional observation method: (1) analysis time can be greatly reduced. For example, it takes only a few seconds to take a one shot picture while more than 10 min even in lucky case by the conventional method. Furthermore, it takes several minutes to take a movie while very long time or even quite difficult by the conventional method, (2) 3D observation is possible, (3) motion of *Euglena* can be controlled, and (4) the living microorganisms can be kept



Figure 2: Picture of living euglena taken using the microchip.

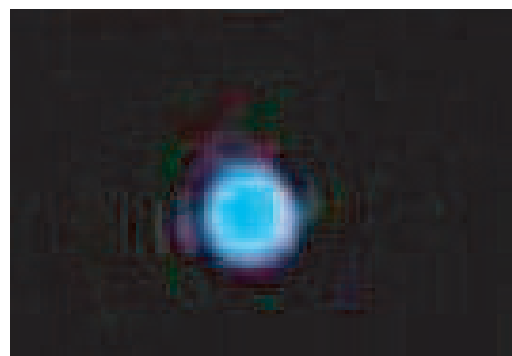


Figure 3: Near field pattern of He-Ne laser beam guided by the 10 mm long optical waveguide written by the fs laser direct writing. Pulse energy and scanning speed were  $0.5 \mu\text{J}$  and  $200 \mu\text{m/s}$ , respectively.

very fresh for long time since the microchannel three-dimensionally confined in the glass can avoid vaporization of water.

#### 4. INTEGRATED MICROCHIP FOR PHOTONIC BIOSENSING

The present technique fabricating 3D hollow microstructures can be also used for embedding some microoptics such as micromirrors [8] and microlenses [15] in a glass chip. Furthermore, the optical waveguide can be written inside the photostucturable glass by fs laser direct writing without annealing and successive wet etching due to refractive index increase of the laser exposed regions [14]. Figure 3 shows an example of near field pattern of He-Ne laser beam guided by the written optical waveguide, showing a single-mode pattern. The propagation loss was evaluated to be approx.  $0.5 \text{ dB/cm}$ .

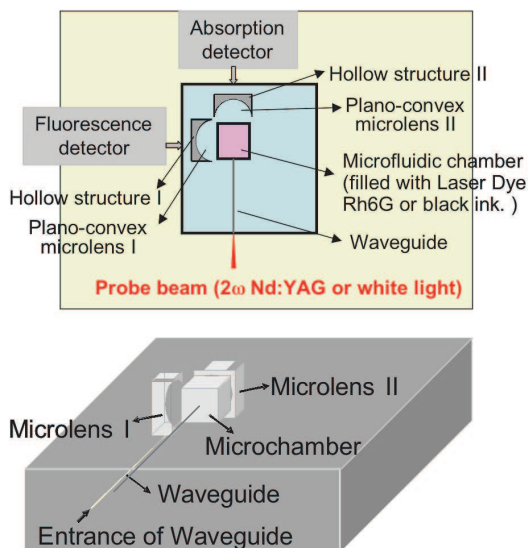


Figure 4: Schematic illustrations of the 3D integrated microchip for photonic biosensing.

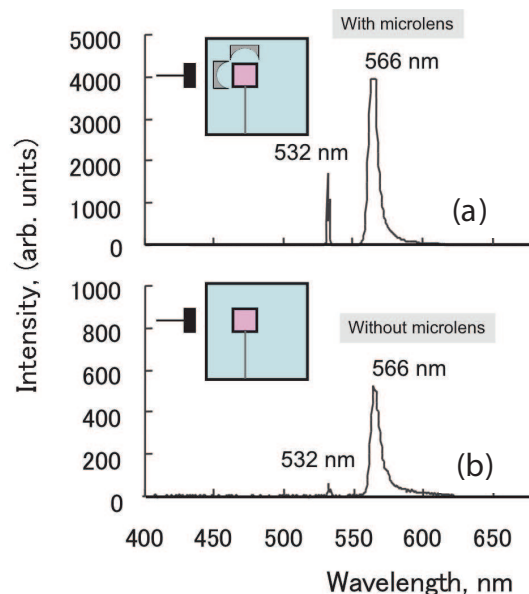


Figure 5: Fluorescence spectra from laser dye Rh6G analyzed by using microchips integrated (a) with and (b) without a microlens.

The microfluidics, microoptics and optical waveguide can be easily integrated in a single glass chip. Figure 4 shows the schematic illustrations of the 3D integrated microchip for photonic biosensing, in which one waveguide of 6 mm length is connected to a microchamber of  $1.0 \times 1.0 \times 1.0 \text{ mm}^3$  volume, and two microlenses of 0.75 mm curvature radius are arranged at the left for fluorescence measurement and opposite sides from the optical waveguide across the microchamber for absorption

measurement at a distance of 200  $\mu\text{m}$ .

For fluorescence analysis of a liquid sample, the microfluidic chamber was filled with laser dye Rh6G of 0.02 mol/L dissolved in ethanol. A pump laser beam of the  $2\omega$  of Nd:YAG laser was guided by the optical waveguide and introduced into the microfluidic chamber. The emission spectra from the laser dye solution were collected in the detector through the plano-convex microlens I. The head of the spectrometer was placed at the end of the glass chip, i.e., behind microlens I, to detect the fluorescence. We measured the emission spectra from the laser dye in the microfluidic chamber at different pump energies. A typical emission spectrum with a central wavelength of 566 nm (the peak at 532 nm is from the pump laser), corresponding to the maximum emission of the dye, was obtained, as shown in Fig. 5. For comparison, the emission measurement was also performed for a microfluidic chamber integrated only with a waveguide but without a microlens. Clearly, the enhanced emission intensity was achieved when a microoptical plano-convex lens was integrated. The enhancement of light intensity by a factor of 8 was realized. Furthermore, for the optical absorption analysis of a liquid sample through the plano-convex microlens II, the black ink at different concentration from 0.1 to 1.0% diluted with water was filled in the microchamber, so that the sensitivity was enhanced by a factor of 3 compared with the microchip without a microlens. These results indicate that the 3D integrated microchip fabricated by our techniques is highly efficient for optical analysis of biochemical samples such as fluorescence and absorption measurement.

## 5. CONCLUSIONS

We have demonstrated 3D microfabrication of photostructurable glass by femtosecond laser direct writing. By fabrication of the hollow microstructures, a variety of microfluidic components and microoptical components like a micromirror, a microlens are successfully integrated in a glass chip. One of the interesting and important applications of microchips, that are referred to as nanoaquarium, fabricated by the present technique is inspection of living cells and microorganisms that has several advantages over the conventional inspection method. The optical waveguide can be further integrated into the identical glass chip after the hollow microstructure fabrication. Such an integrated microchip is of great use for biochemical analysis and medical inspection based on photonic sensing. Finally, we conclude that the technique presented here is very promising for manufacture of highly integrated biophotonic microchips.

## REFERENCES

1. Davis, K. M., K. Miura, N. Sugiimoto, and K. Hirao, *Opt. Lett.*, Vol. 21, 1729, 1996.
2. Kawamura, K., M. Hirano, T. Kamiya, and H. Hosono, *Appl. Phys. Lett.*, Vol 81, 1137, 2002.
3. Watanabe, W., D. Kuroda, K. Itoh, and J. Nishii, *Opt. Express*, Vol. 10, 978, 2002.
4. Marcinkevicius, A., S. Juodkasis, M. Watanabe, M. Miwa, S. Matsuo, H. Misawa, and J. Nishii, *Opt. Lett.*, Vol. 26, 277, 2001.
5. Bellouard, Y., A. Said, M. Dugan, and P. Bado, *Opt. Express*, Vol. 12, 2120, 2004.
6. Masuda, M., K. Sugioka, Y. Cheng, N. Aoki, M. Kawachi, K. Shihoyama, K. Toyoda, H. Helvajian, and K. Midorikawa, *Appl. Phys.*, A76, 857, 2003.
7. Cheng, Y., K. Sugioka, K. Midorikawa, M. Masuda, K. Toyoda, M. Kawachi, and K. Shihoyama, *Opt. Lett.*, Vol 28, 55, 2003.
8. Cheng, Y., K. Sugioka, K. Midorikawa, M. Masuda, K. Toyoda, M. Kawachi, and K. Shihoyama, *Opt. Lett.*, Vol 28, 1144, 2003.
9. Sugioka, K., M. Masuda, T. Hongo, Y. Cheng, K. Shihoyama, and K. Midorikawa, *Appl. Phys.*, A78, 815, 2004.
10. Masuda, M., K. Sugioka, Y. Cheng, T. Hongo, K. Shihoyama, H. Takai, I. Miyamoto, and K. Midorikawa, *Appl. Phys.*, A78, 1029, 2004.
11. Cheng, Y., K. Sugioka, and K. Midorikawa, *Opt. Lett.*, Vol. 29, 2007, 2004.
12. Sugioka, K., Y. Cheng, and K. Midorikawa, *Appl. Phys.*, A81, 1, 2005.
13. Cheng, Y., K. Sugioka, and K. Midorikawa, *Appl. Surf. Sci.*, Vol. 248, 172, 2005.
14. Wang, Z., K. Sugioka, Y. Hanada, and K. Midorikawa, *Appl. Phys.*, A88, 699, 2007.
15. <http://www.mikroglas.com/foturane.htm>
16. Helvajian, H., F. D. Fuqua, W. W. Hansen, and S. Janson, *RIKEN Rev.*, Vol. 57, 2001.
17. Stooky, S., *Photosensitively Opacifiable Glass*, U.S. Patent 2684911, 1954.

18. Hongo, T., K. Sugioka, H. Niino, Y. Cheng, M. Masuda, I. Miyamoto, H. Takai, and K. Midorikawa, *J. Appl. Phys.*, Vol. 97, 063517, 2005.
19. Wang, Z., K. Sugioka, Y. Hanada, and K. Midorikawa, *Appl. Phys.*, A89, 951, 2007.

# A Novel Design of Photonic Crystal Lens Based on Negative Refractive Index

S. Haxha<sup>1</sup> and F. AbdelMalek<sup>2</sup>

<sup>1</sup>Photonics Group, Department of Electronics, University of Kent, Canterbury CT2 7NT, UK

<sup>2</sup>National Institute of Applied Sciences and Technology, BP 676 Cedex 1080, Tunis, Tunisia

**Abstract**— In this study a concave lens based on two dimensional photonic crystal platform with negative refractive index is presented. The proposed lens is employed as a spot-size converter to facilitate coupling of the light from a single mode fibre with a large spot-size area into photonic crystal waveguide with a very small spot-size area, even smaller than the operating wavelength. Optimisation of the lens and its integration with the single mode fibre and photonic crystal waveguide into a single optical chip was performed by employing 2D Finite-Difference Time-Domain (FDTD). A significant reduction of the optical chip dimensions and high coupling efficiency have been achieved by optimizing each device (the lens and the photonic crystal waveguide).

## 1. INTRODUCTION

In 1968, Veselago [1] proposed an artificial material whose permittivity and permeability are simultaneously negative. His study demonstrated that the electric and magnetic field vectors create a left-handed set of vectors with the wave vector. These artificial materials with both negative dielectric permittivity and negative magnetic permeability [1, 2] are also known as metamaterials, or left-handed materials (LHM). Veselago [1] first proposed this type of materials which obey Snell's law with a negative refractive index. Later, it became apparent that such materials can be artificially constructed [2, 3]. In recent years, many research groups around the world have proposed different ideas and suggestions for future applications of these materials, operating at optical and microwave frequencies. In this context, we have proposed a lens based on photonic crystal structure with negative refractive index which operates at optical frequency. Photonic crystal technology can permit strong light confinement in compact structures and can allow for innovative methods for manipulating the guided light. It is already known that conventional lenses are the most widely used to couple the light between various optical components.

However, there are disadvantages of using conventional lenses since they need curved surfaces to form an image and the associated sub-wavelength alignment tolerances lead to high packaging costs. Also, when using such lenses to couple the light between various optical components, the complexity of the circuitry increases. In particular coupling of the light between conventional waveguides and photonic crystal waveguides remains a challenging issue due to the mismatch of the optical mode widths. In this regard photonic crystal lens based on negative refraction plays a significant role in light focusing and light coupling efficiency.

In this paper, we propose and optimise a photonic crystal lens with negative refractive index ( $n = -1$ ) and its integration in a single optical chip, operating at optical frequency. We study integration of a single mode fibre, a photonic crystal lens, and a photonic crystal waveguide. In this optical chip, the light beam propagating through the single mode fibre enters into the photonic crystal lens where it is refracted and then focused at the focusing point. The photonic crystal waveguide is employed to collect the light at the focusing point.

## 2. NUMERICAL METHOD

Several computational methods have been employed to numerically characterise optical properties of photonic crystal devices. Waveguide components are commonly analysed by the beam propagation method, but such a method can only treat small angle bends and crossings, and weakly guided structures. In order to avoid such limitations, we have developed and employed the 2D finite difference time domain computational technique based on the Yee's algorithm [4, 5]. In this study,  $E(x, y)$  the electric and  $H(x, y)$  the magnetic, field components are calculated. We have considered the 2-D plane where the  $z$  direction is normal to the  $x$ - $y$  plane of the grid. The electromagnetic fields are calculated by solving the following time-dependent Maxwell's equations in the FDTD scheme.

$$\frac{\partial H_x}{\partial t} = -\frac{1}{\mu} \frac{\partial E_z}{\partial y} \quad (1)$$

$$\frac{\partial \mathbf{H}_y}{\partial t} = \frac{1}{\mu} \frac{\partial \mathbf{E}_z}{\partial x} \quad (2)$$

$$\frac{\partial \mathbf{E}_z}{\partial t} = \frac{1}{\varepsilon} \left( \frac{\partial \mathbf{H}_y}{\partial x} - \frac{\partial \mathbf{H}_x}{\partial y} - \sigma \mathbf{E}_z \right) \quad (3)$$

where  $\mu$ ,  $\varepsilon$ , and  $\sigma$  are the permeability, permittivity and conductivity, respectively. In this method, we have considered the transverse magnetic (TM) mode. The TM mode has magnetic field components,  $H_x$ , and  $H_y$ , perpendicular to the  $z$ -axis, where  $H_z = 0$ . Here, in the finite difference time domain scheme we have employed as absorbing boundary the perfect matched layer (PML) introduced by Berenger [6]. The key point of the Berenger PML absorbing boundary conditions is the creation of a non-physical absorber adjacent to the outer grid boundary by splitting the field components and introducing a new degree of freedom. The following spatial steps [7] is considered:  $\Delta x = \Delta y = a/40$  and  $\Delta t = 1/(c((1/\Delta x)^2 + (1/\Delta y)^2))^{1/2}$ , where  $c$  is the speed of light and  $\Delta x$  and  $\Delta y$  are meshgrid sizes in the  $x$ - and  $y$ -directions, respectively. It is worth mentioning that the finite difference time domain method represents one of the most powerful and computer efficient numerical techniques dealing with photonic crystal electromagnetic problems.

### 3. SIMULATED RESULTS

The photonic crystal lens considered in this work consists of air holes arranged in a triangular lattice, with a lattice constant  $a$ , in a homogeneous dielectric medium. The photonic crystal structure parameters considered in this study are similar as follows: The air hole radius is  $r = 0.4a$  and the dielectric constant of the background is  $\varepsilon = 12.96$ . First we performed band structure calculations by using plane wave expansion [8] in order to find out the frequency range where the photonic crystal structure exhibits a negative refractive index. Here we have considered only the TM modes (in-plane magnetic field). Calculated band structure results are presented in Fig. 1.

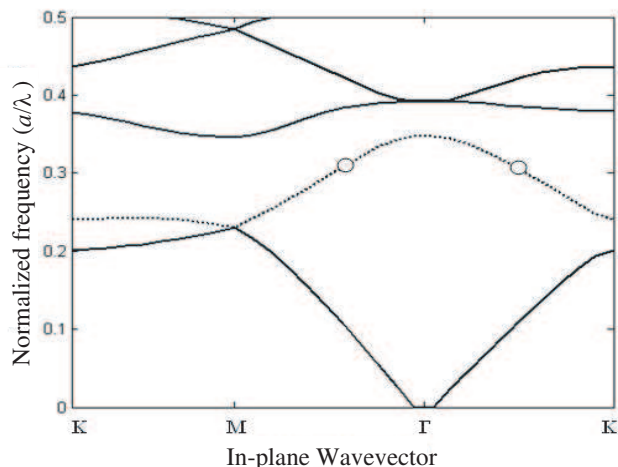


Figure 1: Band structure calculation of the lens based on the photonic crystal structure.

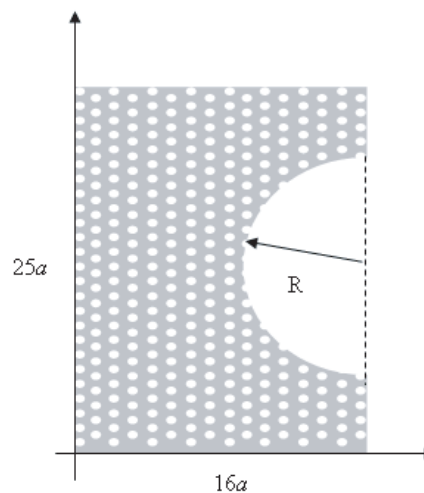


Figure 2: Schematics of the photonic crystal lens.

One can see that this photonic crystal structure in the second band in the range of  $0.25$  to  $0.35 a/\lambda$  possesses bands with negative slope. It is already known that photonic crystal structures that own negative band slope [9] exhibit backwards electromagnetic (EM) wave propagation [1]. This backwards type of (EM) wave propagation can lead to negative refraction when the allowed mode distribution in the wave vector space is isotropic at a certain frequency. In such situations with the satisfaction of some additional restrictions specified in Ref. [9] the photonic crystal structure obeys Snell's law with a negative refractive index. In this study, the operating frequency of the photonic crystal structure is considered to be equal to  $0.305 a/\lambda$ . At this particular frequency the value of the effective refractive index is negative ( $-1$ ) [10].

Next, we have designed a concave lens by cutting the back-side of the photonic crystal structure into a halfcircular shape with the radius  $R$ , as shown in Fig. 2. The lens structure dimensions are

$25 \times 16a$  (unit cells). In our simulations, we have considered 40 mesh grid points per unit cell. In order to obtain a better impedance matching, the normal to surface direction has been placed along the  $\Gamma M$  direction.

In order to achieve high coupling efficiency of a realistic large Gaussian beam source to sub-wavelength size photonic crystal we have optimized the radius of the concave lens,  $R$ . This radius has been investigated to obtain the smallest focused spot,  $S$ , at a desired location, where the light can be focused and coupled to other devices.

Next, the incident Gaussian beam with the beam waist  $10a$  has been launched at the free space on the lefthand side of the lens, illustrated in Fig. 3. The snapshot of the electric field is also presented in this figure.

On the right-hand side of the lens the incident beam has been focused at the point  $P$ , as shown in Fig. 3. The operating wavelength is  $0.305 a/\lambda$ . This is considered to be the optimum behaviour of the plano-concave lens since the refractive index is negative ( $n = -1$ ). One can see from this figure that when the light moves beyond the focusing point,  $P$ , its spot-size area increases rapidly.

Next, we optimised lens where for each value of the radius,  $R$ , we give the size of the focused spot, defined as the full width at half maximum (FWHM) of the beam intensity along  $y$ . Our simulations have indicated that the smallest spot-size can be achieved at a normalized radius equal to 2.1. Therefore, this value remained fixed throughout this study. Location of the focusing point  $P$  has been determined by calculating the focal length which is direct related to the lens radius of curvature, given by  $F = R/(n - 1)$ , where  $n$  is the refractive index [11]. Our numerical simulations indicated that the best focused spot can be achieved at  $F/\lambda = 1.05$ , which corresponds to  $0.305 a/\lambda$ . In the case,  $R = -2F$ , where  $R = 2.1\lambda$ .

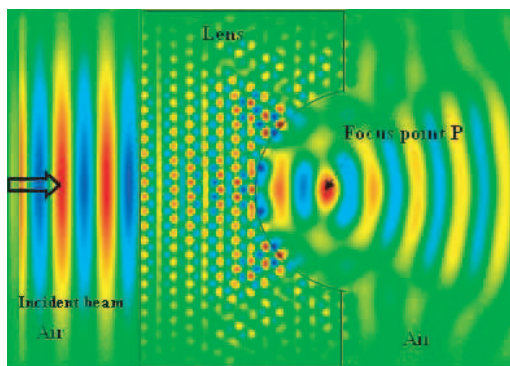


Figure 3: Snapshot of the electric field patterns, when the incident Gaussian beam is launched in free space.

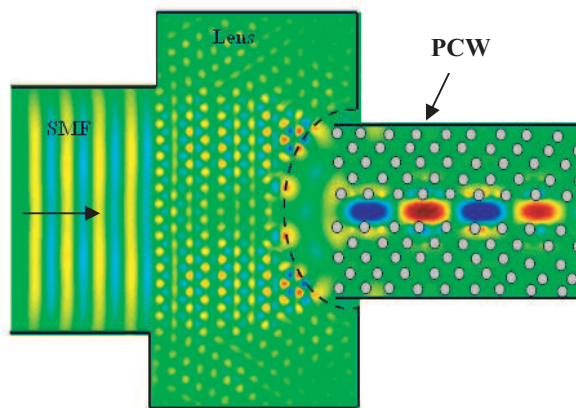


Figure 4: Evolution of the electric field from the SMF to the PCW through the PC lens at the frequency  $f = 0.315 a/\lambda$ .

One can see that there is a small deviation from the value of 1, for the normalized focal length. This is due to the anisotropy in the mode dispersion in wave vector space. The radius of curvature is equal to  $R = -2f$  for a photonic crystal with a negative refractive index equal to  $-1$ ; however, this radius would be shorter in case when the refractive index is positive.

Next, the lens has been placed between the single mode fibre and an ordinary photonic crystal waveguide (PCW), as shown in Fig. 4. The PCW consists of a triangular lattice of dielectric cylinders placed in the air with  $\epsilon = 12.96$  and the radius of  $r = 0.2a'$ , where  $a'$  is the lattice constant [26].

The propagation of the light from the SMF through the lens into the PCW is illustrated in Fig. 4. One can see that, the light is well confined in the PCW. It can be seen that compact integration of SMF, lens and PCW can be achieved by focusing the spot at the desired locations. Next, we investigate the effect of the lens in the light coupling efficiency. Our simulation indicated that in the case when the lens is not used almost 90% of the optical power is lost. On the other hand, a maximum coupling efficiency of about 95% is achieved at the normalised frequency ( $a/\lambda = 0.312$ ) when the lens is used, as shown in Fig. 5. In this figure variation of the coupling efficiency as a function of normalized frequency,  $a/\lambda$ , when the lens is used is illustrated.

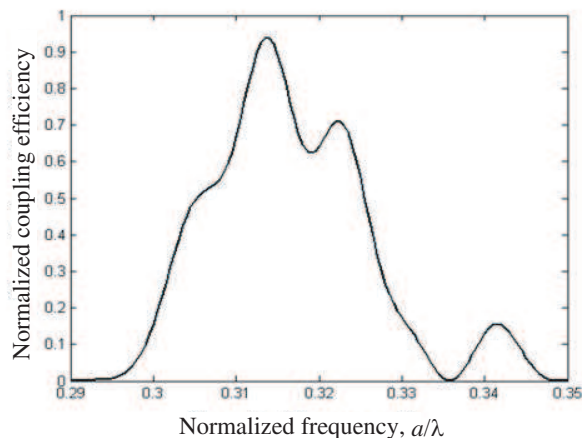


Figure 5: Variation of the coupling efficiency as a function of the normalised frequency.

One can see that the normalised frequency at this point is slightly different from the optimum focusing frequency of  $0.305 a/\lambda$ . This is due to a slight mismatch between the frequency for the optimum performance of the lens, and the optimum performance for the PC waveguide alone. The study presented in this paper opens up the possibility to reduce the optical chip footprint to a few microns. This optical chip design can be significantly important for the effective integration of various optics devices in a very small area.

#### 4. CONCLUSIONS

We have proposed a novel model of a lens which serves as a spot-size converter and is based on a twodimensional photonic crystal platform with a negative refractive index. A numerical method based on twodimensional Finite-Difference Time-Domain is developed and employed to design the photonic crystal lens. The configuration geometry of the PC lens is designed, optimized, and integrated into a single optical chip. The proposed PC lens is deployed to effectively couple the light from a SMF with large core size into a PCW with very small structure dimensions. A significant reduction in the device compactness and coupling efficiency is demonstrated by optimizing the proposed PC lens and the PCW.

#### REFERENCES

1. Veselago, V. G., "The electrodynamic of substances with simultaneously negative values of  $\epsilon$  and  $\mu$ ," *Soviet Physics USPEKI*, Vol. 10, No. 4, 509–514, 1968.
2. Pendry, J. B., A. J. Holden, D. J. Robbins, and W. J. Steward, "Magnetism from conductors and enhanced nonlinear phenomenon," *Microw. Tech. Trans. MTT*, Vol. 47, No. 11, 2075–2084, 1999.
3. Houck, A. A., J. B. Brock, and I. L. Chuang, "Experimental observations of a left-handed material that obeys snell's law," *Phys. Rev. Lett.*, Vol. 90, No. 13, 137401-1–137401-4, 2003.
4. Yee, S. K., "Numerical solution of initial boundary value problems involving Maxwell's equations in isotropic media," *Trans. Anten. and Propag.*, Vol. 14, No. 5, 302–307, 1966.
5. Taflove, A., *Computational Electrodynamics: The Finite Difference Time Domain Method*, Artech House, 1995.
6. Berenger, J. P. A., "Perfectly matched layer for the absorption of electromagnetic waves," *J. Computational Physics*, Vol. 114, No. 2, 185–200, 1994.
7. Masoudi, H. M., M. A. Al-Sunaidi, and J. M. Arnold, "Efficient time-domain beam-propagation method for modelling integrated optical devices," *IEEE J. Lightwave Tech.*, Vol. 19, No. 5, 759–771, 2001.
8. Leung, K. M. and Y. F. Liu, "Full vector wave calculation of photonic band structures in face-centeredcubic dielectric media," *Phys. Rev. Lett.*, Vol. 65, No. 21, 2646–2649, 1990.
9. Foteinopoulou, S. and C. M. Soukoulis, "Electromagnetic wave propagation in two-dimensional photonic crystals: A study of anomalous refractive effects," *Phys. Rev. B*, Vol. 72, 165112, 2005.

10. Moussa, R., S. Foteinopoulou, L. Zhang, G. Tuttle, K. Guven, E. Ozbay, and C. M. Soukoulis, "Negative refraction and superlens behavior in a two-dimensional photonic crystal," *Phys. Rev. B*, Vol. 71, 085106, 2005.
11. Pendry, J. B. and D. R. Smith, *Physics Today*, Vol. 57, No. 6, 37-43, 2004.

# Review of Nonlinear Optics in Metamaterials

Yuanjiang Xiang, Xiaoyu Dai, Shuangchun Wen, and Dianyuan Fan

Research Center of Laser Science and Engineering and School of Computer and Communication  
Hunan University, Changsha 410082, China

**Abstract**— Recent researches on metamaterials (MMs) demonstrated that a nonlinear MM exhibits a rich spatiotemporal dynamics where both linear and nonlinear effective properties can be tailored simply. This provides opportunity to explore the new nonlinear optical phenomena in MMs. This contribution reviews the recent advances on nonlinear interaction between electromagnetic wave with MMs, from the fundamental physical models to unique phenomena and conceived novel devices. The physical origins for the typical nonlinear phenomena, such as second-order harmonic generation (SHG), optical parametric amplification (OPA), four-wave mixing (FWM), optical soliton, self-phase modulation (SPM), and self-focusing in MMs are explained. Several proposals for applications of nonlinear MMs in manipulating light are demonstrated.

## 1. INTRODUCTION

Metamaterials (MMs) are artificial structures that can be pre-designed to show specific electromagnetic properties not commonly found in nature [1–6]. MMs include positive-index regime, absorption regime and negative-index regime [3, 4]. One of the most exciting opportunities for MMs is the development of negative-index metamaterials (NIMs) [1]. NIMs have a number of peculiar properties: reversed Snell refraction, reversed Doppler Effect, reversed radiation tension, negative Cerenkov radiation [1], reversed Goos-Hänchen shift [2] and so on. NIMs have opened new doors in optics and have truly excited the imagination of researchers worldwide. Most of the properties of NIMs have been studied only for linear waves, such as negative refraction and super-lensing [7]. However, it has been already noticed that the NIMs may possess quite complicated nonlinear response. Thanks to rapidly developing nanofabrication and sub-wavelength imaging techniques, the optical NIMs can now be fabricated. The possibility of nonlinear electromagnetic responses, including cubic or quadratic nonlinear responses, in MMs is also demonstrated by the inclusion of nonlinear elements within the MMs, for instance by embedding the split-ring resonators (SRRs) in a Kerr-type dielectric [8], or by inserting certain nonlinear elements (e.g., diodes) in the split-ring resonators' paths [9]. The accessibility of linear and nonlinear MMs exhibiting negative electric and magnetic properties in the infrared and optical frequencies [10–12] have truly excited the imagination of researchers worldwide and stimulated intense investigation on the nonlinear optics of MMs, including second-order nonlinear optical phenomena such as second-harmonic generation and optical parametric amplification [12–18], as well as the 3rd-order nonlinear interaction of ultrashort electromagnetic pulse with MMs [13, 19–24]. It is known that, optical magnetization, which is normally ignored in linear and nonlinear optics of the ordinary media, plays a crucial role in MMs. Several authors have shown that it is the dispersive magnetic permeability that significantly leads to the difference between the propagation models for ultrashort pulses in MMs and in ordinary media. For propagation of ultrashort pulses in MMs with a nonlinear electric polarization, it is demonstrated that the linear dispersive magnetic permeability is incorporated into the nonlinear polarization, resulting in a controllable self-steepening (SS) effect and a series higher-order dispersive nonlinear terms in the propagation models [20–23]. The role of the controllable SS effect in MI has been identified [20, 21].

As the wavelength for which we observe a negative refractive index in MMs continues to push into the optical regime, the study of nonlinear effects will become very important, particularly from an applications point of view. In this paper, we report on the recent progress on investigation of some typical nonlinear optical phenomena in MMs, including third-order nonlinear optical phenomena such as soliton propagation, self-focusing, and spatiotemporal instability. The controllability and the novel properties of the nonlinear phenomena in MMs are demonstrated. Here we consider nonlinear optical processes in a MMs and show that they also exhibit unusual properties with respect to energy conversion and propagation. This will further extends the conventional area of optics, particularly nonlinear optics, and leads to completely new electronic and optical devices to manipulate light waves.

## 2. THE SECOND-ORDER NONLINEAR OPTICAL PHENOMENA IN MMS

In 1961, Franken and his collaborators experimentally discovered second-harmonic generation (SHG) [25], since then, SHG has become one of the most investigated and discussed nonlinear optical processes. Recently, the study of second order processes in MMs has been addressed by Lapine through inserting diodes in the split-ring resonators' paths [9], they have shown that for the case of small amplitudes of the interacting waves, when the diodes are driven by relatively low voltage, the nonlinear response of the MM is described by a quadratic magnetic susceptibility. Subsequently, they analyzed the three-wave coupling processes with a strong pump wave and two weak signals [26]. However, for the quadratic nonlinear, we will more concerns with SHG, optical parametric amplification (OPA), four-wave mixing (FWM).

### 2.1. Second-order Harmonic Generation in MMs

The first analysis of SHG from a semi-infinite NIM was briefly presented by Agranovich et al. [13], who considered that SHG in transmission is badly phase mismatched. Detailed theoretical studies have been made on second harmonic generation [14–17] where one of the important results was the demonstration of the possibility of exact phase matching when the fundamental and second harmonic waves are counter-propagating. Shadrivov et al. demonstrate that the original paper by Agranovich et al. missed an important additional phase-matching condition, quite specific for the harmonic generation by the backward waves [16]. They demonstrate that exact phase matching between a backward-propagating wave of the fundamental frequency (FF) and the forward propagating wave at the second harmonics (SH) is indeed possible. This novel phase-matched process allows the creation of an effective “quadratic mirror” that reflects the SH component generated by an incident FF wave.

Shalaev et al. have also done a lot of work in the second-order nonlinear optical processes. They investigate not only second-harmonic generation and Manley-Rowe relations but also the parametric amplification in NIMs [14]. In the paper, they propose the possibility of a left-handed nonlinear-optical mirror, which converts the incoming radiation into a reflected beam at the doubled frequency with efficiency that can approach 100% for lossless and phase-matched medium considered.

Moreover, Scalora et al. studied pulsed SHG in MMs under the conditions of significant absorption [27]. By tuning the pump in the negative index range, a second harmonic signal is generated in the positive index region, such that the respective indices of refraction have the same magnitudes but opposite signs. This insures that a forward-propagating pump is exactly phase matched to the backward-propagating second harmonic signal. Using peak intensities of  $\sim 500 \text{ MW/cm}^2$ , assuming  $\chi^{(2)} \sim 80 \text{ pm/V}$ , they predicted conversion efficiencies of 12% and 0.2% for attenuation lengths of 50 and  $5 \mu\text{m}$ , respectively. Following this paper, Ceglia et al. studied SHG in a NIM cavity [28], the nonlinear process is made efficient by local phase-matching conditions between a forward-propagating pump and a backward-propagating second harmonic signal. By simultaneously exciting the cavity with counterpropagating pulses, and by varying their relative phase different, one is able to enhance or inhibit linear absorption and the second-harmonic conversion efficiency.

The theoretical research has been followed by a recent experimental demonstration of second harmonic generation in a magnetic MM [15, 18]. They have observed SHG from MMs composed of split-ring resonators excited at 1.5-micrometer wavelength and much larger signals are detected when magnetic-dipole resonances are excited, as compared with purely electric-dipole resonances. The experiments are consistent with the calculations based in the magnetic component of the Lorentz force exerted on metal electrons, where an intrinsic SHG mechanism that plays no role in nature materials, but this mechanism becomes relevant in this experiment as a result of the enhancement and the orientation of the local magnetic fields associated with the magnetic-dipole resonances of the split-ring resonances.

Recently, Roppo et al. analyzed pulsed SHG in ordinary and NIMs under phase mismatched conditions [29], and found that a portion of the generated second-harmonic signal is phase locked, trapped and dragged along by the pump pulse. In the case NIMs, it turns out that the trapped pulse and the pulse back-reflected at the interface constitute a set of twin pulses having the same negative wave vector but propagating in opposite directions as a result of the trapping mechanism, this work thus extends previous investigations done in ordinary materials, and bridges the gap with MMs by revealing exciting new dynamical characteristics hitherto unknown.

## 2.2. Optical Parametric Amplification in MMs

In particularity, Shalaev et al. propose a new approach to compensate losses in NIMs [14]. They demonstrate that the amplification of the left-handed wave can be turned into a cavity-less oscillation when the denominator tends to zero. Further, they have also shown the feasibility of compensating losses in NIMs by OPA. In this process, the wave-vectors of all three coupled waves are co-directed, whereas the energy flow for the signal wave is counter-directed with respect to those for the pump and the idler waves. As seen in Fig. 2, the process is characterized by properties that are in strict contrast with those known for conventional nonlinear-optical crystals. Such extraordinary features allow one to realize optical parametric oscillations (OPOs) without a cavity at frequencies where the refractive index is negative. It is shown that the OPA and OPO in NIMs enable the generation of pairs of entangled counter-propagating right- and left-handed photons inside the NIM slabs.

## 3. THE THIRD-ORDER NONLINEAR OPTICAL PHENOMENA IN MMS

Owing to their unconventional characteristics, MMs with third-order nonlinearity have attracted a lot of recent interest in the properties of wave propagation in such material, which are most investigated in two aspects, the behavior of waves propagating in the bulk homogeneous MMs or across the interface between the conventional medium and the MMs such as the nonlinear MMs slab or the periodic structure composed of MMs and conventional right handed material.

### 3.1. The Propagation Properties for Electromagnetic Wave across the Interface of MMs

When the electromagnetic wave propagates through the interface of MMs, some novel phenomena will happen. Such as surface waves, gap soliton and optical bistability. Surface wave propagate along the interface and decay in the transverse direction, which is particularly important for the lensing effect since the amplification of evanescent modes is responsible for the subwavelength resolution. Darmanyan et al. studied the properties of nonlinear TE-polarized surface modes at the interface between different conventional and NIM and between two NIM [30], the constraints for the mode existence are identified and the energy flow associated with the surface modes was calculated.

Moreover, Hegde et al. have studied a periodic structure which is consisting of alternating layers of positive-index and negative-index materials [31]. They found that a novel band gap where the average refractive index is zero. The zero-n gap differs from the usual Bragg gap in which it is invariant to scale length and relatively insensitive to disorder and input angle [32, 33]. In the presence of Kerr nonlinearity, this zero-n gap can switch from low transmission to a perfectly transmitting state, forming a nonlinear resonance or gap soliton in the process. Furthermore, the phenomena such as hysteresis and bistability have been predicted. Optical bistability is a class of optical phenomena in which a system can exhibit two steady transmission states for the same input intensity, which has attracted interesting for the potential application of the all optical switching.

Recently, Kochara et al. have studied a ring cavity filled with a slab of a right-handed material and a slab of left-handed materials, both layers are assumed to be nonlinear Kerr media [34, 35]. By constructing a mean-field model, they show that the sign of diffraction can be made either positive or negative in this resonator, depending on the thickness of the layers. And they also demonstrated that the dynamical behavior of the modulation instability is strongly affected by the sign of the diffraction coefficient.

### 3.2. The Propagation Properties for Ultrashort Pulses in MMs

There have some investigations of pulse propagation in MMs, especially in NIMs [17–22, 36]. Another important theoretical contribution has been the derivation of a generalized nonlinear Schrödinger equation that can be employed to study pulse propagation and solitary waves in negative index media [19]. It has been demonstrated that the nonlinear MM exhibits a rich spatiotemporal dynamics where both linear and nonlinear effective properties can be tailored by simply engineering the MM [20, 21]. It is known that the most important difference between an ordinary medium and a MM is that the former has a constant permeability, while the latter has a dispersive permeability [37]. Therefore, it can be convinced that the most important difference between the propagation of ultrashort pulses in these two kinds of materials should result mainly from the dispersive permeability. To disclose the features of ultrashort pulse propagation resulting from the unique properties of MMs, it is apparent that a careful re-examination of the propagation of ultrashort pulses is needed. In addition, it is believed that deep understanding of the nonlinear interaction of ultrashort pulses with MMs will lead to new devices with previously inconceivable

properties. We consider pulse propagation in the latter regime, and thus can assume that the pulse is propagating in uniform, bulk material, in which there are no free charges and in which no free currents flow. In addition, we assume the MM has a nonlinear electric polarization and a nonlinear magnetization. The coupled nonlinear Schrödinger equations (NLSEs) for the envelopes of the electric and magnetic fields will be derived by [22]:

$$\begin{aligned}\frac{\partial E}{\partial \xi} &= i\hat{D}E + \frac{i}{2\beta_0\hat{S}_1}\nabla_{\perp}^2 E + \frac{i\mu_0\varepsilon_0\chi_E^{(3)}\omega_0^2}{2\beta_0}\frac{\hat{S}_2}{\hat{S}_1}\hat{G}\left(|E|^2 E\right) + \frac{i\omega_0\mu_0\chi_H^{(3)}}{2}\hat{S}_2\left(|H|^2 H\right) \\ \frac{\partial H}{\partial \xi} &= i\hat{D}H + \frac{i}{2\beta_0\hat{S}_1}\nabla_{\perp}^2 H + \frac{i\varepsilon_0\mu_0\chi_H^{(3)}\omega_0^2}{2\beta_0}\frac{\hat{S}_2}{\hat{S}_1}\hat{Q}\left(|H|^2 H\right) + \frac{i\omega_0\varepsilon_0\chi_E^{(3)}}{2}\hat{S}_2\left(|E|^2 E\right)\end{aligned}\quad (1)$$

For the purpose of calculations, it is convenient to rewrite Eq. (1) in normalized units. To this end we define the  $m$ th-order dispersion length,  $L_{dm} = \tau_p^m/\beta_m$ , where  $\tau_p$  is the pulse width ( $1 = e$ ), the nonlinear polarization length,  $L_{Pnl} = 2\beta_0/(\mu_0\varepsilon_0\nu_0\chi_p^{(3)}|E_0|^2\omega_0^2)$ , the nonlinear magnetization length,  $L_{Mnl} = 2\beta_0/(\varepsilon_0\mu_0\vartheta_0\chi_M^{(3)}|H_0|^2\omega_0^2)$ , and a characteristic length,  $L_{\perp} = \sqrt{|L_{d2}/\beta_0|}$ , and take the transformations,  $U = E/E_0$ ,  $V = H/H_0$ ,  $T = \tau/\tau_p$ ,  $X = x/L_{\perp}$ ,  $Y = y/L_{\perp}$ ,  $Z = \xi/|L_{d2}|$ , where  $E_0$  and  $H_0$  are the initial amplitudes of  $E$  and  $H$ . Eq. (1) is thus transformed to the following form:

$$\begin{aligned}\frac{\partial U}{\partial Z} &= i\tilde{D}U + \frac{i\text{sgn}(\beta_0)}{2\tilde{S}_1}\nabla_T^2 U + iN_e\frac{\tilde{S}_2}{\tilde{S}_1}\left(1 + \tilde{G}\right)\left(|U|^2 U\right) + i\frac{N_E n}{\nu_0\chi}\tilde{S}_2\left(|V|^2 V\right) \\ \frac{\partial V}{\partial Z} &= i\tilde{D}V + \frac{i\text{sgn}(\beta_0)}{2\tilde{S}_1}\nabla_T^2 V + iN_H\frac{\tilde{S}_2}{\tilde{S}_1}\left(1 + \tilde{Q}\right)\left(|V|^2 V\right) + i\frac{N_h n\chi}{\vartheta_0}\tilde{S}_2\left(|U|^2 U\right)\end{aligned}\quad (2)$$

where  $\nabla_T^2 = \partial^2/\partial X^2 + \partial^2/\partial Y^2$ ,  $N_E = |L_{d2}|/L_{Pnl}$ ,  $N_H = |L_{d2}|/L_{Mnl}$ ,  $\chi = \sqrt{\varepsilon_0}\chi_p^{(3)}|E_0|^2 E_0/(\sqrt{\mu_0}\chi_M^{(3)}|H_0|^2 H_0)$ , the linear dispersive operators

$$\tilde{D} = \sum_{m=2}^{\infty} \frac{i^m b_m}{m!} \frac{\partial^m}{\partial T^m}, \quad \tilde{G} = \sum_{m=1}^{\infty} \frac{i^m g_m}{m!} \frac{\partial^m}{\partial T^m}, \quad \tilde{Q} = \sum_{m=1}^{\infty} \frac{i^m q_m}{m!} \frac{\partial^m}{\partial T^m}, \quad (3)$$

where  $L_{dm} = \tau_p^m/\beta_m$ ,  $b_m = |L_{d2}|/L_{dm}$ ,  $g_m = \nu_m/(\nu_0\tau_p^m)$ ,  $q_m = \vartheta_m/(\vartheta_0\tau_p^m)$ , and the SS operators

$$\tilde{S}_1 = 1 + ivs\frac{\partial}{\partial T}, \quad \tilde{S}_2 = 1 + is\frac{\partial}{\partial T}, \quad (4)$$

where  $v = \omega_0\beta_1/\beta_0 = v_p/v_g$ ,  $s = 1/\omega_0\tau_p$ .

The terms on the right-hand side of each equation of the set (2) represent linear dispersion, diffraction, nonlinearity and cross-phase modulation, respectively. The prefactor of the diffraction term denotes the effect of space-time focusing, and the prefactor of the nonlinear term includes the effects of SS, resulted from the SVEA as well as the dispersive permeability (the equation for electric field) and permittivity (the equation for magnetic field), and higher-order dispersive nonlinear terms resulted from the linear dispersive property of MM. From the expressions for  $b_m$ ,  $s$ ,  $g_m$  and  $q_m$ , it is obvious that the higher-order linear and nonlinear dispersion terms become more important as the pulse width decreases. For ordinary dielectrics,  $M_{nl} = 0$  and  $\mu_r = 1$ , and thus  $\tilde{G} = 0$ . In this case, the propagation equation for electric field, i.e., the first equation in Eq. (2) is identical to the few-cycle pulse propagation equation of Ref. [38]. If we further make use of the approximation [19], this equation is reduced to the propagation equation obtained by Brabec and Krausz [39].

It can be seen from the Fig. 1 that the MI gain band shrinks as the self-steepening coefficient increases and disappears after the self-steepening coefficient arrives at a critical value [20, 21]. As stated before, the self-steepening effect can be engineered, thus the MI can be manipulated. These results illustrate not only the unusual nonlinear effects that can be seen in NIMs, but also the new ways of manipulating solitons.

Due to the direction of wave vector is opposite to the Poynting vector in NIM, which will induce anomalous spatial and spatiotemporal MI. There is large different between the spatial MI of NIM and the conditional material, such as, spatial MI only occurs in defocusing NIM, contrary to that

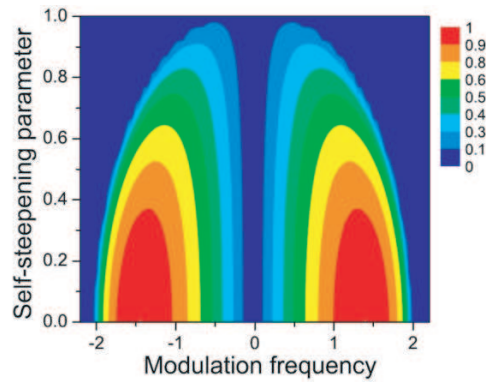


Figure 1: Modulation instability gain spectrum for different SS parameter  $S_1$  in the abnormal dispersion regime of negative-index material (From [21]).

in ordinary material, in which spatial MI only occurs in the focusing regime. This opposition is due to the fact that negative refraction reverses the sign of the diffraction term, with the nonlinearity coefficient unchanged. The special spatial MI will result in anomalous spatiotemporal in NIM. Fig. 2 is the spatiotemporal under three conditions. Comparing the results with those in ordinary nonlinear dispersive material [20,21], we find an interesting fact that the spatiotemporal MI in NIM for a definite combination of dispersion and nonlinearity is just that in ordinary material for a combination of opposite dispersion and opposite nonlinearity. For example, the gain spectra in the three cases, corresponding to Figs. 2(a)–2(c), are, respectively, the same as those in ordinary material for the cases of (i) defocusing nonlinearity and normal dispersion, (ii) focusing nonlinearity and anomalous dispersion, and (iii) focusing nonlinearity and normal dispersion. The physical origin of the fact is that the negative refraction reverses the phase velocity, and thus reverses the diffraction term. This leads to the diffraction and normal dispersion being equivalent when acting with nonlinearity in NIM, while in ordinary material, diffraction is equivalent with anomalous dispersion. In addition, spatiotemporal MI shows how diffraction and dispersion act together to couple space and time. It occurs due to the simultaneous presence of temporal MI and spatial MI in a nonlinear medium, unlike independently occurring temporal MI and spatial MI. Thus the three cases in which spatiotemporal MI can occur can also be obtained by combining the former two kinds of MI, which provide more chance for the form of spatiotemporal soliton.

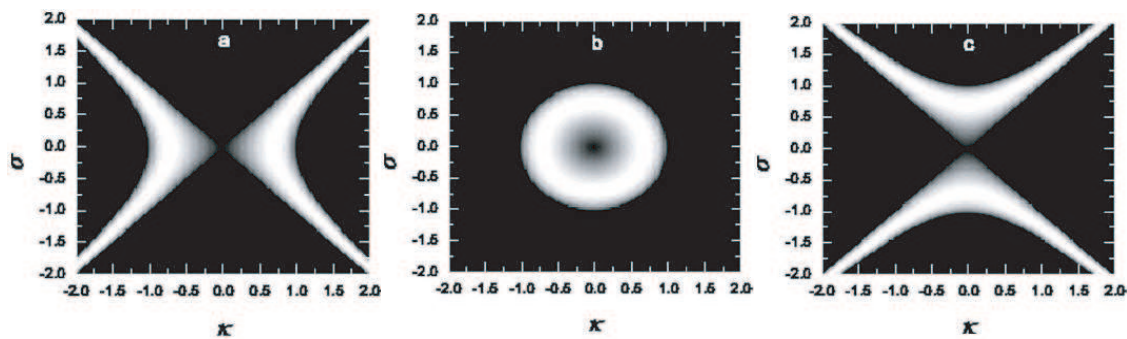


Figure 2: Spatiotemporal MI gain in the  $(\kappa, \sigma)$  plane for the cases of (a) focusing material with anomalous dispersion, (b) defocusing material with normal dispersion, and (c) defocusing material with anomalous dispersion (From [20]).

The dispersive permeability not only will result in the additional SS, but also will result in a series higher-order dispersive nonlinear terms. Wen et al. focus their attention on the additional MI phenomena inducing by the 2nd-order nonlinear dispersion effect in MI and show that a new kind of MI can occur in the normal group-velocity dispersion (GVD) regime and at the zero GVD point of the MMs, which is resulting from the additional 2nd-order nonlinear dispersion term induced by the dispersive magnetic permeability [40]. This provides a method for generating a train of ultrashort pulse in normal GVD regime, and there is significant value in the practical application.

The influence of the 2nd-order dispersion on MI in the forenamed three cases is plotted in Fig. 3.

In the case (a), the 2nd-order nonlinear dispersion parameter can be positive or zero or negative. An abnormal phenomenon is that the coherent MI occurs when  $s_2 < 0$ , as Fig. 3(a) shows. Here the negative 2nd-order nonlinear dispersion acts as the role of the anomalous GVD, and thus makes the otherwise impossible MI possible. In addition, we see from Fig. 3(a) that the partial coherence tends to suppress the MI induced by the 2nd-order nonlinear dispersion.

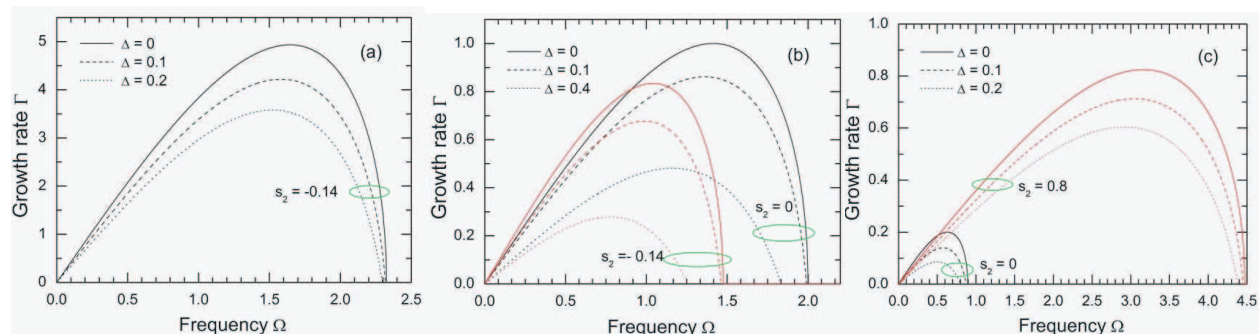


Figure 3: Influence of the 2nd-order nonlinear dispersion on MI in metamaterial. (a) MI gain spectrum in the negative-index region with normal dispersion, (b) MI gain spectrum in the negative-index region with anomalous dispersion, and (c) MI gain spectrum in the positive-index region with anomalous dispersion (From [40]).

In the case (b), the 2nd-order nonlinear dispersion parameter is negative. The influence of 2nd-order nonlinear dispersion on MI in both full and partial coherence is demonstrated in Fig. 3(b). It is shown that, both the 2nd-order nonlinear dispersion and the partial coherence tend to suppress MI in this case. In the case (c), the 2nd-order nonlinear dispersion parameter is positive. We see that the partial coherence tend to suppress MI, while the 2nd-order nonlinear dispersion enhance MI in this case.

To demonstrate this analytical prediction they get the numerical result through the using the standard split-step Fourier method for  $\omega_{pm}/\omega_{pe} = 0.8$  in the case of focusing nonlinearity and no linear dispersion [55]. The initial field distribution is a cosinoidally modulated plane wave,  $u(T, 0) = u_0[1 + a_0 \cos(\Omega T)]$ , where  $u_0 = 10$  is the initial amplitude of background wave and  $a_0$  is the initial amplitude of modulation wave which is set to be 0.05,  $\Omega$  is chosen such that it is the fastest growing frequency for the corresponding case. The numerical results are shown in Fig. 4, and Fig. 4(b) is plotted under the condition of neglecting the SS effect. As shown in Fig. 4(b), the cosinoidally modulated plane wave evolves into a train of pulses with much higher amplitude than the initial modulation as the propagation distance increases. Compared with Fig. 4(b), Fig. 4(a) shows that the center of modulated wave or generated pulse moves toward the leading side and the modulation growth rate is slowed down, which is due to the role of negative SS. These numerical results further demonstrate that MI can appear in the case of no linear dispersion.

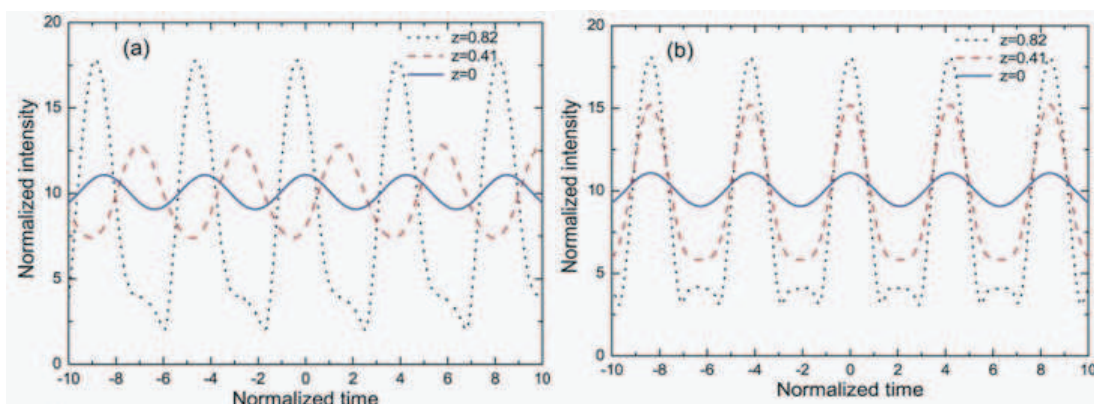


Figure 4: Temporal distributions of the field intensity of cosinoidally modulated plane wave at different propagation distances for different parameters at the zero GVD point (a)  $s_1 = -0.3122$ ,  $s_2 = -0.1424$ ; (b)  $s_1 = 0$ ,  $s_2 = -0.1424$  (From [55]).

#### 4. APPLICATIONS OF NONLINEAR MMS

Nonlinear media with negative index of refraction have a variety of potential application. From a nonlinear applications perspective, nonlinear MMs in the optical regime are very attractive owing to the availability of high intensity light sources. There has been tremendous progress in the area of NIMs in the optical regime with a variety of structures and negative index wavelengths. Nonlinearities of MMs stated above suggest their novel application such as frequency conversion, tunable transmission, nonlinear beam focusing, second-harmonic imaging, soliton propagation, spatiotemporal soliton or light bullet. Furthermore, for the unconventional nonlinear properties of MMs, there are still some novel applications.

##### 4.1. Opaque Nonlinear Left-handed Lenses

Pendry et al. found that the flat slab of NIMs can focus electromagnetic waves, and they argued that a slab of lossless NIM with  $\varepsilon = \mu = -1$  should behave like a perfect lens enabling to obtain an ideal image of a point source through the amplification of the evanescent components of the field [7]. While recent experimental demonstrations confirmed the main features of negative refraction of the NIMs, near-perfect imaging by a flat lens and near-field focusing are severely constrained because of strong dissipation and dispersion of MMs [41, 42]. Nevertheless, numerical studies indicate that nearly-perfect imaging should be expected even under realistic conditions when both dispersion and losses are taken into account [43, 44]. Most of the properties of NIMs have been studied only for linear waves. However, Zharov et al. have studied the second-harmonic generation in a slab of NIM with quadratic nonlinear response [45]. They demonstrated that such a slab can act as a nonlinear lens and it can form an image of the second-harmonic field of the source being opaque at the fundamental frequency, with the resolution that can be made better than the radiation wavelength.

They considered a slab of NIMs and assume that each SRR includes a nonlinear element (a diode inserted into the SRR slot). As a result, the amplitudes of the magnetic momenta induced in the unit cell by the magnetic field  $\mathbf{H}$  and  $-\mathbf{H}$  are different, and the response of such an effective quadratic nonlinear medium should include the second-harmonic field. They choose the material parameters, making the refractive index of second-harmonic wave ( $2\omega$ ) is  $-1$  and the refractive index of fundamental frequency  $\omega$  is imaginary number, and the fundamental waves do not penetrate into the slab. However, an effective nonlinear quadratic response of the MM allows the process of the second-harmonic generation. Using the so-called undepleted pump approximation, they show that the second-harmonic field can propagate through the slab creating an image of the source behind the slab.

##### 4.2. Subwavelength Discrete Solitons

Yongmin Liu et al. studied the metal-dielectric multilayers (MDMLs) [46], this kind MMs is periodic structures consisting of nanoscaled metallic and dielectric slabs [47]. They show that the MDML with nonlinear (Kerr-type) dielectric can exhibit self-focusing of light, and form subwavelength discrete solitons. The formation of such solitons is a result of the threefold interplay between periodicity, nonlinearity, and surface plasmons tunneling, leading to new and intriguing phenomena that are not found in nonlinear DWGAs. They have addressed the issue of the intrinsic loss in such structures, calculated the gain required to compensate such losses, and suggested a feasible configuration in which subwavelength discrete solitons could be experimentally observed.

##### 4.3. Optical Bistability and Optical Switch

NIMs possess simultaneously negative dielectric permittivity and magnetic permeability, which will result in the refract light in the opposite way with respect to what in an ordinary material. According to this special property, Giuseppe D'Aguanno study a Negative Index Fabry-Perot Etalon, and show the presence of bright and dark gap soliton is supported in a single slab of material [48]. It is surprising is that in a single slab of frequency dispersive NIM together with a cubic nonlinearity appears to support both bright and dark gap soliton. Following this work, they predicted the existence of gap solitons in a nonlinear, quadratic Fabry-Perot cavity [49], they found that an intense, fundamental pump pulse is able to shift the band edge of negative index cavity, and make it possible for weak second harmonic pulse initially tuned inside the gap to be transmitted, giving rise to a gap soliton, the process is due to cascading, which causes pulse compression due to self-phase modulation. Moreover, Litchinister et al. investigated nonlinear transmission in a layered structure consisting of a slab of positive index material with Kerr-type nonlinearity and a subwavelength layer of linear negative index material sandwiched between semi-infinite linear dielectrics [50], they

found that a thin layer of NIM leads to significant changes in the hysteresis width when the nonlinear slab is illuminated at an angle near that of total internal reflection, and the unidirectional diodelike transmission with enhanced operational range is demonstrated. These results suggest that NIMs could find further application in all optical switching devices and all-optical buffering, for example.

Nonlinear optical couplers have also attracted interesting for the potential application of the all optical switching, power limiting, and so on. Natalia M. Litchinitser describes a novel nonlinear optical coupler structure that utilizes a NIM [3,12] in one of the channels and a conventional positive index material (PIM) in another channel. They found such a nonlinear coupler (NLC) can be bistable, which is resulted from that the backward coupling between the modes propagating in the PIM and NIM channels enabled by the basic property of NIMs, oppositely directed phase velocity, and the Poynting vector, results in optical bistability in PIM-NIM NLC and gap soliton formation. These effects have no analogies in conventional PIM-PIM couplers composed of uniform (homogeneous) waveguides with no feedback mechanism [51].

#### 4.4. Compensating Losses by Four-wave Mixing

The most detrimental obstacle toward applications of NIMs is strong absorption that is inherent to this class of materials. The possibility to overcome such obstacles based on three wave optical parametric amplification (OPA) in NIMs was shown in [14, 52]. In Section 2.2, it has demonstrated the feasibility of compensating losses in NIMs with second-order nonlinearity by optical parametric amplification. For the MMs with Kerr-nonlinearity, Popov et al. have proposed a approach to compensate losses, which basic idea is that a slab of NIM is doped by four-level nonlinear centers [53]. Chowdhury et al. have shown that second-order and third-order nonlinear susceptibilities and wave-mixing properties of NIM are important [54], especially in this material the three- and four-wave mixing can be naturally phase matched. In the approach, the frequency  $\omega_4$  falls in the NI domain, whereas all the other frequencies are in the positive index domain. They demonstrated that the losses of NIMs for strongly absorbing can be compensated by embedded optical nonlinearities. Further, they have studied the resonant FWM-based OPA in such composite NIM at the frequency of the signal and a positive index for all other coupled waves. In particularly, the strong nonlinear optical response of the composite can be adjusted independently, which is because nonlinear optical response is determined by the embedded four-level nonlinear centers.

## 5. CONCLUSIONS

In this paper, we briefly review some typical nonlinear phenomena of electromagnetic pulse propagate in the nonlinear MMs, such as second-order harmonic generation (SHG), optical parametric amplification (OPA), four-wave mixing (FWM), optical soliton, self-phase modulation (SPM), and self-focusing and so on. Some unique properties of nonlinear MMs have been stated. Furthermore, some potential applications for the nonlinear MMs are also addressed and reviewed. With the rapidly development of nanofabrication and sub-wavelength imaging techniques, the optical MMs will be fabricated more easy, and the nonlinear MMs will get great development. Although further material developments are still needed especially to minimize the losses present in currently available MMs, the novel and controllable properties of nonlinear MMS are very promising and point toward the possibility to achieve various applications in the future optical communication technology.

## ACKNOWLEDGMENT

This work is supported by the National Natural Science Foundation of China (Grant Nos. 10674045 and 10576012), the National High Technology Research and Development Program for Inertial Confinement Fusion of China, the Program for New Century Excellent Talents in University and the Specialized Research Fund for the Doctoral Program of Higher Education of China (Grant No. 20040532005).

## REFERENCES

1. Veselago, V. G., "The electrodynamics of substances with simultaneously negative values of  $\epsilon$  and  $\mu$ ," *Sov. Phys. Usp.*, Vol. 10, No. 4, 509–514, 1968.
2. Berman, P. R., "Goos-Hänchen shift in negatively refractive media," *Phys. Rev. E*, Vol. 66, No. 6, 067603, 2002.

3. Ziolkowski, R. W., "Superluminal transmission of information through an electromagnetic metamaterial," *Phys. Rev. E*, Vol. 63, No. 4, 046604, 2001.
4. Ziolkowski, R. W. and A. D. Kipple, "Causality and double-negative metamaterials," *Phys. Rev. E*, Vol. 68, No. 2, 026615, 2003.
5. Smith, D. R., W. J. Padilla, D. C. Vier, S. C. Nemat-Nasser, and S. Schultz, "Composite medium with simultaneously negative permeability and permittivity," *Phys. Rev. Lett.*, Vol. 84, No. 18, 4184–4187, 2000.
6. Smith, D. R. and N. Kroll, "Negative refractive index in left-handed materials," *Phys. Rev. Lett.*, Vol. 85, 2933–2936, 2000.
7. Pendry, J. B., "Negative refraction makes a perfect lens," *Phys. Rev. Lett.*, Vol. 85, 3966, 2000.
8. Zharov, A. A., I. V. Shadrivov, and Y. S. Kivshar, "Nonlinear properties of left-handed metamaterials," *Phys. Rev. Lett.*, Vol. 91, 037401, 2003.
9. Lapine, M., M. Gorkunov, and K. H. Ringhofer, "Nonlinearity of a metamaterial arising from diode insertions into resonant conductive elements," *Phys. Rev. E*, Vol. 67, 065601, 2003.
10. Shalaev, V. M., W. Cai, U. K. Chettiar, H. K. Yuan, A. K. Sarychev, V. P. Drachev, and A. V. Kildishev, "Negative index of refraction in optical metamaterials," *Opt. Lett.*, Vol. 30, 3356–3358, 2005.
11. Dolling, G., M. Wegener, C. M. Soukoulis, and S. Linden, "Negative-index metamaterial at 780 nm wavelength," *Opt. Lett.*, Vol. 32, 53–55, 2007.
12. Shalaev, V. M., "Optical negative-index metamaterials," *Nature Photonics*, Vol. 1, 41–48, 2007.
13. Agranovich, V. M., Y. R. Shen, R. H. Baughman, and A. A. Zakhidov, "Linear and nonlinear wave propagation in negative refraction metamaterials," *Phys. Rev. B*, Vol. 69, 165112, 2004.
14. Popov, A. K. and V. M. Shalaev, "Negative-index metamaterials: Second-harmonic generation, Manley-Rowe relations and parametric amplification," *Appl. Phys. B*, Vol. 84, 131–137, 2006.
15. Klein, M. W., C. Enkrich, M. Wegener, and S. Linden, "Second-harmonic generation from magnetic metamaterials," *Science*, Vol. 313, 502–504, 2006.
16. Shadrivov, I. V., A. A. Zharov, and Y. S. Kivshar, "Second-harmonic generation in nonlinear left-handed metamaterials," *J. Opt. Soc. Am. B*, Vol. 23, 529–534, 2006.
17. De Ceglia, D., A. D’Orazio, M. De Sario, V. Petruzzelli, F. Prudenzano, M. Centini, M. G. Cappendu, M. J. Bloemer, and M. Scalora, "Enhancement and inhibition of second-harmonic generation and absorption in a negative index cavity," *Opt. Lett.*, Vol. 32, 265–267, 2007.
18. Klein, M. W., M. Wegener, N. Feth, and S. Linden, "Experiments on second- and third-harmonic generation from magnetic metamaterials," *Opt. Express*, Vol. 15, 5238–5247, 2007.
19. Scalora, M., M. S. Syrchin, N. Akozbek, E. Y. Poliakov, G. D’Aguanno, N. Mattiucci, M. J. Bloemer, and A. M. Zheltikov, "Generalized nonlinear Schrödinger equation for dispersive susceptibility and permeability: Application to negative index materials," *Phys. Rev. Lett.*, Vol. 95, 013902, 2005.
20. Wen, S., Y. Wang, W. Su, Y. Xiang, X. Fu, and D. Fan, "Modulation instability in nonlinear negative-index material," *Phys. Rev. E*, Vol. 73, No. 3, 036617-1-6, Copyright © 2006, Optical Society of America, March 24, 2006.
21. Wen, S., Y. Xiang, W. Su, Y. Hu, X. Fu, and D. Fan, "Role of the anomalous self-steepening effect in modulation instability in negative-index material," *Opt. Express*, Vol. 14, No. 4, 1568–1575, Copyright © 2006, Optical Society of America, February 22, 2006.
22. Wen, S., Y. Xiang, X. Dai, Z. Tang, W. Su, and D. Fan, "Theoretical models for ultrashort electromagnetic pulse propagation in nonlinear metamaterials," *Phys. Rev. A*, Vol. 75, 033815, 2007.
23. Lazarides, N. and G. P. Tsironis, "Coupled nonlinear Schrödinger field equations for electromagnetic wave propagation in nonlinear left-handed materials," *Phys. Rev. E*, Vol. 71, 036614, 2005.
24. Kourakis, I. and P. K. Shukla, "Nonlinear propagation of electromagnetic waves in negative-refraction-index composite materials," *Phys. Rev. E*, Vol. 72, 016626, 2005.
25. Franken, P. A., A. E. Hill, C. W. Peters, and G. Weinreich, "Generation of optical harmonics," *Phys. Rev. Lett.*, Vol. 7, 118, 1961.
26. Lapine, M. and M. Gorkunov, "Three-wave coupling of microwaves in metamaterial with nonlinear resonant conductive elements," *Phys. Rev. E*, Vol. 70, 066601, 2004.

27. Scalora, M., G. D'Aguanno, M. Bloemer, et al., "Dynamics of short pulses and phase matched second harmonic generation in negative index materials," *Opt. Express*, Vol. 14, 4746–4756, 2006.
28. De Ceglia, D., A. D'Orazio, M. D. Sario, et al., "Enhancement and inhibition of second-harmonic generation and ansorption in a negative index cavity," *Opt. Lett.*, Vol. 32, 265–267, 2007.
29. Roppo, V., M. Centini, C. Sibilia, et al., "Role of phase matching in pulsed second-harmonic generation: Walk-off and phase-locked twin pulses in negative-index media," *Phys. Rev. A*, Vol. 76, 033829, 2007.
30. Darmanyan, S. A., M. Neviere, and A. A. Zakhidov, "Nonlinear surface waves at the interfaces of left-handed electromagnetic media," *Phys. Rev. E*, Vol. 72, 036615, 2005.
31. Hegde, R. S. and H. G. Winful, "Zero-n gap soliton," *Opt. Lett.*, Vol. 30, 1852–1854, 2005.
32. Li, J., L. Zhou, C. T. Chan, and P. Sheng, "Photonic band gap from a stack of positive and negative index materials," *Phys. Rev. Lett.*, Vol. 90, 083901, 2003.
33. Wu, L., S. He, and L. Chen, "Band structure for a one-dimensional photonic crystal containing left-handed materials," *Phys. Rev. B*, Vol. 67, 235103, 2003.
34. Kockaert, P., P. Tassin, G. V. D'Sande, et al., "Negative diffraction pattern dynamics in nonlinear cavities with left-handed materials," *Phys. Rev. A*, Vol. 74, 033822, 2006.
35. Tassin, P., L. Gelens, J. Danckaert, et al., "Dissipative structures in left-handed material cavity optics," *Chaos*, Vol. 17, 037116, 2007.
36. Kourakis, I., N. Lazarides, and G. P. Tsironis, "Self-focusing and envelope pulse generation in nonlinear magnetic metamaterials," *Phys. Rev. E*, Vol. 75, 067601, 2007.
37. Pendry, J. B. and D. R. Smith, "Reversing light: Negative refraction," *Phys. Today*, Vol. 57, No. 6, 37–44, 2004.
38. Kinsler, P. and G. H. C. New, "Few cycle pulse propagation," *Phys. Rev. A*, Vol. 67, 023813, 2003.
39. Brabec, T. and F. Krausz, "Nonlinear optical pulse propagation in the single-cycle regime," *Phys. Rev. Lett.*, Vol. 78, 3282–3285, 1997.
40. Zhuo, H., S. Wen, X. Dai, Y. Hu, and Z. Tang, "Influence of nonlinear dispersion on modulation instability in metamaterials," *Appl. Phys. B*, Vol. 87, No. 4, 635–641, Copyright @ 2007, Springer, May 17, 2007.
41. Shelby, R. A., D. R. Smith, and S. Schultz, "Experimental verification of a negative index of refraction," *Science*, Vol. 292, 77, 2001.
42. Parazzoli, C. G., R. B. Greigor, K. Li, B. E. C. Koltenbah, and M. Tanielian, "Wave-vector-dependent exciton exchange interaction," *Phys. Rev. Lett.*, Vol. 90, 107401, 2003.
43. Cummer, S. A., "Simulated causal subwavelength focusing by a negative refractive index slab," *Appl. Phys. Lett.*, Vol. 82, 1503, 2003.
44. Feise, M. and Y. S. Kivshar, "Sub-wavelength imaging with a left-handed material flat lens," *Phys. Lett. A*, Vol. 334, 326, 2005.
45. Zharov, A. A. and N. A. Zharova, "Subwavelength imaging with opaque nonlinear left-handed lenses," *Appl. Phys. Lett.*, Vol. 87, 091104, 2005.
46. Liu, Y. M. and G. Bartal, "Subwavelength discrete solitons in nonlinear metamaterials," *Phys. Rev. Lett.*, Vol. 99, 153901, 2007.
47. Economou, E. N., "Surface plasmons in thin films," *Phys. Rev.*, Vol. 182, 539, 1969.
48. D'Aguanno, G., N. Mattiucci, M. Scalora, and M. J. Bloemer, "Bright and dark gap solitons in a negative index Fabry-Pérot etalon," *Phys. Rev. Lett.*, Vol. 93, 213902, 2004.
49. Scalora, M., D. D'Ceglia, G. D'Aguanno, et al., "Gap solitons in a nonlinear quadratic negative-index cavity," *Phys. Rev. E*, Vol. 75, 066606, 2007.
50. Litchinister, N. M., I. R. Gabitov, A. I. Maimistov, and V. M. Shalaev, "Effect of an optical negative index thin film on optical bistability," *Opt. Lett.*, Vol. 32, 151–153, 2006.
51. Litchinitser, N. M. and I. R. Gabitov, "Optical bistability in a nonlinear optical coupler with a negative index channel," *Phys. Rev. Lett.*, Vol. 99, 113902, 2007.
52. Popov, A. K. and V. M. Shalaev, "Compensating losses in negative-index metamaterials with optical parametric amplification," *Opt. Lett.*, Vol. 31, 2169, 2006.
53. Popov, A. K., S. A. Myslivets, T. F. George, and V. M. Shalaev, "Four-wave mixing, quantum control, and compensating losses in doped negative-index photonic metamaterials," *Opt. Lett.*, Vol. 32, 3044–3046, 2007.

54. Chowdhury, A. and J. A. Tataronis, "Nonlinear wave mixing and susceptibility properties of negative refractive index materials," *Phys. Rev. E*, Vol. 75, 016603, 2007.
55. Xiang, Y. J., S. C. Wen, X. Y. Dai, Z. X. Tang, W. H. Su, and D. Y. Fan, "Modulation instability induced by nonlinear dispersion in the nonlinear metamaterials," *J. Opt. Soc. Am. B*, Vol. 24, No. 1, Copyright © 2006, Optical Society of America, 2008 (to be published).

# Transparency Effect Induced by Elastic Metamaterials

Xiaoming Zhou, Jin Hu, and Gengkai Hu

Department of Applied Mechanics, School of Science, Beijing Institute of Technology  
Beijing 100081, China

**Abstract**— In the quasi-static limit, it is shown that the neutral inclusion concept can be applied to predict the transparency phenomenon. The transparency designs for a coated ellipsoid for electromagnetic wave and a multilayered sphere for acoustic wave with metamaterials have been proposed. In this paper, we will show how to cloak a solid object with elastic wave metamaterial, where the shear wave in the system is nontrivial. Based on the Mie theory, it is shown that the effective bulk modulus, mass density, and shear modulus of the assemblage made of the coated spheres dominate the zero, the first and the second order scattering coefficients of one coated sphere, respectively. So letting the first three scattering coefficients vanish, the isotropic coated metamaterial can be determined in order to make a spherical object transparent for elastic wave, this again corresponds to the neutral inclusion concept.

## 1. INTRODUCTION

Since the pioneer work by Alù and Engheta [1], who found that plasmonic metamaterials could make a dielectric sphere with extremely low total scattering cross section, much works are devoted to analyze the transparency induced by metamaterials. In quasi-static limit, this phenomenon can be well predicted with the neutral inclusion concept [2], and it is easily applied for the more complex configurations, such as a coated ellipsoid and particulate composites. This method is suitable to cloak objects with dimension smaller than the operating wavelength. However, several transparent coated spheres joined together to form an object with large electrical size can still be transparent [3]. This may provide a new way to achieve transparency for an object with size larger than the wavelength. By analogy, the acoustic transparency for a coated sphere with acoustic metamaterials can also be designed [4]. Acoustic metamaterial is a kind of material, whose mass density and bulk modulus could be negative. The peculiar properties of this kind of material have been demonstrated experimentally [5, 6]. In this work, we will discuss how to cloak a solid spherical object using elastic wave metamaterials.

## 2. NEUTRAL INCLUSION CONCEPT

Consider a random-shaped region characterized by permittivity  $\varepsilon_*$  and permeability  $\mu_*$  (or bulk modulus  $\kappa_*$ , shear modulus  $G_*$ , and mass density  $\rho_*$ ) embedded in an infinite matrix with  $\varepsilon_0$  and  $\mu_0$  (or  $\kappa_0$ ,  $G_0$  and  $\rho_0$ ), the electromagnetic or acoustic waves propagate through this area as shown in Figure 1. The region can be made of either a homogeneous medium or a heterogeneous material. For the latter,  $\varepsilon_*$  and  $\mu_*$  (or  $\kappa_*$ ,  $G_*$  and  $\rho_*$ ) then denote the effective material parameters of the heterogeneous material. It is not surprised that if the material property of this region is the same as that of the background medium (matrix), the electromagnetic or stress fields outside of this region will not be disturbed. In other word, the region will not be “seen” by an outside observer. When the region is made of a homogeneous material, this is a trivial case. However if the region is made

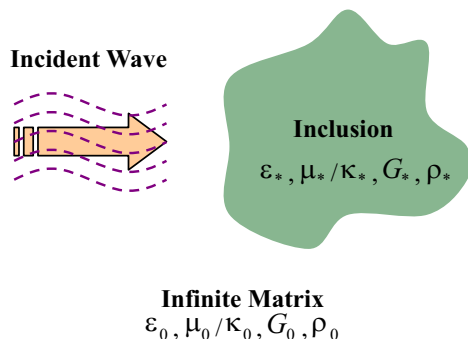


Figure 1: Scheme of neutral inclusion concept.

of a heterogeneous material, there are many design possibilities for equating its effective material property to that of the background medium, i.e., letting  $\varepsilon_* = \varepsilon_0$  and  $\mu_* = \mu_0$  (or  $\kappa_* = \kappa_0$ ,  $\rho_* = \rho_0$  and  $G_* = G_0$ ). This is the basic idea of the “neutral inclusion” concept discussed extensively by Milton [7]. A neutral inclusion is a simple pattern (coated sphere, coated spheroid, etc.). When a neutral inclusion is embedded in a material made of assemblages of such pattern with gradual sizes (in order to fill the whole space), it will not perturb the static electric, magnetic, or mechanical fields outside of this inclusion. Although the neutral inclusion is defined in the static or quasistatic case, it can still provide useful information in the full-wave scattering case.

### 3. ELASTIC WAVE SPHERICAL CLOAK

Consider a coated sphere system characterized by bulk modulus  $\kappa_i$ , shear modulus  $\mu_i$ , and mass density  $\rho_i$ , with the subscript  $i = 1, 2, 3$  representing separately the sphere, the coating, and the host medium. Let  $r_1$  denote the radius of the uncoated sphere and  $r_2$  the radius of the coated sphere. A plane harmonic compressive wave propagates in the system. The total scattering cross section  $Q_{\text{sca}}$  of the coated sphere can be expressed as:

$$Q_{\text{sca}} = \lambda_3^2 \sum_{n=0}^{\infty} \frac{1}{(2n+1)\pi} \left[ |a_n|^2 + n(n+1) \frac{\alpha_3}{\beta_3} |b_n|^2 \right], \quad (1)$$

where  $\alpha_3$  and  $\beta_3$  are propagation constants of longitudinal and transverse waves, respectively.  $\lambda_3 = 2\pi/\alpha_3$  is the wavelength of the compressive wave in the host medium,  $a_n$  and  $b_n$  are the unknown scattering coefficients of scattered waves. Here we consider the host material has a nontrivial shear modulus, the coated sphere will scatter both  $P$  and  $S$  waves due to the coupling mode effect. In the Rayleigh limit, we have derived the first three scattering coefficients based on the Mie theory as follows:

Case I: *Solid* shell and *Solid* host material

$$a_0 = i \frac{\kappa_{\text{eff}}^{\text{HS}} - \kappa_3}{3\kappa_{\text{eff}}^{\text{HS}} + 4\mu_3} (\alpha_3 r_2)^3, \quad a_1 = \frac{\rho_{\text{eff}}^{\text{M}} - \rho_3}{3\rho_3} (\alpha_3 r_2)^3, \quad a_2 = -\frac{20i\mu_3 (\mu_{\text{eff}}^{\text{HS}} - \mu_3) / 3}{6\mu_{\text{eff}}^{\text{HS}} (\kappa_3 + 2\mu_3) + \mu_3 (9\kappa_3 + 8\mu_3)} (\alpha_3 r_2)^3, \\ b_1 = -\frac{\rho_{\text{eff}}^{\text{M}} - \rho_3}{3\rho_3} \alpha_3 \beta_3^2 r_2^3, \quad b_2 = \frac{10i\mu_3 (\mu_{\text{eff}}^{\text{HS}} - \mu_3) / 3}{6\mu_{\text{eff}}^{\text{HS}} (\kappa_3 + 2\mu_3) + \mu_3 (9\kappa_3 + 8\mu_3)} (\beta_3 r_2)^3. \quad (2)$$

Case II: *Fluid* shell and *Solid* host material

$$a_0 = i \frac{\kappa_{\text{eff}}^{\text{HS}} - \kappa_3}{3\kappa_{\text{eff}}^{\text{HS}} + 4\mu_3} (\alpha_3 r_2)^3, \quad a_1 = \frac{\rho_{\text{eff}}^{\text{B}} - \rho_3}{3\rho_3} (\alpha_3 r_2)^3, \quad a_2 = \frac{20i\mu_3}{3(9\kappa_3 + 8\mu_3)} (\alpha_3 r_2)^3, \\ b_1 = -\frac{\rho_{\text{eff}}^{\text{B}} - \rho_3}{3\rho_3} \alpha_3 \beta_3^2 r_2^3, \quad b_2 = -\frac{10i\mu_3}{3(9\kappa_3 + 8\mu_3)} (\beta_3 r_2)^3. \quad (3)$$

Case III: *Solid* shell and *Fluid* host material

$$a_0 = i \frac{\kappa_{\text{eff}}^{\text{HS}} - \kappa_3}{3\kappa_{\text{eff}}^{\text{HS}}} (\alpha_3 r_2)^3, \quad a_1 = \frac{\rho_{\text{eff}}^{\text{M}} - \rho_3}{2\rho_{\text{eff}}^{\text{M}} + \rho_3} (\alpha_3 r_2)^3. \quad (4)$$

Case IV: *Fluid* shell and *Fluid* host material

$$a_0 = i \frac{\kappa_{\text{eff}}^{\text{HS}} - \kappa_3}{3\kappa_{\text{eff}}^{\text{HS}}} (\alpha_3 r_2)^3, \quad a_1 = \frac{\rho_{\text{eff}}^{\text{B}} - \rho_3}{2\rho_{\text{eff}}^{\text{B}} + \rho_3} (\alpha_3 r_2)^3. \quad (5)$$

In every case, the parameter  $b_0$  is not important and thus not given here.

The following parameters  $\kappa_{\text{eff}}^{\text{HS}}$ ,  $\mu_{\text{eff}}^{\text{HS}}$ ,  $\rho_{\text{eff}}^{\text{M}}$  and  $\rho_{\text{eff}}^{\text{B}}$  have been used, which are

$$\kappa_{\text{eff}}^{\text{HS}} / \kappa_2 = 1 + \frac{f(\kappa_1 - \kappa_2)}{\kappa_2 + (1-f)p(\kappa_1 - \kappa_2)}, \quad \mu_{\text{eff}}^{\text{HS}} / \mu_2 = 1 + \frac{f(\mu_1 - \mu_2)}{\mu_2 + (1-f)q(\mu_1 - \mu_2)}, \quad (6)$$

with  $p = \frac{3\kappa_2}{3\kappa_2 + 4\mu_2}$ ,  $q = \frac{6}{5} \frac{\kappa_2 + 2\mu_2}{3\kappa_2 + 4\mu_2}$ ,

$$\rho_{\text{eff}}^{\text{M}} / \rho_2 = 1 + f \frac{\rho_1 - \rho_2}{\rho_2}, \quad \rho_{\text{eff}}^{\text{B}} / \rho_2 = 1 + \frac{3f(\rho_1 - \rho_2)}{3\rho_2 + 2(1-f)(\rho_1 - \rho_2)}, \quad (7)$$

where  $f = (r_1/r_2)^3$ . For a composite filled with coated spheres that are randomly distributed in the host medium and have gradual sizes in order to fill the whole space,  $\kappa_{\text{eff}}^{\text{HS}}$  and  $\mu_{\text{eff}}^{\text{HS}}$  denote its effective bulk modulus and effective shear modulus calculated with the Hashin-Shtrikman (HS) bound [8].  $\rho_{\text{eff}}^{\text{M}}$  is the effective mass density obtained by the volume averaged method, whereas  $\rho_{\text{eff}}^{\text{B}}$  is the effective mass density calculated with Berryman's formula [9]. From Eqs. (2) ~ (5), we immediately get the transparency conditions  $\kappa_{\text{eff}} = \kappa_3$ ,  $\mu_{\text{eff}} = \mu_3$ , and  $\rho_{\text{eff}} = \rho_3$ , which are consistent with those obtained directly from the neutral inclusion concept.

As an example, we employ an acoustic metamaterial to cloak an aluminum sphere (with a radius  $r_1 = \lambda_3/5$ ) immersed in water. The cloaking metamaterial has the desirable material parameters  $\kappa_2 = 0.47\kappa_3$  and  $\rho_2 = 0.4\rho_3$ , which slightly differ from the target value  $\kappa_2 = 0.58\kappa_3$  and  $\rho_2 = 0.55\rho_3$  predicted by the transparency conditions. There is a shifting effect when the quasi-static condition is used to predict the dynamic phenomenon. Figures 2(a) and 2(b) present the near field contour plots of the radial component of the scattered displacement field for an uncoated aluminum sphere and that with an optimized cloak, respectively. It can be seen that a sphere without the metamaterial cover leads to a strong and nonuniform scattering field in the fluid matrix, especially in the region adjacent to the sphere. However, when the cloaking metamaterial is employed as the cover, the scattering is dramatically reduced whilst the field strength within the cloak is large.

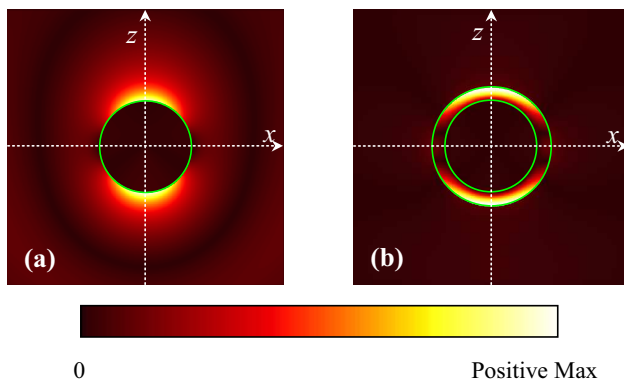


Figure 2: Contour plots of radial component of scattered displacement field for (a) uncoated aluminum sphere, and (b) same sphere with acoustic metamaterial.

#### 4. CONCLUSIONS

With help of neutral inclusion concept, we derive the quasi-static transparency conditions for a solid system. By investigating scattering properties of the composite sphere, we find that the effective bulk modulus, mass density, and shear modulus of the assemblage made of the coated spheres dominate the zero, the first and the second order scattering coefficients of one coated sphere, respectively. These results can be used to obtain the transparency conditions, which agrees with those given by neutral inclusion concept. Numerical results in dynamic case have been given to confirm the proposed conditions.

#### ACKNOWLEDGMENT

This work was supported by the National Natural Science Foundation of China under Grants No. 10325210, No. 90605001, and No. 10702006, and National Basic Research Program of China through Grant No. 2006CB601204.

#### REFERENCES

1. Alù, A. and N. Engheta, "Achieving transparency with plasmonic and metamaterial coatings," *Physical Review E*, Vol. 72, No. 1, 016623, 2005.
2. Zhou, X. M. and G. K. Hu, "Design for electromagnetic wave transparency with metamaterials," *Physical Review E*, Vol. 74, No. 2, 026607, 2006.
3. Alù, A. and N. Engheta, "Cloaking and transparency for collections of particles with metamaterial and plasmonic covers," *Optics Express*, Vol. 15, No. 12, 7578–7590, 2007.
4. Zhou, X. M. and G. K. Hu, "Acoustic wave transparency for a multilayered sphere with acoustic metamaterials," *Physical Review E*, Vol. 75, No. 4, 046606, 2007.

5. Liu, Z. Y., X. Zhang, Y. Mao, et al., “Locally sonic materials,” *Science*, Vol. 289, 1734–1736, 2000.
6. Fang, N., D. Xi, J. Xu, et al., “Ultrasonic metamaterials with negative modulus,” *Nat. Mater.*, Vol. 5, 452–456, 2006.
7. Milton, G. W., *The Theory of Composites*, Cambridge University Press, Cambridge, England, 2002.
8. Hashin, Z. and S. Shtrikman, “A variational approach to the theory of the elastic behavior of multiphase materials,” *J. Mech. Phys. Solids*, Vol. 11, 127–140, 1963.
9. Berryman, J. G., “Long-wavelength propagation in composite elastic media I spherical inclusions,” *J. Acoust. Soc. Am.*, Vol. 68, 1809–1819, 1980.

# Electromagnetic Smart Screen for Tunable Transmission and Reflection Applications

Lie Liu, Serguei Matitsine, and Peng Khiang Tan

Temasek Laboratories, National University of Singapore, Singapore

**Abstract**— Electromagnetic smart screen (ESS) containing conductive strip or patch array loaded with *pin* diodes was investigated with experimental approaches. Transmission and reflection coefficient were measured with free space method and validated by finite element simulation. Tunable transmission coefficient was found from ESS between 3 to 8 GHz which can be used as smart radome or modulator. Tunable reflection coefficient of a layer of ESS with thickness about 0.575 mm on top of metallic substrate is observed between 3 to 4 GHz. The effective working bandwidth can be up to 20% of the central frequency, which is much wider than metamaterials which are not tunable.

## 1. INTRODUCTION

In the past few years, electromagnetic metamaterials have attracted great attention [1]. The main reason lies in that metamaterials can provide certain electromagnetic properties which are not available in nature, such as negative refraction index and sub-wavelength diffraction, *etc* [2, 3]. However, the working frequency band of metamaterials is normally narrow. Depending on the design of the patterns, the relative applicable band width is normally not more than few percents. However, the broadband applications need to cover one to few frequency bands from 2 GHz to 18 GHz [4]. Metamaterials are not tunable or re-deployable as well. Once they are fabricated, the properties, such as working frequency and bandwidth, *etc*, cannot be modified to meet changes in operational requirement. It is therefore appealing to have smart or adaptive screens which are adjustable according to the incident signal. Controllable meta-film has been introduced recently to expand working frequency band [5, 6], which includes a surface with certain amount of electrical small scatterers, turned by bias magnetic fields. Controllable meta-films have the potential in the broadband applications because it overcomes the limitation of the normal meta-materials. However, as compared to electrical voltage or current, uniform magnetic field is more difficult to apply for large working area. Active frequency selective surface (FSS) loaded with *pin* diodes was integrated into a single microwave low reflection layer with reflectivity as a function of diode bias current [7]. As compared with conductive polymer with tunable properties, this type of material does not require high biasing voltage or large devices to achieve large tunability. Since the physics of *p-n* junction is fully understood, it is also easier to compensate for the environmental effect of diodes. Electrically tunable impedance surface with periodic surface texture loaded with varactor has been used to steer the reflected beam over  $+/- 40^\circ$  in two dimensions which has potential for transmission or reflection applications [8]. A reconfigurable beam steering reflector made of similar tunable impedance surface can be varied as a function of the relative position between two layers of circuit boards [9]. The limitation of mechanically tuned surface is that the respond of tuning may not be fast enough to meet the real requirements.

The first aim of this paper is to develop ESS of tunable dual-polarized transmission coefficient with conductive strip array loaded with *pin* diodes, which can be driven by extreme low voltage (few voltages). The second aim is to develop ESS of tunable reflection coefficient with square patch array also loaded with *pin* diodes. Both kind of ESS samples are fabricated with etching method from flexible PCB substrates before measured with free space method.

## 2. SAMPLE PREPARATION AND FREE SPACE MEASUREMENT

ESS was fabricated from a copper-coated flexible dielectric substrate, with total thickness of 75  $\mu\text{m}$ . The permittivity of the substrate was measured with Agilent 4991A material analyzer at 1 GHz. The measured permittivity is 3.5 and loss tangent is about 0.01. Since the permittivity of the flexible substrate is almost constant over the measurement range, the constant permittivity and dielectric loss are used in the simulation. The size of the sample is 20 cm by 20 cm. Surface mounting microwave diodes with working frequency from 1 to 6 GHz were soldered manually. The samples were driven with a portable variable power source, which has AA size batteries providing the biasing voltage up to few volts and enough current to switch on diodes. When the positive

voltage is applied to the diodes, it is switched on with a low  $R_j$ . When no bias voltage is applied, the diodes are switched off with an extremely high  $R_j$ . Fig. 1 shows the strip ESS with tunable transmission coefficient containing two layer of substrates separated by 5 mm Styrofoam spacer. All diodes are in parallel. Only 1 V bias voltage is needed to turn on this sample. The two-layer ESS can tune the transmission of incident wave with parallel and perpendicular polarization. Fig. 2 shows the patch ESS with tunable reflection coefficient. The substrate is back with a layer of Rogers 5880 substrate with thickness about 0.5 mm. The total thickness of patch ESS is 0.575 mm. As indicated in Fig. 2, 6 V bias voltage is needed to turn on the 6 *pin* diode linked in serial in each column.

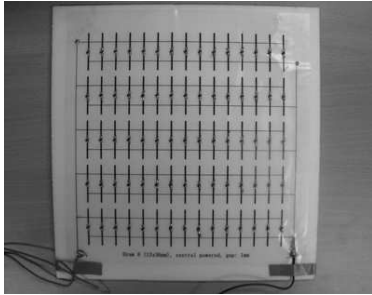


Figure 1: Strip ESS with tunable T.

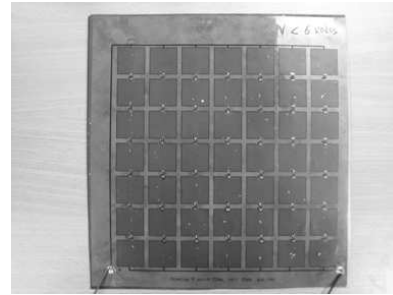


Figure 2: Patch ESS with tunable R.

The transmission or reflection coefficient was measured with the free space method [10]. The measurement setup includes a vector network analyzer, vertically mounted broadband transmitting and receiving electromagnetic horn antennas [10]. The working frequency range is from 2 to 18 GHz. To eliminate multiple scattering between the sample and the horns, time-domain gating was applied. Diffraction effects at the edges of the sample were minimized by attaching a high-quality ring-shaped wave absorber to the transmitting horn.

### 3. RESULTS AND DISCUSSIONS

To valid the free space measurement method, a commercial finite element code (HFSS<sup>TM</sup> v10) and infinite array model were used to simulate a unite element of the single layer strip ESS. Measured and computed transmission coefficients of single layer strip ESS are shown in Fig. 3, with the diodes switched on and off (solid lines and symbols for measured and simulated data, respectively). The resonance frequency is 6.5 GHz when diodes are switched off and 5.5 GHz when diodes are switched on. The transmission coefficient of the ESS is adjustable between 3 to 8 GHz. The difference in the transmission coefficient for the on and off states of the diodes can be taken as the tunability of the smart screen, which varies from 1 dB at 3 GHz to more than 20 dB at 6.5 GHz. Numerical results reasonably agree with measured data which confirm the accuracy of both measurement and simulation results.

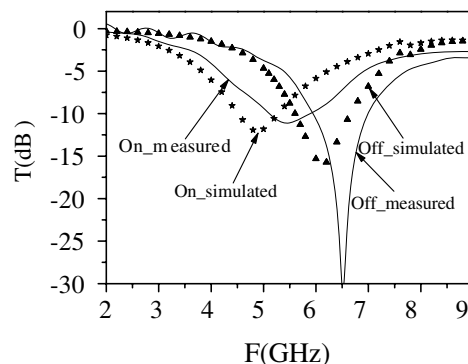


Figure 3: Measured and calculated transmission coefficient.

Numerical methods provide alternative way to optimize the design of the periodic pattern and parameters of diodes. The difference between the simulated and measured resonance frequencies can be mainly attributed to the circuit parameters of the diode in the simulation which is not accurate or frequency dependent within the broad band. Since the RLC values of equivalent circuit of the

diode were obtained at low frequency (1 MHz), more accurate parameters measured at working frequency may improve the simulation results. The details of numerical simulation method and model was discussed elsewhere [11] because it is not the main focus of this paper.

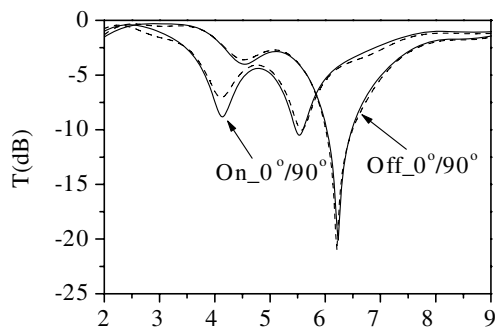


Figure 4: Measured T of strip ESS.

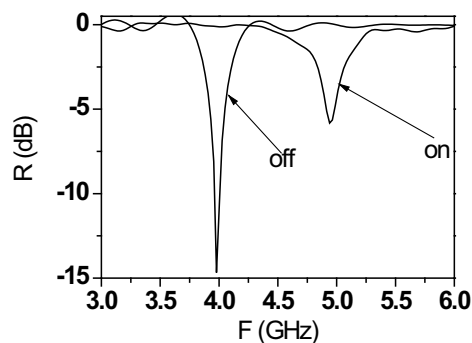


Figure 5: Measured R of patch ESS.

Figure 4 plots the measured transmission coefficient of dual-layer strip ESS with free space method. It is not surprising to find that the responds are almost identical when incident electrical field is in  $0^\circ$  (solid lines) and  $90^\circ$  (dotted lines) due to the symmetry of the sample in both directions. Hence, the dual-layer strip ESS can provide isotropic in-plane tunable transmission. In contrary, the single layer ESS can work for certain polarization only. As compared with the single layer, one more resonance peak for both on and off stage appears at low frequency (4 to 4.5 GHz) which is not found in Fig. 3. It may be attributed to the power lines of the other layer to provide the bias voltage (shown in Fig. 1) which are in parallel to the electrical field of incident wave. The low frequency peak becomes more pronounced when both layers of ESS are turn on, which can be explained by the modified equivalent circuit parameters of the screen by the *pin* diodes.

Figure 5 shows the measured reflection coefficient of patch ESS. When *pin* diodes are switched on, the resonance frequency of the patch shifts from 4 GHz to 5 GHz with attenuation reduced from 15 dB to about 7 dB. It is not impossible to continuously adjust the resonance peak within 1 GHz bandwidth provided the bias voltage and current can be precisely controlled from 0 to 6 V. However, the current power supply can only adjust the bias voltage in step. That is why the resonance peak in between on and off stage has not been captured by the free space measurement. The effective bandwidth of the patch ESS can be more than 20% of the central frequency supposed it can be adjusted continuously with the operation environment, which is much wider than normal metamaterials. If the thickness (less than 0.6 mm) and working frequency band (4 GHz to 5 GHz) are taken into consideration, the performance of patch ESS is much better than conventional iron or ferrite based anti-reflection composites. Anyhow, the loss mechanism of patch ESS could be quite different from conventional high loss EM composites which are either magnetic or dielectric. The superior performances of the artificial or Meta materials need to be explained by new physical mechanism which could be the next step of the ongoing research work.

#### 4. CONCLUSIONS

Electromagnetic smart screen were designed based on periodic strip and patch elements, fabricated from thin flexible high frequency substrate and measured using free space system. The measurement results were validated with finite element simulation. Strip ESS with in-plane isotropic tunable transmission coefficient was obtained which can be used as smart radome, subreflector or modulator. Patch ESS with tunable reflection coefficient has superior attenuation loss and effective working band width as compared with conventional anti-reflection materials.

#### ACKNOWLEDGMENT

The authors appreciate Dr. Moustafaev and other colleagues in ST Engineering for their helps in sample fabrication and free space measurement, Mr. Gan Yeow Beng for fruitful discussions. The research was supported by Defense Science and Technology Agency (DSTA), Singapore under Project No. POD0103671.

## REFERENCES

1. Caloz, C. and T. Itoh, *Electromagnetic Metamaterials: Transmission Line Theory and Microwave Applications*, Wiley-Interscience, John Wiley & Sons, 1–26, 2006.
2. Shelby, R. A., D. R. Smith, and S. Schultz, “Experimental verification of a negative index of refraction,” *Science*, Vol. 292, 77–79, 2001.
3. Pendry, J. B., “Negative refraction makes a perfect lens,” *Phys. Rev. Lett.*, Vol. 85, No. 18, 3966–3969, 2000.
4. Knott, E. F., J. F. Shaeffer, and M. T. Tuley, *Radar Cross Section*, Artech House, Inc., 1993.
5. Kuester, E. F., M. A. Mohamed, M. Piket-May, and C. L. Holloway, “Averaged transition conditions for electromagnetic fields at a metafilm,” *IEEE Trans. on Antenna and Propagation*, Vol. 51, No. 10, 2641–2651, 2003.
6. Holloway, C. L., M. A. Mohamed, E. F. Kuester, and A. Dienstfrey, “Reflection and transmission properties of a metafilm: With an application to a controllable surface composed of resonant particles,” *IEEE Trans. Electromag. Compat.*, Vol. 47, No. 4, 853–865, 2005.
7. Tennant, A. and B. Chambers, “A single-layer tuneable microwave absorber using an active FSS,” *IEEE Microwave and Wireless Components Letters*, Vol. 14, No. 1, 46, 2004.
8. Sievenpiper, D. F., J. H. Schaffner, H. J. Song, R. Y. Loo, and G. Tansonan, “Two-dimensional beam steering using an electrically tunable impedance surface,” *IEEE Trans. on Antenna and Propagation*, Vol. 51, No. 10, 2713–2722, 2003.
9. Sievenpiper, D. F., J. H. Schaffner, R. Y. Loo, G. Tansonan, S. Ontiveros, and R. Harold, “A tunable impedance surface performing as a reconfigurable beam steering reflector,” *IEEE Trans. on Antenna and Propagation*, Vol. 50, No. 3, 2002.
10. Liu, L., S. M. Matitsine, Y. B. Gan, and K. N. Rozanov, “Effective permittivity of planar composites with randomly or periodically distributed conducting fibers,” *J. of Appl. Phys.* 98, 063512, 2005.
11. Liu, L., S. Matitsine, P. K. Tan, and Y. B. Gan, “Smart frequency selective surface with conductive fiber array and diodes,” *Proceeding of Symposium P: Electromagnetic Materials, ICMAT2007*, World Scientific Publishing, 209–211, 2007.

# Enhancement of the Electronic Confinement Improves the Mobility in $p$ - $n$ - $p$ Delta-doped Quantum Wells in $Si$

A. David Ariza-Flores<sup>1</sup> and I. Rodriguez-Vargas<sup>2</sup>

<sup>1</sup>Facultad de Ciencias, Universidad Autónoma del Estado de Morelos  
Av. Universidad 1001, Col. Chamilpa, 62209 Cuernavaca, MOR., México

<sup>2</sup>Unidad Académica de Física, Universidad Autónoma de Zacatecas, Calzada Solidaridad Esquina con  
Paseo la Bufa S/N, 98060 Zacatecas, ZAC., México

**Abstract**— The electronic structure and mobility trends in a  $n$ -type delta-doped quantum well in  $Si$ , matched between  $p$ -type delta-doped barriers of the same material, is presented. The distance between the  $n$ -type well and  $p$ -type barriers is varied from 50 Å to 500 Å; and also the impurity density from  $5 \times 10^{12} \text{ cm}^{-2}$  to  $5 \times 10^{13} \text{ cm}^{-2}$ , for both, donors and acceptors. An increase in the mobility by a factor of 1.6 at interwell distance of 50 Å with donor and acceptor concentrations of  $5 \times 10^{12} \text{ cm}^{-2}$  and  $5 \times 10^{13} \text{ cm}^{-2}$  compared with a single delta-doped well without  $p$ -type barriers is found. This improvement in mobility could be attributed to a better confinement of carriers, which favors excited levels with nodes in the donor plane. This trade-off between carrier concentration and mobility could be exploited in high-speed, high-power and high-frequency applications.

## 1. INTRODUCTION

Carrier densities two-three orders of magnitude greater than those reported in  $GaAs$  systems can be achieved in Silicon systems by means of delta-doping [1]. So, the delta-doped quantum wells in  $Si$  are ideal structures to study the transport properties of ultradense two dimensional electron gases (2DEG) [2, 3] These works make emphasis in parameters such as the mobility, mean free path, and phase coherent length due to their implications in ballistic and coherent nanodevices. Meanwhile the carrier concentration in this kind of systems is ultra high, the mobility is very low, which is opposite to the behavior in  $GaAs/AlGaAs$  systems [4]. An improvement in the conductivity not properly the mobility could be reach via the coupling of delta-doped layers [5]. The main proposal relies in finding the interwell distance at which the mobility is maximum in conjunction with the high carrier density coming from the two delta-doped planes, such that the conductivity -the product of the mobility and the carrier density-enhances [6].

In the present paper we propose and study the implications of matching a  $n$ -type delta-doped quantum well in  $Si$  between  $p$ -type delta-doped barriers ( $pnDD$ ) of the same material. We analyzed the electronic structure and specially the mobility trends as a function of the interlayer distance and the impurity concentration. The Thomas-Fermi approximation and the effective mass theory are used in order to obtain the confining potential and the electron subband levels, respectively. Meanwhile the mobility calculations are performed via an empirical formula previously proposed and applied to  $n$ ,  $p$ , and  $p$ - $n$  delta-doped systems [5, 7, 8]. We find that the electron confinement plays an important role to optimize the mobility. We observed an increase of nearly 60% in the mobility at interwell distance of 50 Å and donor and acceptor concentrations of 5 and 50 in units of  $10^{12} \text{ cm}^{-2}$ .

## 2. MATHEMATICAL METHOD

For a single  $n$ -type  $\delta$ -doped quantum well in  $Si$  centered at  $z = a$  the confining potential can be written as [5],

$$V_{Hn}^*(z) - \mu_n^* = -\frac{\beta^2}{(\beta|z - a| + z_{0n})^4}, \quad (1)$$

with  $\beta = \frac{2}{15\pi}$  and  $z_{0n} = \left(\frac{\beta^3}{\pi n_{2D}^*}\right)^{1/5}$ .  $V_{Hn}^* = V_{Hn}/R_{yn}^*$  and  $\mu^* = \mu/R_{yn}^*$  are given in units of the effective Bohr radius and effective Rydberg,  $a_{0n}^* = \frac{\epsilon_r \hbar}{m^* e^2}$  and  $R_{yn}^* = \frac{e^2}{2\epsilon_r a_{0n}^*}$ .

In the case of a single  $p$ -type  $\delta$ -doped quantum well in  $Si$  centered at  $z = b$  the confining potential can be written as [9],

$$V_{Hp}^*(z) - \mu_p^* = \frac{\alpha^2}{(\alpha|z - b| + z_{0p})^4}, \quad (2)$$

with  $\alpha = \frac{2m_a^{3/2}}{15\pi}$  and  $z_{0p} = \left(\frac{\alpha^3}{\pi p_{2D}^{\alpha u}}\right)^{1/5}$ .  $V_{Hp}^* = V_{Hp}/R_{yp}^*$  and  $\mu_p^* = \mu/R_{yp}^*$  are given in units of the effective Bohr radius and effective Rydberg,  $a_{0p}^* = \frac{\epsilon_r \hbar}{m_h^* e^2}$  and  $R_{yp}^* = \frac{e^2}{2\epsilon_r a_{0p}^*}$ .

The next step is the construction of the  $pnpDD$  potential, so, if we consider the same impurity density in both  $p$ -type planes the system is symmetric with respect to the middle of the  $n$ -type one, then we can restrict ourselves to the half of the plane ( $z \leq 0$ ) and the potential can be written as

$$V_H^*(z) = -\frac{\beta^2}{(\beta|z| + z_{0n})^4} + \frac{\alpha^2}{(\alpha|z + l| + z_{0p})^4} \quad (3)$$

where  $a$  and  $b$  have been taken as 0 and  $l$ .

The latter equation summarizes the model for the conduction band bending profile. Instead of carrying out numerically troublesome self-consistent calculations, we simply solve Schrödinger-like effective mass equations at the zone center  $\mathbf{k} = \mathbf{0}$ , thus obtaining the corresponding subband longitudinal and transverse electron levels.

For the mobility calculations we implement an empirical formula previously proposed and applied to  $n$ ,  $p$  and  $p$ - $n$  delta-doped systems [5, 7, 8],

$$\mu_{rel}^{\delta} = \frac{\mu_{pnpDD}}{\mu_{SDD}} = \frac{\int \int \rho_e^{\delta}(z') \rho_{imp}^{\delta}(z) |z - z'| dz dz'}{\int \int \rho_e^{pnp\delta}(z') \rho_{imp}^{pnp\delta}(z) |z - z'| dz dz'}, \quad (4)$$

where  $\rho_e^{\delta}$  and  $\rho_{imp}^{\delta}$  ( $\rho_e^{pnp\delta}$  and  $\rho_{imp}^{pnp\delta}$ ) represent the density of electrons and impurities of  $SDD$  (of  $pnpDD$ ), respectively. Substituting the density of electrons and impurities and integrating over  $z$  we obtain,

$$\mu_{rel}^{\delta} = \frac{\sum_{ij} m_j \int |F_{ij}^{\delta}(z')|^2 (k_F^{\delta} - E_{ij}^{\delta}) |z'| dz'}{\sum_{ij} m_j \int |F_{ij}^{pnp\delta}(z')|^2 (k_F^{pnp\delta} - E_{ij}^{pnp\delta}) |z'| dz'}, \quad (5)$$

where  $F_{ij}^{\delta}(z')$ ,  $k_F^{\delta}$  and  $E_{ij}^{\delta}$  ( $F_{ij}^{pnp\delta}(z')$ ,  $k_F^{pnp\delta}$  and  $E_{ij}^{pnp\delta}$ ) are the envelope function, the Fermi level and the  $i$ th level respectively of the  $SDD$  (of  $pnpDD$ ).

### 3. RESULTS AND DISCUSSION

We have used standard parameters for  $n$ - and  $p$ -type Silicon [5, 10]. The donor and acceptor concentrations varies from  $1 \times 10^{12} \text{ cm}^{-2}$  to  $1 \times 10^{14} \text{ cm}^{-2}$ .

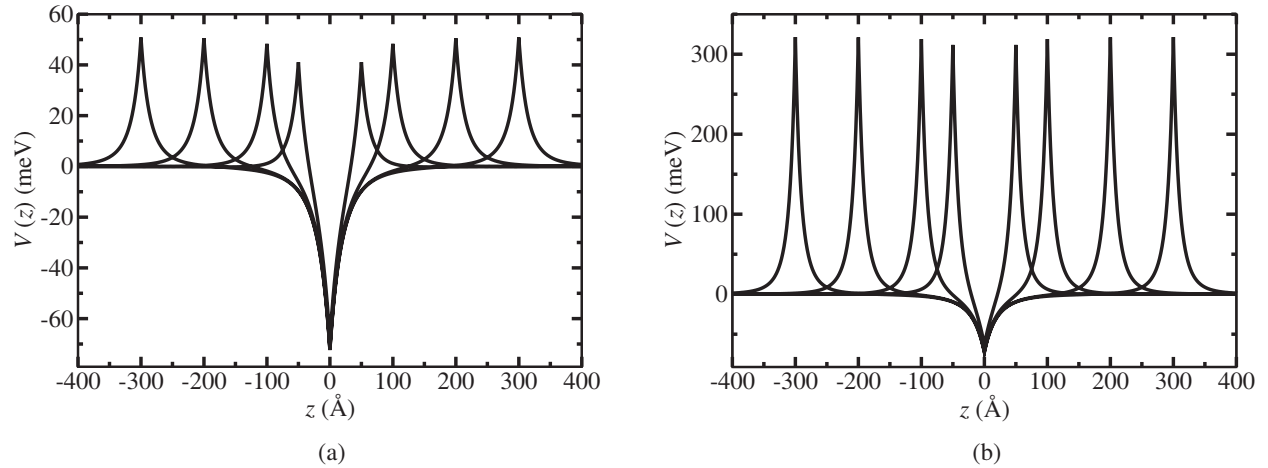


Figure 1: Potential profile of  $pnpDD$  QW's for different interwell distances. (a) and (b) corresponds to acceptor concentrations of 5 and 50 in units of  $10^{12} \text{ cm}^{-2}$ . The donor density is fixed at 5 in units of  $10^{12} \text{ cm}^{-2}$ .

In Fig. 1 we depict the potential profile of  $p$ - $n$ - $p$  delta doped quantum wells in  $Si$  for various distances with (a)  $n_{2D} = 5 \times 10^{12} \text{ cm}^{-2}$  and  $p_{2D} = 5 \times 10^{12} \text{ cm}^{-2}$  and (b)  $n_{2D} = 5 \times 10^{12} \text{ cm}^{-2}$  and

$p_{2D} = 5 \times 10^{13} \text{ cm}^{-2}$ . It is worth mentioning that in all calculations performed only the ground states for longitudinal and transverse electrons are occupied due to the multiple valley degeneracy present in  $n$ -type Silicon.

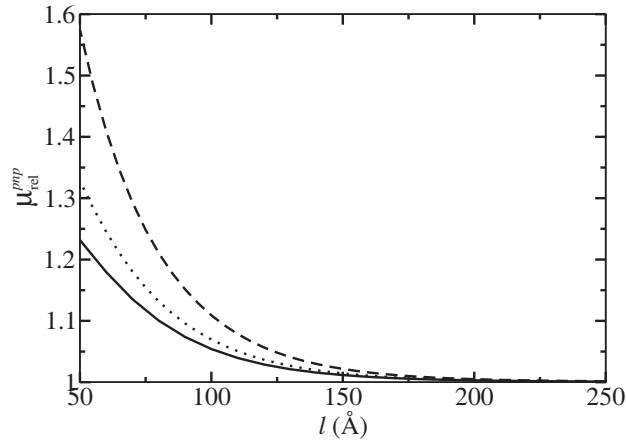


Figure 2: Relative mobility versus the distance between the  $n$ -type well and the  $p$ -type barriers. The donor density remains fix at  $5 \times 10^{12} \text{ cm}^{-2}$ , meanwhile the acceptor concentration takes three values 5 (solid), 10 (dot) and 50 (dash) in units of  $10^{12} \text{ cm}^{-2}$ .

In Fig. 2 we present the mobility of  $p$ - $n$ - $p$  delta doped quantum wells in  $Si$  versus the distance between the donor and acceptor planes. We have fixed the donor concentration at  $5 \times 10^{12} \text{ cm}^{-2}$ , and taken three values for the acceptor one,  $5 \times 10^{12} \text{ cm}^{-2}$ ,  $10 \times 10^{12} \text{ cm}^{-2}$  and  $50 \times 10^{12} \text{ cm}^{-2}$ , solid, dot and dash lines, respectively. There are two important trends in the mobility: (1) the monotonic decrease as the  $p$ -type barriers are separated from the  $n$ -type well and (2) an increase as the acceptor concentration is raised. We find an increase in the mobility of 23%, 32% and 60% at a interplane distance of  $50 \text{ \AA}$  for the three acceptor densities mentioned above. These results reflects that a more effective confinement of electrons could be used as a mechanism to improve the transport properties in delta-doped systems.

#### 4. CONCLUSION

In summary, we study the electronic subband structure and mobility trends of a  $n$ -type delta-doped quantum well in  $Si$  matched between  $p$ -type barriers of the same material. We have analyzed the effects of two paramount parameters in the system, the distance between the  $n$ -type well and the  $p$ -type barriers, and the impurity density in the donor and acceptor planes. We find a more effective confinement as the  $p$ -type barriers are closer to the  $n$ -type well, and we also observe the same effects as the acceptor concentration is raised, which is reflected in an improvement of the mobility of nearly 60%. So, the interplane distance and the impurity density could be used as natural tuning parameters to improve the transport properties in delta-doped systems via enhancement of the electron confinement.

#### ACKNOWLEDGMENT

This work was partially supported by Secretaría general de la UAZ and Consejo Zacatecano de Ciencia y Tecnología (COZCYT).

#### REFERENCES

1. Gossmann, H.-J. and F. C. Unterwald, "Dopant electrical activity and majority-carrier mobility in B- and Sb- $\delta$ -doped  $Si$  thin films," *Phys. Rev. B*, Vol. 47, No. 19, 12618–12624, 1993.
2. Zudov, M. A., C. L. Yang, R. R. Du, T.-C. Shen, J.-Y. Ji, J. S. Kline, and J. R. Tucker, "Weak localization in ultradense 2D electron gas in  $\delta$ -doped Silicon," *Cond-mat/0305482* (unpublished).
3. Goh, K. E. J., L. Oberbeck, M. Y. Simmons, A. R. Hamilton, and M. J. Butcher, "Influence of doping density on electronic transport in degenerate  $Si$ : P  $\delta$ -doped layers," *Phys. Rev. B*, Vol. 73, No. 3, 035401, 2006.

4. Ando, T., A. B. Fowler, and F. Stern, "Electronic properties of two-dimensional systems," *Rev. Mod. Phys.*, Vol. 54, No. 2, 437–672, 1982.
5. Rodriguez-Vargas, I. and L. M. Gaggero-Sager, "Subband and transport calculations in double  $n$ -type  $\delta$ -doped quantum wells in  $Si$ ," *J. Appl. Phys.*, Vol. 99, No. 3, 033702, 2006.
6. Gurtovoi, V. L., V. V. Valyaev, S. Yu Shapoval, and A. N. Pustovit, "Electron transport properties of double delta-doped  $GaAs$  structures grown by low-pressure metalorganic chemical vapor deposition," *Appl. Phys. Lett.*, Vol. 72, No. 10, 1202–1204, 1998.
7. Rodriguez-Vargas, I., L. M. Gaggero-Sager, and V. R. Velasco, "Thomas-Fermi-Dirac theory of the hole gas of a double  $p$ -type  $\delta$ -doped  $GaAs$  quantum wells," *Surf. Sci.*, Vol. 537, No. 1, 75–83, 2003.
8. Gaggero-Sager, L. M, N. Moreno-Martinez, I. Rodriguez-Vargas, R. Pérez-Alvarez, V. V. Grimalsky, and M. E. Mora-Ramos, "Electronic structure as a function of temperature for  $Si$   $\delta$ -doped quantum wells in  $GaAs$ ," *PIERS Online*, Vol. 3, No. 6, 851–854, 2007.
9. Gaggero-Sager, L. M, M. E. Mora-Ramos, and D. A. Contreras-Solorio, "Thomas-Fermi approximation in  $p$ -type  $\delta$ -doped quantum wells of  $GaAs$  and  $Si$ ," *Phys. Rev. B*, Vol. 57, No. 11, 6286–6289, 1998.
10. Rodriguez-Vargas, I. and L. M. Gaggero-Sager, "Hole-level structure of double  $\delta$ -doped quantum wells in  $Si$ : The influence of the split-off band," *Physica B*, Vol. 389, No. 2, 227–233, 2007.

# Electron Subband Structure and Mobility Trends in $p$ - $n$ Delta-doped Quantum Wells in $Si$

A. David Ariza-Flores<sup>1</sup> and I. Rodriguez-Vargas<sup>2</sup>

<sup>1</sup>Facultad de Ciencias, Universidad Autónoma del Estado de Morelos  
Av. Universidad 1001, Col. Chamilpa, 62209 Cuernavaca, MOR., México

<sup>2</sup>Unidad Académica de Física, Universidad Autónoma de Zacatecas, Calzada Solidaridad Esquina con  
Paseo la Bufa S/N, 98060 Zacatecas, ZAC., México

**Abstract**— We present the electronic spectrum of a  $n$ -type delta-doped quantum well in  $Si$  coupled to a  $p$ -type delta-doped barrier within the envelope function effective mass approximation. We applied the Thomas-Fermi approximation to derive an analytical expression for the confining potential, and thus, we obtain the electronic structure in a simple manner. We analyzed the electron subband structure varying the distance between the doping planes ( $l$ ) as well as the impurity density in them ( $n_{2D}$ ,  $p_{2D}$ ). We also study the mobility trends through an empirical formula that is based on the electron levels, the electron wave functions and the Fermi level. We find a monotonic decrease in the mobility as the  $p$ -type barrier moves away from the  $n$ -type well, and optimum parameters,  $l = 70 \text{ \AA}$  and  $n_{2D} = 5 \times 10^{12} \text{ cm}^{-2}$  and  $p_{2D} = 5 \times 10^{13} \text{ cm}^{-2}$ , for maximum mobility.

## 1. INTRODUCTION

Recently, the delta-doping has been used as a backbone technique to improve important characteristics, such as the linearity, in field effect transistor devices for application in millimeter-wave integrated circuits (MMIC) and wireless components [1–7]. The better performance of the mentioned devices relies on an improvement in the transport properties via optimization of the coupling between the delta layers and the heterostructure region.

In particular, high carrier densities, two-three orders of magnitude greater than in  $GaAs$  systems, can be achieved in Silicon systems by means of delta-doping [8]. Delta-doped quantum wells in  $Si$  are ideal structures to study the transport properties of ultra dense two dimensional electron gases (2DEG) [9, 10] Important parameters are the mobility, mean free path and phase coherent length due to their implications in ballistic and coherent nanodevices. Meanwhile the carrier concentration in this kind of systems is ultra high, the mobility is very low, which is opposite to what happen in  $GaAs/AlGaAs$  systems [11]. An improvement in the conductivity, not properly the mobility, could be reach via the coupling of delta-doped layers [12]. The main proposal relies in finding the interwell distance at which the mobility is maximum in conjunction with the high carrier density coming from the two doped planes, such that the conductivity -the product of the mobility and the carrier density-enhances [13].

The aim of the present study is to analyze the implications that represent a  $p$ -type delta-doped barrier near a  $n$ -type delta-doped quantum well in  $Si$ . The electronic structure and the mobility trends as a function of the interlayer distance and the impurity concentration are obtained. The Thomas-Fermi approximation and the effective mass theory are combined to obtain the confining potential and the electron subband levels. The mobility calculations are performed via an empirical formula previously proposed and applied to  $n$ ,  $p$ , and  $p$ - $n$  delta-doped systems [12, 14, 15]. We find that the electron confinement plays an important role to improve the mobility. We obtain an optimization in the mobility at interwell distance of  $70 \text{ \AA}$  and donor and acceptor concentrations of 5 and 50 in units of  $10^{12} \text{ cm}^{-2}$ .

## 2. MATHEMATICAL METHOD

For a single  $n$ -type  $\delta$ -doped quantum well in  $Si$  centered at  $z = a$  the confining potential can be written as [12],

$$V_{Hn}^*(z) - \mu_n^* = -\frac{\beta^2}{(\beta|z - a| + z_{0n})^4}, \quad (1)$$

with  $\beta = \frac{2}{15\pi}$  and  $z_{0n} = \left(\frac{\beta^3}{\pi n_{2D}^* a_{0n}^*}\right)^{1/5}$ .  $V_{Hn}^* = V_{Hn}/R_{yn}^*$  and  $\mu^* = \mu/R_{yn}^*$  are given in units of the effective Bohr radius and effective Rydberg,  $a_{0n}^* = \frac{\epsilon_r \hbar}{m^* e^2}$  and  $R_{yn}^* = \frac{e^2}{2\epsilon_r a_{0n}^*}$ .

In the case of a single  $p$ -type  $\delta$ -doped quantum well in  $Si$  centered at  $z = b$  the confining potential can be written as [16],

$$V_{Hp}^*(z) - \mu_p^* = \frac{\alpha^2}{(\alpha|z - b| + z_0)^4}, \quad (2)$$

with  $\alpha = \frac{2m_a^{3/2}}{15\pi}$  and  $z_{0p} = \left(\frac{\alpha^3}{\pi p_{2D}^*}\right)^{1/5}$ .  $V_{Hp}^* = V_{Hp}/R_{yp}^*$  and  $\mu_p^* = \mu/R_{yp}^*$  are given in units of the effective Bohr radius and effective Rydberg,  $a_{0p}^* = \frac{\epsilon_r \hbar}{m_{ih}^* e^2}$  and  $R_{yp}^* = \frac{e^2}{2\epsilon_r a_{0p}^*}$ .

The next step is the construction of the  $p$ - $n$  delta-doped ( $pnDD$ ) potential well through a proper combination of the potentials for electrons and holes

$$V_H^*(z) = -\frac{\beta^2}{(\beta|z| + z_{0n})^4} + \frac{\alpha^2}{(\alpha|z + l| + z_0)^4} \quad (3)$$

where  $a$  and  $b$  have been taken as 0 and  $l$ .

The latter equation summarizes the model for the conduction band bending profile. Instead of carrying out numerically troublesome self-consistent calculations, we simply solve Schrödinger-like effective mass equations at the zone center  $\mathbf{k} = \mathbf{0}$ , thus obtaining the corresponding subband longitudinal and transverse electron levels.

For the mobility calculations we implement an empirical formula previously proposed and applied to  $n$ ,  $p$  and  $p$ - $n$  delta-doped systems [12, 14, 15],

$$\mu_{rel}^\delta = \frac{\mu_{pnDD}}{\mu_{SDD}} = \frac{\int \int \rho_e^\delta(z') \rho_{imp}^\delta(z) |z - z'| dz dz'}{\int \int \rho_e^{pn\delta}(z') \rho_{imp}^{pn\delta}(z) |z - z'| dz dz'}, \quad (4)$$

where  $\rho_e^\delta$  and  $\rho_{imp}^\delta$  ( $\rho_e^{pn\delta}$  and  $\rho_{imp}^{pn\delta}$ ) represent the density of electrons and impurities of  $SDD$  (of  $pnDD$ ), respectively. Substituting the density of electrons and impurities and integrating over  $z$  we obtain,

$$\mu_{rel}^\delta = \frac{\sum_{ij} m_j \int |F_{ij}^\delta(z')|^2 (k_F^\delta - E_{ij}^\delta) |z'| dz'}{\sum_{ij} m_j \int |F_{ij}^{pn\delta}(z')|^2 (k_F^{pn\delta} - E_{ij}^{pn\delta}) |z'| dz'}, \quad (5)$$

where  $F_{ij}^\delta(z')$ ,  $k_F^\delta$  and  $E_{ij}^\delta$  ( $F_{ij}^{pn\delta}(z')$ ,  $k_F^{pn\delta}$  and  $E_{ij}^{pn\delta}$ ) are the envelope function, the Fermi level and the  $i$ th level respectively of the  $SDD$  (of  $pnDD$ ).

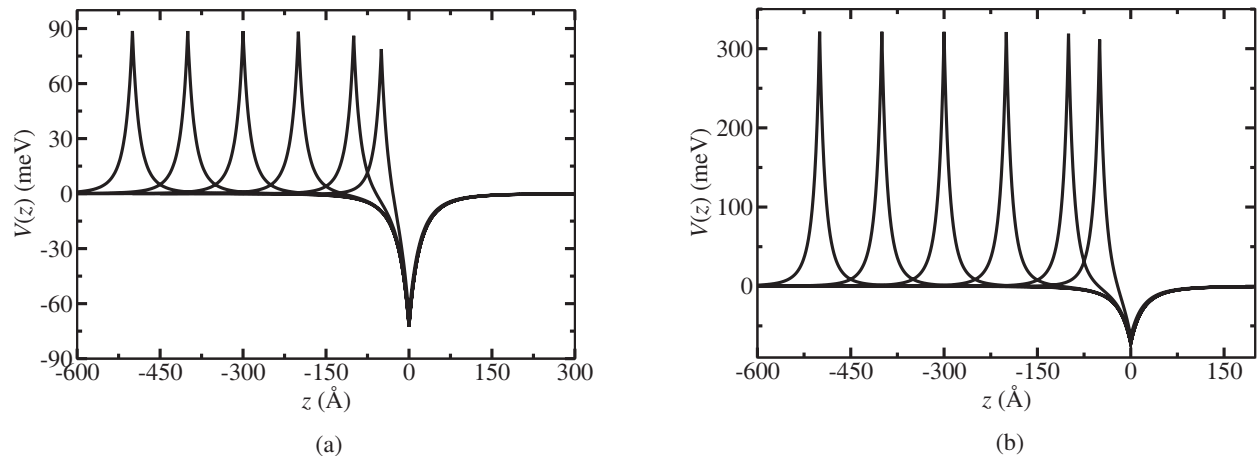


Figure 1: Potential profile of  $p$ - $n$  delta-doped quantum wells for different interwell distances with: (a)  $n_{2D} = 5 \times 10^{12}$  and  $p_{2D} = 1 \times 10^{13} \text{ cm}^{-2}$ , (b)  $n_{2D} = 5 \times 10^{12}$  and  $p_{2D} = 5 \times 10^{13} \text{ cm}^{-2}$ .

### 3. RESULTS AND DISCUSSION

We have found the potential and electronic mobility of a  $p$ - $n$  delta-doped quantum wells in  $Si$ . The donor and acceptor concentrations goes from  $5 \times 10^{12} \text{ cm}^{-2}$  to  $5 \times 10^{13} \text{ cm}^{-2}$ .

In Fig. 1 we present the  $p$ - $n$  potential profile for various interwell distances, from 500 to 50 Å. We can see that there is a small decrement in the altitude of the  $p$ -type well for 100 and 50 Å and a reduced wide in  $n$ -type well, because of the recombination. But in these distances still persist a good confinement of electrons and holes densities. Fig. 2 sketches the mobility, for three concentrations in the  $p$ -type delta-doped barrier remaining fix the donor concentration, as function of the  $p$ - $n$  separation. We found a monotonic growth in the mobility as the  $p$ - $n$  distance decrease. The best improvement in mobility was found in 70 Å interwell distance with donor and acceptor concentrations of  $5 \times 10^{12}$  and  $5 \times 10^{13} \text{ cm}^{-2}$ . The improvement in mobility is attributed to a good confinement of electron densities, so this is a way to enhance the transport properties in  $p$ - $n$  delta-doped quantum wells in  $Si$ .

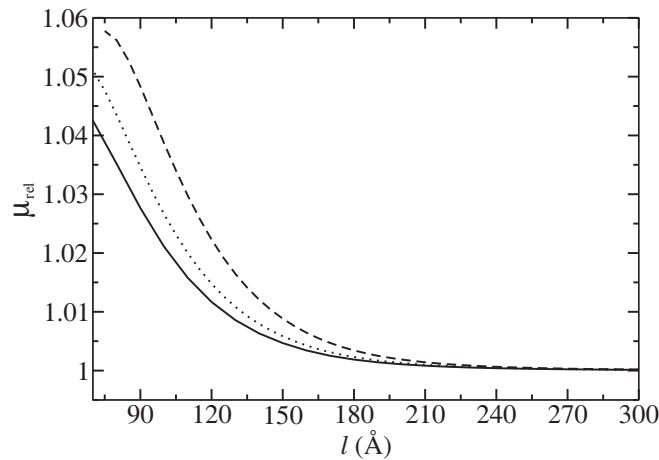


Figure 2: Relative mobility versus the distance between the  $n$ -type well and the  $p$ -type barrier. The donor density remains fix at  $5 \times 10^{12} \text{ cm}^{-2}$ , meanwhile the acceptor concentration takes three values 5 (solid), 10 (dot) and 50 (dash) in units of  $10^{12} \text{ cm}^{-2}$ .

### 4. CONCLUSION

In summary, we study the effects that produces a  $p$ -type barrier near a  $n$ -type delta-doped quantum well in  $Si$ . The Thomas-Fermi theory combined to the effective mass approximation are used for the electron level calculations. An empirical formula is implemented for the mobility-trend analysis. The electronic structure and mobility trends are analysed as a function of the backbone parameters in the system, interlayer distance and impurity density. We find that the electronic confinement plays an important role to optimize the mobility. We obtain an optimization in the mobility at interwell distance of 70 Å and donor and acceptor concentrations of 5 and 50 in units of  $10^{12} \text{ cm}^{-2}$ .

### ACKNOWLEDGMENT

This work was partially supported by Secretaría General de la UAZ and Consejo Zacatecano de Ciencia y Tecnología (COZCYT).

### REFERENCES

1. Huang, D.-H., W.-C. Hsu, Y.-S. Lin, J.-H. Yeh, and J.-C. Huang, "A metamorphic heterostructure field-effect transistor with a double delta-doped channel," *Semicond. Sci. Technol.*, Vol. 22, No. 7, 784–787, 2007.
2. Lee, C.-S., C.-H. Chen, J.-C. Huang, and K.-H. Su, "Comparative studies on double  $\delta$ -doped  $Al_{0.3}Ga_{0.7}As/In_xGa_{1-x}As/GaAs$  symmetrically graded doped-channel field-effect transistors," *J. Electrochem. Soc.*, Vol. 154, No. 5, H374–H379, 2007.
3. Chu, L.-H., H.-T. Hsu, E.-Y. Chang, T.-L. Lee, S.-H. Chen, Y.-C. Lien, and C.-Y. Chang, "Double  $\delta$ -doped enhancement-mode  $InGaP/AlGaAs/InGaAs$  pseudomorphic high electron mobility transistor for linearity application," *Jpn. J. Appl. Phys.*, Vol. 45, No. 35, L932–L934, 2006.

4. Lee, C.-Y., H.-P. Shiao, K.-C. Kuo, H.-Y. Wu, and W.-H. Lin “Mobility and charge density tuning in double  $\delta$ -doped pseudomorphic high-electron-mobility transistors grown by metal organic chemical vapor deposition,” *J. Vac. Sci. Technol. B*, Vol. 24, No. 6, 2597–2600, 2006.
5. Lin, Y.-S., D.-H. Huang, W.-C. Hsu, T. B. Wang, K. H. Su, J.-C. Huang, and C. H. Ho, “Improved *InAlGaP*-based heterostructure field-effect transistors,” *Semicond. Sci. Technol.*, Vol. 21, No. 4, 540–543, 2006.
6. Kalna, K., Q. Wang, M. Passlack, and A. Asenov, “Monte Carlo simulations of  $\delta$ -doping placement in sub-100 nm implant free *InGaAs* MOSFETs,” *Mater. Sci. Eng. B*, Vol. 135, No. 3, 285–288, 2006.
7. Saidi, I., L. Bouzaïene, M. H. Gazzah, H. Mejri, and H. Maaref, “Back doping design in delta-doped *AlGaIn/GaN* heterostructure field-effect transistors,” *Solid State Commun.*, Vol. 140, No. 6, 308–312, 2006.
8. Gossmann, H.-J. and F. C. Unterwald, “Dopant electrical activity and majority-carrier mobility in B- and Sb- $\delta$ -doped Si thin films,” *Phys. Rev. B*, Vol. 47, No. 19, 12618–12624, 1993.
9. Zudov, M. A., C. L. Yang, R. R. Du, T.-C. Shen, J.-Y. Ji, J. S. Kline, and J. R. Tucker, “Weak localization in ultradense 2D electron gas in  $\delta$ -doped Silicon,” *Cond-mat/0305482* (unpublished).
10. Goh, K. E. J., L. Oberbeck, M. Y. Simmons, A. R. Hamilton, and M. J. Butcher, “Influence of doping density on electronic transport in degenerate *Si*: P  $\delta$ -doped layers,” *Phys. Rev. B*, Vol. 73, No. 3, 035401, 2006.
11. Ando, T., A. B. Fowler, and F. Stern, “Electronic properties of two-dimensional systems,” *Rev. Mod. Phys.*, Vol. 54, No. 2, 437–672, 1982.
12. Rodriguez-Vargas, I. and L. M. Gaggero-Sager, “Subband and transport calculations in double *n*-type  $\delta$ -doped quantum wells in *Si*,” *J. Appl. Phys.*, Vol. 99, No. 3, 033702, 2006.
13. Gurtovoi, V. L., V. V. Valyaev, S. Yu Shapoval, and A. N. Pustovit, “Electron transport properties of double delta-doped *GaAs* structures grown by low-pressure metalorganic chemical vapor deposition,” *Appl. Phys. Lett.*, Vol. 72, No. 10, 1202–1204, 1998.
14. Rodriguez-Vargas, I., L. M. Gaggero-Sager, and V. R. Velasco, “Thomas-Fermi-Dirac theory of the hole gas of a double *p*-type  $\delta$ -doped *GaAs* quantum wells,” *Surf. Sci.*, Vol. 537, No. 1, 75–83, 2003.
15. Gaggero-Sager, L. M., N. Moreno-Martinez, I. Rodriguez-Vargas, R. Pérez-Alvarez, V. V. Grimalsky, and M. E. Mora-Ramos, “Electronic structure as a function of temperature for *Si*  $\delta$ -doped quantum wells in *GaAs*,” *PIERS Online*, Vol. 3, No. 6, 851–854, 2007.
16. Gaggero-Sager, L. M., M. E. Mora-Ramos, and D. A. Contreras-Solorio, “Thomas-Fermi approximation in *p*-type  $\delta$ -doped quantum wells of *GaAs* and *Si*,” *Phys. Rev. B*, Vol. 57, No. 11, 6286–6289, 1998.
17. Rodriguez-Vargas, I. and L. M. Gaggero-Sager, “Hole-level structure of double  $\delta$ -doped quantum wells in *Si*: The influence of the split-off band,” *Physica B*, Vol. 389, No. 2, 227–233, 2007.

# Stark Effect in p-type Delta-doped Quantum Wells

A. M. Miteva<sup>1</sup>, S. J. Vlaev<sup>2,4</sup>, and V. Donchev<sup>3</sup>

<sup>1</sup>Space Research Institute, Bulgarian Academy of Sciences, Moskovska Str. 6, Sofia 1000, Bulgaria

<sup>2</sup>Unidad Academica de Fisica, Universidad Autonoma de Zacatecas  
Calzada Solidaridad Esquina con Paseo la Bufa, Zacatecas 98060, Zac., Mexico

<sup>3</sup>Department of Condensed Matter Physics, Faculty of Physics, Sofia University  
blvd. James Bourchier 5, 1164-Sofia, Bulgaria

<sup>4</sup>Facultad de Ciencias, Universidad Autonoma del Estado de Morelos  
Av. Universidad 1001, Col. Chamilpa, Cuernavaca 62210, MOR., Mexico

**Abstract**— In this work tight binding calculations in Be  $\delta$ -doped GaAs quantum wells with an electric field applied along the [001] growth direction are presented. The Stark shifts of the hole electronic states for different impurity concentrations and electric field strengths are calculated. The  $\delta$ -potential is treated as an external potential following the approach described earlier. A comparison with Stark effects in rectangular and graded-gap quantum wells is made.

## 1. INTRODUCTION

For over a decade the properties of single and multiple  $\delta$ -doped GaAs structures have been extensively studied both theoretically and experimentally [1–8]. The planar doping is used in devices to give rise to quantum confinement of carriers. For understanding the operating principles of these devices it is necessary to study the effect of the external constant electric field on the intersubband transitions [9], i.e., quantum confined Stark effect (QCSE).

The purpose of this paper is to describe the QCSE in p-type Be  $\delta$ -doped GaAs quantum wells (QWs). The calculations are conducted by using the empirical tight binding (TB) method. Similar TB calculations have been already performed to treat electric field effects on the electronic and optical properties of various nanostructured materials [10–12]. To the best of our knowledge, there are no TB calculations of the Stark effect in Be  $\delta$ -doped GaAs systems. The Stark effect in these systems have been studied mainly in the effective mass approximation [1–4, 6, 7].

## 2. MODEL AND METHOD

Numerical calculations of hole energy states and their spatial distributions are presented. We consider Be  $\delta$ -doped GaAs QW with two-dimensional impurity concentration  $p_{2D}$  from  $2 \times 10^{12}$  to  $10 \times 10^{12} \text{ cm}^{-2}$  with a step of  $1 \times 10^{12} \text{ cm}^{-2}$  and from  $10 \times 10^{12}$  to  $90 \times 10^{12} \text{ cm}^{-2}$  with a step of  $10 \times 10^{12} \text{ cm}^{-2}$ . The width of the inhomogeneous Be  $\delta$ -doped finite region (the genuine V-shaped  $\delta$ -doped QW) is 250 monolayers (MLs) and it is matched with two semi-infinite homogeneous GaAs barriers. We use the  $sp^3s^*$  spin dependent semi-empirical TB model and the surface Green function matching method [13]. The calculations are performed at the center of the 2D Brillouin zone for the GaAs [001] growth direction. The  $\delta$ -potential is treated as an external potential in the Thomas-Fermi approximation [5, 8]. The external constant electric field  $F$  is applied to the QW in the growth direction. We add the effect of  $F$  as a second external potential to all diagonal elements of the Hamiltonian matrix in each atomic layer  $n$  [11, 12]. The external potential is zero outside the QW. The TB parameters determined in [14] are used. The calculations are made in the low temperature limit. The electric field value has been varied from 0 kV/cm to  $-25 \text{ kV/cm}$  with a 1 kV/cm step. The zero value of the energy is at the top of the bulk GaAs valence band.

## 3. RESULTS AND DISCUSSION

We present here only the results for the negative electric fields. Such electric field direction moves up the right side of the  $\delta$ -doped GaAs QW edge. Fig. 1 represents the effective confining Be  $\delta$ -potential profile of the QW for acceptor concentration  $p_{2D} = 5 \times 10^{12} \text{ cm}^{-2}$  and for different applied electric fields. The  $\delta$ -potential is deeper for larger acceptor concentrations.

At a given  $F$  value, which depends on  $p_{2D}$  a secondary QW appears on the right side of the  $\delta$ -doped QW. That value of  $F$  depends on  $p_{2D}$  as follows:  $p_{2D} = 2$ ,  $F = -1$ ;  $p_{2D} = 20$ ,  $F = -2$ ;  $p_{2D} = 50$ ,  $F = -6$ ;  $p_{2D} = 90$ ,  $F = -17$ . With increasing  $F$  the  $\delta$ -doped QW becomes narrower and shallower, while the secondary QW gets wider and deeper. As a result the bound states

spatial distributions increasingly penetrate in the secondary well. After a given  $F$  value the system represents an asymmetric double QW with corresponding bound states. In this paper we consider only the hole energies which are not influenced by the presence of this secondary QW.

Figure 2 shows the energies of the heavy hole ground (hh0) and first excited (hh1) states and of the light hole ground state (lh0) calculated for four different two-dimensional Be concentrations  $p_{2D}$  (20, 40, 70 and 90) versus the electric field intensity. Here and further the impurity concentration  $p_{2D}$  is given in units  $10^{12} \text{ cm}^{-2}$ . The electric field effects on the hole energy levels are similar for all impurity concentrations. With increasing  $F$  the hole energies increase. These dependencies are almost linear, but their slopes are different. The changes in the hole energies with  $F$  are more pronounced for the ground states hh0 and lh0 (a, b), than for the next heavy hole level hh1 (c).

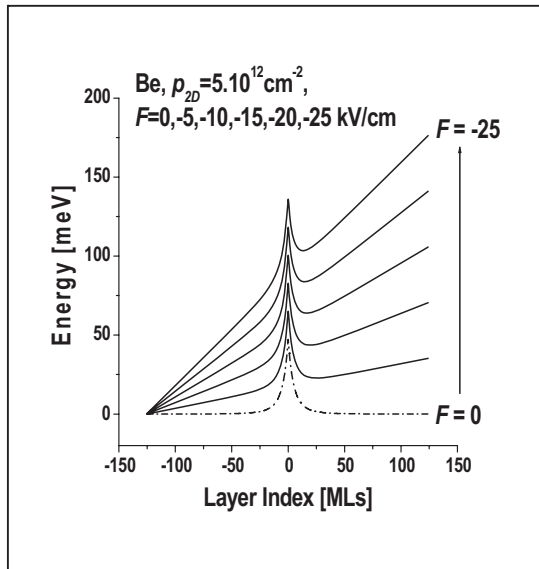


Figure 1: The effective Be  $\delta$ -potential profile for  $p_{2D} = 5.10^{12} \text{ cm}^{-2}$  at zero electric field (dot line) and under the applied electric fields  $F = -5, -10, -15, -20$  and  $-25 \text{ kV/cm}$  from bottom to the top (full curves).

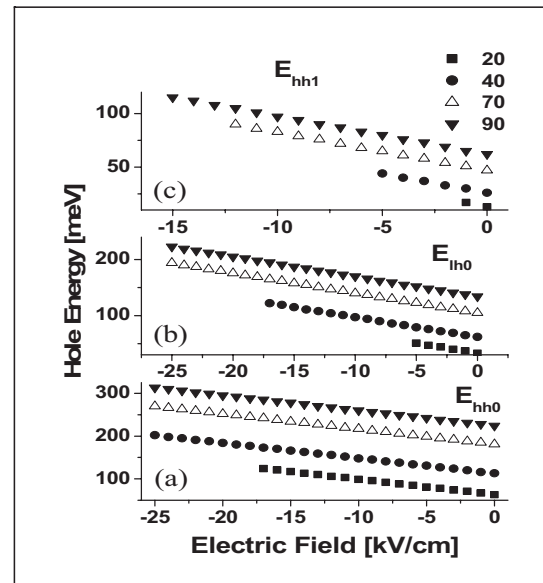


Figure 2: The dependence of the hole energy levels  $E_{hh0}$  (a),  $E_{lh0}$  (b) and  $E_{hh1}$  (c) on the applied electric field intensity as a function of the acceptor concentration  $p_{2D}$ , for a p-type Be  $\delta$ -doped GaAs QW. The acceptor concentrations in units  $10^{12} \text{ cm}^{-2}$  are  $p_{2D} = 20$  (rectangles),  $p_{2D} = 40$  (circles),  $p_{2D} = 70$  (open triangles),  $p_{2D} = 90$  (full triangles).

Figure 3 shows the probability density spatial distributions of some hole states at given values of the acceptor concentration  $p_{2D}$  and of the applied electric field  $F$ , as indicated on the figure. At zero field all spatial distributions are symmetrically situated around the center of the QW. With increasing  $F$  the states get slightly displaced from the center to the right. The influence of  $F$  on spatial distributions is more pronounced for smaller acceptor concentrations. For example the displacement of the lh0 distribution is well seen for  $p_{2D} < 10$  but it is less pronounced for larger  $p_{2D}$  (compare Fig. 3(a) and (c)). At  $p_{2D} > 40$  even high  $F$  values do not result in substantial displacement of the hh0, lh0 and hh1 distributions. (see Fig. 3(b) and (c)).

Figure 4(a), (b) and (c) displays the electric field dependence of the intersubband transition energies  $E_{hh0}-E_{lh0}$  and  $E_{hh0}-E_{hh1}$ , respectively for three different acceptor concentrations:  $p_{2D} = 10$ ,  $p_{2D} = 20$  and  $p_{2D} = 90$ . Two interesting features are observed. First, with increasing  $p_{2D}$  the (hh0–lh0) transition energy increases. Second, the transition energies do not depend on the applied  $F$ . The dependence shows some fluctuations but they are not greater than 1 meV and can be due to calculation errors.

Comparing the present study with our previously obtained results for rectangular and graded-gap QWs [11, 12], we can say that the most important points are the following ones: (1) the hole energies depend on the Be concentration and the applied electric field; (2) the transition energies between hole states depend on the Be concentration, however they show practically zero Stark shift; (3) The spatial overlap between the states is significant at low  $F$  and in general it is larger compared to that in the rectangular and the graded-gap QWs from [11, 12].

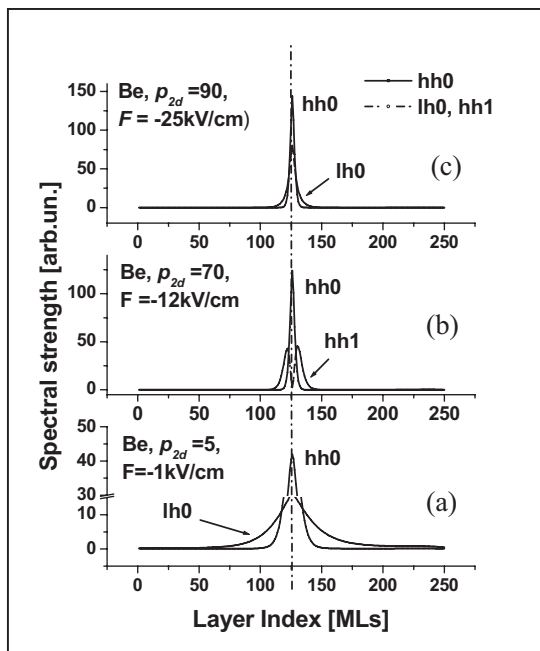


Figure 3: Spectral strength spatial distributions of the hole states hh0 (solid lines) and lh0 and hh1 (dot lines) as a function of the acceptor concentration  $p_{2D}$  and of the applied electric field  $F$ , for a Be  $\delta$ -doped GaAs QW. (a)  $p_{2D} = 5$ , (b)  $p_{2D} = 70$ , (c)  $p_{2D} = 90$ .

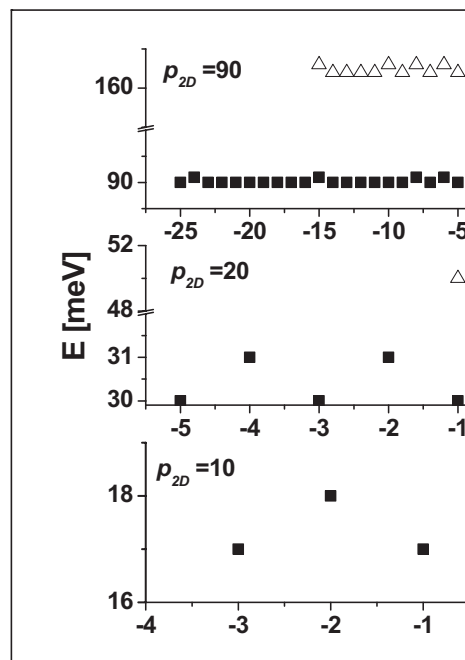


Figure 4: The dependence of the transition energy  $\Delta E$  in meV between the hole states hh0–lh0 (squares), and hh0–hh1 (triangles) on the applied electric field  $F$  as a function of  $p_{2D}$  (in units  $10^{12} \text{ cm}^{-2}$ ) for the QW under study. (a)  $p_{2D} = 10$ , (b)  $p_{2D} = 20$ , (c)  $p_{2D} = 90$ .

#### 4. CONCLUSIONS

The first TB calculation of the QCSE in Be  $\delta$ -doped GaAs QWs is presented. We have studied in details the Stark shifts of the hole states and their spatial distributions, the subband spectra and intersubband transitions of holes. The results give insight into the physics of the  $\delta$ -doping QWs with different impurity densities subjected to an electric field with different magnitudes. Such investigations are very promising in looking for  $\delta$ -doped structures for potential applications in devices based on the hole intersubband and intrasubband transitions e.g., photodetectors and optical modulators. The results demonstrate that the TB method can be used to investigate the Stark effect in a double asymmetric QW system, which is interesting for coherent intraband radiation applications.

#### ACKNOWLEDGMENT

The financial support through the project UAZ-2007-35592 is appreciated. This work was also supported by the Bulgarian National Science Fund (contract No. D01-463/12.07.06).

#### REFERENCES

1. Wagner, J., A. Ruiz, and K. Ploog, "Fermi-edge singularity and band-filling effects in the luminescence spectrum of Be- $\delta$ -doped GaAs," *Phys. Rev. B*, Vol. 43, 12134–7, 1991.
2. Richards, D., J. Wagner, H. Schneider, G. Hendorfer, and M. Maier, "Two-dimensional hole gas and Fermi-edge singularity in Be  $\delta$ -doped GaAs," *Phys. Rev. B*, Vol. 47, 9629–40, 1993.
3. Sipahi, G. M., R. Enderlein, L. M. R. Scolfaro, and J. R. Leite, "Band structure of holes in p-type  $\delta$ -doping quantum wells and superlattices," *Phys. Rev. B*, Vol. 53, 9930–42, 1996.
4. Ben Jazia, A., H. Mejri, H. Maaref, and K. Souissi, "Stark effect studied in  $\delta$ -doped GaAs structures," *Semicond. Sci. Technol.*, Vol. 12, 1388–95, 1997.
5. Vlaev, S. and L. M. Gaggero Sager, "Thomas-Fermi approximation in a tight-binding calculation of  $\delta$ -doped quantum wells in GaAs," *Phys. Rev. B*, Vol. 58, 1142–5, 1998.
6. Ozturk, E. and I. Sokmen, "Intersubband optical absorption in Si  $\delta$ -doped GaAs for the donor distribution and thickness as dependent on the applied electric field," *EPJ Appl. Phys.*, Vol. 25, 3–9, 2004.

7. Osvald, J., "Electronic properties of a near surface Si  $\delta$ -doped GaAs under an applied electric field," *J. Phys. D: Appl. Phys.*, Vol. 37, 2655–9, 2004.
8. Gaggero-Sager, L. M., M. E. Mora-Ramos, and M. A. Olivares-Robles, "Calculation of electronic properties in  $\text{Al}_x\text{Ga}_{1-x}\text{As}$  delta-doped systems," *Microelectronics J.*, Vol. 36, 416–8, 2005.
9. Singh, J., *Physics of Semiconductors and Heterostructures*, McGraw-Hill Book Co., Inc., Singapore, 1993.
10. Di Carlo, A., P. Vogl, and W. Pötz, "Theory of Zener tunneling and Wannier-Stark states in semiconductors," *Phys. Rev. B*, Vol. 50, 8358–77, 1994.
11. Vlaev, S. J., A. M. Miteva, D. A. Contreras-Solorio, and V. R. Velasco, "Stark effect in rectangular and graded gap quantum wells," *Surf. Sci.*, Vol. 424, 331–8, 1999.
12. Vlaev, S. J., A. M. Miteva, D. A. Contreras-Solorio, and V. R. Velasco, "Stark effect in diffused quantum wells," *Superlat. Microstruct.*, Vol. 26, 325–32, 1999.
13. Vlaev, S., V. R. Velasco, and F. Garcia-Moliner, "Electronic states in graded-composition heterostructures," *Phys. Rev. B*, Vol. 49, 11222–9, 1994.
14. Boykin, T. B., G. Klimeck, R. Ch. Bowen, and R. Lake, "Effective-mass reproducibility of the nearest-neighbor  $sp^3s^*$  models: Analytic results," *Phys. Rev. B*, Vol. 56, 4102–7, 1997.

# Miniband Structure Formation of $p$ -type Delta-doped Superlattices in GaAs

I. Rodriguez-Vargas, A. del Rio de Santiago, J. Madrigal-Melchor, and S. J. Vlaev

Unidad Académica de Física, Universidad Autónoma de Zacatecas  
Calzada Solidaridad Esquina con Paseo la Bufa S/N, Zacatecas 98060, ZAC., México

**Abstract**— We present the electronic structure of finite  $p$ -type delta-doped superlattices in  $GaAs$ . We use the first neighbors  $sp^3s^*$  tight-binding approximation including spin for the miniband structure analysis. The calculation is based on analytical expression for the Hartree potential of the inhomogeneous part, previously obtained within the Thomas-Fermi (TF) approximation. This potential is considered as an external potential in the computations, so, it is added to the diagonal terms of the tight-binding Hamiltonian. We give a detail description of the delta-doped superlattices, this is, we study the miniband formation as a function of the impurity density ( $n_{2D}$ ) and the superlattice period ( $d$ ), obtaining the regions of superlattice, multiple well and isolate well behavior. We also compare our results with the theoretical and experimental data available, obtaining a reasonable agreement.

## 1. INTRODUCTION

The delta-doped semiconductor superlattices are important structures for the optoelectronic devices due to their particular properties — high carrier density and miniband formation — that can be exploited in devices based on parallel or vertical transport [1]. Besides, these structures are ideal systems to test the resolution of image techniques [2], to study self-compensation [3] and intermixing effects [4], as well as to analyse the disorder effects [5].

In particular,  $p$ -type delta-doped superlattices have been studied both experimentally and theoretically by several authors [6–14]. Carbon delta-doped superlattices in  $GaAs$  have been successfully grown by chemical beam epitaxy with Carbon tetrabromide ( $CBr_4$ ) as doping source [6, 7]. The Carbon shows a great electrical activation ( $3.5 \times 10^{13} \text{ cm}^{-2}$ ) and very narrow doping profiles (5 Å) mainly due to its high solubility and low diffusivity. Spatially indirect transitions have been reported for the first time in  $Zn$  delta-doped  $GaAs$  layers by optical spectroscopy [8]. It is observed that the transitions depend strongly on the temperature and excitation density. In  $GaN$  and  $AlGaN$  epilayers an enhancement of the  $p$ -type lateral and vertical conductivities is observed [9]. A good material quality is achieved by employing  $Mg$  delta-doping [9]. The systems of [8, 9] are not properly superlattices, however they are very promising systems for lateral and vertical transport devices due to the absence of extra barriers as in the case of heterostructures. There are some theoretical reports in  $p$ -type superlattices in  $GaAs$  and  $Si$  [10–14]. The methodology relies on the  $k \cdot p$  multiband effective mass equation from four, six and eight bands. Detail information about the potential profile, hole subband levels, Fermi level position and luminescence signatures for overall system parameters is given. However, it is important to mention that particularly in  $GaAs$  there are not reports dealing with a detail analysis of the miniband-formation evolution [10–12]. So, the aim of the present work is to fill this gap and to show that the tight-binding methodology together to the Thomas-Fermi approximation are an alternative methodology to study inhomogeneous semiconductors systems.

In the present paper we analyse the miniband structure formation of  $p$ -type delta-doped  $GaAs$  superlattices within the nearest neighbors  $sp^3s^*$  tight-binding model including spin. The confining potential induced by the ionized impurities and the electronic charge is obtained analytically through the Thomas-Fermi approximation. This potential is considered as an external perturbation in the tight-binding methodology and it is added to the diagonal terms of the tight-binding Hamiltonian. A detail information of the miniband structure formation as a function of the impurity density, the interwell distance and the number of periods is given, as well as, a comparison with the available theoretical and experimental data is discussed.

## 2. MATHEMATICAL METHOD

The scheme of calculation starts by modelling the valence band profile, within the local density Thomas-Fermi approximation. The outcome of this approach is an analytical expression for the

one-dimensional potential energy function describing the band bending in a single delta-doped quantum well (SDDQW) [15],

$$V_H^*(z) = \frac{\alpha^2}{(\alpha|z| + z_0)^4} \quad (1)$$

where  $\alpha$  and  $z_0$  are constants that comes in terms of the effective masses, dielectric constant and the impurity density [15]. The corresponding expression for  $V_H^*(z)$  in superlattices (SL's) is constructed with a suitable combination of the potential functions of multiple delta-wells and is incorporated to the diagonal terms of the tight-binding Hamiltonian [16],

$$TB_{ii}(n) = TB_{ii}(0) + V_H^*(n) \quad (2)$$

where the potential  $V_H^*(n)$  is the potential  $V_H^*(z)$  written in discrete coordinates, in which  $n$  numbers the atomic layers.

### 3. RESULTS AND DISCUSSION

The tight-binding calculations are performed in the nearest neighbors spin-dependent  $sp^3s^*$  basis at the center of the two-dimensional Brillouin zone for the (001) direction of the delta-doped *GaAs*. The size of the inhomogeneous doped region (the width of the SL) changes with the interwell distance and the number of periods. The finite inhomogeneous slab is matched with two homogeneous semi-infinite *GaAs* barriers within the frame work of the surface Green function matching method [17–20]. The Green function of the inhomogeneous part is obtained through an algorithm previously presented and applied to this kind of systems [20], meanwhile the Green functions of the barrier are calculated within the usual transfer matrix approach [21, 22].

The tight-binding parameters are taken from [16]. These parameters give good band structure values at  $\Gamma$  point for zero temperature taking into account the spin as well as the commonly accepted effective mass values  $m_e^* = 0.068m_0$ ,  $m_{hh}^* = 0.62m_0$  and  $m_{lh}^* = 0.081m_0$  according to the formulas of Boykin et al. [23]. The values of the diagonal tight-binding parameters and the parameters  $V_{xx}$ ,  $V_{ss}$  are the same as in the work of Priester et al. [24].

The following values of the system parameters were used in the calculations:  $m_{hh}^* = 0.62m_0$ ,  $m_{lh}^* = 0.081m_0$ ,  $\epsilon_r = 12.5$ , and the impurity density ranging from  $1 \times 10^{12} \text{ cm}^{-2}$  to  $10 \times 10^{12} \text{ cm}^{-2}$ .

In Figure 1 we present the miniband-formation evolution, as the number of periods grows as well as the well width increases, through the energy density of states. We have considered delta wells with (a) five, (b) ten and (c) fifteen periods, respectively. We include in each case a single delta-doped well (SDD), delta wells of width 40 ML's and 80 ML's that correspond to the black, red and blue lines. The impurity density is  $p_{2D} = 3 \times 10^{12} \text{ cm}^{-2}$  in all cases. As we can see from the reference system (SDD) there are two hole subband levels at 16 meV and 9 meV that correspond to heavy and light holes. The splitting of these levels is evident in the multiple delta wells, red and blue lines, becoming larger for delta wells with period width of 40 ML's. Heavy holes show a miniband of 1 meV for delta wells with period width of 40 ML's, whilst a clearly degenerate heavy hole subband is presented for delta wells with period width of 80 ML's. The light holes present a wider miniband than the heavy holes, but the density of states curves are very different.

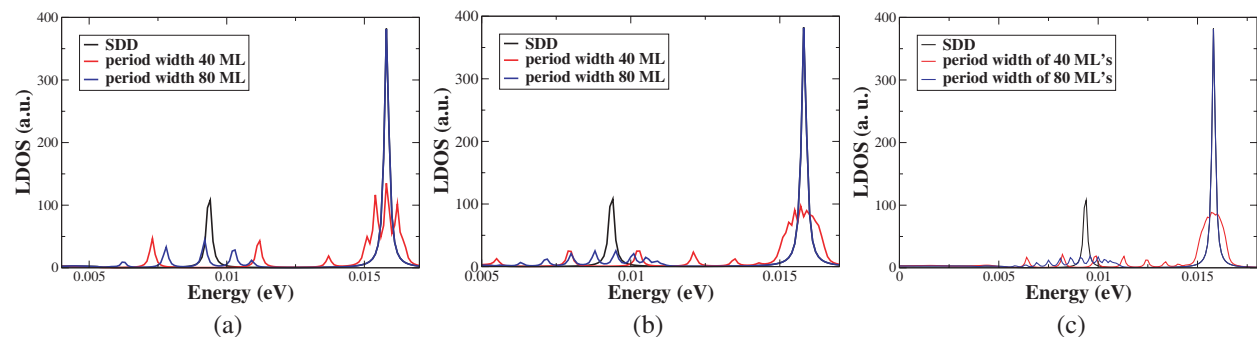


Figure 1: Density of states of delta-doped wells with (a) five, (b) ten and (c) fifteen periods, respectively. The impurity density is  $3 \times 10^{12} \text{ cm}^{-2}$  in all cases. The black, red and blue lines correspond to single delta-doped well (SDD), SL with delta wells of width 40 ML's and 80 ML's, respectively.

In Figure 2, we present the miniband-formation evolution as a function of the impurity density. We have considered three cases (a) 2, (b) 5 and (c) 8 in units of  $10^{12} \text{ cm}^{-2}$ . We include the reference system (SDD) and delta wells of period width of 40 ML's, black and red lines, respectively. The number of periods is ten. If we increase the impurity density, the potential depth increases and the overlap between the hole levels of the different delta wells is much more weaker. As a consequence, the minibands are narrower until become completely degenerate, as we can see for both heavy and light holes in Figure 2.

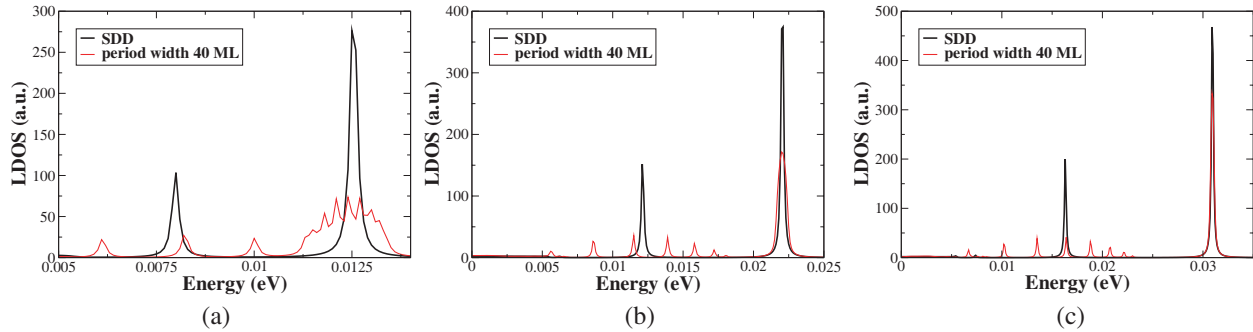


Figure 2: Density of states of delta-doped wells for impurity densities of (a) 2, (b) 5 and (c) 8 in units of  $10^{12} \text{ cm}^{-2}$ . The number of periods is the same (ten) in all cases. The black and red lines correspond to single delta-doped well (SDD) and SL where the delta wells are of width 40 ML's respectively.

Photoluminescence spectroscopy studies on  $Al_xGa_{1-x}As/(Be-doped)GaAs/Al_xGa_{1-x}As$  quantum wells with an intended doping density of  $8 \times 10^{12} \text{ cm}^{-2}$  show the existence of two peaks that could be assigned to radiative transitions of heavy and light holes with electrons in extended states [25]. So, taking the difference between these peaks we can calculate a subband separation of 36 meV. To compare with the experimental data we have taken a period width of 200 ML's, which ensure isolated delta wells, finding a subband separation of 24 meV in relatively good agreement with the experimental value.

Luminescence measurements have been performed in single Be delta-doped layers in GaAs [26]. The recombination involving different subbands permits the study of the subband structure of the quasi-two-dimensional hole gas. In particular, for an acceptor concentration of  $8 \times 10^{12} \text{ cm}^{-2}$  the subband spacing between heavy and light holes is 19 meV. Taking a large period (200 ML's) to ensure isolated delta wells we obtain for the same transition a value of 15 meV.

#### 4. CONCLUSION

In summary, we analysed the miniband structure formation of p-type delta-doped GaAs superlattices within the nearest neighbors  $sp^3s^*$  tight-binding model including spin. We used the Thomas-Fermi approximation to obtain an analytical expression for the SL confining potential. We find that the doping concentration and the period width act as useful tuning parameters for the miniband position, the miniband energy-width and the number of minibands. We show that the tight-binding model combined with the Thomas-Fermi approximation seems to be an efficient tool in the studies of electronic properties in inhomogeneous semiconductor structures, such as delta-doped superlattices.

#### ACKNOWLEDGMENT

This work was supported by the National Science and Technology Council (CONACyT). The authors are especially indebted to the Secretaría General de la UAZ and Consejo Zacatecano de Ciencia y Tecnología (COZCYT) for support.

#### REFERENCES

1. Schubert, E. F., *Delta-doping of Semiconductors*, Cambridge University Press, Cambridge, 1996.
2. Carlino, E., S. Modesti, D. Furlanetto, M. Piccin, S. Rubini, and A. Franciosi, "Atomic resolution composition analysis by scanning transmission electron microscopy high-angle annular dark-field imaging," *Appl. Phys. Lett.*, Vol. 83, No. 4, 662-664, 2003.

3. Modesti, S., R. Duca, P. Finetti, G. Ceballos, M. Piccin, S. Rubini, and A. Franciosi, "Microscopic mechanisms of self-compensation in Si delta-doped GaAs," *Phys. Rev. Lett.*, Vol. 92, No. 8, 086104, 2004.
4. Chaldyshev, V. V., N. A. Bert, Y. G. Musikhin, A. A. Suvorova, V. V. Preobrazhenskii, M. A. Putyato, B. R. Semyagin, P. Werner, and U. Gösele, "Enhanced AsSb intermixing of GaSb monolayer superlattices in low-temperature grown GaAs," *Appl. Phys. Lett.*, Vol. 79, No. 9, 1294–1296, 2001.
5. Willenberg, H., O. Wolts, R. Elpelt, W. Geibelbrecht, S. Malzer, and G. H. Döhler, "Influence of disorder on the vertical transport in wide barrier superlattices," *Phys. Rev. B*, Vol. 65, No. 3, 035328, 2002.
6. Davidson, B. R., L. Hart, R. C. Newman, T. B. Joyce, and T. J. Bullough, "Characterization of carbon delta-doping GaAs superlattices grown by chemical beam epitaxy using  $CBr_4$ ," *J. Cryst. Growth*, Vol. 164, Nos. 1–4, 383–388, 1996.
7. Joyce, T. B., T. J. Bullough, T. Farrell, B. R. Davidson, D. E. Sykes, and A. Chew, "Carbon delta doping in chemical beam epitaxy using  $CBr_4$ ," *J. Cryst. Growth*, Vols. 175–176, No. 1, 377–382, 1997.
8. Zhao, Q. X., M. Willander, P. O. Holtz, W. Lu, H. F. Dou, S. C. Shen, G. Li, and C. Jagadish, "Radiative recombination in p-type  $\delta$ -doped layers in GaAs," *Phys. Rev. B*, Vol. 60, No. 4, R2193–R2196, 1999.
9. Nakarmi, M. L., K. H. Kim, J. Li, J. Y. Lin, and H. X. Jiang, "Enhanced p-type conduction in GaN and AlGaN by Mg-delta-doping," *Appl. Phys. Lett.*, Vol. 82, No. 18, 3041–3043, 2003.
10. Reboredo, F. A. and C. R. Proetto, "Two-dimensional hole gas in acceptor  $\delta$ -doped GaAs," *Phys. Rev. B*, Vol. 47, No. 8, 4655–4661, 1999.
11. Sipahi, G. M., R. Enderlein, L. M. R. Scolfaro, and J. R. Leite, "Band structure of holes in p-type  $\delta$ -doping quantum wells and superlattices," *Phys. Rev. B*, Vol. 53, No. 15, 9930–9942, 1996.
12. Sipahi, G. M., R. Enderlein, L. M. R. Scolfaro, J. R. Leite, E. C. F. da Silva, and A. Levine, "Theory of luminescence spectra from  $\delta$ -doping structures: Application to GaAs," *Phys. Rev. B*, Vol. 57, No. 15, 9168–9178, 1998.
13. Rosa, A. L., L. M. R. Scolfaro, R. Enderlein, G. M. Sipahi, and J. R. Leite, "p-type  $\delta$ -doping quantum wells and superlattices in Si: Self-consistent hole potentials and band structures," *Phys. Rev. B*, Vol. 58, No. 23, 15675–15687, 1998.
14. Rosa, A. L., L. M. R. Scolfaro, J. R. Leite, and G. M. Sipahi, "Rigorous hole band structure calculations of p-type  $\delta$ -doping superlattices in silicon," *Superlattices Microstruct.*, Vol. 25, Nos. 1–2, 67–71, 1999.
15. Gaggero-Sager, L. M., "Exchange energy of a hole gas and the Thomas-Fermi-Dirac Approximation in p-type  $\delta$ -doped quantum wells in Si and GaAs," *Phys. Stat. Sol. (B)*, Vol. 231, No. 1, 243–255, 2002.
16. Vlaev, S. J. and L. M. Gaggero-Sager, "Thomas-Fermi approximation in a tight-binding calculation of  $\delta$ -doped quantum wells in GaAs," *Phys. Rev. B*, Vol. 58, No. 3, 1142–1145, 1998.
17. Muñoz, M. C., V. R. Velasco, and F. García-Moliner, "Electronic structure of AlAs-GaAs superlattices," *Phys. Rev. B*, Vol. 39, No. 3, 1786–1796, 1989.
18. Contreras-Solorio, D. A., V. R. Velasco, and F. García-Moliner, "Electronic structure of (311) AlAs-GaAs superlattices," *ibid*, Vol. 47, No. 8, 4651–4654, 1993.
19. Vlaev, S., V. R. Velasco, and F. García-Moliner, "Tight-binding calculation of electronic states in an inverse parabolic quantum well," *ibid*, Vol. 51, No. 11, 7321–7324, 1995.
20. Vlaev, S., V. R. Velasco, and F. Garcia-Moliner, "Electronic states in graded-composition heterostructures," *Phys. Rev. B*, Vol. 49, No. 16, 11222–11229, 1994.
21. Lopez Sancho, M. P., J. M. Lopez Sancho, and J. Rubio, "Quick iterative scheme for the calculation of transfer matrices: Application to Mo (100)," *J. Phys. F*, Vol. 14, No. 5, 1205–1215, 1984.
22. Lopez Sancho, M. P., J. M. Lopez Sancho, and J. Rubio, "Highly convergent schemes for the calculation of bulk and surface Green functions," *J. Phys. F*, Vol. 15, No. 4, 851–858, 1985.
23. Boykin, T. B., G. Klimeck, R. C. Bowen, and R. Lake, "Effective-mass reproducibility of the nearest-neighbor  $sp^3s^*$  models: Analytic results," *Phys. Rev. B*, Vol. 56, No. 7, 4102–4107, 1997.

24. Priester, C., G. Allan, and M. Lannoo, "Band-edge deformation potentials in a tight-binding framework," *Phys. Rev. B*, Vol. 37, No. 14, 8519–8522, 1988.
25. Wagner, J., A. Ruiz, and K. Ploog, "Fermi-edge singularity and band-filling effects in the luminescence spectrum of Be- $\delta$ -doped GaAs," *Phys. Rev. B*, Vol. 43, No. 14, 12134–12137, 1991.
26. Richards, D., J. Wagner, H. Schneider, G. Hendorfer, M. Maier, A. Fischer, and K. Ploog, "Two-dimensional hole gas and Fermi-edge singularity in Be  $\delta$ -doped GaAs," *Phys. Rev. B*, Vol. 47, No. 15, 9629–9640, 1993.
27. Rodriguez-Vargas, I., J. Madrigal-Melchor, S. J. Vlaev, "Miniband structure analysis of n-type delta-doped GaAs superlattices," *Rev. Mex. Fis. S*, Vol. 53, No. 7, 106–108, 2007.

# Quasi-bound Electronic States in Multiple Delta-doped Quantum Wells

I. Rodriguez-Vargas, A. del Rio de Santiago, and S. J. Vlaev

Unidad Académica de Física, Universidad Autónoma de Zacatecas  
Calzada Solidaridad Esquina con Paseo La Bufa S/N, Zacatecas 98060, ZAC., México

**Abstract**— Multiple delta-doped quantum wells of *n*-type (*Si* doped *GaAs*) and *p*-type (*Be* doped *GaAs*) are studied theoretically looking for quasi-bound electron and hole states. The existence of these states and their strong energy and spatial localizations are demonstrated. The line-width and the mean life time are calculated. The FWHM is less than  $10^{-11}$  eV ( $10^{-9}$  eV) and the corresponding mean life time is greater than  $10^{-5}$  s ( $10^{-7}$  s) for *n*- (*p*-) type wells respectively. A strong spatial localization is observed in both cases.

## 1. INTRODUCTION

The development of the time-resolved spectroscopy permits the detection of the quasi-bound electronic states in different semiconductor heterostructures [1]. The application of the optical transitions involving quasi-bound states in many semiconductor devices has increased recently [2]. Mean life times of the order of pico-seconds or more are sufficiently large for the design of opto-electronic devices where the quasi-bound states play an important role [3]. There are a lot of theoretical and experimental studies about the above barrier resonances and quasi-bound states in superlattices and multiple quantum wells [4]. There are few investigations of the quasi-bound states in single and isolated multiple quantum wells [5]. The delta-doped quantum wells possess confining potentials of a special type. The discrete part of the energy spectrum of these wells is widely studied [6] and numerous applications in modern semiconductor devices as delta-FET, ALD-FET, etc. are realized [7]. There are very few studies of the continuous part of the electronic spectrum in delta-doped wells [8]. The aim of this work is to demonstrate the promising characteristics of the delta-doped quantum wells to confine quasi-bound states in the conduction and valence band. These states have large mean life times and strong spatial localizations suitable for device applications.

## 2. MATHEMATICAL METHOD

Isolated multiple delta-doped quantum wells of *n*-type (*GaAs* doped with *Si*) and *p*-type (*GaAs* doped with *Be*) are considered for the usual impurity concentrations ranging the interval between  $1 \times 10^{12} \text{ cm}^{-2}$  and  $10^{13} \text{ cm}^{-2}$ . The line-width of the quasi-bound states (FWHM) and the corresponding mean life time ( $t$ ) are calculated following the methodology and the numerical scheme published recently [5]. The quantum-mechanical treatment is conducted within the framework of the Surface Green Function Matching method (SGFM) in the context of the discrete semi-empirical tight-binding model working in  $sp^3s^*$  spin dependent basis [9].

## 3. RESULTS AND DISCUSSION

### 3.1. Multiple Delta-doped Quantum Wells of *n*-type

In the Table 1 the main results for the *n*-type wells are presented. The number of the quasi-bound electron states and the quantum-mechanical description of the first state (energy, FWHM and mean life time) are given in dependence on the impurity concentration and the barrier height (well depth). The zero of the energy scale is fixed at the bottom of the *GaAs* conduction band and the energy interval under consideration reaches to 1 eV above the band edge. The number of the quasi-bound states increases from 7 to 21 when the concentration varies from  $n_{2D} = 1 \times 10^{12} \text{ cm}^{-2}$  to  $n_{2D} = 10^{13} \text{ cm}^{-2}$  as consequence of the well depth increase (from 50 meV to 316 meV). When the impurity concentration increases the quasi-bound states move closer to the band edge and move away from the well bottom. The energy changes from 566 meV to 340 meV. This behavior is similar to that of the bound states [10]. A strong energy localization can be observed for all concentrations (the FWHM does not exceed  $10^{-11}$  eV). The mean life times take values greater than  $10^{-5}$  s. The quantum-mechanical characteristics of all quasi-bound states obey similar dependence.

Table 1: *GaAs Si*-doped quantum well. The number of quasi-bound (QB) states, the barrier height (BH), the energy, the full width at half maximum and the mean life time of the first quasi-bound state for different impurity concentrations are given. The zero of the energy is fixed at the bottom of the *GaAs* conduction band. We have look for the quasi-bound states (QB) in the energy interval  $[0.,1.]$  eV. The values in parentheses are measured with respect to the bottom of the quantum well.

$n_{2D}$	1	2	3	4	5	6	7	8	9	10
No.QBS	7	10	12	15	17	18	19	20	21	21
<i>BH</i> <i>meV</i>	50	87	121	152	182	210	238	264	290	316
<i>E(QB 1)</i> <i>meV</i>	566 (616)	535 (622)	507 (628)	480 (632)	455 (637)	431 (641)	408 (646)	385 (649)	362 (652)	340 (656)
<i>FWHM</i> <i>eV</i>	$\leq 10^{-11}$									
t, s	$\geq 10^{-5}$									

Table 2: *GaAs Be*-doped delta quantum well. The number of quasi-bound (QB) states, the barrier height (BH), the energy, the full width at half maximum and the mean life time of the first quasi-bound state for different impurity concentrations are given. The zero of the energy is fixed at the top of the *GaAs* valence band. We have look for the quasi-bound states (QB) in the energy interval  $[0.,-1.]$  eV. The values in parentheses are measured with respect to the bottom of the quantum well.

$p_{2D}$	1	2	3	4	5	6	7	8	9	10
No.QBS	1	1	1	1	1	1	1	1	1	1
<i>BH</i> <i>meV</i>	13	23	31	40	47	55	62	69	76	82
<i>E(QB1)</i> <i>meV</i>	-359 (372)	-357 (380)	-355 (386)	-353 (393)	-351 (398)	-350 (405)	-348 (410)	-346 (415)	-345 (421)	-343 (425)
<i>FWHM</i> <i>eV</i>	$\leq 10^{-9}$									
t, s	$\geq 10^{-7}$									

### 3.2. Multiple Delta-doped Quantum Wells of *p*-type

The results of the *p*-type wells are listed in the Table 2 for the same impurity concentrations as in the *n*-type case. The zero of the energy scale is fixed now at the top of the *GaAs* valence band. The barrier height increases from 13 meV ( $p_{2D} = 1 \times 10^{12} \text{ cm}^{-2}$ ) to 82 meV ( $p_{2D} = 10^{13} \text{ cm}^{-2}$ ). Only one quasi-bound hole state was found for each concentration in the energy interval of 1 eV above the top of the *GaAs* valence band. The energy of this state approaches the band edge and goes away from the well bottom when the doping concentration increases. The energy values are  $-359$  meV and  $-340$  meV for the lowest and highest concentration respectively. The FWHM parameter maintains no greater than  $10^{-9}$  eV and the mean life time is higher than  $10^{-7}$  s.

### 3.3. Comparison between the Multiple Delta-doped Wells of *n*- and *p*-type

In energy intervals of the same magnitude (1 eV) above the band edges the *n*-type wells confine 21 quasi-bound states and the *p*-type wells confine only 1 state. There are two reasons to explain this difference in the capacity to create quasi-bound states. The first reason is that the *n*-type well is deeper for all concentrations, see Tables 1 and 2. The second one consists in the lower bulk density of states of the valence band comparing with the bulk density of states of the conduction band in the corresponding energy intervals. The electron quasi-bound states are much more localized energetically than the hole states. The FWHM takes values of  $10^{-11}$  eV and  $10^{-9}$  eV respectively for *n*- and *p*-type delta well. As a consequence the mean life time is larger in the *n*-type wells ( $10^{-5}$  s) than in the *p*-type wells ( $10^{-7}$  s).

In general, a strong energy localization implies strong spatial localization too. In the Fig. 1 the spectral strengths of the first quasi-bound states for electrons and holes are shown for an impurity concentration of  $10^{13} \text{ cm}^{-2}$ . The electron quasi-bound state is much stronger localized spatially than the hole state. The spectral strengths in the wells differ about 5 times and the oscillations outside the wells approximately 20 times.

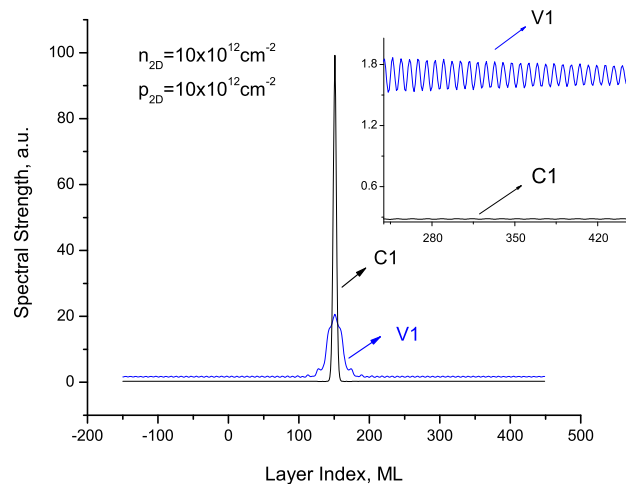


Figure 1: Spectral strengths of the first quasi-bound states for electrons and holes for an impurity concentration of  $10^{13} \text{ cm}^{-2}$ .

The quasi-bound states are well separated (see the Tables) which is an important advantage of the delta-doped wells comparing with the rectangular quantum wells [5].

#### 4. CONCLUSION

The isolated multiple delta-doped quantum wells confine strongly quasi-bound electron and hole states having good energy separation. The mean life times and the spatial localizations of these states permit their experimental detection. Some device applications are quite possible.

#### REFERENCES

- Colocci, M., J. Martinez-Pastor, and M. Gurioli, "Above-barrier resonant transitions in  $Al_xGa_{1-x}As/AlAs/GaAs$  heterostructures," *Phys. Rev. B*, Vol. 48, No. 11, 8089–8094, 1993.
- Levy, M., R. Kapon, A. Sa'ar, R. Beserman, V. Thierry-Mieg, and R. Planel, "Modulated resonant Raman and photoluminescence spectroscopy of Bragg confined asymmetric coupled quantum wells," *Physica E*, Vol. 7, No. 1–2, 245–249, 2000.
- Sung, B., H. C. Chui, E. L. Martinet, and J. S. Harris, Jr., "Control of quasi-bound states by electron Bragg mirrors in  $GaAs/Al_{0.3}Ga_{0.7}As$  quantum wells," *Appl. Phys. Lett.*, Vol. 68, No. 19, 2720–2722, 1996.
- Satanin, A. M. and Y. S. Joe, "Fano interference and resonances in open systems," *Phys. Rev. B*, Vol. 71, No. 20, 205417, 2005.
- Vlaev, S. J. and V. M. González Robles, "Mean lifetimes of quasi-bound electronic states in single rectangular quantum wells," *Phys. Stat. Sol. (C)*, Vol. 2, No. 10, 3653–3656, 2005.
- Gaggero-Sager, L. M. and R. Pérez-Alvarez, "Self-consistent energy levels in  $p$ -type delta-doped quantum wells in GaAs," *J. Appl. Phys.*, Vol. 79, No. 6, 3351–3353, 1996.
- Martínez-Orozco, J. C., L. M. Gaggero-Sager, and S. J. Vlaev, "A simple model for the differential capacitance profile in the atomic layer doped field effect transistor (ALD-FET) in GaAs," *Materials Science and Engineering B*, Vol. 84, No. 3, 155–158, 2001.
- Vlaev, S. J., I. Rodríguez-Vargas, and L. M. Gaggero-Sager, "Resonant states in  $n$ -type  $\delta$ -doped GaAs quantum wells," *Phys. Stat. Sol. (C)*, Vol. 2, No. 10, 3649–3652, 2005.
- Vlaev, S., V. R. Velasco, and F. García-Moliner, "Electronic states in graded-composition heterostructures," *Phys. Rev. B*, Vol. 49, No. 16, 11222–11229, 1994.
- Vlaev, S. J. and L. M. Gaggero-Sager, "Thomas-Fermi approximation in a tight-binding calculation of  $\delta$ -doped quantum wells in GaAs," *Phys. Rev. B*, Vol. 58, No. 3, 1142–1145, 1998.

# Dimensions of the Spectrum of Elementary Excitations in Heterostructures Mimicking a DNA Sequence

R. P. Pérez-Álvarez, M. E. Mora-Ramos, and L. M. Gaggero-Sager

Universidad Autónoma del Estado de Morelos, Ave. Universidad 1001, 62209 Cuernavaca, México

**Abstract**— In the few recent years some authors have claimed the relationship or similarities between the DNA sequences and the man-made quasiregular heterostructures. In order to clarify this connection we have calculated the electromagnetic modes in heterostructures mimicking DNA sequences. Our results indicate that, at least in the analyzed DNA sequences, no similarities can be sustained as the dimension of the spectrum is equal to one. However, some peculiarities of the box-counting curves indicate that the research must continue in this direction.

## 1. INTRODUCTION

In the few recent years some authors have claimed the relationship or similarities between the DNA sequences and the man-made quasiregular heterostructures [1, 2]. This connection is in a certain sense not trivial because the latter have intriguing properties. One of them is the fractal dimension of the spectrum of the elementary excitations propagating along the structure. Meanwhile, no similar property has been so far reported in DNA sequences.

The fractal dimensions of the spectra has been analyzed in several quasiregular heterostructures orderings. As a few examples, the following can be mentioned: Fibonacci, Thue-Morse, Rudin-Shapiro, etc. [3–5]. For some of them, mathematicians have proved useful theorems (see, for example, [6, 7]), but, for the time being, these exact results are limited to the so-called elementary single excitations; i.e., excitations whose master equation is isomorphic with the onedimensional Schrödinger equation. Among these isomorphic excitations one finds transversal horizontal elastic modes, transversal horizontal optical modes, electromagnetic TE and TM modes, etc. However, numerical experiments in non-isomorphic excitations reveal that the key point of the fractal character of the spectra would be the geometric ordering, and not necessarily the complexity of the master equation [3].

This *status quo* has led us to perform the numerical experiment described below in which certain arbitrarily chosen DNA sequence has been mimed by a heterostructure with a few thousands of dielectric active layers disposed in the same ordering of the DNA nucleotide base pairs. The spectrum of excitations in a class of problem isomorphic with the 1D Schrödinger equation -the propagation of TE light modes- has been obtained and its dimensions  $D(q)$  calculated.

In Section 2 the calculation of the spectrum is outlined. Section 3 is devoted to describe in general terms the calculation of the dimension  $D(q)$ . In Section 4 we present the main results. Finally some conclusions are formulated.

## 2. TRANSFER MATRIX APPROACH TO THE CALCULATION OF THE SPECTRUM OF MULTILAYER STRUCTURES

We are dealing with a scalar field  $\Psi(z)$  governed by a second order differential equation isomorphic with 1D Schrödinger equation.  $z$  is the cartesian coordinate along the structure. When we consider the 3D character of the problem a  $(x, y)$  free field  $\Psi(x, y, z) = \Psi(z) \exp[i(k_x x + k_y y)]$  appears, but at the present approach this is irrelevant.

In order to describe these modes we introduce a transfer matrix (TM) as the matrix transferring the values of the field and its derivative from one point to another, i.e.,

$$\begin{pmatrix} \Psi(z) \\ \Psi'(z) \end{pmatrix} = \mathbf{M}(z, z_0) \cdot \begin{pmatrix} \Psi(z_0) \\ \Psi'(z_0) \end{pmatrix}. \quad (1)$$

In [8, 9] many properties can be found on this TM, some other similar magnitudes, and the related Green Function. In particular the secular problem for obtaining the spectrum can be easily written. We address the reader to the cited reference [8, 9] for details.

### 3. FRACTAL DIMENSION $D$

Strange sets appear in many domains of mathematics and physics and in order to characterize them different concepts and procedures have been introduced and studied. We have calculated the so called *fractal dimension*  $D(q)$ . Let  $\{E_i\}$ , with  $i = 1, 2, \dots, N_E$  be the set of points on the real axis representing the eigenvalues. Consider the interval — or set of intervals — occupied by the spectrum, define elementary intervals — 1D boxes — of size  $\epsilon$  and cover the entire interval — or set of intervals — with  $N(\epsilon)$  boxes of size  $\epsilon$ . Let  $q$  be a continuous parameter ranging from  $-\infty$  to  $+\infty$  and  $p_j$  the fraction of points in box  $j$ . The *generalised information of order  $q$*  is defined as (see the book by Rasband [10])

$$I(\epsilon, q) = \frac{1}{1 - q} \log \sum_{j=1}^{N(\epsilon)} p_j^q, \quad (2)$$

and from this the *generalised box-counting dimension*

$$D(q) = - \lim_{\epsilon \rightarrow 0} \frac{I(\epsilon, q)}{\log[\epsilon]}. \quad (3)$$

Some properties of this definition and practical aspects of the evaluation and interpretation of  $D(q)$  can be found in Refs. [4, 5, 10, 11].

### 4. RESULTS

The particular system to which we are applying this mathematical formalism is a dielectric heterostructure made of a porous silicon host material with refractive index  $n_0$  in which dielectric delta-like layers of the same material are inserted following the ordering of the DNA sequence. That is, four other different refractive indices participate, belonging to the constituent elements. The structure is designed in such a way that we can attach to each of these elements a block of the  $n_0$  material having the delta layer inserted (this one having an index given by  $n = n_l$ , where  $l$  labels the nucleotide bases  $A, T, G, C$ ). Then, those elements are arranged according to the chosen sequence. The result is then seen as a non-regular one-dimensional array of dielectric delta layers [12, 13].

The sequence of the layers in the structure follows the ordering of a DNA fraction of the human hemoglobine gen [14]. Then, we have calculated the spectrum of a 2100 layers with zero field at the ends. A set of more than 16,000 eigenvalues have been collected. The input parameters such as the values of the refractive indices (all compatible with different levels of porosity [13]), and the distances between delta layers are displayed in Table 1. Two cases that differ in the layers's widths are considered. The indexes  $\ell$  and  $r$  indicate that distances are between the delta layer and the left and right edges of the corresponding block, respectively. The delta layers are not block-centered, although they might be. This is not an aspect of crucial incidence. Furthermore, we must emphasize that the particular values of the parameters entering the calculation does not influence in principle a so qualitative character of the spectrum as its dimensionality.

Table 1: Refractive index  $n$  of the different delta peaks together with the block layer width for the four different layers of the calculated structure. The host refractive index is  $n_0 = 1.3$ .

refractive index	distances (nm)
$n_A = 2.1$	$d_{A\ell} = 145$ $d_{Ar} = 270$
$n_T = 1.7$	$d_{T\ell} = 120$ $d_{Tr} = 250$
$n_G = 1.9$	$d_{G\ell} = 130$ $d_{Gr} = 220$
$n_C = 1.5$	$d_{C\ell} = 100$ $d_{Cr} = 200$

The information  $I$  for different values of  $q$  parameter ranging from  $-5$  to  $40$  has been plotted against the log of the box size  $\epsilon$ . The slope of the scaled part gives the value  $D(q) = 1$  for all values of  $q$ . However a two-slopes picture appears to be possible. Figures 1 and 2 demonstrate the kind of situation we encounter.

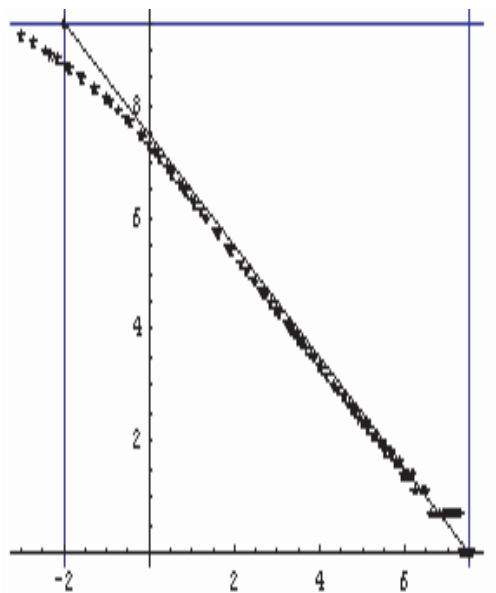


Figure 1: Information *vs* the log of the box size for  $q = 0$ . As a guide of eyes the line with slope  $-1$  is shown.

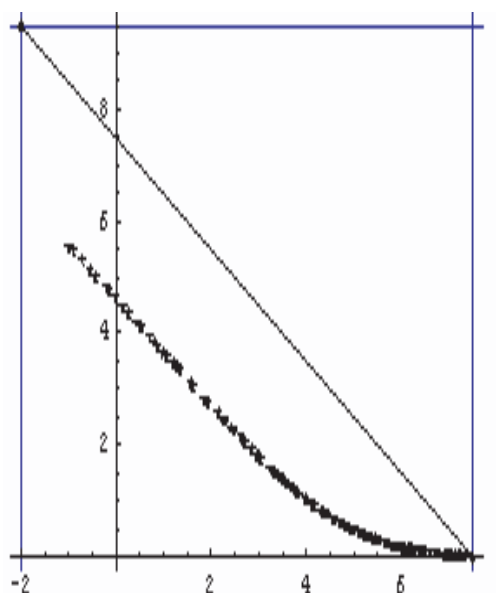


Figure 2: Information *vs* the log of the box size for  $q = 40$ . As a guide of eyes the line with slope  $-1$  is shown.

## 5. CONCLUSION

We have calculated the electromagnetic modes in an heterostructure mimicking DNA sequence in human hemoglobine. Our results indicate that, at least in the analyzed DNA sequence, no similarities can be sustained as the dimension of the spectrum is equal to one for all value of the  $q$  parameter. However, some peculiarities of the box-counting curves indicate that the research must continue in this direction. In particular, a two-slopes situation could be indicating that the spectrum is more complicate than expected.

Our results suggest that the comparison of DNA sequences with the so called Rudin-Shapiro sequence [1] is unjustified, as the latter is known to have a fractal character of the elementary excitations [4].

#### ACKNOWLEDGMENT

One of us (R. P-A) acknowledges hospitality and colleagues of Havana University (Cuba) and Universitat Jaume I (Castelló, Spain) where the first ideas of this work have been elucidated. M. E. M-R. acknowledges support from Mexican CONACYT through grant 52304.

#### REFERENCES

1. Albuquerque, E. L., M. S. Vasconcelos, M. L. Lyra, and F. A. B. F. de Moura, "Nucleotide correlations and electronic transport of DNA sequences," *Phys. Rev. E*, Vol. 71, 021910, 2005.
2. Roche, S., D. Bicout, E. Maciá, and E. Kats, "Long range correlations in DNA: Scaling properties and charge transfer efficiency," *Phys. Rev. Lett.*, Vol. 91, 228101, 2003.
3. Pérez-Alvarez, R., F. García-Moliner, C. Trallero-Giner, and V. R. Velasco, "Polar optical modes in Fibonacci heterostructures," *J. Raman Spectroscopy*, Vol. 31, No. 5, 421–425, 2000.
4. Pérez-Alvarez, R. and F. García-Moliner, "The spectrum of quasiregular heterostructures," invited chapter in *Contemporary Problems of the Condensed Matter Physics*, ed. by S. Vlaey and L. M. Gaggero-Sager, Editorial Nova Science Publishers, Huntington, New York, 2001.
5. Velasco, V. R., R. Pérez-Alvarez, and F. García-Moliner, "Some properties of the elastic waves in quasiregular heterostructures," *J. Phys.: Cond. Matt.*, Vol. 14, 5933–5957, 2002.
6. Bovier, A. and J. M. Ghez, "Spectral properties of one-dimensional Schrödinger operators with potentials generated by substitutions," *Commun. Math. Phys.*, Vol. 158, No. 1, 45–66, 1993.
7. Bovier, A. and J. M. Ghez, "Remarks on the spectral properties of tight-binding and Kronig-Penney models with substitution sequences," *J. Phys. A: Math. Gen.*, Vol. 28, No. 8, 2313–2324, 1995.
8. Pérez-Alvarez, R. and F. García-Moliner, "Transfer matrix, green function and related techniques: Tools for the study of multilayer heterostructures," Universitat Jaume I, Castellón, Spain, 2004.
9. Mora, M., R. Pérez-Álvarez, and C. Sommers, "Transfer matrix in one dimensional problems," *J. Physique*, Vol. 46, No. 7, 1021–1026, 1985.
10. Rasband, S. N., "Chaos dynamics of nonlinear systems," *Wiley Professional Paperback Series*, 199, 1997.
11. Pérez-Álvarez, R., F. García-Moliner, and V. R. Velasco, "Some elementary questions in the theory of quasiperiodic heterostructures," *J. of Phys.: Condens. Matter*, Vol. 13, 3689–3698, 2001.
12. Mora-Ramos, M. E., V. Agarwal, and J. A. Soto Urueta, "Propagation of light in quasi-regular dielectric heterostructures with delta-like layers," *Microelectronics Journal*, Vol. 36, 413–415, 2005.
13. Agarwal, V. and M. E. Mora-Ramos, "Optical characterization of polytype Fibonacci and ThueMorse quasiregular dielectric structures made of porous silicon multilayers," *J. Phys. D: Appl. Phys.*, Vol. 40, 3203–3211, 2007.
14. See GeneBank in <http://www.ncbi.nlm.nih.gov>.

# Transmittance and Fractality in a Cantor-like Multibarrier System

D. S. Díaz-Guerrero, F. Montoya, L. M. Gaggero-Sager, and R. Pérez-Álvarez

Universidad Autónoma del Estado de Morelos, Ave. Universidad 1001, Cuernavaca 62209, México

**Abstract**— The transmittance is studied for a Cantor-like multibarrier system. The calculation are made in the framework of effective mass theory. Some typical values of effective masses and potentials are used in order to have an experimental reference. The techniques of Transfer Matrix are used to calculate the transmittance of the entire structure having some dozens of layers. The results display a complex structure of peaks and valleys. The set of maxima is studied with the tool of the  $q$ -dependent dimension  $D(q)$ . The set of transmittance maxima exhibits a fractal structure, or more exactly, a multifractal structure, i.e., a  $q$ -dependent dimension, characterized as usually with limit one when  $q$  parameter tends to  $-\infty$  but with a limit between 0 and 1 when tends to  $+\infty$ . This numerical experiment demonstrate that spatially bounded potential may exhibit spectrum with fractal character.

## 1. INTRODUCTION

The transmittance, energy levels and wave functions has been studied, among others, for periodic rectangular barriers, superlattices, quasiregular heterostructures and other multilayer onedimensional systems. Nevertheless it is interesting to study non-periodic potentials, such as selfsimilar ones among others. In this case the term selfsimilar potential means that the height and/or the separation between barriers is not constant but it is constructed following some replicative rule. In our case we have chosen the Cantor's set rule [1]. The motivation for studying this kind of potentials comes out because it seems likely to find out that the transmittance reflects the selfsimilar property of the potential through its fractal dimension. In the other hand Lavrinenko et al. [2, 3] studied the propagation of classical waves of the optical Cantor filter. This system is not a self-similitar sistem, because the refractive indices are not scaled. The authors observed that the optical spectra has been shown spectral scalability. In the last few years, a lot of experimental works, concerning the worth noting properties of porous silicon in chemical and biological sensing, have been reported [4]. Moretti et al. have compared the sensitivities of resonant optical biochemical sensor, based on both periodic and aperiodic porous silicon structures, such as Bragg and the Thue-Morse multilayer. They observed that the aperiodic multilayer is more sensitive than the periodic one. Then the task of finding similar systems with bigger sensitivity is important for applications.

## 2. METHODOLOGY

Figure 1 shows the first three generations, each generation having  $2^n - 1$  barriers. Each generation has a main barrier with an energy height  $H_0$  and spatial width  $L_0$ , for the second generation the other two barriers that appear have an energy height  $H_0/3$  and spatial width  $L_0/3$  and they are located in the middle third part where there is a zero potential. The third generation keeps the barriers of the second generation and adds barriers of height  $H_0/9$  and width  $L_0/9$  and they are located in the middle third part where there is a zero potential. With this algorithm one can construct the following generations. The transmittance for the potentials described above is computed, using the transfer matrix technique [5, 6] applied to the onedimensional Schrödinger equation [7].

$$-\frac{\hbar^2}{2m} \frac{\partial^2}{\partial x^2} \Psi(x, t) + V(x) \Psi(x, t) = i\hbar \frac{\partial}{\partial t} \Psi(x, t) \quad (1)$$

Using separation of variables reduces to the time-dependant Shrödinger equation,

$$-\frac{\hbar^2}{2m} \frac{d^2}{dx^2} \psi(x) + V(x) \psi(x) = E \psi(x) \quad (2)$$

Consider first a localized potential  $V$ , restricted to the interval  $(a, b)$ ; the general solution is

$$\psi(x) = \begin{cases} Ae^{ikx} + Be^{-ikx} & \text{if } x < a \\ \psi_{ab}(x) & \text{if } a < x < b \\ Ce^{ikx} + De^{-ikx} & \text{if } b < x \end{cases} \quad (3)$$

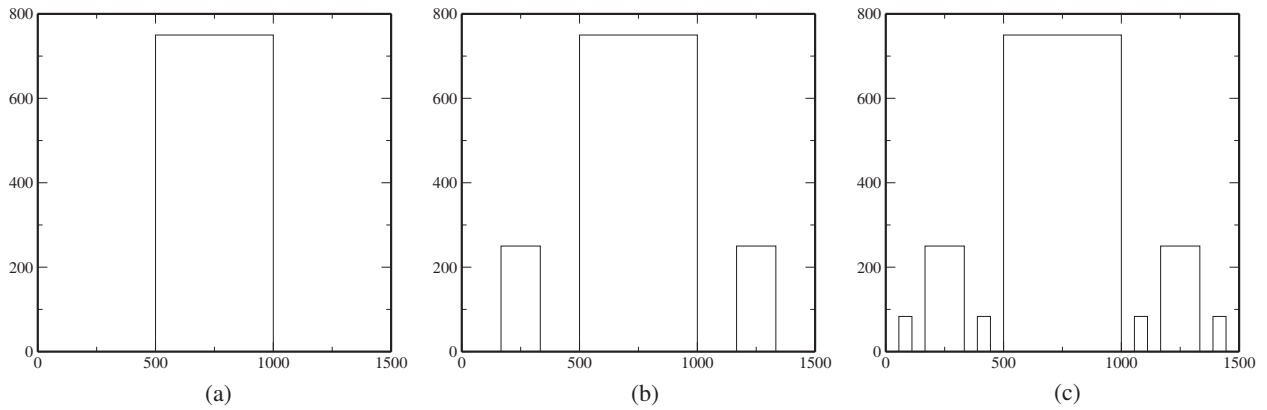


Figure 1: Cantor-like potential. The main barrier has 3 times the energy of the other, and 3 times the length. Panel a/b/c shows the first/second/third generation.

where  $k \equiv \sqrt{2mE/\hbar}$ . When the time factor is included,  $A \exp(ikx)$  and  $C \exp(ikx)$  represent waves propagating to the right, while  $B \exp(-ikx)$  and  $D \exp(-ikx)$  represent waves propagating to the left.

To complete the problem, one solves Eq. (2) for  $\psi(x)$  in  $(a, b)$ . Then, invoking the appropriate boundary conditions at  $a$  and  $b$  [typically, continuity of  $\psi(x)$  and its derivative], one obtains two linear relations among the coefficients  $A$ ,  $B$ ,  $C$  and  $D$ . These can be solved for any two amplitudes in terms of the other two, and the result can be expressed as a matrix equation. Usually one chooses to write the outgoing amplitudes ( $B$  and  $C$ ) in terms of the incoming amplitudes ( $A$  and  $D$ ) using the so-called “ $S$  matrix”.

$$\begin{pmatrix} B \\ C \end{pmatrix} = S \begin{pmatrix} A \\ D \end{pmatrix}$$

We find it more convenient to express the amplitudes to the left of the barrier ( $A$  and  $B$ ) in terms of those to the right ( $C$  and  $D$ ):

$$\begin{pmatrix} A \\ B \end{pmatrix} = M \begin{pmatrix} C \\ D \end{pmatrix}$$

This  $2 \times 2$  matrix

$$M = \begin{pmatrix} M_{11} & M_{12} \\ M_{21} & M_{22} \end{pmatrix}$$

is called the “transfer matrix”.

For this particular work, the energy of the main barrier  $H_0$  is taken as 750 meV and the segment  $L_0$  is of length 500 Å.

Figure 2 shows the transmittance for the first three generations. The behavior of the transmittance for high order generations, above the 6th one, remains approximately the same. This is not surprising considering that the added barriers are of the order of  $H_0/3^n$  and  $L_0/3^n$  or smaller and their contribution is negligible, even when there is  $2^n$  of these barriers. The transmittance, as expected, exhibits a complex structure characterized by many maxima and minima in a relatively small interval of energy. The maxima are related with the discretized spectrum of the set of wells inside the structure. We have collected all these maxima and treated them as a set of points in order to calculate its fractal dimensions  $D(q)$ .

### 3. $Q$ DEPENDENT DIMENSIONS

Following Rasband [8], Pérez-Álvarez [9–11] and coworkers, and the references they cite, we use the so called  $q$ -dependent fractal dimensions in order to describe the strange character of the spectrum as a set of points. The main point is to cover the set with a collection of boxes of size  $\epsilon$  and to study the Information magnitude

$$I(\epsilon, q) = \frac{1}{1-q} \log \sum_{j=1}^{N(\epsilon)} p_j^q, \quad (4)$$

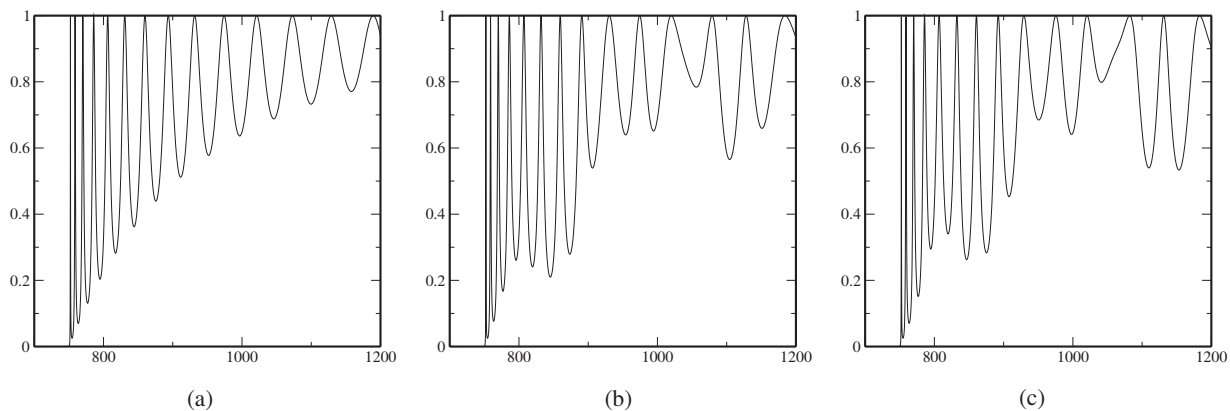


Figure 2: Transmittance for Cantor-like potential. Panel a/b/c shows the first/second/third generation.

and from this the *generalised box-counting dimension*

$$D(q) = -\lim_{\epsilon \rightarrow 0} \frac{I(\epsilon, q)}{\log[\epsilon]} \tag{5}$$

In these formulas  $p_j$  is the fraction of points in the  $j$ -th box.  $N(\epsilon)$  is the number of boxes of size  $\epsilon$ .

In practice the limit in (5) is calculated as the slope of the so called *scaled part* of the curve  $I(\epsilon, q)$  vs  $\log[\epsilon]$ . The reader is addressed to references [10, 12] in order to face some practical aspects and tricks on this matter.

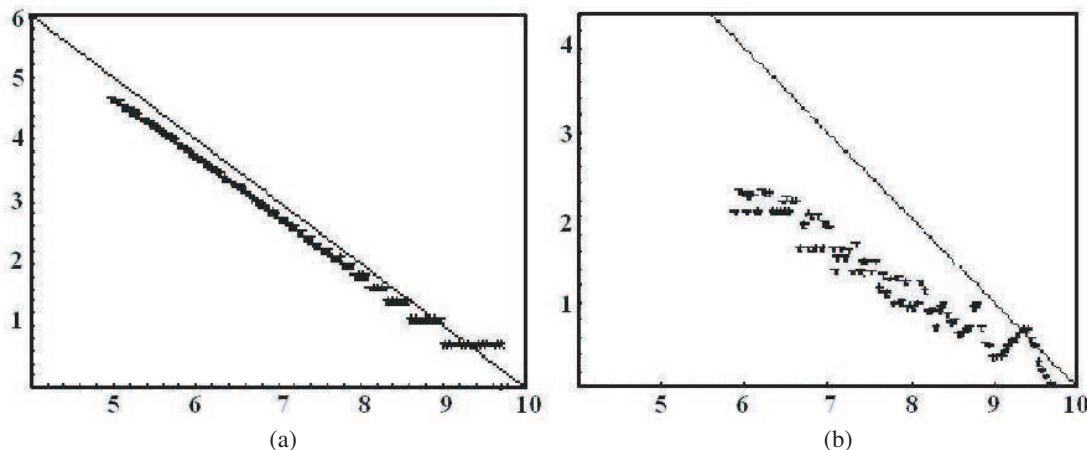


Figure 3:  $I(\epsilon, q)$  vs  $\log[\epsilon]$  curves for  $q = 0$  (left panel) and  $q = 40$  (right panel). A straight line with slope  $-1$  is added as a guide for the eyes. It is clearly seen that dimension at  $q = 40$  is less than unity.

Figure 3 depicts the  $I(\epsilon, q)$  vs  $\log[\epsilon]$  curves for  $q = 0$  and  $q = 40$ . The figures are restricted to the scaled parts of these curves. The  $D(q)$  calculations take as input 725 eigenvalues obtained from the 7th generation. The conclusion is obvious: the spectrum has  $D(0) \approx 1$  but a dimension clearly less than unity for  $q = 40$ , i.e., it has a *distribution* of fractal dimensions. The detailed analysis for  $q \in (-\infty, +\infty)$  shows that  $D(q)$  goes continuously from 1 at  $-\infty$  to  $\approx 0.6$  at  $+\infty$ , as it should be because of very basic principles [12].

#### 4. CONCLUSION

The numerical experiment we present in this paper demonstrate that the spectrum of elementary excitations in spatially bounded potential can have a fractal character. It is not at all trivial.

Mathematicians have proved some theorems about the fractality of the spectrum of Schrödinger-like hamiltonians in some quasiregular sequences [13, 14] but, as far as we know, there is no solid result on potentials defined on bounded intervals. We hope our results open a new field of interest for physicists and mathematicians.

#### ACKNOWLEDGMENT

LM G-S acknowledges E. R. Pujals (IMPA, Rio de Janeiro. Brasil), and O. Sotolongo-Costa (Havana University, Cuba) for many stimulating discussions on this subject. We four acknowledge UAEM (State Autonomous University of Morelos, at Cuernavaca, Mexico) for support.

#### REFERENCES

1. Gaggero-Sager, L. M., E. R. Pujals, and O. Sotolongo-Costa, "Self-similarity in a Cantor-like semiconductor quantum well," *Phys. Stat. Sol. (B)*, Vol. 220, 167–169, 2000.
2. Lavrinenko, A. V., S. V. Zhukovsky, K. S. Sandomirski, and S. V. Gaponenko, "Propagation of classical waves in nonperiodic media: Scaling properties of an optical Cantor filter," *Phys. Rev. E*, Vol. 65, 036621, 2002.
3. Zhukovsky, S. V., A. V. Lavrinenko, and S. V. Gaponenko, "Spectral scalability as a result of geometrical self-similarity in fractal multilayers," *Europhys. Lett.*, Vol. 66, No. 3, 455–461, 2004.
4. Moretti, L., I. Rea, L. de Stefano, and I. Rendina, "Periodic versus aperiodic: Enhancing the sensitivity of porous silicon based optical sensors," *Applied Physics Letters*, Vol. 90, 191112, 2007.
5. Pérez-Alvarez, R. and F. García-Moliner, *Transfer Matrix, Green Function and Related Techniques: Tools for the Study of Multilayer Heterostructures*, Universitat Jaume I, Castellón, Spain, 2004.
6. Mora, M., R. Pérez-Álvarez, and C. Sommers, "Transfer matrix in one dimensional problems," *J. Physique*, Vol. 46, No. 7, 1021–1026, 1985.
7. Griffiths, D. J. and C. A. Steinke, "Waves in locally periodic media," *Am. J. Phys.*, Vol. 69, No. 2, 137–154, 2001.
8. Rasband, S. N., "Chaos dynamics of nonlinear systems," Wiley Professional Paperback Series, 1997.
9. Pérez-Alvarez, R., F. García-Moliner, C. Trallero-Giner, and V. R. Velasco, "Polar optical modes in Fibonacci heterostructures," *J. Raman Spectroscopy*, Vol. 31, No. 5, 421–425, 2000.
10. Pérez-Alvarez, R. and F. García-Moliner, "The spectrum of quasiregular heterostructures," invited chapter in *Contemporary Problems of the Condensed Matter Physics*, ed by S. Vlaev and L.M. Gaggero-Sager, Editorial Nova Science Publishers, Huntington, New York, 2001.
11. Velasco, V. R., R. Pérez-Alvarez, and F. García-Moliner, "Some properties of the elastic waves in quasiregular heterostructures," *J. Phys.: Cond. Matt.*, Vol. 14, 5933–5957, 2002.
12. Pérez-Álvarez, R., F. García-Moliner, and V. R. Velasco, "Some elementary questions in the theory of quasiperiodic heterostructures," *J. of Phys.: Condens. Matter*, Vol. 13, 3689–3698, 2001.
13. Bovier, A. and J. M. Ghez, "Spectral properties of one-dimensional Schrödinger operators with potentials generated by substitutions," *Commun. Math. Phys.*, Vol. 158, No. 1, 45–66, 1993.
14. Bovier, A. and J. M. Ghez, "Remarks on the spectral properties of tight-binding and Kronig-Penney models with substitution sequences," *J. Phys. A:Math. Gen.*, Vol. 28, No. 8, 2313–2324, 1995.

# The Electrostatic Potential Associated to Interface Phonon Modes in Nitride Single Heterostructures

M. E. Mora-Ramos<sup>1</sup>, R. Pérez-Alvarez<sup>1</sup>, and V. R. Velasco<sup>2</sup>

<sup>1</sup>Facultad de Ciencias, Universidad Autónoma del Estado de Morelos, Mexico

<sup>2</sup>Instituto de Ciencia de Materiales de Madrid, CSIC, Spain

**Abstract**— The electrostatic potential associated to the interface oscillation modes in nitride-based heterostructure is calculated with the use of a complete phenomenological electroelastic continuum approach for the long wave optical oscillations, and the Surface Green Function Matching technique. The crystalline symmetries of zincblende and -isotropically averaged- wurtzite are both considered in the sets of input bulk frequencies and dielectric constants.

## 1. INTRODUCTION

The description of the long wavelength polar optical modes in nitride-based heterostructures with wurtzite structure has been put forward since the mid nineties within a formalism that combines the so-called dielectric continuum model (DCM) together with the Loudon's uniaxial model [1]. Studies on the subject have continued until very recently [2–4]. In these works, different polar optical phonon branches have been identified as interface modes, half-space modes, confined or quasi-confined modes, and propagating modes. At the same time, the corresponding electron-phonon interaction Hamiltonians were derived.

In a recent paper Mora-Ramos et al. [5] calculated the interface-polar-optical-phonon-limited mobility for electrons in the conduction band of AlGa<sub>x</sub>N/GaN single heterostructures using the model and interaction Hamiltonian presented in [1]. The outcome of their calculation revealed values for the room temperature mobility well below the most of the experimental reports in such kind of systems. Since several different approaches for the calculation of single electron conduction band states were tested, the problem seems to be related with the particular approach for the optical phonon modes that arises from the uniaxial DCM.

The discussion about the suitability of the DCM for a complete phenomenological description of the optical phonon in polar semiconducting heterostructures dates back to the early nineties [6, 7]. The limitation of the DCM for dealing with the mechanical boundary conditions was then highlighted, and a continuum phenomenological electroelastic model (CPELM) was proposed instead. This model was later applied to the study of polar optical phonon modes in AlGaAs/GaAs single heterostructures [8], in combination with the method of Surface Green Function Matching (SGFM).

## 2. SOME COMMENTS ON THE THEORY

We will use the CPELM-SGFM formalism in the present article. Due to its rather involved mathematical framework, the reader is referred to references [6–9] for details.

The CPELM deals exclusively with systems made of semiconductors with cubic crystalline symmetry. Nevertheless, we believe that some new information, regarding the interface phonon modes, can be derived with its application to heterostructures of materials bearing hexagonal symmetry such as the wurtzite nitrides. For this purpose, the procedure implies the isotropic averaging of the main input parameters of the model. These are the bulk longitudinal and transversal phonon frequencies at the Brillouin Zone center, and the dielectric constants. Besides, it is also needed to average the values of the parameters  $\beta_L$ , and  $\beta_T$ . They are related to the phonon dispersion curves in the bulk, which can be well approximated by  $\omega_L^2(q) = \omega_{LO}^2 - \beta_L^2 q^2$ , and by  $\omega_T^2(q) = \omega_{TO}^2 - \beta_T^2 q^2$ , for the longitudinal and transversal phonons respectively. Since the CPELM is a long wavelength model, its application is usually restricted to a small region -of about 10%- of the Brillouin zone, around the  $\Gamma$  point. This is precisely the region where the parabolic approximation of the dispersion relation appropriately applies.

The work is restricted to deal with GaN-AlGa<sub>x</sub>N structures. We are considering a system that consists of two half-space layers. The one made of Al<sub>x</sub>Ga<sub>1-x</sub>N is located at the  $z < 0$  region, while for  $z > 0$  we have the GaN. For the case of zincblende materials we use the following input parameters:  $\epsilon_\infty(\text{GaN}) = 5.30$ ,  $\epsilon_\infty(\text{AlN}) = 4.46$ ;  $\rho(\text{GaN}) = 6.10 \text{ g/cm}^3$ ,  $\rho(\text{AlN}) = 3.29 \text{ g/cm}^3$ ;  $\omega_{LO}(\text{GaN}) = 748 \text{ cm}^{-1}$ ,  $\omega_{LO}(\text{AlN}) = 920 \text{ cm}^{-1}$ ;  $\omega_{TO}(\text{GaN}) = 562 \text{ cm}^{-1}$ ,  $\omega_{TO}(\text{AlN}) = 670 \text{ cm}^{-1}$ ;

$\beta_L^2(GaN) = 1.52 \times 10^{-11}$ ,  $\beta_L^2(AlN) = 1.44 \times 10^{-11}$ ;  $\beta_T^2(GaN) = 2.87 \times 10^{-13}$ ,  $\beta_T^2(AlN) = 5.89 \times 10^{-12}$ . The corresponding expressions for the cubic alloy  $Al_xGa_{1-x}N$  are obtained by applying the Vegard's law to each of them. That is,  $f(Al_xGa_{1-x}N) = f(GaN) * (1 - x) + f(AlN) * x$ .

In the case of the wurtzite nitrides, we have:  $\epsilon_\infty(GaN) = 5.29$ ,  $\epsilon_\infty(AlN) = 4.68$ ;  $\rho(GaN) = 6.15 \text{ g/cm}^3$ ,  $\rho(AlN) = 3.23 \text{ g/cm}^3$ , with their corresponding Vegard's laws. On the other hand, the parabolic dispersion amplitudes are:  $\beta_{zL}^2(GaN) = 2.78 \times 10^{-12}$ ,  $\beta_{zL}^2(AlN) = 2.47 \times 10^{-11}$ ;  $\beta_{\perp L}^2(GaN) = 7.60 \times 10^{-12}$ ,  $\beta_{\perp L}^2(AlN) = 2.28 \times 10^{-11}$ ;  $\beta_{zT}^2(GaN) = -2.53 \times 10^{-12}$ ,  $\beta_{zT}^2(AlN) = 7.34 \times 10^{-12}$ ;  $\beta_{\perp T}^2(GaN) = -1.21 \times 10^{-12}$ ,  $\beta_{\perp T}^2(AlN) = 2.69 \times 10^{-12}$ ; Vegard's law is also applied to these quantities, in order to deal with their values for the alloy.

The indexes “z” and “ $\perp$ ” label the *A1* and *E1* infrared-active polar optical mode of the wurzite structure, respectively. The dependencies of the frequencies of these optical modes upon the aluminum molar fraction have been studied in greater detail. The longitudinal modes have a one-mode character. The corresponding frequencies are:  $\omega_{zL} = 734 + 153x + 75x(1 - x) \text{ cm}^{-1}$ ,  $\omega_{\perp L} = 7442 + 170x + 65x(1 - x) \text{ cm}^{-1}$ . The transversal modes have two-mode character, GaN-like and AlN-like, with frequencies given by:  $\omega_z(GaN) = 532 + 65x - 2x(1 - x) \text{ cm}^{-1}$ ,  $\omega_z(AlN) = 551 + 55x$ ;  $\omega_{\perp}(GaN) = 557 + 53x \text{ cm}^{-1}$ ,  $\omega_{\perp}(AlN) = 617 + 47x \text{ cm}^{-1}$ . All these data have been collected from different works (see references [10–16]). To grant the application of the CPELM to the wurzite heterostructures, the “z” and “ $\perp$ ” values are isotropically averaged.

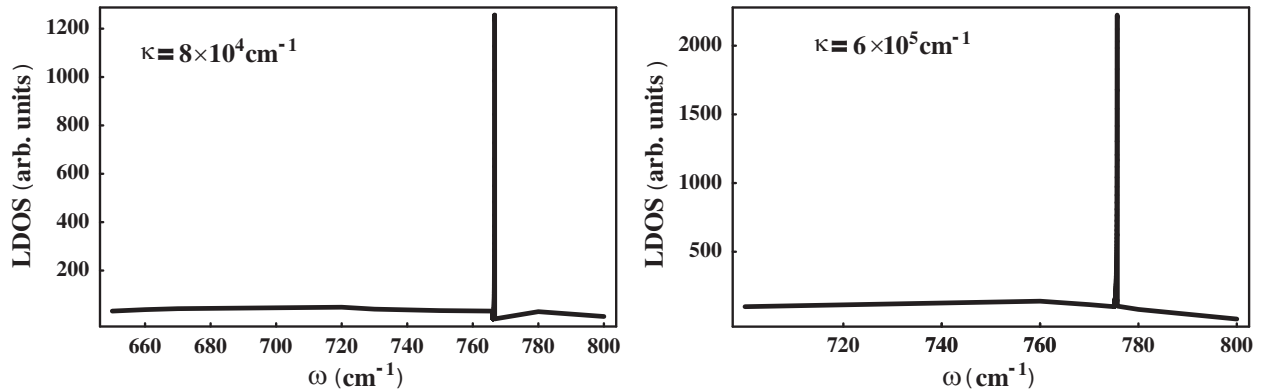


Figure 1: LDOS in a zincblende  $Al_{0.22}Ga_{0.78}N/GaN$  SHS for phonon wavevector  $\kappa = 8 \times 10^4 \text{ cm}^{-1}$  SHS (left), and for a zincblende  $Al_{0.33}Ga_{0.67}N/GaN$  SHS for wavevector  $\kappa = 6 \times 10^5 \text{ cm}^{-1}$  SHS (right).

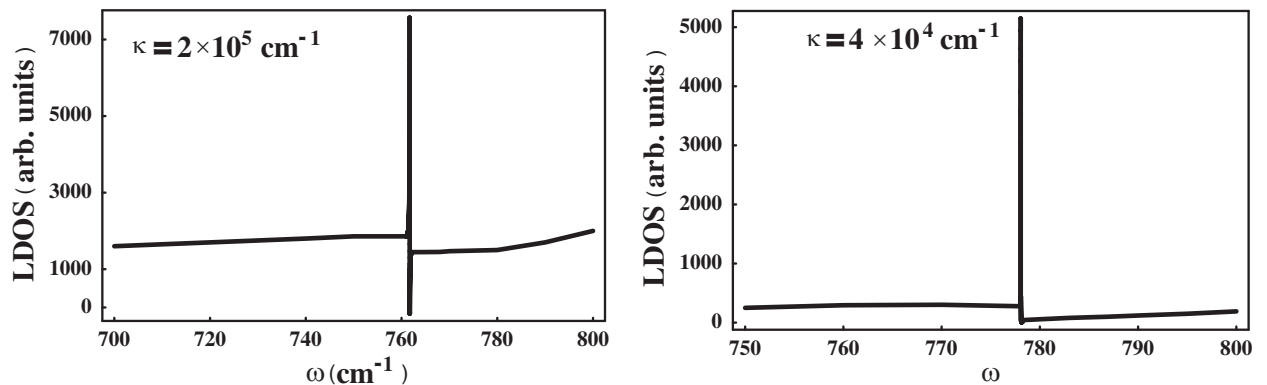


Figure 2: LDOS in a wurzite  $Al_{0.22}Ga_{0.78}N/GaN$  SHS for phonon wavevector  $\kappa = 2 \times 10^5 \text{ cm}^{-1}$  SHS (left), and for a wurzite  $Al_{0.40}Ga_{0.60}N/GaN$  SHS for wavevector  $\kappa = 4 \times 10^4 \text{ cm}^{-1}$  SHS (right).

### 3. RESULTS AND CONCLUSIONS

Figures 1 and 2 show the local density of states (LDOS) for SHS with cubic and hexagonal symmetry, respectively. The peaks correspond to the value of the interface polar optical phonon oscillations. The set of LDOS peaks for different values of the phonon wavevector  $\kappa$  generates the dispersion

relation of the interface mode. These dispersion relations for nitride SHS are shown in figure 3 for some values of the Al molar fraction  $x$ .

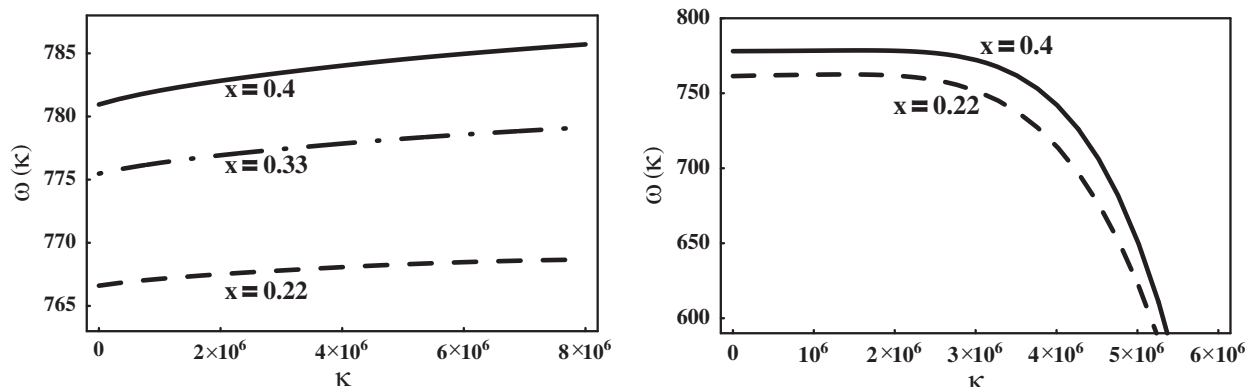


Figure 3: Dispersion relations for the interface polar optical oscillation mode in zincblende  $\text{Al}_x\text{Ga}_{1-x}\text{N}/\text{GaN}$  SHS (left), and wurtzite  $\text{Al}_x\text{Ga}_{1-x}\text{N}/\text{GaN}$  SHS (right).

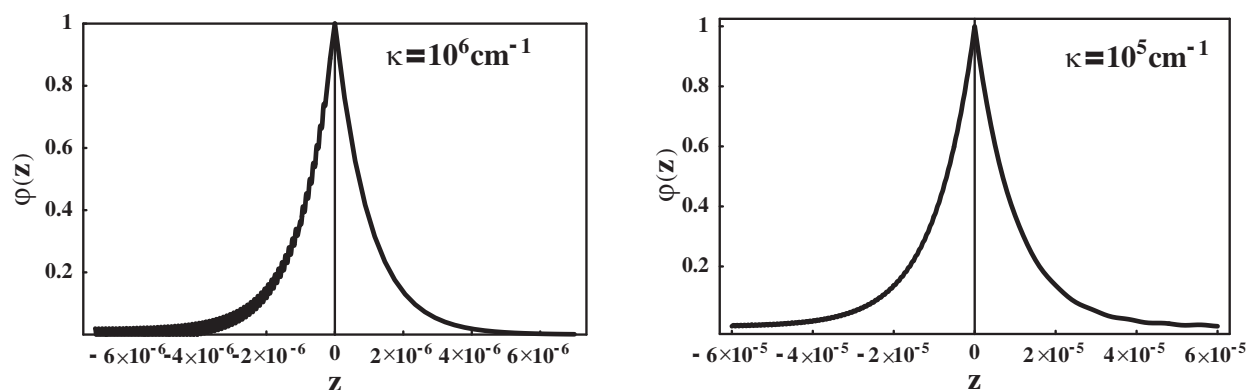


Figure 4: Electrostatic potential function corresponding to the GaN-like interface phonon mode in wurtzite  $\text{Al}_x\text{Ga}_{1-x}\text{N}/\text{GaN}$  SHS. In this case:  $x = 0.22$ ,  $\kappa = 10^6 \text{ cm}^{-1}$  (left figure), and  $x = 0.33$ ,  $\kappa = 10^5 \text{ cm}^{-1}$  (right figure). Arbitrary units are used on both axes.

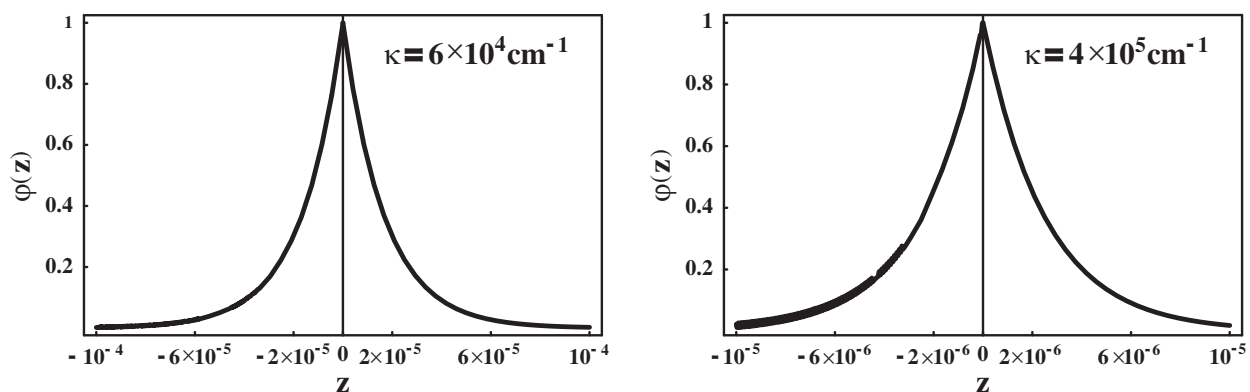


Figure 5: Electrostatic potential function corresponding to the GaN-like interface phonon mode in zincblende  $\text{Al}_x\text{Ga}_{1-x}\text{N}/\text{GaN}$  SHS. In this case:  $x = 0.33$ ,  $\kappa = 6 \times 10^4 \text{ cm}^{-1}$  (left figure), and  $x = 0.40$ ,  $\kappa = 4 \times 10^5 \text{ cm}^{-1}$  (right figure). Arbitrary units are used on both axes.

Figures 4 and 5 present the electrostatic potential corresponding to the GaN-like interface mode in wurtzite and zincblende  $\text{Al}_x\text{Ga}_{1-x}\text{N}/\text{GaN}$  SHS respectively. The values of the phonon wavevector in each case have been chosen just for illustration. A slight oscillatory behavior is observed on the

AlGaN side of the SHS. In fact, the amplitude of the small oscillations of  $\phi$  in that region depends on the magnitude of the phonon wavevector. It is more apparent for higher values of  $\kappa$ . To explain this, one should remember that we are studying the GaN-like modes only. For these modes it fulfills that  $\omega(\kappa) < \omega_{LO}$  in the region  $z < 0$ .

The decaying behavior of  $\varphi$  is readily noticed. It is, in fact, very stepped. Consequently, the width of the region of penetration is extremely narrow. This suggests that the actual contribution of this mode to the electron-phonon matrix elements might be significantly low. Work on this subject is in progress.

#### ACKNOWLEDGMENT

M.E.M.R acknowledges support from CONACyT through Grant 52304.

#### REFERENCES

1. Lee, B. C., K. W. Kim, M. A. Stroscio, and M. Dutta, "Optical-phonon confinement and scattering in wurtzite heterostructures," *Phys. Rev. B*, Vol. 58, No. 8, 4860–4865, 1998.
2. Shi, J.-J., "Interface optical phonon modes and electron-interface-phonon interactions in wurtzite GaN/AlN quantum wells," *Phys. Rev. B*, Vol. 68, No. 16, 165335(1)–165335(11), 2003.
3. Shi, J.-J., X. L. Chu, and E. M. Goldys, "Propagating optical-phonon modes and their electron-phonon interactions in wurtzite GaN/Al<sub>x</sub>Ga<sub>1-x</sub>N quantum wells," *Phys. Rev. B*, Vol. 70, No. 11, 115318(1)–115318(8), 2004.
4. Li, L., D. Liu, and J. J. Shi, "Electron-quasi-confined-optical-phonon interactions in wurtzite GaN/AlN quantum wells," *Eur. Phys. J. B*, Vol. 44, No. 4, 401–413, 2005.
5. Mora-Ramos, M. E., J. Tutor, and V. R. Velasco, "Interface-phonon-limited two-dimensional mobility in AlGaN/GaN heterostructures," *J. Appl. Phys.*, Vol. 100, No. 12, 123708(1)–123708(9), 2006.
6. Trallero-Giner, C., F. García-Moliner, V. R. Velasco, and M. Cardona, "Analysis of the phenomenological models for long wavelength polar optical modes in semiconductor layered systems," *Phys. Rev. B*, Vol. 45, No. 20, 11944–11948, 1992.
7. García-Moliner, F., "Long wave polar optical phonons in heterostructures," in *Phonons in Semiconductor Nanostructures: Proceedings of the NATO Advanced Research Workshop*, Eds. J.-P. Leburton, J. Pascual, C. Sotomayor-Torres. Kluwer Academic Publishers 1993, 1–12, St. Feliu De Guixols, Spain, September 1992.
8. Chubykalo, A., V. R. Velasco, and F. García-Moliner, "Polar optical phonons at semiconductor interfaces," *Surf. Sci.*, Vol. 319, No. 1-2, 184–192, 1994.
9. Mora-Ramos, M. E. and D. A. Contreras-Solorio, "The polaron in a GaAs/AlAs quantum well," *Physica B*, Vol. 253, No. 3-4, 325–334, 1998.
10. Davydov, V. Yu., Yu. E. Kitaev, I. N. Goncharuk, A. N. Smirnov, J. Graul, O. Semchinova, D. Uffmann, M. B. Smirnov, A. P. Mirgorodsky, and R. A. Evarestov, "Phonon dispersion and Raman scattering in hexagonal GaN and AlN" *Phys. Rev. B*, Vol. 58, No. 19, 12899–12907, 1998.
11. Zi, J., X. Wan, G. Wei, K. Zhang, and X. Xie, "Lattice dynamics of zinc-blende GaN and AlN: I. Bulk phonons," *J. Phys.: Cond. Matt.*, Vol. 8, 6323–6328, 1996.
12. Bechstedt, F. and H. Grille, "Lattice dynamics of ternary alloys," *Phys. Stat. Sol. (B)*, Vol. 216, 761–768, 1999.
13. Bechstedt, F., J. Furthmüller, and J.-M. Wagner, "Electronic and vibrational properties of group-III nitrides: Ab initio studies," *Phys. Stat. Sol. (C)*, Vol. 0, 1732–1749, 2003.
14. Santos, A. M., E. C. F. Silva, O. C. Noriega, H. W. L. Alves, J. L. A. Alves, and J. R. Leite, "Vibrational properties of cubic Al<sub>x</sub>Ga<sub>1-x</sub>N and In<sub>x</sub>Ga<sub>1-x</sub>N ternary alloys," *Phys. Stat. Sol. (B)*, Vol. 232, 182–187, 2002.
15. Bougrov, V., M. E. Levinshtein, S. L. Rumyantsev, and A. Zubrikov, "GaN, AlN, InN, BN, SiC, SiGe," in *Properties of Advanced Semiconductor Materials*, Eds. M. E. Levinshtein, S. L. Rumyantsev and M. S. Shur, John Wiley, New York, 2001.
16. Palmer, D. W., <http://www.semiconductors.co.uk>.

# Electronic Spectrum Study of Parabolic $GaAs/Al_xGa_{1-x}As$ Superlattices

I. Rodriguez-Vargas, O. Y. Sanchez-Barbosa, D. A. Contreras-Solorio, and S. J. Vlaev

Unidad Académica de Física, Universidad Autónoma de Zacatecas

Calzada Solidaridad Esquina con Paseo la Bufa S/N, Zacatecas 98060, ZAC., México

**Abstract**— The electronic structure of finite parabolic  $GaAs/Al_xGa_{1-x}As$  superlattices is studied. A detailed analysis of the miniband formation is given and the importance of all system parameters is discussed. The dependence of the equidistant miniband separation on the superlattice size is revealed. A comparison with different theoretical methods and experimental data is presented. The calculations are conducted in the framework of the semi-empirical  $sp^3s^*$  tight-binding model including spin applying the Green function formalism and the Surface Green Function Matching Method (SGFM) method.

## 1. INTRODUCTION

The fast advancement in epitaxial growth techniques has permitted the construction of semiconductor layer systems with arbitrary potential profiles. In particular, the parabolic quantum well (PQW) [1], aside to the square one, is one of the most studied systems both from fundamental and technological points of view [2–7]. This is, partially, because its unique properties such as: equally spaced electronic spectrum, radiative transitions at the same oscillator frequency, interaction with light at the oscillator frequency irrespective of electron-electron interactions, i.e., independence on the number of electrons in the well and on an electric field applied across the well, the so called generalized Kohn theorem [8, 9].

Recently, PQW's have been implemented to study non-linear optical properties [10, 11], the quantum Hall effect [12, 13], charge and spin oscillations in 3D gases [14, 15], magnetic properties for the spin electronics [16, 17], and band gap discontinuities in materials with outstanding characteristics [18, 19].

From the technological point of view, PQW's and PQW superlattices (PQWSL's) can be used as polarization insensitive electroabsorptive modulators [6] and far-infrared resonant tunneling devices [7]. Maranowski et al. [7] have demonstrated the radiative decay through multiple evenly spaced energy levels in PQWSL's as well as an efficient injection when a chirped superlattice acts as an electron filter replacing the barrier.

Here, the miniband structure formation in  $GaAs/Al_xGa_{1-x}As$  parabolic quantum well superlattices within the spin-dependent  $sp^3s^*$  tight-binding semi-empirical model is considered. We study the miniband formation for electrons and holes of finite superlattices as a function of the system parameters, such as, the  $Al$  content, the well and barrier widths.

## 2. MODEL

The parabolic graded  $GaAs/Al_xGa_{1-x}As$  superlattice is constructed as follows: a) a single parabolic well with three fundamental regions: left and right  $Al_xGa_{1-x}As$  barriers of width  $d_B^L$  and  $d_B^R$ , and  $Al$  content  $x_L$  and  $x_R$ , respectively;  $GaAs/Al_xGa_{1-x}As$  quantum well of width  $d_W$  and  $Al$  content varying parabolically from the left barrier ( $x_L$ ) to the center ( $x = 0$ ), and from the center to the right barrier ( $x_R$ ); b) the single parabolic well of point a) is taken as period of the superlattice, so, the finite superlattice is obtained via  $N$  replicas of this period. In the present report the system is symmetrical, so, the left and right barriers are identical  $x_L = x_R = x_B$ . The next step is to embed the superlattice between two  $Al_xGa_{1-x}As$  homogeneous barriers.

The electronic structure calculations are performed within the lines of the spin-dependent  $sp^3s^*$  tight-binding model and the surface Green function matching method [21, 22]. The Green function of the external barriers is calculated by means of the transfer matrix method in the usual way, and the Green function of the superlattice region is computed through an algorithm already used to study this kind of quantum structures [21–23].

All calculations are performed at the center of the two-dimensional Brillouin zone for the (001) growth direction.

Table 1: Conduction miniband-structure formation of ten period PQWSL's for  $x_B = 0.21$ . The barrier and well widths are given in ML's, while the energy in eV. The energy origin is taken at the top of the *AlAs* valence band.

$d_B/2$	$E_0$		$E_1$
	$d_w = 30$	$d_w = 16$	$d_w = 30$
<i>SPQW</i>	2.155	2.196	2.255
100	2.155	2.196	2.255
40	2.155	2.196	2.255
30	2.155	2.196	2.255
20	2.155	2.196	2.255
10	2.155	2.196	2.255
5	2.155	2.195 – 2.199	2.254 – 2.257
2	2.155	2.183 – 2.213	2.248 – 2.273

Table 2: Valence miniband-structure formation of ten period PQWSL's for  $x_B = 0.21$ . The barrier and well widths are given in ML's, while the energy in eV. The energy origin is taken at the top of the *AlAs* valence band.

$d_B/2$	$E_0$		$E_1$	
	$d_w = 30$	$d_w = 16$	$d_w = 30$	$d_w = 16$
<i>SPQW</i>	0.525	0.503	0.505	0.481
100	0.525	0.503	0.505	0.481
40	0.525	0.503	0.505	0.481
30	0.525	0.503	0.505	0.481
20	0.525	0.503	0.505	0.481
10	0.525	0.503	0.505	0.481
5	0.525	0.503	0.505	0.488 – 0.469
2	0.525	0.503	0.508 – 0.506	0.494 – 0.449

### 3. RESULTS AND DISCUSSION

In Table 1 and 2 the miniband structure formation for electrons and holes is presented for ten period PQWSL's. The *Al* barrier concentration is fixed at  $x_B = 0.21$ . We have considered barriers from 200 ML's to 4 ML's for two well widths, 30 ML's and 16 ML's. We also have included a single PQW (SPQW) as a reference system. The energy is given in eV. The energies are measured from the top of the *AlAs* valence band. From Table 1 it is clear that for electrons there are two levels when  $d_W = 30$  ML's, while when  $d_W = 16$  ML's there is only one. This is due to the stronger attractiveness as the well width is increased. PQWSL's behave practically like isolate PQW's from barrier widths of 200 ML's to 20 ML's, in both cases. An evident level splitting is presented for the ground electron level for  $d_W = 16$  ML's and barrier widths of 10 ML's and 4 ML's, with energy-miniband width of 4 meV and 30 meV, respectively. For  $d_W = 30$  ML's the level splitting is present at the same barrier widths as in the case of the electron ground level ( $d_W = 16$  ML's), but for the first excited level. The corresponding energy-miniband widths are 3 meV and 25 meV, respectively. In the case of holes a similar trend is observed as the well width is increased, Table 2. The level splitting is presented only for the ground light hole state in both cases,  $d_W = 30$  ML's and  $d_W = 16$  ML's. The energy-miniband width is 2 meV for  $d_W = 30$  ML's and  $d_B = 4$  ML's, while for  $d_W = 16$  ML's we have 19 meV and 45 meV for barrier widths of 10 ML's and 4 ML's, respectively.

In Fig. 1, we present the density of states of ten period PQWSL's for conduction ((a) and (c)) and valence ((b) and (d)) band with the following set of parameters:  $d_W = 16$  ML's,  $d_B = 4$  ML's,  $x_B = 0.21$  ((a) and (b)) and  $x_B = 0.30$  ((c) and (d)). We also include an isolated PQW for reference. We can see clearly the level splitting for the electron basic level as well as for the basic light hole one. It is important to mention that the number of peaks expected in Fig. 1 are ten,

however the precision used in the calculations does not resolve them properly.

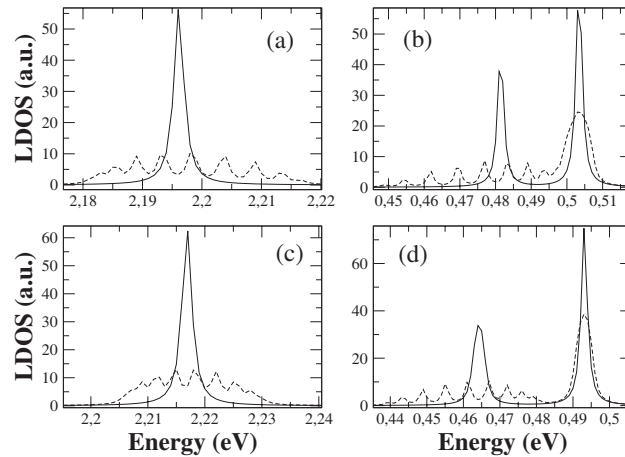


Figure 1: Density of states versus energy of ten period PQWSL's for conduction ((a) and (c)) and valence band ((b) and (d)), for  $x_B = 0.21$  ((a) and (b)) and  $x_B = 0.30$  ((c) and (d)), well width of 16 ML's and barrier width of 4 ML's. The solid line represents an isolated PQW and the dashed line the PQWSL.

Menendez et al. have performed light scattering experiments in parabolic quantum wells [2]. They found that the energy levels are not equally spaced. For a sample quoted to have  $x_B = 0.3$ ,  $d_W = 510 \text{ \AA}$ , they reported  $E_{01} = 25.2 \text{ meV}$  and  $E_{12} = 23.6 \text{ meV}$  with an error of  $0.2 \text{ meV}$ . They attributed the discrepancy to the fact that the structure consist of a large number of square quantum wells rather than a parabolic graded profile. Moreover, from resonance Raman scattering they found the value  $x_B = 0.25$  in disagreement with the value  $x_B = 0.3$  deduced from the growth parameters. For the same system parameters,  $d_W = 510 \text{ \AA}$  and  $x_B = 0.3$  ( $x_B = 0.25$ ), we obtain  $E_{01} = 22 \text{ meV}$  ( $21 \text{ meV}$ ) and  $E_{12} = 22 \text{ meV}$  ( $19 \text{ meV}$ ). In the case of  $x_B = 0.3$  our results are also in closed agreement to the value ( $22.3 \text{ meV}$ ) reported by Miller et al. [1]. Shen et al. have studied the energy levels, wave functions and tunability of two coupled PQW's under applied electric field by means of the transfer-matrix method [4]. They report a value of  $160 \text{ meV}$  (measured from the band edge) for the basic electron level when  $d_B = 30 \text{ \AA}$ ,  $d_W = 100 \text{ \AA}$ , and well depth of  $224 \text{ meV}$ , without bias. We obtain for the same system parameters a value of  $173 \text{ meV}$ .

#### 4. CONCLUSION

In summary, we have computed the electronic structure of parabolic  $GaAs/Al_xGa_{1-x}As$  superlattices within the spin-dependent  $sp^3s^*$  tight-binding model. Clear evidence of the miniband structure formation and the equally spaced energy spectra is found. We also compared our results with the theoretical and experimental data available, obtaining good agreement.

#### ACKNOWLEDGMENT

This work was partially supported by Secretaría general de la UAZ and Consejo Zacatecano de Ciencia y Tecnología (COZCYT).

#### REFERENCES

1. Miller, R. C., A. C. Gossard, D. A. Kleinman, and O. Munteanu, "Parabolic quantum wells with the  $GaAs-Al_xGa_{1-x}As$  system," *Phys. Rev. B*, Vol. 29, No. 6, 3740–3743, 1984.
2. Menéndez, J. and A. Pinczuk, "Light scattering determinations of band offsets in semiconductor heterostructures," *IEEE Journal of Quantum Electronics*, Vol. 24, No. 8, 1698–1711, 1988.
3. Yuen, W.-P., "Exact analytic analysis of finite parabolic quantum wells with and without a static electric field," *Phys. Rev. B*, Vol. 48, No. 23, 17316–17320, 1993.
4. Shen, W. P. and M. L. Rustgi, "Two coupled parabolic wells under an electric field," *J. Appl. Phys.*, Vol. 74, No. 6, 4006–4014, 1993.
5. Vlaev, S., V. R. Velasco, and F. García-Moliner, "Tight-binding calculation of electronic states in an inverse parabolic quantum well," *Phys. Rev. B*, Vol. 51, No. 11, 7321–7324, 1995.

6. Choy, W. C. and E. H. Li, "Polarization-insensitive electroabsorption by use of quantum well interdiffusion," *Appl. Opt.*, Vol. 37, No. 9, 1674–1681, 1998.
7. Maranowski, K. D. and A. C. Gossard, "Far-infrared electroluminescence from parabolic quantum well superlattices excited by resonant tunneling injection," *J. Appl. Phys.*, Vol. 88, No. 1, 172–177, 2000.
8. Kohn, W., "Cyclotron resonance and de Haas-van Alphen oscillations of an interacting electron gas," *Phys. Rev.*, Vol. 123, No. 4, 1242–1244, 1961.
9. Brey, L., N. F. Johnson, and B. Halperin, "Optical and magneto-optical absorption in parabolic quantum wells," *Phys. Rev. B*, Vol. 40, No. 15, 10647–10649, 1989.
10. Wang, G. -H., Q. Guo, and K.-X. Guo, "Third-order nonlinear optical properties of parabolic and semiparabolic quantum wells," *Phys. Stat. Sol. (B)*, Vol. 238, No. 1, 75–80, 2003.
11. Zhang, L. and H.-J. Xie, "Electric field effect on the second-order nonlinear optical properties of parabolic and semiparabolic quantum wells," *Phys. Rev. B*, Vol. 68, No. 23, 235315, 2003.
12. Sergio, C. S., G. M. Gusev, J. R. Leite, E. B. Olshanetskii, A. A. Bykov, N. T. Moshegov, A. K. Bakarov, A. I. Toropov, D. K. Maude, O. Estibals, and J. C. Portal, "Coexistence of a two- and three-dimensional Landau states in a wide parabolic quantum well," *Phys. Rev. B*, Vol. 64, No. 11, 115314, 2001.
13. Gusev, G. M., A. A. Quivy, T. E. Lamas, J. R. Leite, O. Estibals, and J. C. Portal, "Quantum hall ferromagnet in a parabolic well," *Phys. Rev. B*, Vol. 67, No. 15, 155313, 2003.
14. Bratschitsch, R., T. Muller, R. Kersting, G. Strasser, and K. Unterrainer, "Coherent terahertz emission from optically pumped intersubband plasmons in parabolic quantum wells," *Appl. Phys. Lett.*, Vol. 76, No. 24, 3501–3503, 2000.
15. Gusev, G. M., A. A. Quivy, T. E. Lamas, J. R. Leite, O. Estibals, and J. C. Portal, "Transport of the quasi-three-dimensional hole gas in a magnetic field in the ultra-quantum limit," *Physica E*, Vol. 22, Nos. 1–3, 336–340, 2004.
16. Da Cunha Lima, I. C., G. M. Gusev, and J. R. Leite, "Spin polarization by tilted magnetic field in wide  $Ga_{1-x}Al_xAs$  parabolic quantum wells," *Journal of Superconductivity*, Vol. 18, No. 2, 169–173, 2005.
17. Efros, A. L. and E. I. Rashba, "Theory of electric dipole spin resonance in a parabolic quantum well," *Phys. Rev. B*, Vol. 73, No. 16, 165325, 2006.
18. Chung, S. J., N. Dai, G. A. Khodaparast, J. L. Hicks, K. J. Goldammer, F. Brown, W. K. Liu, R. E. Doezema, S. Q. Murphy, and M. B. Santos, "Electronic characterization of InSb quantum wells," *Physica E*, Vol. 7, Nos. 3–4, 809–813, 2000.
19. Ekpunobi, A. J. and A. O. E. Animalu, "Band offsets and properties of AlGaAs/GaAs and AlGaIn/GaN material systems," *Superlattices and Microstructures*, Vol. 31, No. 5, 247–252, 2002.
20. Vlaev, S. J., I. Rodríguez-Vargas, L. M. Gaggero-Sager, and V. R. Velasco, "An alternative way of calculating the superlattice Green function for discrete media," *Surf. Sci.*, Vol. 554, Nos. 2–3, 245–252, 2004.
21. García-Moliner, F. and V. R. Velasco, *Theory of Single and Multiple Interfaces: The Method of Surface Green Function Matching*, Word Scientific, Singapore, 1993.
22. Vlaev, S., V. R. Velasco, and F. García-Moliner, "Electronic states in graded-composition heterostructures," *Phys. Rev. B*, Vol. 49, No. 16, 11222–1229, 1994.
23. Vlaev, S. and D. A. Contreras-Solorio, "Electronic states in diffused quantum wells," *J. Appl. Phys.*, Vol. 82, No. 8, 3853–3856, 1997.

# Transport Properties of Delta Doped Field Effect Transistor

O. Oubram and L. M. Gaggero Sager

Facultad de Ciencias, Universidad Autónoma del Estado de Morelos  
Av. Universidad 1001, Col. Chamilpa, CP 62209, Cuernavaca, Morelos, Mexico

**Abstract**— The first calculation of mobility and conductivity between source and drain as function of gate voltage in a  $\delta$ -doped Field Effect Transistor is presented. The calculation was performed with a model for the  $\delta$ -FET that was shown in [1]. The mobility was calculated using a phenomenological expression that was presented in [2]. That expression does not have empirical form, neither empirical parameter. For the first time a phenomenological expression of the conductivity is presented, which is derived from the mobility expression. The conductivity shows three different regions: a parabolic region and two linear regions. The parabolic region represents the region at which the conduction channel begins to close. On the other hand, the mobility shows a more different behavior. In the mobility there are four regions. These regions correspond to the disappearance of the different conduction channels that form the subbands of the delta-doped quantum well. The different behavior between mobility and conductivity relies on the depletion of the delta-doped quantum well as the gate potential grows.

## 1. INTRODUCTION

The system we are interested in is the  $\delta$ -FET in *GaAs* proposed originally by Schoubert, Ploog and collaborators [3, 4]. They made a field effect transistor in which the channel is formed by growing an *n* type *Si* delta-doped well located between the terminals of the source and the drain of a regular *GaAs* field effect transistor (see Figure 1). The presence of this *n* type quantum well produces a localized two-dimensional electronic gas (2DEG), which participates directly in the conduction channel. The use of this type of doping in semiconductor devices yields a great improvement in the performance of ultra high frequency optoelectronic devices [5]. The  $\delta$ -FET is also expected to exhibit a higher transconductance [4] than a high electron mobility transistor due to the proximity of the delta channel to the gate.

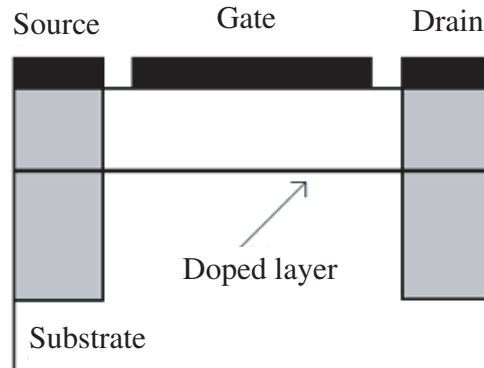


Figure 1: Schematic representation of a  $\delta$ -FET en GaAs.

## 2. THEORETICAL BACKGROUND

The  $\delta$ -doping technique allows one to obtain an extremely sharp doping profile and a high-density-doped layer. Potentials of this system is formed by a metal-semiconductor contact (Schottky barrier), followed by the *n*-type delta-doped quantum-well system. The presence or not of a confined electronic gas depends on the parameters used in the construction of the system.

If there is electronic confinement, our model for describing the conduction band of the semiconductor in the  $\delta$ -FET system has, as its main assumptions, that the potential profile is described by the depletion region approach in the proximity of the metal-semiconductor contact.

$$V_{dep}(z) = \frac{2\pi e^2}{\epsilon_r} N_d (z + d - l)^2 \quad (1)$$

where  $N_d$  is the background impurity density,  $\epsilon_r$  is the electric permittivity constant of GaAs, and  $l$  is the screening distance for the electric field:

The second assumption is that, in the region not too close to the interface, the delta-doped well potential is described within a self-consistent Thomas-Fermi approach [6] by:

$$V_n(z) = -\frac{\alpha_n^2}{(\alpha_n|z| + z_{0n})^4} \quad (2)$$

$\alpha_n = 2/(15\pi)$  and  $Z_{0n} = (\alpha_n^3/\pi N_{2de})^{1/5}$ , is the distance at which the  $n$ -type delta-doped well is positioned,  $N_{2de}$  is the two-dimensional impurity density of the  $n$ -type delta-doped quantum-well. The entire potential is mathematically presented by the following expression [7]:

$$V(z) = V_{dep}(z)\theta(l - z - d) + V_n(z) \quad (3)$$

where  $\theta$  is the unit-step function.

The starting parameters for n-type  $\delta$ -FET in GaAs are:

$$m^* = 0.067, \epsilon_r = 12.5, n_{2D} = 7.5 \times 10^{12} \text{cm}^{-2}$$

(Figure 2) shows the confining potential and the sub-band energies with their envelope wave functions  $n_{2D} = 7.5 \times 10^{12} \text{cm}^{-2}$ , the background impurities is of  $N_d = 10^{18} \text{cm}^{-3}$  at  $T = 0\text{K}$ . Here, n-type delta-doped quantum-well is located at 300 Å from the interface. The dashed curve represents the obtained confining potential profile and the solid curves represent the wave functions, potential profile, eigenvalues and eigenfunctions. Eigenfunctions have an antisymmetric form (extension to right direction) this phenomena due to Schottky potential contact, (Figure 2) presents for  $V_c = 500 \text{meV}$ , eigenvalues  $E_f - E_1 = 248.18 \text{meV}$ ,  $E_f - E_2 = 228.88 \text{meV}$ ,  $E_f - E_3 = 191.15 \text{meV}$  and  $E_f - E_4 = 97.77 \text{meV}$ , with  $E_f$  (Fermi level) is taken to be at the bottom of conduction band.

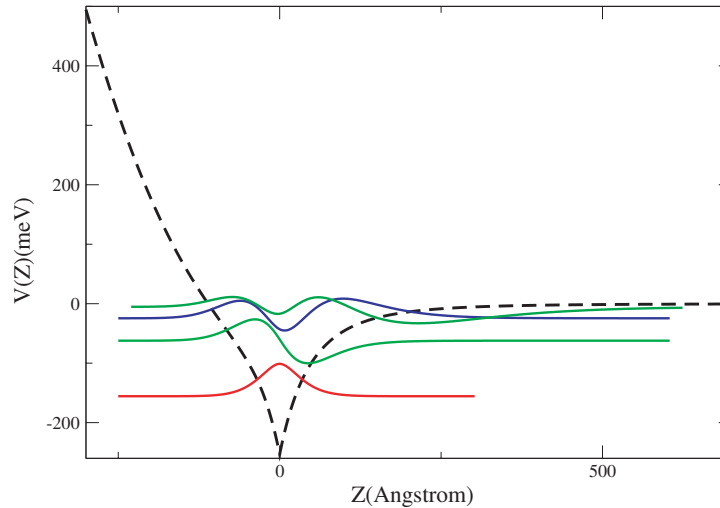


Figure 2: Conduction band, eigenvalues and eigenfunctions for  $V_c = 500 \text{meV}$ .

Based on the Thomas Fermi approximation to this  $\delta$ -FET, we study the electron transport properties of the system. This method also allows us to study the transport properties of the system. We only consider the ionized donor scattering mechanism, because it is the most important at low temperature. The Coulomb scattering potential due to the ionized impurities is considered as distributed randomly in the doped layer. Finally, we take the ratio of the mobility of ( $V_c = 0 \text{meV}$ ) to ( $V_c \neq 0 \text{meV}$ ) the potential contact of the gate.

$$\mu_{rel} = \frac{\mu_{V_c \neq 0}}{\mu_{V_c = 0}} = \frac{\int \int_{IR^2} \rho_e^{V_c=0}(z') \cdot \rho_{imp}^{V_c=0}(z) \cdot |z| \cdot dz \cdot dz'}{\int \int_{IR^2} \rho_e^{V_c \neq 0}(z') \cdot \rho_{imp}^{V_c \neq 0}(z) \cdot |z| \cdot dz \cdot dz'} \quad (4)$$

$\rho_e^{V_c \neq 0}(z')$  ( $\rho_e^{V_c=0}(z')$ ) is the electron density where the potential contact of the gate is  $V_c \neq 0 \text{meV}$  ( $V_c = 0 \text{meV}$ ) and  $\rho_{imp}^{V_c \neq 0}(z)$  ( $\rho_{imp}^{V_c=0}(z)$ ) is the impurity density where the potential contact of the gate is  $V_c \neq 0 \text{meV}$  ( $V_c = 0 \text{meV}$ ). The former expression can be put in the following form:

$$\mu_{rel} = \frac{\sum_1^{ne} \int_{IR} |F_e^{V_c=0}(z')|^2 \cdot (k_F^{V_c=0} - E_i^{V_c=0}) \cdot |z'| \cdot dz'}{\sum_1^{ne} \int_{IR} |F_e^{V_c \neq 0}(z')|^2 \cdot (k_F^{V_c \neq 0} - E_i^{V_c \neq 0}) \cdot |z'| \cdot dz'} \quad (5)$$

where  $F_e^{V_c \neq 0}(z')$ ,  $k_F^{V_c \neq 0}$  and  $E_i^{V_c \neq 0}$ , ( $F_e^{V_c=0}(z')$ ,  $k_F^{V_c=0}$  and  $E_i^{V_c=0}$ ) are the envelope function, the Fermi level and the  $i$ th level respectively of the  $V_c = 0$  ( $V_c \neq 0$ ), the former expression is valid for  $T = 0$  K.

### 3. RESULTS AND DISCUSSION

The (Figure 3) contains the curve of relative mobility *vs.*  $V_c$ . The mobility shows two different behaviors. The first is between 0 meV and 1200 meV where we have the mobility ratio is rising from 1 to 2.06. The second is between 1200 meV and 1500 meV where the mobility is rising also from 2.06 to 4.52. In the first interval, the mobility ratio creases mildly but in the second, it increases rapidly, we can see the potential contact affect more the mobility ratio when  $V_c$  superior 1200 meV. In the mobility ratio characteristic there are four regions, in other words there are three transitions, the first from 150 meV to 200 meV, the second from 600 meV to 650 meV and the last one from 1200 meV to 1250 meV, the responsible of this transitions is the change in the number of state in  $\delta$ -doped quantum well.

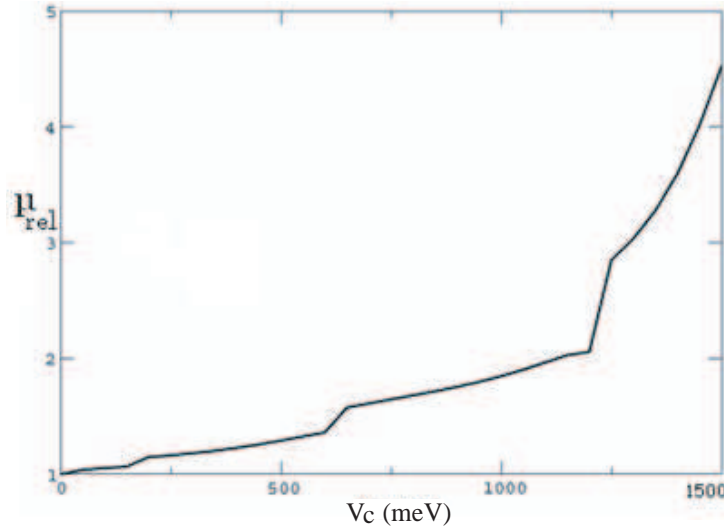


Figure 3: Mobility calculations versus the contact potential ( $V_c$ ) in meV.

$$\sigma_{rel} = n_{rel} \cdot \mu_{rel} \quad (6)$$

$$n_{rel} = \frac{\sum_1^{ne} (k_F^{V_c=0} - E_i^{V_c=0})}{\sum_1^{ne} (k_F^{V_c \neq 0} - E_i^{V_c \neq 0})} \quad (7)$$

$\sigma_{rel}$ : Relative conductivity,  $n_{rel}$ : Relative electronic density of the delta-doped quantum well,  $\mu_{rel}$ : Relative mobility.

Relative conductivity *vs.*  $V_c$  characteristic shows fluctuation of conductivity ratio as a function of  $V_c$ , there are two zones type, the first zone type is linear, it is in [200 meV, 600 meV] and [1250 meV, 1500 meV]. The second zone type is parabolic, it is in [650 meV, 200 meV].

The conductivity ratio has a mild growth when  $V_c$  is in [0 meV, 650 meV] because the mobility ratio rise slowly from 1 to 1.57, in other word the interaction of impurities and free electrons are not low and the variation of electron density in  $\delta$ -doped quantum well is practically constant. On the contrary, when  $V_c \geq 650$  meV the (Figure 4) shows that the conductivity decreases, the reason being that the conduction channel begins to close, due to the strong decrease of confined electrons in the delta-doped well.

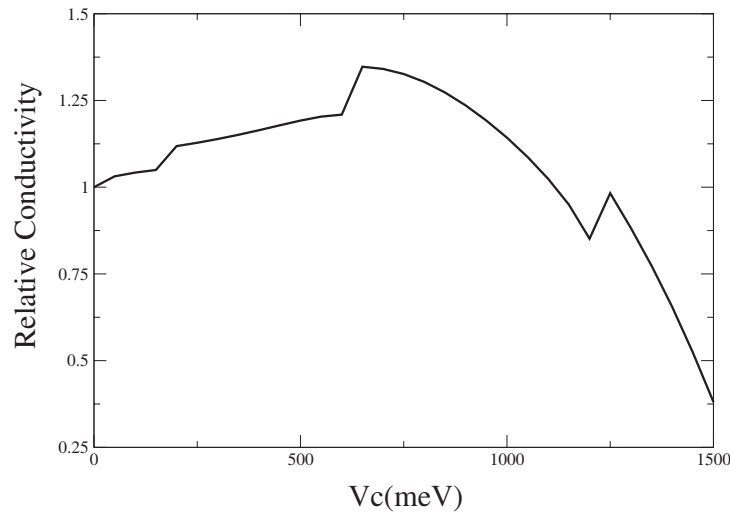


Figure 4: Conductivity calculations versus the contact potential ( $V_c$ ) in meV.

The  $\delta$ -FET permits to have a negative differential resistance (NDR), NDR is seen in intervals [650 meV, 1200 meV] and in [1250 meV, 1500 meV], In electronics we learn that an amplifier coupled with a properly designed positive feedback circuit can be made into an oscillator. We find the optimum  $V_c = 650$  meV Contact potential to achieve the maximum conductivity.

#### 4. CONCLUSIONS

In Summary, we have presented an expression to calculate the relative electronic mobility. In this way it is possible to compare in a reasonable way the mobilities of  $V_c = 0$  meV and  $V_c \neq 0$  meV. This phenomenological formula for the mobility ratio allows us to study the range of parameters governing this problem and to get the best choice of them.

#### ACKNOWLEDGMENT

L. M. G-S acknowledges UAEM (State Autonomous University of Morelos, at Cuernavaca, Mexico) for support. O. O. acknowledges support from Secretaria de Relaciones Exteriores, Mexican Government.

#### REFERENCES

1. Gaggero-Sager, L. M. and R. Pérez-Alvarez, "A simple model for delta-doped field-effect transistor electronic states," *J. App. Phys.*, Vol. 78, No. 7, 4566–4569, 1995.
2. Rodriguez-Vargas, I., L. M. Gaggero-Sager, and V. R. Velasco, "Thomas-Fermi-Dirac theory of the hole gas of a double p-type delta-doped GaAs quantum wells," *Surf. Sci.*, Vol. 537, No. 1, 75–83, 2003.
3. Ploog, K., M. Hauser, and A. Fischer, *Paper Presented at the 18th International Symp. GaAs Related Compounds*, Heraklion, Crete, 1987.
4. Schubert, E. F., A. Fischer, and K. Ploog, *IEEE Transactions on Electron Devices*, Vol. 33, 625, 1986.
5. Kwok, K. Ng., "Characteristics of p- and n-channel poly-Si/Si<sub>1-x</sub>Gex/Si sandwiched conductivitymodulated thin-film transistors," *IEEE* 0018-9383, 1996.
6. Ioriatti, L., "Thomas-Fermi theory of  $\delta$ -doped semiconductor structures: Exact analytical results in the high-density limit," *Phys. Rev. B*, Vol. 41, No. 12, 8340–8344, 1990.
7. Gaggero-Sager, L. M. and R. Perez-Alvarez, "A simple model for delta-doped field-effect transistor electronic states," *J. Appl. Phys.*, Vol. 78, No. 7, 4566–4569, 1995.

# Double Structure of the Wind Jet through the Tsushima Strait

Teruhisa Shimada and Hiroshi Kawamura

Center for Atmospheric and Oceanic Studies  
Graduate School of Science, Tohoku University, Sendai, Japan

**Abstract**— We have investigated the northeasterly/southwesterly wind jets blowing through the Tsushima Strait from two case studies. Using high-resolution winds derived from SAR, we have presented the detailed structure of wind in the strait. The general flow is generally close to geostrophic wind in the strait, inferring from the sea level pressure fields. Wind jets are induced by two channels and by the terrestrial gap at the center of the Tsushima Island. The wind jets are clearly separated from the coastlines.

## 1. INTRODUCTION

The Tsushima Strait is a generic term indicating the sea area between the Korean Peninsula and the Japanese archipelago, with the Japanese islands of Honshu to the east, Kyushu to the south and the Goto Islands to the southeast (Figure 1). In the center of the strait, a slender island, the Tsushima Island is located along the strait. This island principally consists of two mountainous islands. The Tsushima Island divide the strait into eastern and western channels; the width and maximum depth are 140 km and 110 m in the eastern channel, and 40 km and 200 m in the western channel, respectively. Both channels connect the East China Sea and the Japan Sea.

From these geographical conditions, the Tsushima Strait is one of the most important sea areas where the continuous and intense monitoring researches are required from oceanographic and meteorological point of views as well as marine security point of view. Extensive previous studies have investigated the Tsushima Strait hydrography by considering wind effects on it. However, higher-resolution and wider-area wind observations are required for better understanding of the oceanographic and meteorological environment because of the complex coastal topography of the region. This is because few studies pay attention to the formation of wind jets in the strait, wind jet structures, and the role of the Tsushima Island on the formation of the wind jets. These are open issues at the present stage.

The purpose of this paper is to investigate the wind blowing through the Tsushima Strait by using high-resolution satellite wind measurements. We look into the evolution and distribution of the wind jets during representative time periods and illustrate the contribution of the Tsushima Island to the wind jet formation. Specific questions we would like to address are: First question is typical structures of the wind jets found in the Tsushima Strait. When the wind blows through the Tsushima Strait in southwest-northeast direction, strong winds are formed. Second, what are the roles of the Tsushima Island on the formation of the wind jets?

## 2. DATA

We analyze wind fields derived from two SARs. They are the European Space Agency (ESA) Environmental Satellite (ENVISAT) Advanced Synthetic Aperture Radar (ASAR) and the Canadian RADARSAT-1. Both SARs operate at C-band (5.3 GHz). While RADARSAT operates in horizontal (HH) polarization, ENVISAT/ASAR operates in HH or vertical (VV) polarization. In this study, we use wide-swath or ScanSAR mode products. That is, the ENVISAT/ASAR Wide-swath mode images covers an area of approximately  $500 \times 500$  km, with a pixel size of 75 m. The RADARSAT ScanSAR Narrow mode image covers an area of approximately  $300 \times 300$  km, with a pixel size of 25 m.

Wind speed maps are derived from the ENVISAT/ASAR and RADARSAT images by applying SAR wind retrieval by using CMOD IFR2 scatterometer model function [1] and wind direction from objective analysis data (GPV: Grid Point Data). In cases of HH polarization images, a polarization ratio conversion factor [2] is applied. While the C-band geophysical model function is originally developed for VV polarized radar cross section, the polarization ratio conversion factor enables to convert it to HH polarized radar cross section. It has been shown by numerous studies that wind speeds can be retrieved from ENVISAT/ASAR [3] and RADARSAT-1 [4] with a root mean square error of less than 2 m/s and with negligible bias.

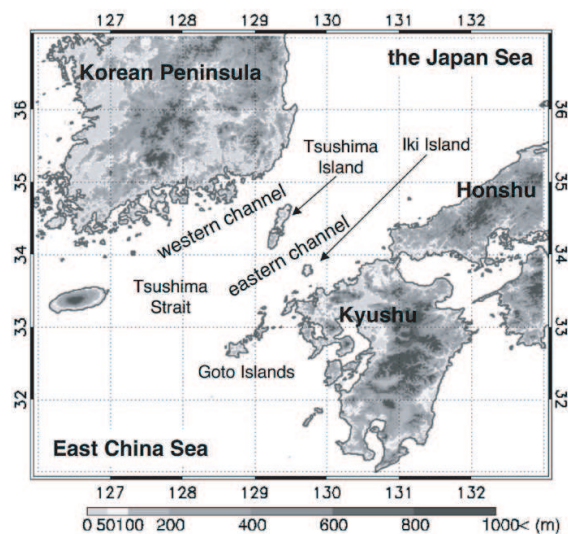


Figure 1: Map of the study area. The color scale indicates the terrain elevation. Geographical locations referred to in this paper are also shown.

### 3. CASE STUDIES: NORTHEASTERLY WIND

Figure 2(a) shows sea level pressure and surface wind fields of NCEP reanalyses at 00:00 UTC 18 Dec. 2002. After a cyclone has passed the south of Japan, a strong anticyclone develops over the Eurasia continent and starts to generate a surge of northerly winds. This is a typical situation associated with East Asian winter monsoon. Surface winds over the Japan Sea are northeasterly. It is suggested that the wind blows toward the Tsushima Strait with converging. The isobars do not cross the strait. The isobars run west-southwest and east-northeast and align with the strait at an angle. This suggests that the geostrophic balance is satisfied on some level.

Let us now look into the wind fields in detail using SAR-derived wind field. Figure 2(b) shows

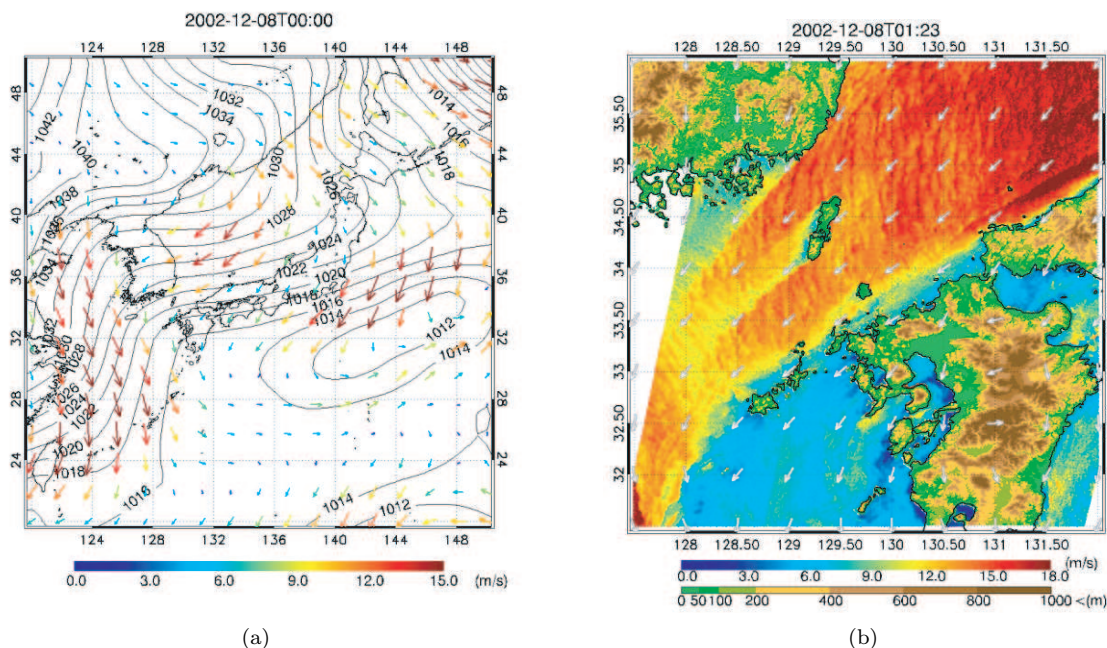


Figure 2: (a) Sea level pressure and 10-m winds from the NCEP reanalyses at 00:00 UTC 8 December 2002. (b) High-resolution wind field derived from ENVISAT/ASR at 01:23 UTC 8 December 2002. Arrows indicate wind directions derived from GPV data.

the wind field derived from an ENVISAT/ASAR image. The image was acquired at 0123 UTC 8 December 2002. The arrows indicate wind direction from the GPV data. Wind speeds are high ( $\sim 18$  m/s) at the Japan Sea side because of wind convergence. The open coastlines of the Korean Peninsula and the Japanese archipelago may enforce the convergence. The winds are detached at the promontories of the Korean Peninsula and the Japanese archipelago and weak wind regions exist along the both sides of the strait. It is noteworthy that we can not obtain any signs of the wind jet from land observations. It is apparent that two wind jets are formed at the western and eastern channels. Along the streamlines, wind speed maximum ( $\sim 15$  m/s) are observed just after passing through the Tsushima. In contrast, a weak wind region extends southwestward in the lee of the Tsushima. The wind speed differences ( $\sim 3$  m/s) keeps over the 200-km downwind.

#### 4. CASE STUDIES: SOUTHWESTERLY WIND

Figure 3(a) shows sea level pressure and surface wind fields of NCEP reanalyses at 18:00 UTC 3 June 2001. A high-pressure system located in the East China Sea. Southwesterly and westerly winds are observed on the northwest of the high-pressure systems, and it should be noted that the winds are generated just near the Tsushima Strait. Thus, the winds blow into the strait.

Figure 3(b) shows the wind field derived from a RADARSAT image. The image is acquired at 2125 UTC 3 June 2001. The arrows indicate the GPV wind direction. Westerly winds blow into the Tsushima Strait. In this case, three wind jets are apparent on the eastern side of the Tsushima. The westerly winds rush through the northern and southern tips of the Tsushima and forms two jets in the western and eastern channels. It should be noted that the wind jets are completely within the channels and that they do not blow cross the coast. Maximum wind speed are observed near the tips of the Tsushima. Another remarkable character is a strong winds extending from the terrestrial gap of the center of Tsushima. In the lee of northern and southern mountains of the Tsushima, weak wind regions with speeds less than 8 m/s are apparent. This wind field is also relatively close to the geostrophic winds. It is not so clear in the sea level field from the  $2.5^\circ$ -gridded NCEP reanalyses because of its low spatial resolution. However, it is confirmed from 10-km-gridded sea level field from the GPV data (not shown).

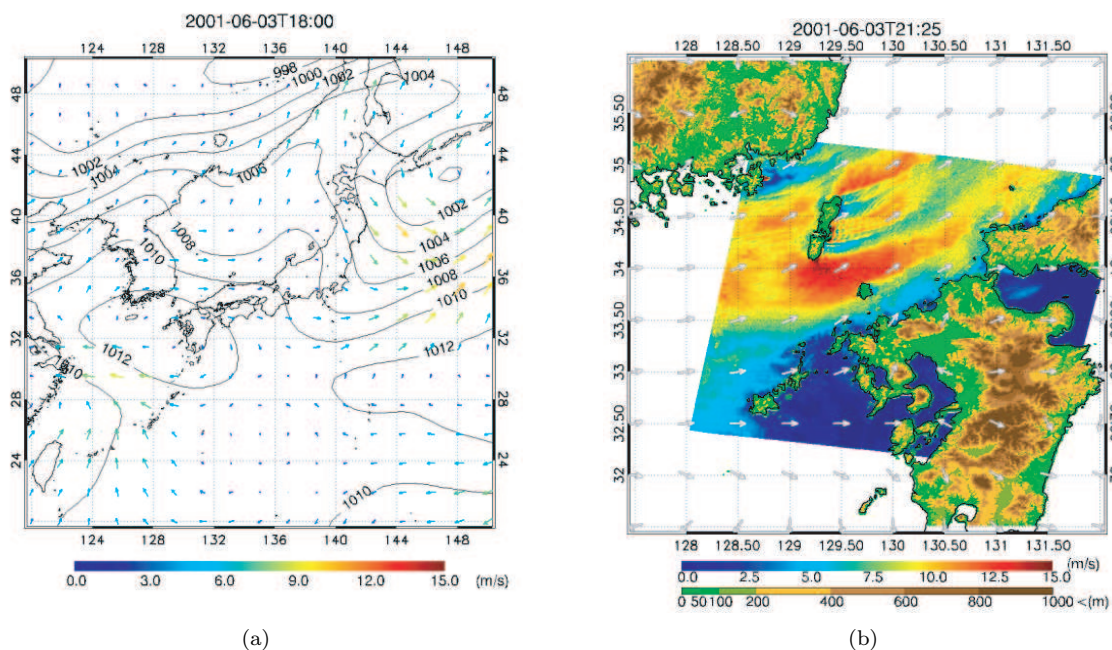


Figure 3: (a) Sea level pressure and 10-m winds from the NCEP reanalyses at 18:00 UTC 3 June 2001. (b) High-resolution wind field derived from RADARSAT at 21:25 UTC 3 June 2001. Arrows indicate wind directions derived from GPV data.

## 5. CONCLUSIONS

We have investigated the northeasterly/southwesterly wind jets blowing through the Tsushima Strait from two case studies. Using high-resolution wind data derived from SAR, we have presented the detailed structure of wind in the strait. The general flow is generally close to geostrophic wind, inferring from the sea level pressure fields. Wind jets are induced by two channels and by the terrestrial gap at the center of the Tsushima. The wind jets are clearly separated from the coastlines. Using the model simulations, we investigate the atmospheric structures of these cases.

## ACKNOWLEDGMENT

ENVISAT/ASAR images are provided by European Space Agency. We purchased the RADARSAT image from ImageONE Co., Ltd. The GPV MSM data were provided by the Japan Meteorological Agency. This study is partly supported by Exploratory Research Program for Young Scientists of Tohoku University, and by Grants-in-Aid for Scientific Research of Japanese Ministry of Education, Culture, Sports, Science and Technology.

## REFERENCES

1. Quilfen, Y., B. Chapron, T. Elfouhaily, K. Katsaros, and J. Tournadre, "Observation of tropical cyclones by high-resolution scatterometry," *J. Geophys. Res.*, Vol. 103, 7767–7786, 1998.
2. Thomson, D. R. and R. C. Beal, "Mapping high-resolution wind fields using synthetic aperture radar," *Johns Hopkins Univ. Tech. Dig.*, Vol. 21, 58–67, Jan. 2000.
3. Kerbaol, V. and F. Collard, "SAR-derived coastal and marine applications: From research to operational products," *IEEE J. Oceanic Engineering*, Vol. 30, No. 3, 472–486, 2005.
4. Monaldo, F. M., D. R. Thompson, W. G. Pichel, and P. Clemente-Colón, "A systematic comparison of QuikSCAT and SAR ocean surface wind speeds," *IEEE Trans. Geosci. Remote Sensing*, Vol. 42, No. 2, 283–291, 2004.

# Surface Wave Parameters Retrieval in Coastal Seas from Spaceborne SAR Image Mode Data

Jian Sun<sup>1,2</sup> and Hiroshi Kawamura<sup>1</sup>

<sup>1</sup> Graduate School of Science, Tohoku University, Sendai, Japan

<sup>2</sup> Physical Oceanography Laboratory, Ocean University of China, Qingdao, China

**Abstract**— We have developed a retrieval scheme of surface wave parameters (wave height and wave propagation direction) from ERS Synthetic Aperture Radar (SAR) image mode data in coastal seas around Japan. In this study, we investigated the energy of simulated SAR spectrum at different wind speed using nonlinear wave-SAR imaging mechanism, derived the criteria to differentiate swell from wind waves, and accordingly processed SAR images containing swell and wind waves in different way respectively. SAR spectra are converted to surface wave spectra of swell-dominated or wind-wave dominated cases. The SAR spectrum and SAR-derived wind speed are used for the derivation of surface wave spectrum. The wind-wave dominated case and swell-dominated case are differentiated by the wind speed of 6 m/s, and processed in different ways because of their different nonlinear degree. It is indicated that the cutoff wavelength for retrieval of the wind-wave dominated spectrum is proportional to the root of significant wave height, which is consistent with the results of previous studies. We generated 66 match-ups coupling the SAR sub-images and the in-situ surface wave parameters, which were measured by the wave gauges installed in near-shore seas. Among them, the number of swell-dominated case is 57, and the number of wind-wave dominated case is 9. The SAR-derived and in-situ significant wave heights agree well with the bias of 0.24 m, the RMS error 0.92 m and the correlation coefficient of 0.66. The averaged absolute deviation of wave propagation directions is  $18.4^\circ$ , and the agreement tendency does not depend on the wave height. It is proven through the comprehensive validation that the developed SAR surface wave spectrum has high accuracy in the Japanese coastal seas.

## 1. INTRODUCTION

Synthetic Aperture Radar (SAR) is one of the most efficient instruments to observe sea surface wave field in a large scope with high resolution. The effort to retrieve surface wave information from SAR data has never stopped. It is generally accepted that for intermediate incident angle like ERS SAR, long waves detected by SAR are due to the existence of decimetric Bragg waves modulated by these long waves. At different phase of long waves (including wind waves and swell), there is the different modulation effect to Bragg waves, which makes long waves appear in SAR images as the wave-like stripes pattern. The modulation of long waves to Bragg waves includes tilt modulation, hydrodynamic modulation and velocity bunching and the modulation transfer function are investigated by some authors [1, 2]. On the basis of the modulation theories [3], a closed spectral integral transform relation between SAR spectra and wave spectra has been proposed and widely accepted [4].

To retrieve wave parameters from SAR data is not a strait-forward procedure. One of the retrieval methods called MPI method [4, 5]. The main idea of the MPI scheme is to use WAM model spectra as first-guess spectra to eliminate the  $180^\circ$  directional ambiguity and augment the spectrum information beyond the azimuthal cut-off. In another scheme call SPRA [6], only SAR image spectra and scatterometer wind vector measurement are needed as input in this model. The model was validated with SAR wave mode data.

Coastal area is important for human activities. The surface wave dynamics in the coastal area is much more complex than that in the deep ocean. It is known that the wave model result is much hampered by the dominance of swell and the dramatic change of the water depth in coastal area. As the result, the direct observation of coastal waves from SAR becomes an important way to acquire wave information. ASAR single look complex (SLC) data is used to extract ocean wave fields near the coast of France recently [7]. However, the application of the image mode SAR images containing wave information is much limited because of the poor knowledge of the retrieval of wave parameters from SAR scene and its validation in coastal areas.

In this study, wave information such as wave height, wave direction and cutoff wavelength is retrieved from SAR image mode precision image (PRI) data around the coast of Japan. The in-situ NOWPHAS wave gauge data is used for matching up the SAR images and for validation. Wind-wave-produced SAR sub-images and swell-produced SAR sub-images are processed using different

retrieval methods respectively according to the methods described in Section 2. In Section 3, the result is shown to demonstrate the relation between cutoff wavelength and the root of wave height and the agreement of wave information from SAR and from in-situ data. The summary and conclusions is given in Section 4.

## 2. DATA AND METHODOLOGY

The ERS SAR image mode data and NOWPHAS in situ data is used in this study.

ERS-1 and ERS-2, which carry Active Microwave Instrument (AMI) operating at C band and VV polarization, was launched in 1991 and 1995 respectively. The swath of the SAR images around 100 km for image mode data. SAR images are produced from raw signal by Sigma SAR Processor [8].

The NOWPHAS (Nationwide Ocean Wave information network for Ports and HARbourS) wave gauge data we use in this study include the data of 21 stations which are located in the coast of Japan. The wave sensors of NOWPHAS include Ultra-sonic Wave Gauge (UWG), Current meter type Wave Directional meter (CWD) and newly developed DWD. These sensor are mounted on the sea bottom with the depth ranging from 10 to 50 meters. NOWPHAS wave gauge data can provide the wave information such as wave propagation direction, significant wave height and significant wave period. NOWPHAS wave observation system has a sample rate of 2 hours.

In this study, the first procedure is to derive a match-up database where the SAR sub-image and wave gauge data is coincident and quasi-simultaneous. The SAR image mode data processed by Sigma0 processor is 6656 pixels in azimuth direction and 5344 pixels in range direction. We choose 5120\*5120 pixels, avoiding the interference of the very dark pixels value at the edge of the image. Then the image is divided into 40\*40 sub-images, each of which has 128\*128 pixels (approximately 1.6\*1.6 km). There are some criteria for matching up. First, for one scene, the sub-image whose location of the center is nearest to a certain wave gauge is preliminarily chosen. Second, it should be satisfied that the distance between the center of the sub-image and the location of the wave gauge less than 0.5 degree. Third, the wave gauge record must be integrate (including wave height, wave direction and wave period) at the nearest time when this scene of SAR image was illuminated. Fourth, there must be clear wave stripe in the sub-image. In detail, the signal to noise (SN) of the corresponding SAR image spectrum should be larger than 3. As the result, we have chosen 98 match-ups. However, there are still some other factors which can affect the degree of these match-ups. First, there is possibility that the sub-image of SAR data and a certain wave gauge locate the different side of the peninsula or island, although they are close. Second, the image quality of the selected sub-image may be deteriorated by other phenomena in SAR image. For example, if there are atmospheric front, as the irregular dark lines or curves, and wave stripes in SAR image simultaneous, the sub-image containing wave stripe will be damaged by the background atmospheric front stripes. Third, if the wave gauge locates in the bay, there will be some mismatch with the increase of the distance between the wave gauge and sub-image owing to the bathymetry. Table 1 shows the statistics of the data match-ups, 32 scenes, about 30% of total 98 scenes, was rejected due to the effect of bathymetry, distance and image quality.

Table 1: Match-up data statistics.

Sample accepted	Swell	57
	Wind wave	9
Sample rejected	Bathymetry	4
	Distance	12
	Quality of image	16
total		98

We first derive the calibrated normalized radar cross section (NRCS) according to the sigma0-derivation formula. NRCS of every pixel in dB can be inverted using SIGMA SAR processor relationship

$$\text{NRCS} = 20 \log_{10}(\text{DN}) + \text{CF},$$

where CF is the conversion parameter provided by JAXA.

Wind speed is estimated by inverting the wind-vector-to-radar-cross-section relationship — CMOD function at the presence of incident angle of radiation, a beam view angle, wind direction and NRCS value [8,9]. The determination of wind direction is according to the background wind direction provided by NCEP/NCAR reanalyzed reanalysis surface wind field.

The SAR sub-images are first filtered by using a Gaussian high pass filter to remove the low wave number signal which has no relation to surface waves. The coarse SAR spectra in Fig. 3(b) are computed by performing 2-dimensional Fast Fourier Transform (2-D FFT) to corrected sub-images. Then the smoothed SAR image spectrum in Fig. 3(c) are derived by performing low pass filter to coarse spectra.

In practice, the observed SAR spectrum  $P_{obs}(\mathbf{k})$  can be described as the combination of a wave image spectrum  $P_I(\mathbf{k})$  and a background clutter noise spectrum  $P_{cl}(\mathbf{k})$ . To the first order,  $P_I(\mathbf{k})$  and  $P_{cl}(\mathbf{k})$  are simply linearly superimposed, the modulation of the clutter noise by the ocean waves being negligible. The clutter spectrum can thus be removed by subtraction. Below the

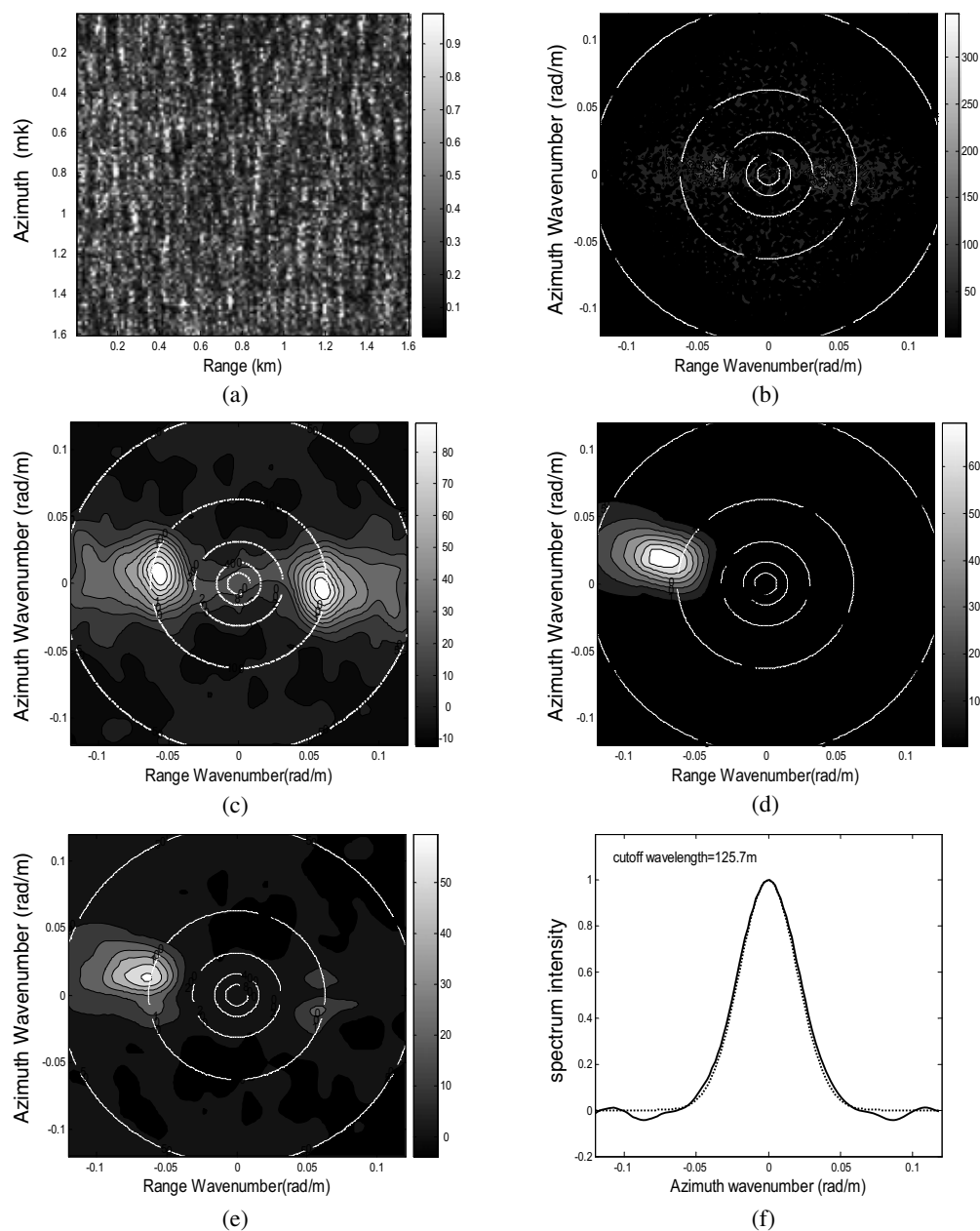


Figure 1: An example of methodology for retrieving wind wave spectrum. (a) SAR sub-image of 128\*128 pixels, (b) coarse SAR image spectrum, (c) filtered SAR image spectrum, (d) first guess spectrum constructed using retrieved wind speed, (e) retrieved wave spectrum, (f) cutoff wavelength calculation.

high wave number roll-off due to the system impulse response function, the clutter spectrum is essentially white. We estimate the clutter noise spectrum by averaging the intensity of observed SAR spectrum of the first 10 bins near Nyquist wave number where there is no wave SAR signal.

Then we treat swell-dominated SAR spectrum  $P_{I.S}(\mathbf{k})$  and wind-wave-dominated SAR image spectrum  $P_{I.W}(\mathbf{k})$  in a different way.

For swell, we retrieved wave spectrum by using linear image relationship

$$P_{I.S}(\mathbf{k}) = k^2 [|T(\mathbf{k})|^2 F(\mathbf{k}) + |T(-\mathbf{k})|^2 F(-\mathbf{k})] \quad (1)$$

giving the standard modulation transfer function. The retrieved elevation wavenumber spectrum by this procedure is known with  $180^\circ$  ambiguity. In order to remove the directional ambiguity and derive the right wave propagation direction, we adopt the fact that swell can only propagate forward the coast instead of backward the coast.

For wind waves, the MPI scheme for retrieving wave spectrum is applied in this study. We use JONSWAP type spectrum [10] and wave direction function [11] to construct a parameterized wind wave spectrum as a first guess spectrum. Then according to the nonlinear imaging mechanism  $P_{I.W}(\mathbf{k}) = \Phi(F(\mathbf{k}))$ , iteratively change wind wave SAR spectrum to match the observed SAR image spectrum by minimize the cost function defined as

$$J = \int [P(k) - \hat{P}(k)]^2 dk + \mu \int [F(k) - \hat{F}(k)]^2 dk \quad (2)$$

where  $\hat{F}(k)$  is first guess spectrum,  $\hat{P}(k)$  is observed SAR spectrum,  $F(k)$  is the best-fit wave spectrum and  $P(k)$  is the best-fit SAR spectrum. The cost function is written as the summation of the difference between best-fit SAR spectrum and the observed SAR spectrum, and the difference between best-fit wave spectrum and the first guess wave spectrum.

SAR spectra are always affected by azimuth cutoff, an effect to roll off SAR spectra in the azimuth direction. The azimuth cutoff is caused by the nonlinearity of wave-SAR relationship in azimuth direction and act as a low-pass Gaussian filter to SAR spectra [12]. The cutoff wavelength has been a parameter which can be calculated by fitting a Gaussian low-pass filter to range-integral SAR spectrum [13]. In this study, we estimate the cutoff wavelength for wind wave cases using the function

$$\exp\left(-\pi \left(\frac{k_x}{k_c}\right)^2\right)$$

where  $k_c = 2\pi/L_c$  and  $L_c$  is cutoff wavelength. The fitting of range-integral SAR spectrum using low pass filter function is shown in Fig. 1(f).

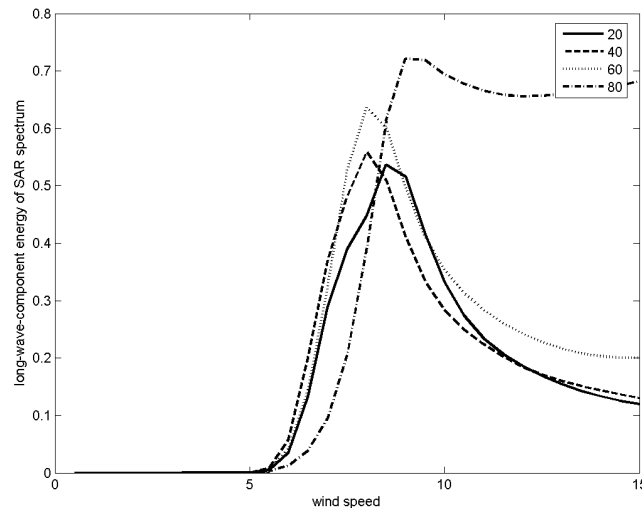


Figure 2: The relation between spectral energy within SAR Nyquist wave number and wind speed at different propagation direction.

### 3. RESULTS

#### 3.1. The Differentiating of Wind Waves and Swell

Figure 2 shows the variation of SAR spectrum within Nyquist wave number with wind speed at the azimuth angle of  $20^\circ$ ,  $40^\circ$ ,  $60^\circ$  and  $80^\circ$ . It is demonstrated that when wind speed is less than 6 m/s, the energy of simulated SAR spectrum in the Nyquist wave number is too weak to be detected. That means if there is detectable signal in SAR image spectrum while the retrieved wind speed is less than 6 m/s, the signal is produced by swell and the wave pattern in SAR image is swell dominated waves.

So we set 6 m/s as a standard of wave category for retrieval. If the wind speed corresponding to SAR image is larger than 6 m/s, it is considered that there is wind wave produced spectrum energy in SAR image spectrum. If less than 6 m/s, it is totally swell produced.

#### 3.2. The Validation of Retrieval

Figure 3 shows the proportional relationship between cutoff wavelength and the root of wave height. The fit implies that in addition to cutoff wavelength, the wave height is another important parameter to reflect the degree of imaging nonlinearity. Wave height is more sensitive to the degree of nonlinearity than any other parameters such as wind speed or wave length.

We now compare SAR-derived parameters to NOWPHAS wave gauge data. The comparison of

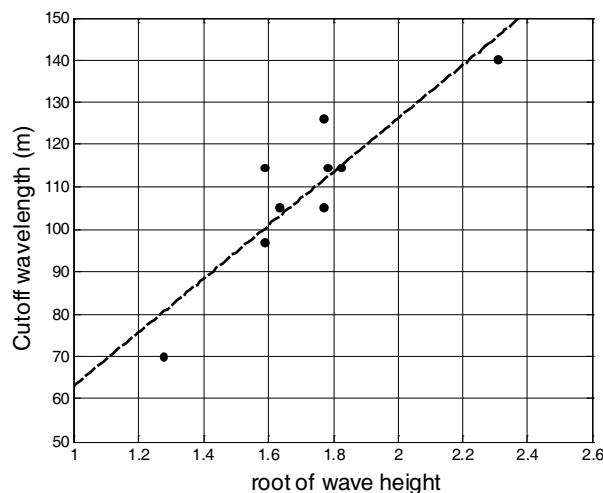
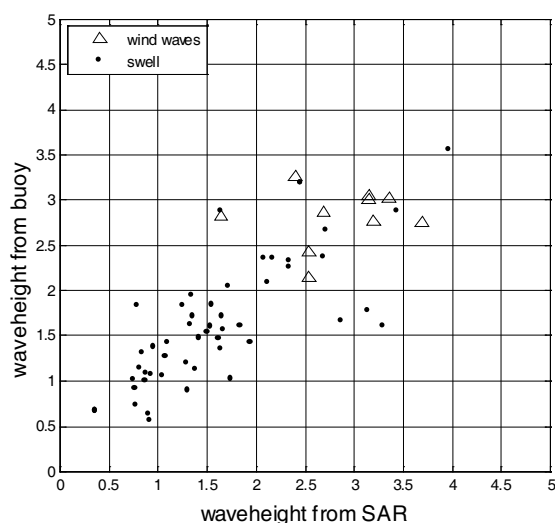
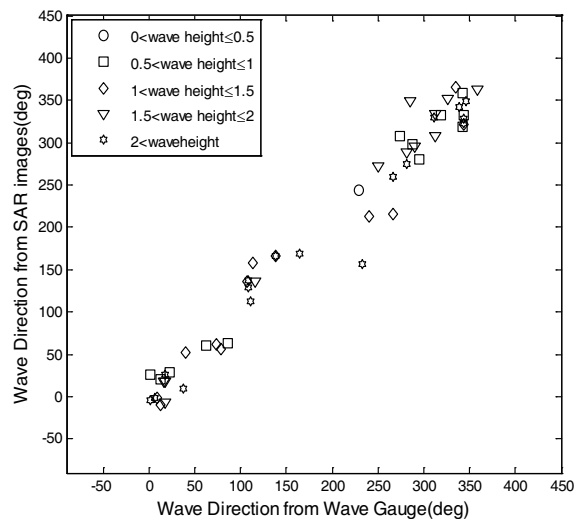


Figure 3: The cutoff wavelength with root of significant wave height for wind waves.



(a)



(b)

Figure 4: The comparison of wave height and wave direction from SAR and wave gauge.

wave height from SAR images and from wave gauge is shown in Fig. 4(a). The comparison gives good agreement except for a few examples showing rather discrepancy. Totally the SAR-derived wave height is underestimated at some degree because the bias is larger than 0 for both wind waves and swell. The swell comparison behaves better than wind waves for its smaller RMS, mainly due to the larger amount of samples and lower wave height samples. For swell, it is more accurate for the cases when the wave height is low, and when wave height increase, the error increase. The wave direction comparison in different wave height categories is shown in Fig. 4(b). The totally agreement is shown with the average difference of the direction below  $20^\circ$ .

#### 4. CONCLUSIONS

In this paper, Using SAR image mode data, we have retrieved and analyzed the parameters of surface waves in the coast region around Japan. The wind speed information is also acquired from SAR data as the additional input information for retrieval. The match-up NOWPHAS wave gauge data is used for validation. The following conclusions are obtained.

ERS-SAR image mode data is capable for wave information retrieval in the coastal region only if the clear wave stripe is available in the sub-image. As for the different nonlinear degree, the wind waves and swell should be dealt with different retrieval methods. The differentiating criteria of swell and wind waves can be reduced to the value of wind speed. The wave height from SAR data and from wave gauge agrees rather well. The bias and RMS of the comparison of swell is better than that of wind waves, mainly due to the degree of nonlinearity.

The cutoff wavelength is proportional to the root of significant wave height. This implies that in addition to cutoff wavelength, the wave height is another important parameter to reflect the degree of imaging nonlinearity. Wave height is more sensitive to the degree of nonlinearity than any other parameters such as wind speed or wave length.

#### REFERENCES

1. Alpers, W. R., D. B. Ross, and C. L. Rufenach, "On the detectability of ocean surface wave by real and synthetic aperture radar," *J. Geophys. Res.*, Vol. 86, No. C7, 6 481–6 498, 1981.
2. Monaldo, F. M. and R. C. Beal, "Comparison of SIR-C SAR wavenumber spectra with WAM model predictions," *J. Geophys. Res.*, Vol. 103, No. C9, 18815–18825, 1998.
3. Hasselmann, K., R. K. Raney, W. J. Plant, W. Alpers, R. A. Shuchman, D. R. Lyzenga, C. L. Rufenach, and M. J. Tucker, "Theory of synthetic aperture radar ocean imaging: A MARSEN view," *J. Geophys. Res.*, Vol. 90, No. C3, 4 659–4 686, 1985.
4. Hasselmann, K. and S. Hasselmann, "On the nonlinear mapping of an ocean wave spectrum into a synthetic aperture radar image spectrum and its inversion," *J. Geophys. Res.*, Vol. 96, No. C6, 10 713–10 729, 1991.
5. Hasselmann, S., C. Bruning, K. Hasselmann, and P. Heimbach, "An improved algorithm for the retrieval of ocean wave spectra from synthetic aperture radar image spectra," *J. Geophys. Res.*, Vol. 101, No. C7, 16 615–16 629, 1996.
6. Mastenbroek, C. and C. F. de Valk, "A semiparametric algorithm to retrieve ocean wave spectra from synthetic aperture radar," *J. Geophys. Res.*, Vol. 105, 3497–3516, 2000.
7. Collard, F., F. Ardhuin, and B. Chapron, "Extraction of coastal ocean wave fields from SAR images," *IEEE Journal of Oceanic Engineering*, Vol. 30, No. 3, 526–533, 2005.
8. Alpers, W., U. Paul, and G. Gross, "Katabatic wind fields in coastal areas studied by ERS-1 synthetic aperture radar imagery and numerical modeling," *J. Geophys. Res.*, Vol. 103, 7875–7886, 1998.
9. Furevik, B. R., O. M., Johannessen, and A. D. Sandvik, "SAR retrieved winds in polar regions- Comparison with in situ data and atmospheric model output," *IEEE Trans. Geosci. Remote Sensing*, Vol. 40, 1720–1732, 2002.
10. Hasselmann, D. E., M. Dunkel, and J. A. Ewing, "Directional wave spectra observed during JONSWAP 1973," *J. Phys. Oceanogr.*, Vol. 10, 1264–1280, 1980.
11. Donelan, M. A., J. Hamilton, and W. H. Hui, "Directional spectra of wind generated waves," *Philos. Trans. R. Soc.*, Vol. 315, 509–562, 1985.
12. Kerbaol, V., B. Chapron, and P. M. Vachon, "A global analysis of ERS-1/2 SAR wave mode images," *J. Geophys. Res.*, Vol. 103, 7833–7846, 1998.
13. Schulz-Stellenfleth, J. and S. Lehner, "Spaceborne synthetic aperture radar observation of ocean waves traveling into sea ice," *J. Geophys. Res.*, Vol. 107, No. C8, 3106, 10.1029/2001JC00837, 2002.

# Statistical Characteristics of Transmitted Nano-meter Electromagnetic Waves in Random Bio-medical Tissues for X-Ray Diagnostic Images

Yasumitsu Miyazaki

Department of Media Informatics, Aichi University of Technology  
50-2 Manori, Nishihazama-cho, Gamagori 443-0047, Japan

**Abstract**— Medical image diagnosis and computer aided diagnosis using X-rays are very important technical tools for physiological diagnosis. Scattered X-ray fields disturb medical image signal properties given by X-ray transmission properties through biological structures concerned with X-ray absorption effects due to biological characteristics. In this paper, in order to improve image diagnosis, statistical analysis of X-ray is discussed for X-ray propagation, attenuation and scattering in random inhomogeneous biological media. Spatial filtering characteristics of grid structure for scattering X-rays particularly, for off-axis X-rays are shown for image X-ray projection by mode theory of lossy waveguides for higher modes. Spatial grid filters consist of waveguide arrays of graded index inhomogeneous waveguides.

## 1. INTRODUCTION

Medical image diagnosis and computer aided diagnosis using nano-meter electromagnetic waves and X-ray are very important medical techniques. Particularly, computer tomography techniques are indispensable medical diagnosis based on transmitted X-ray image processing. However, in X-ray image processing with computed radiography for medical diagnosis, physical and physiological phenomena of X-rays are not so much investigated, based on interaction phenomena between bio-medical material and X-ray. Interaction phenomena between bio-medical material and X-ray are concerned with electromagnetic phenomena of a few KeV energy level interactions between deep electrons and nano-meter electromagnetic waves. Photo-electric absorption, Thomson scatterings and Compton scattering are fundamental phenomena in bio-medical tissues, when X-ray is incident into bio-medical materials. Complex refractive indices of bio-medical materials consisting of high molecules and polymers for nano-meter electromagnetic waves have real values of less than one and relatively large imaginary values, depending on tissue constructions such as bones, muscles and fats [1–2].

Transmitted X-ray responses through biomedical materials are derived by photo-electric absorption and X-ray scatterings. Received X-ray images for medical diagnosis concerned with X-ray absorption are disturbed by X-ray scatterings due to heavy atoms in polymers [3]. If statistical characteristics of X-ray scatterings in random bio-medical tissues are studied and spatial X-ray filter devices for filtering of X-ray scattering for protection of net absorption characteristics are developed, excellent X-ray image diagnosis system may be accomplished.

In this paper, statistical theory of nano-meter electromagnetic waves in bio-medical random media is discussed. Vector wave analysis of X-ray scattering using Green's function is shown for X-ray incident Gaussian beams in short propagation lengths. Based on scattering characteristics for short propagation phenomena, propagation equations for the axial direction are derived using transverse and axial scattering factors and correlation function for random bio-medical media. For long distance propagation, large scattering distribution and axial absorption characteristics are studied by axial propagation equation with transverse and axial scattering factors. Scattering factor has properties of homogeneous scatterings for small correlation length of random bio-medical media and forward scatterings for long correlation length [4]. Back scattering and reflection characteristics are concerned with random bio-medical tissues of small correlation lengths. X-ray image responses depend on mainly forward scattering and X-ray absorptions, with scattering losses due to random bio-medical characteristics of small correlation lengths.

## 2. COMPUTER AIDED DIAGNOSIS AND X-RAY IMAGE

Using computer signal processing for X-ray transmitted images, computer aided diagnosis contributes important medical examinations, of human bodies. Medical and physiological information of interior tissue structures can be obtained by X-ray transmission characteristics. However, transmitted characteristics of X-ray through interior tissues of human bodies depend on X-ray absorption

properties and, also X-ray scattering properties in biological media. X-ray absorption properties with spectral characteristics yield microscopic biological structures of tissues due to atoms and molecules situated along propagation axis. Scattered fields of X-rays by biological molecules and tissues disturb biological information given by absorption properties. Spatial filters consisting grid array of waveguides may exclude such noises due to scattering fields of X-rays. Fundamental spatial filter system for computer aided diagnosis is shown in Fig. 1.

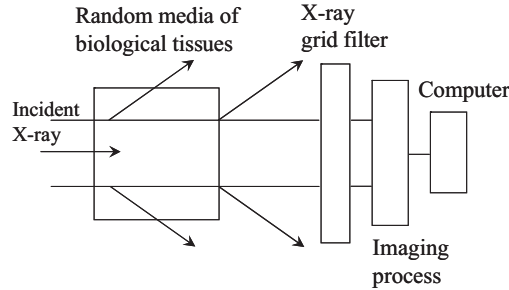


Figure 1: Computer aided diagnosis and scattering X-ray filtering system.

### 3. X-RAY SCATTERING FIELD IN BIOLOGICAL RANDOM MEDIA

In the biological body region, X-ray transmitted and scattered waves through random biomedical media are studied. X-rays, nanometer electromagnetic waves are incident on random media (I) ( $0 \leq z \leq \ell$ ) from left side in Fig. 2. Incident X-ray has  $y$ -direction linearly polarization  $\mathbf{E} = \phi(x, z)\mathbf{i}_y$ . Biological random media in the region (I) have dielectric constants as

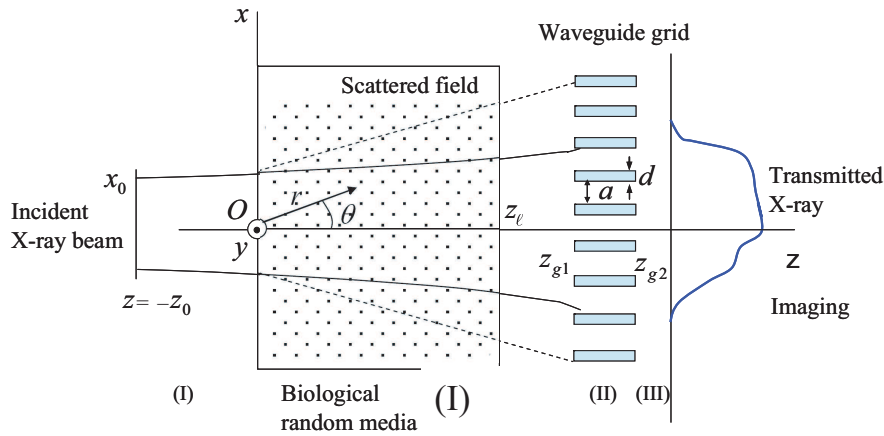


Figure 2: X-ray scattering and X-ray grid.

$$\varepsilon_t = \varepsilon + \varepsilon \Delta\eta(\mathbf{r}_t) \tag{1}$$

where  $\Delta\eta$  is random function and  $\varepsilon = \varepsilon' - j\varepsilon''$ . Here,  $\mathbf{r}_t = x\mathbf{i}_x + z\mathbf{i}_z$ , and we consider two dimensional scattering fields. The field function  $E(x, z)$  concerned with electric field of  $y$  polarization satisfies the following wave equations, using  $k^2 = \omega^2\varepsilon\mu = (k_r - jk_i)^2$

$$\nabla_{xy}^2 E(\mathbf{r}_t) + k^2 E(\mathbf{r}_t) = -\omega^2 \varepsilon \Delta\eta E(\mathbf{r}_t) \tag{2}$$

For incident Gaussian X-ray of  $y$  polarization,  $\mathbf{E}^{inc} = E_{inc}(\mathbf{r}_t)\mathbf{i}_y$  is written as

$$\mathbf{E}_{inc}(\mathbf{r}_t) = \mathbf{i}_y \frac{A}{\sqrt{1-j\zeta}} e^{-jk(z+z_0)} e^{\frac{x^2}{x_0^2(1-j\zeta)}} \tag{3}$$

where beam parameter is  $\zeta = \frac{2(z+z_0)}{kx_0^2}$ , beam waist is  $z = -z_0$ , and beam spot size is  $x_0$ .

Green's function  $G(\mathbf{r}_t, \mathbf{r}'_r)$  for free space is

$$G(\mathbf{r}_t, \mathbf{r}'_r) = -\frac{j}{4} H_0^{(2)}(k|\mathbf{r}_t - \mathbf{r}'_t|) \quad (4)$$

$G$  satisfies the following wave equation

$$\nabla_t^2 G + k^2 G = -\delta(\mathbf{r}_t - \mathbf{r}'_t) \quad (5)$$

Applying Green's formula in random biological media (I) for  $E_{totl} = E_{scatt} + E_{inc}$  and  $G$ ,

$$\int (G \nabla_t^2 E - E \nabla^2 G) dS = \oint \left\{ G \frac{\partial E}{\partial n} - E \frac{\partial G}{\partial n} \right\} dS \quad (6)$$

We have when  $\underline{\mathbf{I}} = G\mathbf{I}$ , using unit dyad  $\mathbf{I}$ ,

$$E_{totl} = E_{inc} - \frac{j}{4} \int_{S_I} dS' (\omega^2 \varepsilon \Delta \eta) E_{totl}(\mathbf{r}'_t) H_0^{(2)}(k|\mathbf{r}_t - \mathbf{r}'_t|) \quad (7)$$

$$\mathbf{E}_{totl} = \mathbf{E}_{inc} + \int k^2 \Delta \eta \underline{\mathbf{I}}(\mathbf{r}_t, \mathbf{r}'_t) \cdot \mathbf{E}(\mathbf{r}'_t) dS' \quad (8)$$

From Maxwell's equation, magnetic field is derived as,

$$\mathbf{H}_{totl} = \mathbf{H}_{inc} - \frac{1}{j\omega\mu} \int k^2 \Delta \eta \nabla \times \underline{\mathbf{I}} \cdot \mathbf{E} dS' \quad (9)$$

Based on the fundamental Equations (8) and (9) in the previous section, we calculate the scattered field by iterative method in this section. Employing the representation of functional analysis, we can solve the integral Equations (8) and (9) in operator forms. If we define vectors  $\mathbf{E}_0$  and  $\mathbf{E}$  in functional space for the vectors  $\mathbf{E}_{inc}$  and  $\mathbf{E}$ , and integral operator  $K_E$  for the integral  $\int k^2 \Delta \eta \underline{\mathbf{I}} \cdot dS'$ , we obtain the field as follows:

$$\mathbf{E} = (\mathbf{I} - K_E)^{-1} \mathbf{E}_0 = \mathbf{E}_0 + K_E \mathbf{E}_0 + K_E K_E \mathbf{E}_0 + \dots \quad (10)$$

Using the similar definition for the magnetic field and Equation (9), we have

$$\mathbf{H} = \mathbf{H}_0 + K_H \mathbf{E} = \mathbf{H}_0 + K_H \mathbf{E}_0 + K_H K_E \mathbf{E}_0 + K_H K_E K_E \mathbf{E}_0 + \dots \quad (11)$$

Equations (10) and (11) express the total electromagnetic field. The optical intensity, which is the most important quantity in the optical range, *i.e.*, the mean intensity of the energy flow in the harmonic electromagnetic field is given by the real part of the complex Poynting vector  $\bar{\mathbf{S}} = \frac{1}{2} \mathbf{E} \times \mathbf{H}^*$ .

$$\mathbf{I} = \text{Re} \bar{\mathbf{S}} = \frac{1}{2} \text{Re}(\mathbf{E} \times \mathbf{H}^*) \quad (12)$$

The conjugate of the vector  $\mathbf{H}$  is indicated by the sign  $\mathbf{H}^*$ .

Consequently, the X-ray intensity is shown as

$$\mathbf{I} = \frac{1}{2} \text{Re} \{ (\mathbf{E}_0 \times \mathbf{H}_0^*) + \mathbf{E}_0 \times (K_H \mathbf{E}_0)^* + (K_E \mathbf{E}_0) \times \mathbf{H}_0^* + K_E \mathbf{E}_0 \times (K_H \mathbf{E}_0)^* \\ + (K_E K_E \mathbf{E}_0) \times \mathbf{H}_0^* + \mathbf{E}_0 \times (K_H K_E \mathbf{E}_0)^* + \dots \} \quad (13)$$

The first term of the right hand side in Equation (13) means the X-ray intensity of the incident wave. The succeeding terms show the light scattering. Particularly, the terms containing multiple  $K'_s$  such as  $(K_H K_E \mathbf{E}_0)^*$  and  $(K_E K_E \mathbf{E}_0)$  imply the multiple scattering due to inhomogeneities.

First order scattered fields corresponding to  $K_E \mathbf{E}_0$  in Equation (10) and  $K_H \mathbf{E}_0$  in Equation (11) are

$$\mathbf{E}_{scatt} = -\frac{j}{4} k^2 \int \Delta \eta(\mathbf{r}'_t) H_0^{(2)}(k|\mathbf{r}_t - \mathbf{r}'_t|) E_{inc}(\mathbf{r}'_t) \mathbf{i}_y dS', \\ \mathbf{H}_{scatt} = -\frac{j}{4} \frac{k^3}{\omega\mu} \int \Delta \eta(\mathbf{r}'_t) H_0^{(2)}(k|\mathbf{r}_t - \mathbf{r}'_t|) (\mathbf{n}(\mathbf{r}') \times E_{inc}(\mathbf{r}'_t)) \mathbf{i}_y dS' \quad (14)$$

The second order scattered fields corresponding to  $K_E K_E \mathbf{E}_0$ , and  $K_E K_H \mathbf{E}_0$  are

$$\begin{aligned} \mathbf{E}_{scatt} &= \left(-\frac{j}{4}k^2\right)^2 \mathbf{i}_y \iint \Delta\eta(\mathbf{r}'_t) \Delta\eta(\mathbf{r}''_t) H_0^{(2)}(k|\mathbf{r}'_t - \mathbf{r}''_t|) H_0^{(2)}(k|\mathbf{r}_t - \mathbf{r}'_t|) E_{inc}(\mathbf{r}''_t) dS' dS'' \\ \mathbf{H}_{scatt} &= \left(-\frac{j}{4}\frac{k^3}{\omega\mu}\right) \left(-\frac{j}{4}k^2\right) \iint \Delta\eta(\mathbf{r}'_t) H_0^{(2)}(k|\mathbf{r}_t - \mathbf{r}'_t|) (\mathbf{n}(\mathbf{r}') \times \mathbf{i}_y) \Delta\eta(\mathbf{r}''_t) H_0^{(2)}(k|\mathbf{r}'_t - \mathbf{r}''_t|) E_{inc}(\mathbf{r}''_t) dS' dS'' \end{aligned} \quad (15)$$

The unit vector  $\mathbf{n}'$  are directed from the point in the sample toward the point of observation and given by  $\mathbf{n}' = \mathbf{n}(\mathbf{r}'_t) = (\mathbf{r}_t - \mathbf{r}'_t) / |\mathbf{r}_t - \mathbf{r}'_t|$ . With the help of Equation (14), the integral operation  $K_E$  of  $K_E \mathbf{E}_0$  in Equations (10), (11) and (13) is described as asymptotic fields,

$$K_E \mathbf{E}_0 \approx -\left(\frac{j}{4}\right) \int k^2 \Delta\eta \sqrt{\frac{2}{\pi k |\mathbf{r}_t - \mathbf{r}'_t|}} e^{-j(k|\mathbf{r}_t - \mathbf{r}'_t| - \frac{\pi}{4})} (E_{inc} \mathbf{i}_y) dS' \quad (16)$$

Similarly, the integral operation  $K_H$  of  $K_H \mathbf{E}_0$  is given by

$$K_H \mathbf{E}_0 \approx \frac{-k}{\omega\mu} k^2 \left(\frac{j}{4}\right) \int \Delta\eta \sqrt{\frac{2}{\pi k |\mathbf{r}_t - \mathbf{r}'_t|}} e^{-j(k|\mathbf{r}_t - \mathbf{r}'_t| - \frac{\pi}{4})} (\mathbf{n}' \times E_{inc} \mathbf{i}_y) dS' \quad (17)$$

Hence, the dominant term of the scattered field in the inhomogeneous medium,  $\frac{1}{2} \text{Re}(K_E \mathbf{E}_0 \times (K_H \mathbf{E}_0)^*)$ , can be written as

$$\begin{aligned} \frac{1}{2} \text{Re}(K_E \mathbf{E}_0 \times (K_H \mathbf{E}_0)^*) &= \frac{k}{\omega\mu} \left(\frac{k^2}{4}\right)^2 \frac{2}{\pi k} \text{Re} \iint \frac{e^{-jk_r |\mathbf{r}_t - \mathbf{r}'_t| + jk_r |\mathbf{r}_t - \mathbf{r}''_t|}}{\sqrt{|\mathbf{r}_t - \mathbf{r}'_t| |\mathbf{r}_t - \mathbf{r}''_t|}} e^{-k_i |\mathbf{r}_t - \mathbf{r}'_t|} e^{-k_i |\mathbf{r}_t - \mathbf{r}''_t|} \\ &\quad \Delta\eta(\mathbf{r}'_t) \Delta\eta^*(\mathbf{r}''_t) \mathbf{n}'' E'_{inc} E''_{inc} dS' dS'' \end{aligned} \quad (18)$$

where we define  $\mathbf{E}'_0 = \mathbf{E}_0(\mathbf{r}'_t)$ ,  $\mathbf{E}''_0 = \mathbf{E}_0(\mathbf{r}''_t)$  and  $\mathbf{n}'' = \mathbf{n}(\mathbf{r}_t, \mathbf{r}''_t) = (\mathbf{r}_t - \mathbf{r}''_t) / |\mathbf{r}_t - \mathbf{r}''_t|$ . These equations are the fundamental formulae for the scattered field.

We assume that the statistical average  $\langle \Delta\eta \rangle$  of fluctuations in the sample is equal to zero, and the correlation function is defined by

$$\langle \Delta\eta(\mathbf{r}'_t) \Delta\eta(\mathbf{r}''_t) \rangle = B_\eta(\mathbf{r}'_t - \mathbf{r}''_t) \quad (19)$$

The statistical average of the total field is expressed as

$$\langle \mathbf{I} \rangle = \mathbf{I}_0 + \frac{1}{2} \text{Re} \langle \{ K_E \mathbf{E}_0 \times (K_H \mathbf{E}_0)^* + \mathbf{E}_0 \times (K_H K_E \mathbf{E}_0)^* + (K_E K_E \mathbf{E}_0) \times \mathbf{H}_0^* + \dots \} \rangle + \dots \quad (20)$$

We study here the dominant term of the X-ray scattering, which leads to the following total intensity  $\langle \mathbf{I} \rangle$

$$\langle \mathbf{I} \rangle \approx \mathbf{I}_0 + \frac{1}{2} \text{Re} \langle K_E \mathbf{E}_0 \times (K_H \mathbf{E}_0)^* \rangle \quad (21)$$

In this case we can write approximately the scattered field as follows:

$$\begin{aligned} \langle \mathbf{I}_s \rangle &\approx \frac{k}{\omega\mu} \left(\frac{k^2}{4}\right)^2 \frac{2}{\pi k} \text{Re} \iint \frac{e^{-jk_r |\mathbf{r}_t - \mathbf{r}'_t| + jk_r |\mathbf{r}_t - \mathbf{r}''_t|}}{\sqrt{|\mathbf{r}'_t - \mathbf{r}''_t| |\mathbf{r}_t - \mathbf{r}''_t|}} e^{-k_i |\mathbf{r}_t - \mathbf{r}'_t|} e^{-k_i |\mathbf{r}_t - \mathbf{r}''_t|} \\ &\quad B_\eta(\mathbf{r}'_t, \mathbf{r}''_t) \mathbf{n}'' E'_{inc} E''_{inc} dS' dS'' \end{aligned} \quad (22)$$

The incident X-ray beam is assumed to be the Gaussian TEM<sub>00</sub> mode. When  $g(k_i |\mathbf{r}_t - \mathbf{r}'_t|) = e^{-2k_i |\mathbf{r}_t - \mathbf{r}'_t|}$ , inside random media of  $\mathbf{r}_t = 1$ , outside,  $\zeta_0 = 2z_0/kx_0^2$  and the correlation function is  $B_\eta(\boldsymbol{\rho}_t) = \overline{\Delta\eta^2} e^{-\rho^2/\rho_0^2}$ , where parameters  $\overline{\Delta\eta^2}$  and  $\rho_0$  give the variances and correlation lengths of fluctuations,

$$\int B_\eta(\boldsymbol{\rho}_t) e^{jk_r (\mathbf{n}' - \mathbf{i}_z) \cdot \boldsymbol{\rho}_t} d^2 \boldsymbol{\rho}_t = \overline{\Delta\eta^2} \rho_0^2 \pi e^{-k_r^2 \rho_0^2 \left(\frac{1 - \mathbf{n}' \cdot \mathbf{i}_z}{2}\right)} \quad (23)$$

For length of random media  $\ell$ , we have for the cylindrical coordinate  $(r, \theta)$  assuming  $g(k_i | \mathbf{r}_t - \mathbf{r}'_t) = e^{-2k_i |z_t - z'_t|}$  in random media of  $0 \leq z \leq z_\ell$ ,

$$\langle \mathbf{I}_s \rangle = \mathbf{i}_r \frac{k}{\omega \mu} \frac{\sqrt{2\pi}}{16} \overline{\Delta \eta^2} A^2 k^3 x_0 \rho_0^2 \frac{1}{|\mathbf{r}|} e^{-k^2 \rho_0^2 \sin^2 \frac{\theta}{2}} e^{-2k_i(z_\ell + z_0)} z_\ell \quad (24)$$

Figure 3 shows angular distribution of Thomson scattering whose parameters  $\rho_0$  is correlation length of random media, and  $k = 2\pi/\lambda$ . For large  $k\rho_0$ , forward scattering is large and small  $k\rho_0$ , scattering is homogeneous.

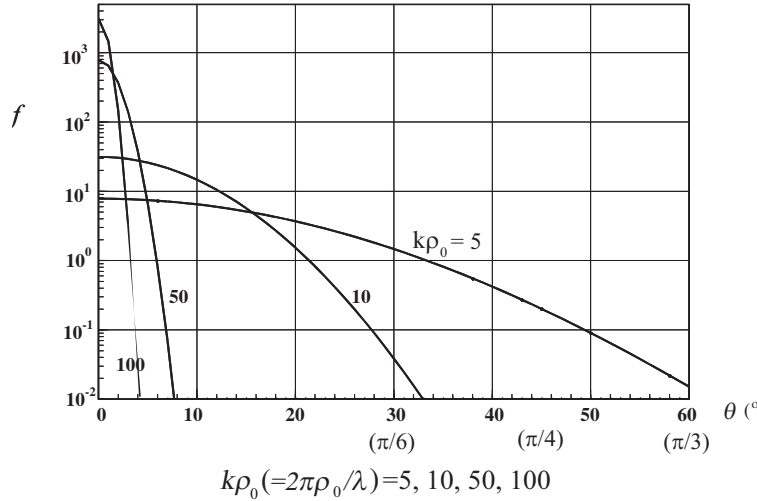


Figure 3: Angular distribution of Thomson scattering.  $\frac{|\mathbf{I}_s|}{|\mathbf{I}_0|} = \overline{\Delta \eta^2}(kx_0) \left( \frac{z_\ell}{|\mathbf{r}|} \right) f$ ,  $f = \frac{\sqrt{2\pi}}{8} (k\rho_0)^2 e^{-(k\rho_0)^2 \sin^2 \frac{\theta}{2}}$ .

3-dimensional Thomson scattering is shown similarly, for incident Gaussian beam with beam waist  $z = -z_0$ , beam spot size  $r_0$ , and polarization of  $\tau$  direction,

$$\langle \mathbf{I}_s \rangle = \mathbf{i}_R \frac{k^4 \pi^{1/2}}{32} I_0 \sum_i r_{0z}^2 \rho_{0i}^3 \overline{\Delta \eta_i^2} \sin^2(\mathbf{i}_R, \boldsymbol{\tau}) \frac{\ell}{R^2} \cdot e^{-k^2 \rho_{0i}^2 \sin^2 \frac{\theta}{2}} \quad (25)$$

Based on these fundamental scattering characteristics, long distance propagation properties with diffusion characteristics can be discussed.

#### 4. FILTERING CHARACTERISTICS IN LOSSY INHOMOGENEOUS GRID WAVEGUIDES

Electromagnetic characteristics of X-rays in lossy waveguide arrays consisting of grid structures are expressed by mode expansions of lossy modes. In the region (II) of grid arrays in Fig. 4, propagation spaces in the core with lossy metal clad are

$$z_{g1} \leq z \leq z_{g2}, \quad \frac{(2s-1)}{2}(a+d) \leq x \leq \frac{(2s+1)}{2}(a+d), \quad s = -m, -(m-1), \dots, -1, 0, 1, \dots, m-1, m.$$

Lossy inhomogeneous waveguides are consisting of graded index waveguides with lossy clads of dielectric constants

$$\begin{aligned} \varepsilon(x_s) &= \varepsilon^{(r)}(x_s) - j\varepsilon^{(i)}(x_s) = \varepsilon' \left[ 1 - (\ell_x x_s)^2 + (D_{IV} \ell_x x_s)^4 + D_{VI} (\ell_x x_s)^6 \right] \\ x_s &= x - s(a+d), \quad \frac{2s-1}{2}(a+d) \leq x \leq \frac{(2s+1)}{2}(a+d) \end{aligned} \quad (26)$$

where complex focusing parameters  $D_{IV}$ ,  $D_{VI}$  are

$$D_{VI} = D_{IV}^{(r)} - jD_{IV}^{(i)}$$

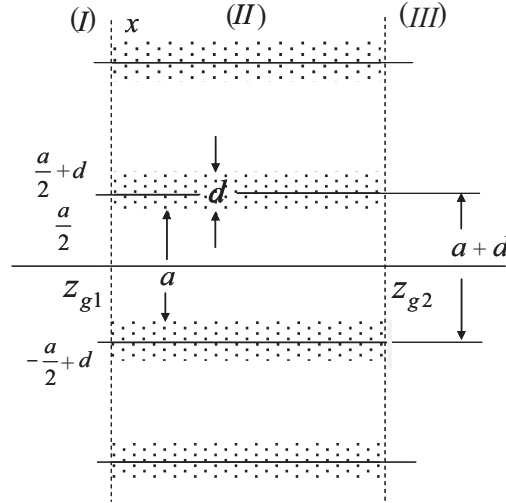


Figure 4: Waveguide type grid structure for scattering filtering.

Electromagnetic eigen fields in section  $s = 0$  of self-focusing optical waveguide with inhomogeneous lossy cladding are derived from inhomogeneous wave equation for the  $y$  polarization

$$\left[ \frac{\partial^2}{\partial x^2} + \frac{\partial^2}{\partial z^2} + \omega^2 \varepsilon(x) \mu \right] E_y + \nabla \left( \frac{\nabla \varepsilon}{\varepsilon} \cdot E_y \mathbf{i}_y \right) = 0 \quad (27)$$

Electric field can be expressed as

$$E_y(x, z) = \int \hat{E}_y(x, \gamma) e^{-j\gamma z} d\gamma \quad (28)$$

Using scalar function  $\Phi = \Psi(x) e^{-j\beta_\Phi z}$  satisfying scalar wave equation

$$\left[ \frac{\partial^2}{\partial x^2} + \frac{\partial^2}{\partial z^2} + \varepsilon_1 \omega^2 \mu \right] \Phi = 0 \quad (29)$$

where eigen functions  $\Phi_m = \Psi_m(x) e^{-j\beta_\Phi(m)z}$  have complete orthogonality characteristics. Eigen functions  $\Phi_m$  are given for  $\varepsilon_1 = \varepsilon' (1 - (\ell_x x)^2)$

$$\Phi_m(x) = \Psi_m(x) e^{-j\beta_\Phi(m)z}, \quad \Psi_m(x) = b_m e^{-j\frac{\alpha_x^2 x^2}{2}} H_m(\alpha_x x), \quad \alpha_x = \beta_1 \ell_x, \quad \beta_1^2 = \omega^2 \varepsilon' \mu, \quad b_m^2 = \frac{a_z}{2^m m! \sqrt{\pi}} \quad (30)$$

Electric field component  $\hat{E}_y$  can be expanded as

$$\hat{E}_y(x, \gamma) = \sum_m a_m(\gamma) \Psi_m(x) \quad (31)$$

Complex propagation constants  $\gamma_m$  are derived as

$$\gamma_m = \beta_m - j\alpha_m \quad (32)$$

where

$$\beta_m = \omega \sqrt{\varepsilon' \mu} \left[ 1 - (2n + 2m + 2) \frac{\ell_x}{\beta_1} - \frac{\ell_x^2}{\beta_1^2} - \frac{\ell_x^2 (1 - 2D_{IV}^{(r)})}{\beta_1^3} (3m + 2) + \frac{D_{IV}^{(r)} \ell_x^2}{4 \beta_1^2} A_m + \frac{D_{IV}^{(i)} \ell_x^3}{8 \beta_1^3} B_m \right]$$

$$\alpha_m = \omega \sqrt{\varepsilon' \mu} \left[ D_{IV}^{(i)} \left\{ \frac{\ell_x^2}{\beta_1^2} \frac{A_m}{4} + \frac{\ell_x^3}{\beta_1^3} (3m + 2) \right\} + \frac{D_{VI}^{(i)} \ell_x^3}{8 \beta_1^3} B_{mn} \right], \quad A_m = 3(m + 1)^2 + 3m^2 + 3 + 2(2m + 1)$$

$$B_m = 6 [(m + 1)^2 + m^2] (m + 2) + 6(3m + 2) + (m + 1)(4m + 6) + m(m - 1)(4m - 2) + 6$$

Using large attenuation characteristics of higher modes in inhomogeneous waveguide of graded index distribution with lossy cladding, spatial filtering of scattered X-rays that are coupled with higher modes in grid filter is accomplished through grid array of inhomogeneous waveguides.

## 5. CONCLUSIONS

Scattering characteristics of X-rays in random bio-medical media consisting of bio-molecules, are studied by statistical theory of electromagnetic field. For X-ray CT in medical diagnosis using X-ray, nano-meter electromagnetic waves, spatial filtering of scattered waves by inhomogeneous waveguides of graded index distribution with lossy cladding is very useful to obtain precise image processing. Attenuation properties of higher modes that are excited by scattered fields of large scattering angles are investigated and based on higher mode characteristics, spatial filtering characteristics of scattered fields are discussed for improvement of precise diagnosis.

## REFERENCES

1. Miyazaki, Y., "Electromagnetic characteristics of grid structures for scattering fields of nano-meter electromagnetic waves and X-rays," *Proc. of PIERS 2006*, 643–647, Tokyo, Aug. 2006.
2. Miyazaki, Y., "Electromagnetic characteristics of waveguide-type grid filters for scattered nano-meter waves in transmitted X-ray diagnostic images," *Proc. of EMTS 2007*, EMTS128, Ottawa, ON, Canada, July 2007.
3. Miyazaki, Y., "Beam propagation and radiation fields in a uniformly curved X ray dielectric gradient waveguides," *Trans. IEE of Japan*, Vol. 120-C, No. 1, 68–73, Jan. 2000.
4. Miyazaki, Y., "Light scattering of laser beams by random micro-inhomogeneities in glasses and polymers," *Jpn. Jour. Appl. Phys.*, Vol. 13, No. 8, 1238–1248, 1974.

# FDTD Parallel Computing of Microwave Scattering and Attenuation Characteristics Due to Randomly Distributed Rainfalls

Yasumitsu Miyazaki<sup>1</sup>, Koichi Takahashi<sup>1</sup>, and Nobuo Goto<sup>2</sup>

<sup>1</sup>Department of Media Informatics, Aichi University of Technology  
50-2 Manori, Nishihassama-cho, Gamagori 443-0047, Japan

<sup>2</sup>Institute of Technology and Science, The University of Tokushima  
2-1 Minamijosanjima-cho, Tokushima 770-8506, Japan

**Abstract**— Rain measurement system using propagation characteristics of microwave and millimeter wave is very important for disaster prevention system to foresee and prevent the occurrence of disasters caused by strong rainfalls and for the sensor of ITS to support safe and automatic driving and cruising. In this study, propagation region is modeled as random media with randomly distributed rainfalls. Propagation of electromagnetic wave in random media is analyzed by three-dimensional FDTD method. FDTD analysis demonstrates the dynamic characteristics of wave scattering and absorption phenomena in rain region where raindrops are distributed randomly. For the analysis of microwave scattering by rain, the analysis space including many raindrops less than and comparable with the wavelength is required and analysis region is much larger than the wavelength and a few meters. Parallel computation of FDTD is shown for efficient analysis of microwave scattering and attenuation characteristics in large rain region.

## 1. INTRODUCTION

Rain measurement system using propagation characteristics of microwave and millimeter wave is very important for disaster prevention system to foresee and prevent the occurrence of disasters caused by strong rainfalls and for the sensor of ITS (Intelligent Transport Systems) to support safe and automatic driving and cruising. Measurement technique of electromagnetic scattering and attenuation characteristics by rain is one of accurate evaluation methods of rainfall rate. Rain measurement system using microwave and millimeter wave has the advantage of rapid measurement of rainfall rate in wide area compared with the direct measurement by rain gauges. To support safe driving and cruising in automatic driving system, sensor of meteorological condition on the road, particularly the amount of rain, fog and snow are indispensable [1]. The sensor using propagation characteristics of microwave and millimeter wave are very useful to detect these road conditions. Also, the efficient design for radio communication channel between automobiles requires accurate propagation characteristics of millimeter waves, it is very important to investigate the characteristics of electromagnetic wave propagation, particularly multiple scattering phenomena with many particles such as raindrops. The application systems of rain measurement using microwave propagation characteristics are shown in Fig. 1.

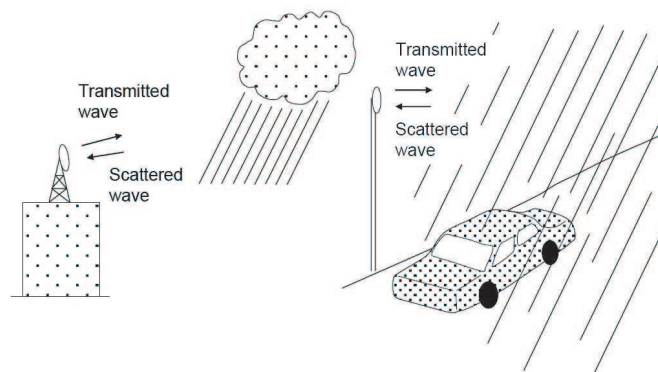


Figure 1: Rain measurement in weather measurement system and ITS.

In this paper, propagation characteristics of microwave in rain region are discussed using FDTD method [2–4]. The effects of multiple scattering and absorption due to randomly distributed raindrops are studied and the relationship between rainfall rate and specific attenuation are evaluated

numerically. The numerical results of specific attenuation are compared with the experimental results to evaluate the accuracy of FDTD computer simulation.

## 2. FDTD ANALYSIS OF ELECTROMAGNETIC SCATTERING AND ATTENUATION BY RAIN

Electromagnetic scattering and attenuation characteristics due to randomly distributed raindrops are very important information for ITS and weather measurement systems. These characteristics can be numerically analyzed by computer simulation. In this paper, electromagnetic propagation characteristics are investigated by FDTD method. Three-dimensional analysis model of rain attenuation is shown in Fig. 2. Analysis region is defined as  $\ell_x \ell_y \ell_z$ .  $z = \ell$  is the observation plane of the transmitted electromagnetic field to obtain the propagation loss per the distance  $\ell$ . Raindrops are distributed randomly in rain region. The incident wave is assumed the Gaussian beam of frequency 20 GHz radiated from the surface  $S_0$  located at  $z = 0$ .

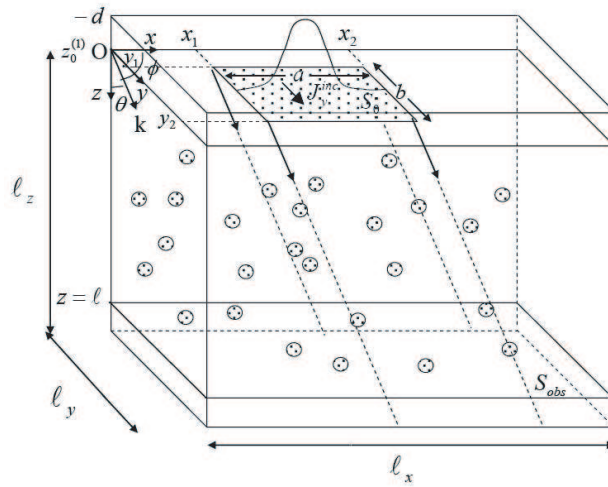


Figure 2: Three dimensional analysis model of FDTD method.

In FDTD method, the analysis region is discretized as  $x = i\Delta s$  ( $0 \leq i \leq Nx$ ),  $y = j\Delta s$  ( $0 \leq j \leq Ny$ ),  $z = k\Delta s$  ( $0 \leq k \leq Nz$ ) and  $t = n\Delta t$  ( $0 \leq n \leq T$ ). The electromagnetic fields at point  $(i, j, k)$  at time  $n\Delta t$  are calculated by difference equation from Maxwell's equation,

$$E_y^n(i, j, k) = c_1 E_y^{n-1}(i, j, k) - c_2 J_y^{n-1}(i, j, k) + c_3 \{H_x^{n-1}(i, j, k) - H_x^{n-1}(i, j, k-1) - H_z^{n-1}(i, j, k) + H_z^{n-1}(i, j, k)\} \quad (1)$$

$$H_y^n(i, j, k) = H_y^{n-1}(i, j, k) - c_4 \{E_x^n(i, j, k+1) - E_x^n(i, j, k) - E_z^n(i+1, j, k) + E_z^n(i, j, k)\} \quad (2)$$

where,

$$c_1 = \frac{1 - \sigma\Delta t/(2\varepsilon)}{1 + \sigma\Delta t/(2\varepsilon)}, \quad c_2 = \frac{\Delta t/\varepsilon}{1 + \sigma\Delta t/(2\varepsilon)}, \quad c_3 = \frac{\Delta t/\varepsilon}{1 + \sigma\Delta t/(2\varepsilon)} \frac{1}{\Delta s}, \quad c_4 = \frac{\Delta t}{\mu\Delta s} \quad (3)$$

Here,  $\Delta s$  is cell size and  $\Delta t$  is time step.  $\varepsilon$ ,  $\mu$  and  $\sigma$  are the dielectric constant, conductivity, and permeability of material. Mur's boundary condition is applied to obtain the electromagnetic fields at the boundary of the analysis space.

In raindrop region, complex dielectric constant  $\varepsilon^*$  and complex refractive index  $n_a^*$  are given by  $\varepsilon^* = \varepsilon + \sigma/(j\omega) = n_r^{*2}\varepsilon_0$ ,  $n_r^* = n_1 - jn_2$ . Here, we consider the time harmonic electromagnetic field with angular frequency  $\omega$ . By using  $n_r^* = n_1 - jn_2$ , dielectric constant and conductivity of raindrops are  $\varepsilon = \varepsilon_0(n_1^2 - n_2^2)$ ,  $\sigma = 2\varepsilon_0\omega n_1 n_2$ . The dielectric constant of background medium is  $\varepsilon_0$ . In this analysis, the shape of a raindrop is assumed to be square. Random scatterers are generated by giving the length of a side length of squares  $a_i$ , positions of one apex  $(x_i, y_i, z_i)$  and relative dielectric constant  $\varepsilon_r(i, j, k) = \varepsilon(i, j, k)/\varepsilon_0$ .

The incident Gaussian beam of  $y$  polarization is given by

$$J_y^n(i, j, 1) = J_0 \varphi(i, j) p(n),$$

$$\varphi(i, j) = \exp \left\{ - \left( \frac{i \Delta s - x_0}{r_0} \right)^2 \right\} \exp \left\{ - \left( \frac{j \Delta s - y_0}{r_0} \right)^2 \right\} \quad (4)$$

Where,  $x_0 = \ell_x/2$ ,  $y_0 = \ell_y/2$ ,  $r_0$  is the beam spot of incident Gaussian beam.

In this analysis, the shapes of raindrops are assumed to be cubic with several side lengths. Random scatterers are generated by giving the number of raindrops  $N$ , with lengths of side lengths of cubic  $a$ , positions of one apex  $(x_i, y_i, z_i)$  and complex dielectric constants  $\epsilon_i^* = \epsilon_i' - j\epsilon_i''$ .

The rain rate  $R$  (mm/h) can be obtained by

$$R = \frac{N}{V} v t a^3 \cdot 10^{-6} \quad (5)$$

where  $a$  (mm) is the average size of raindrops,  $v$  (m/s) is the terminal velocity of raindrops and assumed to be  $4\sqrt{a}$ ,  $t$  is 3600 (sec),  $N' = N/V$  is the number of raindrops per unit volume, where  $V = \ell_x \ell_y \ell$  is the total volume of rain region. Fig. 3 shows the relationship between rain rate  $R$  and the number of raindrops per unit volume  $N/V$ .

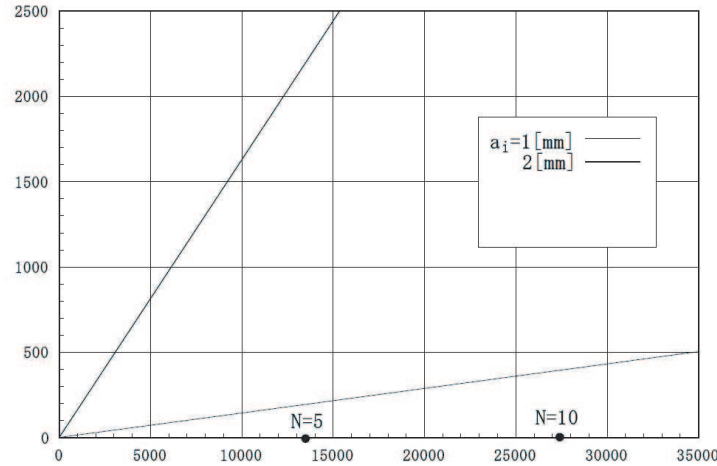


Figure 3: Relationship between rain rate and the number of raindrops per unit volume.

### 3. NUMERICAL RESULTS OF MICROWAVE SCATTERING AND ATTENUATION

As an example of rain scattering and attenuation of microwave propagation, numerical results in small area (Case I) and middle size area (Case II) are discussed.

For  $p(n)$  in Eq. (4) is given by in Case I,

$$p(n) = H_0(n\Delta t) \sin(2\pi f n \Delta t), \quad H_0(n\Delta t) = \begin{cases} 1 & |n\Delta t - t_0| \leq T \\ 0 & |n\Delta t - t_0| > T \end{cases} \quad (6)$$

and in Case II,

$$p(n) = \exp \left\{ - \left( \frac{n\Delta t - t_0}{t_w} \right)^2 \right\} \sin(2\pi f n \Delta t) \quad (7)$$

In Case I,  $\ell_x = \ell_y = 5\lambda = 0.075$  (m),  $x_0 = y_0 = 0.0375$  (m),  $r_0 = \lambda = 0.015$  (m) are used and in Case II,  $\ell_x = \ell_y = 20\lambda = 0.3$  (m),  $\ell_z = 24\lambda = 0.36$  (m),  $x_0 = y_0 = 0.15$  (m),  $r_0 = 2\lambda = 0.03$  (m),  $t_0 = 0.15$  (ns),  $t_w = 0.06$  (ns) are used. In Case II, the propagation distance is  $73.3\lambda = 1.1$  (m) and the intensity of received electric field at  $z = \ell$  is observed to evaluate rain attenuation characteristics. Numerical parameters are shown in Table 1. In Case II, the specific attenuation is obtained by  $A = \langle \alpha \rangle 10^3 / \ell$  (dB/km), where

$$\langle \alpha \rangle = \frac{1}{S} \int \alpha dS, \quad \alpha = -\log_{10} \frac{\langle \overline{W}(x, y) \rangle}{\langle \overline{W}_0(x, y) \rangle}, \quad \overline{W}(x, y, \ell) = \frac{1}{T} \int_t^{t+T} (E_x H_y - E_y H_x)|_{z=\ell} dt (> 0)$$

$\langle\alpha\rangle$  is a loss per propagated distance. The electric field of incident wave is shown in Fig. 4 and Figs. 5–8 show the results of Case I. Three models in Fig. 5 with same raindrop parameters are presented. Figs. 6–8 show the difference  $\Delta E_y$  between total field and the incident field as scattered field. These figures show that spherical scattering waves are generated from the point of scatterers and the distribution of electric field is very complex due to the interference of multiple scattering.

Table 1: Simulation parameters for scattering and attenuation characteristics.

Parameter	Case I	Case II
$f$ : Frequency of incident wave	20 GHz	20 GHz
$\lambda$ : Wavelength of incident wave	0.015 m ( $c/f$ )	0.015 m ( $c/f$ )
$\ell_x$ : Length of analysis space ( $x$ )	0.075 m ( $5\lambda$ )	0.3 m ( $20\lambda$ )
$\ell_y$ : Length of analysis space ( $y$ )	0.075 m ( $5\lambda$ )	0.3 m ( $20\lambda$ )
$\ell$ : Propagation distance	0.065 m ( $4.3\lambda$ )	1.1 m ( $73.3\lambda$ )
$\ell_z$ : Length of analysis space ( $z$ )	0.08 m ( $5.3\lambda$ )	1.16 m ( $77.3\lambda$ )
$V$ : Volume of rain region	$3.66 \times 10^{-4} \text{ m}^3$	$0.099 \text{ m}^3$ ( $\ell_x \ell_y \ell$ )
$x_0$ : Center point of beam ( $x$ )	0.0375 m	0.15 m
$y_0$ : Center point of beam ( $y$ )	0.0375 m	0.15 m
$r_0$ : Beam spot at $z = 0$	0.015 m ( $\lambda$ )	0.03 m ( $2\lambda$ )
$\Delta s$ : Length of a cell	$5 \times 10^{-4} \text{ m}$ ( $\lambda/30$ )	0.001 m ( $\lambda/15$ )
$\Delta t$ : Time increment	0.75 ps ( $T/66.74$ )	1.5 ps ( $T/33.3$ )
$N$ : Number of raindrops	20	114( $R = 20$ ), 143( $R = 40$ )
$a_i$ : Length of a side of a raindrop	2 mm	1–2 mm( $R = 20$ ), 1–3 mm( $R = 40$ )
$n_r^*$ : Complex refractive index of raindrops	6.46– $j$ 2.81	6.46– $j$ 2.81

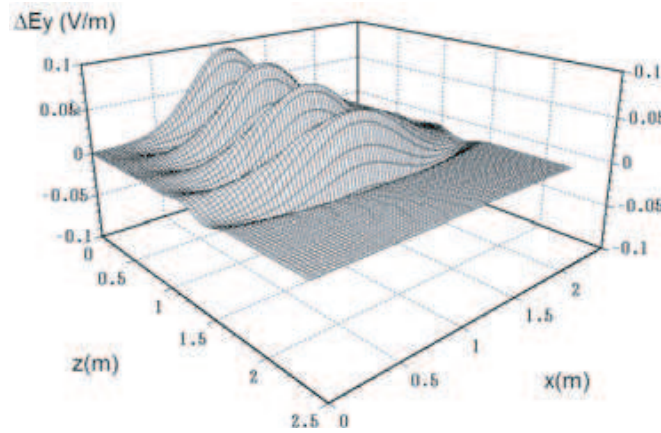


Figure 4: Electric field of incident wave at  $y = 0.0375$  (m),  $t = 250\Delta t = 0.1875$  (ns).

In Case II,  $A = 0.64$  and  $9.62$  are obtained at  $R = 20$  and  $40$ , respectively as shown in Fig. 9. Each dot corresponds to a simulation result using one sample model at  $R = 20$  or  $40$ . Solid curve is a line passing through these two dots and is shown for confirmation of validity of our FDTD analysis. By comparing with the result of other theoretical and experimental study [1], attenuation at  $R = 40$  is considered to be high. Statistical characteristics of electromagnetic propagation, such as average field intensities and field correlation will be derived by statistical data of rainfalls, such as average and correlation of raindrop's size and position, based on these FDTD analyses with a large number of sample models. The effect of multiple scattering is considered by these FDTD simulations.

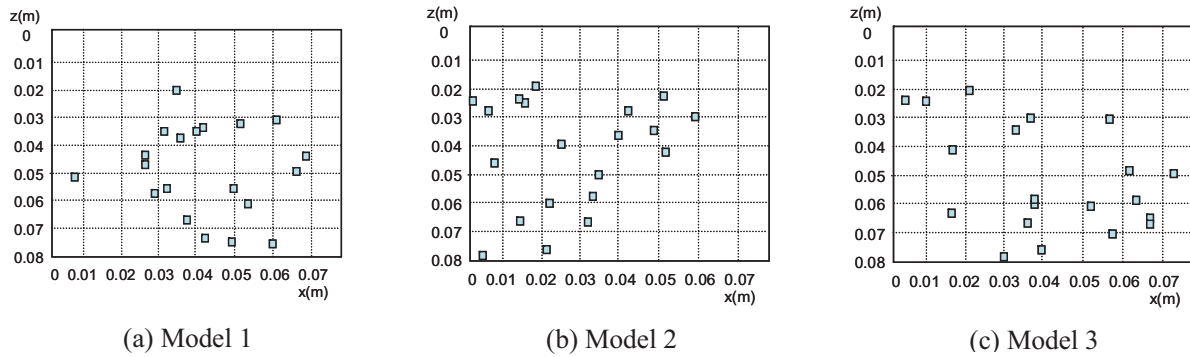


Figure 5: Cross sectional vies of raindrop distribution (Case I),  $N = 20$ ,  $a_i = 2$  (mm),  $n_r^* = 6.46 - j2.81$ .

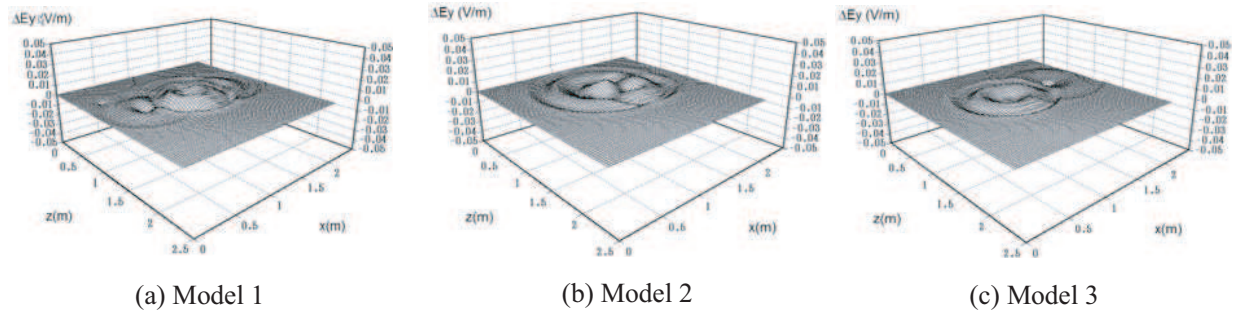


Figure 6: Difference of electric field  $\Delta E_y$  at  $y = 0.0375$  (m),  $t = 250\Delta t = 0.1875$  (ns).

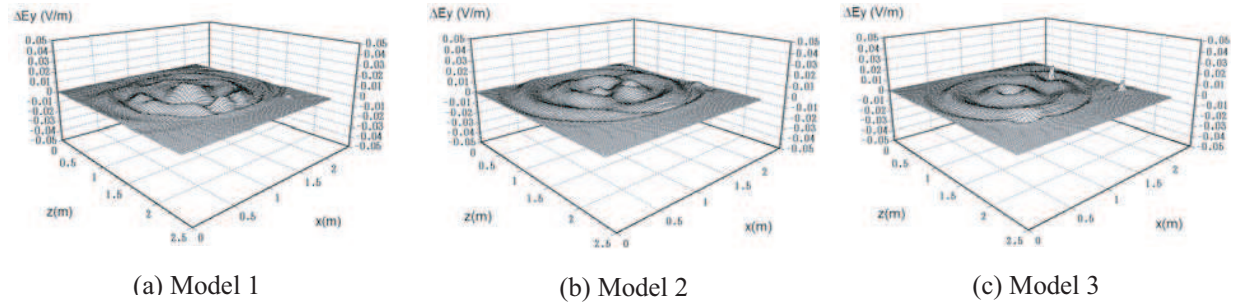


Figure 7: Difference of electric field  $\Delta E_y$  at  $y = 0.0375$  (m),  $t = 300\Delta t = 0.225$  (ns).

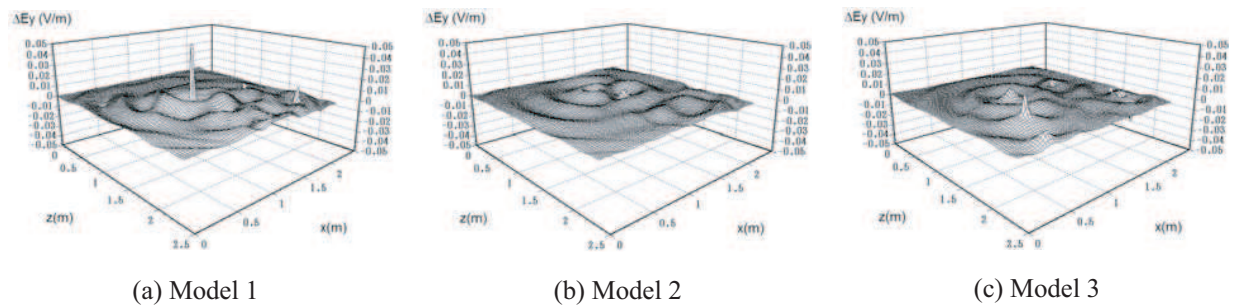


Figure 8: Difference of electric field  $\Delta E_y$  at  $y = 0.0375$  (m),  $t = 400\Delta t = 0.3$  (ns).

#### 4. PARALLEL COMPUTATION FOR LARGE AREA

For the analysis of microwave scattering by rain, the analysis space including many raindrops less than and comparable with the wavelength is required and analysis region is much larger than the wavelength and a few meters. Parallel computation of FDTD using grid computer is indispensably important. To perform parallel processing using grid computer, the total analysis space is divided into subdomains of  $Mz \times My$  as shown in Fig. 10 and one divided subdomain  $D_{u,v}$  is assigned to one of PC computers. The electromagnetic fields in  $D_{u,v}$  ( $1 \leq v \leq My$ ) are calculated by parallel processing. For the calculation of values on the boundary of subdomains, values in the adjacent

subdomain are exchanged and matched for field boundary condition. To proceed the parallel processing, data transfer between adjacent subdomains is carried out using MPI. Along  $z$  direction, electromagnetic fields are calculated successively by storing the electromagnetic fields at the end point of subdomain in the  $z$  direction to computer memory. These stored electromagnetic fields are used as incident field in the domain boundary, to calculate the fields in the next subdomains  $D_{u+1,v}$  ( $1 \leq v \leq My$ ).

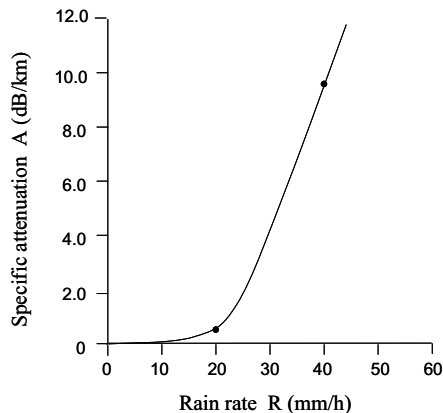


Figure 9: Specific attenuation characteristics by FDTD.

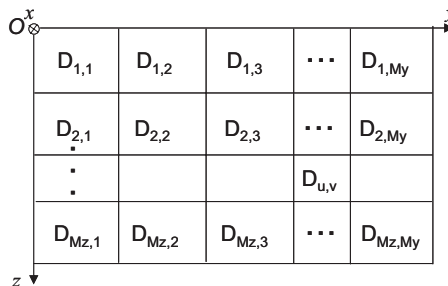


Figure 10: Parallel processing of microwave scattering and attenuation in rain region, subdomain  $D_{u,v}$  ( $1 \leq u \leq Mz, 1 \leq v \leq My$ ).

## 5. CONCLUSIONS

Rain measurement system using microwave and millimeter wave is very significantly important for disaster prevention system to foresee and prevent the occurrence of disasters and for the sensor of ITS. In this paper, parallel FDTD algorithm for the analysis of electromagnetic scattering and attenuation due to rainfall is considered. Rain region is treated as random media consisting of randomly distributed raindrops. The most common parallel algorithm of FDTD requires a large amount of memory. So, successive segmented FDTD [3] is used to decrease the memory required to calculate the electromagnetic fields in large area. In this method, total analysis space is divided into subdomains as shown in Fig. 10 and only a few subdomains where the transmitted pulse wave is propagating, is calculated. By using this algorithm, FDTD computation is demonstrated with less memory requirements and electromagnetic wave scattering and attenuation characteristics in rain can be evaluated numerically.

## REFERENCES

1. Oguchi, T., "Electromagnetic wave propagation and scattering in rain and other hydrometers," *IEEE Proc.*, Vol. 71, 1029–1078, 1983.
2. Takahashi, K. and Y. Miyazaki, "Scattering and attenuation characteristics of microwave and millimeter wave due to rainfall for ITS and weather measurement system," *Proc. of ISAP'04*, POS-B-4, 1081–1084, Sendai, Japan, 2004.
3. Miyazaki, Y. and K. Takahashi, "Computer simulation of X-ray scattering characteristics for medical image diagnosis," *Transactions of the Institute of Electrical Engineers of Japan. C*, Vol. 126, No. 12, 1431–1440, 2006.
4. Rodriguez, G., Y. Miyazaki, and N. Goto, "Matrix-based FDTD parallel algorithm for big areas and its applications to high-speed wireless communications," *IEEE Trans. Antennas and Propagat.*, Vol. 54, No. 3, 785–796, 2006.

# Radar Cross-section of Targets Using Beam Wave Incidence with Linear Polarization

Hosam El-Ocla

Department of Computer Science, Lakehead University, Ontario, Canada

**Abstract**— The scattering problem has been solved as a boundary value problem using a method that has been presented in many of my publications (e.g., [1–4], where other references are available). It has been proved that radar cross section (RCS) changes obviously with the illumination region curvature [1] and polarization [2, 4]. Research on laser radar [5] for target ranging, detection, and recognition [6] has become the one key technology to evaluate and model the characteristics of scattering from a complex target in the military and civil applications. In this regard, the scattering characteristics are analyzed through studying the behavior of laser RCS (LRCS) of the target. In doing that, one can calculate the LRCS by assuming a beam wave incident on a nonconvex target in free space as proposed in [3]. In fact, we can consider the beam wave as a plane wave when the mean size of the target becomes smaller than the beam width, however, this is not usually the general case practically. To detect targets of larger sizes, we should, therefore, handle the case where the beam width is smaller than the target size. Here, we evaluate the effects of the target configuration including size and curvature on the RCS of target for the two cases of plane and beam wave incidences. To Achieve this aim, we draw on our method described earlier to conduct numerical results for the RCS of concave-convex targets of large sizes up to about five wavelengths to be bigger enough than the beam width. Polarization of incident waves is one of the primary keys that affects the scattering waves. Here, we assume linear polarization including E-wave incidence and H-wave incidence.

## 1. INTRODUCTION

The scattering problem has been solved as a boundary value problem using a method that has been presented in many of my publications (e.g. [1–4], where other references are available). It has been proved that radar cross section (RCS) changes obviously with the illumination region curvature [1] and polarization [2, 4]. Research on laser radar [5] for target ranging, detection, and recognition [6] has become the one key technology to evaluate and model the characteristics of scattering from a complex target in the military and civil applications. In this regard, the scattering characteristics are analyzed through studying the behavior of laser RCS (LRCS) of the target. In doing that, one can calculate the LRCS by assuming a beam wave incident on a nonconvex target in free space as proposed in [3]. In fact, we can consider the beam wave as a plane wave when the mean size of the target becomes smaller than the beam width, however, this is not usually the general case practically. To detect targets of larger sizes, we should, therefore, handle the case where the beam width is smaller than the target size. Here, we evaluate the effects of the target configuration including size and curvature on the RCS of target for the two cases of plane and beam wave incidences. To achieve this aim, we draw on our method described earlier to conduct numerical results for the RCS of concaveconvex targets of large sizes up to about five wavelengths to be bigger enough than the beam width. Polarization of incident waves is one of the primary keys that affects the scattering waves. Here, we assume linear polarization including E-wave incidence and H-wave incidence<sup>1</sup>. The time factor  $\exp(-i\omega t)$  is assumed and suppressed in the following section.

## 2. FORMULATION

Let us consider scattering waves from targets with assuming two cases: (1) plane wave incidence, (2) beam waves incidence, in free space. For both scattering problems, geometry of the problem is shown in Figure 1. Here,  $k = \omega\sqrt{\varepsilon_0\mu_0}$  is the wavenumber in free space where  $\varepsilon_0$  and  $\mu_0$  are the free space permittivity and magnetic permeability, respectively, and  $W$  is the beam width. Consider the case where a directly incident wave is produced by a line source  $f(\mathbf{r}')$  distributed uniformly along the  $y$  axis. Then, the incident wave is cylindrical and becomes plane approximately around the target because the line source is very far from the target. We designate the incident wave by  $u_{in}(\mathbf{r})$ , the scattered wave by  $u_s(\mathbf{r})$ , and the total wave by  $u(\mathbf{r}) = u_{in}(\mathbf{r}) + u_s(\mathbf{r})$ . An electromagnetic wave radiated from the line source located at  $\mathbf{r}_t$  propagates in free space, illuminates the target

<sup>1</sup>This work appeared partly in PIER 67 and PIER 56

and induces a surface current on the target. A scattered wave from the target is produced by the surface current and propagates back to the observation point that coincides with the source point. The target is assumed as a conducting cylinder. The cross-section of the cylinder is expressed by  $r = a[1 - \delta \cos 3(\theta - \phi)]$ , where  $a$  is the mean size of the target in which  $a \ll r_t$ ,  $\delta$  is the concavity index, and  $\phi$  is the rotation index which represents the incident angle. Using the current generators  $Y_E$ ,  $Y_H$  and Green's function in free space  $G_0(\mathbf{r}|\mathbf{r}')$ , we can express the scattered wave as

$$u_s(\mathbf{r}) = \int_S d\mathbf{r}_1 \int_S d\mathbf{r}_2 [G_0(\mathbf{r}|\mathbf{r}_2)Y_E(\mathbf{r}_2|\mathbf{r}_1)u_{in}(\mathbf{r}_1|\mathbf{r}_t)] \quad (1)$$

$$u_s(\mathbf{r}) = - \int_S d\mathbf{r}_1 \int_S d\mathbf{r}_2 \left[ \left( \frac{\partial}{\partial n_2} G_0(\mathbf{r}|\mathbf{r}_2) \right) Y_H(\mathbf{r}_2|\mathbf{r}_1)u_{in}(\mathbf{r}_1|\mathbf{r}_t) \right] \quad (2)$$

For the scattering problem with plane wave incidence,  $u_{in}(\mathbf{r}_1|\mathbf{r}_t)$  is expressed as

$$u_{in}(\mathbf{r}_1|\mathbf{r}_t) = G_0(\mathbf{r}_1|\mathbf{r}_t) \quad (3)$$

whose dimension coefficient is understood. Here  $Y_E$  and  $Y_H$  is the operator that transforms incident waves into surface currents on  $S$  and depends only on the scattering body [1–4]. The current generator can be expressed in terms of wavefunctions, which satisfy Helmholtz equation and the radiation condition.

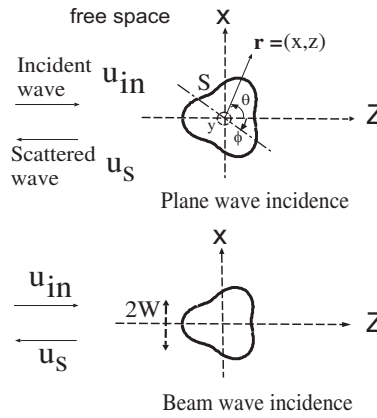


Figure 1: Geometry of the problem of wave scattering from a conducting cylinder.

For the scattering problem with Gaussian beam wave incidence, let us consider  $u_{in}(\mathbf{r}_1|\mathbf{r}_t)$  to be represented by

$$u_{in}(\mathbf{r}_1|\mathbf{r}_t) = G_0(\mathbf{r}_1|\mathbf{r}_t) \exp \left[ - \left( \frac{kx_1}{kW} \right)^2 \right] \quad (4)$$

The beam expression is approximately useful only around the cylinder.

The plane wave can be considered as a beam wave with infinite beam width, that is:

$$W = -\infty \quad \text{for plane wave incidence} \quad (5)$$

In the following section we present results for RCS  $\sigma_0$  for plane wave incidence and LRCS  $\sigma_b$ . We use  $\sigma$  as a general symbol that indicates both  $\sigma_0$  and  $\sigma_b$  and can be calculated as  $\sigma = |u_s(\mathbf{r})|^2 k(4\pi z)^2$ .

### 3. NUMERICAL RESULTS

We define DRCS as the difference in the behavior of RCS  $\sigma$  with  $ka$  between plane and beam wave incidences, i.e., between  $\sigma_0$  and  $\sigma_b$ . To detect the target through calculating its RCS, the target should be surrounded by the incident wave. This condition is realized with the plane wave but not with the beam wave since the later illuminates only a portion of the target. Therefore the beam wave does not cause generating enough surface current needed for correct RCS calculation. We define the surface illuminated by the plane wave incidence and the surface illuminated by the beam wave incidence and restricted by the  $2kW$  are the definitions for  $EIR_p$  and  $EIR_b$ , respectively. Here,

we discuss the numerical results for  $\sigma_0$  and  $\sigma_b$  shown in Figures 2 and 3. It is noticed from these figures that there are two effects on both  $\sigma_0$  and  $\sigma_b$ . The first is the effect of target configuration and can be seen clearly with changing  $\delta$  and  $ka$  as shown in Figure 3. With small  $ka$  and/or large  $\delta$ , DRCS becomes small as a result of the relation  $EIR_p \simeq EIR_b$ . As  $ka$  increases and/or  $\delta$  decreases, as the DRCS augments due to the lack in  $EIR_b$ , and vice versa. To understand such behavior, we have to turn the attention to the beam wave incidence case where the surface current outside  $EIR_b$  is relatively small compared to that at the beam spot that is inside the  $EIR_b$ . Therefore in accordance to (2), as  $EIR_b$  shrinks, as the contribution to the scattered waves wanes clearly. Beam width size  $kW$  is the second effect in which there is a direct relationship between  $\sigma_b$  and  $kW$  as shown in Figure 3. In other words, when  $kW$  increases, the results of  $\sigma_b$  become closer to  $\sigma_0$  especially for small  $ka$  and that agrees with the conclusion published in [7]. In Figure 3, creeping waves make  $\sigma_0$  oscillates largely for relatively small  $ka$ . For larger  $ka$ ,  $\sigma_0$  does not vary with  $ka$  because of two reasons: the effect of creeping waves reduction. Secondly, the generated surface current does not change since the illumination region is always covered by the plane wave incidence. On the other hand,  $\sigma_b$  lessens, in an oscillatory manner, as a result of the shortage in the surface current and that leads to the gradual decrease in the scattered wave contribution with  $ka$ . At certain limit,  $\sigma_b$  will diminish with large enough target and the beam wave becomes incapable of target detection. In general,  $\sigma_0$  and  $\sigma_b$  approach with  $ka$  at certain values that are almost same irrespective of the polarization of incident waves.

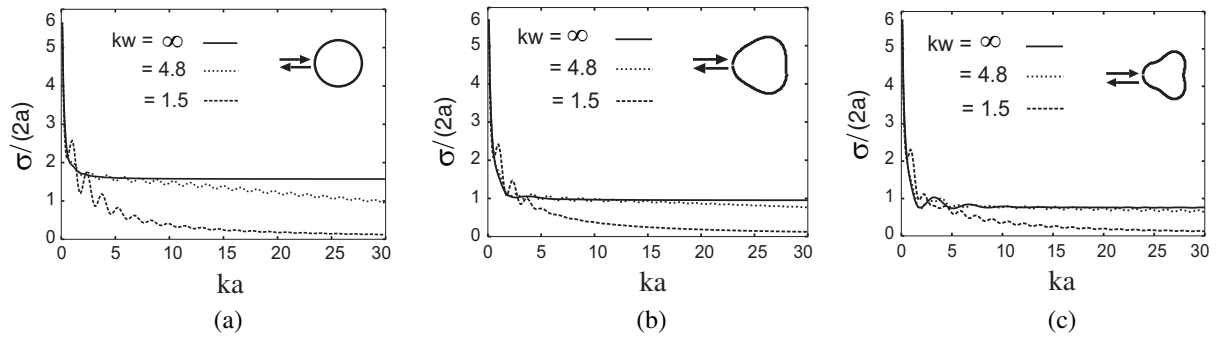


Figure 2: RCS vs. target size for E-wave incidence in free space where (a)  $\delta = 0$ , (b)  $\delta = 0.1$ , and (c)  $\delta = 0.2$ .

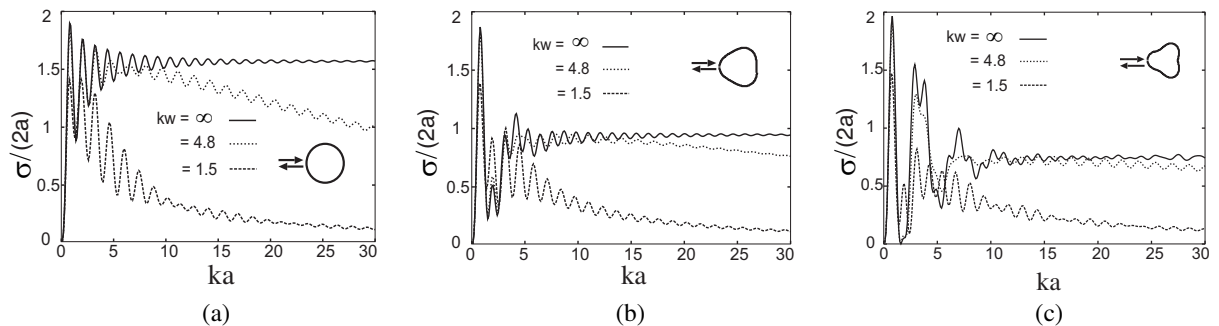


Figure 3: RCS vs. target size for H-wave incidence in free space where (a)  $\delta = 0$ , (b)  $\delta = 0.1$ , and (c)  $\delta = 0.2$ .

#### 4. CONCLUSION

The effect of linear polarization including E-polarization and H-polarization of the incident wave on the behaviour of RCS of targets in free space has been analyzed numerically. The scattering problems of plane wave and beam wave incidences were considered. Target configuration together with beam width  $kW$  has major effects on laser RCS (LRCS). Creeping waves, produced in case of H-polarization, influence the LRCS obviously for limited  $ka$  and their impact diminishes gradually with  $ka$ . LRCS behaves differently from RCS for plane wave incidence in the range  $ka \geq kW$  where target complexity  $\delta$  has a clear effect especially with small  $kW$ . This behaviour contradicts with E-polarization case in which LRCS is almost invariant with  $\delta$  as a result of absence of creeping waves. However, LRCS approaches certain values with  $ka > kW$  irrespective of linear wave polarization.

**ACKNOWLEDGMENT**

This work was supported in part by National Science and Engineering Research Council of Canada (NSERC) under Grant 250299-02.

**REFERENCES**

1. El-Ocla, H. and M. Tateiba, *Waves in Random Media*, Vol. 11, No. 1, 21–32, 2001.
2. El-Ocla, H. and M. Tateiba, *Waves in Random Media*, Vol. 12, No. 3, 387–397, 2002.
3. El-Ocla, H. and M. Tateiba, *IEEE Antennas and Wireless Propagation Letters*, Vol. 2, 173–176, 2003.
4. El-Ocla, H., *Waves in Random and Complex Media*, Vol. 15, No. 1, 91–99, 2005.
5. Jelalian, A. V., *Laser Radar System*, Artech House, Boston, Mass., 1992.
6. Steinvall, O., H. Olsson, G. Bolander, C. Carlsson, and D. Letalick, *Laser Radar Technology and Applications IV*, G. W. Kamerman and C. Werner, eds., *Proc. SPIE*, Vol. 3707, 432–448, 1999.
7. Peng, M. Y. and W. B. Dou, *International Journal of Infrared and Millimeter Waves*, Vol. 22, No. 8, 1277–1286, 2001.

# Polarization of Waves in Reciprocal and Nonreciprocal Uniaxially Bianisotropic Media

Xiangxiang Cheng<sup>1,2</sup>, Jin Au Kong<sup>1,3</sup>, and Lixin Ran<sup>1,2</sup>

<sup>1</sup>The Electromagnetics Academy at Zhejiang University, Zhejiang University, Hangzhou 310058, China

<sup>2</sup>Department of Information and Electronic Engineering, Zhejiang University, Hangzhou 310027, China

<sup>3</sup>Research Laboratory of Electronics, Massachusetts Institute of Technology, Cambridge, MA 02139, USA

**Abstract**— We investigate the polarizations of waves in reciprocal and nonreciprocal uniaxially bianisotropic media, whose corresponding chirality parameter and Tellegen parameter appear only in one direction. By analyzing constitutive parameters for generating circularly polarized waves, we find that the optical-activity effects happen in such kind of uniaxially anisotropic chiral media under certain conditions. On the other hand, similar conditions give birth to linearly polarized waves in nonreciprocal uniaxially bianisotropic media.

## 1. INTRODUCTION

Media can be divided basically into reciprocal and nonreciprocal magnetoelectric materials [1, ?]. There is a long history of optical activity (or rotation of the polarization vector as the wave advances) in physics and chemistry, possibly since the time of Pasteur [3]. Artificial chirality at lower frequencies (RF microwave) was first induced and experimentally verified by Lindeman [4, ?] over 90 years ago, which he accomplished with a random collection of insulated coils of certain handedness. Biisotropic media, analytically proposed by Tellegen [6] over half a century ago, can be nonreciprocal, and is not as popular, possibly because it has not been found in nature. Both chiral and bi-isotropic media are isotropic, and they become polarized when placed in a magnetic field, and magnetized when placed in an electric field.

Recently, a term “metamaterial” is presently applied to artificial discrete media displaying exotic electromagnetic responses unavailable in conventional materials. For example, a uniaxially anisotropic chiral medium is put forward, which may support more kinds of negative refractions than isotropic chiral media and the left-handed materials [7]; a realization of a bianisotropic left-handed material based on the structure of S-ring resonators is further proposed, which has its own double negative permittivity and permeability, combined with an additional chirality produced by subtly introducing some vias inside of the ring [8]; we fabricated and performed free space experimental measurement on a left-handed metamaterial based on bianisotropic S-ring resonator. The realization and experimental results of such bianisotropic S-ring resonator will be discussed in detail in a separate paper.

In this paper, we study the polarizations of waves in reciprocal and nonreciprocal uniaxially bianisotropic media separately, whose corresponding chirality parameter and Tellegen parameter appear only in one direction. Using a wave approach similar to that in [1], through analyzing constitutive parameters for circularly polarized waves, we find that some certain conditions can generate the optical-activity effects in the chiral media we discuss. On the other hand, similar conditions give birth to linearly polarized waves in nonreciprocal uniaxially bianisotropic media.

## 2. RECIPROCAL UNIAXIALLY BIANISOTROPIC MEDIA

Chiral media, which characterize many types of polymers, sugar solutions, or some crystals, such as quartz, are known to rotate the polarization of an incident linearly polarized wave when propagating through a bianisotropic chiral medium described by certain constitutive tensors, yielding optical-activity effects [1]. Such media own chirality factors in all the three orthogonal directions. However, in this paper, we study the constitutive parameters of bianisotropic medium which has chirality element in only one direction, and analyze that the optical-activity effects can also happen in such kind of uniaxially anisotropic chiral media under certain conditions.

The constitutive relations for the uniaxially anisotropic chiral media under consideration are written as follows:

$$\begin{aligned}\overline{D} &= \overline{\epsilon} \cdot \overline{E} + \overline{\xi} \cdot \overline{H}, \\ \overline{B} &= \overline{\zeta} \cdot \overline{E} + \overline{\mu} \cdot \overline{H},\end{aligned}\tag{1}$$

where

$$\bar{\epsilon} = \epsilon_0 \begin{pmatrix} \epsilon & 0 & 0 \\ 0 & \epsilon & 0 \\ 0 & 0 & \epsilon_z \end{pmatrix}, \bar{\mu} = \mu_0 \begin{pmatrix} \mu & 0 & 0 \\ 0 & \mu & 0 \\ 0 & 0 & \mu_z \end{pmatrix}, \bar{\xi} = \frac{1}{c} \begin{pmatrix} 0 & 0 & 0 \\ 0 & 0 & 0 \\ 0 & 0 & -i\xi_0 \end{pmatrix}, \bar{\zeta} = \frac{1}{c} \begin{pmatrix} 0 & 0 & 0 \\ 0 & 0 & 0 \\ 0 & 0 & i\xi_0 \end{pmatrix}, \quad (2)$$

thereinto,  $\epsilon_0$  and  $\mu_0$  are the permittivity and permeability of free space respectively, and  $c$  is the speed of light in free space. Note that  $\epsilon$ ,  $\epsilon_z$ ,  $\mu$ ,  $\mu_z$ , and  $\xi_0$  are all dimensionless quantities and from Eq. (2) we know the medium is reciprocal. The constitutive relations in Eq. (1) are in the  $\bar{E}\bar{H}$  representation and they can be inverted and written as:

$$\begin{aligned} \bar{E} &= \bar{\kappa} \cdot \bar{D} + \bar{\chi} \cdot \bar{B}, \\ \bar{H} &= \bar{\nu} \cdot \bar{B} + \bar{\gamma} \cdot \bar{D}, \end{aligned} \quad (3)$$

which are called in the  $\bar{D}\bar{B}$  representation. From Eq. (2), through the inversion of the system of Eq. (1) into Eq. (3), we directly get

$$\begin{aligned} \bar{\kappa} &= \frac{1}{\epsilon_0} \begin{pmatrix} 1/\epsilon & 0 & 0 \\ 0 & 1/\epsilon & 0 \\ 0 & 0 & \mu_z/(\epsilon_z\mu_z - \xi_0^2) \end{pmatrix}, \bar{\nu} = \frac{1}{\mu_0} \begin{pmatrix} 1/\mu & 0 & 0 \\ 0 & 1/\mu & 0 \\ 0 & 0 & \epsilon_z/(\epsilon_z\mu_z - \xi_0^2) \end{pmatrix}, \\ \bar{\chi} &= c \begin{pmatrix} 0 & 0 & 0 \\ 0 & 0 & 0 \\ 0 & 0 & i\chi_0 \end{pmatrix}, \bar{\gamma} = c \begin{pmatrix} 0 & 0 & 0 \\ 0 & 0 & 0 \\ 0 & 0 & -i\chi_0 \end{pmatrix}, \end{aligned} \quad (4)$$

thereinto,  $\chi_0 = \xi_0/(\epsilon_z\mu_z - \xi_0^2)$ .

For the study of the optical-activity effect, we use the analytical method described in [1] to rewrite the electromagnetic fields and flux in the  $kDB$  system defined by three vectors ( $\hat{e}_1, \hat{e}_2, \hat{e}_3$ ), and in which  $\bar{k} = \hat{e}_3 k$ . So in the  $kDB$  system,

$$\begin{aligned} \bar{E}_k &= \bar{\kappa}_k \cdot \bar{D}_k + \bar{\chi}_k \cdot \bar{B}_k \\ \bar{H}_k &= \bar{\nu}_k \cdot \bar{B}_k + \bar{\gamma}_k \cdot \bar{D}_k \end{aligned} \quad (5)$$

where

$$\begin{aligned} \bar{\kappa}_k &= \bar{T} \cdot \bar{\kappa} \cdot \bar{T}^{-1}, \\ \bar{\chi}_k &= \bar{T} \cdot \bar{\chi} \cdot \bar{T}^{-1}, \\ \bar{\nu}_k &= \bar{T} \cdot \bar{\nu} \cdot \bar{T}^{-1}, \\ \bar{\gamma}_k &= \bar{T} \cdot \bar{\gamma} \cdot \bar{T}^{-1}, \end{aligned}$$

thereinto,  $\bar{T}$  is the transformation matrix defined in [1], and  $\theta$  is the angle between  $\bar{k}$  and  $z$  axis. Since  $B_3 = D_3 = 0$ , Maxwell's equations can be rewritten as a succession of  $2 \times 2$  matrix multiplies, which is substantially simpler than the original  $3 \times 3$  systems.

Eliminating  $\bar{B}_k$  from the Maxwell equations in  $kDB$  system, we obtain

$$\begin{bmatrix} \frac{u^2}{\nu_{22}} - \kappa_{11} & u \frac{\chi_{22}}{\nu_{22}} \\ -u \frac{\chi_{22}}{\nu_{22}} & \frac{u^2}{\nu_{11}} - \frac{\chi_{22}^2}{\nu_{22}} - \kappa_{22} \end{bmatrix} \begin{bmatrix} D_1 \\ D_2 \end{bmatrix} = 0 \quad (6)$$

where  $u = \omega/k$  is the phase velocity for characteristic waves inside the medium. For nontrivial solutions for  $\bar{D}_k$ , we set the determinant of the  $2 \times 2$  matrix equal to zero and obtain:

$$u^2 = \frac{2 \cos^2 \theta}{\epsilon \mu} + \frac{\sin^2 \theta}{\epsilon_z \mu_z - \xi_0^2} \left( \frac{\mu_z}{\mu} + \frac{\epsilon_z}{\epsilon} \right) \pm \frac{\sin^2 \theta}{|\epsilon_z \mu_z - \xi_0^2|} \sqrt{\left( \frac{\mu_z}{\mu} - \frac{\epsilon_z}{\epsilon} \right)^2 + \frac{4\xi_0^2}{\epsilon \mu}}, \quad (7)$$

and the dispersion relation relating the wave number in free space  $k_0$  and the wave vector inside the media  $\bar{k}$ :

$$\frac{1}{\epsilon^2 \mu^2} k_z^4 + \frac{1}{(\mu_z \epsilon_z - \xi_0^2) \epsilon^2 \mu^2} k_s^4 + \frac{\mu_z / \mu + \epsilon_z / \epsilon}{(\mu_z \epsilon_z - \xi_0^2) \epsilon \mu} k_z^2 k_s^2 - \frac{2k_0^2}{\epsilon \mu} k_z^2 - \frac{(\mu_z \epsilon + \epsilon_z \mu) k_0^2}{(\mu_z \epsilon_z - \xi_0^2) \epsilon \mu} k_s^2 + k_0^4 = 0. \quad (8)$$

The two components of the field vector  $\bar{D}_k$  are related by

$$\frac{D_2}{D_1} = i \frac{\left( \frac{\mu_z}{\mu} - \frac{\epsilon_z}{\epsilon} \right) \pm \frac{\sin^2 \theta}{\text{sign} \{ \epsilon_z \mu_z - \xi_0^2 \}} \sqrt{\left( \frac{\mu_z}{\mu} - \frac{\epsilon_z}{\epsilon} \right)^2 + \frac{4\xi_0^2}{\epsilon \mu}}}{\sqrt{2\xi_0} \sqrt{\frac{2 \cos^2 \theta}{\epsilon \mu} + \frac{\sin^2 \theta}{\epsilon_z \mu_z - \xi_0^2} \left( \frac{\mu_z}{\mu} + \frac{\epsilon_z}{\epsilon} \right) \pm \frac{\sin^2 \theta}{|\epsilon_z \mu_z - \xi_0^2|} \sqrt{\left( \frac{\mu_z}{\mu} - \frac{\epsilon_z}{\epsilon} \right)^2 + \frac{4\xi_0^2}{\epsilon \mu}}}}. \quad (9)$$

Equation (7) and Eq. (9) tell that, as long as  $\theta \neq 0$  or  $\pi$  and the expression under the square root of Eq. (7) is larger than 0 which is  $\left( \frac{\mu_z}{\mu} - \frac{\epsilon_z}{\epsilon} \right)^2 + \frac{4\xi_0^2}{\epsilon \mu} > 0$ , there are two characteristic waves propagating at two different phase velocities in the medium, both of which are elliptically polarized; When  $\bar{k}$  lies in  $z$  axis, it becomes a degenerate isotropic case.

However, there exists a special case which is that the expression under the square root of Eq. (7) is equal to 0:

$$(\mu_z / \mu - \epsilon_z / \epsilon)^2 + 4\xi_0^2 / \epsilon \mu = 0, \quad (10)$$

then there is only one solution for phase velocity  $u$  in Eq. (7)

$$u^2 = \frac{\frac{2 \cos^2 \theta}{\epsilon \mu} + \frac{\sin^2 \theta}{\epsilon_z \mu_z - \xi_0^2} \left( \frac{\mu_z}{\mu} + \frac{\epsilon_z}{\epsilon} \right)}{2}, \quad (11)$$

and  $D_2/D_1$  in Eq. (9)

$$\frac{D_2}{D_1} = i \frac{\left( \frac{\mu_z}{\mu} - \frac{\epsilon_z}{\epsilon} \right)}{\sqrt{2\xi_0} \sqrt{\frac{2 \cos^2 \theta}{\epsilon \mu} + \frac{\sin^2 \theta}{\epsilon_z \mu_z - \xi_0^2} \left( \frac{\mu_z}{\mu} + \frac{\epsilon_z}{\epsilon} \right)}} = i \frac{\left( \frac{\mu_z}{\mu} - \frac{\epsilon_z}{\epsilon} \right)}{2\xi_0 u}. \quad (12)$$

So there is only one characteristic wave existing in the medium, and this one characteristic wave may not be a linearly polarized one by looking at Eq. (12), except that  $\xi_0$  is a pure imaginary, which means the medium is not a lossless medium, but a totally lossy one. This situation is not in our consideration, so we exclude this possibility and find out that the only one characteristic wave is still elliptically polarized. Under the presupposition that  $\xi_0$  is not a pure imaginary but has nonzero real part, some of the parameters among  $\epsilon$ ,  $\epsilon_z$ ,  $\mu$  and  $\mu_z$  should have negative real parts in order to satisfy Eq. (10), and this condition could be realized by the super-developed design and manufacture of metamaterials. Note that Eq. (10) is independent of  $\theta$ , which means this happens for every  $\theta$  angle.

Different from biisotropic chiral media, the uniaxially anisotropic chiral media investigated in this paper need its constitutive parameters to satisfy some condition to make the waves inside them circularly polarized ( $\frac{D_2}{D_1} = \pm i$ ), which is

$$\frac{u^2}{\nu_{22}} - \kappa_{11} = \frac{u^2}{\nu_{11}} - \frac{\chi_{22}^2}{\nu_{22}} - \kappa_{22}. \quad (13)$$

This can be decomposed into two sub-conditions:  $\frac{1}{\nu_{22}} = \frac{1}{\nu_{11}}$  and  $\kappa_{11} = \frac{\chi_{22}^2}{\nu_{22}} + \kappa_{22}$ .

Substituting the values for the constitutive tensor elements, we simplify the condition and yield:

$$\xi_0^2 = \epsilon_z (\mu_z - \mu), \quad (14)$$

$$\epsilon_z = \frac{\epsilon(\mu - \mu_z) \sin^2 \theta + \epsilon \mu_z}{\mu}. \quad (15)$$

From Eq. (14) we can see that  $\mu_z$  must not be equal to  $\mu$  to guarantee  $\xi_0 \neq 0$ ; on the other hand, based on the precondition  $\mu_z \neq \mu$ , from Eq. (15) we discover that when  $\theta = 90^\circ$  the demand for the permittivity tensor components becomes  $\epsilon_z = \epsilon$  which means the medium degenerates from uniaxially anisotropic to isotropic for its permittivity. This is illustrated clearly in Fig. 1, all the curves assemble at the point (90, 1). As in this case of heterodox medium with isotropic permittivity, uniaxially anisotropic permeability, and charily existing only in  $\hat{z}$  direction whose value is coincident with the condition in Eq. (14), a linearly polarized wave entering this medium along the  $\hat{z}$  direction is broken up into two characteristic waves that propagate at different velocities, both of which are circularly polarized but with opposite handedness. This is exactly the condition for *optical activity*.

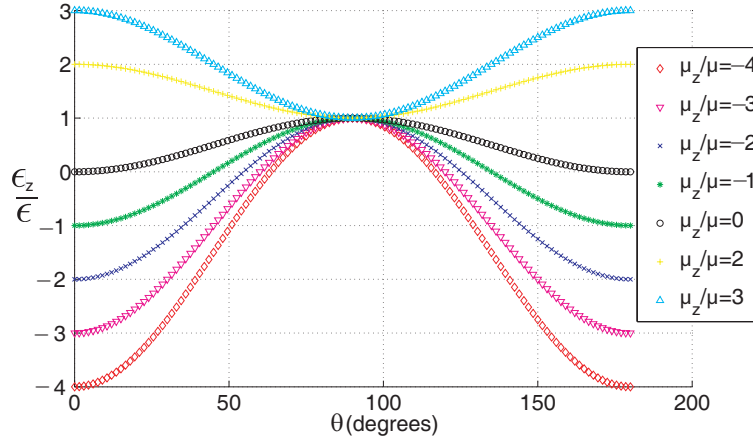


Figure 1: (Color online) The optical activity condition for the uniaxially anisotropic chiral media. The curves of ratio value  $\epsilon_z/\epsilon$  changing with angle  $\theta$  at different  $\mu_z/\mu$  ratio values.

Besides, according to Fig. 1, not only for normal incidence ( $\theta = 90^\circ$ ), but the optical activity also happens for all the other  $\theta$  values, as soon as the ratio of  $\epsilon_z/\epsilon$ , the ratio of  $\mu_z/\mu$  and  $\xi^2$  satisfy the condition (Eq. (14) and Eq. (15)) simultaneously. Therefore, taking the advantage of quickly developing matematerial designing and manufacturing nowadays, we can control the parameters values and make a medium described above to realize optical activity only when the wave incident in a certain angle as demanded.

### 3. NONRECIPROCAL UNIAXIALLY BIANISOTROPIC MEDIA

The nonreciprocal uniaxially bianisotropic medium has the following constitutive relations:

$$\begin{aligned} \bar{D} &= \epsilon_0 \begin{pmatrix} \epsilon & 0 & 0 \\ 0 & \epsilon & 0 \\ 0 & 0 & \epsilon_z \end{pmatrix} \cdot \bar{E} + \frac{1}{c} \begin{pmatrix} 0 & 0 & 0 \\ 0 & 0 & 0 \\ 0 & 0 & \xi_0 \end{pmatrix} \cdot \bar{H}, \\ \bar{B} &= \frac{1}{c} \begin{pmatrix} 0 & 0 & 0 \\ 0 & 0 & 0 \\ 0 & 0 & \xi_0 \end{pmatrix} \cdot \bar{E} + \mu_0 \begin{pmatrix} \mu & 0 & 0 \\ 0 & \mu & 0 \\ 0 & 0 & \mu_z \end{pmatrix} \cdot \bar{H}, \end{aligned} \quad (16)$$

thereinto,  $\epsilon_0$  and  $\mu_0$  are the permittivity and permeability of free space respectively, and  $c$  is the speed of light in free space. Here  $\epsilon$ ,  $\epsilon_z$ ,  $\mu$ ,  $\mu_z$ , and  $\xi_0$  are all dimensionless quantities, and  $\xi_0$  is the non-reciprocity parameter, which is also called *Tellegen* parameter in many places [2]. As we can see, the non-reciprocity parameter also exists only in  $\hat{z}$  direction just like the chirality parameter in previous section for the reciprocal medium. Similarly as what we do to the reciprocal uniaxially bianisotropic medium in the previous section, we obtain the key matrix for this nonreciprocal medium in  $kDB$  system just like Eq. (6), which is

$$\begin{bmatrix} \frac{u^2}{\nu_{22}} - \kappa_{11} & -u \frac{\chi_{22}}{\nu_{22}} \\ -u \frac{\chi_{22}}{\nu_{22}} & \frac{u^2}{\nu_{11}} - \frac{\chi_{22}^2}{\nu_{22}} - \kappa_{22} \end{bmatrix} \begin{bmatrix} D_1 \\ D_2 \end{bmatrix} = 0 \quad (17)$$

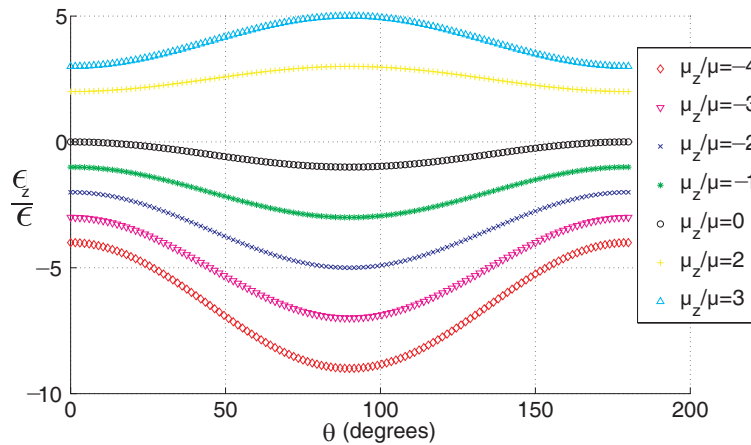


Figure 2: (Color online) The condition for the uniaxially anisotropic nonreciprocal media to obtain linearly polarized wave. The curves of ratio value  $\epsilon_z/\bar{\epsilon}$  changing with angle  $\theta$  at different  $\mu_z/\mu$  ratio values.

where  $u = \omega/k$  is the phase velocity for characteristic waves inside the medium. The tiny difference between the two matrixes in Eq. (6) and Eq. (17) is that there is one more minus sign for the off-diagonal element in the first line of the matrix for nonreciprocal medium, and  $\chi_{22} = -\chi_0 \sin^2 \theta$  which is also a little different from reciprocal medium, changing  $i$  into a minus sign. If Eq. (13) still holds in this case, these two little changes will cause two consequences:

1. The condition is not for circularly polarized waves any more, on the contrary, it is for linearly polarized wave, as there is no  $i$  in the ratio of  $D_2/D_1$ . There is only one kind of polarization in the nonreciprocal medium under this condition and it is linearly polarized.
2. Equation (14) remains the same, while Eq. (15) becomes

$$\epsilon_z = \frac{\epsilon(\mu_z - \mu) \sin^2 \theta + \epsilon\mu_z}{\mu} \quad (18)$$

for this nonreciprocal bianisotropic medium as Fig. 2 shows. As we can see, comparing to the uniaxially anisotropic chiral media, there is no such point of intersection as in Fig. 1.

#### 4. CONCLUSIONS

In conclusion, the polarizations of waves in reciprocal and nonreciprocal uniaxially bianisotropic media are studied, whose corresponding chirality parameter and Tellegen parameter appear only in one direction. By analyzing constitutive parameters for generating circularly polarized waves, we find that the optical-activity effects happen in such kind of uniaxially anisotropic chiral media under certain conditions. On the other hand, similar conditions give birth to linearly polarized waves in nonreciprocal uniaxially bianisotropic media.

#### ACKNOWLEDGMENT

This work was supported by the Chinese Natural Science Foundation under Grant No. 60531020.

#### REFERENCES

1. Kong, J. A., *Electromagnetic Waves Theory*, EMW Publishing, Cambridge, MA, USA, 2005.
2. Serdyukov, A., I. Semchenko, S. Tretyakov, and A. Sihvola, *Electromagnetics of Bi-Anisotropic Materials*, OPA, Amsterdam, 2001.
3. Pasteur, L., *Ann. Chim. Phys.*, Vol. 28, 56, 1850.
4. Lindeman, K., *Ann. Phys.*, Leipzig, Vol. 63, 621, 1920.
5. Sommerfeld, A., *Optics*, Academic, New York, 1954.
6. Tellegen, B. D. H., *Philips Res. Rep.*, Vol. 3, 81, 1948.
7. Cheng, Q. and T. J. Cui, *Phys. Rev. B*, Vol. 73, 113104, 2006.
8. Cheng, X. X., H. S. Chen, L. X. Ran, B.-I. Wu, T. M. Grzegorczyk, and J. A. Kong, *Phys. Rev. B*, Vol. 76, 024402, 2007.

# Identification of Defects in Materials with Surface Conductivity Distribution

J. Dědková

Department of Theoretical and Experimental Electrical Engineering  
Brno University of Technology  
Kolejní 2906/4, Brno 612 00, Czech Republic

**Abstract**— The images of the electrical surface conductivity distribution can be reconstructed from the voltage measurement captured on the boundaries of an object. This very well known technique is named Electrical Impedance Tomography. The image reconstruction problem is an ill-posed inverse problem of finding such conductivity  $\sigma_s$  that minimizes some optimisation criterion, which can be given by a suitable primal objective function. This paper describes new algorithms based on stochastic methods to be used for the acquirement of more accurate reconstruction results and stable solution. The proposed methods are expected to non-destructive test of materials. It will be shown examples of the identification of voids or cracks in special structures called honeycombs. Instead of the experiments we used phantom evaluated voltage values based on the application of finite element method. The advantages of a new approach are compared with properties of a deterministic approach to the same image reconstructions.

## 1. INTRODUCTION

In EIT an approximation of the internal conductivity or resistivity distribution is computed based on the knowledge of the voltages and currents on the surface of the body. We have studied the possibilities of using stochastic and deterministic methods to reconstruct static two-dimensional (2D) conductivity distribution of thin conductive layers of unknown surface conductivity and known geometry. An arrangement of 2D model for experiment and an example of the honeycombs structure are shown in Fig. 1.

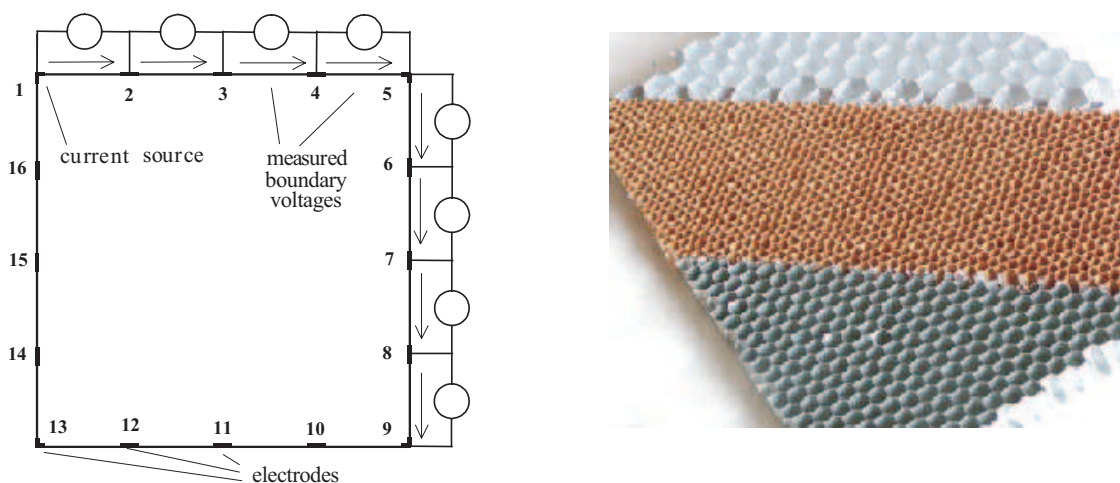


Figure 1: An arrangement of 2D model, an example of honeycombs structure.

We will show that the 2D static images obtained from the solution of inverse problems are able to recover the original values by means of suitable algorithms based on stochastic or deterministic methods. In inverse problems the forward problem is used to predict the observation. The frequency range of the applied current sources used in EIT is of the order of kHz. The corresponding wavelength of the electromagnetic wave is much larger than the dimension of the specimen under inspection so that curl electric field components as well as displacement current influence can be neglected and only the conductive currents are considered. Further we assume the existence of the thin conductive layers only. Let  $\text{grad}_s$  and  $\text{div}_s$  be the surface gradient and the surface divergence operators on such conductive layer. This field is described by the continuity equation

$$\text{div}_s \sigma_s \text{grad}_s U = 0. \quad (1)$$

Here,  $U$  is the potential and  $\sigma_s$  is the unknown surface conductivity distribution in  $S$ . The problem is solved as a static one. The solution of (1) satisfies the Dirichlet and Neumann boundary conditions, too. Equation (1) together with the complete electrode model [1] is discretized by the Finite Element Method (FEM) in the usual way. We approximated (1) from nodal values  $U_j$  using approximation functions  $W_j$  on a grid of linear triangular finite elements

$$U = \sum_{nodes} U_j W_j(x, y) \quad (2)$$

Applying the Galerkin method to (1) and integrating by parts we have ( $\mathbf{m}$  is the outer unit normal to the thin layer)

$$\int_{layer} \sigma_s \text{grad}_s W_i \cdot \text{grad}_s U \, dl - \int_c \sigma_s W_i \text{grad}_s U \cdot \mathbf{m} \, dc = 0. \quad (3)$$

The line integral along  $c$  is nonzero only for those nodes  $i$  that belong to curve  $c$  common to layer  $l$  and to the surface of the current supply electrodes. We include the electrode contact impedances according to [1] in (3) and we obtain the resulting discretized system of linear equations of the form (forward model)

$$\mathbf{K}U = \mathbf{F} \quad (4)$$

where the contribution of nodes  $i, j$  of the finite element (e) to  $\mathbf{K}$  is

$$\Delta k_{ij}^{(e)} = \int_{layer} \sigma_s^{(e)} \text{grad}_s W_i^{(e)} \cdot \text{grad}_s W_j^{(e)} \, dl. \quad (5)$$

## 2. PROPOSED TECHNIQUES FOR INVERSE PROBLEM

From a mathematical perspective, the EIT inverse problem searches for parameters in a high-dimensional space. Let define the primal objective function

$$\Psi(\sigma_s) = \frac{1}{2} \sum \|U_M - U_{FEM}(\sigma_s)\|^2. \quad (6)$$

Here  $\sigma_s$  is the surface conductivity distribution vector in the object,  $U_M$  is the vector of measured voltages on the boundary, and  $U_{FEM}(\sigma_s)$  is the vector of computed peripheral voltages in respect to  $\sigma_s$ , which can be obtained using FEM. To minimize the objective function  $\Psi(\sigma_s)$  we can use a lot of different methods based on both deterministic and stochastic approaches [2, 3]. When we apply the deterministic method based on the Least Squares (LS) method due to the ill-posed nature of the problem, regularization has to be used. It is possible to apply the widely known Tikhonov Regularization Method (TRM) or the Total Variation Primal Dual Interior Point Method (TV PD-IPM), described in [4, 5]. With respect to regularization the object function of TRM can be written in the form

$$\Psi(\sigma_s) = \frac{1}{2} \sum \|U_M - U_{FEM}(\sigma_s)\|^2 + \alpha \|A\sigma_s\|^2 \quad (7)$$

Here,  $\alpha$  is the regularization parameter, and  $A$  is the so-called regularization matrix. The primal objective function  $\Psi(\sigma_s)$  for TV PD-IPM algorithm

$$\Psi(\sigma_s) = \frac{1}{2} \sum \|U_M - U_{FEM}(\sigma_s)\|^2 + \alpha \sum \sqrt{\|A\sigma_s\|^2 + \beta}. \quad (8)$$

Here  $A$  is a suitable regularization matrix again and  $\beta$  is a small positive parameter, which represents an influence on the smoothing of  $\Psi(\sigma_s)$ . For the solutions of (7) and (8) we can apply a Newton-Raphson method. The iterative procedures are likely to be trapped in local minima and so sophisticated regularization must be taken into account to obtain the stable solution.

A little bit different approach present global optimizing evolutionary algorithms, such as genetic algorithms, which have been recently applied to the EIT problem [6, 7]. Compared to the genetic algorithms, the Differential Evolution Algorithm (DEA) is a relatively new heuristic approach to minimizing nonlinear and non-differentiable functions in a real and continuous space. DEA can converge faster and with more certainty than many other global optimization methods according

to various numerical experiments. It requires only a few control parameters and it is robust and simple in use. The details of the algorithm based on DEA can be found for example in [8]. Furthermore the algorithm so-called the Controlled Selection of Non-homogeneities (CSN) can be used to the reconstruction of the conductivity distribution [9]. The optimization of the primal objective function (6) based on the CSN is a relatively new technique with a very simple basic principle. All the briefly introduced methods were used to reconstruction of the surface conductivity distribution.

### 3. EXAMPLE AND COMPARISON OF RECONSTRUCTION RESULTS

A simple example of 2D grid of the honeycombs structure is given in Fig. 2. The grid is fully described by its nodes and edges. The mesh for the calculation of the gradients, voltage reference values, and the Jacobians du ring iterations, has a total of 384 edges, and 272 nodes. The same finite element mesh is used for the forward and the inverse calculations. The volume conductivity is assumed to be zero. The surface conductivity  $\sigma_s$  has non-zero value 72 700 S (on black edges) except the red colored edges, where the actual value of conductivity  $\sigma_s$  has zero value and these edges represent some cracks in honeycombs structure (see the original conductivity distribution in the Fig. 2). We assume the constant distribution of the conductivity  $\sigma_s$  on all edges.

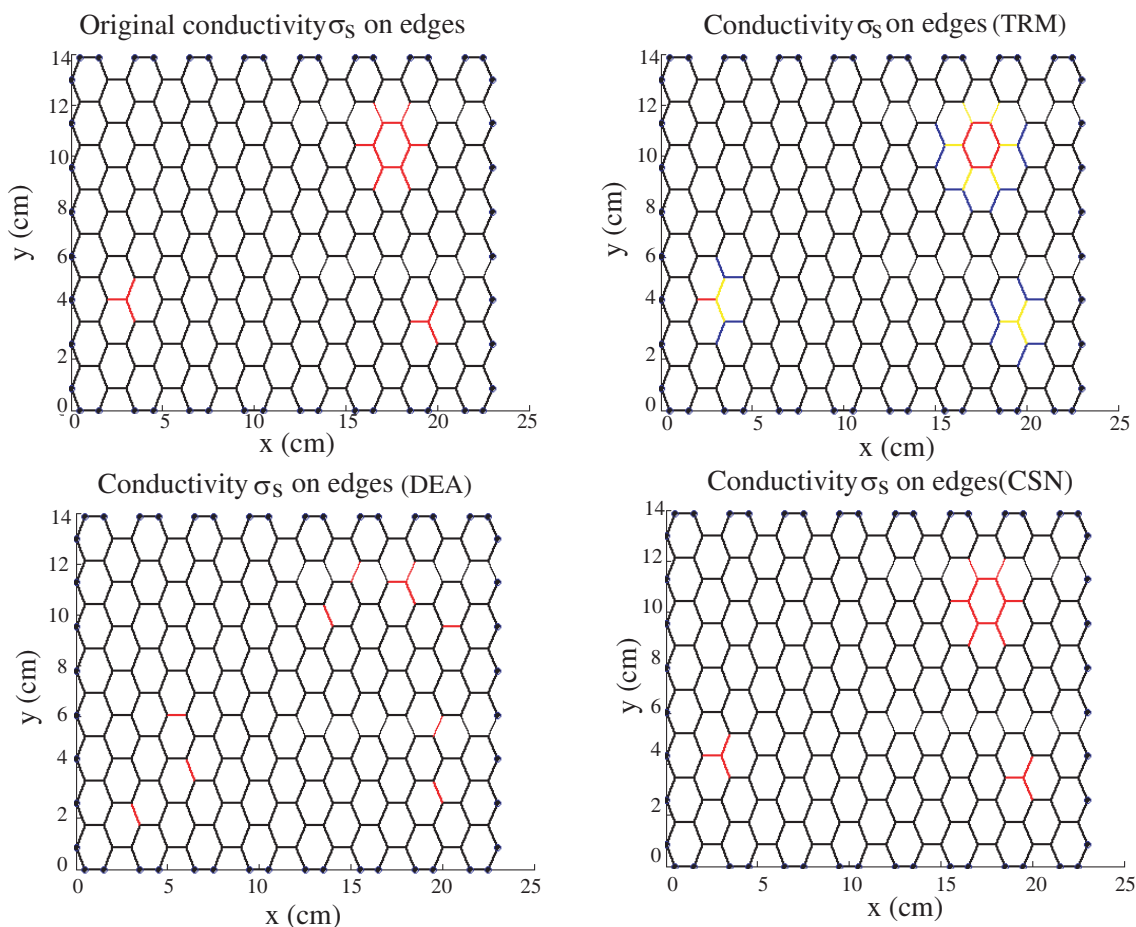


Figure 2: Example 1 of reconstruction results.

Two simple examples of some results of numerical experiments are presented in following figures. The number of current supply and voltage electrodes was 48 and the exciting currents were distributed trigonometrically with magnitude 1 mA. All the recovered values were obtained using modification of the TRM, PD-IPM, DEA and CSN algorithms. In the Fig. 2 are presented conductivity  $\sigma_s$  distributions on edges obtained using TRM, DEA and CSN algorithms. The conductivity distribution  $\sigma_s$  obtained using PD-IPM is not shown because it is very similar to results obtained using TRM, the accuracy of recovering results is a little bit worse in case of using PD-IPM. We needed 5 iterations to obtained results presented in Fig. 2 and the accuracy is strong depending on the value of the regularization parameter  $\alpha$ . We can see that the best result of reconstruction we

obtain in this case using CSN algorithm.

In Fig. 3 is presented another example of cracks distributions and recovered conductivity  $\sigma_s$  using TRM only, because the conductivity distribution obtained using PD-IPM is again very similar to results obtained using TRM, and the conductivity distribution  $\sigma_s$  obtained using CSN is the same as the original conductivity on edges. It was verified that the algorithm based on DEA is not suitable to solve the inverse problem of this above described category.

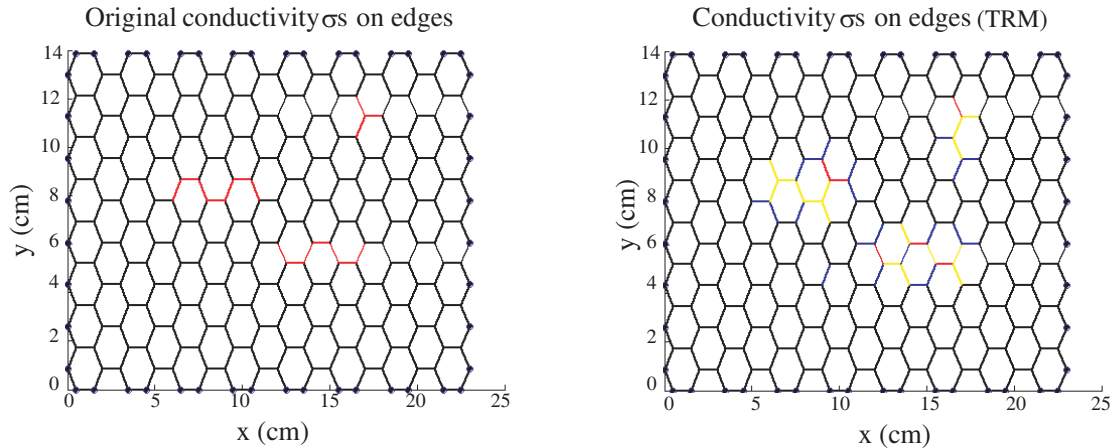


Figure 3: Example 2 of reconstruction results.

#### 4. CONCLUSION

In this paper a new possibilities to the reconstruction of non-homogeneities distribution has been presented. The all algorithms based on both deterministic and stochastic approaches have been adapted to reconstruction of conductivity distributions in special honeycombs structures. Many numerical experiments performed during the above-described algorithms and methods have resulted in the conclusion that only the application of the CSN reconstruction algorithm has an advantage over the TRM in better accuracy and stability of the reconstruction process. On the other hand the CSN is very time-consuming technique. The stability of the TRM algorithm is a bit sensitive to the setting of the starting value of conductivity. The regularization parameter controls the relative weighting allocated to the prior information. Its optimal choice provides balance between the accuracy and stability of the solution. On the basis of many numerical experiments, it is supposable that we obtain higher accuracy of the reconstruction results for smaller value of the parameter  $\alpha$ , but if the value of  $\alpha$  is decreasing, the instability of the solution is increasing. The results stated above as well as many other examples were obtained using a program written in MATLAB by author.

The next paper will presented other possibilities and some examples to obtain the effective reconstruction results in more practical cases with respect to the best accuracy, stability and space resolution of non-homogeneities.

#### ACKNOWLEDGMENT

The research described in the paper was financially supported by the research programs MSM 0021630513.

#### REFERENCES

1. Vilhunen, T., J. P. Kaipio, T. Savolainen, and M. Vauhkonen, "Simultaneous estimation of internal admittivity distribution and electrode contact impedances," Report 1, Univ. of Kuopio, 2002.
2. Cheney, M., D. Isaacson, and J. C. Newwell, "Electrical impedance tomography," *SIAM Rev.*, Vol. 41, No. 1, 85–101, 1999.
3. Michalewicz, Z., *Genetic Algorithms + Data Structure = Evolution Programs*, 2nd ed., Springer Verlag, Berlin, 1994.

4. Vauhkonen, M., D. Vadásy, P. A. Karjalainen, E. Somersalo, and J. P. Kaipio, "Tikhonov regularization and prior information in electrical impedance tomography," *IEEE Trans. Med. Eng.*, Vol. 17, 285–293, 1998.
5. Borsic, A., "Regularization methods for imaging from electrical measurement," *PhD. Thesis*, Oxford Brookes University, 2002.
6. Olmi, R., M. Bini, and S. Priori, "A genetic algorithm approach to image reconstruction in electrical impedance tomography," *IEEE Trans. Evol. Comp.*, Vol. 4, 83–88, 2000.
7. Yorkey, T. J., J. G. Webster, and W. J. Tomkins, "Comparing reconstruction algorithms for electrical impedance tomography," *IEEE Trans. Biomed. Eng.*, Vol. 34, 843–852, 1987.
8. Bachorec, T., T. Jirku, and J. Dedkova, "New numerical technique for non-destructive testing of the conductive materials," *PIERS Online*, Vol. 3, No. 5, 709–713, Beijing, China, 2007.
9. Kubásek, R., T. Bachorec, and J. Dědková, "Identification of defects in materials using EIT," *Electronic Devices and Systems*, 285–289, Brno, Czech Republic, September 2006.

# Image Reconstruction Using Combination Deterministic and Stochastic Method

J. Dědková

Department of Theoretical and Experimental Electrical Engineering  
Brno University of Technology  
Kolejní 2906/4, Brno 612 00, Czech Republic

**Abstract**— This paper proposes a new algorithm based on the combination of deterministic and stochastic methods to be used to obtain the best results of a reconstruction process of the surface conductivity distribution. The images of the electrical surface conductivity distribution can be reconstructed from voltage measurement captured on the boundaries of an object. The image reconstruction problem is an ill-posed inverse problem of finding such surface conductivity that minimizes the suitable optimisation criterion. The advantages of a new approach are compared with properties of deterministic and stochastic approaches during the same image reconstructions. It will be shown that proposed algorithm is a very effective way to obtain the satisfying identification of cracks in special structures called honeycombs.

## 1. INTRODUCTION

Electrical impedance tomography (EIT) is used to reconstruct the conductivity distribution by the measured surface electric potential distribution around the phantom when injecting current into the object [1]. The electric potential distribution on the surface generated by the injected current could be obtained as a solution of the Laplace equation. Many published papers have already described the recovering of volume conductivity. But it is well known that some industrial products can better be described by surface conductivity or by the combination of both parameters. The theoretical background of EIT with surface conductivities is given in [2]. EIT image reconstruction problem is an ill-posed inverse problem of finding such surface conductivity  $\sigma_s$  that minimizes certain optimisation criterion, which can be given by the suitable objective function. Let define the primal objective function

$$\Psi(\sigma_s) = \frac{1}{2} \sum \|U_M - U_{FEM}(\sigma_s)\|^2. \quad (1)$$

Here  $\sigma_s$  is the surface conductivity distribution vector in the object,  $U_M$  is the vector of measured voltages on the boundary, and  $U_{FEM}(\sigma_s)$  is the vector of computed peripheral voltages in respect to  $\sigma_s$ , which can be obtained using FEM. To minimize the objective function  $\Psi(\sigma_s)$  we can use a lot of different methods based on both deterministic and stochastic approaches [3–6]. When we apply the deterministic method based on the Least Squares (LS) method due to the ill-posed nature of the problem, regularization has to be used. It is possible to apply the widely known Tikhonov Regularization Method (TRM), described in [4]. With respect to regularization the primal object



Figure 1: Some cracks in honeycombs.

function of TRM can be written in the form

$$\Psi(\sigma_s) = \frac{1}{2} \sum \|U_M - U_{FEM}(\sigma_s)\|^2 + \alpha \|A\sigma_s\|^2 \quad (2)$$

Here,  $\alpha$  is the regularization parameter, and  $A$  is the so-called regularization matrix. For the solutions of (2) we can apply a Newton-Raphson method. The iterative procedures are likely to be trapped in local minima and so sophisticated regularization must be taken into account to obtain the stable solution.

A little bit different approach present global optimizing evolutionary algorithms, such as genetic algorithms, which have been recently applied to the EIT problem [3, 5]. We have been applied to the reconstruction of the conductivity distribution the algorithm based on the Controlled Selection of Non-homogeneities (CSN) described in [7]. The optimization of the primal objective function (1) based on the CSN is a relatively new technique with a very simple basic principle,

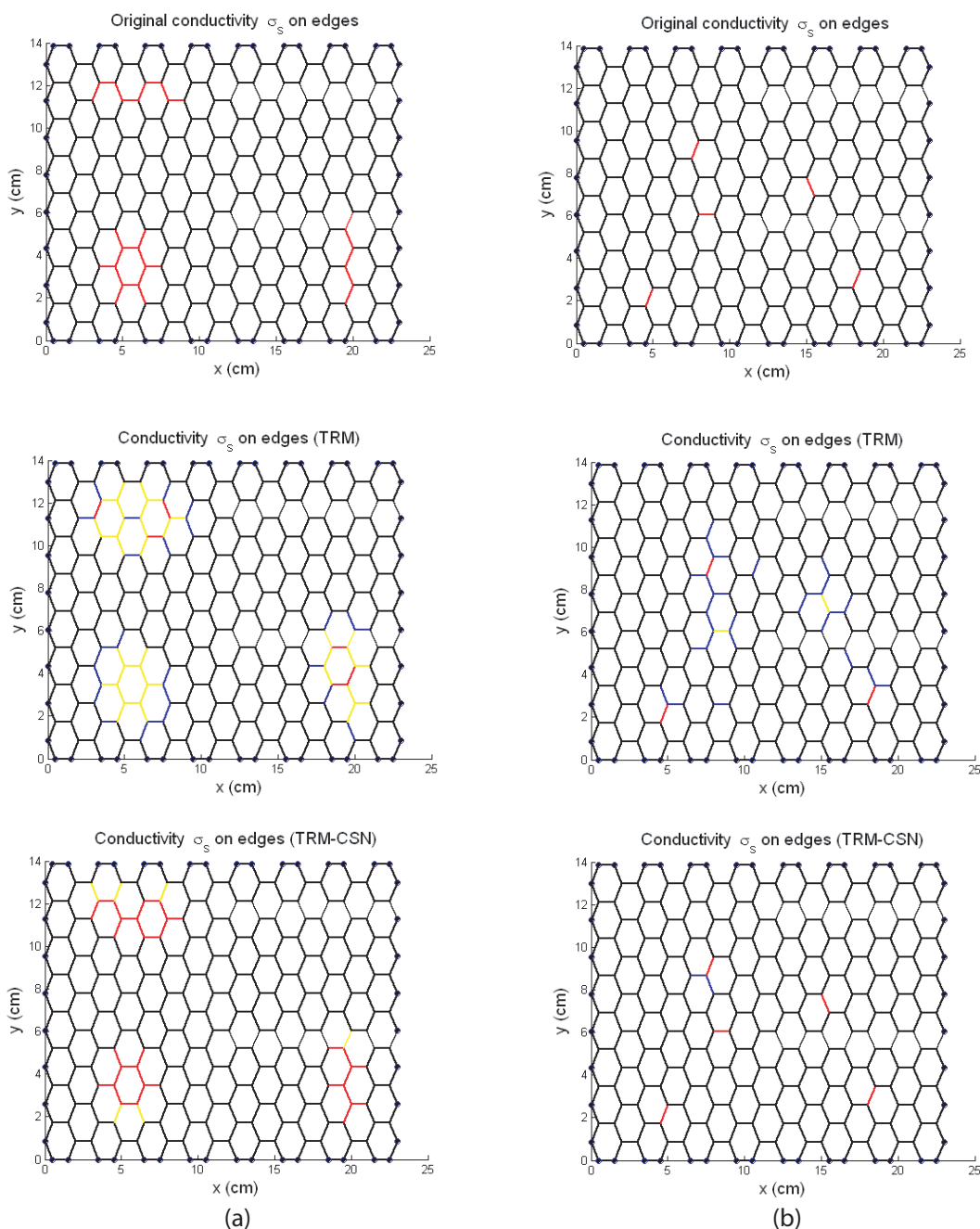


Figure 2: Reconstruction results, length of edge is 1 cm.

but it is unfortunately a very time-consuming algorithm. To obtain the effective method for the image reconstruction process we propose algorithm based on the both above mentioned methods. First we apply the TRM to find subregions where the non-homogeneities can occur and then it is possible to specify effectively the accurate distribution of the non-homogeneities using the CSN. The proposed algorithm can be used to practical detection of cracks in honeycombs structures, see Fig. 1.

## 2. VERIFICATION AND RESULTS

Simple examples of 2D grid of honeycombs structures are given in Fig. 2 (respectively in Fig. 3). The mesh has a total of 384 edges and 272 nodes, (respectively 2400 edges and 1640 nodes). The surface conductivity  $\sigma_s$  has non-zero value 72 700 S (on black edges), on the red colored edges are

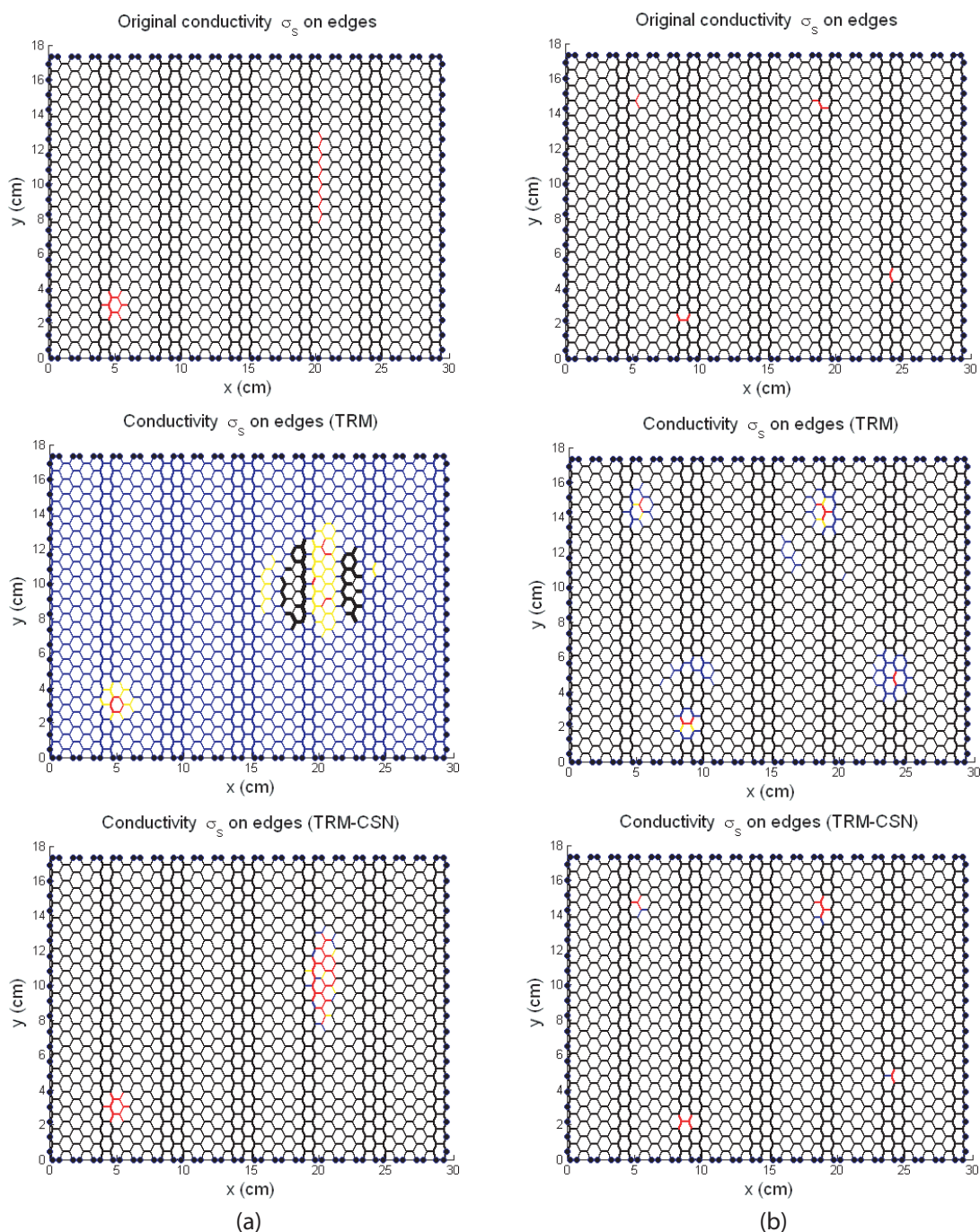


Figure 3: Reconstruction results, length of edge is 0.5 cm.

assume zero value of conductivity and these edges represent some cracks in honeycombs structure (see the original conductivity distribution in Fig. 2 and in Fig. 3).

In the Fig. 2 are presented conductivity  $\sigma_s$  distributions on edges obtained using the TRM, CSN and TRM-CSN algorithms for two cases of cracks distribution. When we used the TRM we needed 5 iterations to obtain presented results and the accuracy and the stability was strong depending on the value of the regularization parameter  $\alpha$ . The best results of the reconstruction we obtain using the CSN algorithm, but the needed time was ten times greater then the time needed for TRM algorithm for an arrangement due to Fig. 2 and more then three hundred times greater for an arrangement due to Fig. 3. When we used to reconstruction proposed algorithm TRM-CSN, we obtained the satisfactory reconstruction results in the same time which is needed for the TRM.

### 3. CONCLUSION

In this paper has been presented one effective algorithm to a reconstruction of the cracks distributions in special materials structures. Many numerical experiments performed during the above-described methods have resulted in the conclusion that the application of the CSN reconstruction algorithm has a significant advantage over the TRM in better accuracy and the stability of the reconstruction process, but on the other hand the CSN is a very time-consuming technique. The algorithm TRM-CSN based on combination of the both methods was proposed and verified. On the basis of many numerical experiments, we can confidently say that the TRM-CSN algorithm is a very effective tool to detect the cracks distributions in honeycombs structures with respect to the best accuracy, the stability and the space resolution. The results stated above as well as many other examples were obtained using a program written in MATLAB by author.

The next work will focused to enlarge the possibility to reconstruction of the cracks distributions in 3D honeycombs structures.

### ACKNOWLEDGMENT

The research described in the paper was financially supported by the research programs MSM 0021630513.

### REFERENCES

1. Cheney, M., D. Isaacson, and J. C. Newwell, "Electrical impedance tomography," *SIAM Rev.*, Vol. 41, No. 1, 85–101, 1999.
2. Dědková, J., "Identification of defects in materials with surface conductivity distribution," *Proceedings of PIERS*, (in print), Hangzhou, China, March 24–28, 2008.
3. Michalewicz, Z., *Genetic Algorithms+Data Structure=Evolution Programs*, 2nd ed., Springer Verlag, Berlin, 1994.
4. Vauhkonen, M., D. Vadásy, P. A. Karjalainen, E. Somersalo, and J. P. Kaipio, "Tikhonov regularization and prior information in electrical impedance tomography," *IEEE Trans. Med. Eng.*, Vol. 17, 285–293, 1998.
5. Olmi, R., M. Bini, and S. Priori, "A genetic algorithm approach to image reconstruction in electrical impedance tomography," *IEEE Trans. Evol. Comp.*, Vol. 4, 83–88, 2000.
6. Yorkey, T. J., J. G. Webster, and W. J. Tomkins, "Comparing reconstruction algorithms for electrical impedance tomography," *IEEE Trans. Biomed. Eng.*, Vol. 34, 843–852, 1987.
7. Kubásek, R., T. Bachorec, and J. Dědková, "Identification of defects in materials using EIT," in *Electronic Devices and Systems*, 285–289, Brno, Czech Republic, September 2006.

# Laplace Transform and FDTD Approach Applied to MTL Simulation

J. Dědková<sup>1</sup> and L. Brančík<sup>2</sup>

<sup>1</sup>Department of Theoretical and Experimental Electrical Engineering  
Brno University of Technology

Kolejní 2906/4, Brno 612 00, Czech Republic

<sup>2</sup>Department of Radio Electronics, Brno University of Technology  
Purkyňova 118, Brno 612 00, Czech Republic

**Abstract**— The paper proposes two different approaches to simulation of multiconductor transmission lines (MTL). Numerical results of MTL simulations based on both the Laplace transform and Finite Difference Time Domain (FDTD) method are presented and compared. Fundamental algorithms were programmed in Matlab language. Some typical situations are solved as illustration of the results.

## 1. INTRODUCTION

Let us suppose a simple MTL linear system consisting of a uniform  $(n + 1)$ -conductor transmission line terminated at both ends (left (1), right (2)) by linear lumped-parameter networks, see Fig. 1.

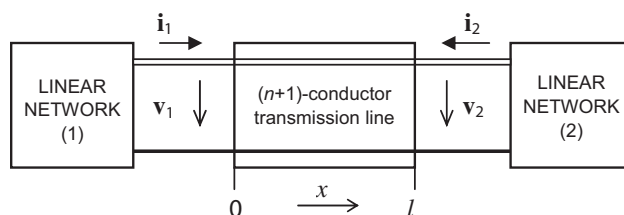


Figure 1: Simple MTL linear system.

The MTL is considered to be of a length  $l$ , with per-unit-length  $n \times n$  matrices  $\mathbf{R}_0$ ,  $\mathbf{L}_0$ ,  $\mathbf{G}_0$  and  $\mathbf{C}_0$ . The basic MTL equations can be expressed as [1]

$$-\frac{\partial \mathbf{v}(t, x)}{\partial x} = \mathbf{R}_0 \mathbf{i}(t, x) + \mathbf{L}_0 \frac{\partial \mathbf{i}(t, x)}{\partial t}, \quad -\frac{\partial \mathbf{i}(t, x)}{\partial x} = \mathbf{G}_0 \mathbf{v}(t, x) + \mathbf{C}_0 \frac{\partial \mathbf{v}(t, x)}{\partial t}, \quad (1)$$

where  $\mathbf{v}(t, x)$  and  $\mathbf{i}(t, x)$  are  $n \times 1$  column vectors of instantaneous voltages and currents of  $n$  active wires at a distance  $x$  from MTL's left end respectively.

To solve the above stated system two basic approaches will be considered. First, the Equation (1) will be treated in the  $s$ -domain after the Laplace transform is applied, and then a proper method for numerical inversion of Laplace transform (NILT) will be used to get the required time-domain solution. In principle, both one- and two-dimensional Laplace transforms can be utilized for this purpose, see e.g., [1–3]. Second, the Equation (1) will be treated in the time-domain directly. Among many other methods, the FDTD approach seems to be very well applicable [4–6]. The Laplace transform approach does not make it possible to consider a nonlinear MTL in general. On the other hand, it is relatively easy to incorporate boundary conditions defined by terminating networks just in the  $s$ -domain. The FDTD approach can handle both linear and nonlinear cases. The connection of distributed and lumped parts, however, can be more complicated.

## 2. LAPLACE TRANSFORM APPROACH

Herein, only a method based on the one-dimensional Laplace transform will be considered. After performing Laplace transform with respect to time, and considering only zero initial voltage and current distributions along the MTL's wires ( $\mathbf{v}(0, x) = \mathbf{i}(0, x) = 0$ ), the Equation (1) lead to a compact matrix form [1]

$$\frac{d}{dx} \begin{bmatrix} \mathbf{V}(s, x) \\ \mathbf{I}(s, x) \end{bmatrix} = \begin{bmatrix} 0 & -\mathbf{Z}(s) \\ -\mathbf{Y}(s) & 0 \end{bmatrix} \cdot \begin{bmatrix} \mathbf{V}(s, x) \\ \mathbf{I}(s, x) \end{bmatrix}, \quad (2)$$

where  $\mathbf{Z}(s) = \mathbf{R}_0 + s\mathbf{L}_0$  and  $\mathbf{Y}(s) = \mathbf{G}_0 + s\mathbf{C}_0$  is a per-unit-length series impedance and shunting admittance matrix respectively. The solution of (2) can be expressed as

$$\begin{bmatrix} \mathbf{V}(s, x) \\ \mathbf{I}(s, x) \end{bmatrix} = \exp \left( \begin{bmatrix} 0 & -\mathbf{Z}(s) \\ -\mathbf{Y}(s) & 0 \end{bmatrix} x \right) \cdot \begin{bmatrix} \mathbf{V}(s, 0) \\ \mathbf{I}(s, 0) \end{bmatrix} = \begin{bmatrix} \Phi_{11}(s, x) & \Phi_{12}(s, x) \\ \Phi_{21}(s, x) & \Phi_{11}^T(s, x) \end{bmatrix} \cdot \begin{bmatrix} \mathbf{V}(s, 0) \\ \mathbf{I}(s, 0) \end{bmatrix}, \quad (3)$$

where  $\mathbf{V}(s, 0)$  and  $\mathbf{I}(s, 0)$  are given by boundary conditions. The matrix exponential function, called a chain matrix  $\Phi(s, x)$ , is decomposed into square submatrices in (3). Then the solution can be split into separate matrix equations

$$\mathbf{V}(s, x) = \Phi_{11}(s, x)\mathbf{V}(s, 0) + \Phi_{12}(s, x)\mathbf{I}(s, 0), \quad \mathbf{I}(s, x) = \Phi_{21}(s, x)\mathbf{V}(s, 0) + \Phi_{11}^T(s, x)\mathbf{I}(s, 0). \quad (4)$$

The boundary conditions can be expressed by generalized Thvenin or Norton equivalents in the form

$$\mathbf{V}_{1(2)}(s) = \mathbf{V}_{i1(2)}(s) - \mathbf{Z}_{i1(2)}(s)\mathbf{I}_{1(2)}(s) \quad \text{or} \quad \mathbf{I}_{1(2)}(s) = \mathbf{I}_{i1(2)}(s) - \mathbf{Y}_{i1(2)}(s)\mathbf{V}_{1(2)}(s), \quad (5)$$

while new designations were taken into account as  $\mathbf{V}_1(s) = \mathbf{V}(s, 0)$ ,  $\mathbf{I}_1(s) = \mathbf{I}(s, 0)$ , and  $\mathbf{V}_2(s) = \mathbf{V}(s, l)$ ,  $\mathbf{I}_2(s) = -\mathbf{I}(s, l)$  for the left and right MTL's side respectively. Here  $\mathbf{V}_i(s)$  and  $\mathbf{I}_i(s)$  are  $n \times 1$  vectors of internal voltages and currents,  $\mathbf{Z}_i(s)$  and  $\mathbf{Y}_i(s)$  mean  $n \times n$  internal impedance and admittance matrices respectively. For example, when using generalized Norton equivalents, the equation can be derived as [2]

$$\mathbf{V}_1(s) = \left[ (\Phi_{11}^T(s) - \mathbf{Y}_{i2}(s)\Phi_{12}(s)) \mathbf{Y}_{i1}(s) + \mathbf{Y}_{i2}(s)\Phi_{11}(s) - \Phi_{21}(s) \right]^{-1} \left[ (\Phi_{11}^T(s) - \mathbf{Y}_{i2}(s)\Phi_{12}(s)) \mathbf{I}_{i1}(s) + \mathbf{I}_{i2}(s) \right], \quad (6)$$

and the  $\mathbf{I}_1(s)$  is given by the corresponding equation in (5). Here  $\Phi_{ij}(s)$ ,  $i, j = 1, 2$ , mean square submatrices of the full chain matrix  $\Phi(s) = \Phi(s, l)$ . Having substituted (5) and (6) into (3), this equation can be treated by a proper NILT method to get the time-domain solution. In this paper the NILT [7] has been applied, see examples below.

### 3. FDTD APPROACH

For a numerical solution of the above described wave equation system (1) the widely known Finite Difference Time Domain method can also be used. The main aim is to approximate the temporal and spatial derivatives by the suitable difference expression, which ensures the best stability and the highest accuracy of the numerical solution. There are a lot of possibilities how to replace the above mentioned derivatives. One of them is to use the implicit Wendorff formula, which can be described for the  $n$ -th time step and for the  $k$ -th spatial element of transmission line by the following expression

$$\frac{\partial \mathbf{v}(t, x)}{\partial t} \approx \frac{1}{2} \left( \frac{\mathbf{v}_k^n - \mathbf{v}_k^{n-1}}{\Delta t} + \frac{\mathbf{v}_{k+1}^n - \mathbf{v}_{k+1}^{n-1}}{\Delta t} \right), \quad \frac{\partial \mathbf{v}(t, x)}{\partial x} \approx \frac{1}{2} \left( \frac{\mathbf{v}_{k+1}^n - \mathbf{v}_k^n}{\Delta x} + \frac{\mathbf{v}_{k+1}^{n-1} - \mathbf{v}_k^{n-1}}{\Delta x} \right). \quad (7)$$

Here the derivatives of voltages (currents) are replaced by a combination of both forward and backward differences. Some interesting results based on the application of the described formula can be found in [4, 5], where practical examples of a numerical modeling of the surge phenomena on transmission lines caused by the lightning stroke and on  $hv$  and  $vhv$  three phase transmission lines with earth wire are presented.

The aim of our investigation was to find an effective algorithm for numerical simulation of the current or voltage wave propagation on multiconductor transmission line. Therefore we carried out a lot of tests with the different way of replacing derivatives by the difference expression. When we used the backward differences the solution was often unstable, but when we used the forward differences, we obtained a stable solution but the accuracy deteriorated. The best solution was obtained by using so-called leapfrog method, when the spatial and temporal derivatives were replaced by the combination of both central and forward differences. This modification of FDTD was discussed for example in [6] and it was applied to the numerical simulation of electromagnetic wave propagations in a free space. So, the temporal and spatial derivatives in wave Equation (1) were replaced by the

four following expressions

$$\begin{aligned} \frac{\partial \mathbf{v}(t, x)}{\partial t} &\approx \frac{\mathbf{v}_k^{n+\frac{1}{2}} - \mathbf{v}_k^{n-\frac{1}{2}}}{\Delta t}, & \frac{\partial \mathbf{v}(t, x)}{\partial x} &\approx \frac{\mathbf{v}_{k+1}^{n+\frac{1}{2}} - \mathbf{v}_k^{n+\frac{1}{2}}}{\Delta x}, \\ \frac{\partial \mathbf{i}(t, x)}{\partial t} &\approx \frac{\mathbf{i}_{k+\frac{1}{2}}^{n+1} - \mathbf{i}_{k+\frac{1}{2}}^n}{\Delta t}, & \frac{\partial \mathbf{i}(t, x)}{\partial x} &\approx \frac{\mathbf{i}_{k+\frac{1}{2}}^n - \mathbf{i}_{k-\frac{1}{2}}^n}{\Delta x}. \end{aligned} \tag{8}$$

To simulate the current and voltage distributions  $\mathbf{v}(t, x)$  and  $\mathbf{i}(t, x)$  along all lines of MTL in arbitrary time  $t = n\Delta t$ , the implicit formula can be expressed in a compact matrix form

$$\begin{bmatrix} \mathbf{v}(x_1, \dots, x_{M+1}) \\ \mathbf{i}(x_1, \dots, x_{M+1}) \end{bmatrix}^{n+1} = \mathbf{A}^{-1} \left( \mathbf{B} \begin{bmatrix} \mathbf{v}(x_1, \dots, x_{M+1}) \\ \mathbf{i}(x_1, \dots, x_{M+1}) \end{bmatrix}^n + \mathbf{D} \right). \tag{9}$$

The coefficients of matrices  $\mathbf{A}$  and  $\mathbf{B}$  are given by the per-unit-length matrices, the matrix  $\mathbf{D}$  is given by sources.

#### 4. ERROR ANALYSIS

Both the above mentioned numerical methods were used to simulate the current and voltage wave propagation along a transmission line. As an example we suppose an infinitely long line with a negligible leakage and inductance, so-called Thomson cable, with  $G_0 = 0$  and  $L_0 = 0$ , see Fig. 2 [8].

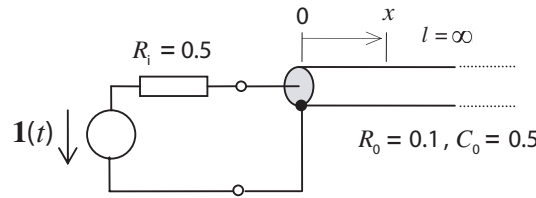


Figure 2: Model and parameters of Thomson cable.

The remaining primary parameters  $R_0$  and  $C_0$  are given in normalized forms. The cable is excited from the source of unit step voltage  $v_i(t) = \mathbf{1}(t)$  and resistance  $R_i$ , which can represent internal resistance of this voltage source. In that case the closed form solution exists and the accuracy of both numerical approaches can be verified. We used the closed form solution which is derived for example in [8]

$$\begin{aligned} i(t, x) &= \frac{1}{R_i} \exp\left(\frac{R_0}{R_i^2 C_0} t + \frac{R_0}{R_i} x\right) \cdot \operatorname{erfc}\left(\frac{1}{R_i} \sqrt{\frac{R_0}{C_0}} t + \frac{x}{2} \sqrt{\frac{R_0 C_0}{t}}\right), \\ v(t, x) &= \operatorname{erfc}\left(\frac{x}{2} \sqrt{\frac{R_0 C_0}{t}}\right) - R_i i(t, x). \end{aligned} \tag{10}$$

In the above formulae  $\operatorname{erfc}$  means a complementary error function. In Fig. 3 and Fig. 4 you can see the calculated current  $i(t, x)$  and voltage  $v(t, x)$  distributions along the line together with the absolute errors in logarithmic scales of FDTD and Laplace transform approaches.

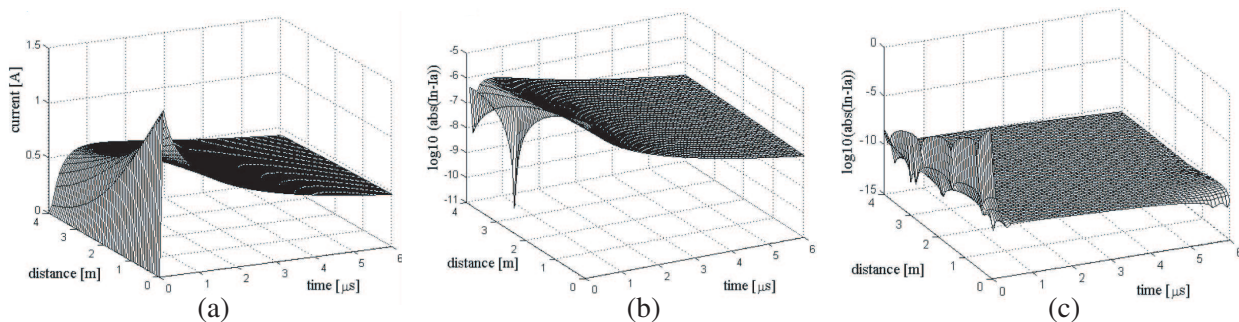


Figure 3: Current distribution (a) with FDTD error (b) and Laplace transform error (c).

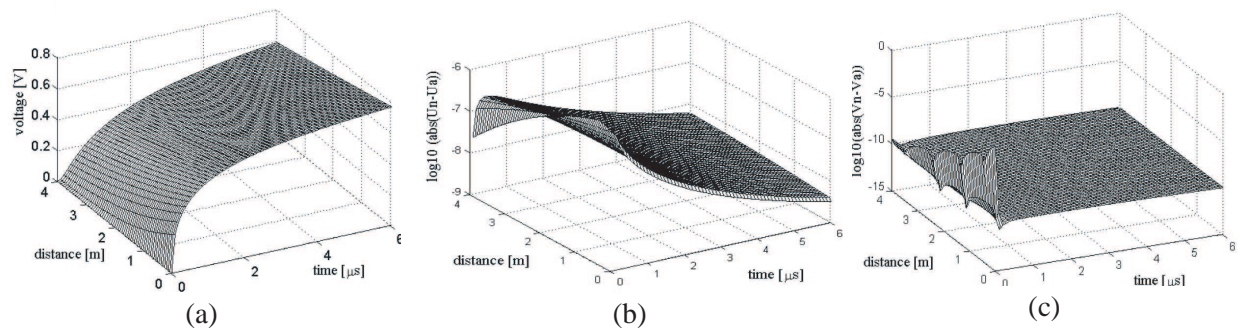


Figure 4: Voltage distribution (a) with FDTD error (b) and Laplace transform error (c).

### 5. PRACTICAL EXAMPLE

To illustrate the practical application of Laplace transform and FDTD method we consider a (3+1)-conductor uniform transmission line, see Fig. 5.



Figure 5: The (3+1)-conductor TL.

We suppose unsymmetrical loads which are represented by the terminating resistors  $R_{11} = 10 \Omega$ ,  $R_{12} = 1 \Omega$ ,  $R_{13} = 100 \Omega$  on the left side, and  $R_{21} = 10 \text{ k}\Omega$ ,  $R_{22} = 1 \Omega$ ,  $R_{23} = 10 \Omega$  on the right side. The MTL is of the length  $l = 1 \text{ m}$ , with per-unit-length matrices

$$\mathbf{R}_0 = \begin{bmatrix} 41.7 & 0 & 0 \\ 0 & 41.7 & 0 \\ 0 & 0 & 41.7 \end{bmatrix} \frac{\Omega}{m}, \quad \mathbf{L}_0 = \begin{bmatrix} 2.4 & 0.69 & 0.64 \\ 0.69 & 2.36 & 0.69 \\ 0.64 & 0.69 & 2.4 \end{bmatrix} \frac{\mu H}{m},$$

$$\mathbf{G}_0 = \begin{bmatrix} 0.6 & 0 & 0 \\ 0 & 0.6 & 0 \\ 0 & 0 & 0.6 \end{bmatrix} \frac{mS}{m}, \quad \mathbf{C}_0 = \begin{bmatrix} 21 & -12 & -4 \\ -12 & 26 & -12 \\ -4 & -12 & 21 \end{bmatrix} \frac{pF}{m}.$$

The input voltage source driving the central wire of the MTL has the waveform  $v_{12}(t) = \sin^2(\pi t/2 \cdot 10^{-9})$  if  $0 \leq t \leq 2 \cdot 10^{-9}$ , and  $v_{12}(t) = 0$  otherwise. The solution in  $(t, x)$ -domain was obtained using both FDTD method and LT method. All the results of numerical calculated voltage and current distributions are the same. Fig. 6 shows the voltage waves on the excited wire (b) and the voltage waves induced on the neighboring wires of the transmission line (a, c), only as an example.

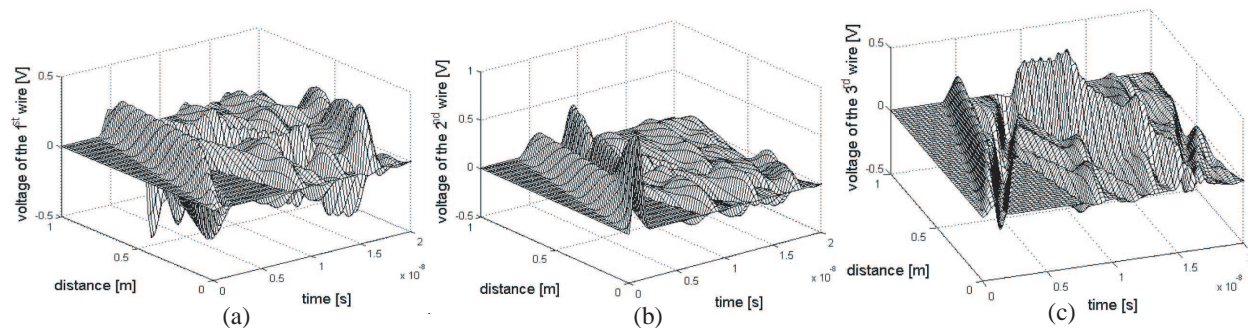


Figure 6: Voltage distributions along the MTL wires.

## 6. CONCLUSIONS

This paper presents two different approaches which can be used successfully for numerical solution of the voltage and current distributions along three-phase transmission line with earth wire. A new variant of the FDTD so-called leapfrog method is proposed and verified. The correctness of both used methods was verified and the obtained results indicate that both methods are very effective numerical tools for the simulation of time-spatial dependences. The accuracy of both methods is comparable, but the FDTD is more time-consuming than LT. On the other hand the FDTD can be used for the simulation of both linear and nonlinear systems.

## ACKNOWLEDGMENT

The research described in the paper was financially supported by the research programs MSM 0021630513 and MSM 0021630503.

## REFERENCES

1. Paul, C. R., *Analysis of Multiconductor Transmission Lines*, John Wiley & Sons, New York, 1994.
2. Brančík, L., "Transient analysis in multiconductor transmission line systems using numerical ILT," *Proceedings of International Conference Radioelektronika'98*, Vol. 2, 344–347, Brno, Czech Republic, April 1998.
3. Brančík, L., "Simulation of multiconductor transmission lines using two-dimensional Laplace transformation," *Proceedings of the 15<sup>th</sup> ECCTD'01*, Vol. 2, 133–136, Espoo, Finland, August 2001.
4. Benešová, Z. and V. Kotlan, "Propagation of surge waves on interconnected transmission lines induced by lightning stroke," *Acta Technica IEE CSAV*, Vol. 51, No. 3, 301–316, 2006.
5. Kotlan, V. and Z. Benešová, "Inductive coupling effect on induced voltage on three-phase transmission line in consequence of lightning stroke," *Proceedings of International Conference AMTEE'07*, V-7–V-8, Pilsen, Czech Republic, September 2007.
6. Sullivan, D. M., *Electromagnetic Simulation Using the FDTD Method*, IEEE Press, New York, 2000.
7. Brančík, L., "Improved numerical inversion of Laplace transforms applied to simulation of distributed circuits," *Proceedings of the XI International Symposium ISTET'01*, 51–54, Linz, Austria, August 2001.
8. Brančík, L. and J. Valsa, "A fast computing method of numerical inversion of two-dimensional Laplace transforms using FFT algorithms," *Proceedings of International Conference SSCC'98*, Vol. 2, 102–106, Durban, South Africa, September 1998.